2017

Effect of Minerals on Coke Analogue Carbon Bonding and Reactivity

Oluwatosin Adekunle Aladejebi
University of Wollongong

Effect of Minerals on Coke Analogue Carbon Bonding and Reactivity

A thesis submitted in fulfilment of the

requirements for the award of the degree

Doctor of Philosophy

from

University of Wollongong

by

Oluwatosin Adekunle Aladejebi, BEng. MEng.

Faculty of Engineering and Information Sciences

School of Mechanical, Materials, Mechatronic and Biomedical Engineering

November 2017

Certification

I, Oluwatosin Adekunle Aladejebi, declare that this thesis, submitted in partial fulfillment of the requirements for the award of Doctor of Philosophy, in the Faculty of Engineering and Information Sciences, University of Wollongong, is my own work unless otherwise referenced or acknowledged. This document has not been submitted for qualifications at any other academic institution.

OLUWATOSIN ADEKUNLE ALADEJEBI

06th November 2017

Abstract

Metallurgical coke is an essential reagent in the ironmaking blast furnace process. A better understanding of coke behaviour (graphitisation and reactivity) in the blast furnace is critical to improving its performance in the blast furnace. This study introduces and evaluates a new approach to study coke behaviour, through the use of a coke analogue. A coke analogue is a laboratory tool developed to minimise the uncertainty associated with the complexity and inherent heterogeneity of metallurgical coke. In this study, the principal aim was to establish how representative of metallurgical coke is the coke analogue and develop a fundamental understanding of the effects of elemental/metallic Fe on the carbon (sp^2–sp^3) bonding and reactivity of the coke analogue. The form of the Fe addition was examined by adding elemental iron (Fe) and magnetite (Fe_3O_4) to the coke analogue. The magnetite was reduced to metallic iron (Fe) during the production of the coke analogue.

How representative the coke analogue was of metallurgical coke was established by characterisation with respect to porosity, microstructure, carbon bonding (sp^2–sp^3) and reactivity testing in CO_2. From this characterisation, it was found that the coke analogue was in general representative of metallurgical coke. The characterisation and findings are summarised below.

- The porosity and pore size distribution of the coke analogue were evaluated using three different but complementary porosity measurements of optical microscopy, mercury porosimetry and neutron radiography (Dingo). The porosity and pore size distribution of the coke analogue were found to be well controlled and reproducible relative to metallurgical coke. The porosity of the coke analogues was highest in the 10–100μm range and broadly represents metallurgical coke in the range <200μm. The pores in the coke analogue are highly interconnected in three dimensions and typical of the interconnected pores in metallurgical coke.
- The microstructure of the coke analogues was characterised using optical and electro-optical microscopy. The coke analogue microstructure was uniform and well controlled. It was made up of carbon (graphite grains and carbonised phenolic resin), Fe/minerals and pores. The coke analogue graphite grains were

similar in character to that of the reactive maceral derived component (RMDC) in metallurgical coke. The carbonised phenolic resin was similar in character to that of the inert maceral derived component (IMDC) in metallurgical coke. To a large degree, the nature of the carbon component was a constant in the experimental program, that is, the rank of the coke analogue was fixed. The production of the coke analogue allowed control of the Fe or mineral component (non-carbon phases) of the coke analogue. The added Fe or mineral phase (particle size, composition and morphology) and dispersion throughout the coke analogue are well controlled. This resulted in a less complex, homogenous and well controlled mineralogy relative to metallurgical coke. The control of the Fe or mineral and carbon components was key in minimising the uncertainty in the experimental program.

- The sp^2 and sp^2–sp^3 carbon bonding of the coke analogue were evaluated using Raman spectroscopy. The carbon bonding of the coke analogue was found to be a combination of ordered sp^2 and disordered sp^2–sp^3 bonding types (0.16–1.55 for $I_{(D)}/I_{(G)}$ and 0–0.41 for $I_{(V)}/I_{(G)}$). These values, though broader than that of the metallurgical coke, cover the range of data for metallurgical coke measured in this study (1.16–1.45 for $I_{(D)}/I_{(G)}$ and 0.38–0.62 for $I_{(V)}/I_{(G)}$) and the metallurgical coke reported in the literature.
- The kinetic studies of the reaction of the coke analogues in CO_2 were evaluated using a large sample (~8g) thermogravimetric technique at temperatures between 900°C and 1350°C. It was found that the reactivity of the coke analogues was in general similar to that of the metallurgical coke, both in terms of trends with time and the effects of temperature. Further, the reactivity of the coke analogue is more controlled and reproducible relative to the metallurgical coke.
- Utilising the Walker Arrhenius approach, two temperature zones corresponding to different kinetic control regimes, chemical reaction controlled (zone I) and mixed controlled (zone II) were identified in the coke analogues. The zone I activation energy value obtained for the base coke analogue (273.6±0.5 $kJ.mol^{-1}$) was similar to the published results for metallurgical coke (222–266 $kJ.mol^{-1}$). The similar activation energy value indicates that the reaction mechanism of the coke analogue is typical of metallurgical coke.

The use of the analogue allowed evaluation and quantification of elemental/metallic Fe effects on carbon bonding and the reactivity of the coke analogue in CO_2 gas. With the addition of elemental Fe and Fe_3O_4 to the coke analogue it was found that,

- the Raman technique identified an increase in the graphitic nature (increases sp^2) of the carbon bonding as a result of the addition of Fe and Fe_3O_4 to the analogue. This effect was localised near to or at the Fe particle–carbon interface. The effect was discernible at a distance <5μm from the interface.
- elemental Fe and Fe added as magnetite (Fe_3O_4) increased the reactivity of the coke analogue in CO_2 relative to the base coke analogue. It was thought that elemental/metallic Fe increased the number of active carbon sites (C_f) in the coke analogue through carbon dissolution into Fe and the transfer of electrons from carbon into Fe. Further possible additional effects of Fe relate to the promotion of oxygen delivery to the active carbon sites (C_f) through the dissociation of CO_2 on Fe surface and redox reactions between Fe and CO_2 to form iron oxide and CO, followed by reduction of the iron oxide on reaction with carbon. The effects of Fe added as elemental Fe and Fe_3O_4 on the reactivity of the coke analogue was linearly proportional to the surface area of the Fe particles. There was a linear relationship between R_C and Fe particle surface area. The Fe initially added as Fe_3O_4 gave a higher reactivity of the coke analogue relative to elemental Fe at a constant concentration and similar total surface area of Fe. Elemental/metallic Fe did not change the rate controlling mechanism for the reaction of the coke analogue in CO_2. Hence, there was no change in the zone I activation energy value for the reaction of the coke analogue in CO_2.

After developing a fundamental understanding of the effects of Fe on carbon bonding and analogue reactivity in CO_2, the secondary aim of this study was evaluated. That is, the effects of quartz (SiO_2) and Fe bonded within a complex mineral (enstatite ferroan ($Mg_{1.56}Fe_{0.44}Si_2O_6$) and phlogopite ferroan [$K(Mg,Fe)_3(Al,Fe)Si_3O_{10}(OH,F)_2$]) on carbon bonding and reactivity of the coke analogue relative to the effects of elemental Fe were also evaluated. It was found that,

- quartz (SiO_2) had no significant effect on the sp^2 and sp^2–sp^3 bonding of the coke analogue. The addition of quartz (SiO_2) also decreased the reactivity of the coke analogue in CO_2 relative to the base coke analogue. The relative rate of reaction of the analogues were quartz < base < elemental Fe. It is not clear from the results obtained in this study why the addition of quartz lowered the analogue reactivity.
- Fe bonded within a complex mineral (enstatite ferroan ($Mg_{1.56}Fe_{0.44}Si_2O_6$) and phlogopite ferroan [$K(Mg,Fe)_3(Al,Fe)Si_3O_{10}(OH,F)_2$]) had no significant effect on the sp^2 and sp^2–sp^3 bonding of the coke analogue. The Fe containing minerals increased the reactivity of the coke analogue relative to the base coke analogue. In comparison with elemental Fe, their relative effects on coke analogue reactivity were base < enstatite ferroan < phlogopite ferroan < elemental Fe. The Fe containing mineral may have increased the analogue reactivity by promoting oxygen delivery to the active carbon sites (C_f).

The findings of this study have shown that the coke analogue is representative of a simplified metallurgical coke having porosity, carbon bonding, microstructure and reaction behaviour similar to metallurgical coke. Further, the effect of elemental/metallic Fe on carbon bonding and analogue reactivity was established. It has been interpreted that a coke analogue is a suitable tool for the study of metallurgical coke behaviour in the ironmaking blast furnace and by extension other coke related studies.

Table of contents

List of Tables

List of Figures

Nomenclature and Abbreviations

Symbol	Definition/meaning in the text
A	Surface area, m^2
Ai	Surface area of a single particle, m^2
$A_{T/100g}$	Total surface area per 100g of coke analogue carbonaceous, $m^2/100g$
BET	Brunauer-Emmett-Teller
C_f	Carbon active sites
C(O)	Chemisorbed oxygen on carbon (intermediate)
ΔC	Concentration change of gaseous reactants, $g.m^{-3}$
C_s	Carbon concentration at the surface
C_i	Initial carbon concentration
$\overline{C}$	Average carbon composition at time t,
CRI	Coke reactivity index and
CSR	Coke strength after reaction
d	Diameter of particles, μm
D	Diffusion coefficient
D	Equivalent pore diameter, μm
$d_{(002)}$	Interlayer spacing
Ea	Activation energy, $J.mol^{-1}$
FWC	Fractional weight change
FWHM	Full width at half maximum of the (002) carbon peak
ICDD	International centre for diffraction data
$I_{(D)}$	Intensity of the D band
$I_{(2D)}$	Intensity of the 2D band
$I_{(G)}$	Intensity of the G band
$I_{(V)}$	Intensity of the valley between D and G bands
IMDC	Inert maceral derived component
k	Reaction rate constant, $g.s^{-1}.m^{-2}$

k_0	Pre exponential factor, s^{-1}
L	Semi-thickness, cm
La	Crystallite width
Lc	Crystallite height
n	Order of the reaction
N	Total number of particles in coke analogue carbonaceous
m	Mass of particles, g
P_{OP}	Optical porosity of the coke analogue
P_1	Porosity value at the coke analogue centre, position '1'
P_a	Porosity value at the coke analogue annulus
Q	Reaction quotient
R	Gas constant, $J.K^{-1}.mol^{-1}$
R_C	Initial reaction rate, $g.g^{-1}.s^{-1}$
R_O	Mean reflectance
RMDC	Reactive maceral derived component
SEM	Scanning electron microscopy
t	Time, s
T	Temperature, K or °C
TEM	Transmission electron microscopy
TGA	Thermogravimetric analyzer
V	Volume% of the pore
V_i	Volume of a single particle, m^3
V_T	Total volume of particles in coke analogue carbonaceous, m^3
W	Weight of the sample at time t, g
X	Fractional carbon conversion
XRD	X-ray diffraction
λ	Radiation wavelength of the X-ray source
β	Full width at half maximum (FWHM) of the carbon peak
ρ	Density, $g.cm^{-3}$

θ	Bragg scattering angle of the diffraction peak
σW_0	Error of initial weight obtained from the TGA scale that has a quantifiable uncertainty associated with the balance and buoyancy effect
σdt	Error of the resolution of the reading
σX	Error of carbon conversion
σR_C	Error of initial reaction rate
(I)	Higher mass of addition

Acknowledgment

This project was carried out and completed with the support of unique individuals, and I would like to use this opportunity to show my appreciation.

I would like to express my sincere gratitude to my supervisor Professor Brian J. Monaghan for guidance, encouragement, intellectual support, brilliant ideas, thoughtful analyses and feedback throughout this study. During this work, I benefited from Brian's positive viewpoint and contributions. He contributed enormously to the thesis writing, especially in helping me articulate my scientific arguments. I am grateful for the financial support Brain provided during this study.

I express my special thanks to my co-supervisors, Prof Marc in het Panhuis and Dr. Mark H. Reid for their immense contribution to the success of this study. I acknowledge the support of Marc in the Raman spectroscopy. He provided financial support during this study. I acknowledge the support of Mark in the neutron radiography (Dingo) and optical porosity measurement. They both contributed enormously to the thesis writing, especially in helping me articulate my scientific arguments.

I am very grateful to Dr. Raymond J. Longbottom for his selfless help, time and guidance throughout this study. I acknowledge the support of Ray in the use of the MTDATA thermodynamic software and other facilities in the research laboratories. Ray contributed enormously to the thesis writing, especially in helping me articulate my scientific arguments.

I would like to highlight the contribution and assistance of the following individuals towards the success of this study,

- Dr. Harold Rogers assisted with the polarised optical microscopy and the SEM/EDS images from the ZEISS EVO 50 SEM instrument.
- Dr. David Wexler for XRD training.
- Associate Professor Peter Innis and Dr. Patricia Hayes for the use of their Raman equipment.

- Greg Tillman, Nick Mackie, Tony Romeo and other UOW technical staff for training in metallography and XRD.

- Dr. Ulf Garbe, Dr. Bevitt Joseph and Dr. Filomena Salvemini, Australian Nuclear Science and Technology Organisation (ANSTO), for training in image reconstruction of neutron radiography (Dingo) data.

I acknowledge the financial support of the Federal Government of Nigeria through the Federal University of Technology Akure during this study.

I acknowledge the financial support of the Australian Centre for Neutron Scattering, Australian Nuclear Science and Technology Organisation (ANSTO) for the grant value for the use of the neutron radiography (Dingo) during this study.

I offer my special thanks and appreciation to my adorable wife (Olawunmi Aladejebi) and my dearest siblings (Oluwaseun, Opeyemi, Olubunmi and Ifeoluwa) for their love, prayers, support, encouragement, patience and understanding. These were the fuel that kept me going during this study.

I am grateful for the financial support of the University of Wollongong through the International Postgraduate Tuition Awards (IPTA) and Matching Scholarship without which this study would not have been possible.

Finally, I express my sincere thankfulness to God Almighty for making this study a reality.

I dedicate this work to my loving Dad and Mum

1. Introduction

Metallurgical coke is a key material in the ironmaking blast furnaces. It is the furnace fuel for the high-temperature process and the primary source of carbon monoxide gas for the reduction of iron oxide to iron. Coke also provides the structural support to maintain the furnace permeability required for high production rates. The performance of coke in the ironmaking blast furnace is related to its hot strength and reactivity. A number of factors affect the reactivity of metallurgical coke in the blast furnace [1-10]. These include carbon forms, coke texture, pore size distribution, connectivity and morphology, the inherent reactivity of the minerals in the metallurgical coke, and the chemical and physical environment it is exposed to during the blast furnace operation.

Ideally, from an operational perspective, it would be desirable to predict the reactivity of metallurgical coke from these factors, but the current understanding of coke reactivity critically limits such predictions [3, 7, 11, 12]. This is because coke is a complex material that consists of different carbonaceous forms or textural components (originating from the parent coal macerals) and minerals, with a pore distribution and morphology dependent on the volatile matter in the parent coal (and coking conditions). In addition, it has significant heterogeneity in most metric(s) used to characterise its textural grouping, mineralogy, phase dispersion, morphology and porosity [3, 5, 7, 8, 11-21].

The mineral matter in coke is typically 8–12 mass%, which comes from the inorganic matter in the parent coal [2-4, 7, 8, 18, 21-25]. The mineralogy of coke is important as it is known to affect coke reactivity and graphitisation and slag formation in the blast furnace. A lack of understanding of the effects of mineralogy on metallurgical coke carbon when exposed to high temperatures and reactive atmospheres significantly limits coke reactivity predictions. In particular, a clear delineation of the effects of mineralogy on coke reactivity has proved difficult due to the potential non-additive effects of minerals on coke reactivity.

Some minerals and metals are known to promote the graphitisation (increase the sp^2 bonding) of carbonaceous materials [4, 7, 10, 26-41]. The process by which minerals and metals promote the graphitisation of carbonaceous materials is often referred to as catalytic graphitisation. The catalytic graphitisation of carbon by metals and minerals involves carbon dissolution and precipitation, or carbide formation and decomposition [26, 30, 31, 33, 35, 38-48]. With respect to metallurgical cokes, minerals and metallic iron promotes graphitisation [4, 7, 26, 45-49]. It is the metallic components in the minerals that promote graphitisation [4, 26, 46-48] and it is consistent with catalytic graphitisation of graphitisable and non-graphitisable carbons [26, 30, 32-44, 50-52].

The use of metallurgical coke to test the specific effects of minerals and metallic iron on carbon bonding and reactivity is problematic due to the inherent complexity of coke (carbonaceous forms, mineral components and pore structure), along with the heterogeneous nature of coke's constituents and structure [3, 5, 7, 8, 11-21]. This results in uncertainty and makes it difficult to isolate the effects of specific minerals on coke behaviour in experimental studies. This uncertainty can be minimised by using a coke analogue [11-13, 15, 16, 53-55]. The coke analogue is made from a number of carbonaceous materials, and minerals can be added to it for study. In the coke analogue, mineralogy as well as porosity can be controlled. In previous studies that used the coke analogue, the researchers were able to distinguish the specific effects of selected minerals and mineral combinations [12, 13, 16, 53] and coke ash [11] on the coke analogue's reactivity with carbon dioxide at high temperatures. Further, it has also been demonstrated that the reaction mechanism and kinetics of the coke analogue reactivity in carbon dioxide with temperature is similar to that of metallurgical coke [15, 54, 55].

As the coke analogue offers the possibility of being used to study some key aspects of metallurgical coke behaviour [11-13, 15, 16, 53-55], it is not clear whether the coke analogue has similar carbon bonding to that of metallurgical coke. A goal of this study is to answer this question, focusing on establishing whether the coke analogue is representative of the metallurgical coke. If so it can then be used as a control tool to evaluate the effects of metallic iron, iron as magnetite, iron bonded within an oxide and quartz on the carbon bonding and reaction kinetics of the coke analogue. The study of

the effects of metallic iron, iron containing minerals and quartz on coke analogue carbon bonding and reactivity are justifiable, because iron is often reported as metallic iron [7, 21, 24, 27, 56, 57], iron oxides [7, 11, 27, 56-59], iron bonded within an oxide [24, 27, 56, 57] and sulphides [7, 24, 27, 56, 57] in coke mineralogy. Quartz is also present in coke mineralogy [20, 22, 27, 56, 57, 59].

The primary aims of this study are,

1. To establish whether the coke analogue is representative of metallurgical coke.

2. To investigate the effect of Fe in its elemental form and Fe added as magnetite (Fe_3O_4) on the carbon bonding and reactivity of the coke analogue.

To further understand the effects of Fe on carbon bonding and coke reactivity secondary aims to deal with comparative effects of elemental Fe relative to

3. quartz (SiO_2) on the carbon bonding and reactivity of the coke analogue.

4. Fe bonded within a complex mineral (enstatite ferroan ($Mg_{1.56}Fe_{0.44}Si_2O_6$) and phlogopite ferroan [$K(Mg,Fe)_3(Al,Fe)Si_3O_{10}(OH,F)_2$]) on the carbon bonding and reactivity of the coke analogue.

To achieve the aims, the specific objectives of this study are,

a) To evaluate the microstructure* of the coke analogues using optical and electro-optical microscopy,

b) To evaluate the carbon bonding of the coke analogues using Raman spectroscopy,

c) To evaluate the porosity and pore size distribution of the coke analogues using three separate but complementary porosity measurements of optical microscopy combined with image analysis, mercury porosimetry and neutron radiography (Dingo), and

* In the metallurgical coke literature researchers often use the expression microtexture when dealing with coke microstructure. Generally, in this thesis, it is the microstructure that is being evaluated.

d) To establish the reaction kinetics of the coke analogues with carbon dioxide during a reactivity test using a large sample thermogravimetric analyser (TGA).

The research outcomes will be used to provide information to better understand the effects of Fe and minerals on the carbon bonding and reactivity of the metallurgical coke.

2. Literature review

2.1. The ironmaking blast furnace

The ironmaking blast furnace (see schematic given in Figure 2-1) is a high temperature chemical reactor. The main product of the blast furnace is molten iron and the by-products are molten slag and gas. Molten iron production involves charging raw materials (iron oxide, coke and fluxes) into the furnace from the top and blowing preheated air and injectants, usually pulverised coal or natural gas, into the furnace through tuyeres located at the bottom of the furnace. The iron oxides, generally haematite (Fe_2O_3) or magnetite (Fe_3O_4), may be charged as sinter, pellets, ore or a combination of these materials. The primary source of the blast furnace fuel is metallurgical coke. In addition, coke is key in controlling the permeability of the blast furnace and also performs a chemical role in the production of CO gas to reduce the iron oxides. The blast furnace fluxes (limestone and magnesia) are added directly to the furnace or included in blast furnace sinter or pellets [1, 2, 8, 9, 44, 60-62].

The temperature profile of a blast furnace, from the top of the furnace to the bottom of the furnace, and the type of chemical reactions that occur within three temperature zones of a typical blast furnace [1] are given in Figure 2-1. The three zones are the direct reduction, thermal reserve and preheat zones.

The chemistry of the blast furnace involves the reaction of hot air, blown (blast) through the tuyeres, with metallurgical coke to form carbon monoxide. The reaction is sequential, initially forming carbon dioxide (reaction 2-1) then carbon monoxide (reaction 2-2).

$$C_{(s)} + O_{2(s)} \rightarrow CO_{2(g)} \qquad \Delta G^\circ = -394100 - 0.84T \ J.mol^{-1} \ [63] \qquad 2\text{-}1$$

$$CO_{2(g)} + C_{(s)} \rightarrow 2CO_{(g)} \qquad \Delta G^\circ = 165300 - 170.76T \ J.mol^{-1} \ [63, 64] \qquad 2\text{-}2$$

Reaction 2-2 is known as the Boudouard reaction, coke gasification reaction or the solution loss reaction [1, 6, 9, 44, 63].

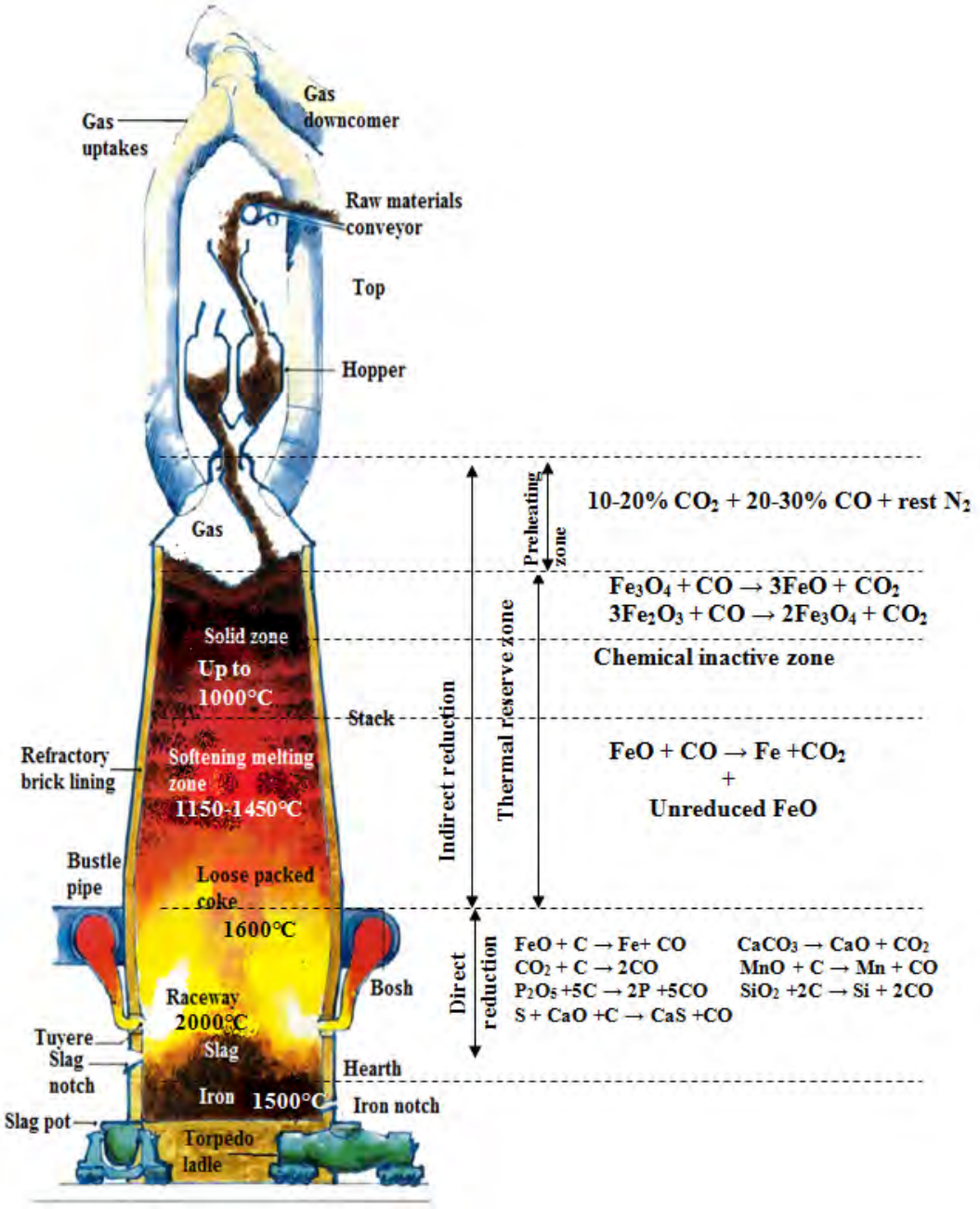

Figure 2-1: A schematic of a blast furnace, showing the distribution of gases and solids along its height and the chemical reactions occurring in the three temperature zones [1, 60].

In the indirect reduction zone given in Figure 2-1, iron oxides react with carbon monoxide to produce iron and carbon dioxide, the reactions can be represented by equations 2-3 to 2-5,

$$3Fe_2O_{3(s)} + CO_{(g)} \rightarrow 2Fe_3O_{4(s)} + CO_{2(g)} \quad \Delta G^\circ = -30260 - 51.54T \text{ J.mol}^{-1} \text{ [63, 64]} \quad 2\text{-}3$$

$$Fe_3O_{4(s)} + CO_{(g)} \rightarrow 3FeO_{(s)} + CO_{2(g)} \quad \Delta G^\circ = 32560 - 40.14T \text{ J.mol}^{-1} \text{ [63, 64]} \quad 2\text{-}4$$

$$FeO_{(s)} + CO_{(g)} \rightarrow Fe_{(s)} + CO_{2(g)} \quad \Delta G^\circ = -20100 + 22.41T \text{ J.mol}^{-1} \text{ [63, 64]} \quad 2\text{-}5$$

In the direct reduction zone given in Figure 2-1, iron oxide reacts with carbon to produce iron and carbon monoxide, reactions 2-6 and 2-7.

$$FeO_{(l)} + C_{(s)} \rightarrow Fe_{(s)} + CO_{(g)} \quad \Delta G^\circ = 118300 - 131.11T \text{ J.mol}^{-1} \text{ [63, 64]} \quad 2\text{-}6$$

$$FeO_{(l)} + C_{(s)} \rightarrow Fe_{(l)} + CO_{(g)} \quad \Delta G^\circ = 132107.2 - 138.72T \text{ J.mol}^{-1} \text{ [64, 65]} \quad 2\text{-}7$$

2.2. Metallurgical coke

Metallurgical coke can be described as a complex composite material comprising of different carbonaceous forms, minerals and a pore structure. Coke is made by heating coals, preferably of low inorganic minerals, in a coke oven to approximately 1000–1200°C in the absence of air. During the coke making process, coke microstructure and microtexture, and mineralogy are developed. The process also involves the release of volatile matter containing methane, carbon dioxide, carbon monoxide, hydrogen sulphides and hydrogen [2, 4, 7, 66-68].

The properties of metallurgical coke are progressively changed as the coke descends towards the lower part of the blast furnace. Coke performance is affected by its composition and blast furnace operational conditions. It reacts with furnace gases, alkalis, inherent minerals and slag phases [6, 7, 10, 21, 24, 69, 70]. An example of the expected properties and composition of typical metallurgical cokes used in the ironmaking blast furnace is given in Table 2-1 [6, 8, 71-75].

Table 2-1: An example of the expected properties and composition of metallurgical cokes used in the ironmaking blast furnace [6, 8, 21, 71-75].

Properties and composition of typical metallurgical coke	
Mean size distribution	45–70 mm
ASTM stability	60–64
Coke Strength after Reaction (CSR)	50–74
Coke Reactivity Index (CRI)	18–30
Moisture	1–6 wt.(%)
Volatile matter*	<1 wt.(%)
Ash*	8–12 wt.(%)
Sulphur*	0.5–0.9 wt.(%)
Phosphorus*	0.02–0.06 wt.(%)
Alkalis*	<0.3 wt.(%)

*dry-based

2.2.1. Metallurgical coke mineralogy

Metallurgical coke contains approximately 8–12 mass% inorganic minerals [2, 4, 7, 8, 10, 18, 21-25, 76, 77]. The minerals in metallurgical cokes are formed from the progenitor minerals from the parent coal. They are formed when minerals in coal undergo chemical, physical/chemical and structural transformations during coke making [3, 20, 25, 78-80]. Iron, iron containing minerals and quartz are some of the minerals reported in cokes [3, 7, 11, 20, 22, 24, 25, 27, 56-59, 66-68, 70, 80].

The common techniques used in the characterisation of minerals in metallurgical cokes are X-ray diffraction (XRD) and scanning electron microscopy (SEM) [4, 7, 25, 56, 57, 59, 68, 70, 81-85]. A detailed list of minerals and their compositions identified in some metallurgical cokes [3, 7, 25, 27, 56, 57, 67, 68, 80, 81, 83] is given in Table 2-2.

Table 2-2: A list of selected minerals and their composition identified in metallurgical cokes by different authors [3, 7, 25, 27, 56, 57, 67, 68, 80, 81, 83]

Minerals	**Composition**	**Minerals**	**Composition**
Akermanite	$Ca_2Mg_2Si_2O_7$	Iron	Fe
Albeit	$NaAlSi_3O_8$	Iron phosphate	$FePO_4$
Alumina	Al_2O_3	Iron silicon	Fe_3Si
Anatase	TiO_2	Jarosite Hydronian	$(K,H_3O)Fe_3(SO_4)_2(OH)_6$
Bassanite	$CaSO_4.\ 0.5H_2O$	Leucite	$KAlSi_2O_6$
Brookite	TiO_2	Magnetite	Fe_3O_4
Calcite	$CaCO_3$	Mullite	$Al_6Si_2O_{13}$
Coquimbite	$Fe_2(SO_4)_3.9H_2O$	Oldhamite	CaS
Cristobalite	SiO_2	Pyrrhotite	$Fe_{1-x}S$
Diopside	$CaMgSi_2O_6$	Quartz	SiO_2
Fayalite	Fe_2SiO_4	Rutile	TiO_2
Fluorapatite	$Ca_5(PO_4)_3F$	Spinel	$MgAl_2O_4$
Gehlenite	$Ca_2Al_2SiO_7$	Troilite	FeS
Hematite	Fe_2O_3	Wustite	FeO
Hercynite	$FeAl_2O_4$		

Gupta, et al. [7] and Rodrigues, et al. [68] used XRD to determine the nature mineral phases in metallurgical coke. The same authors [7, 68] used the SEM to assess the morphology, dispersion, and chemical composition of minerals in metallurgical coke. An example of the SEM images showing heterogeneity of mineral sizes and distributions in metallurgical cokes is given in Figure 2-2 [7, 83].

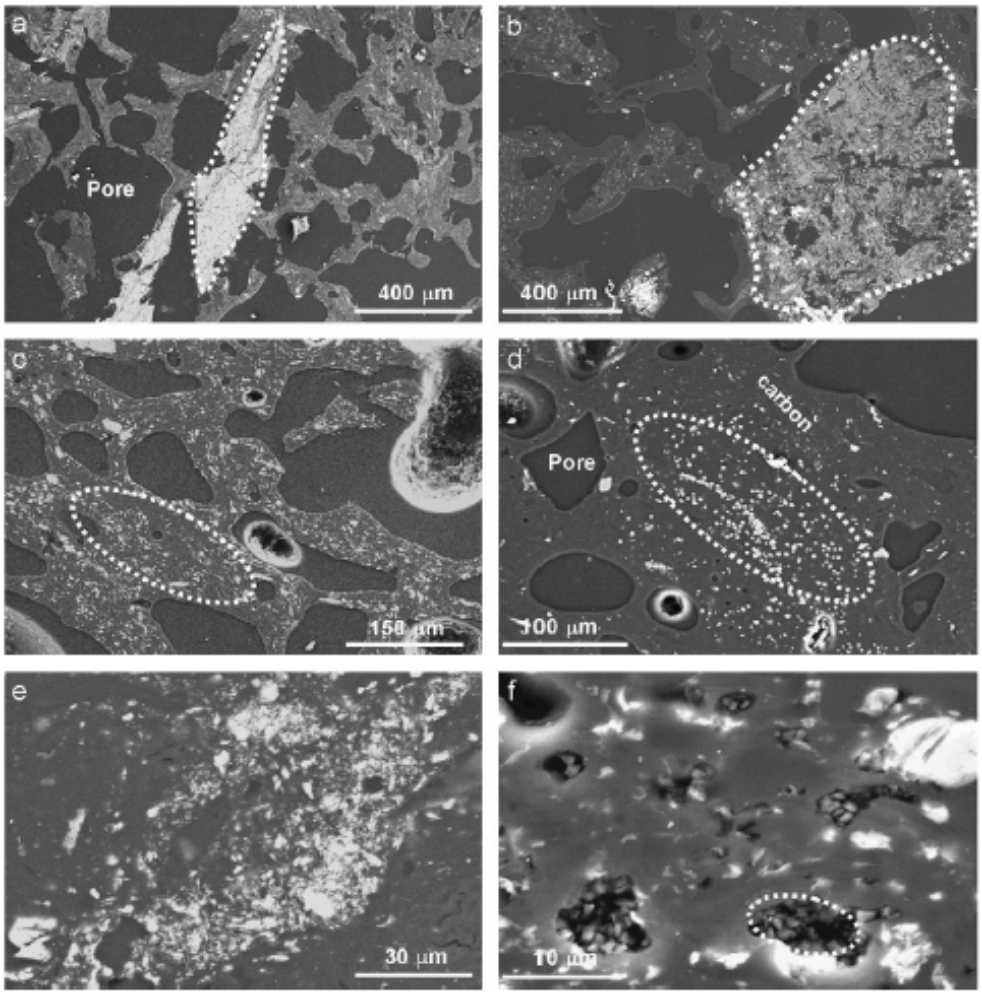

Figure 2-2: An example of the SEM images showing heterogeneity of mineral sizes and distributions in metallurgical cokes [7, 83].

During coke making, minerals in coal can undergo chemical and structural transformation and can react with other minerals or carbon to form new mineral species or phases in metallurgical coke [25, 26, 46, 68, 78-80, 86-91]. The chemical transformation may include mineral phase decomposition, the formation of carbides, and formation of new crystalline and glass phases. The structural transformation may include expansion (or swelling) of aluminosilicate and temperature-related polymorphs of quartz [20, 68, 78, 79, 87-89, 92-95]. For example, Rodrigues et al. [68] carbonised coal at 1000°C to form metallurgical coke, then heat treated the samples under the flow of argon to temperatures of 1500°C, 2000°C and 2500°C. The minerals identified in their study were characterised using both SEM and XRD techniques and given in Figure 2-3.

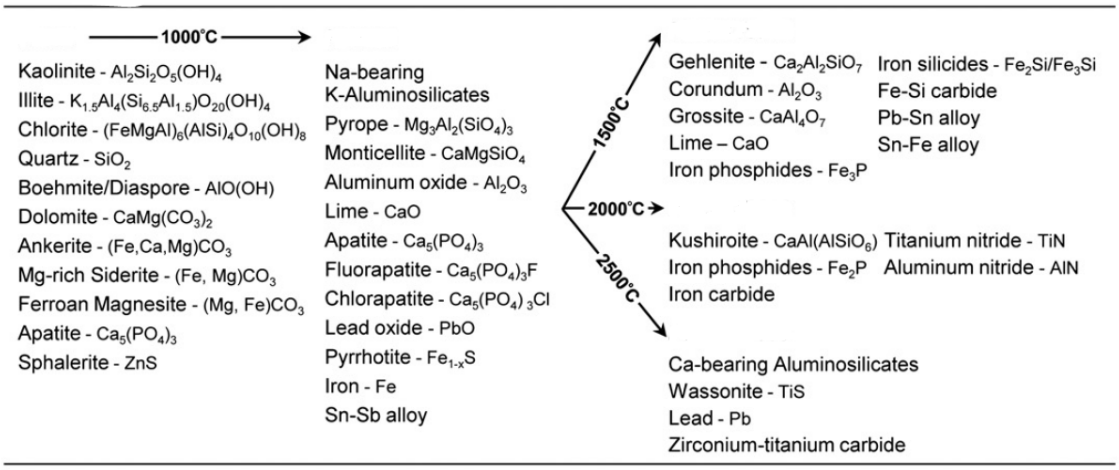

Figure 2-3: Minerals identified in a coke and its heat treated sample [68].

During coke reactivity testing in CO_2, some minerals and metals transform from one form to the other and also react with one another and with carbon dioxide to form new mineral phase(s) or specie(s) [25, 27, 81, 96-98]. For example, Grigore et al. [81] studied mineral transformation during coke reactivity testing in CO_2. They found that some mineral phases present in the unreacted metallurgical cokes were either absent or lower in the reacted samples, and some mineral phase(s) absent in the unreacted metallurgical cokes were found in the reacted samples. A typical example of minerals found in unreacted and reacted metallurgical cokes is given in Table 2-3.

Table 2-3: The list of minerals and composition identified in unreacted and reacted (15% and 75% carbon conversion) metallurgical cokes by weight% [81].

Mineral phase	Chemical formula	Coke B			Coke C			Coke F		
		Raw	15%	75%	Raw	15%	75%	Raw	15%	75%
Anorthite	$(Ca,Na)(Si,Al)_4O_8$		0.02	0.11		0.04	0.17		0.06	0.24
Akermanite	$Ca_2MgSi_2O_7$		0.01	0.07	0.04	0.05		0.03	0.08	0.09
Diopside	$CaMgSi_2O_6$				0.04			0.03		
Diopside–jadeite	$(Ca,Na)(Mg,Fe^{+2},Fe^{+3},Al)Si_2O_6$			0.04		0.07	0.10			
Rankinite	$Ca_3Si_2O_7$									0.14
Calcium ferrite	$Ca_4Fe_9O_{17}$					0.04	0.06		0.08	0.06
Fluorapatite	$Ca_5(PO_4)_3F$	0.21	0.09	0.06	0.44	0.32	0.17	0.36	0.21	0.08
Calcite	$CaCO_3$		0.05			0.09			0.03	0.02
Oldhamite	CaS	0.02	0.01	0.01	0.05	0.04		0.14	0.06	0.02
Iron	Fe	0.03	0.01		0.06	0.02		0.16	0.01	
Pyrrhotite	$Fe_{1-x}S$	0.03	0.01		0.12	0.03		0.48	0.02	
Hematite	Fe_2O_3		0.02	0.03	0.05					0.03
Magnetite	Fe_3O_4		0.03	0.05		0.16	0.17		0.38	0.17
Magnesioferrite	$MgFe_3O_4$		0.05	0.01		0.12	0.07		0.08	0.04
Wüstite	FeO	0.04		0.01						
Hercynite	$FeAl_2O_4$					0.11	0.51		0.09	0.61
Iron phosphate	$FePO_4$	0.01	0.02		0.04	0.02	0.06	0.03	0.01	
Fayalite	$(Fe,Mg)_2SiO_4$					0.06	0.07		0.06	0.14
Leucite	$KAlSi_2O_6$	0.03	0.03	0.02	0.04	0.01	0.05		0.02	0.03
Mullite	$Al_6Si_2O_{13}$	1.1	0.99	1.6	1.6	1.5	2.2	0.58	0.42	0.96
Spinel	$MgAl_2O_4$				0.16	0.02	0.04	0.06	0.06	0.42
Aluminium oxide	Al_2O_3	0.02								
Cristobalite	SiO_2	0.01	0.01	0.07	0.01	0.01	0.24		0.01	0.09
Quartz	SiO_2	2.4	2.7	2.3	1.8	2.1	1.8	3.4	3.5	2.8
Tridymite	SiO_2			0.05			0.04			
Anatase	TiO_2	0.02	0.02	0.01	0.02			0.02	0.02	
Brookite	TiO_2				0.06					
Rutile	TiO_2	0.03	0.09	0.08	0.01	0.06	0.08	0.03	0.07	0.03
Amorphous		5.0	4.7	4.4	7.6	7.3	6.2	4.5	4.5	3.9

The stability of mineral phases in metallurgical cokes with temperatures can be predicted using multiphase equilibria thermodynamic software packages. An example of the multiphase equilibria thermodynamic software packages are MTDATA [99] and FactSage [100]. The phase equilibria calculation is based on Gibb's free energy minimisation to predict the equilibrium phase stability.

2.2.2. Carbonaceous forms in metallurgical coke

The carbonaceous forms in metallurgical coke are formed from the progenitor macerals in the parent coal. Its structural and textural properties depend on the rank of the parent coal [5, 60, 101-103]. In general, the carbonaceous forms in metallurgical coke are classified as inert maceral derived component (IMDC) and reactive maceral derived component (RMDC) [3, 5, 25, 60, 98, 101-113]. There are many techniques used in the characterisation of carbonaceous materials in metallurgical cokes. Optical microscopy, Raman spectroscopy, transmission electron microscopy (TEM), SEM and XRD are among the most common [3, 4, 10, 17, 18, 44, 62, 70, 82, 101, 105, 108, 110, 114-121].

The IMDC of coke is mainly isotropic, has less obvious or little grain structure, shows no variation in reflectance and colour, and the structure is poorly ordered. The RMDC of coke is mainly anisotropic, has a grain structure, shows variation in reflectance and colour and the structure is well ordered [3, 10, 17, 18, 44, 62, 101, 105, 108, 110, 114-120]. The anisotropic character is generally classified according to their form and grain size of their mosaic texture (Figure 2-4) [101].

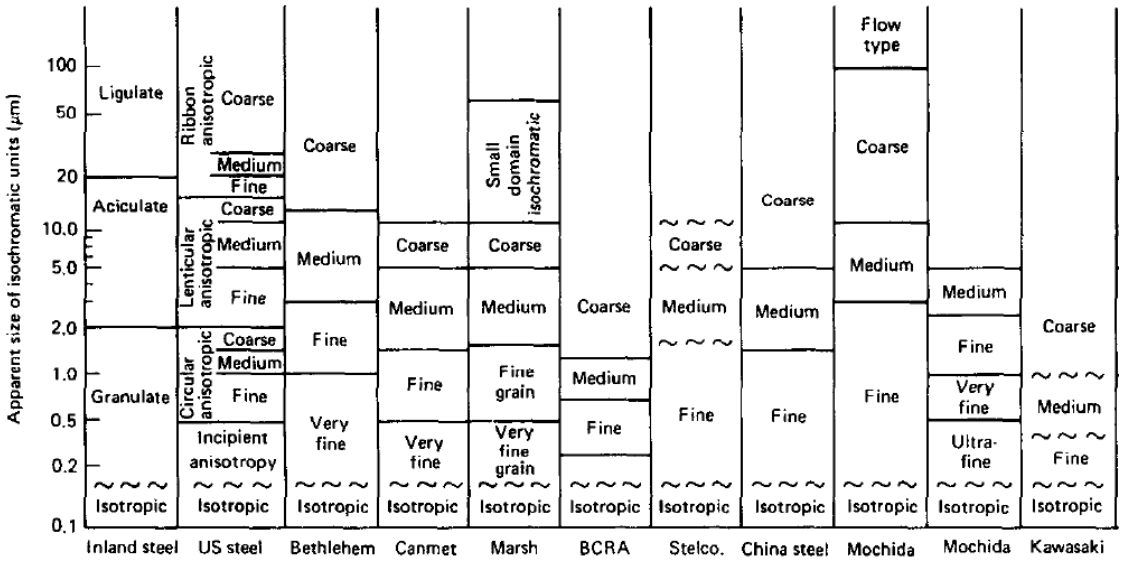

Figure 2-4: An example of the classification and comparison of the anisotropic character in cokes by different users [101].

Raman spectroscopy has been used to study the structural order (ordered sp^2 and disordered sp^2–sp^3 bonding) in metallurgical cokes [17, 18, 26, 62, 114-117, 122]. An example of typical Raman spectra of metallurgical cokes is given in Figure 2-5. The G band is associated with the perfect sp^2 bonding (that is, no form of structural defect) of pristine graphite [123]. The D and 2D bands are associated with the sp^2 bonding consisting of structural defects (that is, reduction in crystallite size or when graphene planes are bent) [18, 62, 116, 123-126]. The V band is associated with the less ordered carbonaceous materials (that is, sp^3 like defect in sp^2 bonding) [18, 127-131].

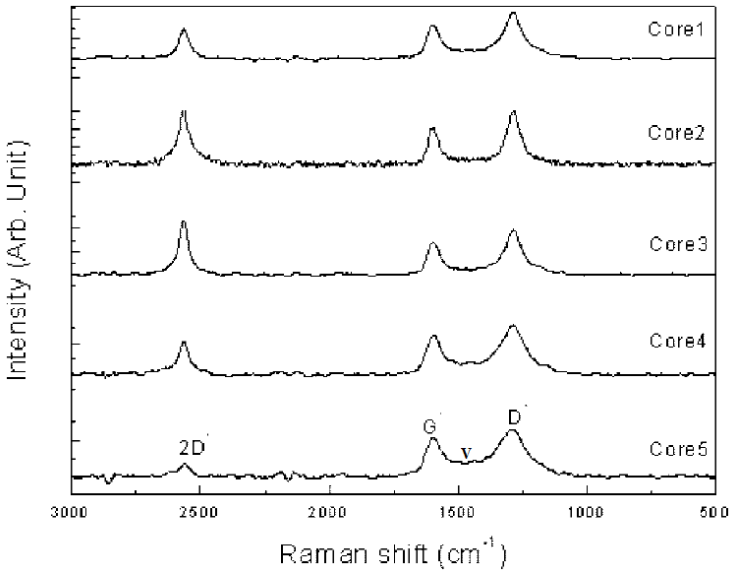

Figure 2-5: An example of Raman spectra of metallurgical coke samples [116].

The ratios of the Raman bands (equations 2-8 to 2-10) are used to indicate the type of carbon bonding present in charcoal, coal, coke and graphite [17, 18, 26, 62, 114-117, 123, 125, 126, 129, 131-138]. The commonly used ratios are,

$$\text{ratio of the D band to the G band} = \frac{I_{(D)}}{I_{(G)}} \qquad 2\text{-}8$$

$$\text{ratio of the V band to the G band} = \frac{I_{(V)}}{I_{(G)}} \qquad 2\text{-}9$$

$$\text{ratio of the 2D band to the G band} = \frac{I_{(2D)}}{I_{(G)}} \qquad 2\text{-}10$$

The $I_{(D)}/I_{(G)}$ and $I_{(2D)}/I_{(G)}$ are used to indicate the degree of structural defects in sp^2 bonding in graphite, while the $I_{(V)}/I_{(G)}$ is used to indicate the degree of disordered sp^2–sp^3 bonding in coal and cokes [18, 115, 123, 133]. An example of data calculated from the Raman spectra of coal, coke or graphite using the ratios of the Raman bands is given in Table 2-4.

Table 2-4: An example of data calculated from the Raman spectra of different carbonaceous materials using the ratios of the Raman bands.

Materials	Ratios of Raman Bands			Band positions (cm^{-1})				Reference
	$I_{(D)}/I_{(G)}$	$I_{(V)}/I_{(G)}$	$I_{(2D)}/I_{(G)}$	G	D	V	2D	
Metallurgical coke	1.26–1.40	0.10–0.55	0.10–1.68	1596–1598	1287–1295	1460–1470	2564–2566	[115, 116]
Metallurgical coke	0.10–1.70	0–0.60	#	1580–1600	1330–1360	1480–1500	#	[17, 18]
Metallurgical coke	0.82–1.1 9	0.20–0.68	#	1573–1595	1340–1355	1470–1520	#	[117]
Metallurgical coke	0.67–1.59	0–0.10	0.46–3.50	1578–1588	1353–1361	1470–1500	2702–2741	[26]
Metallurgical coke	0.78–1.06	0.25–0.40	#	1580	1350	1460	#	[62]
Metallurgical coke	0.40–0.50	0.20–0.30	#	1610–1612	1367–1385	1470–1520	#	[114]
Metallurgical coke	0.90–1.30	0.10–0.45	#	1595–1605	1345–1355	1490–1500	#	[122]
Coal	0.27–0.72	0–0.25	#	1599–1609	1325–1365	1480–1520	#	[135]
Coal	0.82–1.75	0.25–0.60	#	1590–1598	1350–1378	1480–1500	#	[134]
Charcoal	1.00–1.10	0.55–0.57	#	1580	1360	1470	#	[133]
Activated charcoal	0.96	0.45	#	1575	1355	1465	#	[123]
Graphite	0	0	0.48	1580	*	*	2670	[132]
Single crystal of graphite	0	0	#	1575	*	*	#	[123]

not reported * no peak

XRD has been used to study structural order in cokes [18, 25, 62, 70, 116, 119, 122, 139-141]. A typical XRD profile of coke materials illustrating the carbon peaks ((002), (100) and (110)) is given in Figure 2-6. The (002) peak is the average stacking height of the aromatic planes of carbon crystallite, while (100) peak at approximately 44° (2θ) and (110) peak at approximately 81° (2θ) are ascribed to the hexagonal ring structure [18, 25, 62, 116, 119, 122, 141].

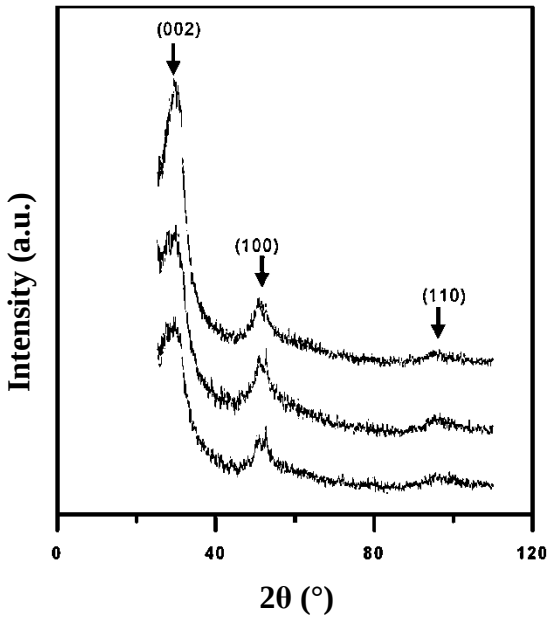

Figure 2-6: A typical XRD profile of coke materials illustrating the carbon peaks ((002), (100) and (110)). The XRD was carried out with cobalt Kα radiation (wavelength λ = 1.789Å) [62].

XRD analysis can be used to calculate structural parameters such as the crystallite height (L_c), crystallite width (L_a) and interlayer spacing (d_{002}) [18, 25, 84, 111, 116, 119, 139, 140, 142]. An example of typical L_c, L_a and d_{002} data for metallurgical cokes are given in Table 2-5.

Table 2-5: An example of typical L_c, L_a and d_{002} data for metallurgical cokes.

L_c(Å)	**L_a**(Å)	**d_{002}**(Å)	**Reference**
46.6–92.7	90.9–132.6	3.44–3.50	[116]
18.1–46.1	#	#	[141]
10.0–150.0	18.0–40.0	3.41–3.48	[18]
12.0–26.0	#	3.45–3.56	[62]
18.0–17.0	#	3.43–3.52	[122]
16.1–16.6	33.3–37.4	#	[25]
30.0–115.0	#	#	[119]
20.0–40.0	#	#	[70]
13.9–17.2	35.3–39.6	#	[111]

not reported

In general, the L_c measurement is used for assessing the structural order in metallurgical coke. An increase in L_c indicates increase in the structural order [18, 70, 116, 119, 139, 142]. L_c can be calculated using the Scherrer's equation [143], given as,

$$L_C = \frac{K\lambda}{\beta \cos\theta} \qquad 2\text{-}11$$

where K is the shape factor of 0.89 radians, λ is the radiation wavelength of the X-ray source, β is the full width at half maximum (FWHM) of the carbon peak and θ is the Bragg scattering angle of the diffraction peak.

It is generally argued that the carbon bonding of metallurgical coke can be modified by a number of factors. These factors are,

1. physical distortion [44, 130, 144],
2. annealing [18, 43, 44, 70, 115, 119, 145] and
3. catalytic graphitisation [4, 25, 26],

Alkali metals (potassium and sodium) can also interact with coke by diffusing into coke micropores or by intercalating with coke carbon without affecting the coke carbon bonding significantly [70, 82, 146, 147].

Physical distortion

Physical distortion in carbon bonding is in the form of twisting, sliding or bending of graphene layers so that they are not aligned with one another. Physical distortion can lead to increase in the degree at which bonding is disordered, that is, increase in the amounts of sp^3 bonding [44, 130, 144].

The layers of hexagonal arrangements of the carbon atoms in graphite can be described as graphene layers. These layers do not lie immediately above and below each other but are displaced to form an ABABAB sequence (Figure 2-7) [44, 121].

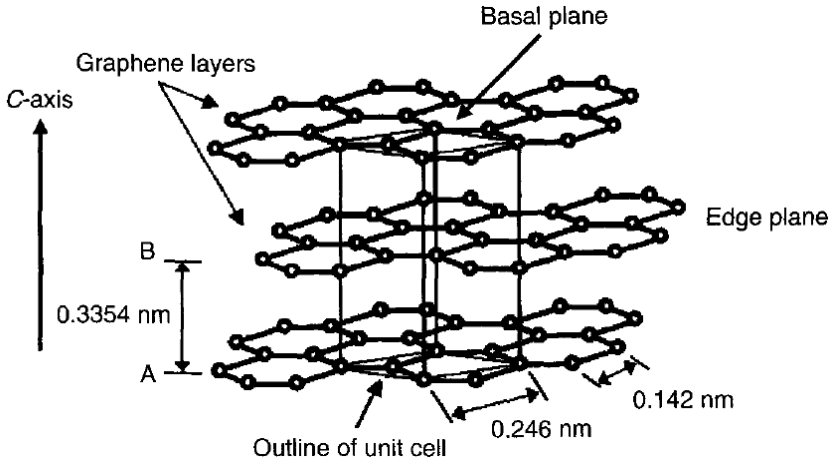

Figure 2-7: The structure of hexagonal graphite [121].

The graphene layers are held loosely together by van der Waals forces [44, 121]. The energy needed to slide the graphene layers over one another is low. With respect to metallurgical coke, Gornostayev et al. [89] suggests that changes in the volume of quartz (SiO_2) as a result of phase transformation to tridymite (SiO_2) during coke making can lead to the formation of cavities and cracks near the silica particle–coke interface (Figure 2-8). The resulting effect of change in the volume of silica (SiO_2) on coke carbon bonding was not evaluated in their study [89].

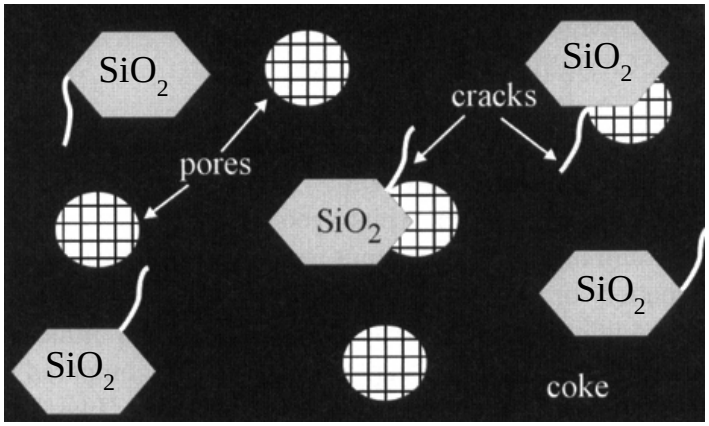

Figure 2-8: Influence of silica (SiO_2) particles on the formation of cavities and cracks related to volume increase during coking [89].

The effect of silica on carbon bonding was evaluated by Grobert et al. [144]. They studied a carbon–silica system heat treated at approximately 1200°C. On cooling the interface between the carbon–silica system was assessed using transition electron

microscopy. A significant sliding of the graphene layers was observed at the carbon–silica interface [144] indicating an increase in sp^3 bonding at the interface [130].

Annealing

Metallurgical coke is graphitised during heat treatment, that is, becomes more sp^2 in character [18, 43, 44, 70, 115, 119, 145]. The graphitisation represents an increase in structural order brought about by the movement of carbon atoms across surfaces and edges of graphene layers to sites of reduced energy and maximum stability [18, 35, 40, 43, 44, 145].

Kawakami et al. [18] used Raman spectroscopy to study the overall structural ordering in metallurgical coke with temperatures. In their study, they observed increasing ordering from a disordered sp^2–sp^3 bonding to ordered sp^2 bonding with increasing temperature. The observation was expressed using the $I_{(D)}/I_{(G)}$ versus $I_{(V)}/I_{(G)}$ plot and given in Figure 2-9 [18]. From Figure 2-9, decrease in $I_{(D)}/I_{(G)}$ values indicate a decrease in the amount of structural defects in the ordered sp^2 bonding, while a decrease in $I_{(V)}/I_{(G)}$ values indicate a decrease in the amount of sp^3 bonding or an increase in the amount of sp^2 bonding in a disordered sp^2–sp^3 bonding of the metallurgical cokes [18, 115, 116, 123-130, 138]. The degree of graphitisation depends on temperature and time allowed to anneal the carbon structure [43, 44, 121, 148]. This is consistent with what is known about metallurgical coke using XRD Lc measurement [18, 70, 116, 119, 139, 142]. A typical example of metallurgical coke XRD Lc measurement with temperature is given in Figure 2-10. The steps involved in structural ordering from a disordered sp^2–sp^3 bonding to an ordered sp^2 bonding are given in Figure 2-11 [43, 145].

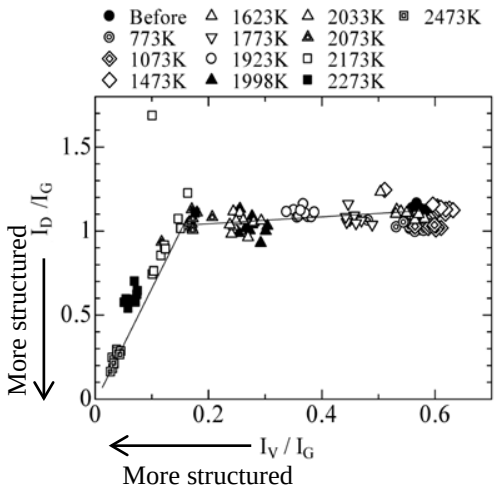

Figure 2-9: A plot of $I_{(D)}/I_{(G)}$ versus $I_{(V)}/I_{(G)}$ showing structural ordering in metallurgical coke with temperature [18].

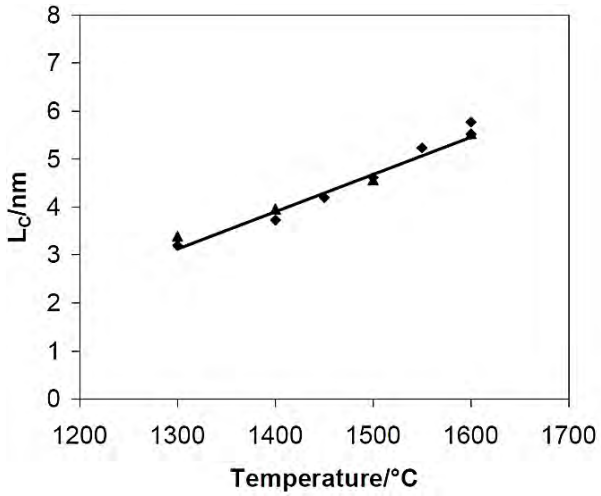

Figure 2-10: A plot of XRD Lc measurement of metallurgical coke with temperature [119].

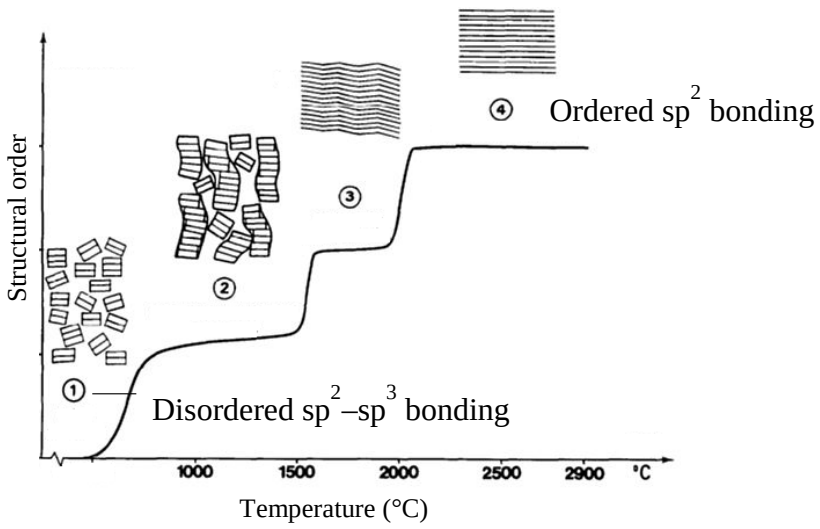

Figure 2-11: The schematics of steps involved in structural ordering from a disordered sp^2–sp^3 bonding to an ordered sp^2 bonding with temperature [43, 145].

Catalytic graphitisation

It is well known that some minerals and metals promote graphitisation (increase sp^2 bonding) of metallurgical coke. The process is referred to as catalytic graphitisation. It is generally argued that catalytic graphitisation occur through either dissolution and precipitation (Reaction 2-12), or carbide formation and decomposition (Reaction 2-13) steps [4, 7, 25, 26, 30, 32, 33, 38, 40, 41, 43, 45-49, 52, 149-152].

$$\text{Minerals or metals} + \text{Carbon} \xrightarrow{\text{Heating}} \text{Carbon in solution} \xrightarrow{\text{Cooling}} \text{Metal} + \text{Graphitised carbon} \quad 2\text{-}12$$

$$\text{Minerals or metals} + \text{Carbon} \xrightarrow{\text{Heating}} \text{Carbide formation} \xrightarrow{\text{Cooling}} \text{Metal} + \text{Graphitised carbon} \quad 2\text{-}13$$

With respect to metallurgical coke, Wang et al. [26] studied the effect of iron on coke graphitisation using Raman spectroscopy. In their study, iron was added to a metallurgical coke sample and the mixture was heat treated at 1600°C for 1 hour. On cooling, they reported the formation of graphitised carbon (increased in sp^2 bonding) around the iron particle with the graphitisation effect decreasing with increasing distance from the iron particle [26]. This is consistent with what is known of minerals that graphitise metallurgical coke [4, 25].

Elements such as Al, Ca, Fe, K, Mg, Mn, O, P, S, Si and Ti are often reported in the mineral matter found in coke, with metallic iron also found in coke ash [3, 7, 25, 27, 56, 57, 67, 68, 80]. The dissolution of carbon into metals is a function of temperature [63, 153, 154] and is well established by Fick's Second Law for non-steady state diffusion. The kinetics can be represented by equation 2-14 [155, 156],

$$\frac{\overline{C} - C_s}{C_i - C_s} = \frac{8}{\pi^2} \exp\left[\frac{-\pi^2}{4} \cdot \frac{Dt}{L^2}\right] \quad 2\text{-}14$$

where C_s is the carbon concentration at the surface, C_i is the initial carbon concentration, $\overline{C}$ is the average carbon composition at time t, D is the diffusion coefficient and L is the semi-thickness.

The range of diffusion coefficients of interstitial and substitutional elements in iron is given in Figure 2-12.

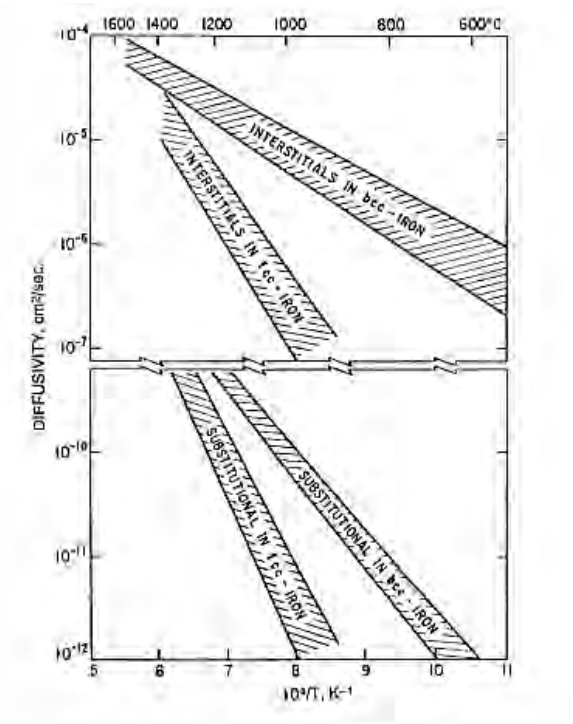

Figure 2-12: The range of diffusion coefficients of interstitial and substitutional elements in iron [63].

Intercalation

Intercalation in coke occurs when alkali (mostly potassium and sodium) present in coke minerals intercalates between the layers in coke crystal lattice (Figure 2-13).

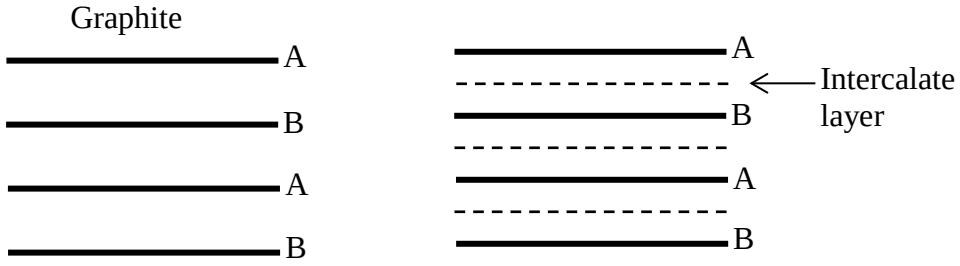

Figure 2-13: Intercalation of alkali metal in graphite [44]. A, B are graphene layers.

The intercalation of Na and K within coke crystal lattice could lead to an expansion of the coke carbon structure (to form cracks), increase stress, modify the coke surface area, weaken coke microstrength and weaken coke structure without affecting the coke carbon bonding significantly [70, 82, 104, 116, 146, 147]. Most intercalation studies in cokes were carried out by adding K in its elemental form, K as K_2CO_3 or K as K_2O [10, 82, 104, 146]. There was no evidence of intercalation in metallurgical cokes (containing alkali bearing minerals) obtained from the tuyere level of the ironmaking blast furnace [116].

The common alkali bearing minerals found in coking coals are illite $K(Al,Mg,Fe)_2(OH)_2[(Si,Al)_4O_{10}]H_2O$, biotite $K(Mg,Fe^{2+})_3[AlSi_3O_{10}](OH)_2$, muscovite $KAl_2[AlSi_3O_{10}](OH)_2$, and montmorillonite $(Na,Ca)(Al,Mg,Fe)_2(OH)_2[Si_4O_{10}]nH_2O$ [81, 147, 157-160].

2.2.3. Metallurgical coke pore structure

The pore structure of metallurgical cokes is linked to the voids left after the escape of volatile matter during coke making, while fissures in metallurgical cokes are produced by internal stresses [2]. The pore size distribution in metallurgical coke is classified into coarse pores (pore diameter >10µm), macropores (pore diameter 0.05µm to 10µm), and micropores (pore diameter <0.002µm) and is consistent with other types of porous carbons in the context of physisorption [2, 76, 161, 162]. The pore size distribution and porosity of coke has a significant variation or scatter from lump to lump and is different for different positions in the coke oven [2, 3, 5, 163-166]. The porosity of typical metallurgical cokes ranges between 35% and 70% [2, 5, 11, 77, 108, 165, 167, 168] while the pore size distributions in metallurgical coke showing variation from lump to lump and different positions in the coke oven are given in Figure 2-14 [2].

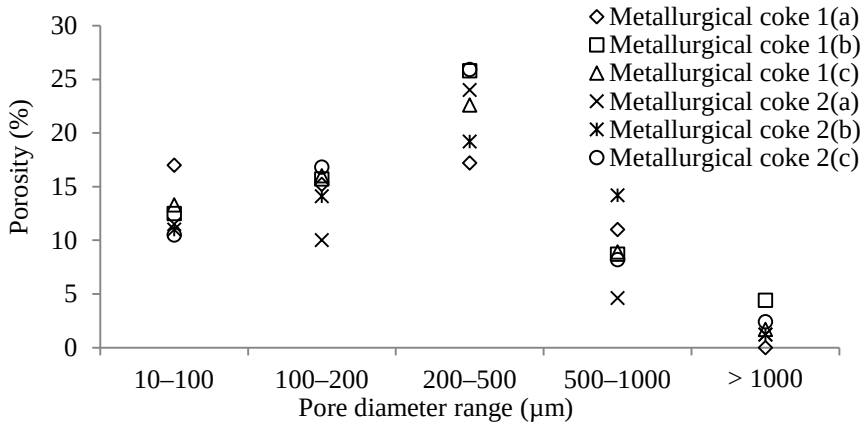

Figure 2-14: A plot of pore size distribution in metallurgical coke samples. 1(a, b, c) are from the same batch, 2(a, b, c) from a different batch, while (a, b, c) indicate different positions in the coke oven [2].

Optical microscopy [2, 3, 5, 44, 77, 163, 165, 167, 168] and mercury porosimetry [76, 77, 163, 169, 170] are widely used to characterise the pore structure of coke. The Mahoney group [164, 171, 172] have used the Imaging and Medical Beamline of the Australian Synchrotron to perform micro-computed tomography (micro-CT) imaging on coke. The technique was used to study the three-dimensional pore structures of cokes.

Optical microscopy is commonly used to characterise porosity, pore size distribution and pore shape of metallurgical cokes [2, 5, 77, 165, 167, 168]. The pore shape of a metallurgical coke can be circular, elliptical, rectangular, triangular or slit-like [163]. Table 2-6 lists the pore properties of typical metallurgical coke [5].

Table 2-6: Metallurgical coke pore properties [5].

PARAMETERS	SCHEMATIC REPRESENTATION	DESCRIPTION
Porosity (%)		Total area occupied by the pores. The ratio of total pore area and the total area of the image gives the sample porosity.
Pore size distribution (µm)		The equivalent diameter of the pores.
Shape (Feret ratio) $= \frac{a}{b}$	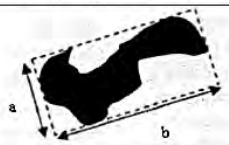	Measures the elongation of the pores using the ratio of the shortest axial length (a) to the longest axial length (b)
Shape (Solidity %) $= \frac{A}{CHA}$ Shape (Concavity %) $= \frac{CHA - A}{CHA}$	 Pore Area (A) Applied Convex Hull Area (CHA)	These parameters give a measure of the degree of surface irregularity or roughness of a pore area.
Shape (Convexity %) $= \frac{CHP}{P}$	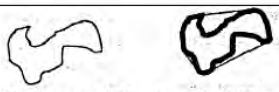 Perimeter (P) Applied Convex Hull Perimeter (CHP)	This parameter provides another measure of pore deviation from fully convex using perimeter rather than area.
Shape (Form factor) $= \frac{4\pi(Area)}{P^2}$	 Perimeter (P)	This parameter quantifies the shape of the pores using both area (A) and perimeter (P). A circle would have a form factor of 100%.

Mercury porosimetry has demonstrated an effective capability in characterising pores with equivalent diameter as low as 0.0035µm [163, 169, 170]. These pores may be difficult to measure with other porosity characterisation techniques, such as optical microscopy. The primary shortcoming of this method is that it measures the largest entrance towards a pore but not the inner size of a pore (see Figure 2-15) [169].

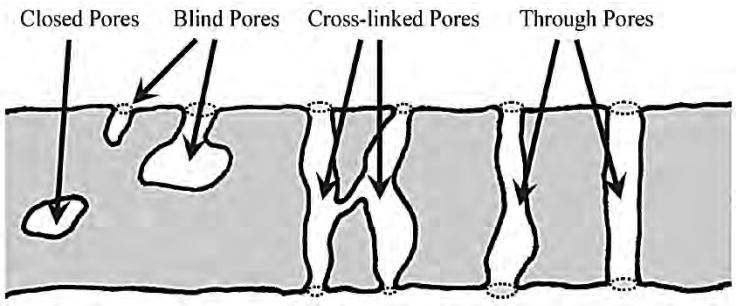

Figure 2-15: A schematic showing typical example of pores measurable with mercury porosimetry [169].

Using the micro-CT imaging porosity, pore size distribution and connectivity of pores in metallurgical cokes can be determined [164, 171, 172]. For example, Jenkins et al. [171] used this technique to characterise three-dimensional pore structure of different coke samples. The spacial resolution of the technique was ~8µm. The dimension of each sample was approximately 17mm diameter and 10mm thickness. The pore diameter range measured with this method was between 8–800µm. The study showed that pores in the metallurgical coke samples were highly interconnected in 3D (Table 2-7) [171].

Table 2-7: Porosity and voids connected in different coke samples with 16mm diameter and 10mm thickness [171].

Coke	Sample	Porosity (%)	% of voids connected
A	1	46.5	99.4
	2	39.5	99.0
	3	42.6	99.2
B	4	50.4	99.5
	5	52.8	99.5
	6	56.4	99.4
C	7	48.5	99.7
	8	54.6	99.7
	24	51.6	99.8
F	10	52.0	99.8
	11	48.0	99.6
	12	50.7	99.8
E	13	37.6	99.2
E/F BLEND	16	42.2	99.4
D	19	40.3	99.2

The Brunauer-Emmett-Teller (BET) technique can be used to determine the surface area of porous carbonaceous materials [161, 173]. It has the technique has the capability to characterise pores with equivalent diameter <2nm [162]. Prior to the BET measurement, samples are degassed, but degassing may lead to the decomposition of hydroxides or carbonates, formation of surface defects or irreversible changes in the texture of the sample [161]. The surface area of coke can range between 1.6 and 38.3 $m^2.g^{-1}$ [21, 56, 108].

2.3. Coke Reactivity in CO_2

Coke reactivity in CO_2 involves carbon, carbon dioxide and carbon monoxide. The reaction of carbon and carbon dioxide to form carbon monoxide was given in reaction 2-2 and reproduced in the following text.

$$CO_{2(g)} + C_{(s)} \rightarrow 2CO_{(g)} \quad \Delta G^\circ = 165300 - 170.76T \ J.mol^{-1} \quad [63, 64]$$

The reaction mechanism of the coke–carbon dioxide reaction is based on the ability of the coke carbon to remove an oxygen atom from a carbon dioxide molecule and retain it on certain sites by chemical bonding. The oxygen is then released as carbon monoxide and a new carbon atom is exposed to the carbon dioxide for the reaction to continue. The coke–carbon dioxide reaction is generally reported to follow the oxygen exchange mechanism [44, 60, 174-178] given in reaction 2-15 and 2-16.

$$C_f + CO_{2(g)} \underset{j_1}{\overset{i_1}{\rightleftarrows}} C(O) + CO_{(g)} \qquad 2\text{-}15$$

$$C(O) \xrightarrow{j_3} CO_{(g)} \qquad 2\text{-}16$$

where C_f is active carbon site, C(O) is the chemisorbed oxygen on carbon and i_1, j_1, and j_3 are the rate constants for the reactions.

As suggested by previous investigators [44, 60, 174-178], both the forward and backward reactions 2-15 are very rapid and there is an equilibrium between the CO and CO_2 in the system. The reaction 2-16 is the slowest step, assuming the concentration of the CO_2 gas inside and outside the solid carbon is uniform [174]. The rate constants are functions of temperature and are common to all carbons having trigonal (coplanar) bonds regardless of source, particle size, porosity and crystallinity [174].

The reaction of carbon with carbon dioxide fits into the Langmuir–Hinshelwood type equation [60, 77, 177, 179] given as,

$$R_C = \frac{k_1 p_{CO_2}}{1 + k_2 p_{CO} + k_3 p_{CO_2}} \qquad 2\text{-}17$$

$$k_1 \equiv i_1 \sum c, \quad k_2 \equiv \frac{j_1}{j_3}, \quad k_3 \equiv \frac{i_1}{j_3}, \qquad 2\text{-}18$$

where R_C is the reaction rate, $g.g^{-1}.s^{-1}$, p is the partial pressures of the CO and CO_2, Σ_c represents the total available active carbon sites and k_1, k_2 and k_3 are the rate constants.

Aderibigbe and Szekely [77] in their study on coke reactivity in CO_2, found that as temperature increases the values of k_1 increase while the value of both k_2 and k_3 decreases. A typical plot of k_1, k_2, and k_3 with temperature for coke reactivity in CO_2 is given in Figure 2-16.

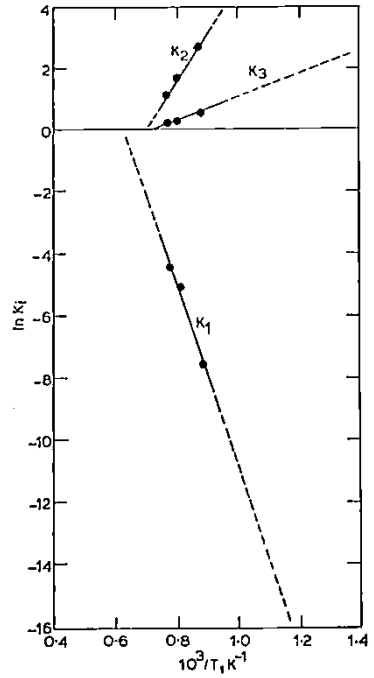

Figure 2-16: The plot of ln k_i (i = 1,2,3) versus 1/T for coke reactivity in CO_2 [77].

The reaction rates of carbon with carbon dioxide can be calculated using the following equations [44, 60, 77, 175, 176, 180-182],

$$R_C = -\frac{1}{W}\frac{dW}{dt} \qquad 2\text{-}19$$

where W is the weight of the sample at time t (g), t is the time (s).

The reaction rate can be related to fractional carbon conversion, X,

$$X = \frac{W_0 - W}{W_0} \qquad 2\text{-}20$$

where W_0 is the initial mass of the sample (g), then,

$$R_C = \frac{1}{(1-X)}\frac{dX}{dt} \qquad 2\text{-}21$$

The rate coefficient, k, is related to temperature via an Arrhenius expression,

$$k = k_0\, e^{-\frac{E_a}{RT}} \qquad 2\text{-}22$$

where k_0 is the pre–exponential factor (s^{-1}), E_a is the activation energy ($kJ.mol^{-1}$), R is the gas constant ($J.mol^{-1}.K^{-1}$), and T is the temperature (K).

A linear form of equation 2-22, given in 2-23, can be used to study the effect of temperature on the rate constants (see Figure 2-16). In addition, activation energies can be calculated from the plot (lnk versus 1/T) generated using equation 2-23.

$$\ln k = -\frac{E_a}{R}\frac{1}{T} + \ln k_0 \qquad 2\text{-}23$$

While the Arrhenius equation is usually written for the rate constant rather than the reaction rate, it can also be adapted to determine the temperature dependency on the reaction rate [44, 176, 181, 182].

$$R_C = k_0\, e^{-\frac{E_a}{RT}} \qquad 2\text{-}24$$

The reactivity of coke in CO_2 can be influenced by a number of factors. These factors include,

1. temperature [15, 21, 44, 60, 77, 175, 176, 181],
2. constituent minerals and metals [10, 29, 56, 59, 96, 180, 183-187],
3. carbonaceous form [3, 25, 98, 105, 108, 110-112, 188] and
4. porosity [2, 3, 5, 165].

The properties of the parent coal (coal rank and maceral composition) and the carbonisation conditions can also influence the porosity and carbonaceous form of coke, and as a consequence affect its reactivity in CO_2.

Coke reactivity in carbon dioxide involves several steps [44, 77, 175, 181],

1. The mass transport of the CO_2 reactant gas and CO product across the gas film between the exterior surface of the solid carbon and the main gas stream.
2. The mass transport of the CO_2 reactant gas from the exterior surface to an active carbon site below the surface of the solid carbon and the mass transport of the CO product in the opposite direction.
3. The adsorption of the CO_2 reactant gas on the carbon surface to form C(O) and the desorption of C(O) from the carbon surface and formation of new active carbon sites.
4. The chemical reactions occur at the reaction sites.

Steps 1–4 are functions of temperature [77, 174, 181]. Coke reactivity in CO_2 can be divided into three temperature zones as illustrated in Figure 2-17 with an idealized Arrhenius plot [175, 176, 181]. The corresponding variations in the CO_2 reactant gas concentration through the solid carbon is given in Figure 2-18, where R is the radius of the solid coke, δ is the thickness of the surrounding gas film and C_g is the CO_2 bulk reactant gas concentration [181].

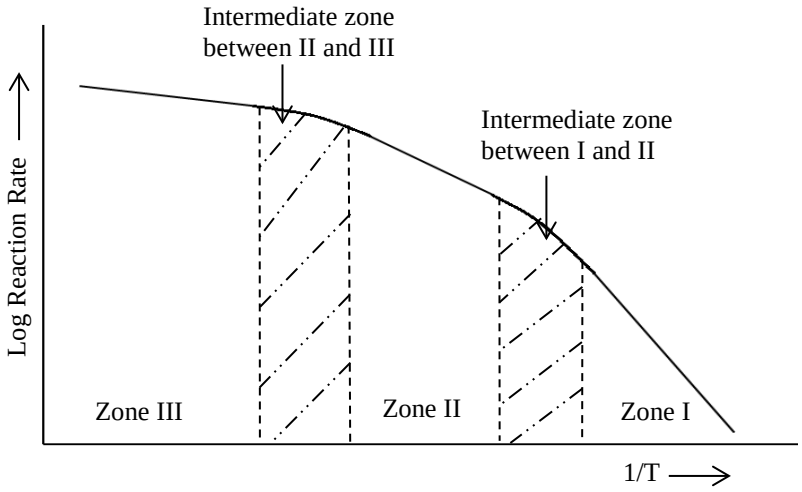

Figure 2-17: An ideal representation of three zones of coke reactivity in CO_2 with temperature [181].

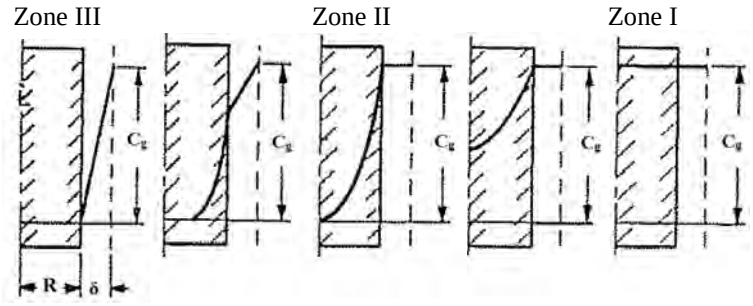

Figure 2-18: The variations in the CO_2 reacting gas concentration through the solid coke at each zone [181].

Zone I is the low-temperature chemical reaction controlled zone, where the rate is controlled by Steps 3 and 4, and there is no impediment to CO_2 reactant gas reaching the carbon surface. The CO_2 reactant gas concentration is uniform throughout the bulk of the solid carbon or coke and is equal to the concentration in the gas phase [15, 44, 77, 175, 181]. Zone II, the intermediate temperature zone, is a mixed controlled zone, where the rate is controlled by steps 2, 3 and 4 [44, 176, 181]. In zone II, there is lower probability (relative to zone I) for CO_2 reactant gas to penetrate deep into the solid carbon/coke, with the reaction occurring closer to the external surface of the solid carbon or coke. This lower penetration is a consequence of pore diffusion (molecular or Knudsen) [15, 44, 77, 175, 176, 181, 189]. Zone III is the high-temperature gas phase mass transfer, where the rate is controlled by Step 1. The reaction is limited to the external surface of the solid carbon or coke. The reaction starts soon after the CO_2

reactant gas gets to the external surface of the solid carbon or coke, and the interior is unaffected until it is exposed to CO_2 reactant gas [60, 175, 176, 181].

The two intermediate zones show the transition between the ideal zones and represent transition from a single controlling mechanism to another, and are in part determined by the gas flow rate, gas composition and gas pressure as well as the coke material, particle size, porosity and the concentration of the active carbon sites [15, 175, 176, 181].

The activation energy values for the reaction of coke, char, graphite and activated carbon in CO_2 at each reaction zone are given in Table 2-8 [60, 174, 190-195].

Table 2-8: The activation energy values for the reaction of coke, char, graphite and activated carbon in CO_2 at each reaction zone.

Carbon types	**Zone I activation energy with temperature range**		**Zone II activation energy with temperature range**		**Ref**
	$kJ.mol^{-1}$	°C	$kJ.mol^{-1}$	°C	
Metallurgical coke	222–266	770–931	–	–	[60]
Metallurgical coke	249±47	850–1000	–	–	[77]
Metallurgical coke	216–239	650–900	–	–	[190]
Petroleum coke	203–235	745–905	–	–	[191]
Petroleum coke	260±24	900–975	–	–	[192]
Petroleum coke	214–231	650–900	–	–	[190]
Petroleum coke	198	975–1050	–	–	[196]
Coal char	185–244	650–900	–	–	[190]
Char	174	1000–1200	95	1200–1600	[193]
Graphite	305	900–1100			[194]
Activated carbon	200	800–900	40	900–1100	[195]
Activated carbon	247	700–1000	–	–	[174]

–Not reported

Effects of minerals and metals on coke reactivity in CO_2

It is well known that minerals in coke affect the reactivity of coke in CO_2. The presence of minerals in coke could lead to an increase or a decrease in coke reactivity.

Minerals and Metals that increase coke reactivity

It is generally argued that some minerals and metals in coal and coke increase the C–CO_2 reaction rate. This increase is a function of nature, size, dispersion, chemical state and amounts of the mineral and metals involved. Examples of minerals and metals that increase reaction rate includes alkali metals [10, 59, 183-186, 197], alkaline earth metals [10, 59, 183, 186, 198] and transition metals such as iron and their oxides [12, 27, 29, 56, 59, 96, 97, 180, 184, 186, 187, 199-202]. They increase the reaction rate through the mechanisms given below [10, 44, 56, 70, 82, 96, 97, 104, 116, 146, 147, 152, 174, 176, 178, 186, 188, 197-214].

- Dissolution of carbon into metals

The carbon–catalyst interaction allows carbon to dissolve into metals [152, 154, 201, 202, 208, 215, 216]. When carbon diffuses into metals the carbon–carbon bonds at the carbon metal interface are weakened. The weakened carbon–carbon bonds act as an active carbon sites to increase reaction rates.

- Dissociation of CO_2 reactant gas on mineral or metal surfaces

In this case the CO_2 reactant gas dissociates on the mineral or metal surfaces to form CO and absorbed oxygen atoms. Once oxygen atoms are formed they react with the active carbon sites at the catalyst–carbon interface, and can also spill over from the mineral/metal surface to find an active carbon. The CO_2 dissociation reaction mechanism can be written as reaction 2-25 to 2-27, and 2-28 and 2-29 [44, 97, 152, 178, 199-202, 205, 206, 208, 210-215, 217].

$$M_{(s)} + CO_{2(g)} \rightarrow M(O) + CO_{2(g)} \qquad 2\text{-}25$$

$$M(O) + C_{(s)} \rightarrow M_{(s)} + C(O) \qquad 2\text{-}26$$

$$C(O) \rightarrow CO_{(g)} \qquad 2\text{-}27$$

$$MO_{(s)} + CO_{2(g)} \rightarrow MO.CO_2 \quad \text{2-28}$$

$$MO.CO_2 + C_{(s)} \rightarrow MO_{(s)} + 2CO_{(g)} \quad \text{2-29}$$

where M represents a metal, MO a metallic oxide, M(O) is chemisorbed oxygen on metal.

With respect to C–CO_2 reactions catalysed by metallic iron, the excess carbon in the metallic iron must be removed on reaction with CO_2 in order to activate the metallic iron surface. That is, excess carbon in metallic iron could inhibit the catalytic efficient of Fe. The activated metallic iron surface would then be able to dissociate CO_2 gas [215]. Both carbon in solution in liquid iron ([C]) and carbon as graphite <C> can react with CO_2 reactant gas to release CO product gas (see reaction 2-30 and 2-31 respectively).

$$[C] + CO_{2(g)} \rightarrow 2CO_{(g)} \qquad \Delta G^\circ = 142706 - 128.50T \text{ J.mol}^{-1} \text{ [63, 64]} \quad \text{2-30}$$

$$< C > + CO_{2(g)} \rightarrow 2CO_{(g)} \qquad \Delta G^\circ = 165300 - 170.76T \text{ J.mol}^{-1} \text{ [63, 64]} \quad \text{2-31}$$

<C> reference state is pure graphite and [C] reference state is 1wt% standard state.

- Redox reaction involving CO_2 and metals

The redox reaction suggests that Fe is oxidised by CO_2, yielding an iron oxide and CO as products (reaction 2-32). The iron oxide is subsequently reduced by carbon giving CO and Fe (reaction 2-33), and the formation of new active carbon sites. The Fe is continuously renewed in reaction 2-33 to resume the redox cycle. The continuous contact between iron oxide and carbon surface is key to maintain the catalytic action of Fe [200, 212, 213].

$$y\,Fe_{(s)} + xCO_{2(g)} = Fe_yO_{x(s)} + xCO_{(g)} \quad \text{2-32}$$

$$Fe_yO_{x(s)} + xC_{(s)} = yFe_{(s)} + xCO_{(g)} \quad \text{2-33}$$

- The transfer of electrons from carbon into minerals or metals

According to Long and Sykes [206, 217] the transfer of electrons from carbon into minerals or metals would catalyse the C–CO_2 reaction. The transfer of electrons results in a redistribution of the π electrons in the carbon structure at the carbon–mineral/metal interface. The redistribution of the π electrons creates new active carbon sites. This mechanism could be applicable to metallic Fe because it can accept electrons with its unfilled d-orbital [215].

- Formation of intercalates in between the crystal structure of graphite

The presence of K and Na in minerals are known to form intercalates in the crystal structure of graphite. The formation of intercalates can cause an expansion of the coke carbon structure (to form cracks), increase stress, modify the coke surface area, weaken coke microstrength and weaken coke structure to increase the reaction rate. That is, the formation of intercalates in between the crystal structure of graphite generates active carbon sites [70, 82, 104, 116, 146, 147].

Minerals that decrease coke reactivity

Some minerals are reported to decrease coke reactivity in CO_2. Most of these minerals decrease reactivity by covering the pores and pore walls of coke and covering coke surface [79, 89, 163, 168, 176, 186, 206, 218, 219]. For example, aluminosilicate in coke has been found to form a thin layer of molten slag that seals the interior walls of the coke pore structure against gas penetration [163]. Other studies also reported that quartz (SiO_2) decrease coke reactivity [89, 168, 186, 219].

Effects of coke carbonaceous form on coke reactivity in CO_2

The carbonaceous forms (inert maceral derived component (IMDC) and reactive maceral derived component (RMDC)) in metallurgical coke affect coke reactivity in CO_2. In general, the IMDC reacts faster in CO_2 than the RMDC [3, 25, 98, 105, 108, 110-112, 188]. This is in part due to the differences in the structural order of the RMDC and IMDC, which is higher for RMDC compared to IMDC [108, 111]. An example of

changes in the carbonaceous form of metallurgical coke after reaction in CO_2 at 1100°C for 2 hours is given in Figure 2-19 [108]. The micrograph shows significant loss of carbon in the IMDC part of the coke compared to the RMDC.

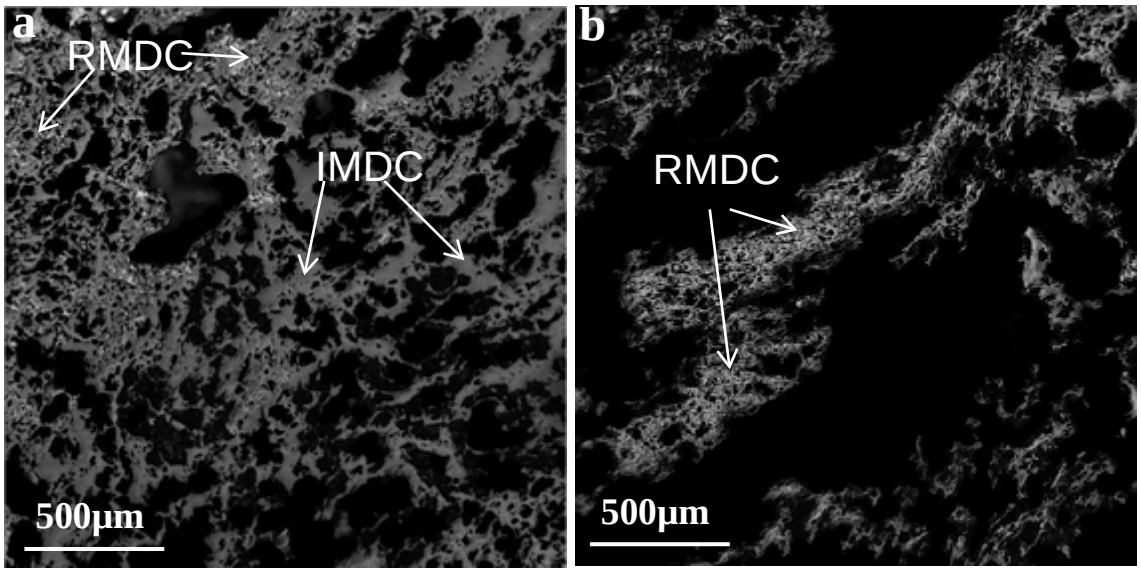

Figure 2-19: An example of change in IMDC and RMDC of metallurgical coke, (a) pre reactivity test and (b) after reaction with CO_2 at 1100°C for 2 hours [3].

Effect of porosity on coke reactivity

The porosity of coke plays a part in the reactivity of metallurgical coke in CO_2 [2, 3, 5, 165, 168]. Patrick and Walker [165] studied the effect of porosity on the reactivity of three metallurgical cokes in CO_2 at 1000°C. The metallurgical cokes used in their study had different initial porosity values. Image analysis was used to measure porosity in the pore diameter range 5.45–4000µm. In their study, they found that the initial porosity of the metallurgical coke sample is related to the reactivity of the metallurgical coke samples in CO_2 (Figure 2-20).

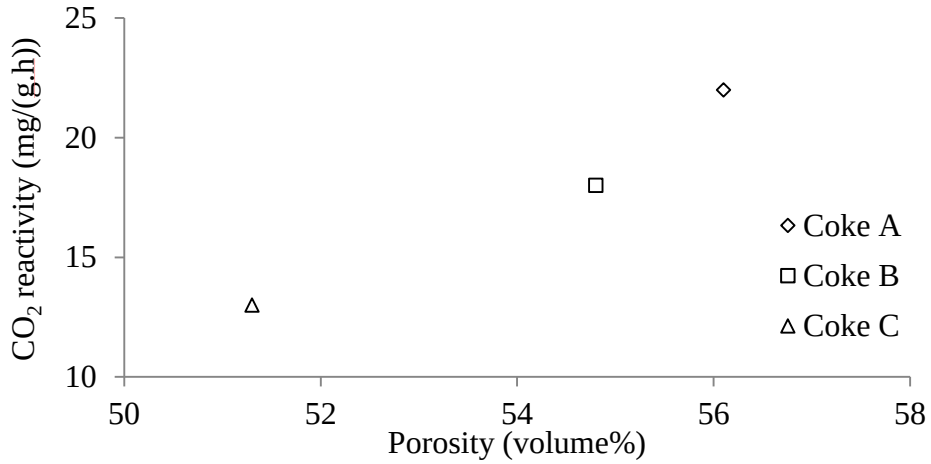

Figure 2-20: The plot of metallurgical coke CO_2 reactivity versus porosity [165].

The porosity of coke increases after reaction in CO_2 (relative to porosity before reaction in CO_2) [77, 108]. For example, Aderibigbe and Szekely [77] studied the evolution of porosity in metallurgical coke reacted in CO_2 at 1000°C. They found that the porosity of the metallurgical coke increases with loss of carbon due to reaction (Figure 2-21). The figure also shows how the loss of carbon due to the reaction affects the relative proportion of the large (>35μm) and the small (<32nm) diameter pores. The molecular diffusion predominates in the large pores while the Knudsen diffusion dominates in the small pores [77].

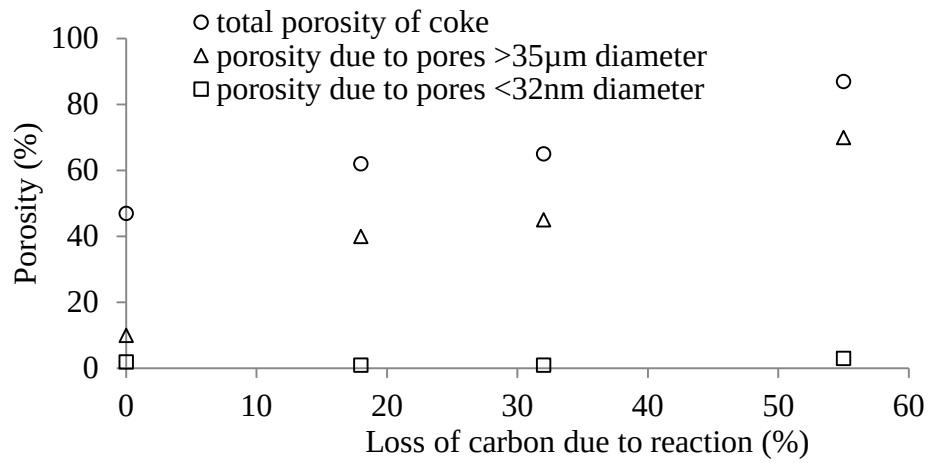

Figure 2-21: The plot of variation of porosity as a function of loss of carbon due to reaction [77].

2.3.1. Coke reactivity testing

There are many coke reactivity tests used to measure the performance of metallurgical coke. The main characteristics of the different methods are given in Table 2-9 [179].

Table 2-9: A summary of the main characteristic of different coke reactivity tests [179].

Method	**Mass of coke sample, (g)**	**Particle size of coke, (mm)**	**Reaction temperature, (°C)**	**Reaction time, (mins)**	**Flow rate, ($m^3.h^{-1}$)**
NSC	200	19–21	1100	120	0.3
ECE	7–10	1–3	1000	15 or 30	0.072
ECE–INCAR	7	1–3	1000	60	0.072
NCB	20000	>20	1069	360–480	5.4
Gost 10089–73	200	3–6	1000	60	0.12
IRSID–CERCHAR	400	20–30	1200	Until 25% weight loss	2.0
Okstad and Hoy	7	425000–870000	750–1000	10	Adjusted to 10% conversion

NSC, Nippon Steel Corporation,
ECE, Economic Commission for Europe,
INCAR, Instituto Nacional del Carbon,
NCB, National Coke Board.
IRSID-CERCHAR, Ingenieur au Centre d'Etudes et Recherches des Charbonnages de France.

The NSC procedure is the most commonly used of all the methods given in Table 2-9 [3, 21, 70, 108, 120, 179, 186, 188, 220-225]. The test is used to measure coke reactivity index (CRI) and coke strength after reaction (CSR). The CRI is determined as,

$$CRI = \frac{\text{loss in weight}}{\text{original weight}} \text{ X } 100\% \qquad 2\text{-}34$$

CSR is determined as,

$$CSR = \frac{\text{weight of} > 10\text{mm after 600 revolutions}}{\text{weight after reactions}} \text{ X } 100\% \qquad 2\text{-}35$$

An example of CRI and CSR values reported for metallurgical cokes are given in Table 2-10, with an example of the linear relationship between the CRI and CSR for approximately 60 coke samples produced from coals of different sources, ranks and blends given in Figure 2-22 [179] and consistent with the findings of other authors [3, 21, 188, 221, 224, 225].

Table 2-10: An example of CRI and CSR values reported for metallurgical cokes

CRI	CSR	References
15–80	0–75	Menendez et al. [179]
20–60	20–60	Miroshnichenko et al. [225]
14–38	50–79	Sakurovs et al. [188]
30–55	25–82	Koszorek et al. [221]
26–59	24–62	Krzesinska et al. [224]
21–47	32–70	Xing et al. [69]
17–31	58–68	Haapakangas et al. [21]
30–44	37–61	Pusz et al. [108]

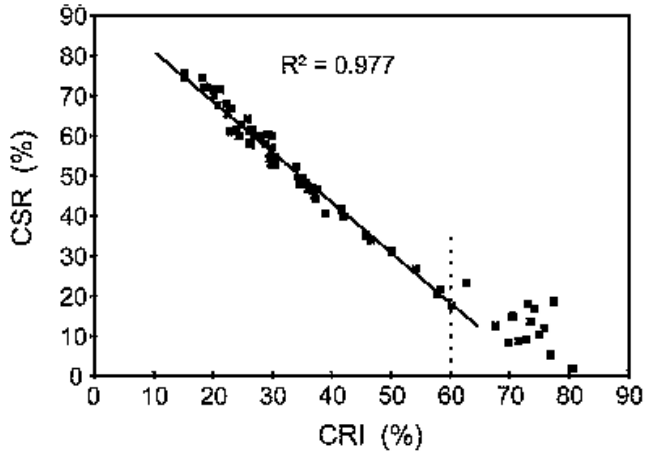

Figure 2-22: The relationship between the CRI and CSR of metallurgical cokes [179].

The limitations of the CRI/CSR test compared to real blast furnace performance are [21, 59, 69],

1. that very high CO_2 levels are used,
2. a single temperature (1100°C) is used for testing, whereas in the blast furnace coke is exposed to temperatures of up to 2000°C, and
3. ex-situ measurements.

The thermogravimetric analysis (TGA) is the most common laboratory method used to study coke reactivity under varying conditions, such as varying gas composition, temperature, initial sample mass and particle size [11, 21, 60, 70, 77, 115, 226, 227]. A schematic of the TGA used by Aderibigbe and Szekely [77] in their coke reactivity study is given in Figure 2-23. The major components of the TGA set-up are given in the figure. In that study, metallurgical coke samples were placed in a platinum basket, suspended from one arm of a recording balance with the help of platinum suspension wire. The sample was preheated under the flow of argon gas to the desired reaction temperature. Then the CO_2 reactant gas was supplied at a predetermined rate into the TGA for the coke reactivity test [77].

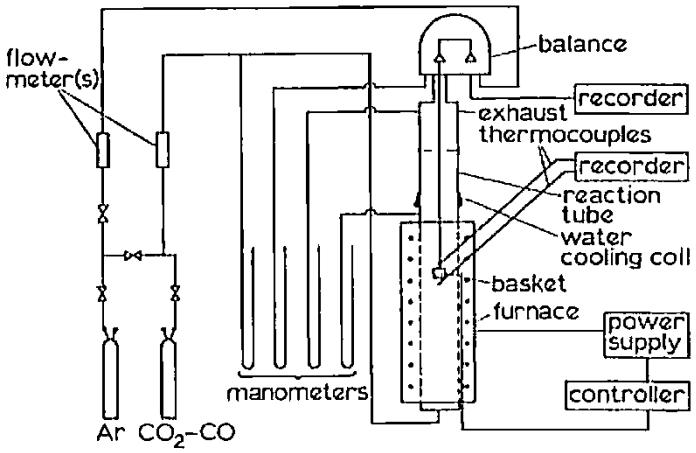

Figure 2-23: A schematic diagram of the TGA system used for coke reactivity test [77].

An example of fractional weight change, FWC, of the metallurgical coke samples as they reacted in CO_2 at 1100°C in a TGA system is given in Figure 2-24. The FWC was calculated as,

$$FWC = \frac{W - W_0}{W_0} \qquad 2\text{-}36$$

where W represents the mass of the coke analogue at time t and W_0 represents the mass of the coke analogue at time zero (the changeover of gas from Ar to CO_2).

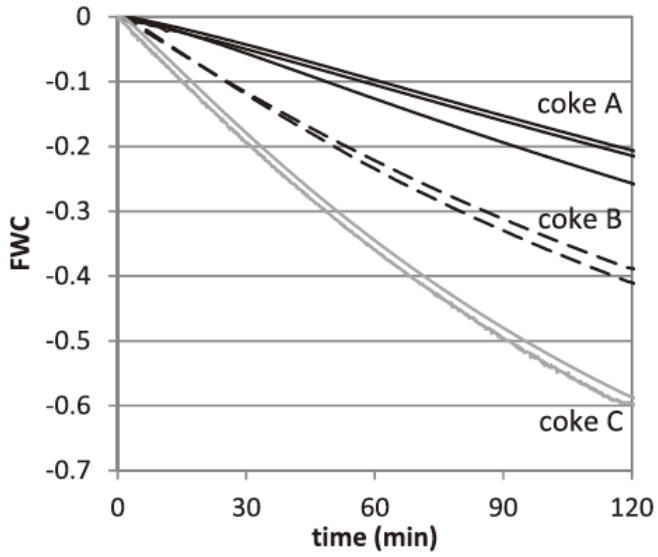

Figure 2-24: The FWC curves for the reaction of three metallurgical coke samples with CO_2 at 1100°C [11].

2.4. Coke analogue

As mentioned previously, investigations of metallurgical coke behaviour are problematic due to the complexity and heterogeneous issues. These issues can be minimised or lessened with the use of a coke analogue. A coke analogue, of controlled porosity, mineralogy and mineral dispersion has been used to study selected aspects of metallurgical coke reactivity [11-13, 15, 16, 53-55, 58, 228].

Longbottom et al. [53] and Reid et al. [12] studied the effects of selected minerals and metallic iron on the reactivity of the coke analogue in CO_2. The reactivity testing was carried out in a 100% CO_2 atmosphere at a single temperature of 1100°C. In the Longbottom et al. [53] study, the coke analogues were prepared with silica in the form of quartz and cristobalite. It was found that silica addition decreased the reactivity of the coke analogue relative to the coke analogue prepared with no silica (Figure 2-25). Further increasing the quartz concentration decreased reactivity. Silica added as quartz and cristobalite at a constant concentration and similar particle sizes have the same effect on reactivity. The study also showed that at a constant concentration, the coke analogue containing smaller sized quartz particles (–38µm) decreased reactivity relative to the coke analogue containing larger sized quartz particles (125–150µm) [53].

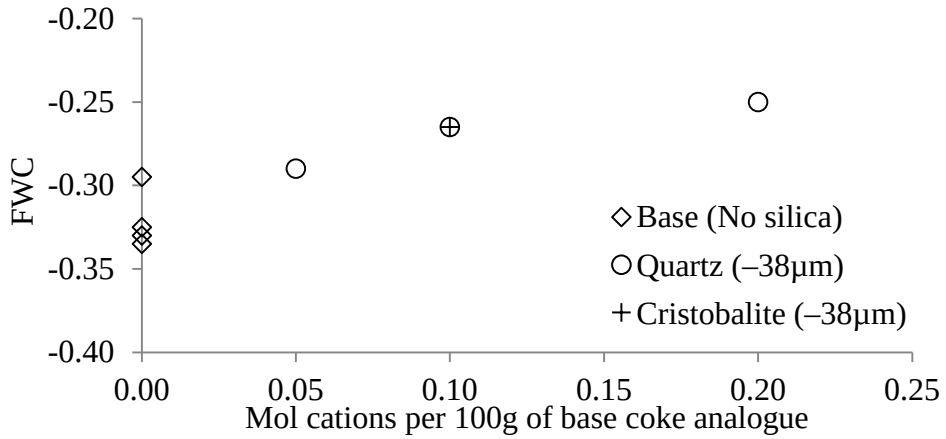

Figure 2-25: The FWC of the coke analogue samples after reaction in CO_2 at 1100°C for 2 hours [53].

In the Reid et al. [12] study, single minerals and metallic iron were added to the coke analogue at a constant concentration of 0.1mol cations per 100g of the coke analogue carbonaceous materials. The study showed that the addition of pyrite, gypsum, iron, troilite, magnetite, lime and hematite increased the reactivity of the coke analogue relative to the base coke analogue. Also, the addition of Na feldspar, K feldspar, quartz and kaolinite decreased the reactivity of the coke analogue relative to the base coke analogue (Figure 2-26) [12].

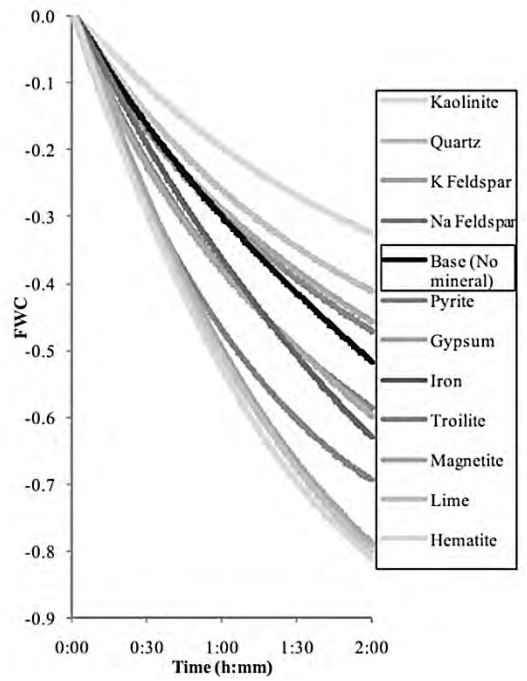

Figure 2-26: The FWC versus time for coke analogues containing single minerals at constant concentration reacted in CO_2 at 1100°C for 2 hours [12].

The coke analogue has also been used to study the effect of selected minerals and mineral combinations [12, 13, 16, 53, 58, 228] and coke ash [11] on coke analogue reactivity in CO_2. With respect to the coke ash reactivity study, Longbottom et al. [11] added mineral matter from three metallurgical coke ash to the coke analogue at a constant proportion of 10 mass% and a particle size of –38µm, eliminating the effect of carbon type and rank. The study showed that the coke analogue was able to replicate the reactivity of metallurgical coke [11].

In studies that focused on the effects of binary and ternary combinations of minerals on coke analogue reactivity in CO_2 [13, 16, 58, 228], it was found that the reactivity trends in the binary and ternary combinations were similar, with the testing allowing better understanding and prediction of the combined effect of minerals on the reactivity of metallurgical cokes.

Jayasekara et al. [15, 54] studied the kinetic behaviour of the coke analogue reacted in CO_2. The study was carried out over the temperature range 900°C–1350°C. Both studies showed that the coke analogue was able to replicate the kinetic behaviour of metallurgical coke. In the first study [15] they used the base coke analogue. In this study it was shown that the reaction mechanism of the base coke analogue reacted in CO_2 was similar to that of metallurgical coke. The kinetics of the reaction of the coke analogue in CO_2 was characterised into chemical reaction controlled (zone I) and mixed (pore diffusion and chemical reaction) controlled (zone II). The plot of the $\ln(R_C)$ versus 1/T of the coke analogue is given in Figure 2-27 and is consistent with Figure 2-17 for cokes/carbon. The zone I activation energy value for the reaction of the base coke analogue (273.6±0.5 $kJ.mol^{-1}$) is similar to the zone I activation energy value of metallurgical cokes given in Table 2-8.

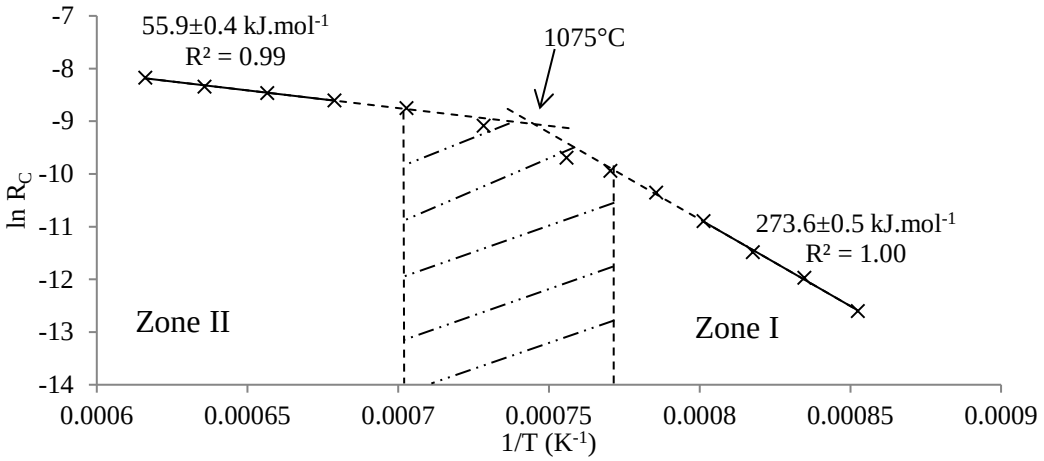

Figure 2-27: The plot of ln(R_C) against 1/T for base coke analogue reacted in CO_2 with temperature and showing reaction zones [15].

In the second study [54] they studied the catalytic effect of lime on the reaction rate of the coke analogue in CO_2. The study indicated that lime increased the reaction rate and decreased the zone I activation energy value (119.8±1.5 kJ.mol^{-1}) of the reaction of the coke analogue relative to the base coke analogue (273.6±0.5 kJ.mol^{-1}) [54].

2.5. Key issues in the literature that need to be considered

Metallurgical coke is an intricate material that is made up of diverse carbonaceous forms, mineral components and has a pore size distribution with pores of various morphologies. The carbonaceous forms, inorganic minerals and pore structures of the metallurgical coke influence its reactivity in the iron making blast furnace. The key issues established from the coke literature are that,

- metallurgical coke textural component grouping, mineralogy, phase dispersion, morphology and pore structure can differ within a metallurgical coke batch or lump and from metallurgical coke to coke type [3, 5, 7, 8, 11-20],

- it is difficult to assess the effects of specific minerals on the behaviour of metallurgical coke due to its complexity and heterogeneity issues, potential non–

additive effects of minerals, and experimental uncertainties associated with the use of metallurgical coke,

- the carbon bonding in the metallurgical coke is primarily the disordered sp^2–sp^3 bonding. Metallic iron has been reported to promote the formation of ordered sp^2 bonding close to the metallic iron–metallurgical coke interface. The roles played by iron as oxides in the form of magnetite (Fe_3O_4), enstatite ferroan ($Mg_{1.56}Fe_{0.44}Si_2O_6$) and phlogopite ferroan [$K(Mg,Fe)_3(Al,Fe)Si_3O_{10}(OH,F)_2$], and quartz ($SiO_2$) on the carbon bonding of the metallurgical coke is not well known, and

- the minerals and metals in metallurgical cokes are known to either increase or decrease coke reactivity with CO_2. Minerals and metals could increase coke reactivity by creating more active carbon sites, while they could decrease coke reactivity by blocking pore walls and pore surface, and carbon surface.

This literature review highlights the need to have a laboratory tool that is representative of simplified metallurgical coke with controlled porosity, mineralogy and mineral dispersion throughout the coke, with the aim being to better understand the specific effects of minerals on coke reactivity and carbon bonding. This is what the present study seeks to resolve using a coke analogue.

3. Experimental

This investigation is focused on elucidating the effects of metals and minerals on the carbon bonding and CO_2 reactivity of coke analogue with a specific focus on metallic/elemental iron. To expand the relevance of this work, quartz (SiO_2) and Fe bonded within a complex mineral (enstatite ferroan ($Mg_{1.56}Fe_{0.44}Si_2O_6$) and phlogopite ferroan [$K(Mg,Fe)_3(Al,Fe)Si_3O_{10}(OH,F)_2$]) were also evaluated. The quartz and Fe bonded within mineral effects on carbon bonding and analogue reactivity were simply contrasted with those of the elemental Fe. To achieve this, the following approaches were used.

- Raman spectroscopy to characterise the carbon bonding in the coke analogue. The technique was also used to assess the effect of metallic iron and minerals on the carbon bonding in the coke analogue. This work was augmented with optical and electro-optical microscopy techniques.

- Three separate but complementary porosity measurement techniques. Optical microscopy linked to image analysis, mercury porosimetry and Dingo neutron radiography were used to assess the coke analogue porosity. This was principally carried out to ensure the structure of the coke analogue was characterised but also to aid comparison of reactivity experiments.

- CO_2 reactivity experiments using a large sample (~8g) thermogravimetric analyser (TGA).

In addition, the coke analogue systems studied were subjected to thermodynamic analysis using the MTDATA thermodynamic software, version 5.10 [99]. The characterisation approach was required as the coke analogue is a relatively new material. To further evaluate coke analogue performance, selected measurements (Raman spectroscopy, optical microscopy linked to image analysis, optical porosity and Dingo neutron radiography) were also carried out on the metallurgical coke for comparison.

Given the coke analogue is a relatively new material and the primary material used in this study, its production has been brought to the beginning of this experimental chapter.

3.1. Coke analogue production

The coke analogues were prepared by mixing carbonaceous materials, graphite and phenolic resins (Bakelite and Novolac), and non-carbonaceous materials. The full details of the materials used, their purity, proportional addition, supplier and particle size are given in Table 3-1.

Table 3-1: The purity, proportional addition, supplier and particle sizes of the materials used to make the coke analogue.

Materials	**Purity (%)**	**Proportional addition**	**Supplier**	**Particle size (µm)**
Graphite Powder 1[#]	>99.99	28% of dry mass	Sigma–Aldrich	<45
Graphite Powder 2[#]	>99.99	28% of dry mass	Sigma–Aldrich	<150
Phenolic resin (Bakelite)*	NA	44% of dry mass	LECO Metallurgical Supplies	100–250
Phenolic resin (Novolac)[+]	99.8	Ratio of 0.52 liquid/dry mix	Momentive Ltd	NA
Hexamethylene-tetramine (HTMA) powder	99.5	3 mass % of phenolic resin (novolac)	Ajax Finechem Pty Ltd	NA
Non-carbonaceous[&]	-	0.10mol cation/100g of Carbonaceous[≠]	-	38–53†

[#]Full details are given in Appendix I – Material purity.

*The phenolic resin (Bakelite) used in this study is a carbonaceous material that contains small amounts of mineral matter. The loss on ignition test showed approximately 4 mass % was mineral matter. The mineral matter consisted of alumina–silica–calcia oxide.

[+]The phenolic resin (Novolac) was dissolved in propylene glycol in a mass ratio of 1:1 to form a resin. A VMA Getzmann cavitation mixer was used to homogenise the resin at a temperature of ~60°C. The mixer speed was ~5000rpm and the process takes ~20 minutes.

[&]The backscattered SEM images of the green additions are given in Figure 3-1.

[≠]Coke analogues containing metallic iron of 0.20 mol cation/100g of carbonaceous materials and magnetite of 0.16 mol cation/100g of carbonaceous materials were also evaluated.

†Coke analogues containing metallic iron of <10µm and 75–90µm were also evaluated.

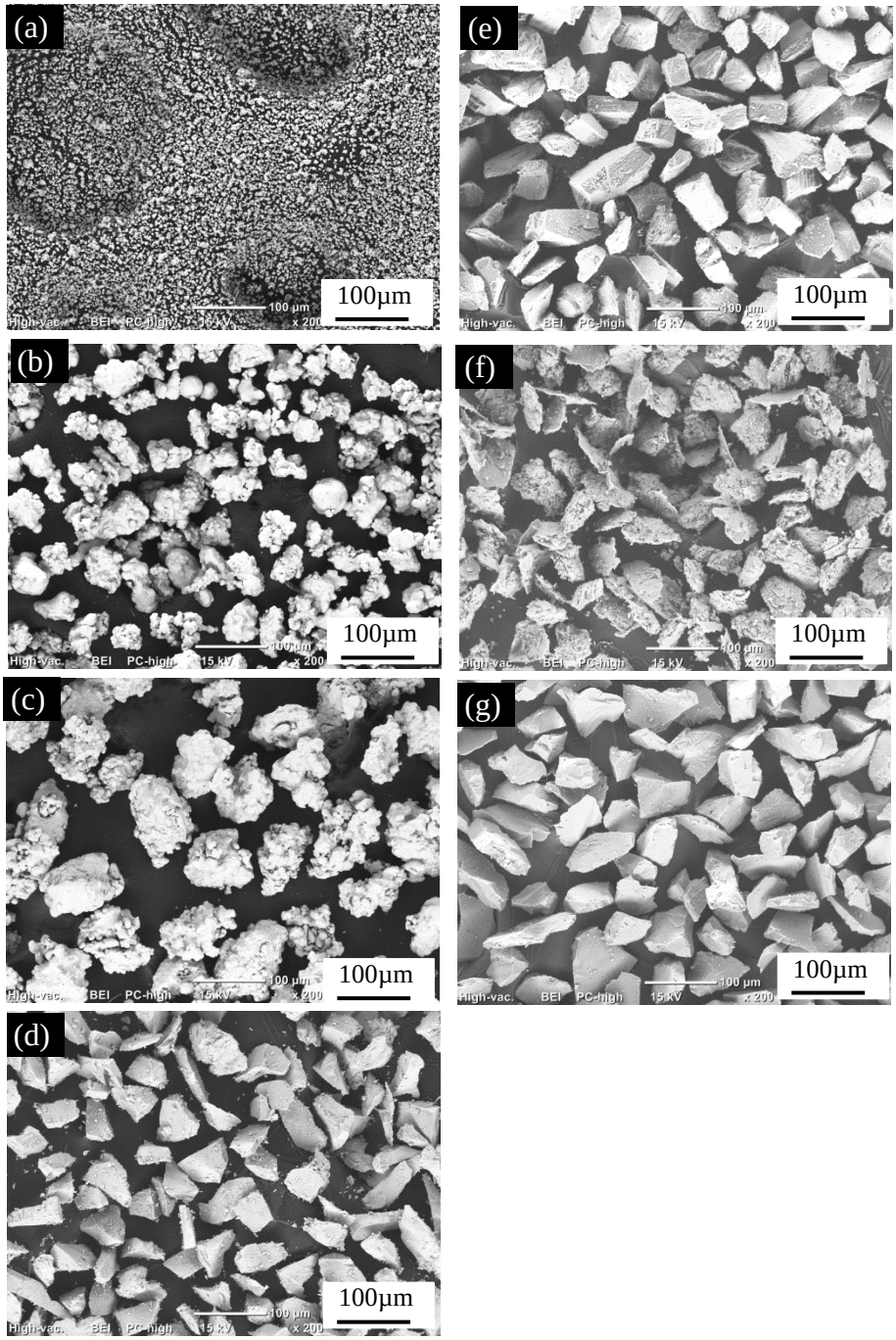

Figure 3-1: Typical backscattered SEM images of the non-carbonaceous materials used to make the coke analogues. (a) Metallic iron (Fe) of <10µm particle size, (b) metallic iron (Fe) of 38–53µm particle size, (c) metallic iron (Fe) of 75–90µm particle size, (d) magnetite (Fe_3O_4) of 38–53µm particle size, (e) enstatite ferroan ($Mg_{1.56}Fe_{0.44}Si_2O_6$) of 38–53µm particle size, (f) phlogopite ferroan [$K(Mg,Fe)_3(Al,Fe)Si_3O_{10}(OH,F)_2$] of 38–53µm particle size and (g) quartz (SiO_2) of 38–53µm particle size.

The details of the non-carbonaceous materials (metallic iron, iron containing minerals and quartz) used to make the coke analogues are given in Table 3-2.

Table 3-2: The purity, supplier and size description of non-carbonaceous materials used to make the coke analogues.

Non-carbonaceous materials*	**Purity (%)**	**Suppliers**	**Size description**
Metallic iron 1, (Fe)[#]	>99.9	Sigma-Aldrich	<10µm powder
Metallic iron 2, (Fe)[#]	>99.5	Höganäs	<150µm powder
Low carbon aluminium killed (LCAK) steel[#]	99.62	BlueScope	2mm x 7mm x 9mm
Magnetite, (Fe_3O_4) [#]	72 mass% of Fe, with O as balance	Höganäs	<500µm powder
Enstatite Ferroan, $(Mg_{1.56}Fe_{0.44}Si_2O_6)^+$	NA	Wards' Science	1–10 mm diameter flake
Phlogopite Ferroan, $[K(Mg,Fe)_3(Al,Fe)Si_3O_{10}(OH,F)_2]^+$	NA	Wards' Science	1–10 mm diameter flake
Quartz, (SiO_2)	NA	Creswick Quartz	1–5mm diameter grain

*These names represent green additions to the coke analogue. For example, magnetite in the coke analogue was reduced to iron during the firing process. The phases of the non-carbonaceous materials (metallic iron, iron containing minerals and quartz) used to make the coke analogue and their states in the fired coke analogues were confirmed using XRD (see Table 3-3). Where more than one mineral phase was identified Maud diffraction software version 2.55 [229] linked to crystallography database of crystal structures [230] was used to quantify the phases in weight%. The XRD patterns are given in Appendix II.

[#]Full details are given in Appendix I – Material purity.

[+]Enstatite ferroan and phlogopite ferroan are commercial mineral samples. They are described with the matching XRD diffraction database system [231, 232]. They were calcined to 500°C in air before they were used to make the coke analogue. This was carried out to ensure the coke analogue porosity was controlled, but not to decompose the minerals. It was also carried out to remove bonded OH and F from the phlogopite ferroan. Their detailed chemical composition as measured by XRF is given in Table II-4 [233].

Table 3-3: The phases of the non-carbonaceous materials used to make the coke analogue and their stability in the fired coke analogue and after ashing at 520°C.

Non-carbonaceous materials	**Prior to addition**	**Phases identified in the coke analogue using the XRD**	
		Without ashing	**After ashing at 520°C**
Metallic iron 1 (Fe)	Iron (Fe)	Iron (Fe)	–
Metallic iron 2 (Fe)	Iron (Fe)	Iron (Fe)	–
Magnetite (Fe_3O_4)	Magnetite	Iron (Fe)	–
Enstatite Ferroan ($Mg_{1.56}Fe_{0.44}Si_2O_6$)	Enstatite ferroan ($Mg_{1.56}Fe_{0.44}Si_2O_6$)	Enstatite ferroan ($Mg_{1.56}Fe_{0.44}Si_2O_6$)	Enstatite ferroan ($Mg_{1.56}Fe_{0.44}Si_2O_6$)
Phlogopite Ferroan $[K(Mg,Fe)_3(Al,Fe)Si_3O_{10}(OH,F)_2]$	Phlogopite ferroan $[K(Mg,Fe)_3(Al,Fe)Si_3O_{10}(OH,F)_2]$ 81.3% and osumilite ($KMg_2Al_3(Si_{10}Al_2)O_{30}$) 18.7%.	Phlogopite ferroan $[K(Mg,Fe)_3(Al,Fe)Si_3O_{10}(OH,F)_2]$ 14.7% and osumilite ($KMg_2Al_3(Si_{10}Al_2)O_{30}$) 85.3%	Forsterite (Mg_2SiO_4) 50.9%, sanidine ($KAlSi_3O_8$) 41.1%, gedrite $[(Fe,Mg,Al)_7Al_2Si_6O_{22}(OH)_2]$ 4.6%, hematite (Fe_2O_3) 3.4% and magnetite (Fe_3O_4) (trace amount)
Quartz (SiO_2)	Quartz (SiO_2)	Quartz (SiO_2)	–

–Not measured

3.1.1. The coke analogue production procedure

A step by step guide for the coke analogue production is given as follows.

The ‘dry’ materials (graphite powders, phenolic resin (Bakelite), HTMA, non-carbonaceous materials) were weighed. The powders were then mixed in a helical mixer at 5 rpm for 1 hour. The dry component was then added to phenolic resin (Novolac) and mixed by hand until a homogeneous mixture was obtained (this process took approximately 30 minutes). The mixture was then divided into ~14 g parts and rolled into a ball.

Each 14 g ball was then rolled into a rod to fit into a 19 mm diameter and 50 mm length steel die. The rod was then hydraulically pressed to form cylindrical shaped green analogue. A ram pressure of approximately 40 Pa was used.

The green analogue was cured in an industrial oven in air at 170°C for 24 hours. In this step, the Novolac resin reacted with the HTMA and hardened.

It was then fired in a two-stage process (see Figure 3-2 for firing details). The firing was carried out in a high-temperature resistance tube furnace under argon (see schematic given in Figures 3-3 and 3-4). The analogues were placed in steel tube and graphite crucible in 1st (at 950°C) stage and 2nd (at 1200°C) stage firing respectively. The mass of a coke analogue after the 2nd stage firing was approximately 8 g.

> Note, the analogue was fired at 1200°C to simulate coke oven operational temperature. Coke is made in a coke oven at approximately 1000–1200°C.

After firing, the analogues were stored in a desiccator to minimize moisture adsorption.

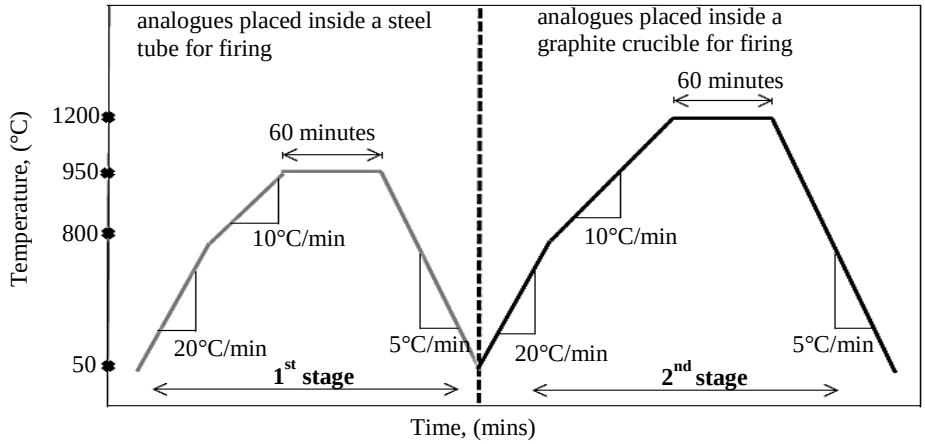

Figure 3-2: A schematic illustration of the firing regimes used in the coke analogue production showing heating time and heating/cooling rates.

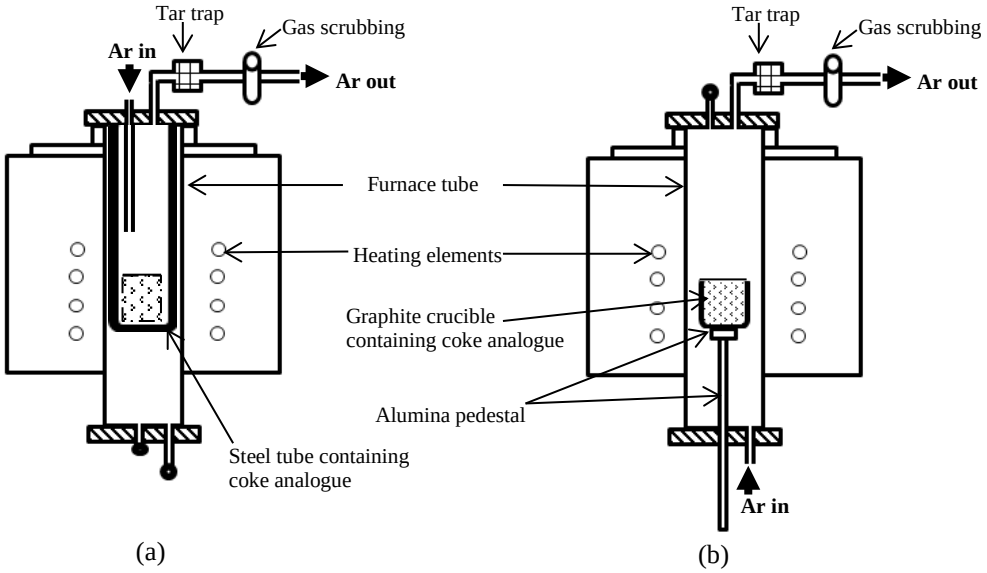

Figure 3-3: A schematic of the coke analogue production furnace, showing (a) 1st stage set up and (b) 2nd stage set up.

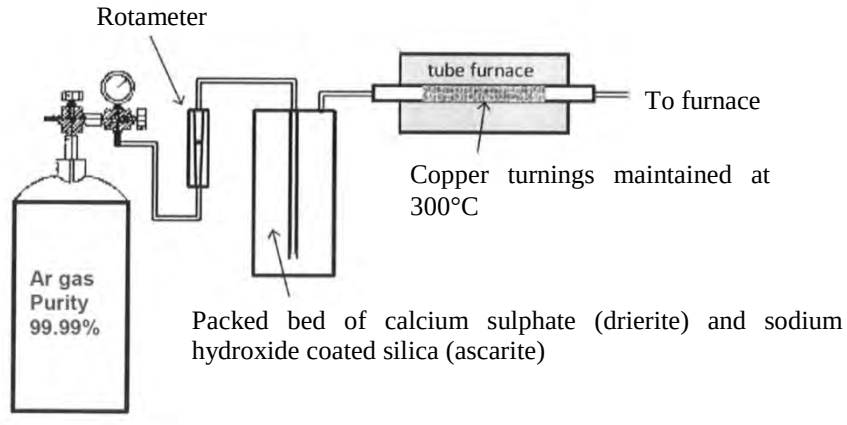

Figure 3-4: A schematic of the gas cleaning system for Ar prior to entering the furnace.

The decomposition of the phenolic resins, used to make the coke analogue, during coke analogue firing can be summarized as [24, 234-239],

(1) At temperatures <600°C there was liberation of gaseous products. The products are H_2O, carbon dioxide, carbon monoxide, methane, phenol, cresols and xylenols, and

(2) At temperatures >600°C there was formation of carbon matrix from the carbonised phenolic resin.

A typical non-polarised optical micrograph showing the carbon microstructure of the base coke analogue is given in Figure 3-5.

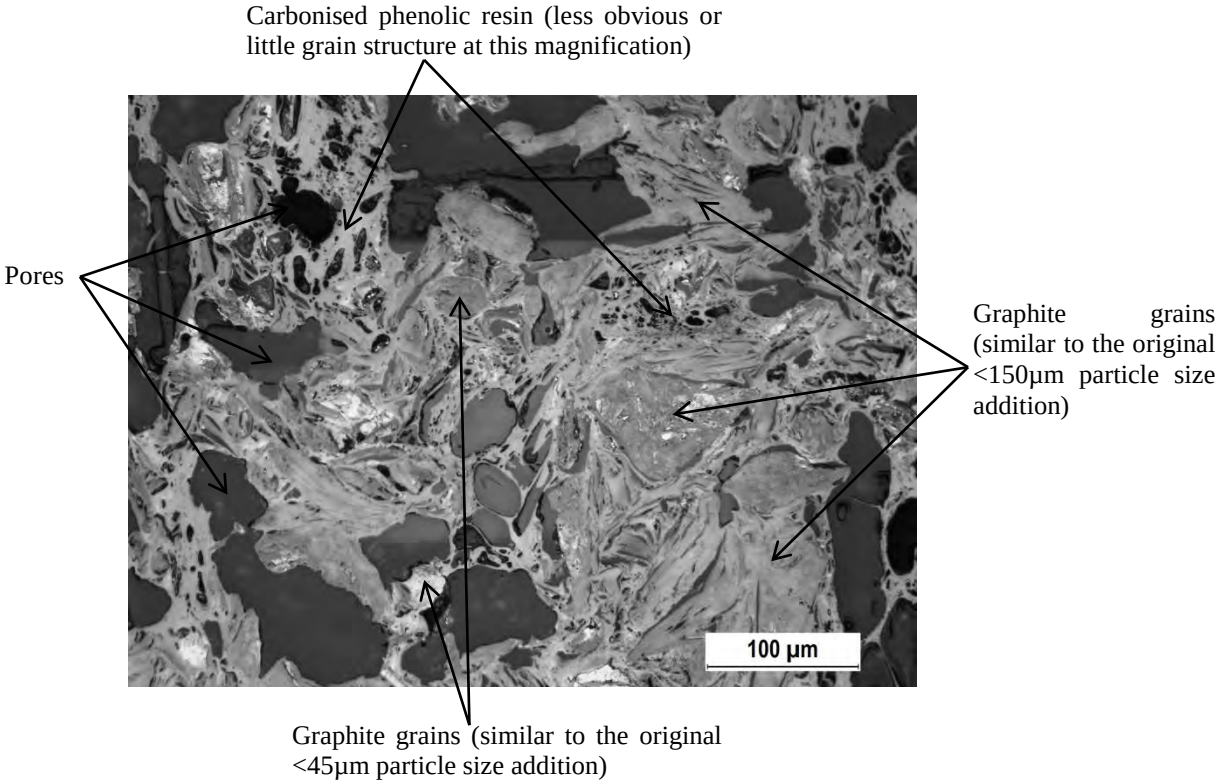

Figure 3-5: A typical non-polarised optical micrograph of the base coke analogue showing the carbon microstructure.

3.1.2. Coke analogue production furnace calibration

A high temperature resistance tube furnace was used to fire the analogues under argon (see Figures 3-3 and 3-4). Prior to firing the analogues, the resistance tube furnace was calibrated with respect to temperature under argon. The thermal profile for the resistance tube furnace was established to determine the position and length of the stable hot zone. A type R thermocouple was used to measure the resistance furnace thermal profile by progressively lowering it into the furnace equidistant from the furnace wall. A period of approximately 10 minutes was allowed to stabilise thermally, and then the temperature was recorded. The temperature profile for the furnace is given in Figure 3-6.

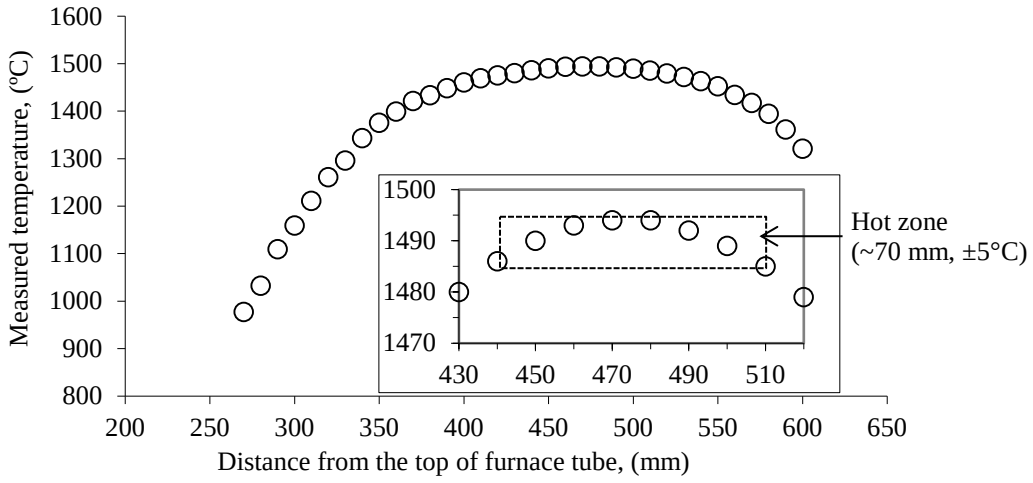

Figure 3-6: The thermal profile for the resistance furnace used to fire the coke analogues. Furnace set point = 1550°C.

A sample experimental temperature was established using the thermocouple/coke analogue set-up given in Figure 3-7. The thermocouple/coke analogue set-up was lowered into the centre of the furnace hot zone (see Figure 3-6). The furnace temperature was then stepped through series of temperature that spanned the coke analogue experimental temperature range. At each temperature, the furnace was left for approximately 30 minutes to stabilise thermally and then the temperature was recorded. This was carried out in an argon atmosphere. A plot of the sample experimental temperature against furnace set temperature is shown in Figure 3-8. The temperature

response measurement was taken in both the steel tube and graphite crucible used in the 1st stage and 2nd stage coke analogue firing regimes respectively.

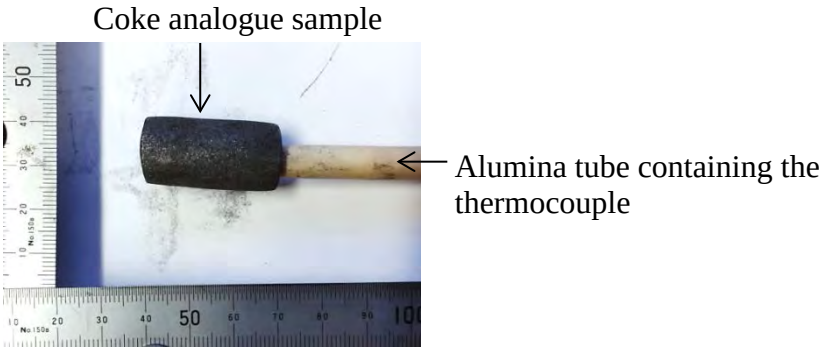

Figure 3-7: The thermocouple/coke analogue set-up used to establish the sample experimental temperature.

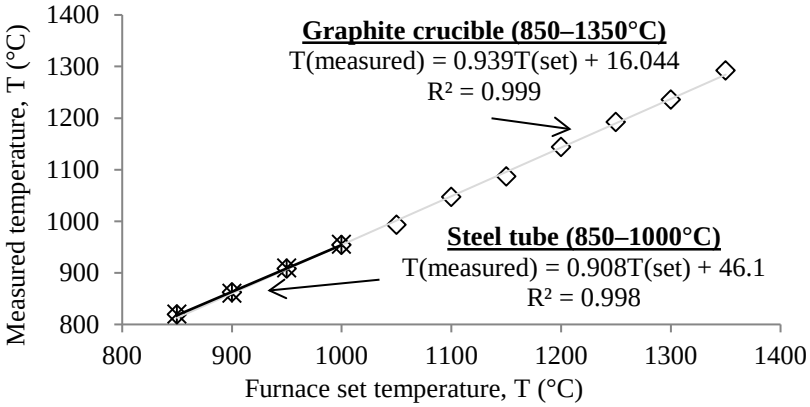

Figure 3-8: A plot of measured temperature versus the furnace set temperature for the coke analogue production furnace. The straight lines are linear fits of the data.

Key output from coke analogue production

The key output from coke analogue production was coke analogues of controlled porosity and metallic iron/minerals composition and dispersion. Full details of the coke analogues produced are given in Table 3-4.

3.2. Characterisation techniques

The characterisation techniques used to evaluate the coke analogues and metallurgical coke are given in Table 3-5.

Table 3-4: The details of the coke analogues produced.

Coke analogue name identifier*	**Metallic iron/minerals added**					**Optical porosity, (%) 10–500µm**
	Name	Particle size or dimension	Concentration, (mol cation/100g C)	Total surface area[#], (m^2/100 g C)	Density, (g/cm^3)	
Base	None	-	-	-	-	29.3±2.3
Metallic iron 5µm	Metallic iron (Fe)	<10µm	0.10	0.903	7.87 [93]	31.8
Metallic iron 46µm	Metallic iron(Fe)	38–53µm	0.10	0.099	7.87 [93]	31.9
Metallic iron 46µm (I)	Metallic iron(Fe)	38–53µm	0.20	0.213	7.87 [93]	31.4
Metallic iron 83µm	Metallic iron(Fe)	75–90µm	0.10	0.055	7.87 [93]	30.9
Low carbon aluminium killed (LCAK) steel	LCAK	2mm x 7mm x 9mm	-	-		-
Magnetite 46µm	Magnetite (Fe_3O_4)	38–53µm	0.10	-	5.17 [93]	29.7
Equivalent Fe from Fe_3O_4 46 µm[+]	-	-	-	0.130	7.87 [93]	-
Magnetite 46µm (I)	Magnetite (Fe_3O_4)	38–53µm	0.16	-	5.17 [93]	30.7
Equivalent Fe from Fe_3O_4 46 µm (I)[+]		-	-	0.213	7.87 [93]	-
Enstatite ferroan ($Mg_{1.56}Fe_{0.44}Si_2O_6$)	Enstatite ferroan ($Mg_{1.56}Fe_{0.44}Si_2O_6$)	38–53µm	0.10	0.221	3.38 [240]	31.3
Phlogopite ferroan $[K(Mg,Fe)_3(Al,Fe)Si_3O_{10}(OH,F)_2]$	Phlogopite ferroan $[K(Mg,Fe)_3(Al,Fe)Si_3O_{10}(OH,F)_2]$	38–53µm	0.10	0.262	3.00 [93]	28.7
Quartz (SiO_2)	Quartz (SiO_2)	38–53µm	0.10	0.318	2.65 [93]	28.5

*The coke analogue name identifier will be used to refer to the coke analogues in this thesis.

[#]The total surface area was calculated using the mass and density of the metallic Fe/minerals added. Assuming the mean of the particle size range can be used to characterise the diameter of the metallic Fe/mineral and approximation of spherical particles.

[+]The total surface area has been corrected to compensate for the reduction of Fe_3O_4 as green addition to Fe after the firing process and assuming no loss of metallic Fe content. The mass of Fe after firing and the density of Fe were used to calculate the change in the total surface area.

Table 3-5: A summary of the characterisation techniques used in this work and the samples they were used to measure.

Characterisation techniques	**Coke analogues**											**Metallurgical coke**
	Base	Metallic iron 5µm	Metallic iron 46µm	Metallic iron 46µm (I)	Metallic iron 83µm	LCAK	Magnetite 46µm	Magnetite 46µm (I)	Enstatite ferroan	Phlogopite ferroan	Quartz	
Raman spectroscopy	√	√	√	–	√	–	√	–	√	√	√	√
Optical microscopy combined with image analysis	√	√	√	√	√	–	√	√	√	√	√	√
SEM–EDS	√	√	√	–	√	–	√	–	√	√	√	–
Non-polarised optical microscopy	√	√	√	–	√	–	√	–	√	√	√	√
Polarised optical microscopy	√	–	–	–	–	–	–	–	–	–	–	–
Hg porosimetry	√	–	–	–	–	–	√	–	–	–	–	–
Neutron radiography (Dingo)	√	–	√	–	–	–	√	–	–	–	√	√
XRD	√	√	√	√	√	–	√	√	√	√	√	–
LECO carbon and sulphur	–	–	–	–	–	√	–	–	–	–	–	–

√ carried out, – not measured.

3.2.1. General sample preparation for the coke analogue characterisation

A polished sample surface is required for the Raman spectroscopy, optical and electro-optical microscopy and optical porosity. A step by step guide for sample preparation for the coke analogue characterisation is given as follows,

- A mark was created on the side of the coke analogue (see Figure 3-9).

  Note, the mark was used as reference position to aid navigation on the coke analogue surface.

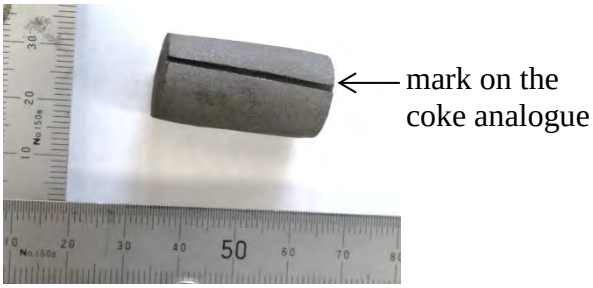

Figure 3-9: The set-up used to establish the coke analogue sample reference position.

- The coke analogue was sectioned at ~10mm depth from the top of the sample (see Figure 3-10).

  Note, an automated Struer Accutom-50 precision cutter was used to section the coke analogues. The cutter wheel and feed speed used were 3000 rpm and 0.10mm/s respectively.

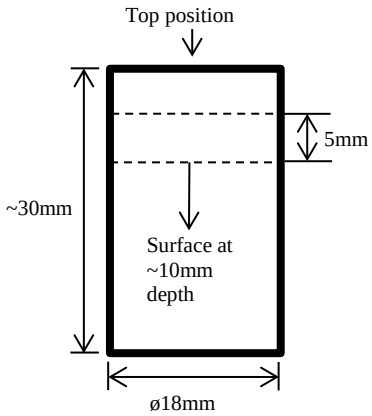

Figure 3-10: A schematic of the set up used to establish the coke analogue sample sectioning position.

- The coke analogue disc was mounted in epoxy resin.

- A vacuum chamber was used to impregnate the coke analogue with resin. The chamber was evacuated for 1 minute and then after 10 minutes the sample removed.
- Grinding and polishing (see Table 3-6 for the coke analogue grinding and polishing schedule).

Table 3-6: The coke analogue grinding and polishing schedule.

Stages	Grit	Surface	Schedule	Force (N)	Lubricant	Time (mins)
1	P500*	Silicon carbide paper	Grinding	20	Distilled water or glycol resin[#]	1.5
2	P1200	Silicon carbide paper	Grinding	20	Distilled water or glycol resin[#]	0.5
3	9µm	MD-Largo	Polishing	20	Struers DP-Lubricant green suspension	4
4	3µm	MD-Dac	Polishing	20	Struers DP-Lubricant green suspension	3
5	1µm	MD-Dur	Polishing	15	Struers DP-Lubricant green suspension	3
6	0.25µm	MD-Dur	Polishing	10	Struers DP-Lubricant green suspension	4

*Continue until the resin and marks from the cutting are no longer visible on the sample surface.
[#] Distilled water for samples prepared for optical porosity measurement but glycol resin for samples prepared for Raman spectroscopy, optical microscopy and SEM–EDS measurements.

3.2.2. Optical microscopy technique

Non-polarised and polarised optical microscopies were used to characterise both the coke analogues structure and identify metallic iron and minerals in the coke analogues. The surfaces of samples characterised with these techniques were prepared using the general sample preparation approach described in section 3.2.1.

Non-polarised microscopy

A Leica DM/RM optical microscope equipped with a Leica DFC295 digital camera (see schematic given in Figure 3-11) was used to take non-polarised optical micrographs of the coke analogues in unreacted and reacted conditions.

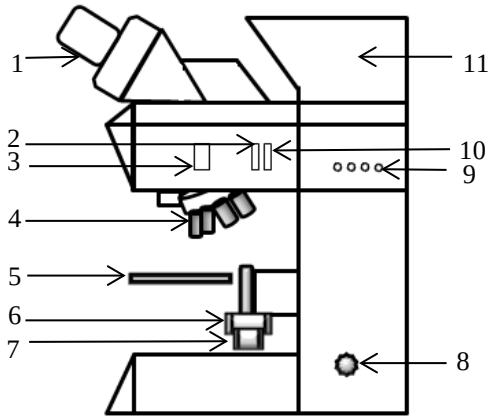

1	Eye piece
2	Field diaphragm
3	Reflector
4	Objective
5	Sample stage
6	Y- stage orientation
7	X- stage orientation
8	Focus knob
9	Filter magazine
10	Aperture diaphragm
11	Leica DFC295 digital camera

Figure 3-11: A schematic of Leica DM/RM optical microscope [241].

Unreacted coke analogues

To ensure representative characterisation of the coke analogues microstructure, 20 micrographs were taken from the surface of all the polished samples. The approximate positions where the micrographs were taken is given in Figure 3-12. The micrographs were acquired at 250x magnification.

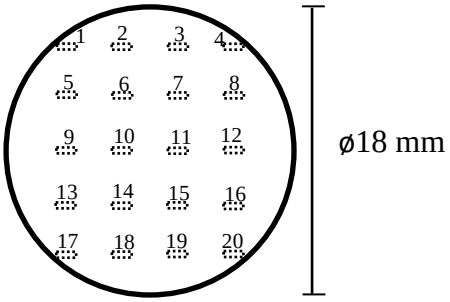

Figure 3-12: A schematic of the positions where the micrographs were taken on the sample horizontal cross section. The boxes numbered 1–20 represent the approximate positions of the micrographs.

Reacted coke analogues

The horizontal and vertical cross sectional approaches were adopted to assess the reacted coke analogues. The micrographs were acquired at 50x magnification to ensure wider coverage. Micrographs of the unreacted samples were also taken at 50x magnification for comparison.

- **An horizontal cross sectional approach**

A schematic of the approximate positions where the micrographs were taken was given in Figure 3-12.

- **A vertical cross sectional approach**

A schematic of the approximate positions where the micrographs were taken is given in Figure 3-13.

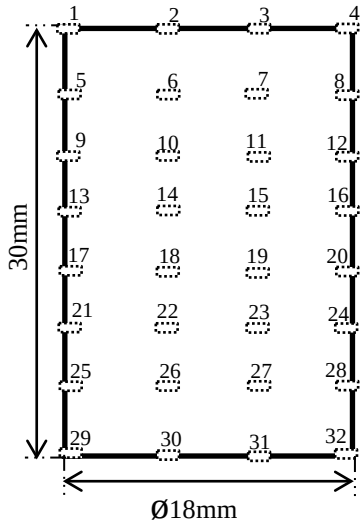

Figure 3-13: A schematic of the positions where the micrographs were taken on the sample vertical cross section. The boxes numbered 1–32 represent the approximate positions of the micrographs.

Polarised microscopy

A Leitz orthoplan microscope (see schematic given in Figure 3-14) was used to take polarised optical micrographs of the coke analogues in unreacted and reacted conditions. The microscope was set up in accordance with the ASTM D5061-07 'standard test method for microscopical determination of the textural components of metallurgical coke'* [242].

*Assistance from Harold Rogers, a coke reactivity expert, is acknowledged for this measurement

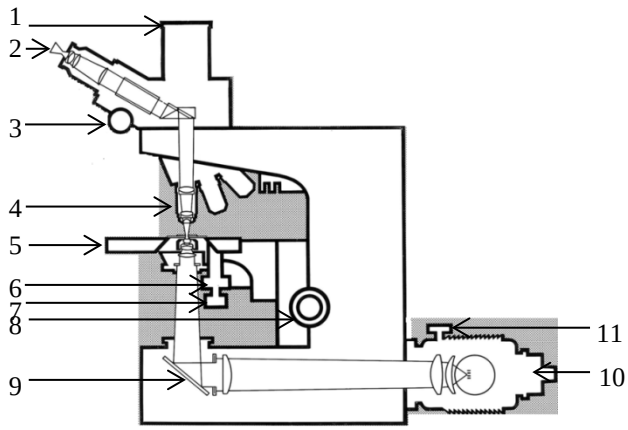

1	Removable cover for photo tube
2	Eyepiece
3	Interpupillary distance adjustment knob
4	Objective
5	Sample stage
6	Y- stage orientation
7	X- stage orientation
8	Focus knob
9	Mirror
10	Lamp for incident light
11	Incident light adjustment knob

Figure 3-14: A schematic of Leitz orthoplan microscope [243].

Unreacted coke analogues

The polarised optical micrographs were taken from random positions on the unreacted base coke analogue to characterise its carbon microstructure. The micrographs were taken using an oil immersion objective lens.

Reacted coke analogues

The polarised optical micrographs were also taken from the external surface of the coke analogues (base, metallic iron 46µm, magnetite 46µm and quartz) reacted in CO_2 at 1100°C for 20 minutes to characterise their microstructure. The micrographs were taken with air objective lens.

Key outputs of the optical (polarised and non-polarised) microscopy

- A representative characteristic feature of the coke analogues microstructure,
- Identification and distribution of the metallic iron and mineral in the coke analogues, and
- Selective reactivity features of the coke analogues.

3.2.3. SEM-EDS analysis

Three different SEM-EDS systems were utilized in this study to meet specific analysis requirements for the coke analogues in unreacted and reacted conditions. The details of the SEM-EDS systems used in this work and the coke analogues they were used to analyze are given in Table 3-7.

Table 3-7: The details of the SEM-EDS systems used in this work and the coke analogues they were used to analyse.

SEM instrument	**EDS system software**	**Coke analogues**	**Sample preparation**
JEOL JSM 6490 LV SEM	Aztec Energy microanalysis software from Oxford Instruments	See Table 3-5	In accordance with the approach described in Section 3.2.1 and then carbon coated.
ZEISS EVO 50 SEM	INCA system energy dispersive analysis (standardless software) from Oxford Instruments	The external surface of coke analogue–Fe 46µm reacted in CO_2 at 1100°C for 20 minutes	In accordance with the approach described in Section 3.2.1 and then gold coated.
Neoscope SEM-JSM 6000	Energy dispersive x-ray (EDS) analysis from JEOL	Non-carbonaceous materials used to make the coke analogue (see Figure 3-1)	Carbon coated.

The significance of the ZEISS EVO 50 SEM instrument

The instrument can provide indicative values of oxygen/iron ratios[†]. The atomic oxygen/iron ratio $\frac{O^*}{Fe}$ was calculated using equation 3-1 [244],

$$\frac{O^*}{Fe} = \frac{\text{EDS O atom\% - (O atom\% associated with coexisting elements in typical oxide stoichiometry)}}{\text{EDS Fe atom\%}} \quad 3\text{-}1$$

Typical values for iron oxide phases are given in Table 3-8.

[†] Assistance from Harold Rogers is acknowledged for this measurement

Table 3-8: An atomic oxygen/iron ratio $\frac{O^*}{Fe}$ for iron oxide phases [244].

Phase(s)	$\frac{O^*}{Fe}$	$\frac{O}{Fe}$ (Stoichiometry)
Iron	~0(<0.1)	0
Wustite	~1.0 (typical range 0.8–1.2)	1
Magnetite	~1.5 (typical range 1.2–1.8)	1.33
Hematite	~2.0 (typical range (1.8–2.2)	1.5

Key outputs of the SEM-EDS analysis

- general micrographic characterisation,
- EDS elemental maps, and
- EDS composition of spot analyses.

3.2.4. Raman spectroscopy technique

A Jobin Yvon (JY–HR800) Raman micro-spectrometer unit (see schematic given in Figure 3-15) was used to characterise the carbon bonding of the coke analogues. The main components of the instrument are detailed in the figure. The specific samples analysed are given in Table 3-5. The surfaces of samples characterised with this technique were prepared using the general sample preparation approach described in section 3.2.1.

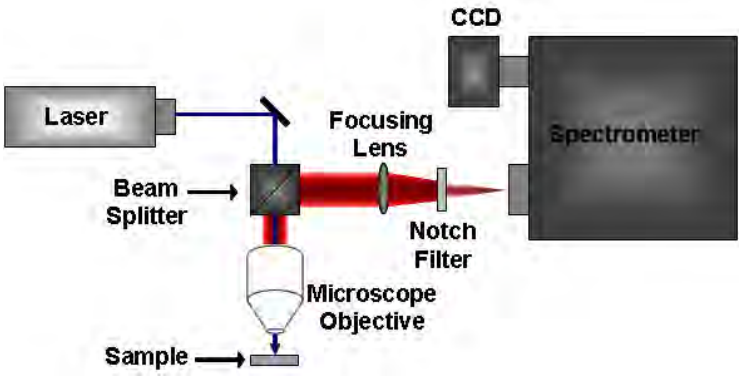

Figure 3-15: A schematic of the Raman instrument [245].

The Raman microscope enables convenient image characterisation of the sample surface and acquisition of Raman spectra from the same area. Prior to carbon bonding

measurements, the instrument was calibrated with a standardised silicon sample. The Raman calibration settings are listed in Table 3-9.

Table 3-9: A list of Raman calibration settings used in this work

Raman parameters	**Calibration settings**
Laser wavelength	632.81 nm
Filter	None
Hole	1100µm
Slit	200µm
Grating	300
Spectrometer	1154.82 cm^{-1}
Objective lens	100x
Exposure time	2 seconds
Extended scan exposure time	2 seconds
Accumulation number	5
Peak position	520±0.8 cm^{-1}

A LabSpec 6 application package, version 5.45.09 [246] was used to take spectra from the samples. The spectra were acquired over an acquisition range of 500–3500cm^{-1}. The software also generated quantitative information such as the Raman band positions and the intensities of the bands. A typical spectrum showing the band positions and the intensities of the bands for a coke analogue is given in Figure 3-16.

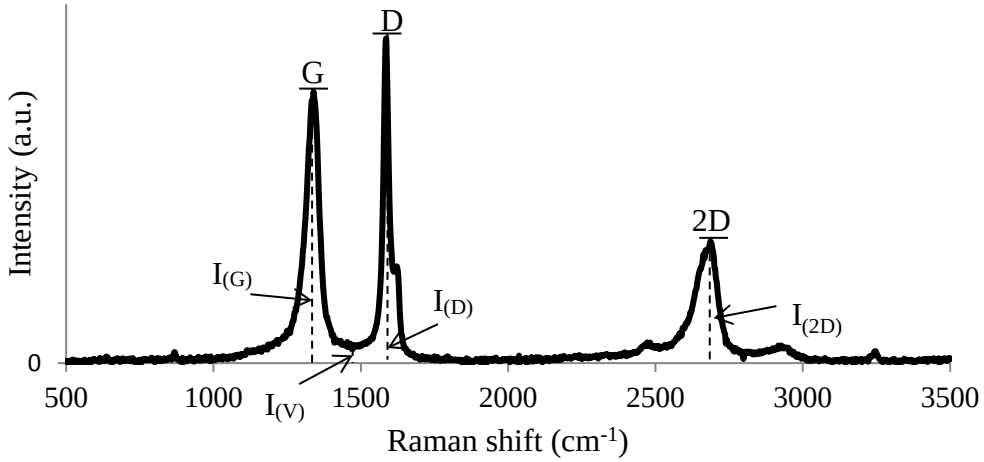

Figure 3-16: A schematic of a typical Raman spectrum for the coke analogue, showing the D, G, V and 2D band positions. $I_{(D)}$, $I_{(G)}$, $I_{(V)}$ and $I_{(2D)}$ are intensities of the bands.

The quantitative information derived from Figure 3-16 and used in this study were the,

- D, G, V and 2D band positions, and
- ratio of the intensities (I) of the bands [$I_{(D)}/I_{(G)}$ and $I_{(V)}/I_{(G)}$].

The Raman bands are related to carbon bonding and the relationship is given in Table 3-10.

Table 3-10: The relationship between Raman band positions and carbon bonding.

Band name	Band Position (cm^{-1})	Bond type	References
D	~1335	sp^2	[18, 116, 126, 129, 136, 138]
V	~1480	sp^2, sp^3	[18, 116, 129, 131]
G	~1590	sp^2	[18, 116, 123, 136, 138]
2D	~2680	sp^2	[116, 136]

Coke analogue carbon bonding measurement

The bulk and localised Raman measurements around metallic iron and mineral approaches were adopted to measure the carbon bonding of the coke analogues. The measurements were taken from the areas that are typical of the coke analogues. The typical areas were identified using the approach described in section 3.2.2 for the unreacted coke analogues.

Bulk measurement approach

For the bulk Raman measurement, approximately 150 spectra were taken from the surface of each coke analogue. The positioning of the laser was carried out manually on the coke analogue with the aid of the in-built microscope. Areas of mounting resin, voids and metallic iron and minerals were avoided in the measurement. The measurement was taken at a distance that was >5µm from the metallic iron and minerals in the coke analogue. This approach was also used on the individual carbonaceous materials used to make the coke analogue (see Table 3-1) and on the metallurgical coke. The plot of the $I_{(D)}/I_{(G)}$ versus $I_{(V)}/I_{(G)}$ was used to resolve the carbon bonding from the bulk measurement as discussed in section 2.2.2 (literature review chapter).

Localised measurement around metallic iron/mineral particle approach

This approach was applied to the coke analogues containing metallic iron and minerals. The measurement was carried out in the vicinity of the metallic iron and mineral particles (see schematic given in Figure 3-17), but at a distance that was >0.5µm from the particles. This minimised the possibility of compromising the carbon bonding measurement with the metallic iron and minerals. The point and radial measurements were adopted to resolve the carbon bonding nearer the metallic iron and minerals.

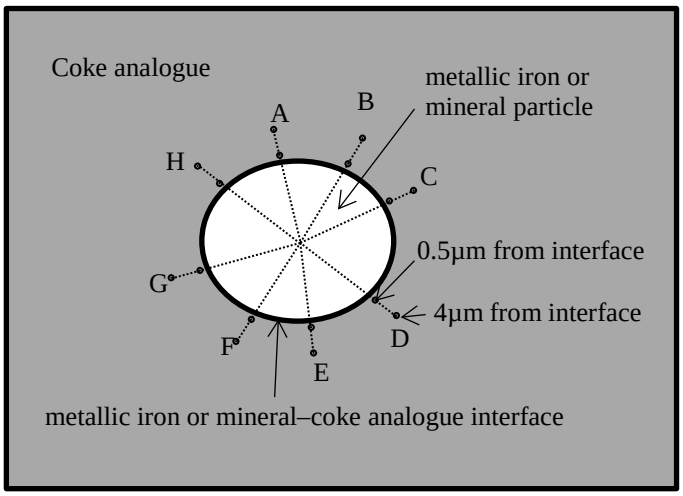

Figure 3-17: A schematic showing positions of localized measurements around metallic iron/mineral in the coke analogue. The positions were labelled clockwise and alphabetically.

- **Point measurement**

In the point measurement around the metallic iron and minerals, approximately 10 positions were measured in each coke analogue. The measurement was taken at a distance of 0.5µm and 4µm from the metallic iron or mineral–coke analogue interface. The plot of the $I_{(V)}/I_{(G)}$ versus Raman position was used to resolve the carbon bonding from the point measurement because it indicated progression or changes in sp^2–sp^3 carbon bonding. The plot of $I_{(D)}/I_{(G)}$ versus Raman position was not effective to resolve the carbon bonding from the point measurement due to its low sensitivity to changes in carbon bonding. A typical example of $I_{(D)}/I_{(G)}$ versus Raman position, and $I_{(V)}/I_{(G)}$ versus Raman position plots around Fe–coke analogue interface is given in Figure 3-18.

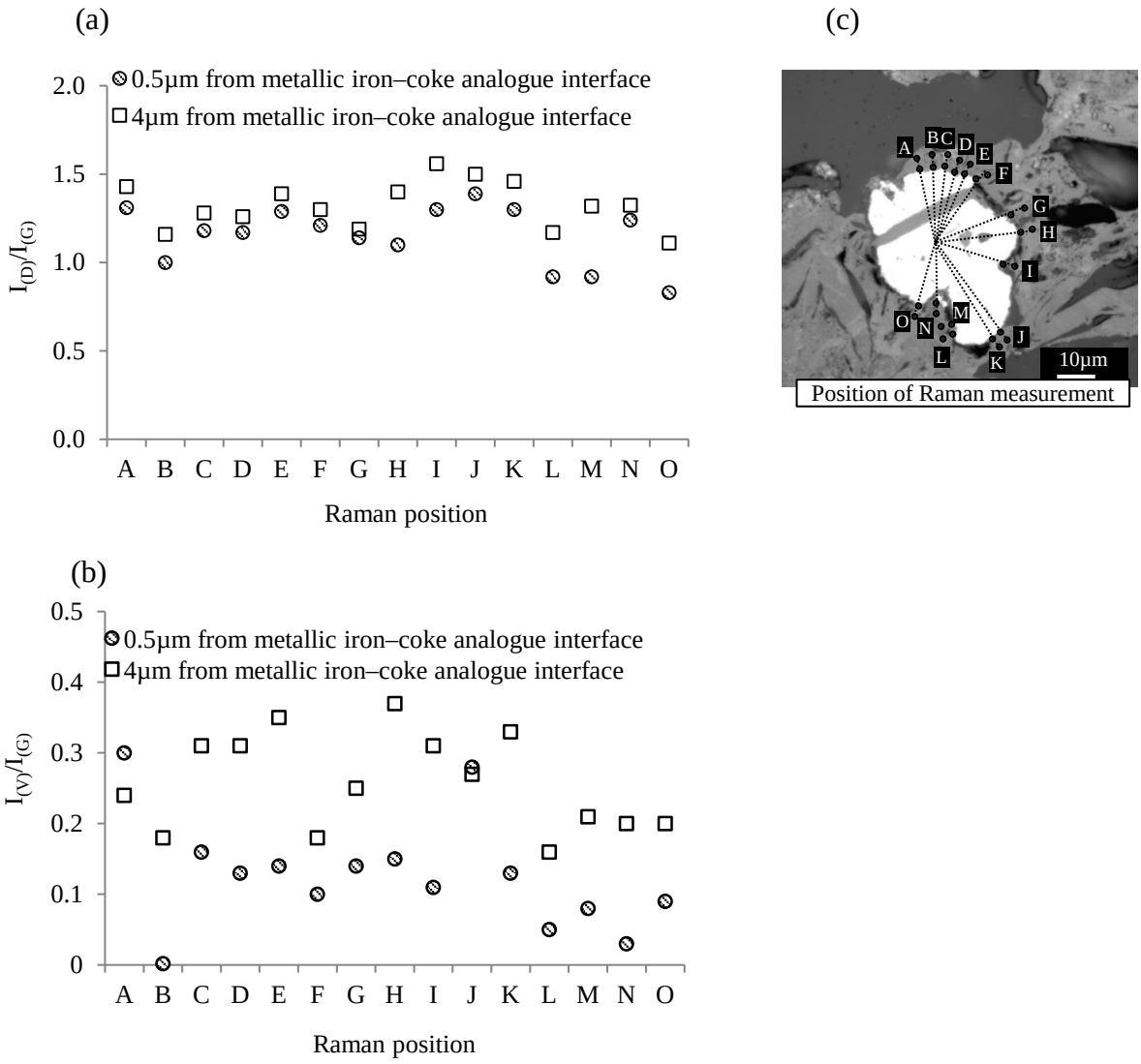

Figure 3-18: (a) A plot of $I_{(D)}/I_{(G)}$ versus Raman position around Fe particle, (b) a plot of $I_{(V)}/I_{(G)}$ versus Raman position around iron particle and (c) non-polarised optical micrograph showing position of localised Raman measurements in coke analogue–Fe 46µm.

- **Radial measurement**

The radial measurement around the Fe and mineral particles was taken at 0.25µm intervals, starting at 0.5µm from the interface and ending at 4µm from the interface. The plot of the $I_{(V)}/I_{(G)}$ versus distance from Fe or mineral–coke analogue interface was used to resolve the carbon bonding from the radial measurement. Figure 3-19 shows a typical measurement using this approach.

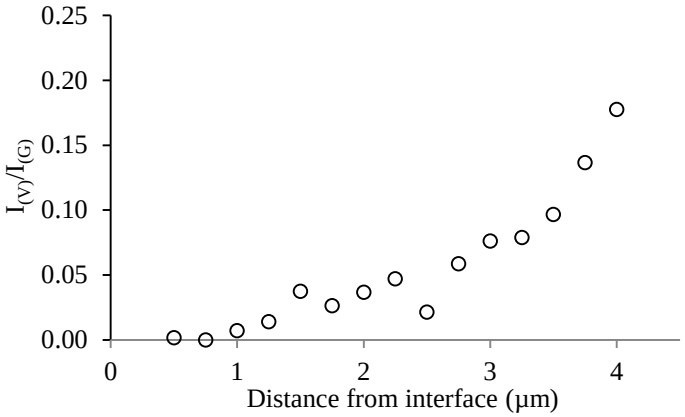

Figure 3-19: The plot of $I_{(V)}/I_{(G)}$ versus distance from the Fe–coke analogue interface at position B of the optical image given in Figure 3-18(a).

Key outputs of the Raman measurement

- The Raman spectra of the coke analogues, carbonaceous materials used to make the coke analogue and metallurgical coke, and
- The data relating to sp^2 and sp^3 carbon bonding of the coke analogues, carbonaceous materials used to make the coke analogue and metallurgical coke.

3.2.5. Optical microscopy combined with image analysis

A Leica DM/RM optical microscope equipped with a Leica DFC295 digital camera (see schematic given in Figure 3-11) was used to take the micrographs used to measure the optical porosity of the coke analogues. The specific samples are given in Table 3-5. The micrographs were taken using a high intensity green filtered light by selecting only the green channel on the filter magazine (see Figure 3-11) of the Leica microscope. The surface of the coke analogues was prepared for optical porosity using the approach described in section 3.2.1. The only modification to section 3.2.1 was the number of surfaces prepared (see schematic given in Figure 3-20(a)).

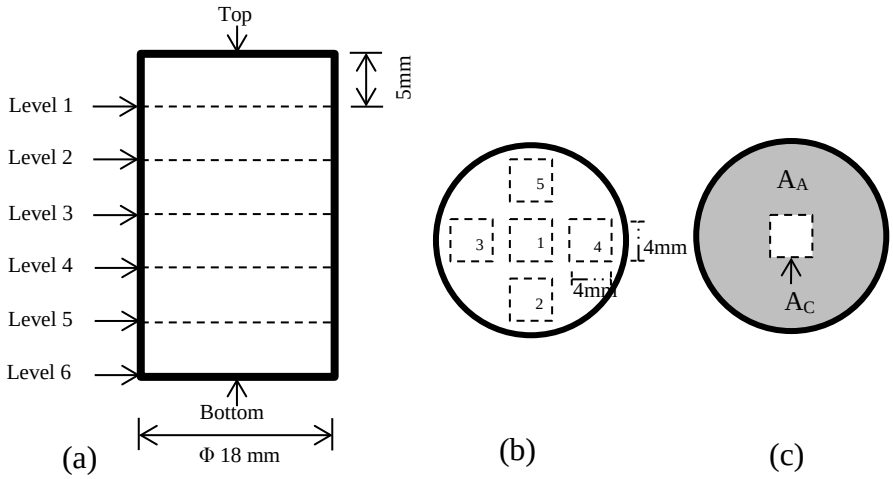

Figure 3-20: A schematic of the set up used to establish the sample sectioning positions, showing (a) vertical positions prepared for measurement (b) radial positions where the micrographs were obtained, and (c) showing areas A_A and A_C.

Using three base coke analogue samples, the porosity at positions '2' to '5' were similar and have been assumed to be the same, while in some cases position '1' is larger. The optical porosity was calculated as follows,

$$\text{Area of the coke analogue surface, } A_S \text{ (Figure 3-20(c))} = \pi r^2 = 254.5\text{mm}^2 \quad 3\text{-}2$$

$$\text{Area of the coke analogue centre, } A_C \text{ (Figure 3-20(c))} = L^2 = 16.0\text{mm}^2 \quad 3\text{-}3$$

$$\text{Area of the coke analogue annulus, } A_A \text{ (shaded area of Figure 3-20(c))} = \pi r^2 - L^2 = 238.6\text{mm}^2 \quad 3\text{-}4$$

where r, radius of the coke analogue is 9 mm, and L, length of the micrograph/position where the micrographs were taken, is 4 mm. r and L were constants for all coke analogues.

The optical porosity of the coke analogue, P_{OP}, is expressed as,

$$P_{OP} = \frac{A_C}{A_S} \times P_1 + \frac{A_A}{A_S} \times P_a \quad 3\text{-}5$$

$$P_{OP} = 0.063\,P_1 + 0.937 P_a \quad 3\text{-}6$$

where P_1, is the porosity value at the coke analogue centre, position '1'. P_a, is the porosity value at the coke analogue annulus. P_a could be any of positions '2' to '5'.

To obtain a micrograph of 4 mm x 4 mm, a total of 12 micrographs were taken at 50x magnification, stitched together and cropped. The micrograph was then processed using ImageJ application package version 1.48 [247] (see Table 3-11 for settings). The ImageJ software was then used to measure percentage porosity, excluding pores with an equivalent diameter <10µm (considered unreliable at the magnification used) and pores with an equivalent diameter >500µm (considered to be fissures rather than porosity). An example of optical micrograph used for optical porosity measurement set up is given in Figure 3-21.

Table 3-11: A list of ImageJ settings used for optical porosity measurements.

Parameter	**Settings**
Threshold color	Hue (0, 255) Saturation (0, 255) Brightness (0, 123)
Thresholding method	Default
Threshold color	Red
Color space	HSB

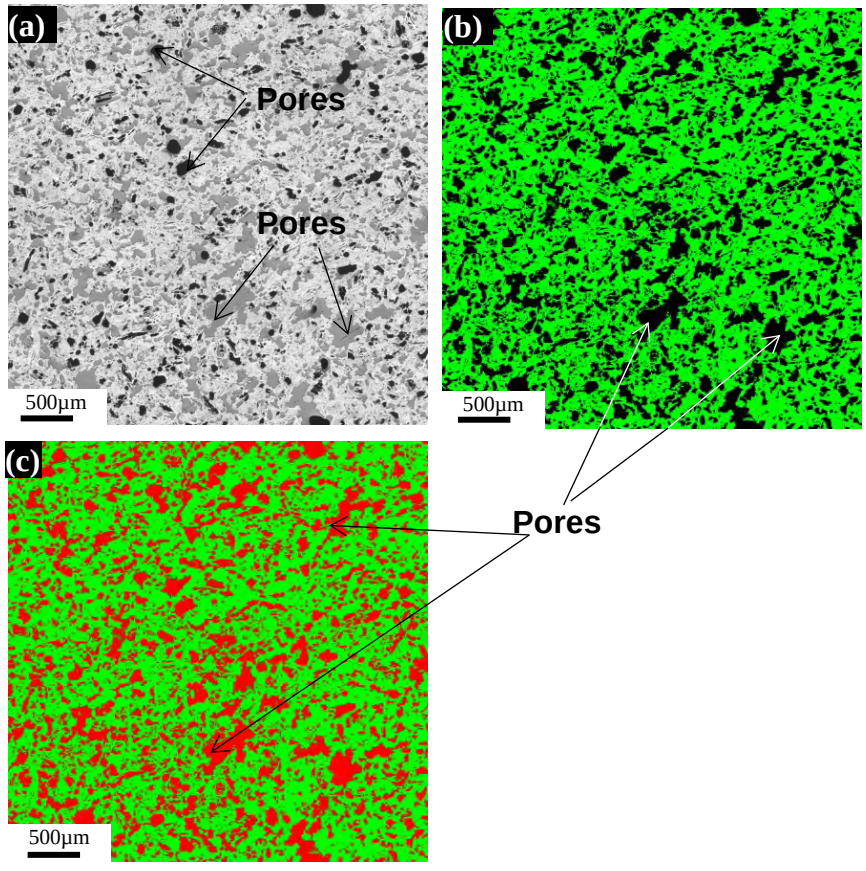

Figure 3-21: An example of optical micrograph of the base coke analogue used for optical porosity measurement set up, (a) without filter, (b) with green filter and (c) ImageJ processed image.

The error associated with the optical porosity of the coke analogue has been determined by using three base coke analogue samples from two different batches. The optical porosity of the three base coke analogue samples was 29.3%, and the variance associated with the optical porosity is ±2.3%. There was no significant variation in porosity along the length of the coke analogue, though values measured for area 1, the center of the analogue (see Figure 3-20(b)) tended to be marginally greater than areas 2 to 5 near the wall. The optical pore size distribution of the three base coke analogue samples is given in Figure 3-22.

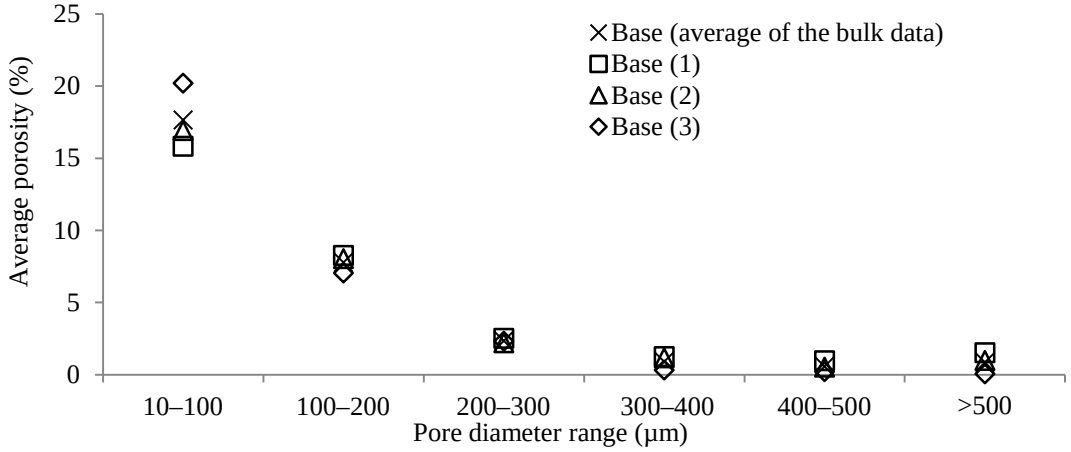

Figure 3-22: The average optical pore size distribution in the vertical and radial sections of the three base coke analogues compared to the average of the bulk data. (1) and (2) from the same batch and (3) from a different batch.

After establishing the error associated with this method, surface at ~10mm depth or level '2' of Figure 3-20(a) was prepared for optical porosity for the rest of the coke analogues produced in this study. The statement of error and uncertainty that comes from a more extensive investigation is detailed in the results and discussion chapters.

Correction for minerals in the coke analogue optical porosity

To correct for minerals that were identified as pores in the optical micrographs, backscattered electron micrographs of the same position were taken (see Figure 3-23). In this study, only quartz particles showed this effect. The phase expert tool of Leica Application Suite, version 4.0.0 [241] was then used to quantify the area% of the quartz

in the backscattered micrograph of the coke analogue. The area% of the quartz was subtracted from the optical porosity of the coke analogue–quartz.

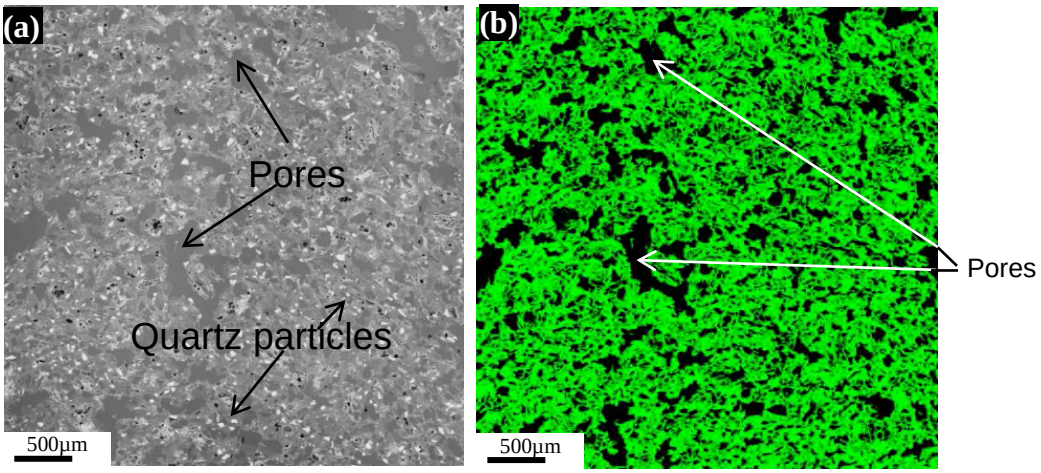

Figure 3-23: An example of set up used to correct for quartz in the optical porosity of the coke analogue–quartz, (a) SEM backscattered micrograph and (b) optical micrograph taken with green filter.

Reacted coke analogues

The optical porosity of base coke analogue and coke analogue–metallic iron 46µm reacted in CO_2 at 950°C for 1 hour were also measured in this study.

Metallurgical coke optical porosity

The optical porosity of the metallurgical coke used in this study was also measured using the approach similar to the coke analogue. The three samples were prepared from two batches of the same metallurgical coke. The sample positioning (vertical and radial) on the metallurgical coke was arbitrary.

Key output of the optical porosity measurement

The key output of the optical porosity was the evaluation of pores with equivalent diameter range 10–500µm.

3.2.6. Mercury porosimetry

A Micrometrics Autopore 9600 Mercury Porosimeter was used to further characterise the porosity of three base coke analogues from two batches and a coke analogue–magnetite 46µm. Coke analogue–magnetite 46µm was measure to specifically check whether the reduction of magnetite (Fe_3O_4) to iron (Fe) during the coke analogue firing have any effect on porosity. The measurement was carried out external to the University by Particle and Surface Science Pty Limited, Gosford, New South Wales, Australia. The measurement procedure complied with the Standard ISO 15901-1 ‘pore size distribution and porosity of solid materials by mercury porosimetry and gas adsorption’ [248].

Key output of the mercury porosimetry

The primary output from this measurement was the evaluation of pores with equivalent diameter range <10µm (not measured with the optical method).

3.2.7. Neutron radiography (Dingo)

Neutron radiography (Dingo) instrument located at Australian Centre for Neutron Scattering, Australian Nuclear Science and Technology Organization (ANSTO) was used to characterise the coke analogue structure. The specific samples are given in Table 3-5. The samples were characterised in their unreacted and reacted conditions. A high resolution neutron beam set up (see schematic given in Figure 3-24) was used to take radiographs of the samples. The main components of the instrument are detailed in the figure. The radiographs were taken from the samples using the settings given in Table 3-12. The sequence at which the radiographs of each sample were taken is given in Table 3-13.

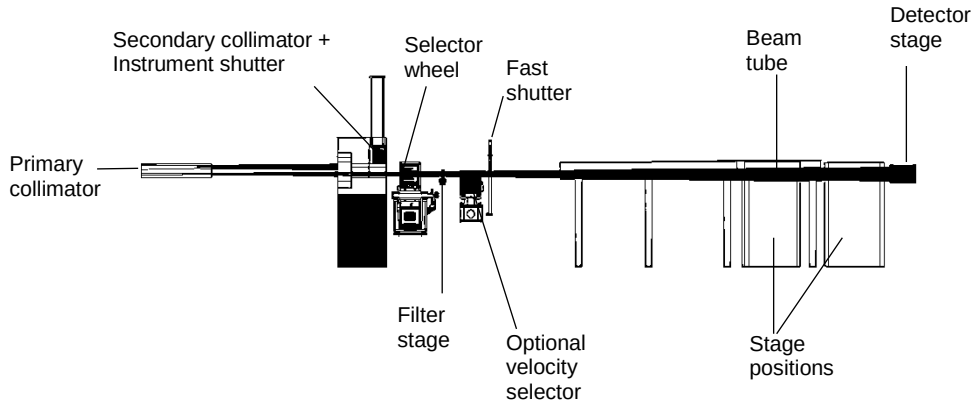

Figure 3-24: A schematic of the high-resolution neutron beam arrangement used to take radiographs from the coke analogues [249].

Table 3-12: A list of neutron radiography (Dingo) instrument settings used to take radiographs of the coke analogues.

Parameters	**Settings**
Acquisition step	0.18°
Acquisition exposure time	50 seconds
Number of steps	1000
Acquisition range	0–180°
Instrument resolution	~26.8µm
Instrument flux	5.3 x 10^7 n/cm^2s
Distance between sample position and detector	3 cm

Table 3-13: A list of the sequence at which radiographs of the coke analogues were taken.

Sequences	**Activities**
1	Neutron radiography (Dingo) of the unreacted coke analogues
2	1st stage reaction (the samples were reacted in CO_2 at 1100°C for 10 minutes)
3	Neutron radiography (Dingo) of the 1st stage reacted coke analogues
4	2nd stage reaction (the samples were further reacted in CO_2 at 1100°C for 10 minutes)
5	Neutron radiography (Dingo)of the 2nd stage reacted coke analogues

The Octopus reconstruction package version 8.8.2 [250] was used to produce 3D images of the coke analogue from 2D sections. The image resolution was ~26.8µm. After reconstruction, the VGStudio MAX application package [251] was used to render images of different slice thicknesses of the coke analogue. An example of the images of

the base coke analogue is given in Figure 3-25. The image models were created using the volume rendering tool of the VGStudio MAX package. The settings used are given in Table 3-14.

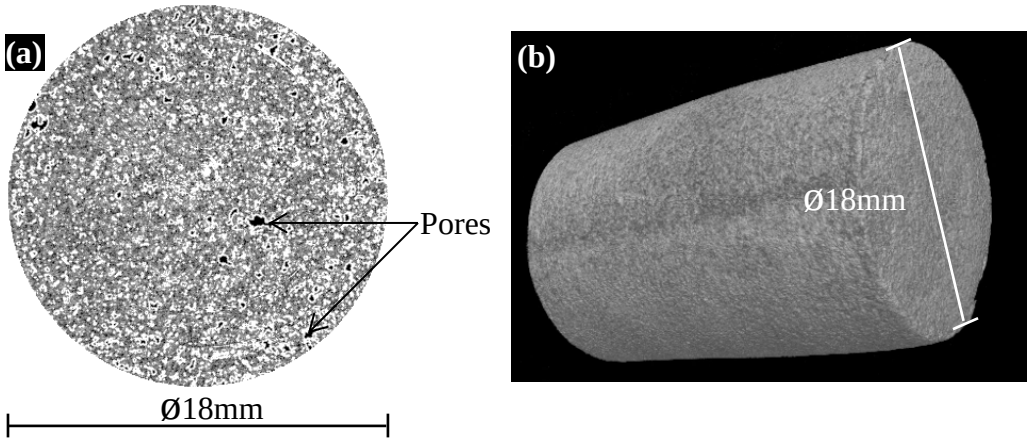

Figure 3-25: An example of the image of the base coke analogue, (a) a single image of ~26.8µm thickness and (b) the whole image of ~30 mm height.

Table 3-14: A list of volume rendering tool settings used to create the image models.

Parameters	Settings
Opacity manipulation region	42200
Appearance (Intensity)	20
Rendering settings	Isosurface renderer
Oversampling	1.0

Dingo porosity

The VGStudio MAX application package [251] was used to measure the volume% of pores in the coke analogue.

The equivalent diameter of the pore, D, was calculated using equation 3-7,

$$D = \left(\frac{6V}{\pi}\right)^{\frac{1}{3}} \qquad 3\text{-}7$$

where V is the volume of the pore.

The schematic of the position measured for Dingo porosity is given in Figure 3-26. The numbers of images combined to form images of different thicknesses are given in Table 3-15.

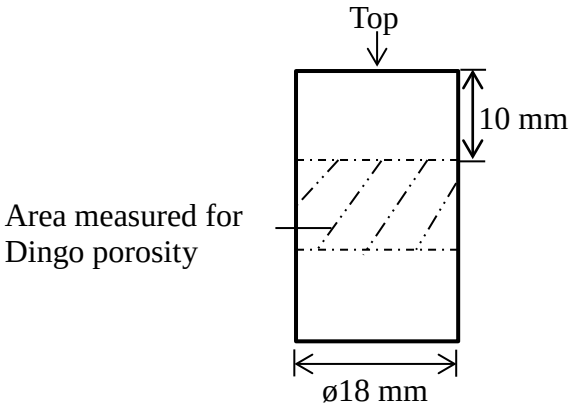

Figure 3-26: A schematic of an area of the coke analogue measured for Dingo porosity.

Table 3-15: A list of numbers of images combined to form varying images of different slice thicknesses

Numbers of image(s)	1	2	4	8	16	25	50	100	200	400
Slice thickness (mm)	0.03	0.05	0.10	0.21	0.43	0.67	1.34	2.68	5.36	10.72

Note, for Dingo porosities, pores with equivalent diameter >500µm were considered and included in the porosity data to evaluate interconnected pores. This was based on the pore distribution data obtained in this measurement. For a single slice (~0.03 mm thickness) there was no pore >500µm diameter but as the slice thickness increases the pore becomes interconnected.

$$\%\ \text{of pores connected} = \frac{\text{porosity of pores with equivalent diameter} > 500\mu\text{m}}{\text{total porosity}} \times 100\% \qquad 3\text{-}8$$

The neutron radiography (Dingo) was also used to measure the Dingo porosity of the metallurgical coke used in this study.

Key outputs of the Dingo porosity measurement

- The porosity values for different slice thicknesses of the analogues, and
- The evaluation of interconnected pores in the analogues.

3.2.8. X-Ray diffraction (XRD)

A GBC MMA XRD unit was used to characterise the phases of non-carbonaceous materials used to make the coke analogue and their stability in the coke analogue system. The coke analogue materials were detailed in Table 3-5. The XRD analysis was carried out with Copper Kα radiation (wavelength λ = 1.54Å). The XRD patterns were recorded using a Visual XRD software ViX122D [231] over 2θ diffraction angle range 20–70°. The patterns are given in Appendix II. The generated patterns were subsequently processed using Trace X-ray processing software V6 combined with the international centre for diffraction data (ICDD) database system [231, 232].

3.2.9. Thermodynamic analysis of the coke analogue systems

The MTDATA thermodynamic software, version 5.10, is a commercial multiphase equilibria thermodynamic software developed at National Physical Laboratory U.K. with ISO 9001 registration [99]. It was used for thermodynamic assessment of the coke analogue system. The databases used in the thermodynamic assessments were SUB_SGTE, SGSOL, NPLOXF, and NPLOX_5NI. Both NPLOXF and NPLOX_5NI are custom databases developed for the University of Wollongong.

3.2.10. LECO carbon and sulphur analysis

A LECO CS444LS analyser was used to measure the mass% of carbon in the LCAK steel removed from the coke analogue system. The LECO combustion analysis for carbon and sulphur content in iron is an established technique [252]. The LECO CS444LS used the HF400 induction furnace and measured carbon and sulphur content by infrared absorption.

The analysis of the iron samples was conducted in accordance with the ASTM E1019 ‘standard test methods for determination of carbon, sulphur, nitrogen and oxygen in iron, nickel and cobalt alloys’ [242] and the relevant LECO application notes [253]. A minimum of two calibrations, using known standards, were used to maintain the

accuracy of the LECO CS444LS instrument. The standards (given in Table 3-16) were chosen such that they spanned the range of carbon expected and measured in this study. The plot of carbon content (mass %) for the measured values versus the certified values for standards used are given in Figure 3-27.

Table 3-16: A list of the standards used to calibrate the LECO CS444LS instrument.

Materials	**Description**	**Source**	**Certified carbon (mass %)**
Blank	-	LECO	-
Standard sample 0.058	Iron rod	Midwest Instrument Co. US	0.058
Pin Standard carbon and sulphur	Iron rod Lot #100	LECO	0.071
Standard sample 0.390	Iron standard Lot #0662	LECO	0.390
Standard sample 0.934	Iron rod	LECO	0.934
Standard sample 82a	Cast iron Nickel-chromium	National bureau of standards US	2.24

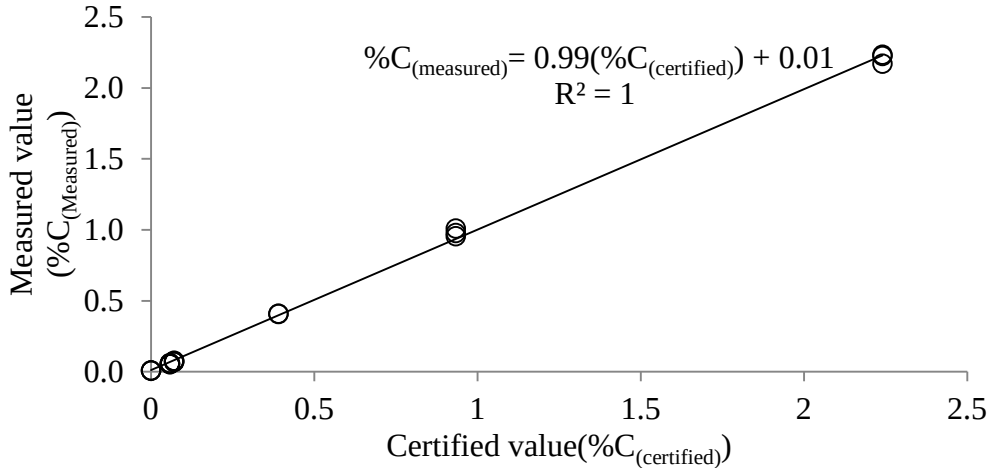

Figure 3-27: The carbon contents (mass %) of the standards used to calibrate the LECO CS444LS instrument.

3.2.11. Particle size analysis for materials used to make the coke analogues

The particle sizes of materials used to make the coke analogues were screened into the required size range using sieves. In most cases, the aggregates were ground to suitable particle sizes in a Labtechnics pneumatic ring grinder. The resulting powder was shaken over nested sieves (see Table 3-17 for size apertures used). The sieves were shaken on a mechanical EFL2000 Endacott Sieve Shaker for approximately 10 minutes. The individual mass retained on each sieve and pan was recorded.

Table 3-17: A list of sieve apertures used for material screening.

Sieve aperture (µm)	Targeted particle size range (µm)	Material
106, 250	100–250	Bakelite
38, 53, 75, 90	38–53 75–90	Non-carbonaceous materials listed in Table 3-2

3.3. Reaction of the coke analogue in CO_2 gas using a large sample thermogravimetric analyser (TGA)

The kinetics of the reaction between the coke analogues and CO_2 were studied using a large sample TGA. The TGA testing was carried out under conditions similar to the commonly used NSC reactivity test indices (CSR and CRI) [220]. See section 2.3.1 (literature review chapter) for more detail of this test.

The TGA system was used to track the weight change of the coke analogue with time and temperature in a CO_2 gas atmosphere. A schematic of the TGA experimental apparatus is given in Figure 3-28 and the alumina pedestal for holding the coke analogue is given in Figure 3-29. The gases (Ar and CO_2) used were high purity (99.99%) and cleaned by passing through calcium sulphate (drierite) and sodium hydroxide–coated silica (ascarite) prior to entering the furnace. The Ar was further cleaned by passing it through copper turnings at 300°C (see Figure 3-4).

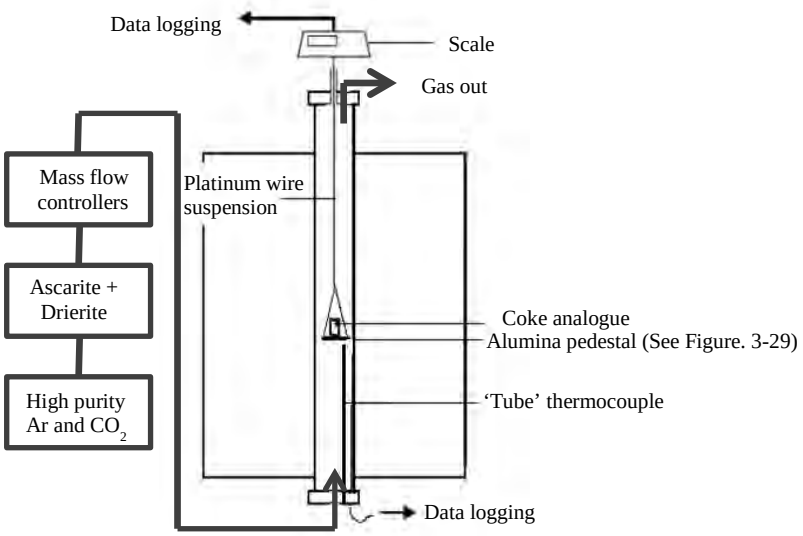

Figure 3-28: A schematic diagram of the TGA system used for the coke analogue reactivity experiments.

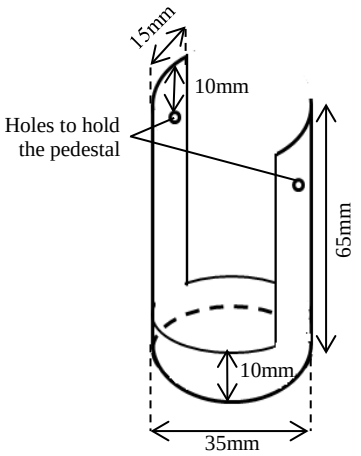

Figure 3-29: A schematic diagram of the alumina pedestal used in the coke analogue reactivity experiments.

3.3.1. Coke analogue reactivity experiment

In the reactivity test, ~8g of the coke analogue, approximately 18mm diameter and 30mm height, was weighed and then placed on an alumina pedestal (Figure 3.29) suspended from a balance in the TGA system using a platinum wire. The experimental temperatures examined in this study were in the range of 900°C to 1350°C. A schematic showing key experimental conditions is given in Figure 3-30, and the summary of the temperature conditions the coke analogues were reacted for is given in Table 3-18.

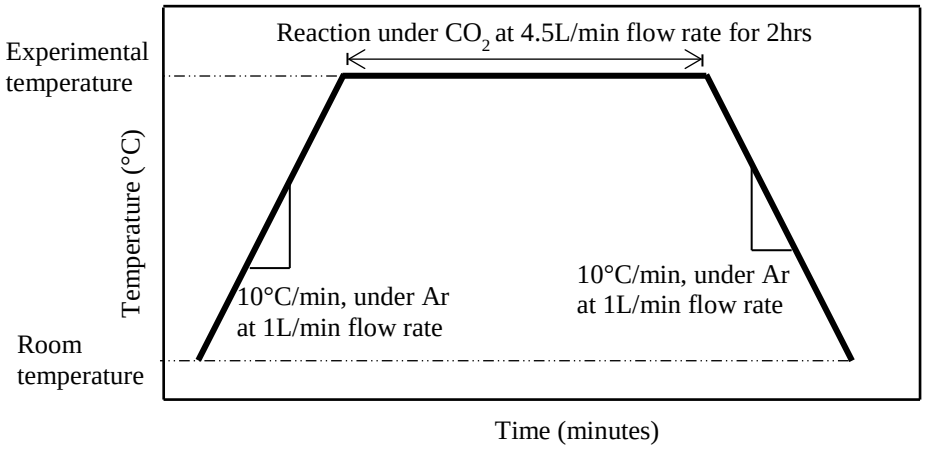

Figure 3-30: A schematic of the gases, gas flow rates and heating/cooling rates used in the coke analogue reactivity experiments.

Table 3-18: A summary of the coke analogues reacted in CO_2 and the temperature range of the reaction.

Coke analogues	**Temperature range (°C)**
Base	900–1350
Metallic iron 5µm	900–1025 and 1100
Metallic iron 46µm	900–1350
Metallic iron 46µm (I)	950 and 1100
Metallic iron 83µm	900–1025 and 1100
LCAK	950 and 1025
Magnetite 46µm	900–1350
Magnetite 46µm (I)	950 and 1100
Enstatite ferroan	900–1350
Phlogopite ferroan	900–1350
Quartz	900–1350

The physical appearances and features of the coke analogues after the reactivity experiments were observed and detailed in the result section.

A typical weight change versus time curve for three base coke analogue samples reacted in CO_2 at 1100°C is given in Figure 3-31. 1100°C is the temperature used in the industrial CRI test and represents an intermediate temperature used in this experimental study. The three samples were used to test for the repeatability of the coke analogue in CO_2. The difference between the average FWC and the FWC of Base 2 (the experiment with the highest variation) is only 0.005. This difference is negligible and demonstrates the repeatability of the coke analogue in the reactivity test.

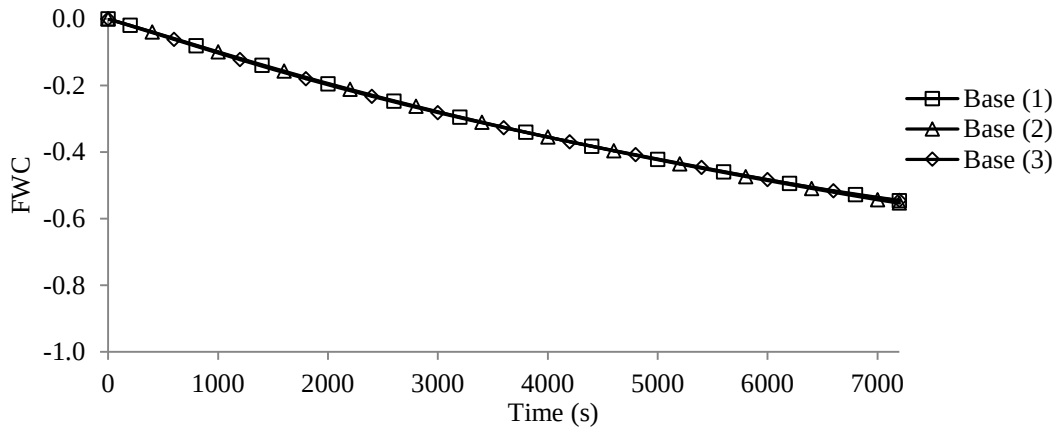

Figure 3-31: A typical weight change versus time plot of three base coke analogue samples at 1100°C for 2 hours. (1) and (2) from the same batch and (3) from a different batch.

A fractional weight change, FWC, of the coke analogue is calculated from the data using equation 2-36 and reproduced in the following text.

$$FWC = \frac{W - W_0}{W_0}$$

A reaction rate, R_C, was calculated using equation 2-21 (reproduced in the following text). The initial linear part of the weight change versus time curve (generally the first 10 minutes, see Figure 3-31) was used to calculate R_C,

$$R_C = \frac{1}{(1 - X)} \frac{dX}{dt}$$

where X is the fractional conversion of the coke analogue and is defined in equation 3-9 [44, 176],

$$X = \frac{W_0 - W}{W_0} = \frac{\Delta W}{W_0} = -FWC \qquad 3\text{-}9$$

The reaction rate, R_C, was evaluated as a function of temperature using the Arrhenius equation given in equation 2-24 (reproduced in the following text) [44, 176, 181, 182],

$$R_C = k_0\, e^{-\frac{Ea}{RT}}$$

equation 3-10, a linear form of equation 2-24, was used to evaluate the reaction mechanism of the coke analogue,

$$\ln(R_C) = -\left(\frac{E_a}{R}\right)\left(\frac{1}{T}\right) + \ln k_0 \qquad 3\text{-}10$$

The TGA system was also used to study the kinetics of the reaction of metallurgical coke used in this study.

3.3.2. Calculation of error associated with coke analogue reaction rate measurements

The reaction rate measurement involves some variables independent of the measurement. The measurement was accompanied with uncertainties independent of each other. These uncertainties were confirmed using the propagation of error formula [253]. For example, if a quantity, F, is a function of variable u and v,

$$F = f(u, v) \qquad 3\text{-}11$$

The total derivation of F is derived from the partial derivative of F with respect to each of the variables and is given in equation 3-12.

$$dF = \left(\frac{\partial F}{\partial u}\right)_v du + \left(\frac{\partial F}{\partial v}\right)_u dv \qquad 3\text{-}12$$

squaring both sides of equation 3-12 gives,

$$(dF)^2 = \left(\frac{\partial F}{\partial u}\right)^2 (du)^2 + \left(\frac{\partial F}{\partial v}\right)^2 (dv)^2 + 2\left(\frac{\partial F}{du}\right)\left(\frac{\partial F}{dv}\right)(du)(dv) \qquad 3\text{-}13$$

the value of the last term on the right-hand side in equation 3-13 is insignificant and the equation can be reduced to equation 3-14,

$$(dF)^2 = \left(\frac{\partial F}{\partial u}\right)^2 (du)^2 + \left(\frac{\partial F}{\partial v}\right)^2 (dv)^2 \qquad 3\text{-}14$$

the equation 3-14 can be considered as the square of the standard deviation and is given in equation 3-15,

$$(\sigma F)^2 = \left(\frac{\partial F}{\partial u}\right)^2 (\sigma u)^2 + \left(\frac{\partial F}{\partial v}\right)^2 (\sigma v)^2 \qquad 3\text{-}15$$

the standard deviation of F is given as [254],

$$\sigma F = \left[\left(\frac{\partial F}{\partial u}\right)^2 (\sigma u)^2 + \left(\frac{\partial F}{\partial v}\right)^2 (\sigma v)^2\right]^{\frac{1}{2}} \qquad 3\text{-}16$$

where σ_u and σ_v are the standard deviation of u and v measurements respectively.

The application of equation 3-16 can be used to derive the errors associated with the R_C, X and ln(R_C) measurements,

from equation 2-21 R_C is a function of variables dX, dt and X,

$$R_C = f(dX, dt, X) \qquad 3\text{-}17$$

by applying equation 3-17, the error of R_C can be estimated using equation 3-18,

$$\sigma R_C = \left[R_C^2\left(\frac{(\sigma dX)^2}{(dX)^2} + \frac{(\sigma dt)^2}{(dt)^2} + \frac{(\sigma X)^2}{X^2}\right)\right]^{\frac{1}{2}} \qquad 3\text{-}18$$

from equation 3-9, X is a function of ΔW and W_0

$$X = f(\Delta W,\ W_0) \qquad 3\text{-}19$$

by applying equation 3-16, the error of X can be estimated using equation 3-20,

$$\sigma X = \left[X^2\left(\frac{(\sigma \Delta W)^2}{(\Delta W)^2} + \frac{(\sigma W_0)^2}{(W_0)^2}\right)\right]^{\frac{1}{2}} \qquad 3\text{-}20$$

where σW_0 was obtained from the TGA scale that has a quantifiable uncertainty associated with the balance and buoyancy effect, σdt was the resolution of the reading, σdX was the error of conversion change and σX was the error of conversion. The values of σW_0 and σdt were ±0.001g and ±1second respectively. The σdX and σX were obtained from the FWC curves.

The error of $\ln(R_C)$ can be estimated by applying equation 3-16,

$$\sigma\ln(R_C) = \left(\frac{\sigma R_C}{R_C}\right) \qquad 3\text{-}21$$

The error associated with $\ln(R_C)$ measurement was ±0.06, while the $\ln(R_C)$ typically was between -8 and -13.

3.3.3. Determination of CO_2 flowrate independent reactivities

The coke analogue reactivity experiment was performed with a CO_2 flow rate that eliminated gas boundary layer control kinetics, thereby being independent of flow rate. The CO_2 independent flow rate was determined through series of coke analogue reactivity experiments using different CO_2 flow rates (stepwise from 1 to 5L/min) at 1350°C (the maximum temperature in the current experimental series). The reaction rate, R_C, at each flow rate was calculated using equation 2-19. A plot of R_C against CO_2 flow rate is given in Figure 3-32. The figure shows that at CO_2 flow rates >4L/min the R_C is independent of the gas flow. Based on these data a CO_2 flow rate of 4.5L/min was used for the reactivity experiments.

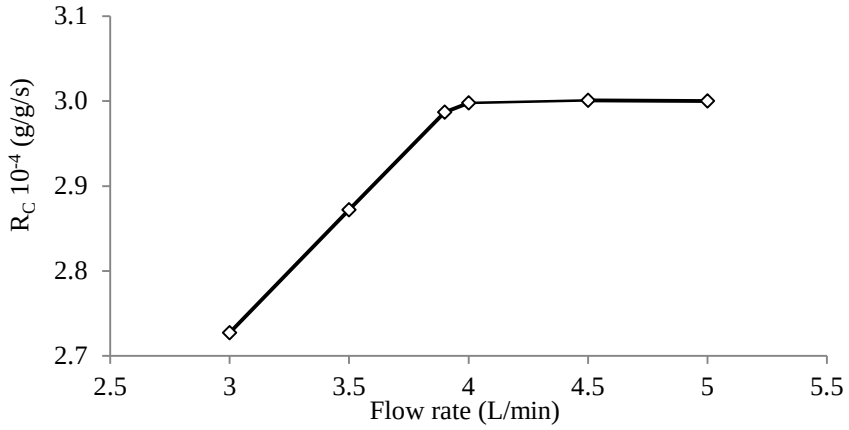

Figure 3-32: A plot of the coke analogue reaction rate against CO_2 flow rate.

3.3.4. Temperature calibration of the TGA furnace

Prior to the reactivity test, the TGA furnace was calibrated with respect to temperature. The thermal profile for the TGA furnace was established to determine the position and length of the stable hot zone. A type R thermocouple was used to measure the TGA furnace thermal profile and temperature response. The TGA furnace thermal profile and temperature response are given in Figures 3-33 and 3-34 respectively. The TGA furnace was calibrated by adopting the approach used to calibrate the coke analogue production furnace (see section 3.1.2).

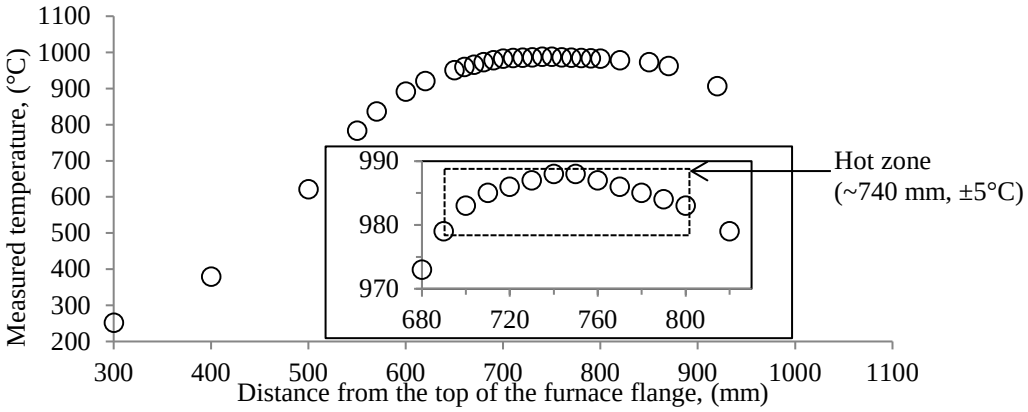

Figure 3-33: The thermal profile of the TGA furnace used in the coke analogue reactivity experiments. The furnace set point was 1000°C.

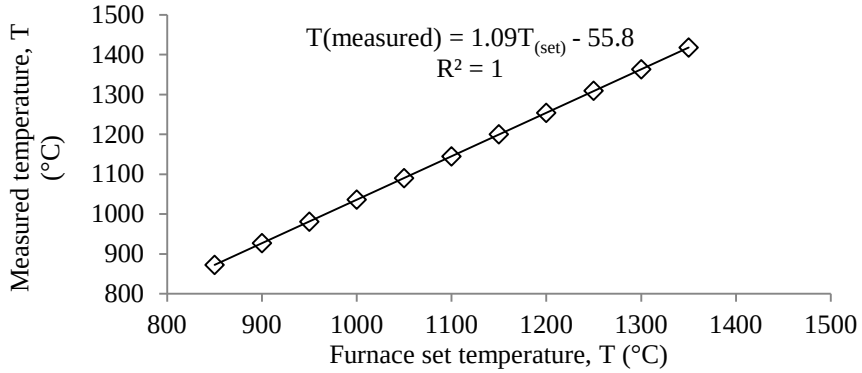

Figure 3-34: A temperature calibration plot for the TGA furnace. The straight line is a linear fit of the data.

Key outputs of the reactivity experiments

- weight change versus time curves,
- reaction rate, R_C, and
- physical appearance of the reacted coke analogues.

3.4. Metallurgical coke

The metallurgical coke used in this study was obtained from BlueScope Australia. The coke contains 0.40–0.45 mass % of sulphur and 11.60–11.80 mass % of mineral matter. A detailed chemical composition of the mineral matter as measured by XRF after ashing of the coke at 815°C is given in Table 3-19.

Table 3-19: The chemical composition of the mineral matter in the metallurgical coke [24].

Mineral Matter	**SiO_2**	**Al_2O_3**	**Fe_2O_3**	**CaO**	**P_2O_5**
Mass (%)	54.80	32.30	4.90	2.90	1.42
Mineral Matter	**MgO**	**K_2O**	**TiO_2**	**Na_2O**	**Mn_3O_4**
Mass (%)	1.00	0.51	1.40	0.38	0.05

The metallurgical coke mineral matter was quantified by SIROQUANT method [254]. It was found to contain 52.1% crystalline phases and 47.9% amorphous material. A full analysis is given in Table 3-22. The amorphous material was predominantly a mixture of silica and alumina.

Table 3-20: A list of crystalline phases present in the metallurgical coke mineral matter [24].

Mineral species observed		**Mass %**	**Mineral species observed**		**Mass %**
Anatase	TiO_2	0.1	Jarosite	$(K,H_3O)Fe_3(SO_4)_2(OH)_6$	0.3
Anorthite	$(Ca,Na)(Si,Al)_4O_8$	0.2	Maghemite	γ-Fe_2O_3	0.4
Bassanite	$CaSO_4x_{0.5}H_2O$	0.8	Magnetite	Fe_3O_4	0.6
Calcite	$CaCO_3$	0.3	Martensite	$C_{0.055}Fe_{1.945}$	0.1
Cristobalite	SiO_2	3.6	Mullite	$Al_6Si_2O_{13}$	29.7
Fluorapatite	$Ca_5(PO_4)_3F$	1.8	Pyrrhotite	FeS	0.2
Gehlenite	$Ca_2Al_2SiO_7$	0.1	Quartz	SiO_2	13.5
Iron	Fe	0.4	-	-	-
Total mineral matter (mass%) = 11.8 **Amorphous (mass%) = 47.9**					

The rank of the BlueScope coke as given by mean reflectance, R_o is 1.13. The industrial CRI value of the coke is 19.4% [11].

4. Results

The results of the characterisation and experimental work carried out in this study have been presented in separate sections as detailed below.

4.1 Optical and electro-optical microscopy and associated EDS analysis,

4.2 Raman spectroscopy,

4.3 Porosity,

4.4 Thermodynamic analysis for metallic iron and mineral stability in the coke analogue using MTDATA, a multiphase thermodynamic software package, and

4.5 Coke analogue reactivity in CO_2.

This chapter is primarily focused on the coke analogue but where applicable the results of the metallurgical coke are also presented.

4.1. Optical and electro-optical microscopy and associated EDS analysis

4.1.1. Non-polarised optical and electro-optical microscopy and associated EDS analysis of the fired coke analogues and a metallurgical coke

The non-polarised optical and electro-optical microscopy and associated EDS analysis were carried out to assess the microstructure of the fired coke analogues and a metallurgical coke. Due to the large number of the micrographs of the samples, a summary that is representative of the results is given in Table 4-1. A complete set of micrographs is given in Appendix III. Figures 4-1 to 4-8 show typical non-polarised optical micrographs that represent the characteristic features of the microstructure of the coke analogues. SEM backscattered micrographs and EDS elemental maps associated with the typical non-polarised optical micrographs are also presented in Figures 4-1 to 4-8. The positions marked '+' with a number on the SEM backscattered micrographs indicate positions of the EDS spot analyses. The composition of the EDS spot analyses

is given in the table placed beside the micrographs. An area marked with a rectangle on the SEM backscattered micrographs is an indication of the area where a magnified section was acquired (to resolve the metallic iron and mineral particles better).

The non-polarised optical and electro-optical micrographs and associated EDS analysis of a metallurgical coke used in this work are given in Figure 4-9. The full sets of the micrographs are also given in Appendix III.

Table 4-1: A summary of the non-polarised and electro-optical microscopy and associated EDS analysis results.

Samples	**The non-polarised and electro-optical microscopy and associated EDS analysis results of the fired coke analogues and a metallurgical coke**
Base coke analogue	Figures 4-1 and III-1 show the microstructure of the fired base coke analogue. It is made up of carbon, pores and a small amount of oxide. • The graphite grains appeared to be of similar size to the graphite powders (<45µm and <150µm particle size range) used to make the coke analogue, • The carbonised phenolic resin appeared to have a less obvious or little grain structure and was associated with smaller sized pores. If there is a grain structure, it is likely to be <1µm in size and not resolved in the microscopy approaches used in this study, and • Small amounts of alumina-silica-calcia oxide are present, <1mass%. Its source was the phenolic resin (Bakelite).
Coke analogue–metallic iron 5µm	Figures 4-2 and III-2 show the microstructure of the fired coke analogue–metallic iron 5µm. It is made up of carbon, metallic iron and pores. • The carbon microstructure of graphite grains and carbonised phenolic resins are the same as or similar to that of the fired base coke analogue, • The metallic iron (Fe) particles have size similar to the initial particle size (<10µm) used to make the coke analogue, and • It is difficult to assess whether the metallic iron (Fe) particle have a morphology similar to that of the initial particles before addition (see Figure 3-1(a)), or whether the morphology of the particles had changed. This was due to the small size (<10µm) which was difficult to resolve in the microscopy approaches used in this study.

Table 4-1 (continued): A summary of the non-polarised and electro-optical microscopy and associated EDS analysis results.

Samples	**The non-polarised and electro-optical microscopy and associated EDS analysis results of the fired coke analogues and a metallurgical coke**
Coke analogue–metallic iron 46µm	Figures 4-3 and III-3 show the microstructure of the fired coke analogue–metallic iron 46µm. It is made up of carbon, metallic iron and pores. • The carbon microstructure of graphite grains and carbonised phenolic resins are the same as or similar to that of the fired base coke analogue, • The metallic iron (Fe) particles have size similar to the initial particle size (38–53µm) used to make the coke analogue, • The metallic iron (Fe) particles are more rounded than the original particle addition (see Figure 3-1(b), indicating it may have gone through a liquid Fe phase during the coke analogue firing, and • There is evidence of graphite flakes forming within the metallic iron particle.
Coke analogue–metallic iron 83µm	Figures 4-4 and III-4 show the microstructure of the fired coke analogue–metallic iron 83µm. It is made up of carbon, metallic iron and pores. • The carbon microstructure of graphite grains and carbonised phenolic resins are the same as or similar to that of the fired base coke analogue, • The metallic iron (Fe) particles have size similar to the initial particle size (75–90µm) used to make the coke analogue, • The metallic iron (Fe) particles are more rounded than the original particle addition (see Figure 3-1(c), indicating it may have gone through a liquid Fe phase during the coke analogue firing, and • There is evidence of graphite flakes forming within the metallic iron particle.
Coke analogue–magnetite 46µm	Figures 4-5 and III-5 show the microstructure of the fired coke analogue–magnetite 46µm. It is made up of carbon, iron and pores. • The carbon microstructure of graphite grains and carbonised phenolic resins are the same as or similar to that of the fired base coke analogue, • The initial magnetite (Fe_3O_4) particles has been reduced to iron (Fe) particles, • It appeared that the iron (Fe) particles have size similar to the initial particle size (38–53µm) used to make the coke analogue. If there is a change in particle size, it is likely to be at a scale that is difficult to assess in the microscopy approaches used in this study, • The iron (Fe) particles are more rounded relative to the initial angular morphology (see Figure 3-1(d)), indicating it may have gone through a liquid Fe phase during the coke analogue firing, and • There is evidence of graphite flakes forming within the iron particle.

Table 4-1 (continued): A summary of the non-polarised and electro-optical microscopy and associated EDS analysis results.

Samples	**The non-polarised and electro-optical microscopy and associated EDS analysis results of the fired coke analogues and a metallurgical coke**
Coke analogue–enstatite ferroan	Figures 4-6 and III-6 show the microstructure of the fired coke analogue–enstatite ferroan. It is made up of carbon, enstatite ferroan and pores. • The carbon microstructure of graphite grains and carbonised phenolic resins are the same as or similar to that of the fired base coke analogue, • The enstatite ferroan ($Mg_{1.56}Fe_{0.44}Si_2O_6$) particles have size similar to the initial particle size (38–53µm) used to make the coke analogue, and • The enstatite ferroan ($Mg_{1.56}Fe_{0.44}Si_2O_6$) particles have angular morphology similar to that of the initial angular morphology (see Figure 3-1(e)) used to make the coke analogue.
Coke analogue–phlogopite ferroan	Figures 4-7 and III-7 show the microstructure of the fired coke analogue–phlogopite ferroan. It is made up of carbon, phlogopite ferroan and pores. • The carbon microstructure of graphite grains and carbonised phenolic resins are the same as or similar to that of the fired base coke analogue, • The phlogopite ferroan [$K(Mg,Fe)_3(Al,Fe)Si_3O_{10}(OH,F)_2$] particles have size similar to the initial particle size (38–53µm) used to make the coke analogue, and • The phlogopite ferroan [$K(Mg,Fe)_3(Al,Fe)Si_3O_{10}(OH,F)_2$] particles have angular morphology similar to that of the initial angular morphology (see Figure 3-1(f)) used to make the coke analogue.
Coke analogue–quartz	Figures 4-8 and III-8 show the microstructure of the fired coke analogue–quartz. It is made up of carbon, quartz and pores. • The carbon microstructure of graphite grains and carbonised phenolic resins are the same as or similar to that of the fired base coke analogue, • The quartz (SiO_2) particles have size similar to the initial particle size (38–53µm) used to make the coke analogue, and • The quartz (SiO_2) particles have angular morphology similar to that of the initial angular shape (see Figure 3-1(g)) used to make the coke analogue.
Metallurgical coke	Figures 4-9 and III-9 show the microstructure of metallurgical coke. It is made up of carbon (inert maceral derived components (IMDC) and reactive maceral derived components RMDC), minerals and pores. • The RMDC appeared to have a grain structure with size of approximately 50µm or larger, • The IMDC appeared to have a less obvious or little grain structure at the magnification used in this work and associated with minerals and smaller sized pores, and • The mineral phase has high variability in size, morphology and distribution.

Base coke analogue

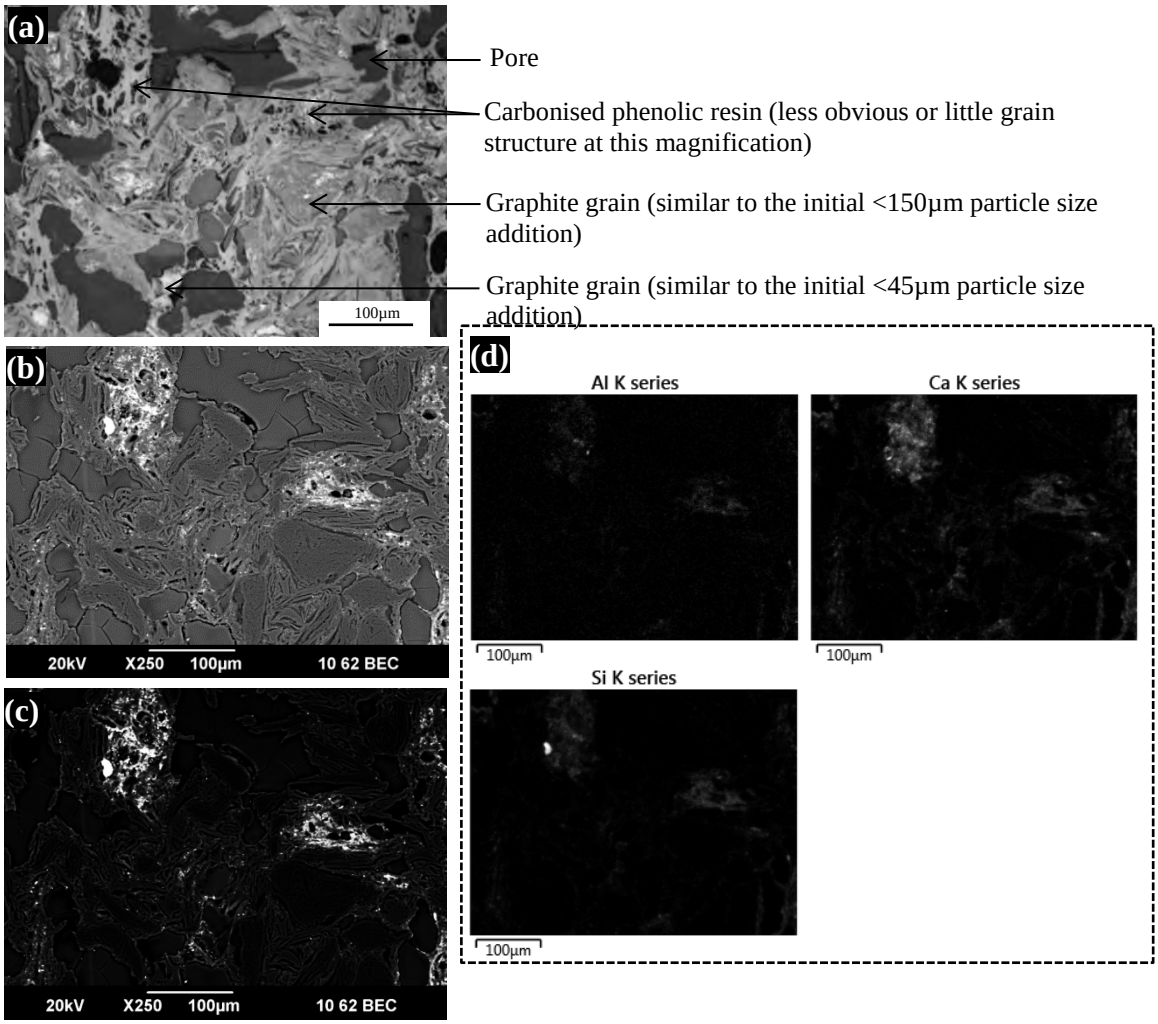

Figure 4-1: A typical non-polarised optical micrograph and associated SEM backscattered micrographs and EDS elemental maps of the base coke analogue. (a) optical micrograph from position 10 on Figure III-1, (b) backscattered micrograph optimised for carbon microstructure, (c) backscattered micrograph optimised for oxide microstructure and (d) the EDS elemental maps.

Coke analogue containing metallic iron and iron containing minerals

Metallic iron 5µm, Fe

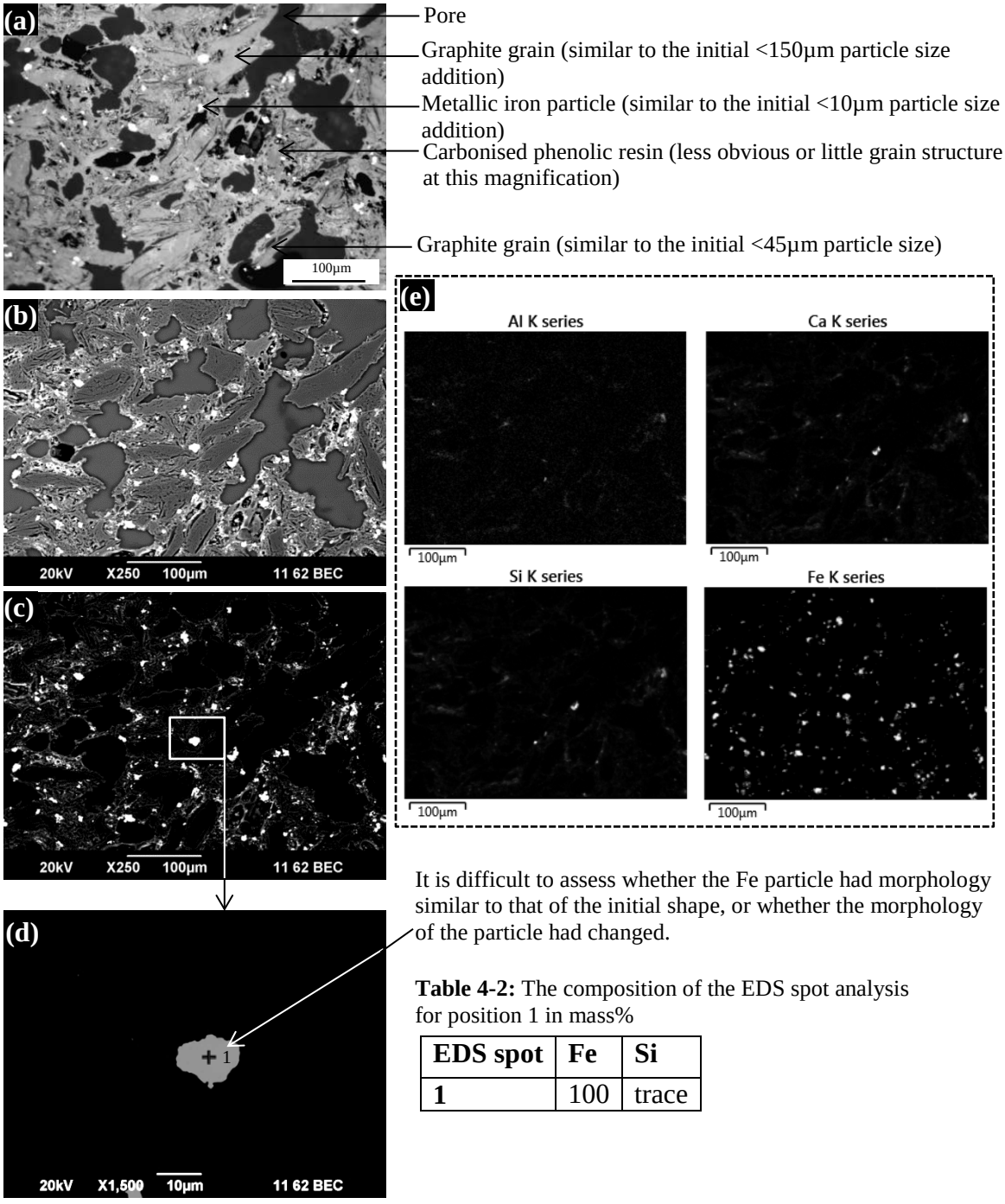

It is difficult to assess whether the Fe particle had morphology similar to that of the initial shape, or whether the morphology of the particle had changed.

Table 4-2: The composition of the EDS spot analysis for position 1 in mass%

EDS spot	Fe	Si
1	100	trace

Figure 4-2: A typical non-polarised optical micrograph and associated SEM backscattered micrographs and EDS elemental maps of the coke analogue–metallic iron 5µm. (a) optical micrograph from position 2 on Figure III-2, (b) backscattered micrograph optimised for carbon microstructure, (c) and (d) backscattered micrographs optimised for metallic iron microstructure and (e) the EDS elemental maps.

Metallic iron 46µm, Fe

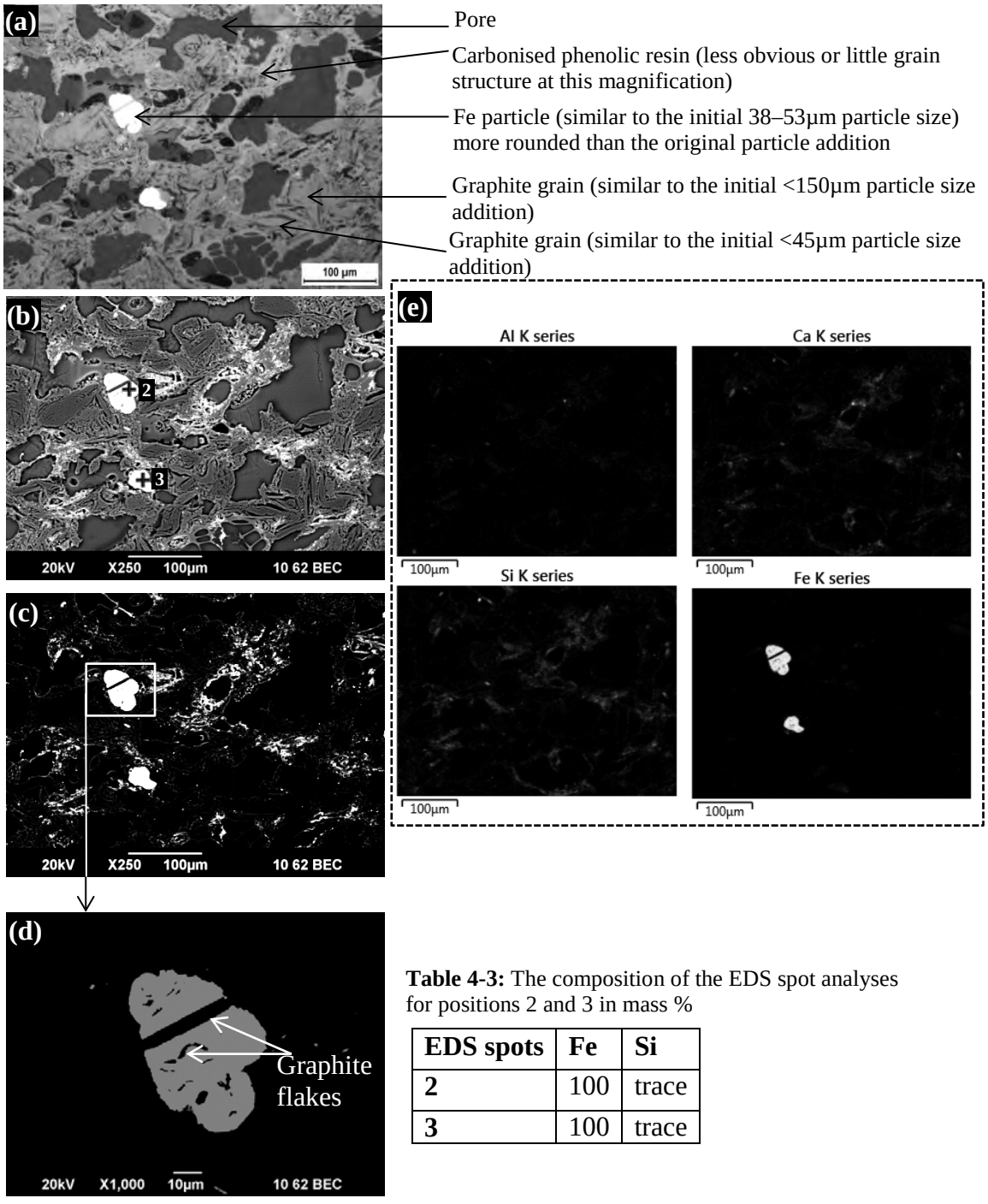

Table 4-3: The composition of the EDS spot analyses for positions 2 and 3 in mass %

EDS spots	Fe	Si
2	100	trace
3	100	trace

Figure 4-3: A typical non-polarised optical micrograph and associated SEM backscattered micrographs and EDS elemental maps of the coke analogue–Fe 46µm. (a) optical micrograph from position 8 on Figure III-3, (b) backscattered micrograph optimised for carbon microstructure, (c) and (d) backscattered micrographs optimised for Fe microstructure and (e) the EDS elemental maps.

Metallic iron 83µm, Fe

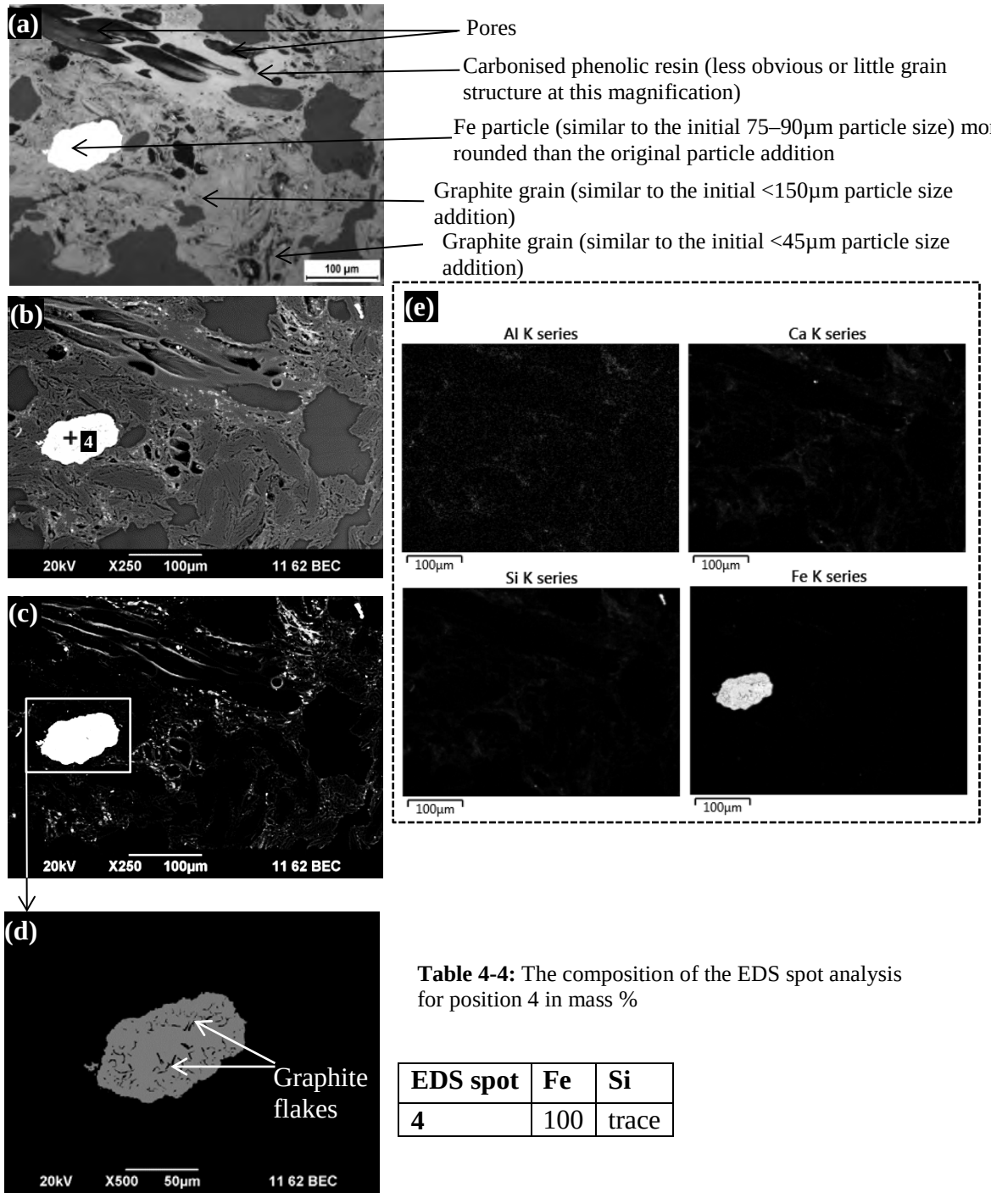

Table 4-4: The composition of the EDS spot analysis for position 4 in mass %

EDS spot	Fe	Si
4	100	trace

Figure 4-4: A typical non-polarised optical micrograph and associated SEM backscattered micrographs and EDS elemental maps of the coke analogue–Fe 83µm. (a) optical micrograph from position 7 on Figure III-4, (b) backscattered micrograph optimised for carbon microstructure, (c) and (d) backscattered micrographs optimised for metallic iron microstructure and (e) the EDS elemental maps.

Magnetite 46µm, Fe_3O_4

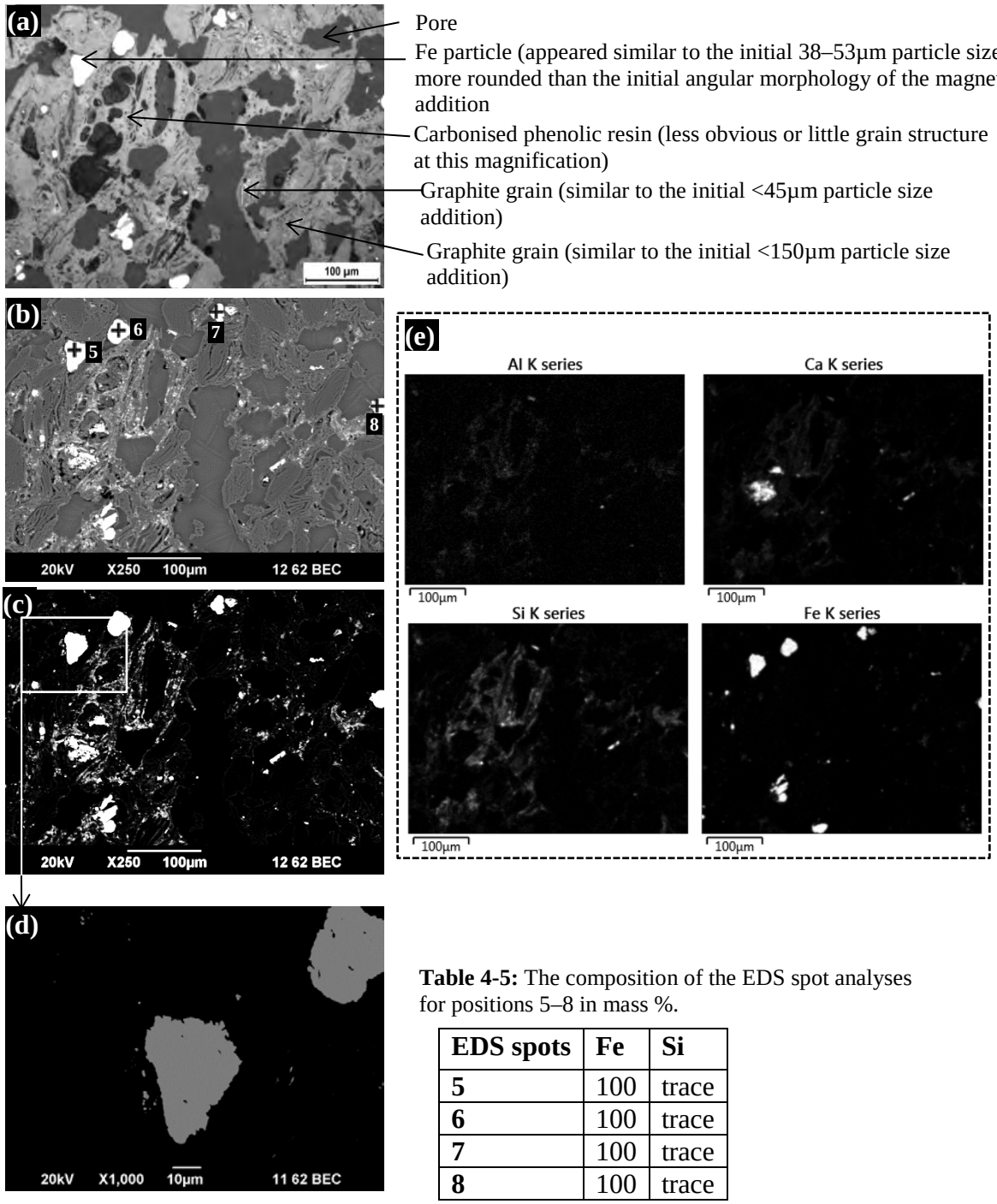

Table 4-5: The composition of the EDS spot analyses for positions 5–8 in mass %.

EDS spots	Fe	Si
5	100	trace
6	100	trace
7	100	trace
8	100	trace

Figure 4-5: A typical non-polarised optical micrograph and associated SEM backscattered micrographs and EDS elemental maps of the coke analogue–Fe_3O_4 46µm. (a) Optical micrograph from position 10 on Figure III-5, (b) backscattered micrograph optimised for carbon microstructure, (c) and (d) backscattered micrographs optimised for Fe microstructure and (e) the EDS elemental maps.

Enstatite ferroan, $Mg_{1.56}Fe_{0.44}Si_2O_6$

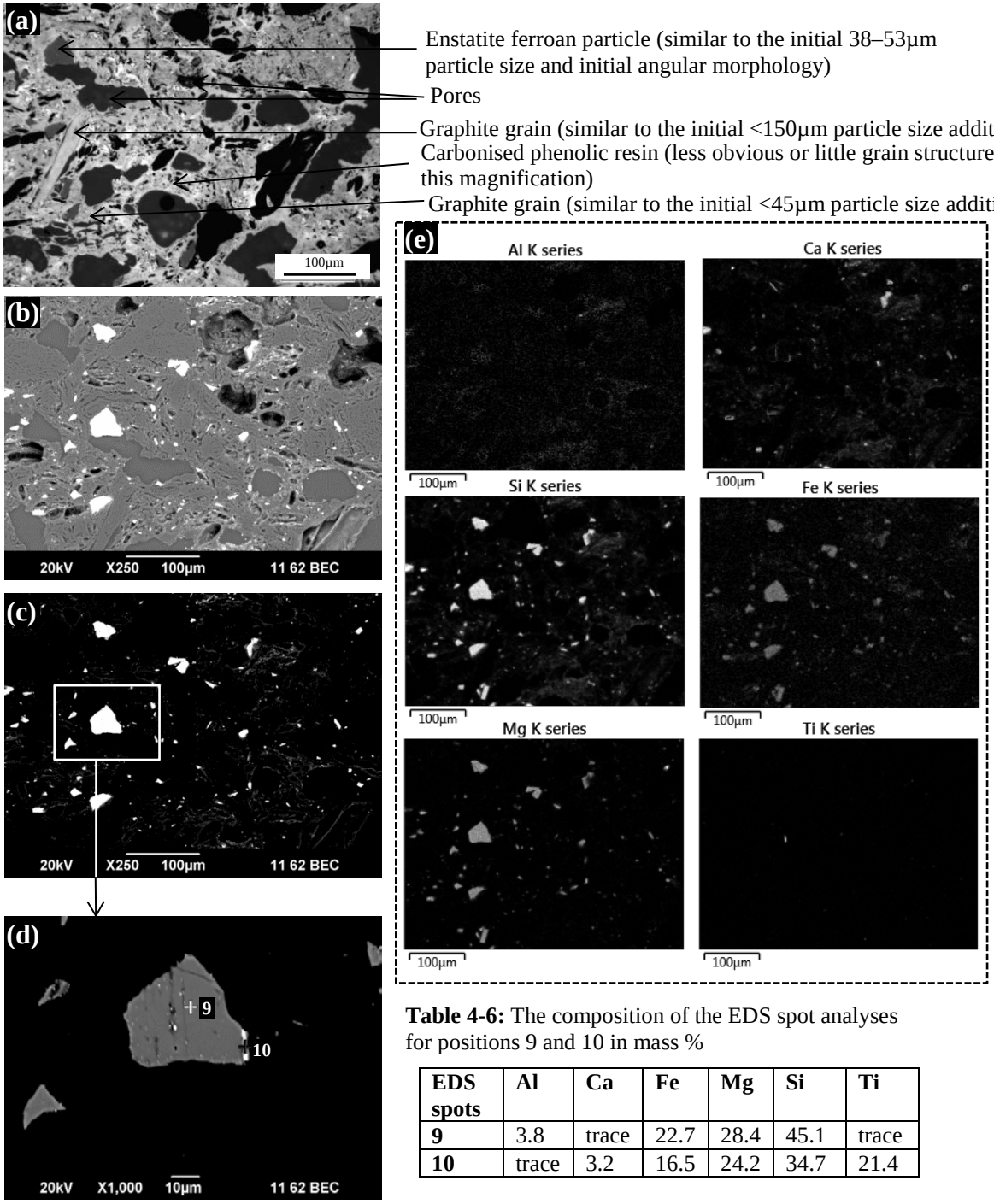

Table 4-6: The composition of the EDS spot analyses for positions 9 and 10 in mass %

EDS spots	Al	Ca	Fe	Mg	Si	Ti
9	3.8	trace	22.7	28.4	45.1	trace
10	trace	3.2	16.5	24.2	34.7	21.4

Figure 4-6: A typical non-polarised optical micrograph and associated SEM backscattered micrographs and EDS elemental maps of the coke analogue–enstatite ferroan. (a) Optical micrograph from position 18 on Figure III-6, (b) backscattered micrograph optimised for carbon microstructure, (c) and (d) backscattered micrographs optimised for enstatite ferroan microstructure and (e) the EDS elemental maps.

Phlogopite ferroan, $K(Mg,Fe)_3(Al,Fe)Si_3O_{10}(OH,F)_2$

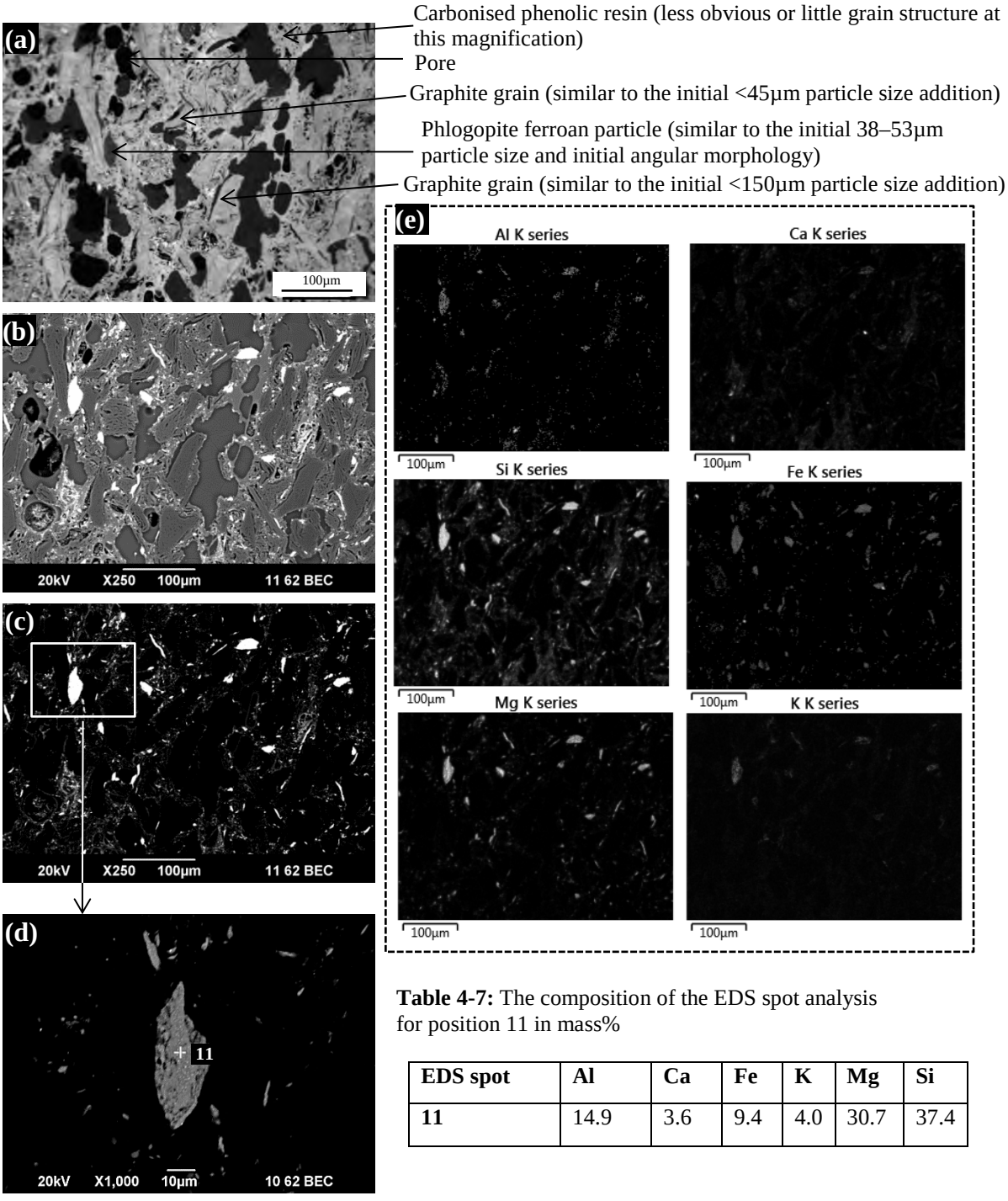

Table 4-7: The composition of the EDS spot analysis for position 11 in mass%

EDS spot	Al	Ca	Fe	K	Mg	Si
11	14.9	3.6	9.4	4.0	30.7	37.4

Figure 4-7: A typical non-polarised optical micrograph and associated SEM backscattered micrographs and EDS elemental maps of the coke analogue–phlogopite ferroan. (a) Optical micrograph from position 1 on Figure III-7, (b) backscattered micrograph optimised for carbon microstructure, (c) and (d) backscattered micrographs optimised for phlogopite ferroan microstructure and (e) the EDS elemental maps.

Coke analogue containing quartz (SiO_2)

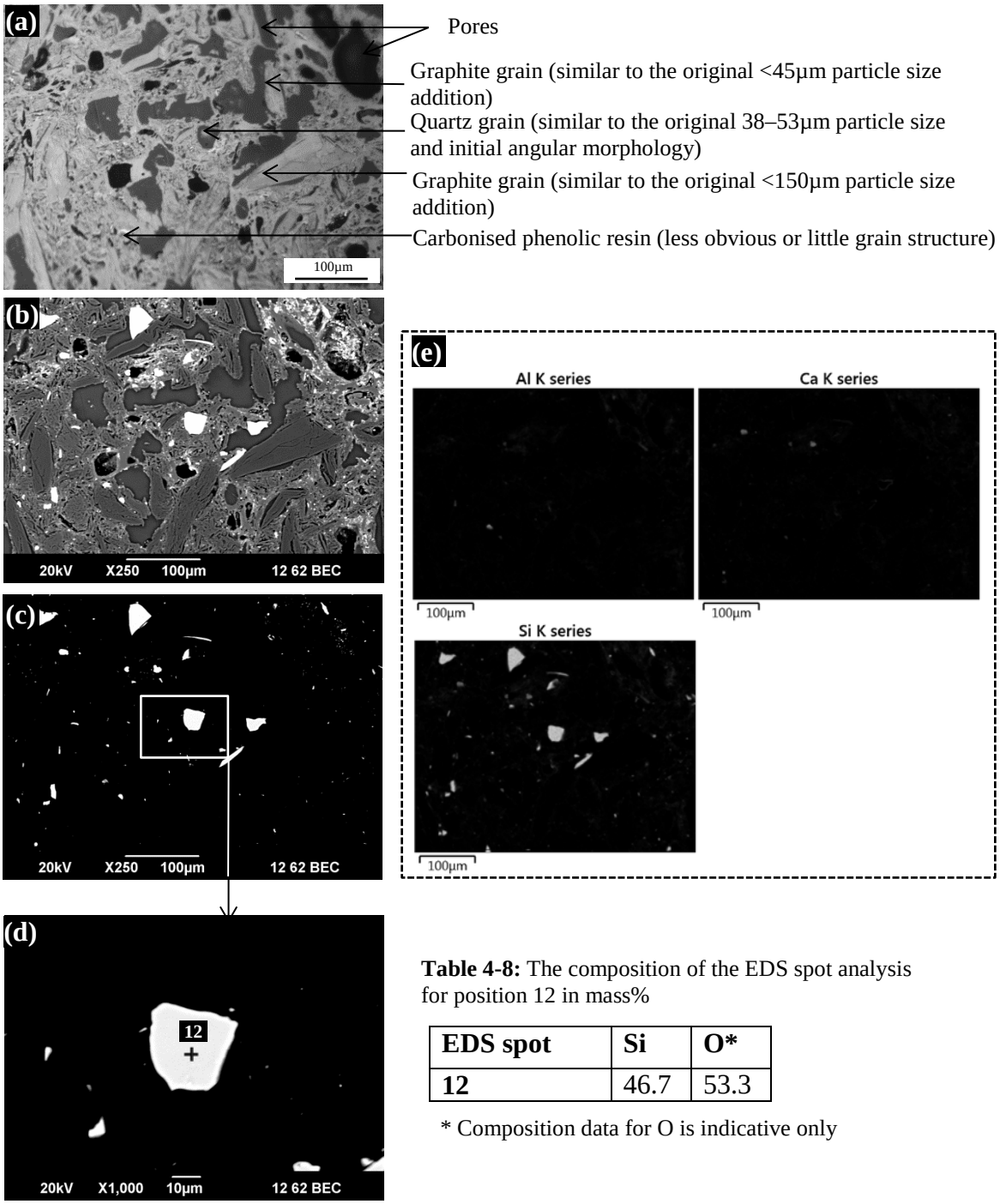

Table 4-8: The composition of the EDS spot analysis for position 12 in mass%

EDS spot	Si	O*
12	46.7	53.3

* Composition data for O is indicative only

Figure 4-8: A typical non-polarised optical micrograph and associated SEM backscattered micrographs and EDS elemental maps of the coke analogue–quartz. (a) Optical micrograph from position 11 on Figure III-8, (b) backscattered micrograph optimised for carbon microstructure, (c) and (d) backscattered micrographs optimised for quartz microstructure and (e) the EDS elemental maps.

Metallurgical coke

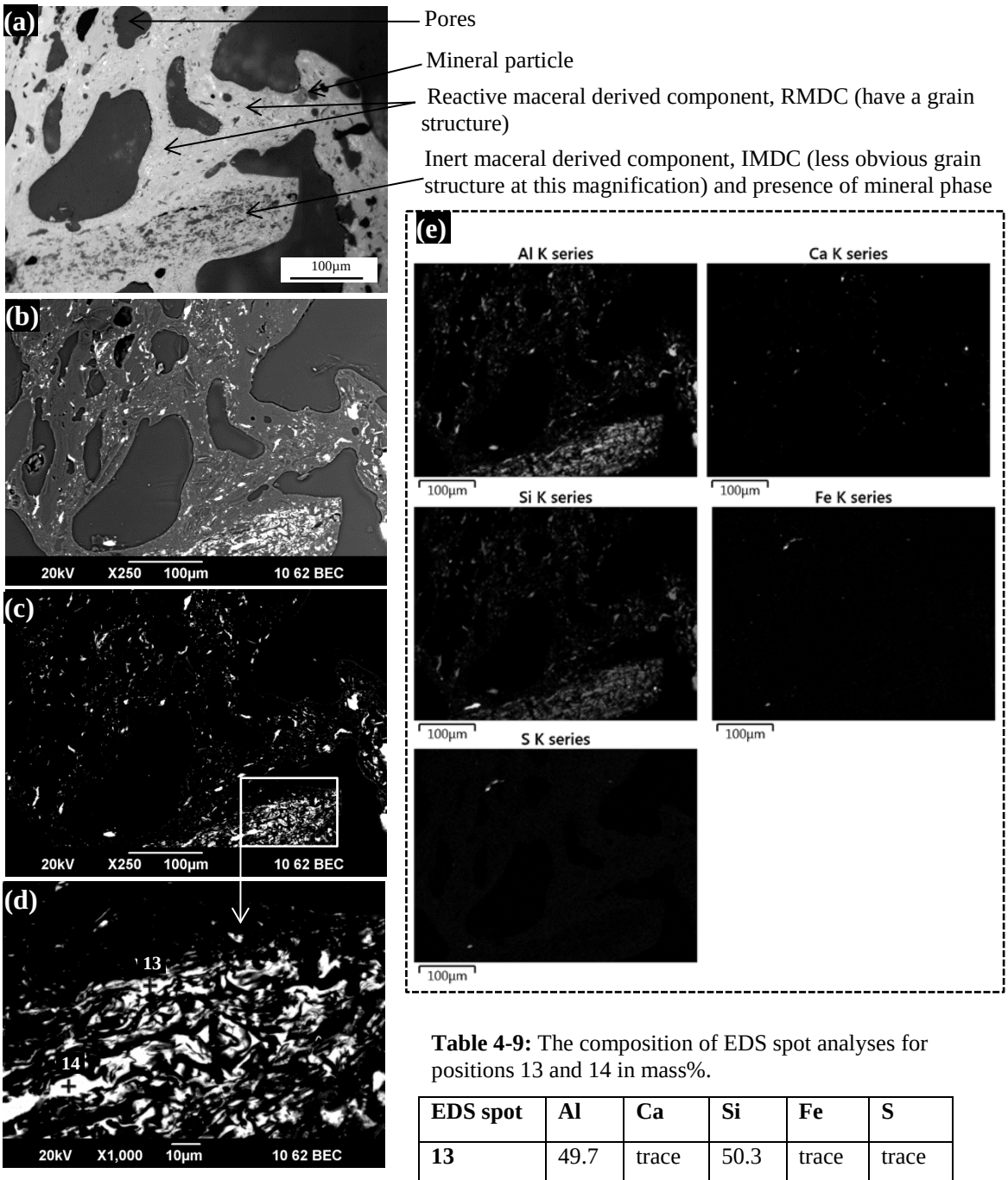

Table 4-9: The composition of EDS spot analyses for positions 13 and 14 in mass%.

EDS spot	Al	Ca	Si	Fe	S
13	49.7	trace	50.3	trace	trace
14	50.2	trace	49.8	trace	trace

Figure 4-9: A non-polarised optical micrograph and associated SEM backscattered micrographs and EDS elemental maps of a metallurgical coke. (a) Optical micrograph from position 2 on Figure III-9, (b) backscattered micrograph optimised for carbon microstructure, (c) and (d) backscattered micrographs optimised for mineral microstructure and (e) the EDS elemental maps.

4.1.2 Non-polarised optical microscopy of the reacted samples

Non-polarised optical microscopy was carried out to characterise the microstructure of the coke analogues (base and metallic iron 46μm) after reaction in CO_2 for 1 hour at two different temperatures of 950°C and 1025°C. The samples were reacted for only 1 hour to ensure its initial cylindrical shape was maintained. That is, to avoid the sample breaking up on transferring from the furnace alumina pedestal to sample container at 1025°C. The microstructures of the fired samples were also characterised for comparison. Table 4-10 gives a representative summary of the non-polarised micrographs. The full details of the micrographs are given in Figures III-10 to III-21.

Table 4-10: A summary of the non-polarised optical microscopy of the fired and reacted coke analogues.

Coke analogues	**Non-polarised optical microscopy results**	
	Fired or unreacted	Post reacted at 950° and 1025°C, and arrested after 1 hour.
Base	Figures III-10 and III-16 show the microstructure of the fired base coke analogue in horizontal and vertical views respectively. It is made up of carbon (carbonised phenolic resins and graphite grains), a small amount of oxide and pores (as per the detailed description given for the base coke analogue in Table 4-1).	Figures III-11, III-12 and III-17, III-18 show the microstructure of the post reacted base coke analogue in horizontal and vertical views respectively. The microstructure is similar to the fired base coke analogue, but also show • evidence of preferential loss of carbonised phenolic resin compared to graphite grains (remaining only particles of the size similar to the particle size of the initial graphite used to make the coke analogue) at the external surface of the sample. It was difficult to resolve this closer to the interior of the sample at the magnification used, and • a weakened external surface of the sample due to the removal of carbon.
Fe 46µm	Figures III-13 and III-19 show the microstructure of the fired coke analogue–Fe 46µm in horizontal and vertical views respectively. It is made up of carbon (carbonised phenolic resins and graphite grains), metallic iron particles and pores (as per the detailed description given for the coke analogue–Fe 46µm in Table 4-1).	Figures III-14, III-15 and III-20, III-21 show the microstructure of the post reacted coke analogue–Fe 46µm in horizontal and vertical views respectively. The microstructure is similar to the fired coke analogue–Fe 46µm, but also show • evidence of preferential loss of carbonised phenolic resin (same as the base coke analogue), • a weakened external surface of the sample due to removal of carbon, • appearance of preferential loss of carbon around Fe particle, and • evidence of darker phase around Fe particles closer to the external surface of the sample (thought to be iron oxides, see section 4.1.5).

4.1.3 Polarised optical microscopy of the fired base coke analogue

Polarised optical microscopy was carried out to better elucidate the characteristic features of the fired base coke analogue microstructure not seen under the non-polarised optical microscopy. Figure 4-10 shows the polarised (plane and crossed) optical micrographs of the fired base coke analogue. Under the polarised light, the graphite grains exhibited anisotropic character (sensitive to reflection in plane polarised and cross polarised views) while the areas thought to be carbonised phenolic resin exhibited isotropic character (not sensitive to reflection in plane polarised and crossed polarised views).

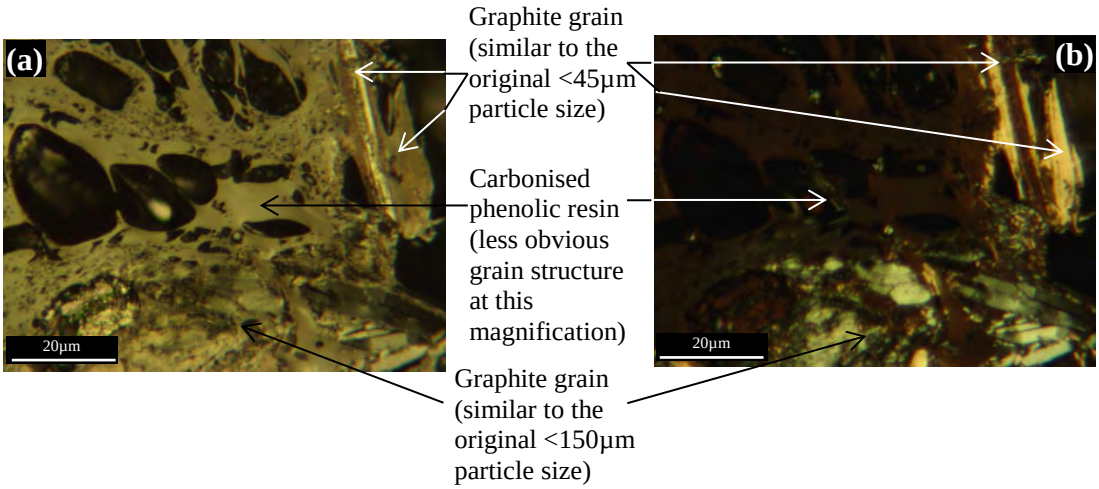

Figure 4-10: The polarised optical micrographs of the fired base coke analogue. (a) Plane polarised and (b) crossed polarised.

4.1.4 Polarised optical microscopy of the post reacted samples

Polarised optical microscopy was carried out to characterise the microstructure of coke analogues (base, Fe 46µm, Fe_3O_4 46µm and quartz (SiO_2)) after reaction in CO_2 at 1100°C and arrested after 20 minutes. The plane polarised optical micrographs of the post reacted coke analogues are given in Figures 4-11 to 4-14. The micrographs were taken closer to the external surface of the samples. Figures 4-11 to 4-14 show coke analogue carbon microstructure that have grains of particle size similar to the initial graphite grains but the absence of the less obvious grain structure associated with the carbonised phenolic resins. Figure 4-12 shows the presence of a non-metallic phase around the Fe particle. The phases that appeared similar to that in Figure 4-12 were then assessed under the ZEISS EVO 50 SEM using the same sample and given in section 4.1.5. These phases were only identified at the external surface of the sample.

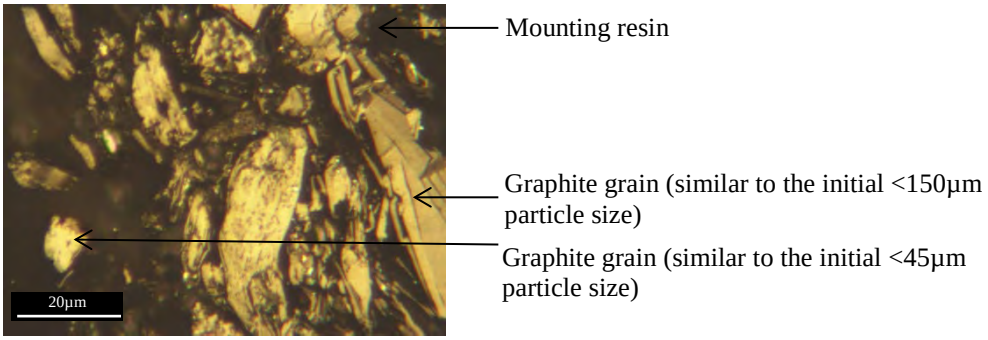

Figure 4-11: A polarised optical micrograph of the external surface of base coke analogue reacted in CO_2 at 1100°C for 20 minutes.

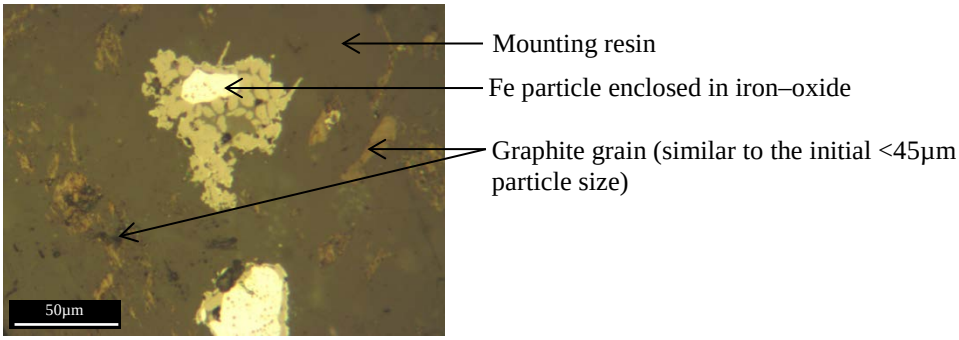

Figure 4-12: A polarised optical micrograph of the external surface of coke analogue–Fe 46µm reacted in CO_2 at 1100°C for 20 minutes.

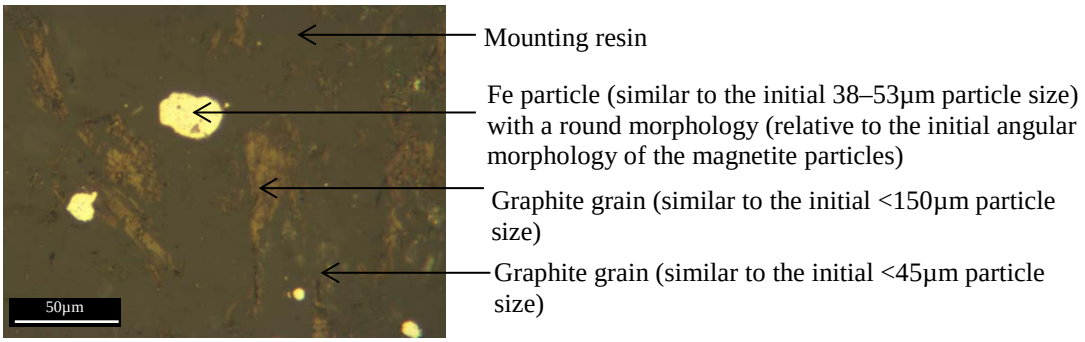

Figure 4-13: A polarised optical micrograph of the external surface of coke analogue–Fe_3O_4 46µm reacted in CO_2 at 1100°C for 20 minutes.

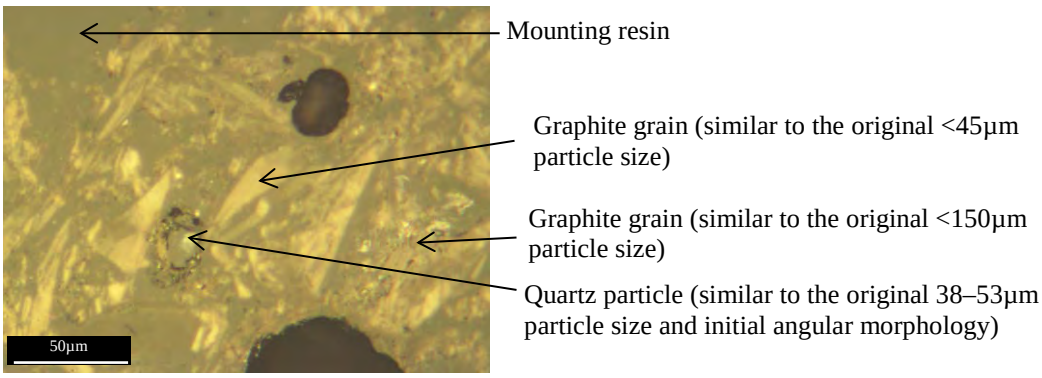

Figure 4-14: A polarised optical micrograph of the external surface of coke analogue–quartz (SiO_2) reacted in CO_2 at 1100°C for 20 minutes.

4.1.5 SEM-EDS analysis of the external surface of coke analogue–Fe 46µm reacted in CO_2 at 1100°C for 20 minutes

SEM-EDS analysis of the external surface of coke analogue–Fe 46µm reacted in carbon dioxide at 1100°C and arrested after 20 minutes was carried out to characterise the darker phase observed around the metallic iron particle. The SEM backscattered micrographs of the reacted sample focused on metallic iron microstructure are given in Figure 4-15. The positions marked '+' and a number on the SEM backscattered micrographs indicate where the EDS spot analyses were taken. The composition of the EDS spot analyses is given in Table 4-11 and 4-12. Table 4-11 shows spot analyses of iron-alumina-silica-calcia oxide dominated phases while Table 4-12 shows spot analyses of iron oxide dominated phases. The (O*/Fe) value indicative of the iron oxide phase is given in Table 4-13. Table 4-13 shows that the iron oxide phases around the metallic iron were magnetite (Fe_3O_4) and hematite (Fe_2O_3) rather than wustite (FeO). Figure 4-15 also shows some small sized pores and graphite flake on the Fe particle.

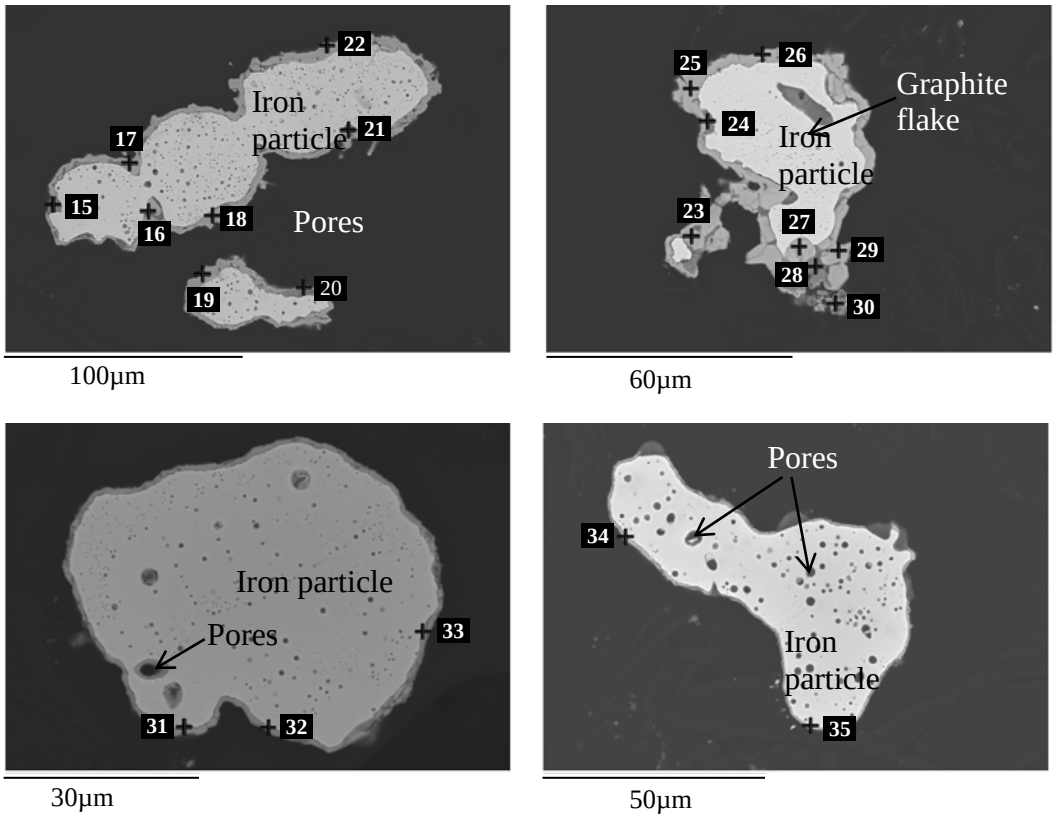

Figure 4-15: The SEM backscattered micrographs at the external surface of coke analogue–Fe 46µm reacted in CO_2 at 1100°C for 20 minutes. The micrographs were optimised for Fe microstructure.

Table 4-11: The composition of the EDS spot analyses for iron-alumina-silica-calcia oxide dominated phases in atom%.

EDS spots	Ca	Mg	Fe	Si	Al	O
15	4.8	trace	17.7	11.7	trace	65.8
16	2.8	-	34.6	7.8	2.3	52.5
20	6.6	-	18.7	11.6	-	63.1
21	3.6	-	20.6	11.0	trace	64.8
24	9.2	-	17.8	12.1	2.6	58.3
28	11.7	trace	9.4	9.4	4.5	65.0
30	trace	trace	14.2	trace	18.8	67.0

Table 4-12: The composition of the EDS spot analyses for iron oxide dominated phases in atom %.

EDS Spots	17	18	19	22	23	25	26
Fe	34.6	34.3	32.7	35.8	36.6	36.5	36.5
O	65.4	65.7	67.3	64.2	63.4	63.5	63.5
O*/Fe	1.9	1.9	2.1	1.8	1.7	1.7	1.7
EDS Spots	**27**	**29**	**31**	**32**	**33**	**34**	**35**
Fe	44.2	39.4	37.8	35.7	38.3	45.7	45.0
O	55.8	60.6	62.2	64.3	61.7	54.3	55.0
O*/Fe	1.3	1.5	1.7	1.8	1.6	1.2	1.2

Table 4-13: The iron oxide phases identified in Table 4-12.

Iron oxide phases[+]	**EDS spots**	O*/Fe **(average and standard deviation)**
Fe_3O_4	22, 23, 25, 26, 27, 29, 31, 32, 33, 34 and 35	1.6±0.2
Fe_2O_3	17, 18 and 19	2.0±0.1

+see equation 3-1 and Table 3-8 for the definition of (O*/Fe)

A summary of the optical and electro-optical microscopy and associated EDS analysis results

- Characteristic features of the coke analogues microstructure indicating that the graphite grains were similar to the initial graphite grains (<45μm and <150μm particle sizes) used to make the coke analogue. The graphite grains exhibited anisotropic character in plain and crossed polarised lights (Figures 4-1 to 4-8, 4-10 and III-1 to III-8).

- Characteristic features of the coke analogues microstructure indicating that the carbonised phenolic resin has a less obvious or little grain structure. If there is a

grain structure, it is likely to be <1µm in size and not resolved in the microscopy approaches used in this study. It is associated with small sized pores and exhibited isotropic character in plain and crossed polarised lights (Figures 4-1 to 4-8, 4-10 and III-1 to III-8).

- The presence of small amounts of alumina-silica-calcia oxide (<1 mass%) in the coke analogue (Figures 4-1 to 4-8). The source is the phenolic resin (Bakelite).

- The Fe particles in the coke analogues (Figures 4-2 to 4-5 and III-2 to III-5) appeared to have sizes similar to the initial particle sizes (Figure 3-1(a) to 3-1(d)). The Fe particles are more rounded than the original Fe particle addition (Figure 3-1(b, c)) and initial angular morphology for Fe_3O_4 particle addition (Figure 3-1(d)), indicating they may have gone through a liquid Fe phase during coke analogue firing. There was evidence of graphite flakes within the iron particles. It is difficult to resolve the shape and presence of graphite flake within the metallic iron with <10µm particle size in the microscopy approaches used in this study.

- Enstatite ferroan ($Mg_{1.56}Fe_{0.44}Si_2O_6$), phlogopite ferroan ($K(Mg,Fe)_3(Al,Fe)Si_3O_{10}(OH,F)_2$) and quartz ($SiO_2$) particles in the coke analogues (Figures 4-6, 4-7, 4-8 and III-6, III-7 and III-8) have sizes similar to the initial particle sizes (Figure 3-1(e), 3-1(f) and 3-1(g)). They also have angular morphology similar to that of the initial angular morphology used to make the coke analogue.

- The elucidation of the microstructure of the fired and post reacted base coke analogue in horizontal and vertical views (Figures III-10 to III-12, III-16 to III-18 and Table 4-10). The samples were prepared by arresting the reaction with CO_2 after 1 hour at two different temperatures of 950°C and 1025°C. The microstructure of the post reacted samples (Figures III-11, III-12 and III-17, III-18) was similar to the fired samples (Figures III-10 and III-16), but also shows a weakened external surface due to the removal of carbon. There was evidence of preferential loss of carbonised phenolic resin compared to the graphite grains (remaining only particles of the size similar to the particle size of the initial

graphite used to make the coke analogue). The preferential loss of carbon was evident at the external surface of the sample, but difficult to resolve closer to interior of the sample at the magnification used in the study.

- The elucidation of the microstructure of the fired and post reacted coke analogue–Fe 46μm in horizontal and vertical views (Figures III-13 to III-15, III-19 to III-21 and Table 4-10). The reactivity testing was similar to the base coke analogue above. The microstructure of the post reacted samples (Figures III-14, III-15 and III-20, III-21) was similar to the microstructure of the fired samples (Figures III-13 and III-19). There was evidence of preferential loss of carbonised phenolic resin (similar to the base coke analogue above). It appeared that carbon was preferentially lost around the iron particles. Furthermore, closer to the external surface of the post reacted samples, a darker phase was observed on the surface of the Fe particles and is thought to be iron oxide (Figures III-14, III-15 and III-20, III-21),

- The elucidation of the microstructure of the external surface of coke analogues (base, Fe 46μm, Fe_3O_4 46μm and quartz (SiO_2)) reacted in CO_2 at 1100°C and arrested after 20 minutes given in Figures 4-11 to 4-15. There was preferential loss of carbonised phenolic resin compared to the graphite grains. There was formation of iron oxide (magnetite and hematite) phases around the iron particles in the post reacted coke analogue–Fe 46μm (Figures 4-12 and 4-15 and Table 4-13).

- The features of metallurgical coke microstructure indicating reactive maceral derived components (RMDC), inert maceral derived component (IMDC), mineral phase and pores (Figures 4-9 and III-9). The RMDC appeared to have a grain structure with size of approximately 50μm or larger. The IMDC appeared to have a less obvious grain structure at the magnifications used in this study. The IMDC is associated with minerals and smaller sized pores. The mineral phases have high variability in size, shape and distribution.

4.2. Raman spectroscopy

The results of the carbon bonding measurements (bulk and localised around particles) carried out in this study are presented in this section. The localised measurements were only applicable to the coke analogues containing metallic iron and minerals. The bulk measurement result of the metallurgical coke used in this work and the carbonaceous materials used to make the coke analogue are also presented. The Raman measurements were taken from positions identified as typical for the samples given in section 4.1.1.

The carbon bonding of the coke analogues and other carbonaceous materials used in this study have been characterised using

1. A plot of $I_{(D)}/I_{(G)}$ versus $I_{(V)}/I_{(G)}$,
2. A plot of $I_{(V)}/I_{(G)}$ versus Raman position near the metallic iron and mineral particles, and
3. A plot of $I_{(V)}/I_{(G)}$ versus distance from the metallic iron or mineral–coke analogue interface.

In these plots, decreasing values of $I_{(D)}/I_{(G)}$ and $I_{(V)}/I_{(G)}$ represent an increasing graphitic nature. The non-polarised optical micrographs showing positions of the localised measurements are shown next to the Raman results.

Key summary of the carbon bonding characterisation of the coke analogues are,

1. A plot of $I_{(D)}/I_{(G)}$ versus $I_{(V)}/I_{(G)}$ (Figures 4-17 to 4-24) show that the carbon bonding of the coke analogues extended over a broad range of sp^2 bonding (0.16–1.55 for $I_{(D)}/I_{(G)}$) and sp^2–sp^3 bonding (0–0.41 for $I_{(V)}/I_{(G)}$). It appeared to represent a combination of the carbon bonding of the carbonised carbonaceous materials used to make the coke analogue (Figure 4-16). Fe and minerals appeared to have no clear discriminating effect on carbon bonding as resolved with this approach.

2. A plot of $I_{(V)}/I_{(G)}$ versus the Raman position near the Fe or mineral particle, and a plot of $I_{(V)}/I_{(G)}$ versus distance from the Fe or mineral–coke analogue interface (Figures 4-18 to 4-24) show that Fe and minerals are having an effect on the sp^2–sp^3 bonding.
    - Fe (Figures 4-18(c, d), 4-19 (c, d), 4-20 (c, d) and 4-20 (c, d)) increased sp^2 bonding. The white area of enstatite ferroan ($Mg_{1.56}Fe_{0.44}Si_2O_6$), thought to be Ti (Figure 4-22(e)), also increased sp^2 bonding, and
    - Enstatite ferroan ($Mg_{1.56}Fe_{0.44}Si_2O_6$) (Figure 4-22(c, d)), phlogopite ferroan [$K(Mg,Fe)_3(Al,Fe)Si_3O_{10}(OH,F)_2$] (Figure 4-23(c, d)) and Quartz (SiO_2) (Figure 4-24 (c, d)) had no significant discriminating effect on the sp^2–sp^3 bonding.

3. A plot of $I_{(D)}/I_{(G)}$ versus $I_{(V)}/I_{(G)}$ (Figure 4-25) show that the carbon bonding of the metallurgical coke extended over range a tighter range of sp^2 bonding (1.16–1.45 for $I_{(D)}/I_{(G)}$) and sp^2–sp^3 bonding (0.38–0.62 for $I_{(V)}/I_{(G)}$).

Carbonaceous materials used to make the coke analogue

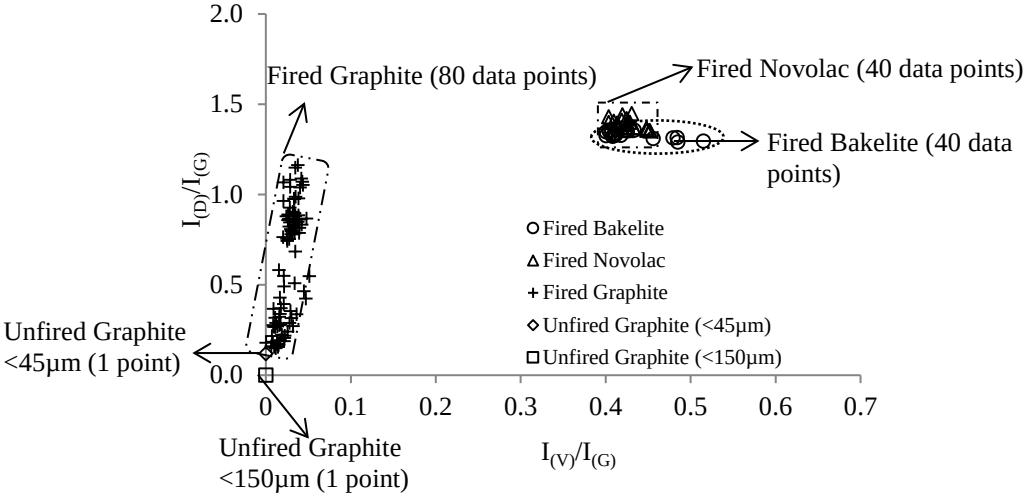

Figure 4-16: A plot of $I_{(D)}/I_{(G)}$ versus $I_{(V)}/I_{(G)}$ showing the carbon bonding of the carbonaceous materials used to make the coke analogue.

Base coke analogue

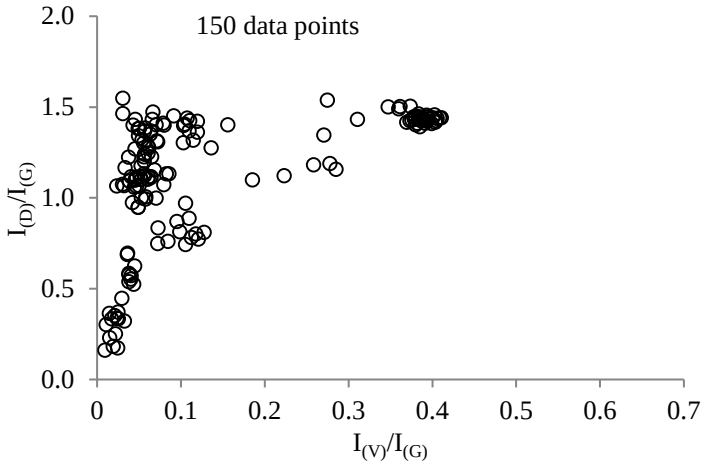

Figure 4-17: A plot of $I_{(D)}/I_{(G)}$ versus $I_{(V)}/I_{(G)}$ showing the carbon bonding of the base coke analogue.

Coke analogues containing Fe and Fe containing minerals

Fe 5µm

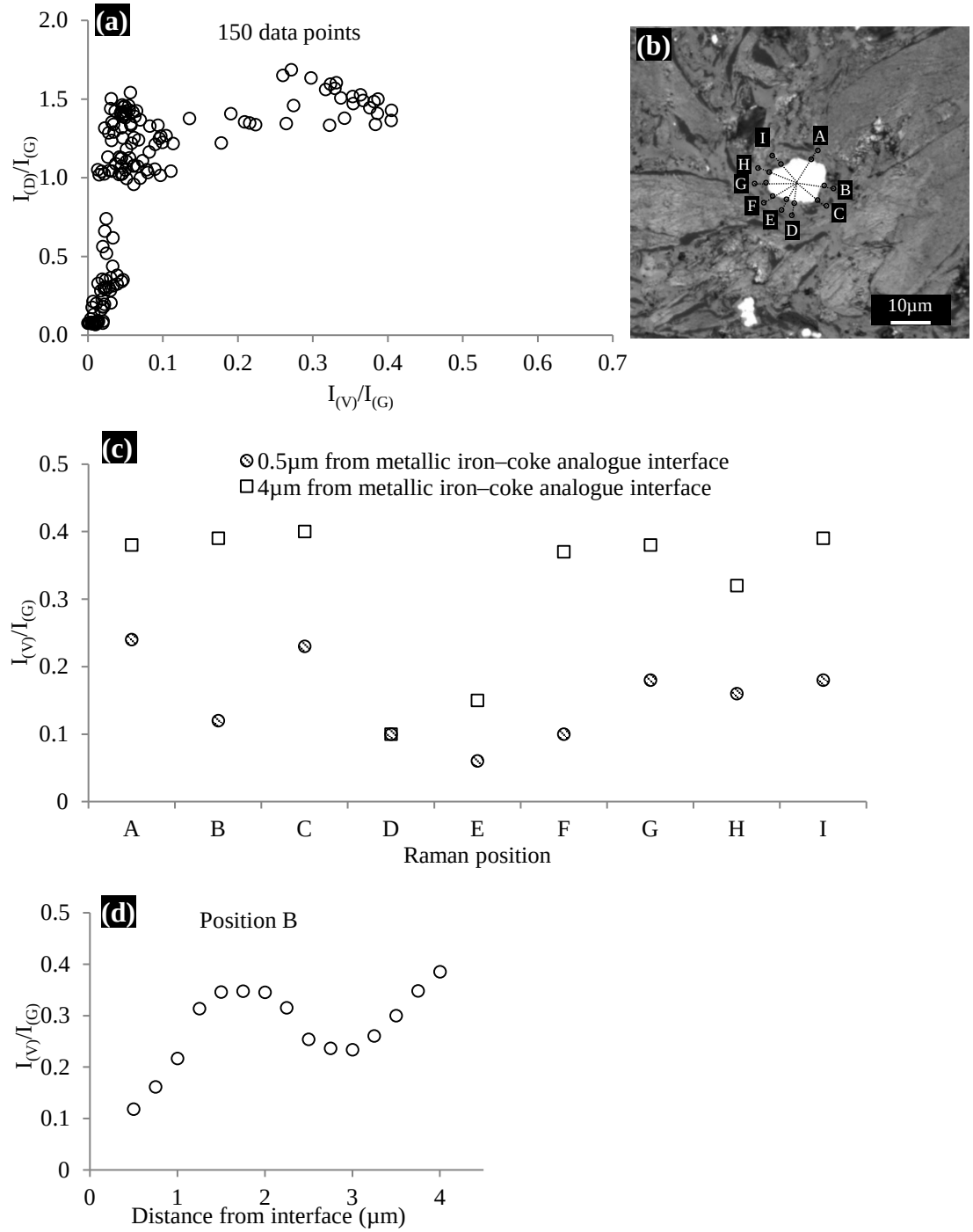

Figure 4-18: (a) A plot of $I_{(D)}/I_{(G)}$ versus $I_{(V)}/I_{(G)}$ showing the carbon bonding, (b) non-polarised optical micrograph showing the position of the localised Raman measurements, (c) a plot of $I_{(V)}/I_{(G)}$ versus the Raman position and (d) a plot of $I_{(V)}/I_{(G)}$ versus distance from the interface of the coke analogue–Fe 5µm.

Fe 46µm

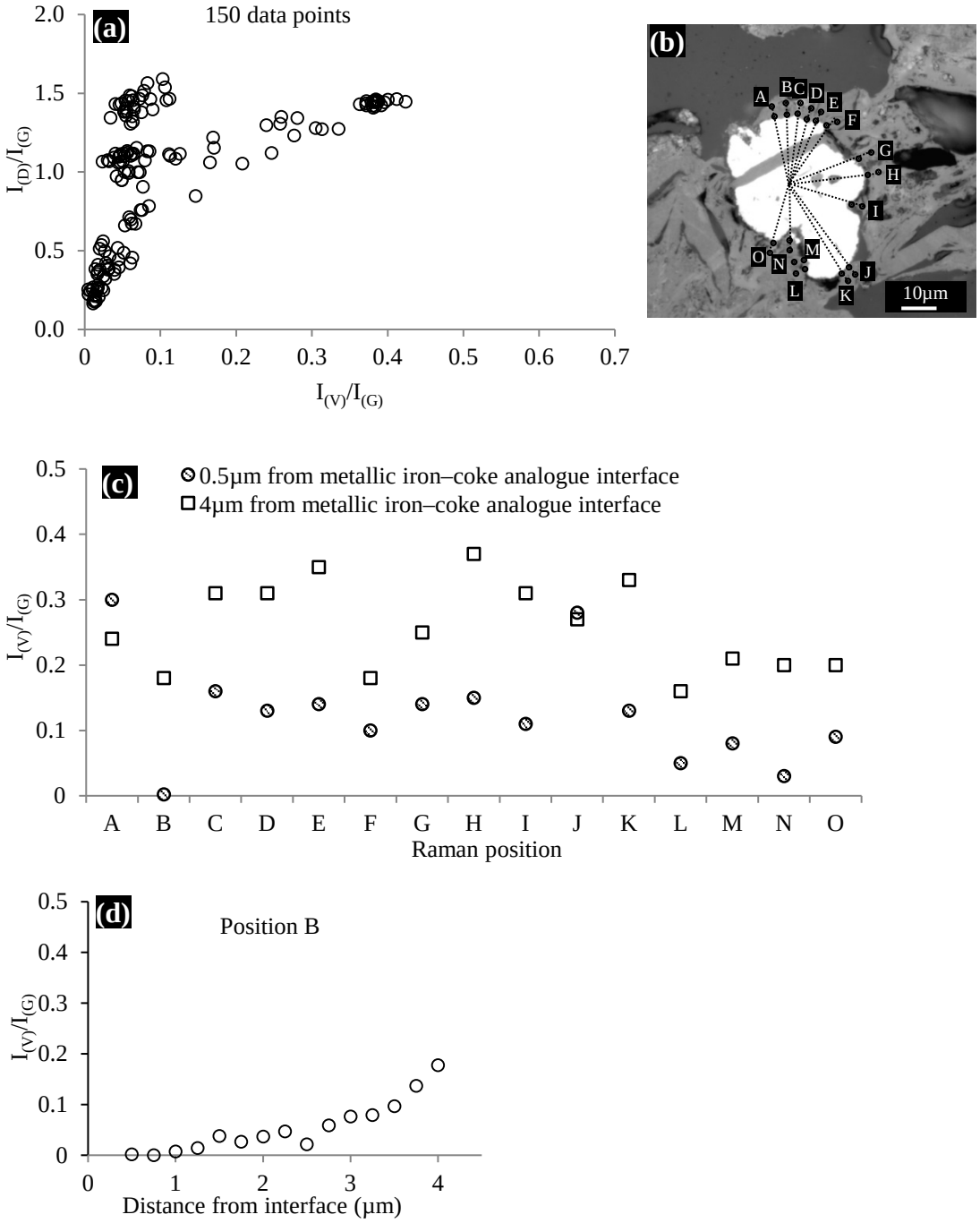

Figure 4-19: (a) A plot of $I_{(D)}/I_{(G)}$ versus $I_{(V)}/I_{(G)}$ showing the carbon bonding, (b) non-polarised optical micrograph showing the position of the localised Raman measurements, (c) a plot of $I_{(V)}/I_{(G)}$ versus the Raman position and (d) a plot of $I_{(V)}/I_{(G)}$ versus distance from the interface of the coke analogue–Fe 46µm.

Fe 83µm

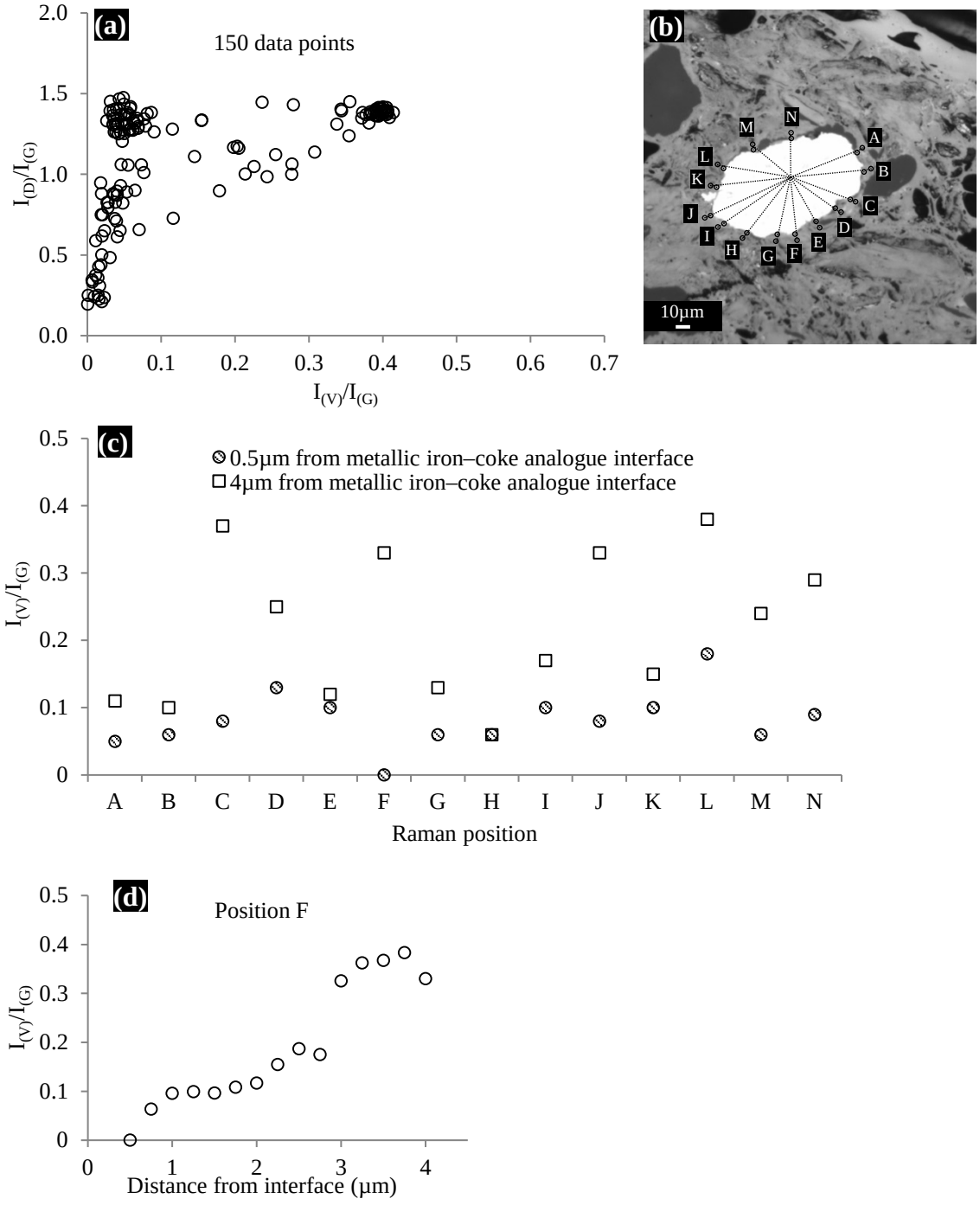

Figure 4-20: (a) A plot of $I_{(D)}/I_{(G)}$ versus $I_{(V)}/I_{(G)}$ showing the carbon bonding, (b) non-polarised optical micrograph showing the position of the localised Raman measurements, (c) a plot of $I_{(V)}/I_{(G)}$ versus the Raman position and (d) a plot of $I_{(V)}/I_{(G)}$ versus distance from the interface of the coke analogue–Fe 83µm.

Fe_3O_4 46µm

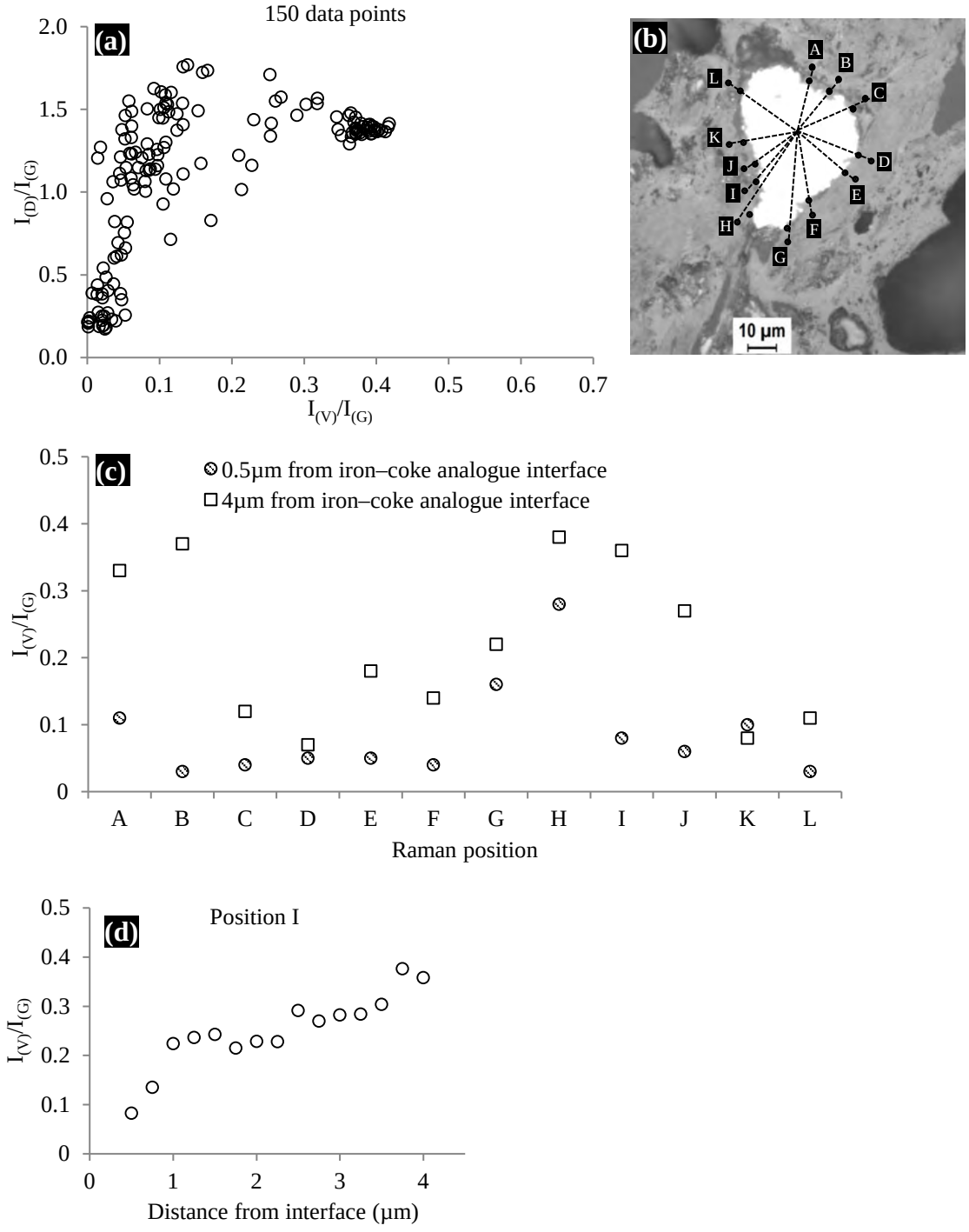

Figure 4-21: (a) A plot of $I_{(D)}/I_{(G)}$ versus $I_{(V)}/I_{(G)}$ showing the carbon bonding, (b) non-polarised optical micrograph showing the position of the localised Raman measurements, (c) a plot of $I_{(V)}/I_{(G)}$ versus the Raman position and (d) a plot of $I_{(V)}/I_{(G)}$ versus distance from the interface of the coke analogue–Fe_3O_4 46µm.

Enstatite ferroan, $Mg_{1.56}Fe_{0.44}Si_2O_6$

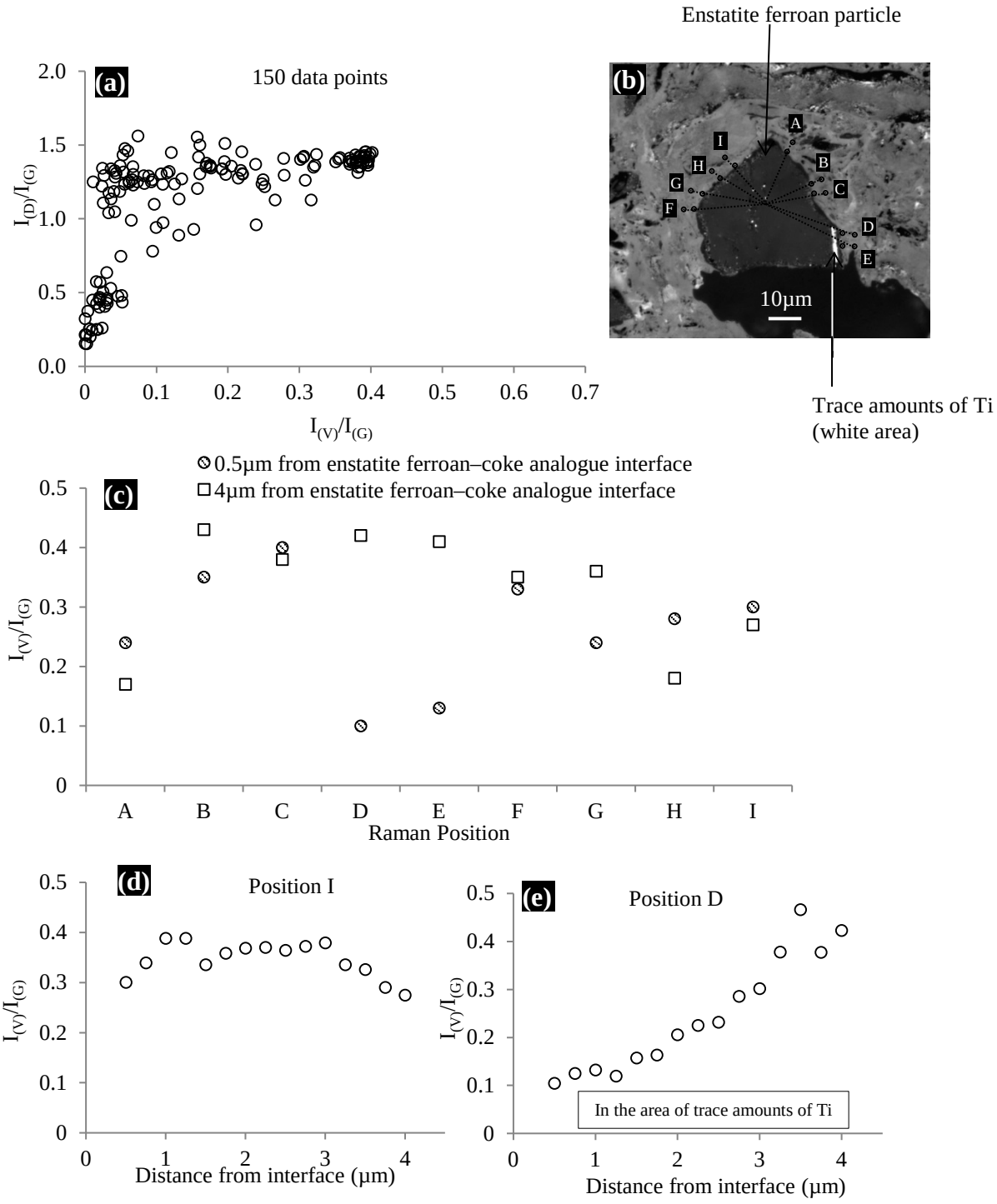

Figure 4-22: (a) A plot of $I_{(D)}/I_{(G)}$ versus $I_{(V)}/I_{(G)}$ showing the carbon bonding, (b) non-polarised optical micrograph showing the position of the localised Raman measurements, (c) a plot of $I_{(V)}/I_{(G)}$ versus the Raman position and (d and e) plots of $I_{(V)}/I_{(G)}$ versus distance from the interface of the coke analogue–enstatite ferroan.

Phlogopite ferroan, $K(Mg,Fe)_3(Al,Fe)Si_3O_{10}(OH,F)_2$

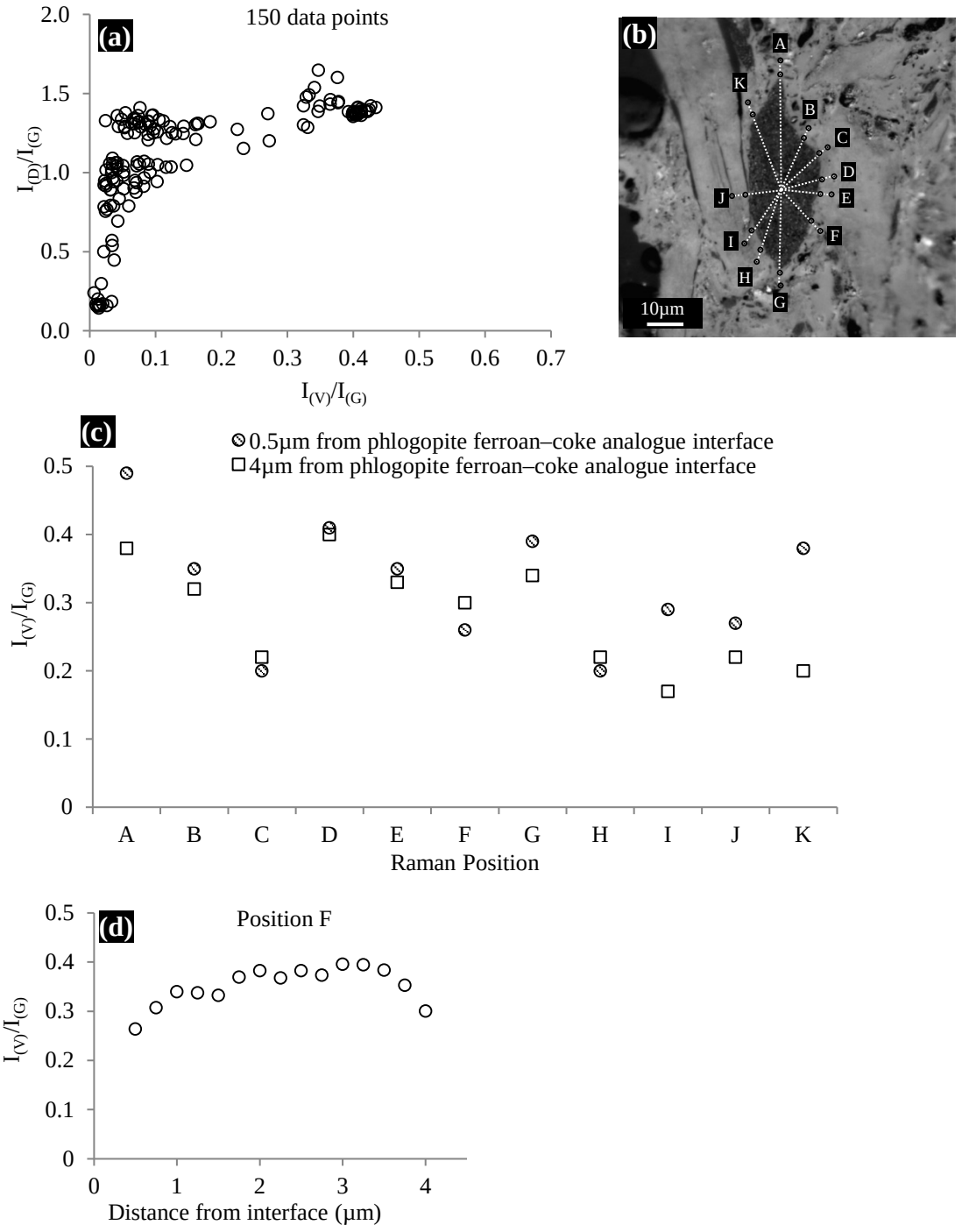

Figure 4-23: (a) A plot of $I_{(D)}/I_{(G)}$ versus $I_{(V)}/I_{(G)}$ showing the carbon bonding, (b) non-polarised optical micrograph showing the position of the localised Raman measurements, (c) a plot of $I_{(V)}/I_{(G)}$ versus the Raman position and (d) a plot of $I_{(V)}/I_{(G)}$ versus distance from the interface of the coke analogue–phlogopite ferroan.

Coke analogue containing quartz (SiO_2)

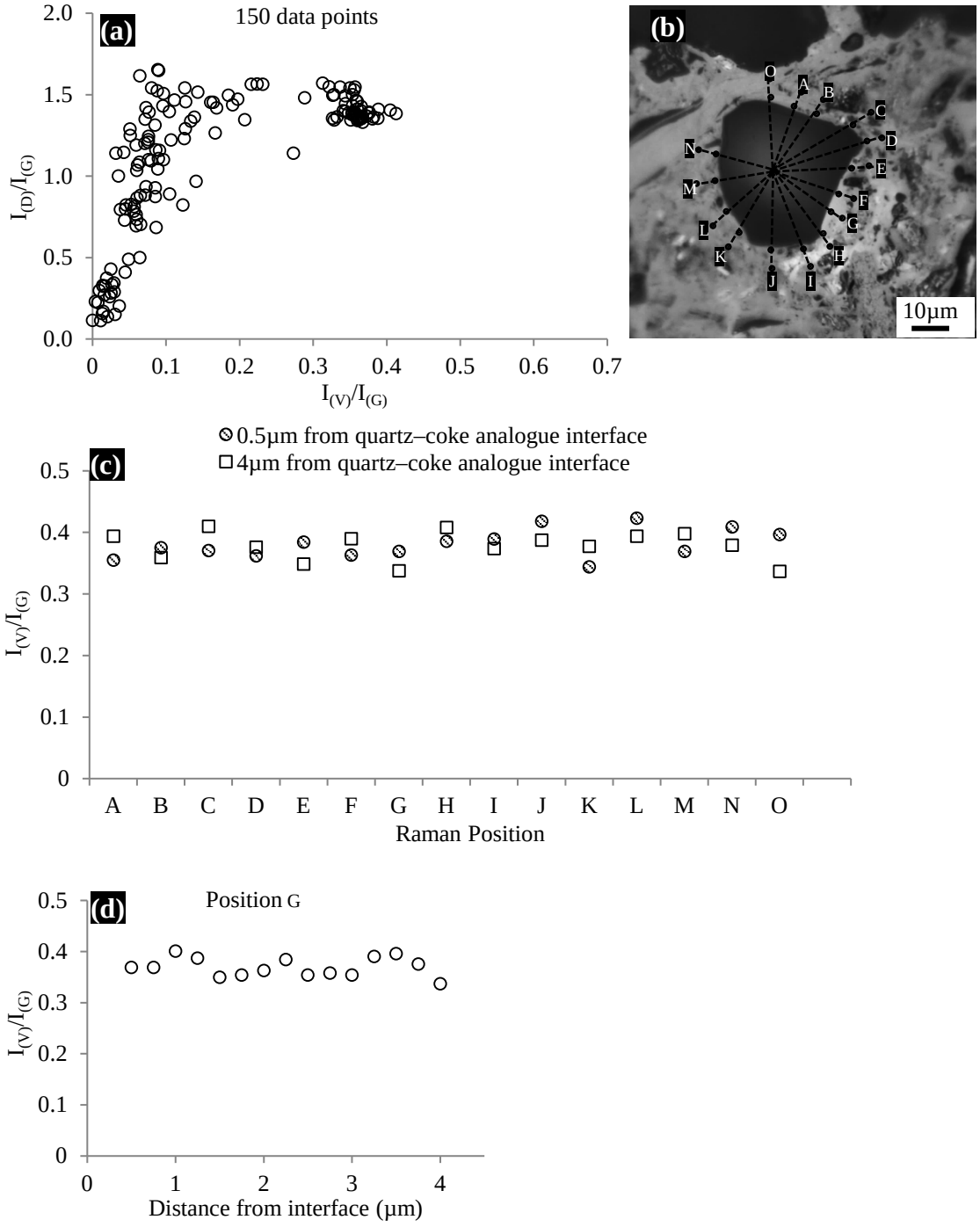

Figure 4-24: (a) A plot of $I_{(D)}/I_{(G)}$ versus $I_{(V)}/I_{(G)}$ showing the carbon bonding, (b) non-polarised optical micrograph showing the position of the localised Raman measurements, (c) a plot of $I_{(V)}/I_{(G)}$ versus the Raman position and (d) a plot of $I_{(V)}/I_{(G)}$ versus distance from the interface of the coke analogue–quartz.

Metallurgical coke

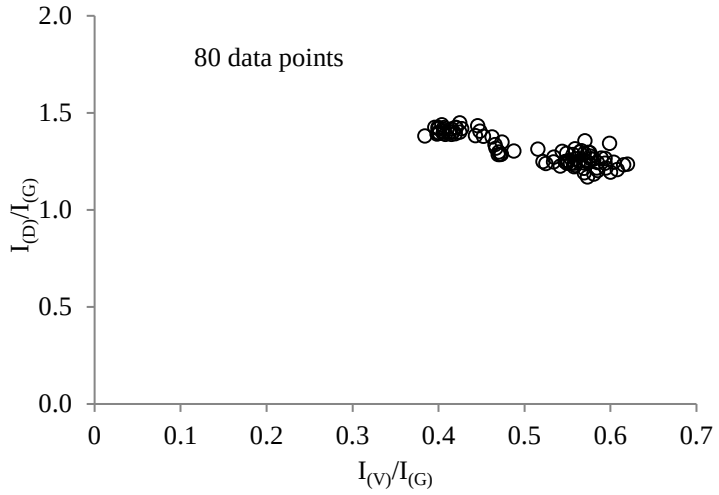

Figure 4-25: A plot of $I_{(D)}/I_{(G)}$ versus $I_{(V)}/I_{(G)}$ showing the carbon bonding of the metallurgical coke.

4.3. Porosity

Three separate but complementary porosity techniques of optical microscopy combined with image analysis, mercury porosimetry and neutron radiography (Dingo) were used in this study to test whether the porosity and pore size distribution of the coke analogues were well controlled and reproducible. Neutron radiography (Dingo) was also used to evaluate pore interconnectivity. The results for the metallurgical coke used in this study are also given.

4.3.1. Optical porosity and pore size distribution of the fired coke analogues and a metallurgical coke

The optical porosity in the vertical and radial sections of the three base coke analogues and optical porosity of a single surface (10mm depth) of the coke analogues containing metallic iron and minerals was given in Table 3-4. The optical porosity from the extensive measurements of a single surface of eight base coke analogues was 29.6% with a variation of ±1.0%. This is less than the ±2.3% variation obtained from the vertical and radial section of three base coke analogues given in Table 3-4 and Figure 3-22.

The average of the optical pore size distribution of the three base coke analogues (Figure 3-22) was compared to the data of a single surface of the coke analogues (Figures 4-26 to 4-28). This was carried out to verify whether the optical pore size distributions of a single surface of the coke analogues were similar to those obtained from the vertical and horizontal sections of the base coke analogues.

Table 3-4 and the optical porosity of the eight base coke analogues show that the porosity of the coke analogues was well controlled and reproducible. Figures 4-26 to 4-28 show that the optical pore size distribution of the coke analogues was well controlled and reproducible. It was highest in the 10–100µm pore diameter range.

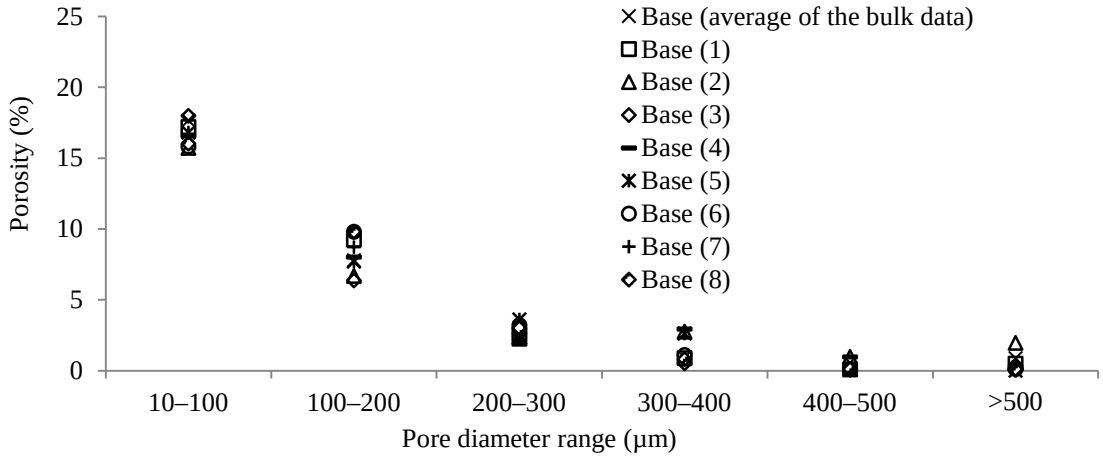

Figure 4-26: A plot of porosity versus pore diameter range of a single surface of the eight base coke analogues compared to the average of the bulk data given in Figure 3-22. (1) and (2) from the same batch and (3) – (8) from different batches.

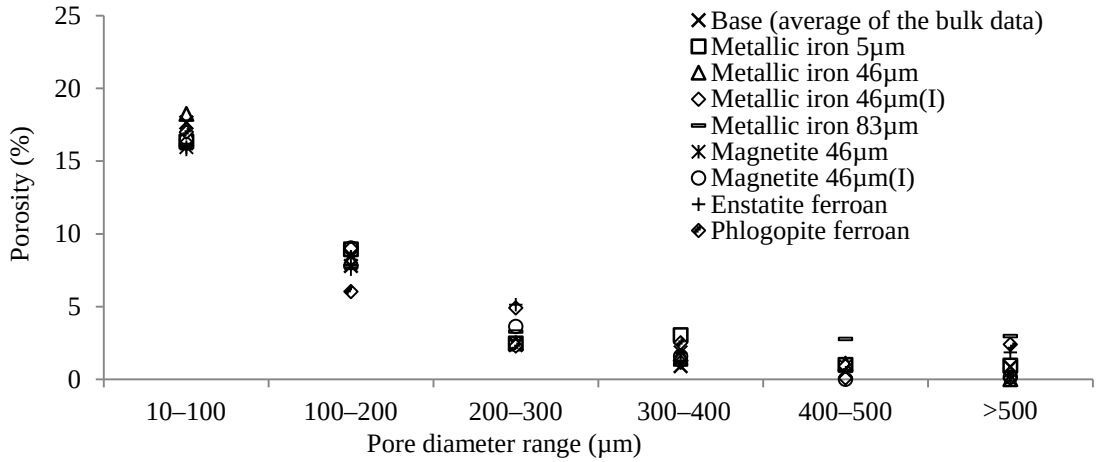

Figure 4-27: A plot of porosity versus pore diameter range of a single surface of the coke analogues containing Fe and Fe containing minerals compared to the average of the bulk data given in Figure 3-22.

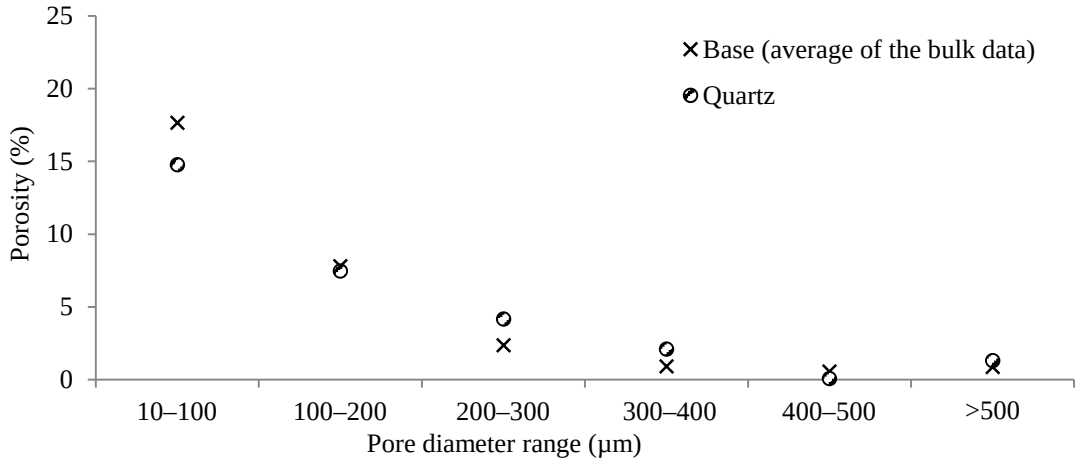

Figure 4-28: A plot of porosity versus pore diameter range of a single surface of the coke analogue–quartz (SiO_2) compared to the average of the bulk data given in Figure 3-22.

The optical porosity values of the three metallurgical coke samples (from the same source) used in this study were 24.7%, 30.9% and 37.5%. The optical pore size distribution of the three metallurgical cokes is given in Figure 4-29. Figure 4-29 shows that the area fraction of the metallurgical coke is mainly independent of the pore size.

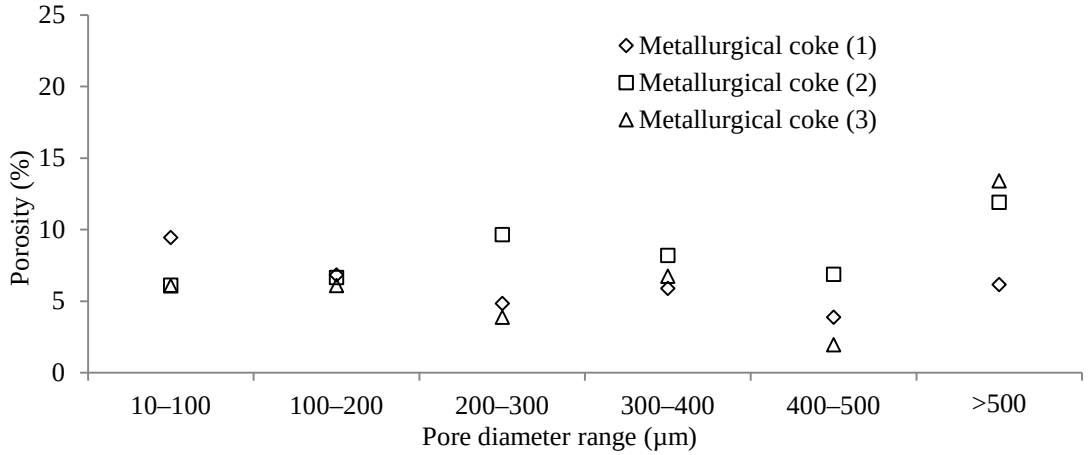

Figure 4-29: A plot of porosity versus pore diameter range of three metallurgical coke samples. The samples are from the same source.

4.3.2. Optical porosity and pore size distribution of reacted samples

The optical porosity and pore size distribution of the coke analogues (base and Fe 46µm) after reaction in CO_2 at 950°C and arrested after 1 hour are given in Table 4-14 and Figure 4-30 respectively. The results were compared to their unreacted (fired) samples. Table 4-14 shows that the optical porosities for the unreacted and reacted coke analogues were relatively similar, but with a possible slight increase in the reacted samples relative to the unreacted samples. Figure 4-30 shows that the optical pore size distributions of the unreacted and reacted coke analogues were relatively similar.

Table 4-14: The optical porosities of the unreacted and reacted coke analogues.

Coke analogues	**Optical porosity (%)**	
	Unreacted	Reacted at 950°C for 1hour
Base	29.3±2.3	30.7
Fe 46µm	31.9	32.4

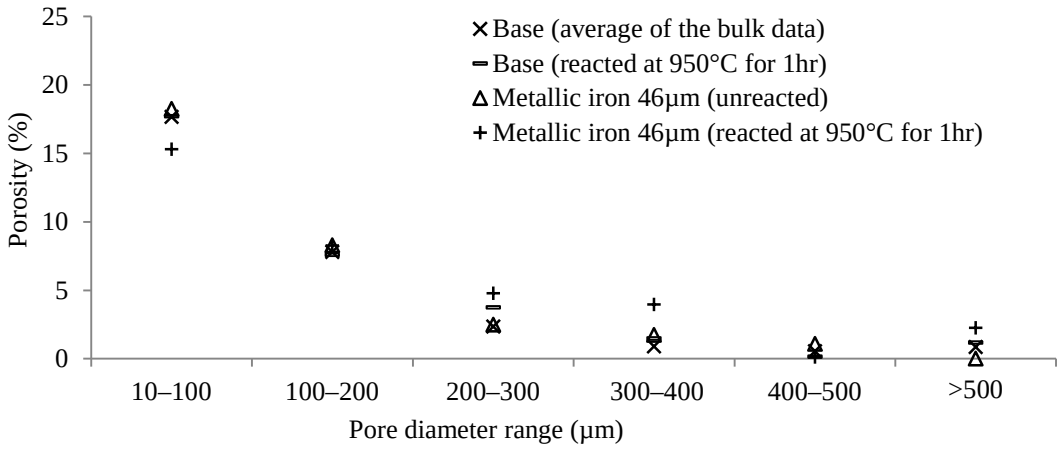

Figure 4-30: The optical pore size distribution of the unreacted and reacted coke analogues (base and Fe 46µm).

4.3.3. Dingo porosity and pore size distribution of the fired coke analogues and a metallurgical coke

The porosities and percentage of connected pores with the slice thickness of the coke analogues (base, Fe 46µm, Fe_3O_4 46µm and quartz (SiO_2)) and a metallurgical coke are given in Table 4-15. Neutron radiography (Dingo) shows that porosity values were relatively similar with increasing slice thickness.

The Dingo pore size distribution with slice thickness of the coke analogues (base, Fe 46µm, Fe_3O_4 46µm and quartz (SiO_2)) and metallurgical coke are given in Figures 4-31 to 4-35. The slice thickness in mm is given in the black box on the figures. Figures 4-31 to 4-34, for the coke analogues, show that at slice thickness <0.05mm the pores were largely in the <300µm equivalent diameter range. These pores appeared to be interconnected to one another at slice thickness ≥0.21mm to form pores with equivalent diameter >500µm. Figure 4-35, for the metallurgical coke, shows that at slice thickness <0.05mm the pores were largely in the 100–500µm equivalent diameter range and appeared to be interconnected to one another at slice thickness ≥0.21mm to form pores with equivalent diameter >500µm. Figures 4-31 to 4-35 indicate that the pores in the samples were interconnected with increasing slice thickness.

Table 4-15: Porosities and % of connected pores of the coke analogues and metallurgical coke using neutron radiography (Dingo).

Slice thickness (mm)	**Coke analogues**								**Metallurgical coke**	
	Base		Fe 46µm		Fe_3O_4 46µm		Quartz (SiO_2)			
	Porosity (%)	% of connected pores	Porosity (%)	% of connected pores	Porosity (%)	% of connected pores	Porosity (%)	% of connected pores	Porosity (%)	% of connected pores
0.03	25.3	0	25.0	0	23.3	0	22.4	0	29.8	0
0.05	25.6	4.1	24.7	4.5	23.6	5.9	22.7	2.4	29.9	14.7
0.10	25.6	19.2	24.8	21.9	23.5	18.7	22.9	22.5	30.2	55.6
0.21	25.1	54.3	24.6	58.4	23.4	47.6	22.4	48.8	30.5	80.3
0.43	24.2	77.0	24.3	81.2	23.6	71.0	22.4	73.8	31.4	91.2
0.67	23.5	80.8	24.1	81.1	23.8	80.3	22.3	78.7	31.9	95.1
1.34	23.5	80.8	23.9	83.0	23.1	84.3	22.0	87.6	29.3	95.8
2.68	23.9	82.7	23.3	82.9	23.7	84.2	22.4	89.0	30.5	97.1
5.36	23.2	85.9	23.5	82.9	23.7	87.1	23.4	89.1	31.7	97.7
10.72	23.7	86.0	23.3	82.7	23.8	87.7	23.1	89.9	30.0	97.4

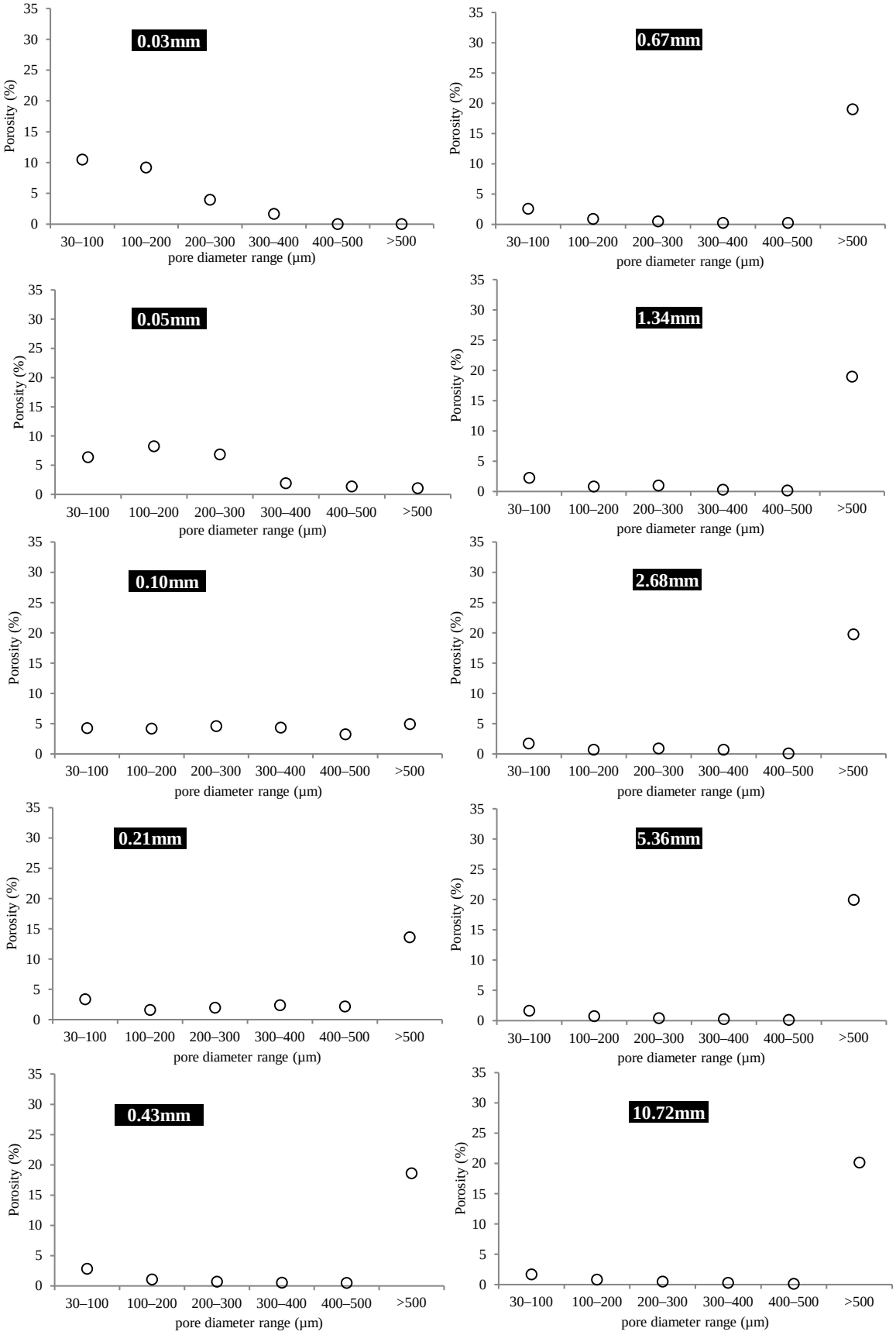

Figure 4-31: A plot of porosity versus pore diameter range of the base coke analogue, showing pore size distribution with slice thickness using Dingo method. The text in the black box indicating the slice thickness of the coke analogue.

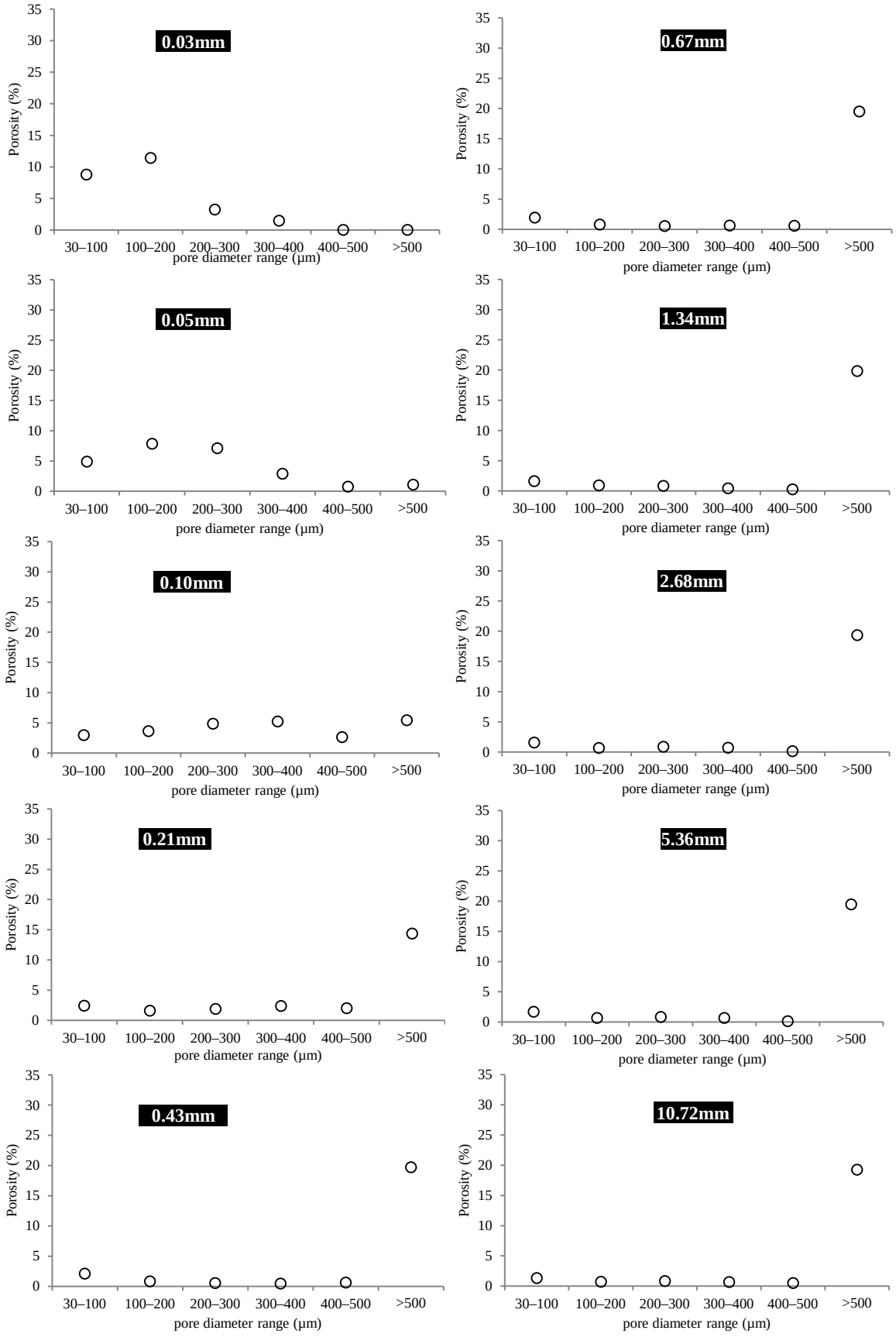

Figure 4-32: A plot of porosity versus pore diameter range of the coke analogue–Fe 46µm, showing pore size distribution with slice thickness using Dingo method. The text in the black box indicating the slice thickness of the coke analogue.

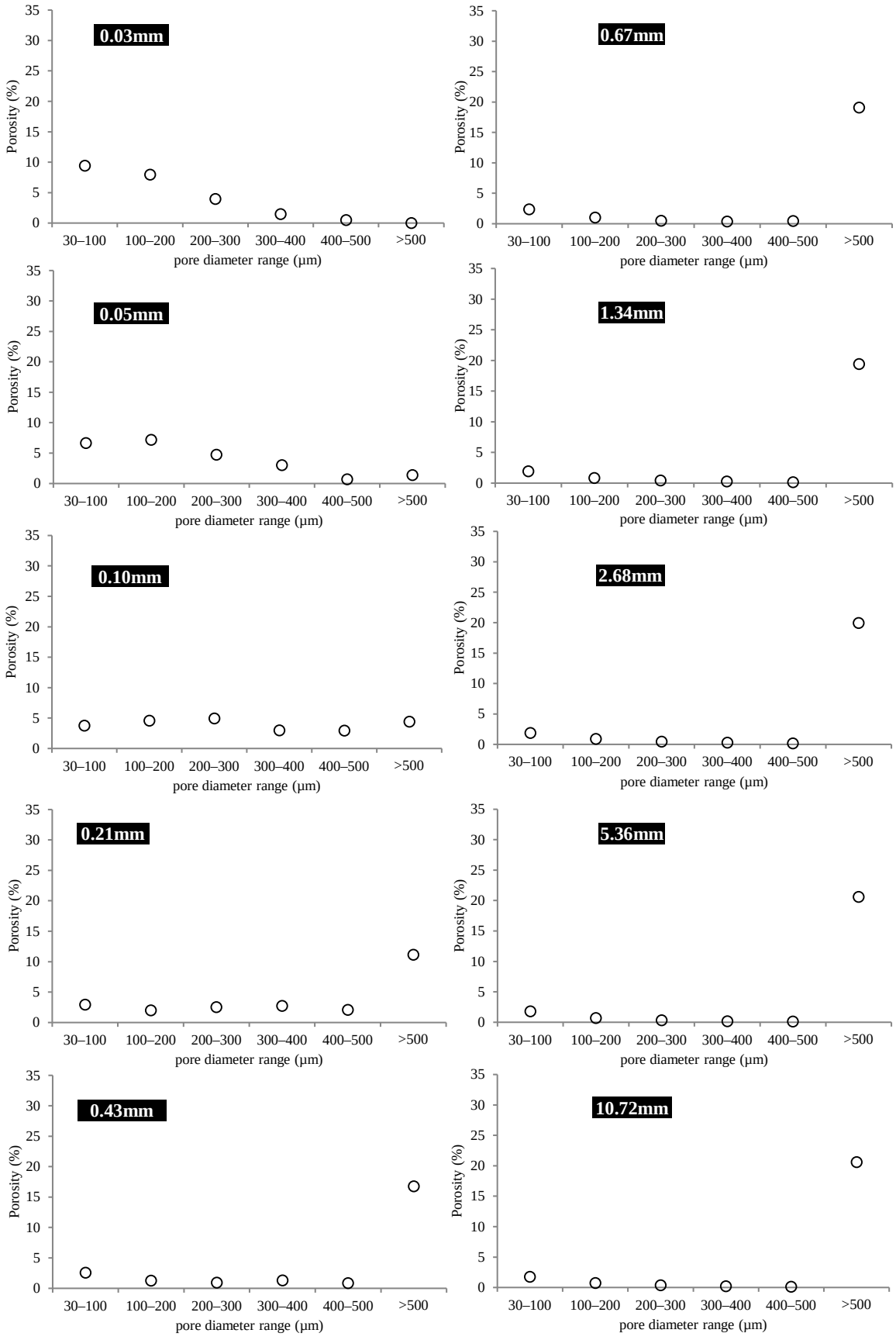

Figure 4-33: A plot of porosity versus pore diameter range of the coke analogue–Fe_3O_4 46µm, showing pore size distribution with slice thickness using Dingo method. The text in the black box indicating the slice thickness of the coke analogue.

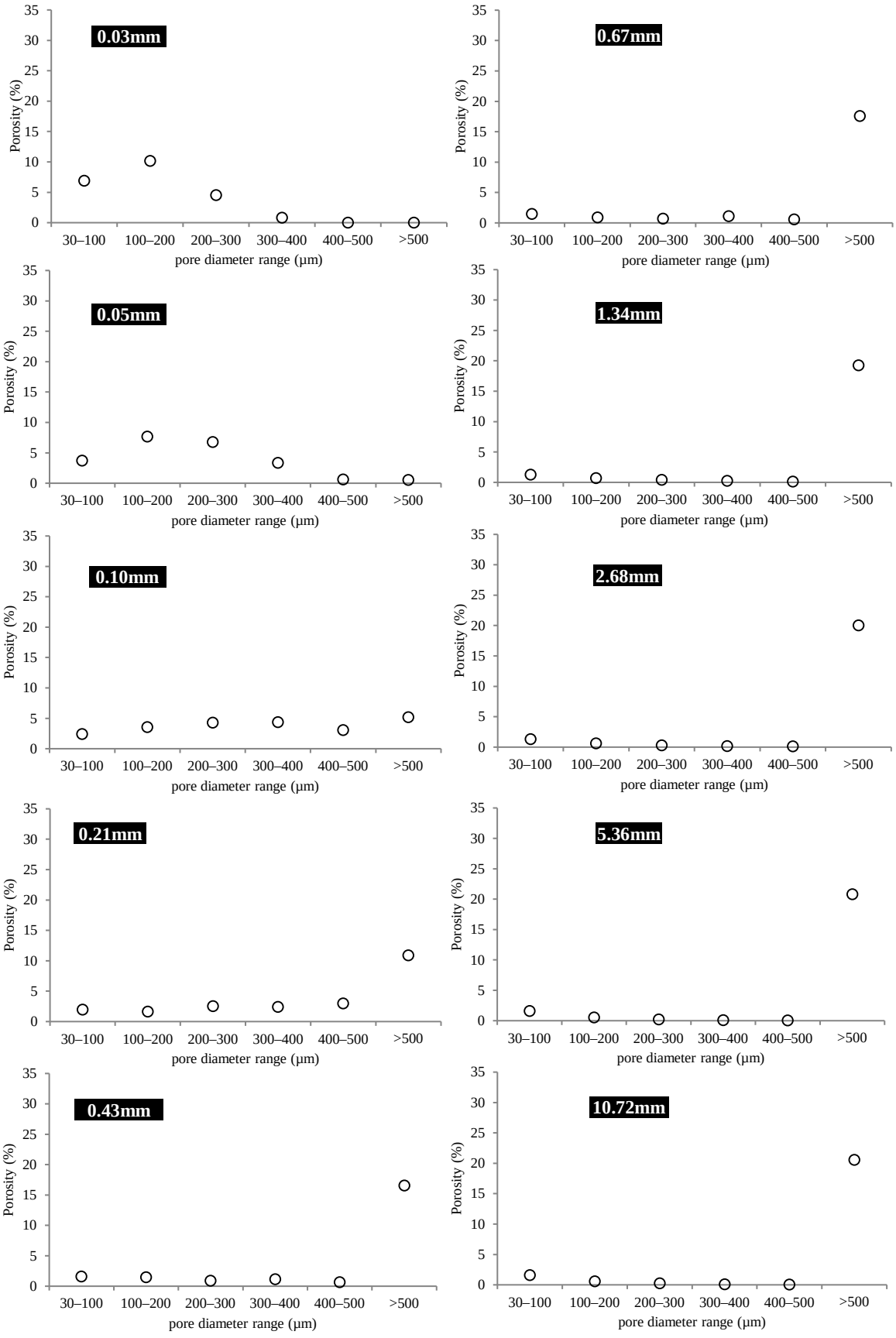

Figure 4-34: A plot of porosity versus pore diameter range of the coke analogue–quartz (SiO_2), showing pore size distribution with slice thickness using Dingo method. The text in the black box indicating the slice thickness of the coke analogue.

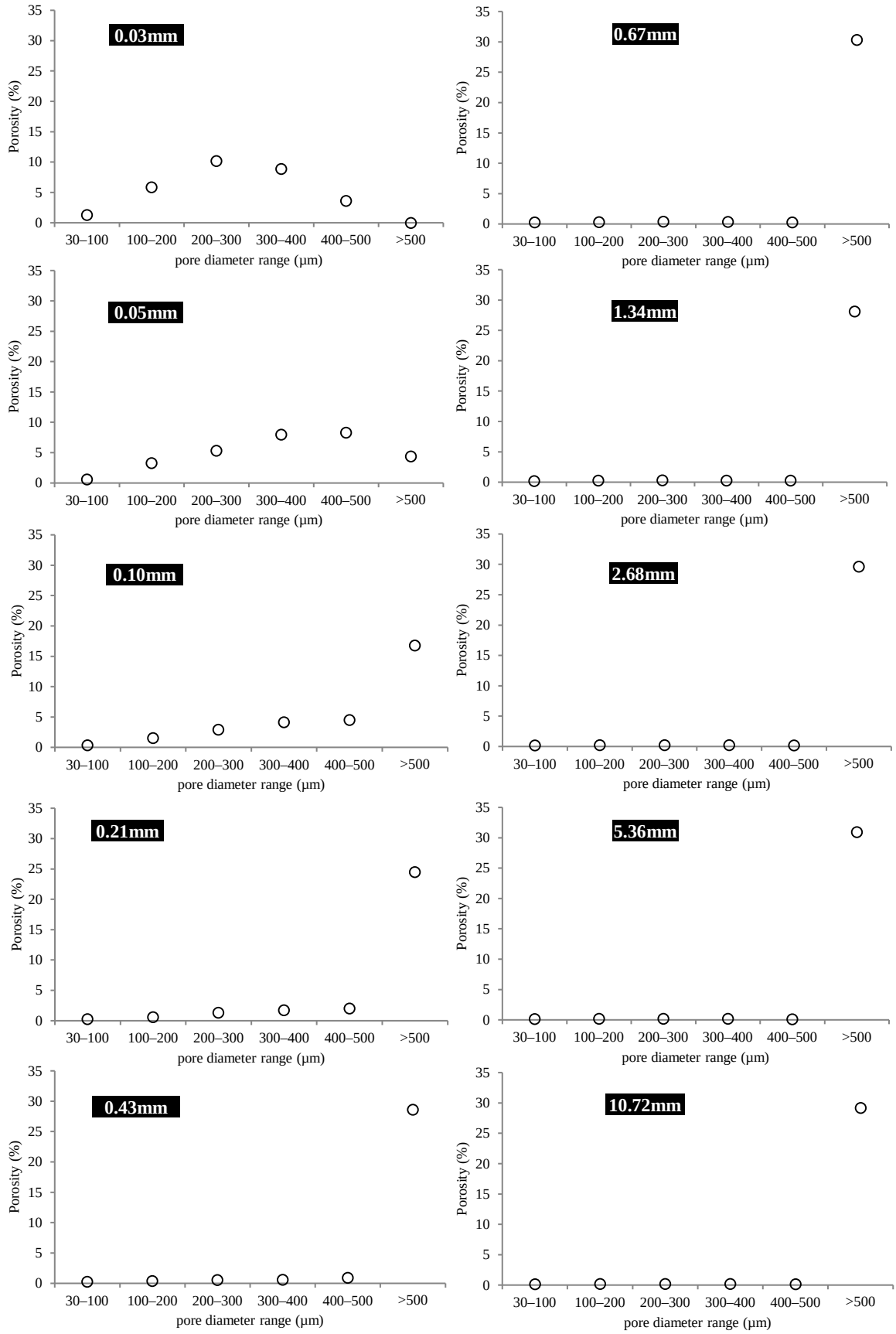

Figure 4-35: A plot of porosity versus pore diameter range of the metallurgical coke, showing pore size distribution with different slice thicknesses using Dingo method. The text in the black box indicating the slice thickness of the metallurgical coke.

4.3.4. Dingo porosity and pore size distribution of reacted samples

The Dingo porosity and pore size distribution of the coke analogues (base, Fe 46µm, Fe_3O_4 46µm and quartz (SiO_2)) reacted in CO_2 at 1100°C with time (arrested after 10 minutes and a further 10 minutes (20 minutes in total)) are given in Table 4-16 and Figure 4-36 respectively. Table 4-16 shows that porosity increases with increasing reaction time at this experimental temperature (1100°C). Figure 4-36 shows that large size pores with equivalent diameter >500µm were formed with reaction time.

An example of 2D image of the coke analogue–quartz (SiO_2) in fired condition and after CO_2 reactivity testing at 1100°C with time is given in Figure 4-37. Figure 4-37 shows "sponge-like" pore structure at the external surface of the reacted sample. This "sponge-like" pore structure increase with reaction time but the core of the reacted sample appeared to remain unreacted, indicating that at this experimental condition the enlargement of the pores occurred mainly at the external surface of the sample.

Table 4-16: Dingo porosity of the unreacted and reacted coke analogues.

Coke analogues	**Dingo porosity % (slice thickness is 0.03mm)**		
	Unreacted	Reacted at 1100°C	
		for 10 minutes	for 20 minutes
Base	25.3	27.9	30.5
Fe 46µm	25.0	28.0	31.2
Fe_3O_4 46µm	23.3	28.5	33.6
Quartz (SiO_2)	22.4	25.2	27.8

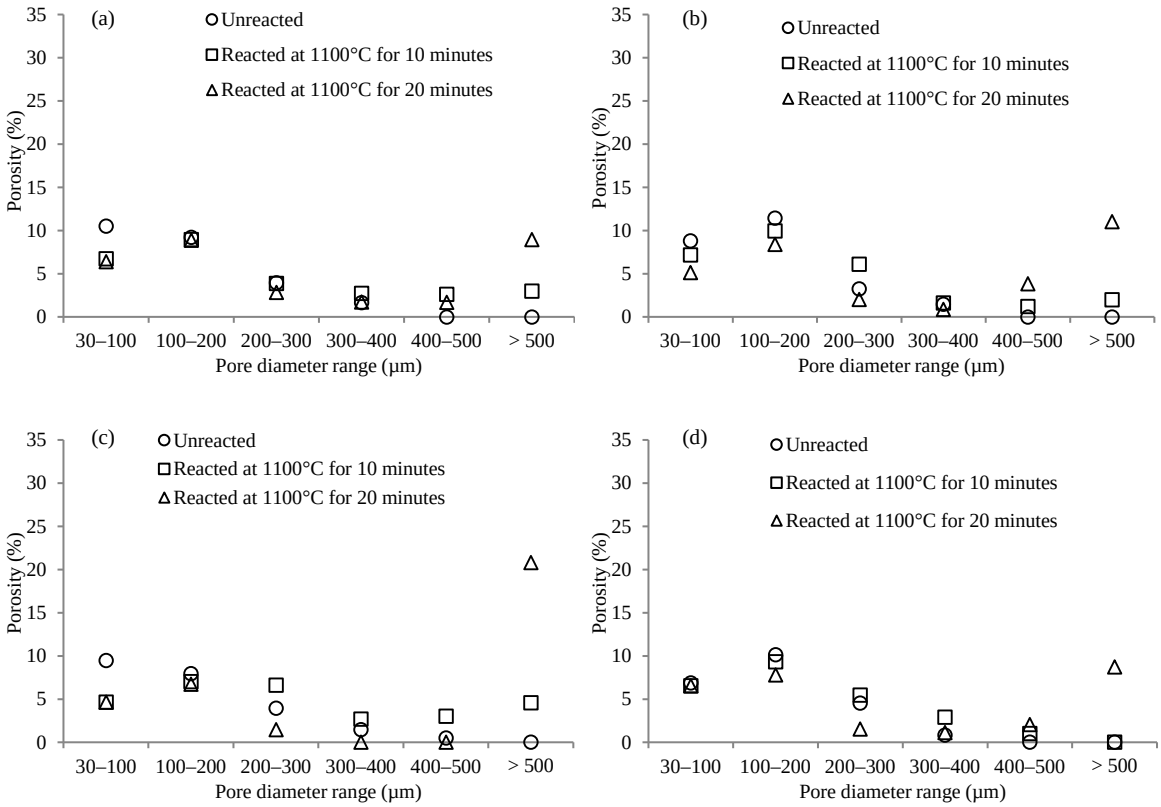

Figure 4-36: A plot of porosity versus pore diameter range of the coke analogues, showing pore size distribution with reaction time using Dingo method. (a) Base, (b) Fe 46µm (c) Fe_3O_4 46µm and (d) quartz (SiO_2). The slice thickness is ~0.03mm.

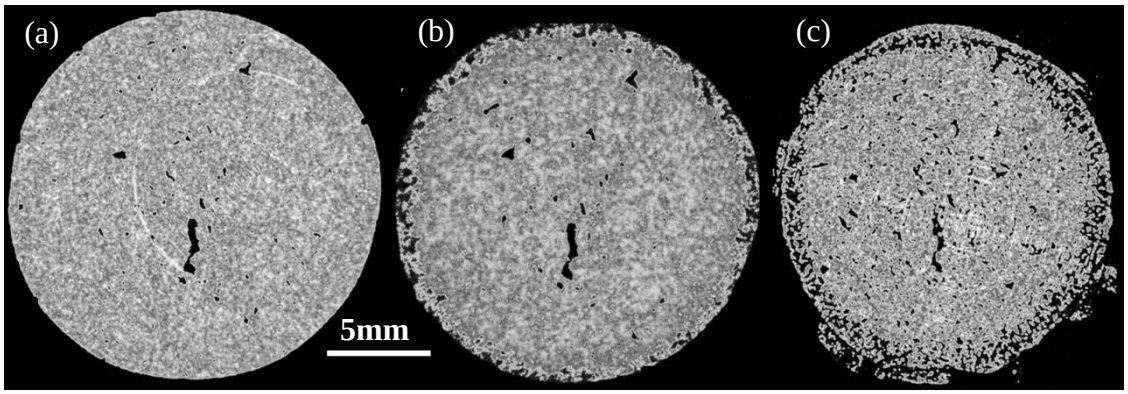

Figure 4.37: An example of 2D image of the coke analogue–quartz (SiO_2). (a) Fired condition, (b) after CO_2 reactivity testing at 1100°C for 10 minutes and (c) after CO_2 reactivity testing at 1100°C for a further 10 minutes (20 minutes in total). The slice thickness is 0.03mm.

4.3.5. Mercury porosimetry of the fired coke analogue

The mercury porosimetry provided data for pores with equivalent diameter <10µm in addition to the pores in the diameter range 10–500µm measured with the optical microscopy. This method measured pores in the diameter range 0.003–300µm. The porosity of the coke analogue samples (three base and a coke analogue–Fe_3O_4 46µm) are given in Table 4-17. The similar porosity values of the coke analogues indicate that the porosity of the coke analogues is well controlled and reproducible.

Table 4-17: Porosity of coke analogue samples measured using mercury porosimetry.

Coke analogues	**Porosity, % (0.003–300µm)**
Base	39.6 ± 2.8 (average of 3 samples)
Magnetite 46µm	40.0

Note, the coke analogue–Fe_3O_4 46µm was measured to check whether the reduction of Fe_3O_4 to Fe during coke analogue production affected the porosity of the sample.

A summary of the porosity results

- The three different techniques (optical (Figures 3-22, 4-26 to 4-28 and Table 3-4), mercury porosimetry (Table 4-17) and neutron radiography (Dingo) (Figures 4-31 to 4-34)) indicated that the porosity and pore size distribution of the coke analogues were similar, well controlled and reproducible.
- The mercury porosimetry was able to measure pores with equivalent diameter as low as 0.003µm.
- The optical porosity and pore size distribution of the coke analogues (base and Fe 46µm) in fired and post reacted (in CO_2 at 950°C and arrested after 1 hour) conditions were relatively similar (Table 4-14 and Figure 4-30), but with possible slight increase in the porosity of the reacted samples relative to the unreacted samples,
- The neutron radiography (Dingo) indicated that the pores of the coke analogues (Figures 4-31 to 4-34) and metallurgical coke (Figure 4-35) were highly interconnected with increasing slice thickness or in three dimensions,
- The neutron radiography (Dingo) indicated that porosity increases and pores were enlarged when the coke analogues were reacted in CO_2 at 1100°C with

time (Table 4-16 and Figure 4-36). The pore enlargement occurred mainly at the external surface of the reacted sample (Figure 4-37), and

- The optical porosity of the three metallurgical coke samples (same source) used in this study was not similar. Likewise, their pore size distribution has significant variation (Figure 4-29).

4.4. Thermodynamic analysis of metallic iron and mineral stability in the fired coke analogues

The results of MTDATA thermodynamic assessment of metallic iron and mineral stability in the fired coke analogues are presented in this section. The thermodynamic calculation was based on the proportional addition of the carbonaceous and non-carbonaceous materials used to make the coke analogue, as given in Table 3-1. The mass % of the thermodynamically stable phases and the components in the phases at the coke analogue firing temperature of 1200°C are given in Table 4-18. Only phases at 1200°C have been considered. The MTDATA predicts that at 1200°C, Fe and Fe_3O_4 would be in a liquid Fe phase with the release of CO gas from Fe_3O_4 on reaction with carbon. Enstatite ferroan ($Mg_{1.56}Fe_{0.44}Si_2O_6$) and phlogopite ferroan [$K(Mg,Fe)_3(Al,Fe)Si_3O_{10}(OH,F)_2$] would decompose into other thermodynamically stable phases accompanied by the release of gases. Quartz (SiO_2) would undergo phase transform to form tridymite (SiO_2). Plots of the effect of temperature on the phase stability of iron and minerals in the coke analogue as predicted by MTDATA are given in Figures 4-38 to 4-42.

The compounds $Mg_{1.56}Fe_{0.44}Si_2O_6$ and $K(Mg,Fe)_3(Al,Fe)Si_3O_{10}(OH,F)_2$ were not available in the MTDATA database. To deal with this, the following approach was used and the following inputs used in the calculation.

- An equivalent mass of the compounds (~5g) and carbon (80g),
- an equivalent mass of the elements in the compounds (based on the number of moles of the elements in the compounds), and
- OH was replaced with an equivalent amount of O to maintain electron balance.

The assumptions underlying this calculation were that,

1. energy of formation or reaction of $Mg_{1.56}Fe_{0.44}Si_2O_6$ and $K(Mg,Fe)_3(Al,Fe)Si_3O_{10}(OH,F)_2$ with carbon can be represented by a simple mass approach,
2. equilibrium state of formation is only dependent on the amounts of each components and temperature, and
3. OH and F are unstable at high temperature, and OH will decompose to simple oxides.

Table 4-18: The stable phases (in mass %) and components in the phases (in mass %) as predicted by MTDATA.

Coke analogues	**Stable phases at 1200°C**	**Mass% of the phases**	**Components in the phases**	**Mass% of components in the phases**
Metallic iron (Fe)	Graphite	94.2	C	100.0
	Liquid Fe	5.8	C	4.5
			Fe	95.5
Magnetite (Fe_3O_4)	Graphite	90.5	C	100.0
	Liquid Fe	5.8	C	4.5
			Fe	95.5
	CO gas	3.7	C	42.9
			O	57.1
Enstatite ferroan ($Mg_{1.56}Fe_{0.44}Si_2O_6$)*	Graphite	94.5	C	100.0
	Protopyroxene $MgSiO_3$	3.9	Mg	24.2
			O	47.8
			Si	28.0
	Tridymite SiO_2	0.7	O	53.3
			Si	46.8
	Liquid Fe	0.6	C	4.5
			Fe	95.5
	CO gas	0.3	C	42.9
			O	57.1
Phlogopite ferroan $[K(Mg,Fe)_3(Al,Fe)Si_3O_{10}(OH,F)_2]$ *	Graphite	94.0	C	100.0
	Sanidine $KAlSi_3O_4$	1.7	O	46.1
			Si	30.4
			K	14.0
			Al	9.6
	Liquid Fe	1.5	C	4.5
			Fe	95.5
	Forsterite Mg_2SiO_4	1.2	O	45.4
			Mg	34.6
			Si	20.0
	$K_2Si_4O_9$	0.9	O	42.9
			Si	33.6
			K	23.5
	Gas phase	0.6	O	48.9
			C	36.5
			F	6.6
			K	6.5
			Al	1.0
			Si	0.5
	MgF_2	0.1	F	61.2
			Mg	38.8
Quartz (SiO_2)	Graphite	94.0	C	100.0
	Tridymite SiO_2	6.0	O	53.3
			Si	46.7

* As described earlier, the compounds were not available in the MTDATA database.

Fe and Fe containing minerals stability in the fired coke analogue

Fe

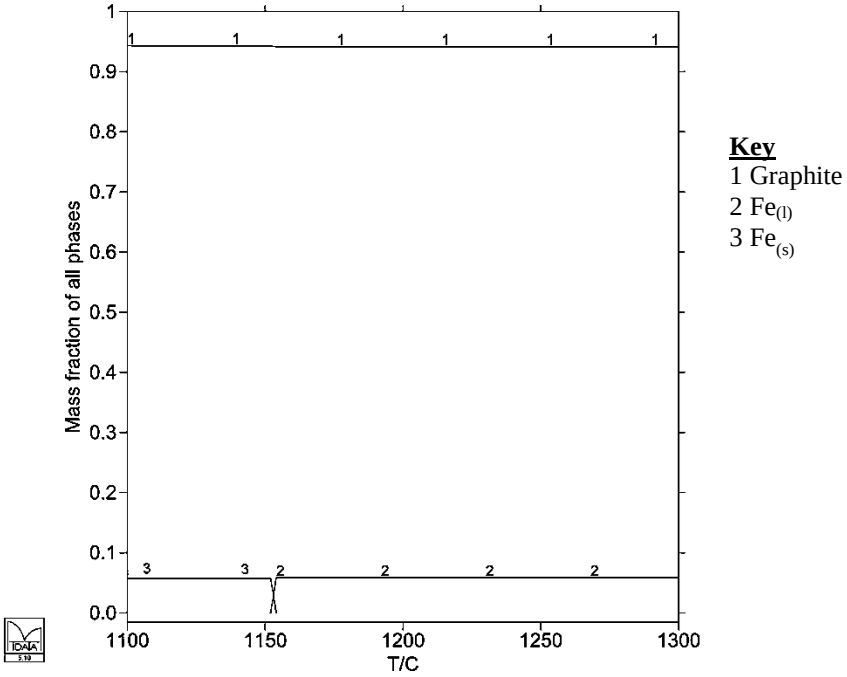

Figure 4-38: The effect of temperature on the phase stability of Fe in the coke analogue as predicted by MTDATA.

Fe_3O_4

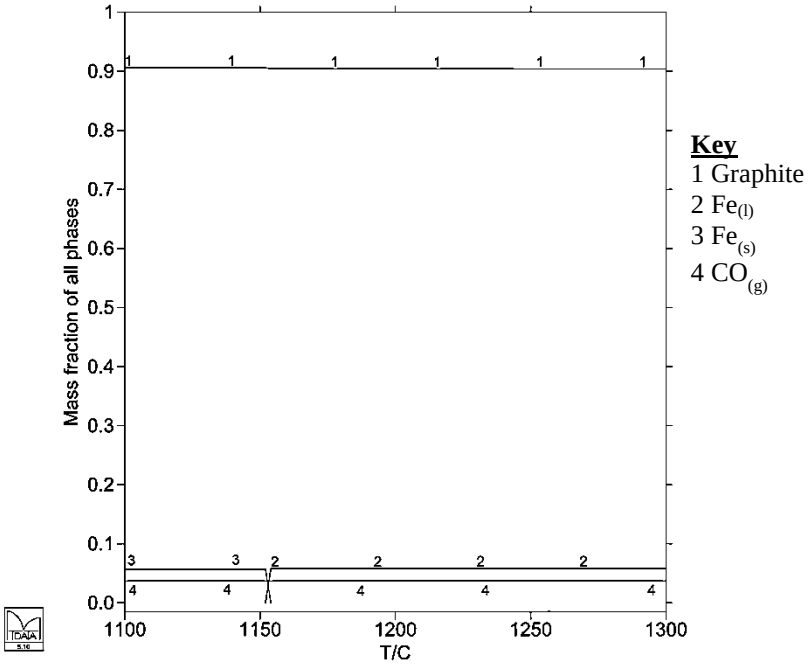

Figure 4-39: The effect of temperature on the phase stability of Fe_3O_4 in the coke analogue as predicted by MTDATA.

Enstatite ferroan, $Mg_{1.56}Fe_{0.44}Si_2O_6$

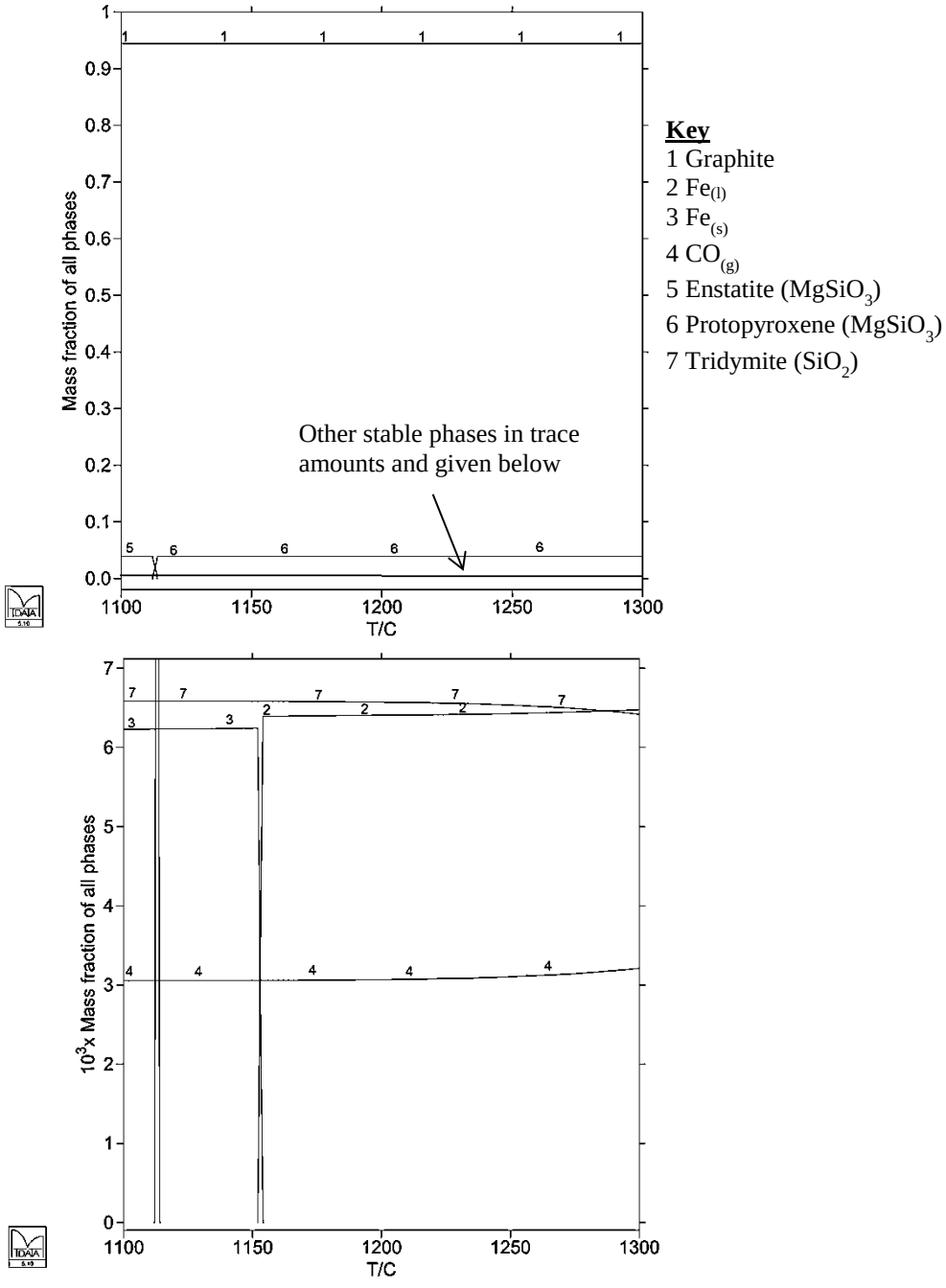

Figure 4-40: The effect of temperature on the phase stability of enstatite ferroan ($Mg_{1.56}Fe_{0.44}Si_2O_6$) in the coke analogue as predicted by MTDATA.

Phlogopite ferroan, $K(Mg,Fe)_3(Al,Fe)Si_3O_{10}(OH,F)_2$

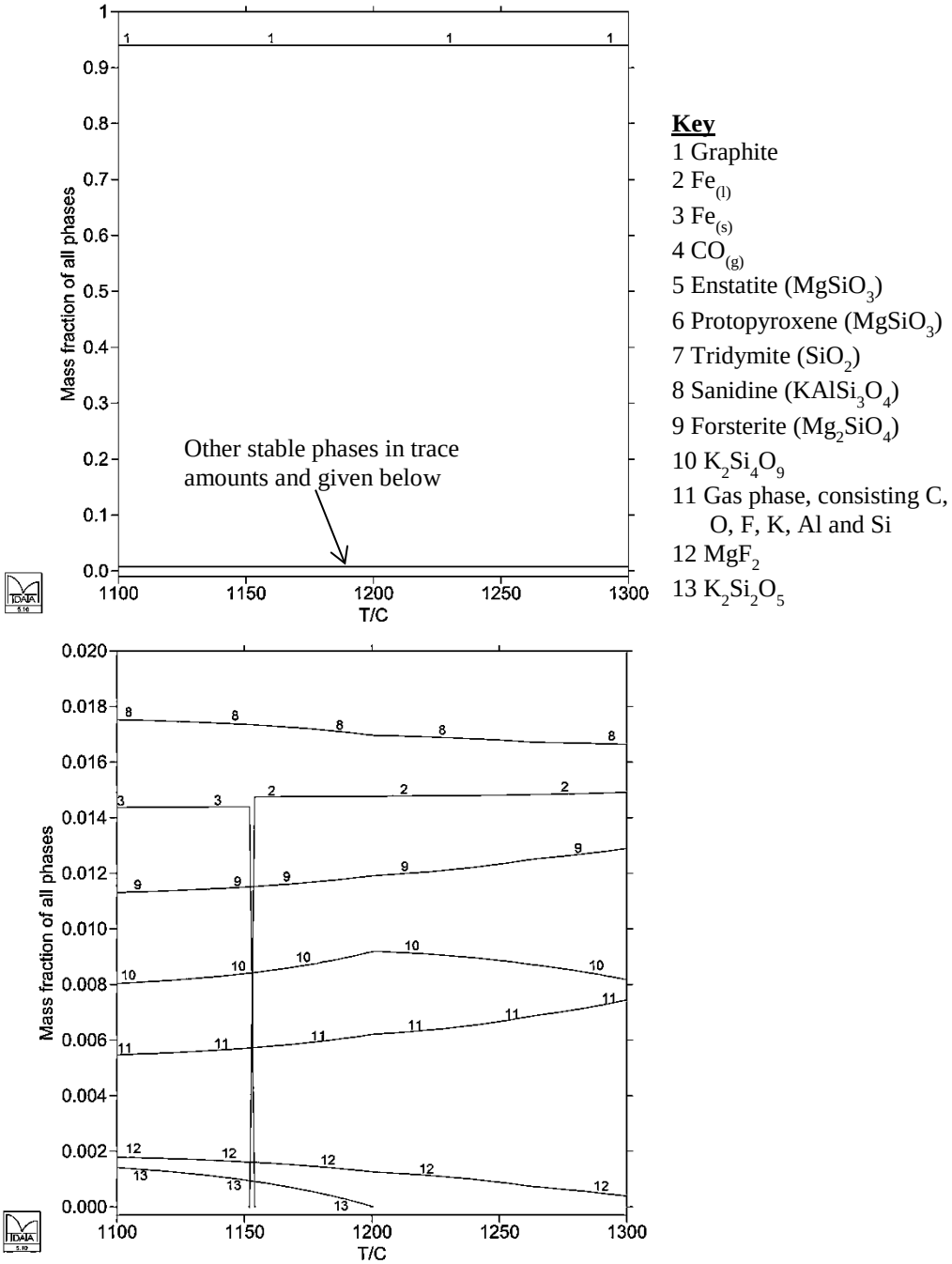

Figure 4-41: The effect of temperature on the phase stability of phlogopite ferroan [$K(Mg,Fe)_3(Al,Fe)Si_3O_{10}(OH,F)_2$] in the coke analogue as predicted by MTDATA.

Quartz (SiO_2) stability in the fired coke analogue

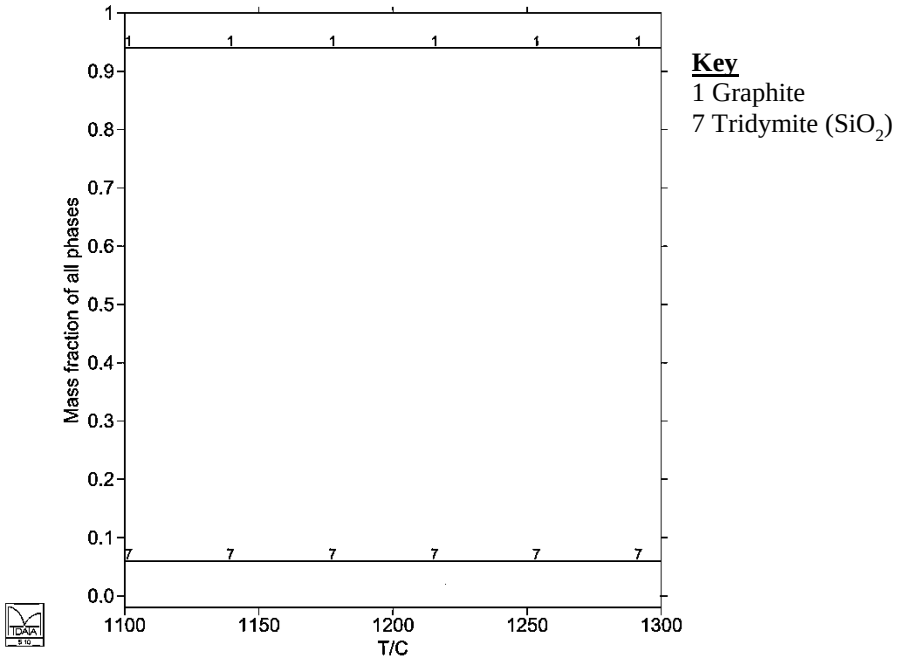

Figure 4-42: The effect of temperature on the phase stability of quartz (SiO_2) in the coke analogue as predicted by MTDATA.

The comparison of the MTDATA thermodynamic predictions (at 1200°C) and the XRD measurement (at approximately 25°C) for phase stability of non-carbonaceous materials in coke analogue is given in Table 4-19.

Table 4-19: A comparison of the MTDATA thermodynamic predictions and XRD measurements for phase stability of non-carbonaceous materials in the coke analogue.

Non-carbonaceous materials used to make the coke analogue	**MTDATA thermodynamic predictions for stable phases at 1200°C**	**XRD results for stable phases in the coke analogue**	
		Without ashing	After ashing at 520°C
Metallic iron (Fe)	$Fe_{(l)}$	α-$Fe_{(s)}$	–
Magnetite (Fe_3O_4) Enstatite Ferroan ($Mg_{1.56}Fe_{0.44}Si_2O_6$)	$Fe_{(l)}$ Protopyroxene ($MgSiO_3$), tridymite (SiO_2) and $Fe_{(l)}$	α-$Fe_{(s)}$ Enstatite ferroan ($Mg_{1.56}Fe_{0.44}Si_2O_6$)	– Enstatite ferroan ($Mg_{1.56}Fe_{0.44}Si_2O_6$)
Phlogopite Ferroan $[K(Mg,Fe)_3(Al,Fe)Si_3O_{10}(OH,F)_2]$	Sanidine ($KAlSi_3O_4$), $Fe_{(l)}$, forsterite (Mg_2SiO_4), $K_2Si_4O_9$ and magnesium fluoride (MgF_2)	Phlogopite ferroan $[K(Mg,Fe)_3(Al,Fe)Si_3O_{10}(OH,F)_2]$ and osumilite ($KMg_2Al_3(Si_{10}Al_2)O_{30}$)	Forsterite (Mg_2SiO_4), sanidine ($KAlSi_3O_8$), gedrite $[(Fe,Mg,Al)_7Al_2Si_6O_{22}(OH)_2]$, hematite ($Fe_2O_3$) and magnetite ($Fe_3O_4$).
Quartz (SiO_2)	Tridymite (SiO_2)	α-Quartz (SiO_2)	–

– not measured

4.5. Coke analogue reactivity

4.5.1. General reactivity in CO_2

The FWC versus time curves with temperatures of the coke analogues and metallurgical coke reacted in CO_2 for 2 hours is given in Figures 4-43 to 4-53. The figures show that the final FWC became more negative with temperature. Figures 4-47 and 4-48 show that the coke analogues were completely reacted at ~1 hour at temperatures >1250°C and >1200°C respectively.

Base coke analogue

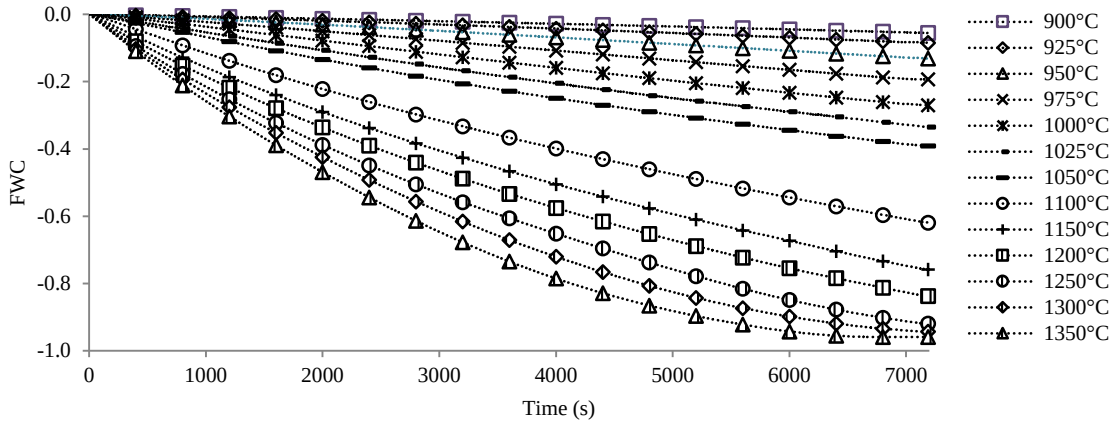

Figure 4-43: The FWC versus time curves with temperatures of the base coke analogue reacted in CO_2 for 2 hours.

Coke analogues containing Fe and Fe containing minerals

Fe 5µm

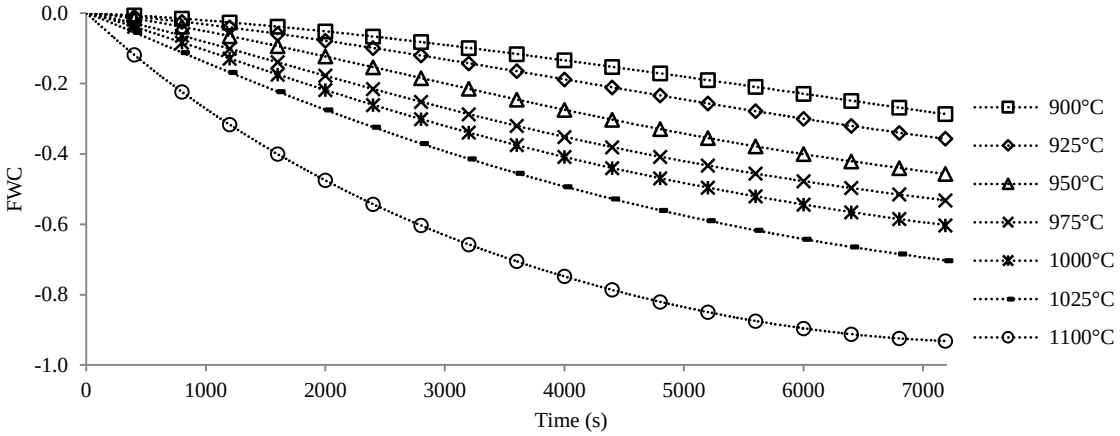

Figure 4-44: The FWC versus time curves with temperatures of the coke analogue–Fe 5µm reacted in CO_2 for 2 hours.

Fe 46µm

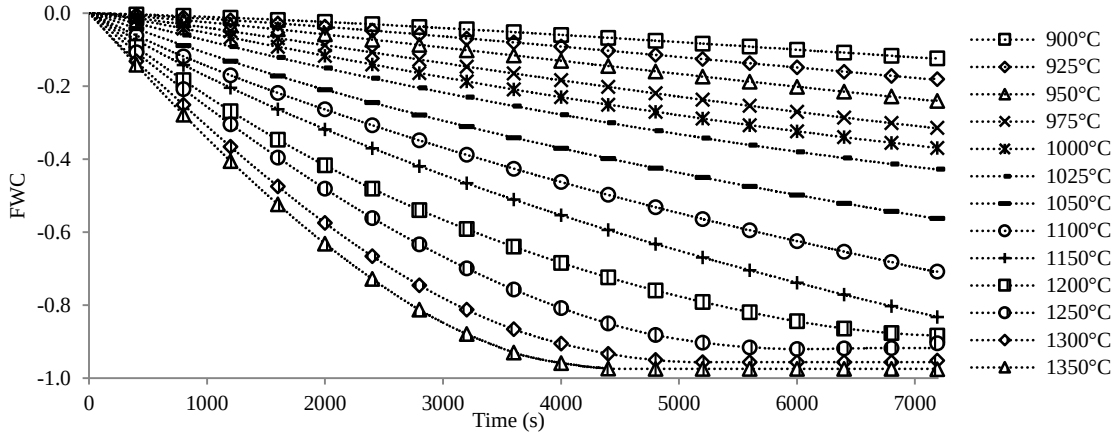

Figure 4-45: The FWC versus time curves with temperatures of the coke analogue–Fe 46µm reacted in CO_2 for 2 hours.

Fe 46µm (I)

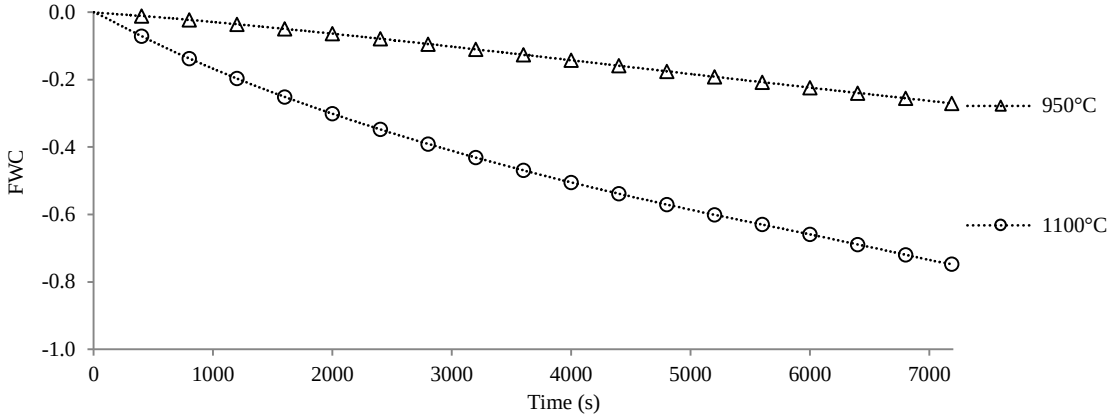

Figure 4-46: The FWC versus time curves with temperatures of the coke analogue–Fe 46µm (I) reacted in CO_2 for 2 hours.

Fe 83µm

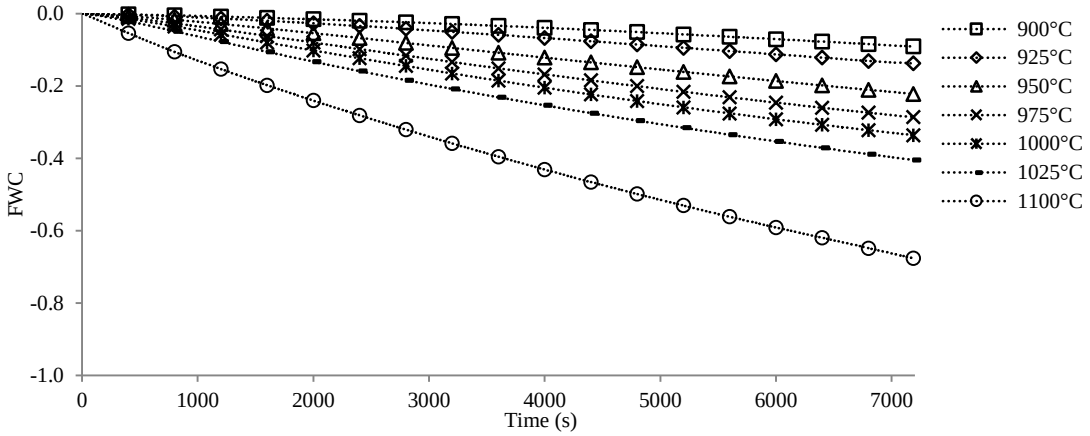

Figure 4-47: The FWC versus time curves with temperatures of the coke analogue–Fe 83µm reacted in CO_2 for 2 hours.

Fe_3O_4 46µm

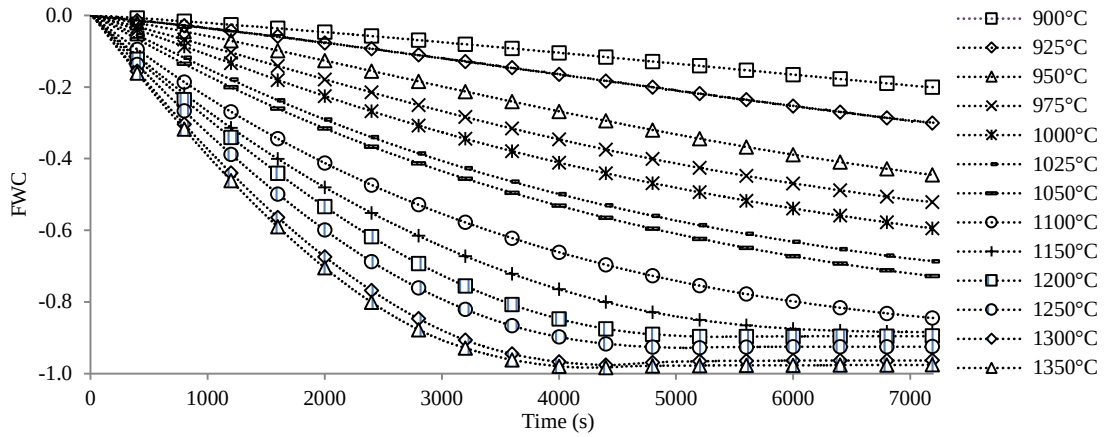

Figure 4-48: The FWC versus time curves with temperatures of the coke analogue–Fe_3O_4 46µm reacted in CO_2 for 2 hours.

Fe_3O_4 46µm (I)

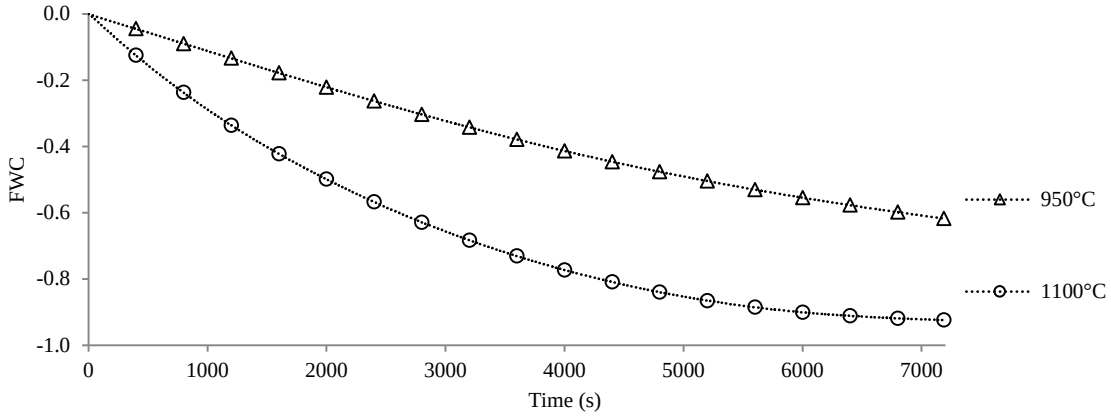

Figure 4-49: The FWC versus time curves with temperatures of the coke analogue–Fe_3O_4 46µm (I) reacted in CO_2 for 2 hours.

Enstatite ferroan, $Mg_{1.56}Fe_{0.44}Si_2O_6$

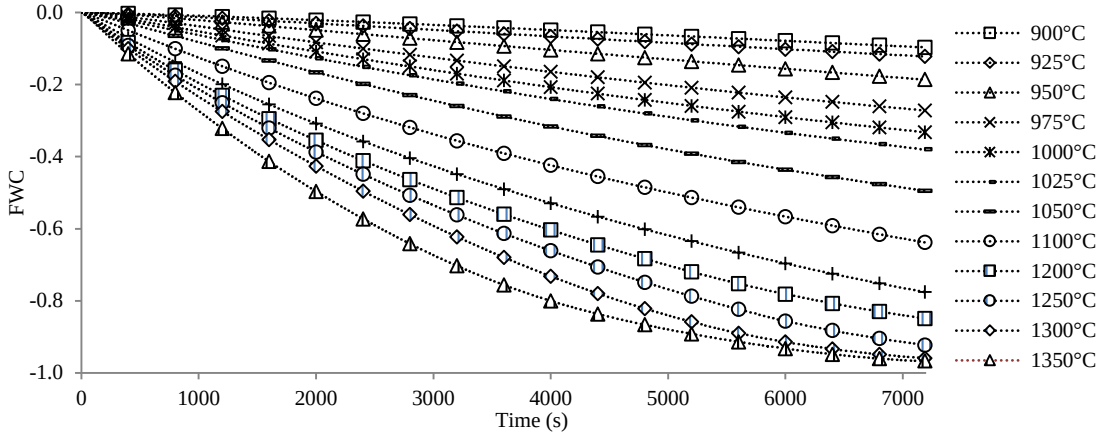

Figure 4-50: The FWC versus time curves with temperatures of the coke analogue–enstatite ferroan reacted in CO_2 for 2 hours.

Phlogopite ferroan, $K(Mg,Fe)_3(Al,Fe)Si_3O_{10}(OH,F)_2$

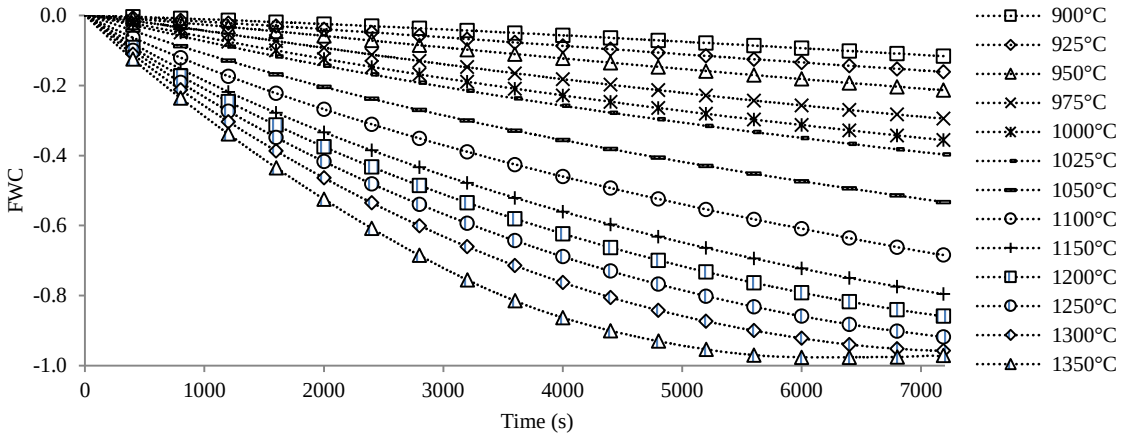

Figure 4-51: The FWC versus time curves with temperatures of the coke analogue–phlogopite ferroan reacted in CO_2 for 2 hours.

Coke analogue containing quartz (SiO_2)

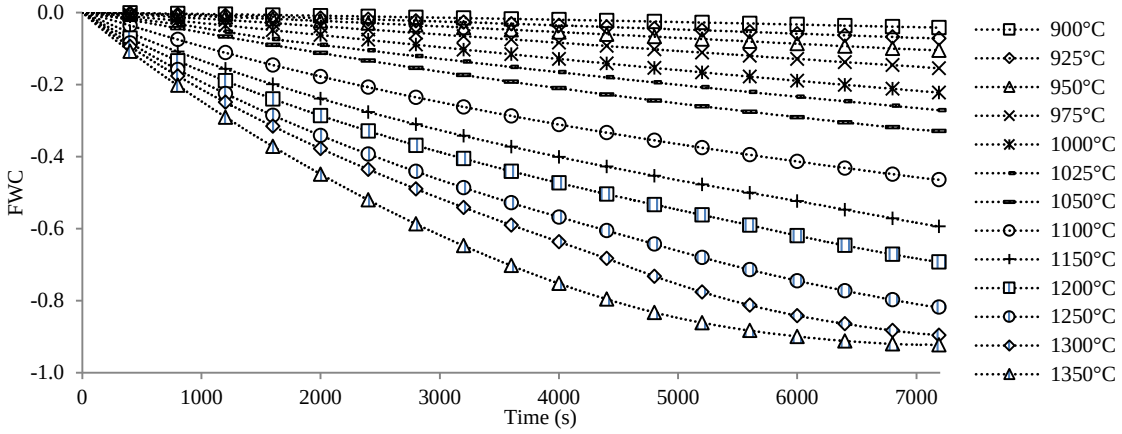

Figure 4-52: The FWC versus time curves with temperatures of the coke analogue–quartz (SiO_2) reacted in CO_2 for 2 hours.

Metallurgical coke

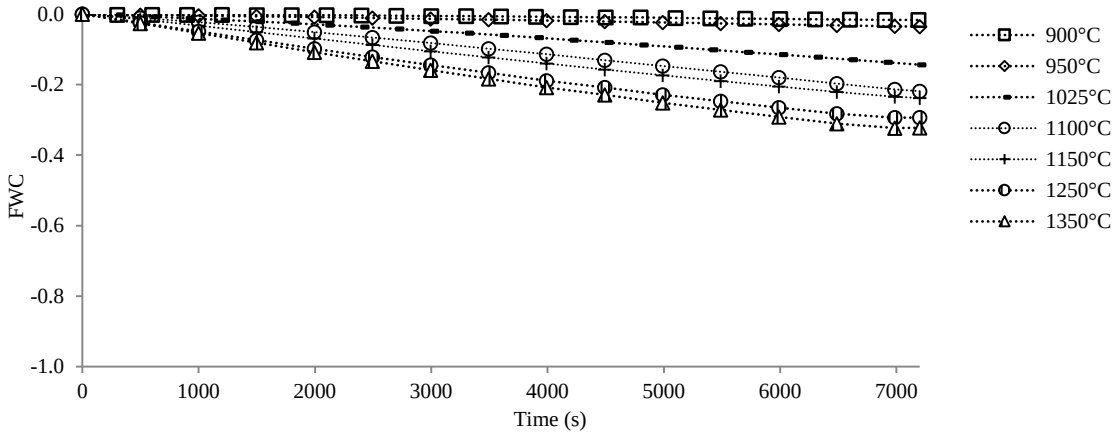

Figure 4-53: The FWC versus time curves with temperatures of the metallurgical coke reacted in CO_2 for 2 hours.

4.5.2. Post reactivity experimental observation and analysis

The physical appearance and features of the coke analogues reacted (post-experimental) in CO_2 for 2 hours is given in Table 4-20. In general, the geometry of the samples remained unchanged up to approximately 1150°C, but deviate significantly from the initial cylindrical shape with increasing temperature.

Table 4-20: The physical appearance and features of the post reacted coke analogues (reacted in CO_2 for 2 hours).

Coke analogues	**Temperature (°C)**												
	900	925	950	975	1000	1025	1050	1100	1150	1200	1250	1300	1350
Base	#	#	#	#	#	*	β	β	β	+	+	≠	≠
Fe 5µm	#	#	*	*	β	β	-	+	-	-	-	-	-
Fe 46µm	#	#	#	*	*	β	β	β	β	+	†	^	^
Fe 46µm (I)	-	-	#	-	-	-	-	β	-	-	-	-	-
Fe 83µm	#	#	#	*	*	β	-	β	-	-	-	-	-
Fe_3O_4 46µm	#	#	*	*	β	β	β	+	+	+	†	^	^
Fe_3O_4 46µm (I)	-	-	*	-	-	-	-	+	-	-	-	-	-
Enstatite ferroan	#	#	#	#	#	*	β	β	β	+	+	^	^
Phlogopite ferroan	#	#	#	#	*	β	β	β	β	+	+	^	^
SiO_2	#	#	#	#	#	*	β	β	β	+	+	$	$

- reactivity not measured
\# maintained the initial cylindrical shape,
* maintained the initial cylindrical shape with powdered external surface,
β maintained the initial cylindrical shape with powdered external surface but broke up on transferring from the furnace alumina pedestal to sample container,
\+ deviated from the initial shape and in powder form,
† no more coke analogue but presence of particles thought to be either iron or iron oxide,
≠ no more coke analogue,
^ no more coke analogue but presence of solidified residue, and
$ no more coke analogue but presence of white powder.

Summary of coke analogue reactivity results

1. The FWC of the coke analogues (Figures 4-43 to 4-52) and metallurgical coke (Figure 4-53) became more negative with increasing temperature.
2. At the same temperature, the FWC of the coke analogues (Figures 4-43 to 4-52) is more negative relative to the FWC of the metallurgical coke (Figure 4-53).
3. At the same temperature, the FWC of the coke analogues became more negative with increase in the concentration of Fe (Fe 46µm (I) > Fe 46µm, and Fe_3O_4 46µm (I) > Fe_3O_4 46µm). The FWC curves are given in Figures 4-46, 4-45, 4-49 and 4-48 respectively.

4. At the same temperature and constant Fe concentration, the FWC of the coke analogues became more negative with change in particle size of Fe (5µm > 46µm > 83µm). The FWC curves are given in Figures 4-44, 4-45 and 4-47.
5. At the same temperature the effect of Fe and minerals (0.1mol per 100g of coke analogue carbonaceous materials and 38–53µm particle size range) on the FWC of the coke analogues can be ranked as quartz (SiO_2) < base < enstatite ferroan ($Mg_{1.56}Fe_{0.44}Si_2O_6$) < phlogopite ferroan [$K(Mg,Fe)_3(Al,Fe)Si_3O_{10}(OH,F)_2$] < Fe 46µm < Fe_3O_4 46µm. The FWC curves are given in Figures 4-52, 4-43, 4-50, 4-51, 4-45 and 4-48 respectively.
6. The post reacted samples deviated from the initial cylindrical shape with increasing temperature (Table 4-20).

4.6. LECO analysis of coke analogue system containing Fe

The LECO analysis result of carbon pick up and loss from the iron during firing and reaction with CO_2 respectively is given in Table 4-21.

Table 4-21: The carbon (mass %) in the Fe

LCAK steel sample condition	**Carbon (mass %)**
As-received	0.06
Removed from fired coke analogue	1.72
Removed from post reacted coke analogue (in CO_2 at 950°C for 2hours)	0.48
Removed from post reacted coke analogue (in CO_2 at 1025°C for 2hours)	0.46

The measurement indicates that Fe picked up carbon after the analogue was fired at 1200°C for 1 hour. The carbon level in the Fe decreased after reaction (post-experimental) in CO_2 for 2 hours at two different temperatures of 950°C and 1025°C.

4.7. Assessment of Intercalation

Intercalation has been assessed by considering the broadening of the (002) carbon peak. The assessment of the full width at half maximum (FWHM) of the (002) carbon peak is being carried out to establish the effects of iron and minerals. The FWHM and peak position of the (002) carbon peak of the base coke analogue is given in Figure 4-54. Figure 4-54 is typical of other analogue materials tested. The full details of these are given in section II.2 of Appendix II.2.

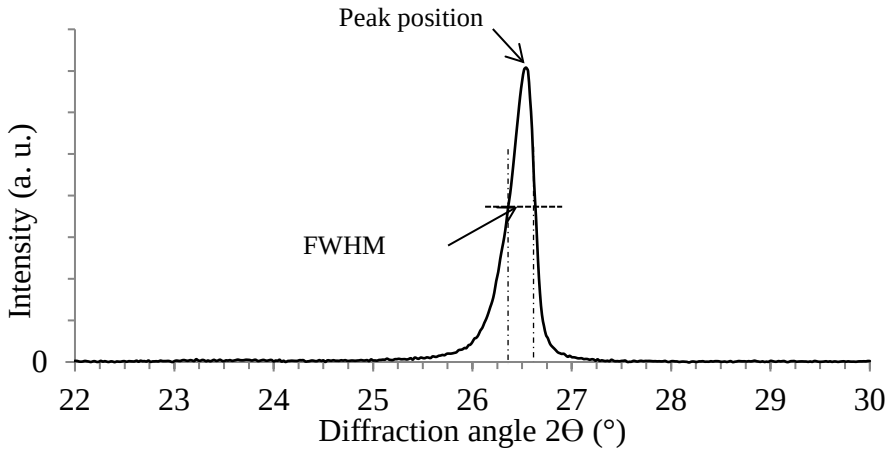

Figure 4-54: The XRD pattern of fired base coke analogue showing FWHM and position of the (002) carbon peak.

Table 4-22: The FWHM and position of (002) carbon peak in the coke analogues

Coke analogues	**Fired**		**Post experimental at 1100°C for 2hrs**	
	FWHM (°)	Peak Position (°)	FWHM (°)	Peak Position (°)
Base	0.286	26.54	0.336	26.58
Fe 5µm	0.226	26.56	–	–
Fe 46µm	0.218	26.58	0.222	26.64
Fe 83µm	0.240	26.54	–	–
Fe_3O_4 46µm	0.248	26.56	0.332	26.52
Enstatite ferroan ($Mg_{1.56}Fe_{0.44}Si_2O_6$)	0.296	26.50	0.302	26.56
Phlogopite ferroan $[K(Mg,Fe)_3(Al,Fe)Si_3O_{10}(OH,F)_2]$	0.250	26.58	0.256	26.60
Quartz (SiO_2)	0.244	26.58	0.284	26.52

– Not measured

From Table 4-22, it can be seen that FWHM values of the coke analogues are relatively similar both in fired and post reacted conditions. It appears Fe and mineral additions do not affect the (002) carbon peak, that is no broadening of the peak. That is there appears to be no intercalation effect of these minerals.

5. Discussion: How representative of metallurgical coke is the coke analogue?

Metallurgical coke is a complex material that consists of different carbonaceous forms or textural components, mineral components and has a pore size distribution with pores of various morphologies. In addition, it has significant heterogeneity in most metric(s) used to characterise its carbon form, carbon texture, mineralogy, mineral dispersion, mineral size and morphology, and porosity. The complexity and heterogeneity of coke make it difficult to evaluate mineral effects on coke behaviour.

To overcome the complexity and heterogeneity issues a coke analogue was developed that represents a simplified metallurgical coke with controlled porosity, mineralogy, mineral dispersion throughout the coke and reactivity in CO_2. While carbon type is not controlled, it is to a large degree set by the analogue production method and for the most part reasonably constant for all the analogues.

The primary aims of this thesis are encapsulated in two questions.

1. Is the coke analogue representative of metallurgical coke?
2. Using the coke analogue, what are the effects of metallic/elemental iron on carbon bonding and analogue reactivity?

Further with aims 3 and 4, there has been an attempt to quantify the relative effects (relative to Fe) of quartz (SiO_2) and iron bonded with an oxide (enstatite ferroan ($Mg_{1.56}Fe_{0.44}Si_2O_6$) and phlogopite ferroan [$K(Mg,Fe)_3(Al,Fe)Si_3O_{10}(OH,F)_2$]) on the carbon bonding and analogue reactivity in CO_2.

The coke analogue used in this study is a relatively new material. This Chapter (Chapter 5) is focused on the characterisation of the coke analogue and will assess how representative of metallurgical coke is the coke analogue. This Chapter addresses aim 1 of this thesis. Aims 2, 3 and 4 of this thesis will be addressed in the subsequent chapters as,

- Chapters 6, 7 and 8 will address aim 2,
- Chapter 9 will address aim 3, and
- Chapter 10 will address aim 4.

5.1. How representative of metallurgical coke is the coke analogue?

For the coke analogue to provide a realistic representation of the metallurgical coke it is required to replicate some key characteristic properties of, and behave in a similar manner to, metallurgical coke. The characteristic properties and behaviours evaluated in this study include

1. Porosity,
2. Microstructure,
3. Carbon bonding,
4. General reactivity of the coke analogue in CO_2, and
5. General mechanism of reaction of the coke analogue in CO_2.

In order to use the coke analogue for understanding metallurgical coke, it is important that its key properties are controlled, while the behaviour of the coke analogue is reproducible.

5.1.1. Porosity

The porosity of the coke analogue as characterised by optical microscopy combined with image analysis, mercury porosimetry and neutron radiography (Dingo) will be discussed in this section.

Importance of porosity control

Reactivity in CO_2 and mineral interactions with metallurgical coke or coke analogue are heterogeneous reaction systems and proportional to the contact area of the coke or coke analogue. Generally, this contact area is the surface area of the coke or coke analogue and can be considered a function of porosity. The contact area–porosity of coke is highly variable, even within a coke batch or lump and from coke to coke type. The porosity of coke can range between 35% and 70% [2, 5, 11, 77, 108, 165, 167, 168]. This variability can cause significant uncertainty in isolating specific reactivity effects of minerals. If an analogue can be produced that has low variation in porosity then the

uncertainty in comparing the effects of minerals or other factors can be reduced and perhaps the reactivity of coke can be better understood.

A general rate equation for a heterogeneous reaction could be written as,

$$\frac{dX}{dt} = k.A.\Delta C^{n} \qquad 5\text{-}1$$

where k is the reaction rate constant $g.s^{-1}.m^{-2}$, A is the contact area in m^2, ΔC is the concentration change of gaseous reactants in $g.m^{-3}$ and n is the order of the reaction.

From equation 5-1, it can be seen that the rate of reaction is a function of reaction rate constant k, contact area A of the reactants, order of the reaction n and a gas concentration change ΔC, which can be approximated to the thermodynamic driving force for the reaction. The specific or appropriate values for k, A, n and ΔC in equation 5-1 are dependent on the prevailing rate controlling mechanism. The rate controlling mechanism is a function of temperature.

The contact area–porosity relationship in metallurgical coke or coke analogue will be different for a different rate controlling mechanism. For chemical reaction control, A is greater than that for the mixed control, which in turn will be greater than that for the mass transfer in the gas boundary layer control. In a chemical reaction control system, all surfaces, including pores and pore walls, providing the CO_2 gas can reach the pores, are available for reaction. In a mixed control system, the penetration of the pores with the reactant CO_2 gas is at least a function of the pore size and pore connectivity, which limits the depth of penetration and therefore the area available for reaction. In a mass transfer control system the appropriate area of the solid is its external geometry. It can therefore be expected that with increasing temperature, moving from chemical reaction control (zone I) to mixed control (zone II) to mass transfer in the gas boundary layer control (zone III), will result in a decrease in the effective contact area, A [15, 181].

In the coke analogue used in this study, the initial porosity of 29.3% ± 2.3% and pore size distribution were controlled, fixed and reproducible (Table 3-4 and Figures 3-22, 4-26 to 4-28). The control and fixing of initial porosity of the coke analogue samples used in this study should minimise or eliminate porosity as a variable in reactivity testing.

There is the potential for the evolution of porosity on reaction to be different for different coke analogues. To address this, post-experimental porosity measurements were made on selected coke analogues that were reacted in CO_2 at 950°C and arrested after 1 hour (Table 4-14 and Figure 4-30). The porosity values after reaction for the base coke analogue and coke analogue–Fe 46µm were 30.7% and 32.4% respectively, corresponding to FWC values of -0.07 and -0.12 for the base and Fe 46µm respectively. While slightly larger than the original (unreacted) values of 29.3% ± 2.3% (for base) and 31.7% (for Fe 46µm), they are also similar and show no preferential increase in porosity associated with Fe addition. This is not to say there is no biasing of porosity associated with Fe addition, but given the post-experimental porosity values after reactivity testing, it is unlikely to be a significant variable in the differences in reactivities of the coke analogues tested.

There was an attempt to use the BET [161, 173] to study the effects of gas-solid contact area in this study, but as the baseline values proved difficult due to degassing issues associated with the carbonaceous materials [161], this approach was discontinued.

Comparison of porosity measurements using different measurement techniques

The optical microscopy, mercury porosimetry and neutron radiography (Dingo) used in this study indicated consistency in the porosity of the coke analogues (Table 5-1).

Table 5-1: The porosity of the base coke analogue measured using optical microscopy, mercury porosimetry and neutron radiography (Dingo).

Method	Porosity (%)	Pore diameter range (µm)	Advantages	Disadvantages
Neutron radiography (Dingo, slice thickness of 0.03mm)	25.3	30–500	(1) Gives pore interconnectivity in 3D, and (2) Non-destructive.	(1) Resolution on sample was ~30µm, (2) The analysis is time intensive (~24 hours for one analysis), and (3) Non-standard technique (still under development).
Optical microscopy	29.3±2.3	10–500	(1) Simple method, (2) Repeatable, (3) Readily available in UOW laboratory, and (4) The analysis is not time intensive.	Cannot measure pore diameter <10µm.
Mercury porosimetry	39.6±2.8	0.003–300	(1) Can measure pore diameter as low as 0.003µm, and (2) Standard technique	(1) Cost: Not available in UOW laboratory, and (2) Sample damage during measurement (not reusable)

The mercury porosimetry value was significantly higher relative to both optical microscopy and neutron radiography (Dingo). As the mercury porosimetry could measure porosity not assessed by the other techniques, it is therefore not surprising that it gives higher values.

The interconnectivity of pores: 3D analysis

The neutron radiography (Dingo) indicated that the apparent porosity of the coke analogues did not change significantly with increasing slice thickness (volume analysed). For example, the porosity value for a base coke analogue at slice thickness 0.03mm was 25.3% compared to slice thickness 10.72mm with 23.7% (Table 4-15). What did change though was the apparent pore size of the pores that made up the

porosity. The apparent pore size increased with increasing thickness of the analogue sample analysed. This is only likely to be correct when the pores are interconnected.

The high pore interconnectivity as indicated by the Dingo 3D measurements showed that the majority of the pores (~90%) and pore walls of the coke analogues would be accessible for CO_2 gas penetration. Similar behaviour of high pore interconnectivity in 3D was also found in a metallurgical coke sample used in this study (Figure 4-35). The results of this study is consistent with the recent results of Jenkins et al. [171] where micro-CT imaging with a resolution of ~8µm was used to characterise the 3D pore structure of coke samples. In the Jenkins study, they found that ~99% of the pores in the coke samples were highly interconnected in 3D [171].

The coke analogue has high interconnectivity in 3D and representative of metallurgical coke used in this study and reported by Jenkins et al. [171].

Comparison of coke analogue porosity with metallurgical coke porosity

A comparison of the porosity of the base coke analogue and metallurgical cokes (this study and reported in the literature [2, 5, 165]) measured using the optical microscopy is given in Table 5-2. The metallurgical coke measured in this study was used to show the inherent significant variation in coke porosity from the same source.

Table 5-2: A comparison of the porosity of base coke analogue and metallurgical cokes measured using the optical microscopy.

Coke analogue and metallurgical coke	**Porosity (%)**
Base coke analogue	29.3±2.3
Metallurgical coke (this study)	24.7–37.5
Metallurgical coke [2]	51.3–67.1
Metallurgical coke [5]	49.8–64.9
Metallurgical coke [165]	38.0–70.0

A comparison of the pore size distribution of the coke analogue and metallurgical coke (this study and reported in the literature [2]) measured using the optical microscopy is given in Figure 5-1.

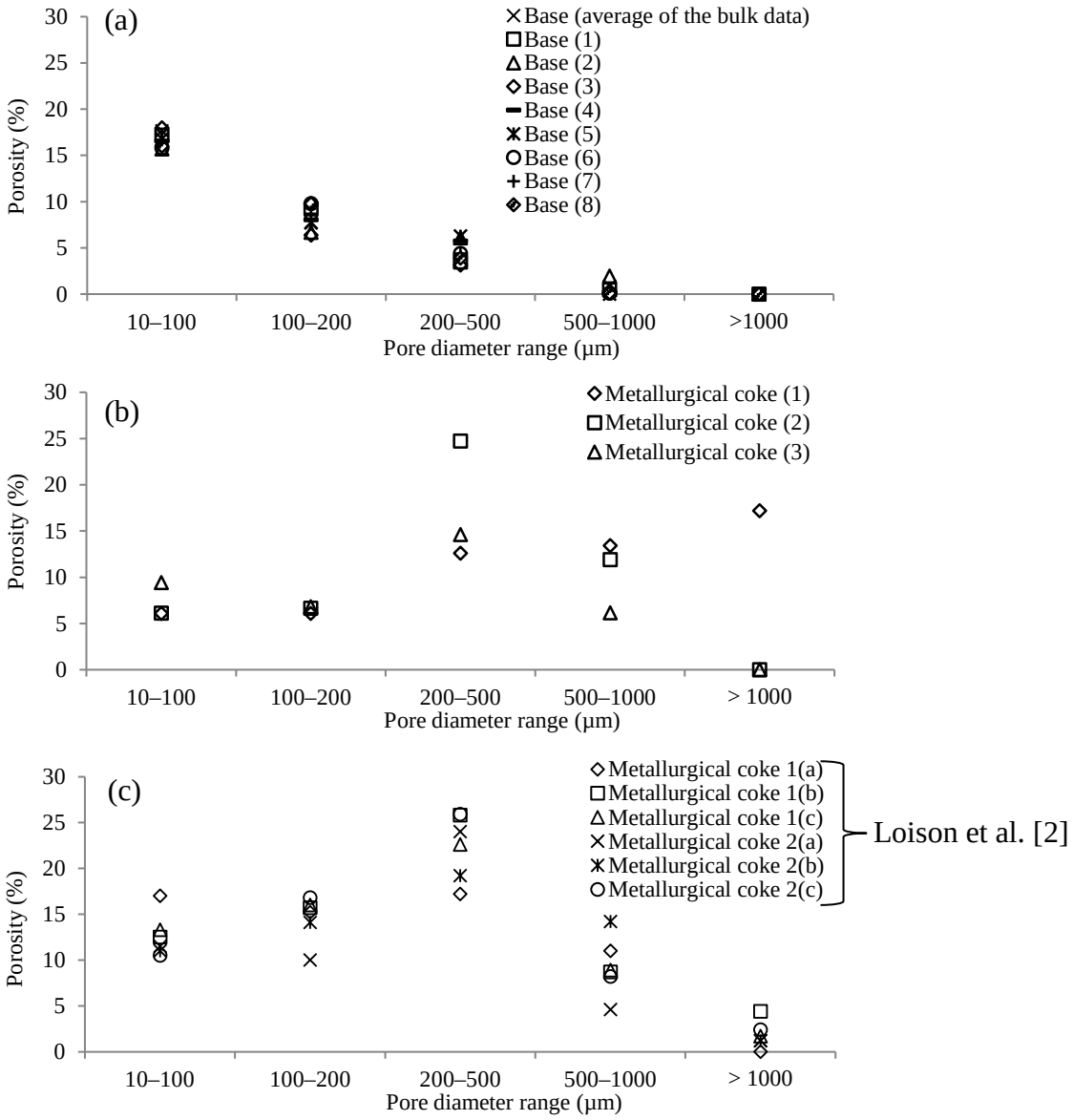

Figure 5-1: A plot of pore size distribution in (a) base coke analogue, (b) metallurgical coke (this study) and (c) metallurgical coke from the literature [2]. The base coke analogue (1) and (2) are from the same batch, (3)–(8) from different batches. The metallurgical cokes (1) to (3) used in this study is from the same source. The metallurgical coke (from the literature) 1(a, b, c) are from the same batch, 2(a, b, c) from a different batch.

From Table 5-2 and Figure 5-1, it can be seen that the porosity and pore size distribution of the coke analogue is well controlled, reproducible and less scattered relative to the metallurgical cokes. The majority of the porosity (~60% of the total porosity) of the coke analogue is in the 10–100μm diameter range. It can also be seen that in comparison with metallurgical coke (Figure 5-11(c)), the data is comparable in size range 10–200 μm. This is encouraging as the principal aim of developing the coke analogue is to produce a research tool, representative of key aspects of coke, that is more controlled and reproducible.

The well-controlled and reproducible initial porosity of the base coke analogue is significant and likely responsible for the relative similarity in the FWC values of the three base coke analogue samples reacted in CO_2 at 1100°C for 2 hours (Figure 3-31, reproduced in the following text). This would not be possible with the metallurgical coke due to its heterogeneity issues [11, 21, 179, 188, 225].

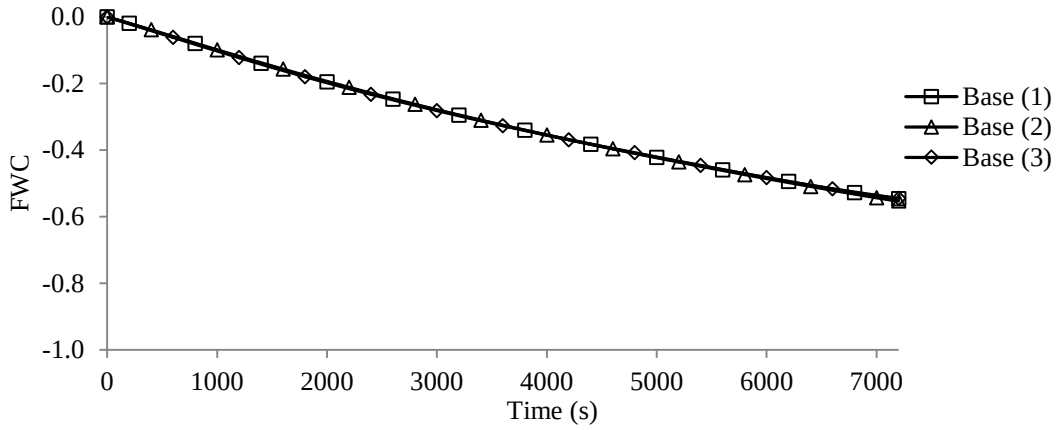

A FWC versus time plot of three base coke analogue samples reacted in CO_2 at 1100°C. (1) and (2) from the same batch and (3) from a different batch (see Figure 3-31).

5.1.2. Microstructure

The microstructure of coke analogue as characterised with optical and electro-optical microscopy and associated EDS analysis is discussed in this section. The microscopy methods used in this study are the commonly used methods to characterise the microstructure of metallurgical coke [2, 3, 5, 7, 10, 20, 22, 24, 25, 27, 56, 57, 59, 60, 67, 68, 77, 80, 98, 101-113, 165, 167]. This should allow a direct comparison of the microstructure of coke analogue to that of metallurgical coke. The microstructure of metallurgical coke is made up of

1. Carbons (reactive maceral derived component (RMDC) and inert maceral derived component (IMDC))
2. Pores, and
3. Minerals.

The components that make up the microstructure of the coke analogue are carbon (graphite grains and carbonised phenolic resin), Fe/minerals (excluding the base coke analogue) and pores (Table 4-1, Figures 4-1 to 4-8, 4-10 and III-1 to III-8).

To facilitate the analogue comparison with coke, Figure 4-3(a, b) for the coke analogue–Fe 46μm is reproduced in Figure 5-2 with a metallurgical coke. The metallurgical coke details were originally given in Figure 4-9.

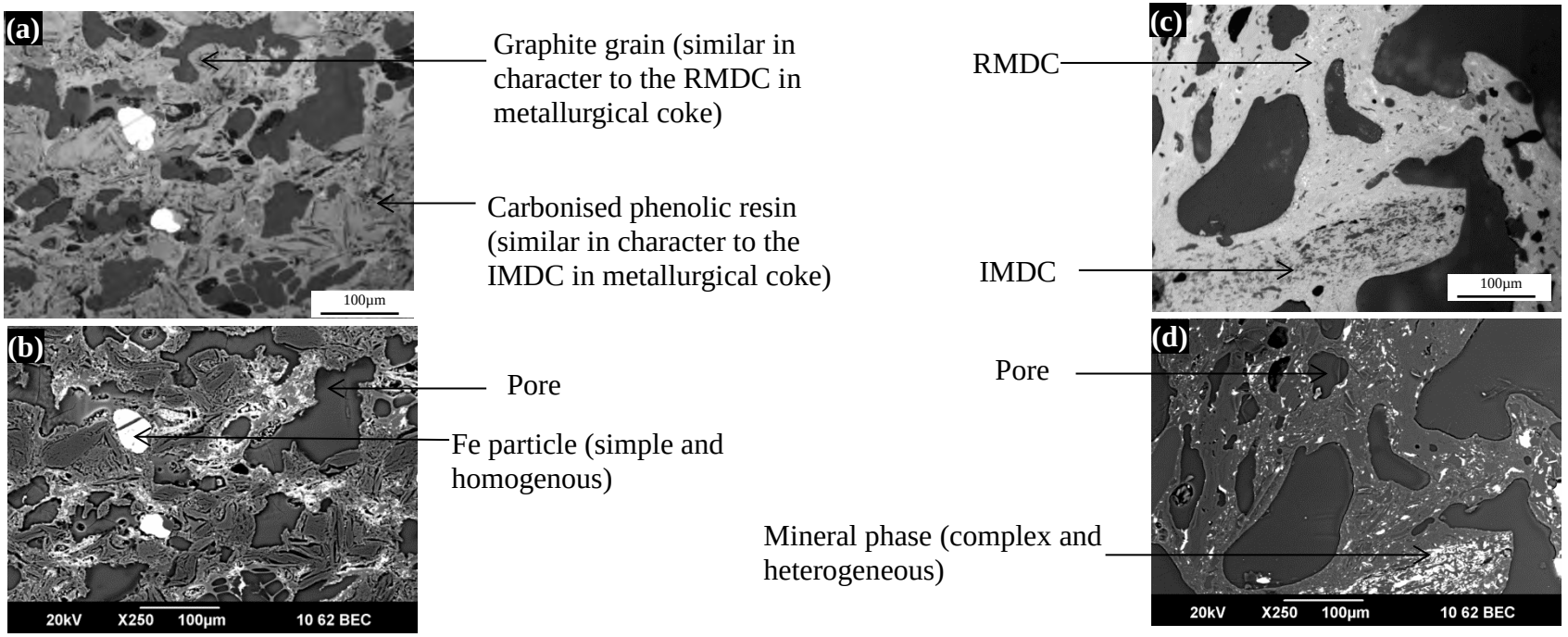

Figure 5-2: A comparison of the microstructure of the analogue and metallurgical coke. (a) non-polarised optical micrograph of the coke analogue–Fe 46µm, (b) SEM backscattered micrograph of the coke analogue–Fe 46µm, (c) non-polarised optical micrograph of metallurgical coke and (d) SEM backscattered micrograph of metallurgical coke.

The carbon (graphite grains and carbonised phenolic resin) microstructure of coke analogue is simple and well controlled (Table 4-1, Figures 4-1 to 4-8, 4-10 and III-1 to III-8). The graphite grains have sizes similar to the initial graphite powders used to make it (<45µm and <150µm particle sizes) and exhibited an anisotropic character under the polarised (plane and crossed) light (Figure 4-10). The carbonised phenolic resin in the coke analogues have little or a less obvious grain structure and exhibited an isotropic character under the polarised (plane and crossed) light (Figure 4-10).

In general terms both the grain structure and the anisotropic character of the graphite component in the coke analogue have features similar to the RMDC type in metallurgical cokes (used in this study (see Figure 5-2) and the literature [2, 3, 5, 10, 60, 101-108, 120]). Also, both the less obvious grain structure and the isotropic character of the carbonised phenolic resin component in the coke analogue have features similar to the IMDC type in metallurgical cokes. The RMDC/IMDC like features in the analogue reasonably aligns with what would represent a coke made from a very low rank coal (R_o max <0.8) [2].

Fe and mineral phase, morphology and dispersion

The Fe and mineral phase in the coke analogues are well controlled and evenly distributed (Figures 4-2 to 4-8 and III-2 to III-8) compared to metallurgical cokes used in this study (Figures 4-9 and III-9) and that reported in the literature [7, 83]. The even distribution and controlled dispersion of Fe and minerals in the coke analogues will minimise heterogeneity issues associated with the particles, which is a significant issue in the use of metallurgical coke.

The Fe particles in the coke analogues (Figures 4-2 to 4-5 and III-2 to III-5) appeared to have sizes similar to the initial particle sizes used to make the coke analogues (Figure 3-1(a) to 3-1(d)). They also have a round morphology (relative to the initial morphology of agglomerated small spherical particles for Fe (Figure 3-1(b) and 3-1(c) and initial angular morphology for Fe_3O_4 (Figure 3-1(d)), indicating that they may have gone

through a liquid Fe phase during coke analogue firing at 1200°C. This is consistent with the MTDATA thermodynamic prediction at 1200°C (Figures 4-38 and 4-39 and Table 4-18). From the MTDATA thermodynamic analysis (Figures 4-38 and 4-39), it can be seen that liquid Fe would form at ~1147°C (the eutectic temperature). This temperature is lower than the firing temperature of the coke analogue. There was evidence of graphite flakes within the Fe particles and this may have consequences for changes in sp^2–sp^3 bonding at the Fe–coke analogue interface (to be discussed in detail in Chapter 6).

The magnetite (Fe_3O_4) was found to be elemental Fe in the coke analogue after firing (Figures 4-5, II-4 and III-5). The reduction of magnetite (Fe_3O_4) with carbon (see equation 5-2) [63, 64] has a negative $\Delta G°$ at 1200°C.

$$Fe_3O_{4(s)} + 4C_{(s)} \rightarrow 3Fe_{(s)} + 4CO_{(g)} \qquad \Delta G° \text{ at } 1200°C = -332754J \text{ [63, 64]} \quad 5\text{-}2$$

The negative $\Delta G°$ value indicates that the formation of Fe is thermodynamically spontaneous and the reaction will proceed from left to right when Fe_3O_4 is fired within the coke analogue at 1200°C.

The enstatite ferroan ($Mg_{1.56}Fe_{0.44}Si_2O_6$), phlogopite ferroan [$K(Mg,Fe)_3(Al,Fe)Si_3O_{10}(OH,F)_2$] and quartz ($SiO_2$) particles in the coke analogues (Figures 4-6, 4-7, 4-8 and III-6, III-7 and III-8) have sizes similar to the initial particle sizes used to make the coke analogues (Figure 3-1(e), 3-1(f) and 3-1(g)). They also have an angular morphology similar to the initial angular morphology used to make the coke analogues.

The XRD analysis of the coke analogues prepared with enstatite ferroan (Figure II-5) and phlogopite ferroan (Figure II-6) indicate that the minerals did not decompose into the phases predicted by the MTDATA thermodynamic predictions at 1200°C (Figures 4-40, 4-41 and Table 4-19).

It was not possible to carry out a full thermodynamic analysis of enstatite ferroan ($Mg_{1.56}Fe_{0.44}Si_2O_6$) and phlogopite ferroan [$K(Mg,Fe)_3(Al,Fe)Si_3O_{10}(OH,F)_2$] as these phases were not in the MTDATA databases. While it was not possible to do the full analysis, equivalent masses of each element in the mineral (mass of mineral is ~5g) and an excess carbon (80g) were inputted into MTDATA. The stable phases predicted were

1. protopyroxene ($MgSiO_3$), tridymite (SiO_2) and $Fe_{(l)}$ for enstatite ferroan, and
2. sanidine ($KAlSi_3O_4$), $Fe_{(l)}$, forsterite (Mg_2SiO_4), $K_2Si_4O_9$ and magnesium fluoride (MgF_2) for phlogopite ferroan.

The phases predicted by MTDATA may not have formed either because of the set-up of the calculations (1 and 2 above) are not well founded or because the decomposition of the $Mg_{1.56}Fe_{0.44}Si_2O_6$ and $K(Mg,Fe)_3(Al,Fe)Si_3O_{10}(OH,F)_2$ are kinetically limited, that is the predicted phases did not have enough time to form.

Summary of main points

- The microstructure of the coke analogue appeared similar to the microstructure of metallurgical coke, with the graphite grains and carbonised phenolic resin similar in character to the RMDC and IMDC respectively.
- Though similar, the coke analogue microstructure is simpler/less complex than metallurgical coke.
- The coke analogue microstructure is relatively homogenous and reproducible with respect to mineral phase (size, composition, morphology and dispersion).

5.1.3. Carbon bonding

The carbon bonding of the coke analogue as characterised with Raman spectroscopy is discussed in this section. The Raman spectroscopy has been used to characterise the structural order or carbon bonding of metallurgical coke [17, 18, 26, 62, 114-117, 122]. This should allow direct comparison of the carbon bonding of the coke analogue to metallurgical coke (measured in this study and reported in literature). The specific effects of Fe and minerals on carbon bonding will also be discussed.

It is generally argued that a number of factors can modify the carbon bonding of metallurgical coke. These factors are,

1. annealing [18, 43, 44, 70, 115, 119, 145],
2. catalytic graphitisation [4, 25, 26] and
3. physical distortion [44, 130, 144].

Annealing and catalytic graphitisation increase sp^2 bonding while physical distortion increases sp^3 bonding. These factors were discussed in detail in the literature review chapter (section 2.2.2).

The carbon bonding of the base coke analogue is given in Figure 4-17. In order to explain this result, the carbon bonding of the carbonised carbonaceous materials used to make the coke analogue (Figure 4-16) will be discussed first.

In Figure 4-16, the unfired and fired graphite have low $I_{(V)}/I_{(G)}$ values, as would be expected for graphite and graphitised carbons with ordered sp^2 bonding [18, 62, 116, 123-126]. The fired graphite has higher $I_{(D)}/I_{(G)}$ values compared to unfired graphite. This is due to thermal distortion of the graphite lattice [123]. The thermal distortion of the graphite lattice introduces defects into the graphite structure changing the sp^2 bonding. The fired Bakelite and fired Novolac have high $I_{(D)}/I_{(G)}$ and $I_{(V)}/I_{(G)}$ values. These are what would be expected for less structured carbonaceous materials with disordered sp^2–sp^3 bonding [18, 115, 116, 123-130].

From comparison of Figures 4-16 and 4-17, it can be seen that the carbon bonding of the base coke analogue appeared to be the combination of the carbon bonding of the carbonised carbonaceous materials used to make it. The carbon bonding of the base coke analogue extends from the ordered sp^2 bonding of the fired graphite to the disordered sp^2–sp^3 bonding of the carbonised phenolic resin (Figure 5-3) [18, 115, 123, 125, 127-129, 133]. In retrospect, this range of values would be expected from a material made up of graphite, and fired Bakelite and fired Novolac. The Raman measurements represent the extreme (individual) values of the materials and possible values in between representing measurement of mixtures of the carbonaceous materials.

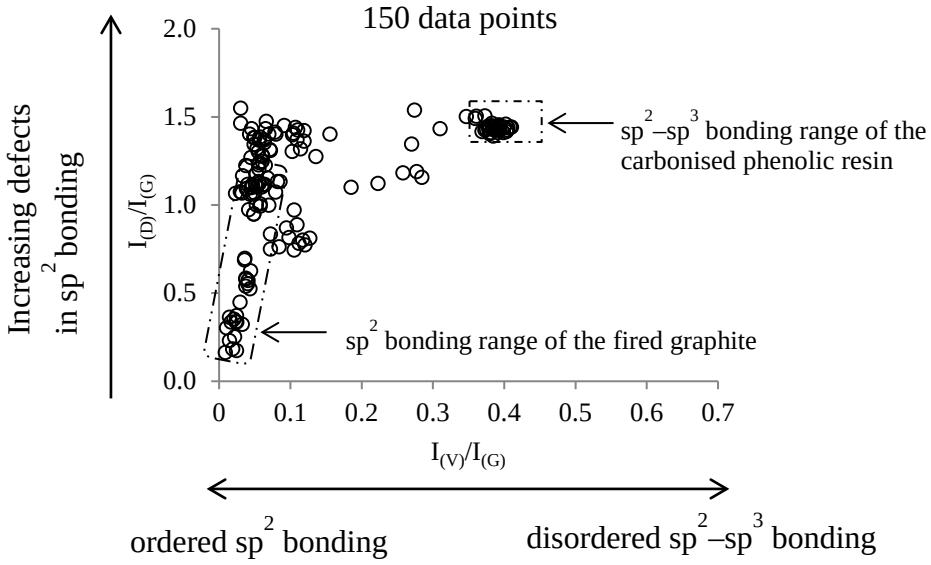

Figure 5-3: An illustration of the ordered sp^2 bonding and disordered sp^2–sp^3 bonding of the base coke analogue.

Comparison of coke analogue carbon bonding with metallurgical coke carbon bonding

In order to understand whether the carbon bonding as measured in the base coke analogue was similar to that of the metallurgical coke, it was compared with metallurgical coke measured in this study (Figure 4-25) and Raman measurements of coke found in the literature [18, 115, 117]. The comparison is given in Figure 5-4.

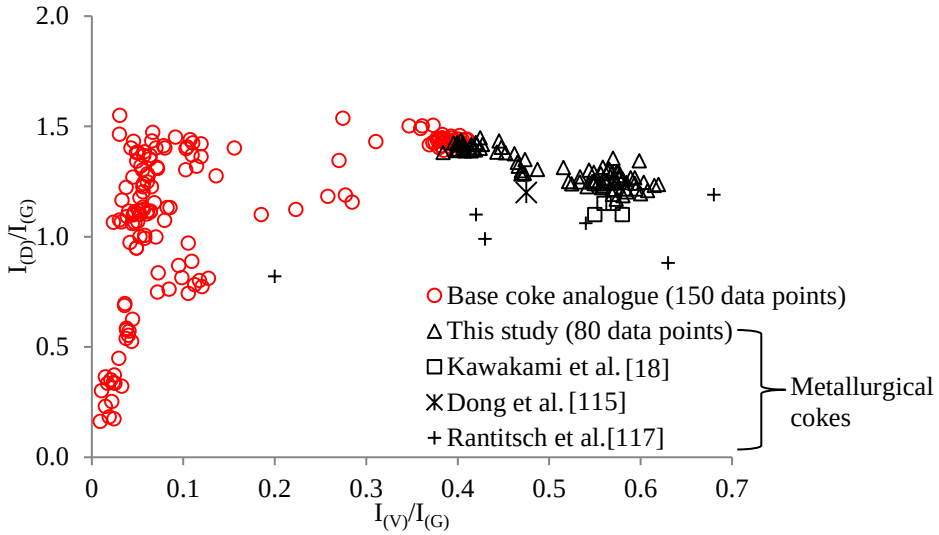

Figure 5-4: A comparison of the carbon bonding in the coke analogue and metallurgical coke samples using plot of $I_{(D)}/I_{(G)}$ versus $I_{(V)}/I_{(G)}$ approach.

The Raman measurements on the metallurgical coke used in this study (1.16–1.45 for $I_{(D)}/I_{(G)}$ and 0.38–0.62 for $I_{(V)}/I_{(G)}$) agree well with that reported in the literature [17, 18, 26, 62, 114-117, 122]. The literature data are from metallurgical coke samples that were not subjected to high temperature annealing. These grouped $I_{(D)}/I_{(G)}$ and $I_{(V)}/I_{(G)}$ values are characteristic of disordered sp^2–sp^3 carbon bonding.

The carbon bonding of the base coke analogue (0.16–1.55 for $I_{(D)}/I_{(G)}$ and 0–0.41 for $I_{(V)}/I_{(G)}$) overlaps with that for the metallurgical coke measured in this study and reported in the literature (Figure 5-4), but cover a much broader range. The broader range of values for the base coke analogue raises a question about its representation of metallurgical coke. Ultimately, this may limit the coke analogue's usefulness in predicting metallurgical coke behaviour, but it is envisaged that it will be a consistent or near consistent starting point for what could be referred to as carbon bonding type to assess the discriminating effects of minerals on carbon bonding and subsequent effects on reactivity.

Effects of elemental Fe, Fe containing minerals and quartz (SiO_2) on sp^2–sp^3 bonding: $I_{(D)}/I_{(G)}$ versus $I_{(V)}/I_{(G)}$ approach

Attempts were made to assess the effects of elemental Fe, Fe containing minerals and quartz (SiO_2) on the sp^2–sp^3 bonding in the coke analogue, using plots of $I_{(D)}/I_{(G)}$ versus $I_{(V)}/I_{(G)}$ (see Figures 4-18(a) to 4-24(a)). The general character of these plots was compared with a similar approach for base coke analogue (Figures 4-17 and 5-3).

In comparing these figures, while it could not be argued that all the plots of $I_{(D)}/I_{(G)}$ versus $I_{(V)}/I_{(G)}$ were the same, the trends and scatter were such that no clear discriminating effect of elemental Fe, Fe containing minerals and quartz (SiO_2) on the sp^2–sp^3 bonding could be observed. This was surprising, particularly with respect to elemental Fe, Fe containing minerals and quartz (SiO_2) reactivity effects reported in the literature [10, 29, 56, 59, 96, 180, 183-187] and the reactivity results of this study shown in the Results section 4.5. In both the literature [10, 29, 56, 59, 96, 180, 183-187] and measurements made in this study, the reactivity was shown to be significantly affected by the mineral addition.

The effects of elemental Fe, Fe as oxides in the form of magnetite (Fe_3O_4), enstatite ferroan ($Mg_{1.56}Fe_{0.44}Si_2O_6$) and phlogopite ferroan [$K(Mg,Fe)_3(Al,Fe)Si_3O_{10}(OH,F)_2$], and quartz ($SiO_2$) on carbon bonding will be further analysed and discussed in detail in Chapters 6, 9 and 10.

Summary of main points

- The coke analogue sp^2 bonding and sp^2–sp^3 bonding characteristics, while overlapping with metallurgical coke, covers a wider range/broader than that of metallurgical coke.
- The carbon bonding as assessed by $I_{(D)}/I_{(G)}$ versus $I_{(V)}/I_{(G)}$ plots is not discriminating with respect to elemental Fe and mineral addition.

5.1.4. Coke analogue reactivity in CO_2

In this section the focus is “how representative of metallurgical coke reactivity is the coke analogue reactivity?” A general discussion regarding the reaction kinetics of the coke analogue and metallurgical coke is also considered. A more detailed analysis of the effects of minerals on reactivity will be dealt with in later chapters (Chapter 7, 8, 9 and 10).

The reactivity of the coke analogue in CO_2 was characterised using a large sample TGA. Approximately 8g of the analogue was reacted in a 100% CO_2 atmosphere, similar in principle to the commonly used NSC reactivity test (CRI and CSR) [220]. This is expected to allow the coke analogue reactivity testing to be put in the context of many other metallurgical coke studies, and facilitate comparison of the coke analogue reaction behaviour with metallurgical coke [3, 11, 21, 70, 108, 120, 179, 186, 188, 220-223].

All the coke analogue results show similar reaction behaviour in CO_2 (as expressed as FWC with time in Figures 4-43 to 4-52). A more negative FWC indicates a more reactive coke or coke analogue. The reactivity increased with increasing temperature.

A comparison of the reactivity of the base coke analogue (FWC at 2 hours is –0.62 or 62%) and the reactivity of metallurgical cokes (CRI values 15%–80%) [3, 21, 179, 188, 221, 224, 225] suggests that the coke analogue is typical of highly reactive cokes. Also, the coke analogue is more reactive in CO_2 than the metallurgical coke used in this study (see Figure 5-5 produced using Figure 4-43 (for base coke analogue) and 4-53 (for metallurgical coke)). The metallurgical coke used in this study has been reported to be a low reactivity coke, with previous study showing both low FWC value of -0.23 at 1100°C and low CSR value of 19.4% [11].

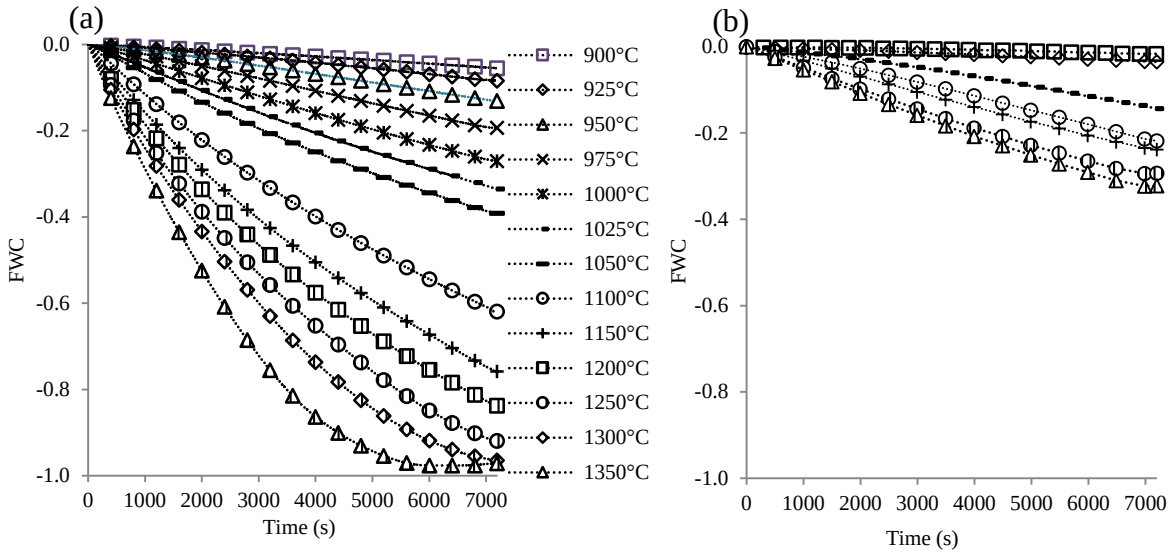

Figure 5-5: The FWC versus time curves with temperatures of samples reacted in CO_2 for 2 hours. (a) base coke analogue and (b) metallurgical coke used in this study.

In terms of trend with time and the effects of temperature, the kinetics of reactivity of the analogue is in general similar to that of the metallurgical coke measured in this study and metallurgical coke reported in the literature [11, 21, 77, 196, 222].

Further, the reactivity of the coke analogue is more controlled and reproducible relative to metallurgical coke (see Figure 5-6 reproduced from Figure 2-24 [11] (for metallurgical coke) and 3-31 (for analogue)). The metallurgical coke samples were measured in a similar TGA system to the coke analogue [11].

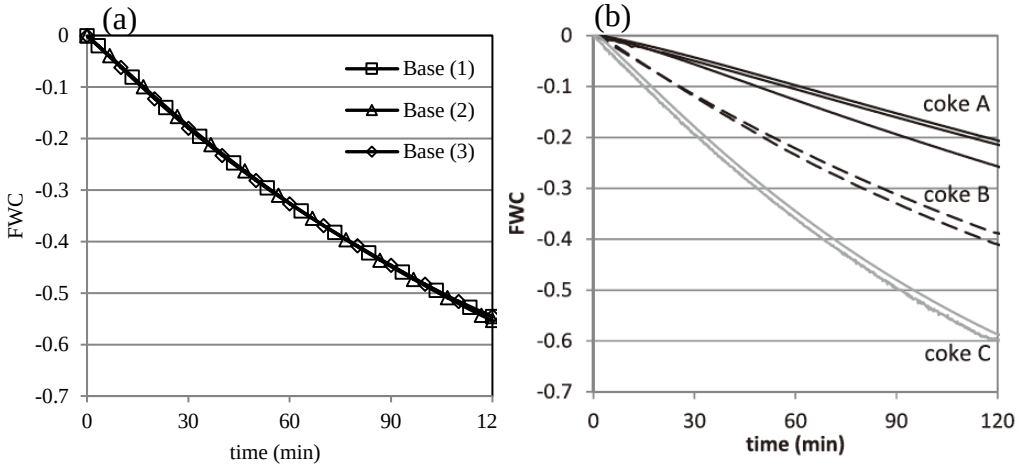

Figure 5-6: The FWC versus time curves of samples reacted in CO_2 at 1100°C. (a) base coke analogue and (b) metallurgical coke [11]. The base coke analogue (1) and (2) are from the same batch, (3) from a different batch. The coke A, B and C are from different sources.

Summary of main points

- The kinetics of the reactivity of the coke analogue is similar to metallurgical coke both in terms of trend with time and the effects of temperature.
- The reactivity of the coke analogue is highly reproducible.

5.1.5. General mechanism of reaction of the coke analogue in CO_2

Walker et al. [181] developed a general approach for establishing the rate controlling mechanism of metallurgical coke with temperature. This is a standard approach used by many researchers to study metallurgical coke [15, 60, 77, 190, 192, 196] and detailed in the literature review (section 2.3).

An Arrhenius approach (see equation 2-24, and reproduced in the following text) is used to assess the general mechanism of reaction of the coke analogue in CO_2.

$$R_C = k_0 \, e^{-\frac{E_a}{RT}}$$

From a plot of ln R_C against 1/T, it is possible to define three distinct reaction zones, as shown in Figure 2-17 from section 2.3 and reproduced in the following text.

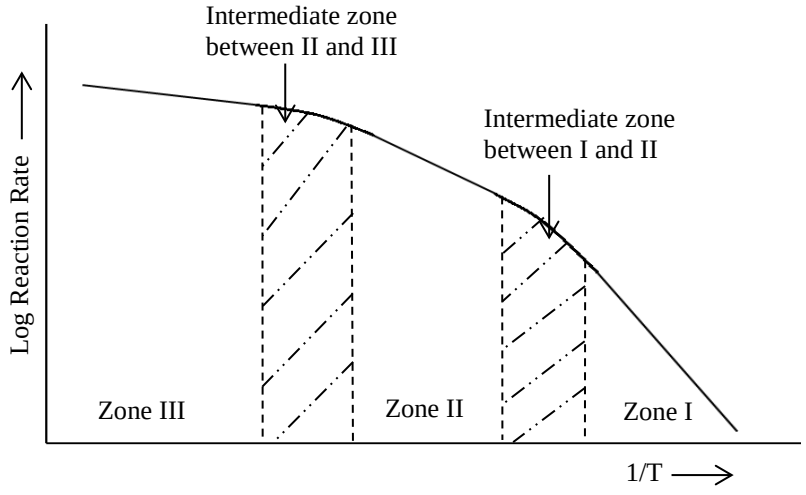

An ideal representation of three zones of coke reactivity in CO_2 with temperature [181], see Figure 2-17.

The zones I, II and III are the chemical reaction control regime, mixed control regime (both chemical reaction and pore diffusion control) and gas phase mass transfer control regime respectively.

The application of the Walker et al's [181] Arrhenius approach to the coke analogue may be a useful method to assess the analogue's coke–like characteristics. The FWC measurement, detailed in section 3.3.3 of the experimental chapter, has been carried out so that the measurement is independent of gas flow and should not be controlled by gas phase mass transfer. Therefore we should only expect the coke analogue to show zones I and zone II.

A plot of ln R_C against 1/T for the base coke analogue is given in Figure 5-7.

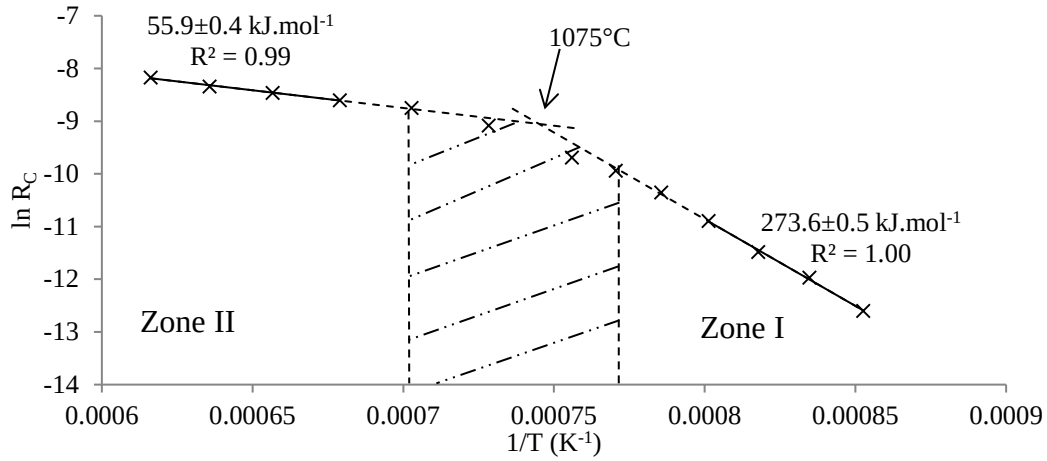

Figure 5-7: The plot of ln R_C against 1/T for base coke analogue reacted in CO_2 with temperature and showing reaction zones.

From comparison of Figure 5-7 with 2-17, it appears that the coke analogue does show similar reaction behaviour to metallurgical coke [176, 181]. From the ln R_C versus 1/T analysis, the base coke analogue does have zones I and II. Figure 5-7 is typical of other materials tested. Full details of the other analogues ln R_C versus 1/T behaviour are given in Appendix VI.

Comparison of the activation energy with previous study

Much of the published work on coke reactivity in CO_2 has been carried out in zone I. A comparison of the coke analogue with the literature data on coke in zone I is given in Figure 5-8 [15, 60, 77, 192, 196].

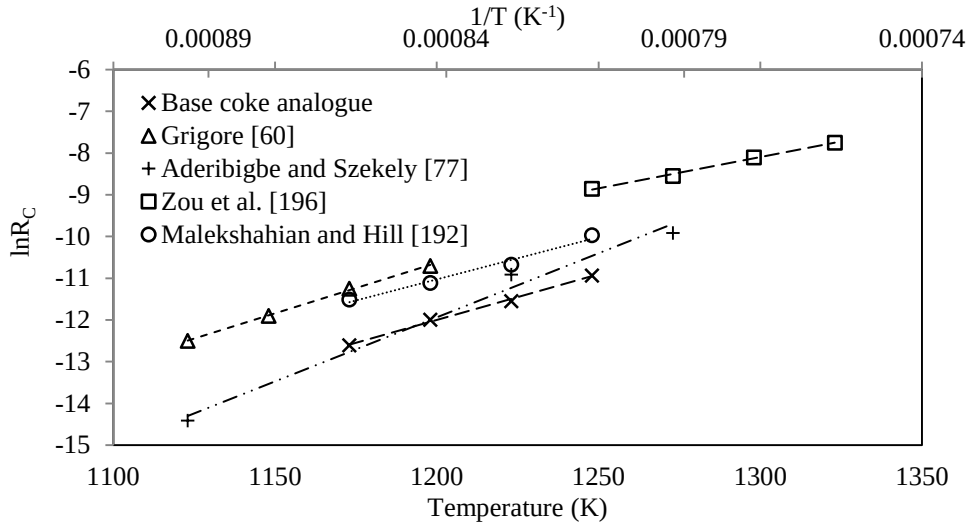

Figure 5-8: A comparison of ln R_C in zone I for base coke analogue and cokes.

From Figure 5-8, it can be seen that coke analogue has similar reaction behaviour to metallurgical coke. A comparison of the zones I and II activation energies of the base coke analogue with cokes, char and activated carbon reacted in CO_2 are given in Table 5-3. No activation energies were reported for zone II of metallurgical coke. To facilitate a comparison with the analogue, data for zone II for char and activated carbon have been included.

Table 5-3: The activation energies of the base coke analogue and cokes reacted in CO_2.

Coke analogues and coke	**Activation energies (kJ.mol^{-1})**	
	Zone I	Zone II
Base coke analogue	273.6±0.5	55.9±0.4
Metallurgical coke [60]	222–266	–
Metallurgical coke [77]	249±47	–
Petroleum coke [196]	198	–
Petroleum coke [192]	260±24	–
Char [193]	174	95
Activated carbon [195]	200	40

– not measured or reported

The zone I activation energy of the base coke analogue is close to the activation energies of cokes (Table 5-3). Also, the zone II value of the analogue is of a similar order of magnitude to those of char and activated carbon.

The activation energy values in zone I, the chemical reaction controlled region, are associated with bond breaking and bond formation [255]. Therefore, the similarity of the activation energies of the coke analogues and cokes suggest that they both follow the same reaction mechanism for reaction in CO_2. This is consistent with the suggestion that the coke analogue has both carbon microstructure and carbon bonding that is representative of coke (as discussed previously in section 5.1.2 and 5.1.3 respectively).

Given that the starting mixture for the coke analogue contains approximately 50% by mass graphite, it might be expected that the activation energy for zone I for the coke analogue would be similar or close to graphite. The activation energy for graphite is 305 $kJ.mol^{-1}$ [194]. This is significantly higher than that for the coke analogues. From these activation energies, it can be concluded that the coke analogue reactivity in CO_2 more replicates coke than graphite.

Summary of how representative of metallurgical coke is the coke analogue?

A summary of the findings of how representative of metallurgical coke is the coke analogue from the different perspectives tested (porosity, pore size distribution, 3D pore interconnectivity, microstructure (carbon and mineral phase), carbon bonding ($I_{(D)}/I_{(G)}$ and $I_{(V)}/I_{(G)}$), reactivity in CO_2 and zone I activation energy of reaction) is given in Table 5-4.

Table 5-4: How representative of metallurgical coke is the coke analogue?

Characteristic behaviours tested	**Coke Analogue**	**Metallurgical Coke and reference where applicable**	**Comments**
Porosity (%)	29.3±2.3	24.7–37.5 (this study) 35.0–70.0 [2, 5, 11, 165]	Similar but highly controlled in a coke analogue.
Pore size distribution	Majority in the 10–100μm diameter range	Highly variable	Coke analogue porosity distribution overlaps with that of metallurgical coke.
3D pore interconnectivity	Pores are highly interconnected	Pores are highly interconnected	Coke analogue is similar to metallurgical coke.
Microstructure: Carbon	(1) Graphite grain is similar in character to RMDC, and (2) Carbonised phenolic resin is similar in character to IMDC	RMDC and IMDC	The coke analogue had a simpler but similar microstructure to that of metallurgical coke.
Microstructure: Mineral phase	(1) Simple and homogenous mineralogy, and (2) well defined in terms of particle size, morphology and has controlled dispersion	(1) Complex and heterogeneous mineralogy, and (2) highly variable in terms of particle size, morphology and dispersion	The mineral phase in the analogue is less complex than that found in metallurgical coke and key mineral properties are more controlled than would be in metallurgical coke.
Carbon Bonding: $I_{(D)}/I_{(G)}$	0.16–1.55	1.16–1.45	The bonding in the analogue covers a greater range than that of metallurgical coke, which overlaps with that of metallurgical coke.
Carbon Bonding: $I_{(V)}/I_{(G)}$	0–0.41	0.38–0.62	
Reactivity in CO_2	Reproducible and well controlled	Highly variable	The reactivity trends with time and temperature of the analogue and metallurgical coke are similar but the analogue reactivity has a greater repeatability.
Zone I activation energy ($kJ.mol^{-1}$)	273.6±0.5	216–266 [60, 190]	The activation energy of the analogue for zone I is comparable with that of metallurgical coke.

From a number of perspectives it would appear that the coke analogue is similar to metallurgical coke. It is also highly controllable with respect to porosity, mineralogy, mineral dispersion throughout the coke analogue and reactivity in CO_2. This similarity and controllability should allow the testing and evaluation of the specific effects of metallic/elemental Fe and minerals on the carbon bonding and reactivity of the coke analogue and by extension metallurgical coke.

6. Effects of elemental Fe and Fe added as Fe_3O_4 on sp^2–sp^3 carbon bonding at the Fe–carbon interface

The effects of elemental Fe and Fe added as readily reducible Fe_3O_4 on both sp^2–sp^3 bonding in the coke analogue is discussed in this chapter.

Surface effect versus bulk effect on sp^2–sp^3 bonding

As discussed previously in section 5.1.3, elemental Fe and Fe added as Fe_3O_4 had no clear discriminating effect on the sp^2–sp^3 bonding in the coke analogue as characterised with $I_{(D)}/I_{(G)}$ versus $I_{(V)}/I_{(G)}$ approach (see Figures 4-18(a) to 4-21(a)). This result was surprising as it is widely reported [12, 16, 96, 97, 176, 187] that Fe increases reactivity of metallurgical coke in CO_2. This is often argued as a catalysing effect whereby elemental Fe promote graphitisation (increase sp^2 bonding) and hence reactivity [4, 7, 10, 25, 26, 29, 30, 32, 33, 38, 40, 41, 43, 45-49, 52, 56, 59, 84, 96, 149-152, 180, 183-187]. In contrast to the carbon bonding results, the FWC results of this study shown in Figures 4-44 to 4-49, indicate that Fe and Fe containing minerals increased the reactivity of the coke analogue in CO_2. It may be that the catalytic effect is local to the Fe/mineral–coke analogue interface and is not observed in the "bulk" Raman assessment detailed in section 5.1.3.

To test this effect, measurements were made of the $I_{(V)}/I_{(G)}$ near the Fe/mineral–coke analogue interface, radiating out from the interface (see Figures 4-18(c, d) to 4-21(c, d)). This $I_{(V)}/I_{(G)}$ approach was used as other researchers [18, 115, 123, 133] have found it is more sensitive to changes in sp^2–sp^3 bonding than the $I_{(D)}/I_{(G)}$ versus $I_{(V)}/I_{(G)}$ approach. It also allows convenient testing of proximity or position effects in the coke analogue.

To aid the analysis, Figures 4-18(c) to 4-21(c) have been amended to show the sp^2 bonding range of graphite. This bonding range is based on the literature values [44, 123] and measurements made in this study (Figure 4-16). These amended graphs are given in Figure 6-1(a) to (d) with the shaded area indicating sp^2 bonding region.

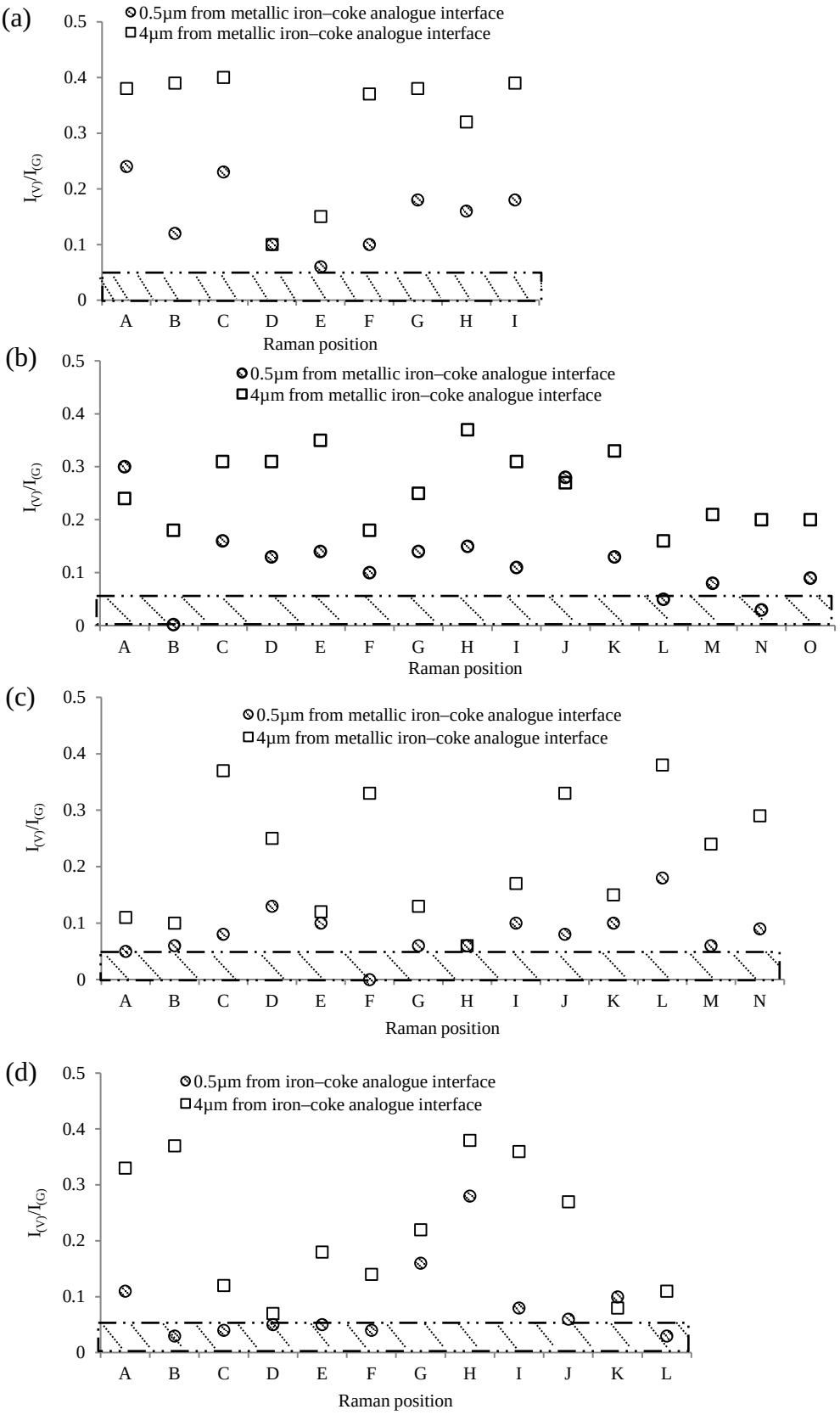

Figure 6-1: An illustration of sp^2–sp^3 bonding around particle in coke analogues. The hashed area is representative of the range of sp^2 bonding. (a) coke analogue–Fe 5µm, (b) coke analogue–Fe 46µm, (c) coke analogue–Fe 83µm and (d) coke analogue–Fe_3O_4 46µm.

From Figure 6-1(a) to (d), the localised effects of elemental Fe and Fe added as Fe_3O_4 on the sp^2–sp^3 bonding are summarised in Table 6-1.

Table 6-1: The localised effects of elemental Fe and Fe added as Fe_3O_4 on sp^2–sp^3 bonding

Elemental Fe and Fe added as Fe_3O_4	**Increased sp^2 bonding character at or near the interface**	**Comments**
Fe 5µm	Yes	-
Fe 46µm	Yes	-
Fe 83µm	Yes	-
Fe_3O_4 46µm	Yes	Note, Fe_3O_4 is reduced to Fe on firing of the coke analogue. The bonding values are very similar to that of the Fe addition.

'Yes' indicates that sp^2 bonding was found to increase at the Fe–coke analogue interface.

The $I_{(V)}/I_{(G)}$ approach confirms that when Fe is added in its elemental form or in a readily reduced form such as Fe_3O_4 it does cause an increase in sp^2 bonding (graphitisation) albeit local to the Fe–coke analogue carbon interface. This is consistent with what Wang et al. [26] observed in metallurgical coke impregnated with Fe.

As mentioned previously, it is well known that Fe promotes graphitisation. Often this is explained in terms of carbon dissolving into Fe at temperature and precipitating carbon in the form of graphite on cooling [26, 30, 39, 151]. During the production of the coke analogues prepared with Fe and Fe_3O_4, the coke analogue was fired at 1200°C and held at this temperature for 1 hour. Based on what other researchers have reported [22, 24-26, 30, 39, 84, 85, 97, 151, 156, 215], it would be expected that the Fe should pick up carbon. To assess this, two experiments were carried out using analogues containing large pieces of iron (see experimental section 3.2.10). It was found that the carbon level in the Fe increased from 0.06 mass% to 1.72 mass% (see Table 4-21). The carbon level in the Fe (1.72 mass%) is well above the saturation level of α-Fe at room temperature.

According to the Fe–C equilibrium phase diagram (Figure 6-2) [99], at the coke analogue firing temperature of 1200°C, the possible stable phase fields are γ-Fe (a solid solution of carbon in face centered cubic iron), liquid Fe + γ-Fe, liquid Fe or graphite + liquid Fe. The likelihood of having a liquid Fe phase (at 1200°C) was in part supported by the detailed microscopy analysis (Figures 4-3 to 4-5 and III-3 to III-5). Both the Fe and Fe_3O_4 additions show signs of being liquid Fe with a more rounded morphology than the original particles added to the coke analogue (see Figure 3-1(a–d) for the original particle morphology).

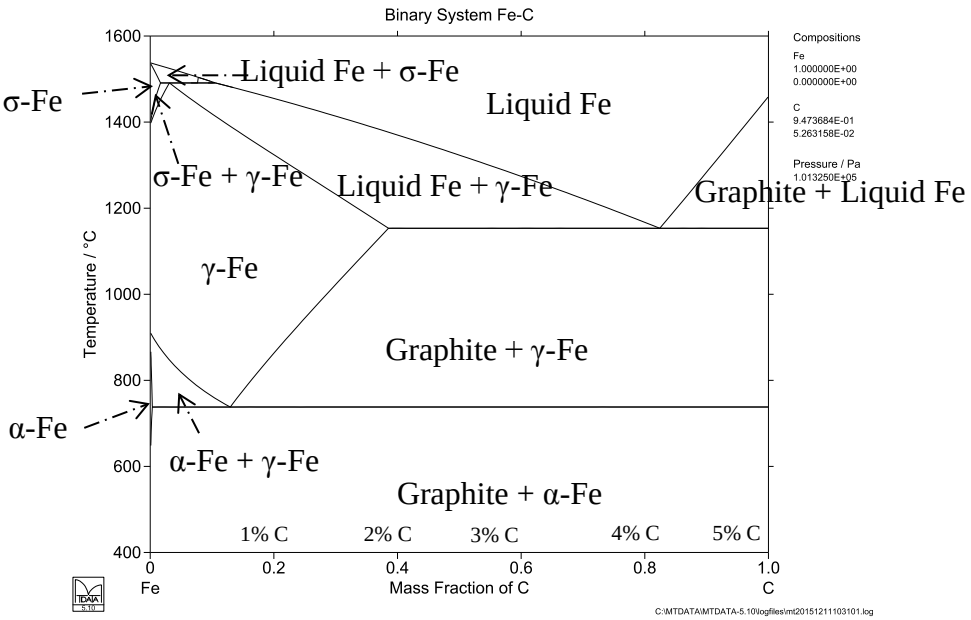

Figure 6-2: The MTDATA output of Fe–C binary system with temperature [99].

Upon cooling to room temperature, the stable phase is expected to be graphite + α-Fe (a solid solution of carbon in body centered cubic iron). It is possible for carbon to diffuse from the Fe on cooling (the cooling rate was 10°C/min) to form a graphite layer. The α-Fe was confirmed by XRD at room temperature of approximately 25°C (see Figures II-2 to II-4). Further evidence in support of carbon pick up comes from the microscopy analysis of coke analogue materials prepared with Fe and Fe_3O_4 (Figures 4-3, 4-4, III-3 to III-5). Graphite flakes were observed within the particles. The graphite flakes are only possible within the particle if carbon has been dissolved in the Fe.

Experimental observations (microscopy, Raman and LECO) indicate that Fe (both in its elemental form and in a readily reduced form of Fe_3O_4) promotes sp^2 bonding. This is best explained in terms of graphitisation caused by dissolution of carbon into Fe during firing at 1200°C followed by precipitation of carbon from Fe during cooling. This finding is broadly consistent with the literature [26, 30, 39, 151].

Summary of main points

- The Fe added as elemental Fe and readily reducible Fe_3O_4 promotes sp^2 bonding character locally near the Fe–carbon interface.
- There was evidence of carbon pick up by the Fe with the carbon level in the Fe increased from 0.6 mass% to 1.72% and graphite flakes around the particles after firing.

7. Effects of elemental Fe and Fe added as Fe_3O_4 particle surface area on reaction rate

The effects of the particle surface area of elemental Fe and Fe added as readily reducible Fe_3O_4 on the reactivity of the coke analogue is discussed in this chapter.

The addition of elemental Fe and Fe added as Fe_3O_4 to the coke analogue increased the reactivity of the coke analogue in CO_2 relative to the base coke analogue. The reaction mechanism of coke or coke analogue in CO_2 has often been separated into two steps (reaction 2-15 and 2-16, reproduced below) [44, 60, 174-178].

$$C_f + CO_{2(g)} \underset{j_1}{\overset{i_1}{\rightleftarrows}} C(O) + CO_{(g)}$$

$$C(O) \xrightarrow{j_3} CO_{(g)}$$

The reaction 2-16 is the rate controlling step assuming the concentration of the CO_2 gas inside and outside the coke and coke analogue is uniform [174]. An increase in the amount of the active carbon sites (C_f in reaction 2-15) will have the effect of increasing reactivity of coke. This is likely to be true also for the coke analogue. The amounts of active carbon sites are known to be strongly affected by the presence of Fe in coke. This would be expected to be a function of Fe particle size, chemical state or phase, amount and total surface area [44, 56, 96, 97, 178, 186, 188, 203]. That is, though the primary reaction under investigation is CO_2 with carbon, the fact that carbon reactivity is affected by Fe through increased C_f, it can be expected that the rate of reaction would be, at least in part, proportional to the contact area of carbon with Fe.

7.1. Testing for the effect of particle surface area of Fe and Fe_3O_4 on coke analogue reactivity

In order to test the effect of contact area on reaction rate, three series of experiments were carried out.

Series 1: The size of the Fe particles added to the analogue was varied. For a constant mass of addition, this results in a change in surface area of the particles. See Figure 7-1(a) and 7-1(b) showing the change in FWC at 950°C and 1100°C respectively

for Fe particles 5µm, 46µm and 83µm. Though limited data sets are available for other temperatures, the data are consistent with Figure 7-1(a) and (b). A full set of data are given in Appendix VII).

Series 2: The amount of the Fe particles added to the analogue was varied for a constant particle size range. This would result in a change in the contact area of the particles. These data are also shown in Figure 7-1(a) and 7-1(b) for 46µm particle addition. The (I) denotes higher mass of Fe addition.

Series 3: Similar to series 2, two mass levels of magnetite (Fe_3O_4) have been used at a constant particle size range. These data are shown in Figure 7-2(a) and 7-2(b), the (I) denotes higher mass of magnetite (Fe_3O_4) addition

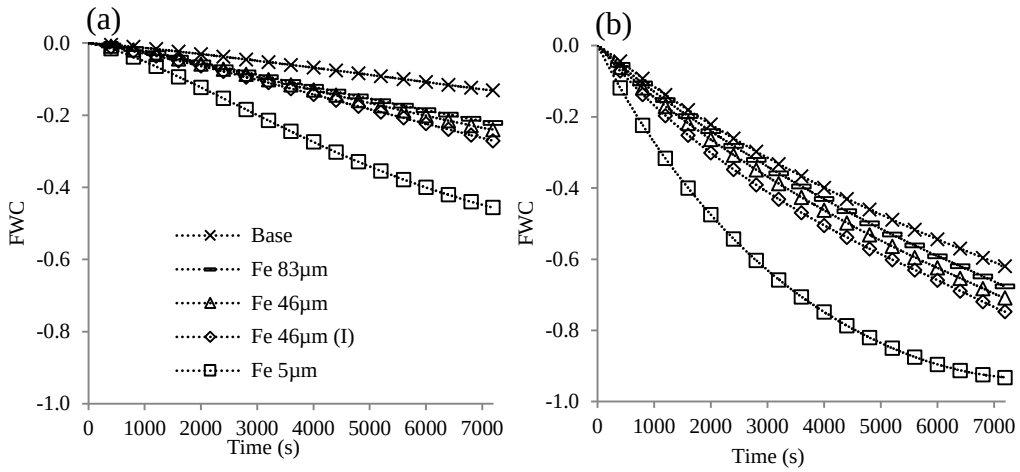

Figure 7-1: The FWC versus time of the base coke analogue and coke analogues prepared with metallic iron (Fe) reacted in CO_2 at different temperatures. (a) 950°C and (b) 1100°C.

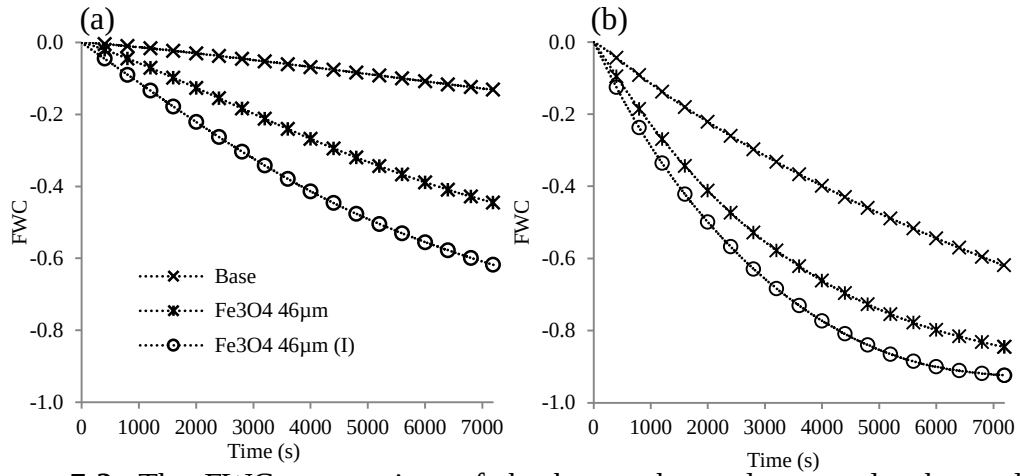

Figure 7-2: The FWC versus time of the base coke analogue and coke analogues prepared with magnetite (Fe_3O_4) reacted in CO_2 at different temperatures. (a) 950°C and (b) 1100°C.

From Figures 7-1 and 7-2, it can be seen that reducing the particle size of Fe, increasing the mass addition of the Fe and increasing the mass addition of the Fe_3O_4 all resulted in an increased reaction rate (more negative FWC). Both smaller particle sizes and increasing mass will result in an increased surface area of Fe. Therefore the results from these figures are consistent with what might be expected with increased contact area effects on an heterogeneous reaction, that is, increased contact area of reagents increasing the rate of reaction.

In an attempt to be more quantitative about this particle surface area effect, the following approach was adopted. The total surface area of elemental Fe and Fe added as Fe_3O_4 used to make the coke analogue was calculated using the known mass and density of the elemental Fe and magnetite (Fe_3O_4). Assuming the mean of the particle size range can be used to characterise the particle diameter and approximating the particles to a sphere, the surface area of the particles can be calculated. Details of the surface area calculation for the analogue are given in Table 7-1.

Table 7-1: The total surface area of elemental Fe and magnetite (Fe_3O_4) based on average particle size

Coke analogues	**Fe and Fe_3O_4 added**										
	Particle size µm	Diameter, d µm	Conc. mol cation / 100g C	Mass, m g	Density, ρ $10^6 g/m^3$	Volume of a single particle, V_i $10^{-14} m^3$ $V_i = \frac{4}{3}\pi\left(d/2\right)^3$	Surface area of a single particle, A_i $10^{-6} m^2$ $A_i = 4\pi\left(d/2\right)^2$	Total volume of particles in C, V_T $10^{-6} m^3$ $V_T = \frac{m}{\rho}$	Total number of particles in C, N 10^7 $N = V_T / V_i$	Total surface area in C, A_T (m^2) $A_T = N \times A_i$	Total surface area per 100g of C, $A_{T/100g}$ $(m^2/100g\ C)$ $A_{T/100g} = A_T \times \left(100/80\right)$
Fe 5µm	<10	5	0.10	4.74	7.87 [93]	0.00655	0.0785	0.60	919.86	0.72	0.90
Fe 46µm	38–53	45.5	0.10	4.74	7.87 [93]	4.93	6.51	0.60	1.22	0.08	0.10
Fe 46µm (I)	38–53	45.5	0.20	10.18	7.87 [93]	4.93	6.51	1.29	2.62	0.17	0.21
Fe 83µm	75–90	82.5	0.10	4.74	7.87 [93]	29.4	21.3	0.60	0.20	0.04	0.05
Fe_3O_4 46µm	38–53	45.5	0.10	5.17	5.17 [93]	4.93	6.51	1.29	2.62	–	–
Equivalent Fe in Fe_3O_4 46µm[+]	–	35.5	–	4.84	7.87 [93]	2.35	3.96	0.62	2.62	0.10	0.13
Fe_3O_4 46µm (I)	38–53	45.5	0.16	10.98	5.17 [93]	4.93	6.51	2.12	4.31	–	–
Equivalent Fe in Fe_3O_4 46µm (I)[+]	–	35.5	–	7.95	7.87 [93]	2.35	3.96	1.01	4.31	0.17	0.21

[+]The total surface area has been corrected to compensate for the reduction of Fe_3O_4 as green addition to Fe after the firing process and assuming no loss of metallic Fe content. The mass of Fe after firing and the density of Fe were used to calculate the change in the total surface area.

Fe in its elemental form

To test for the effect of elemental Fe on the reactivity of the coke analogue in CO_2, a plot of FWC versus total surface area of Fe (Figure 7-3(a)) and a plot of R_C versus total surface area of Fe (Figure 7-3(b)) were used. The plots show data sets at two different temperatures (950°C and 1100°C).

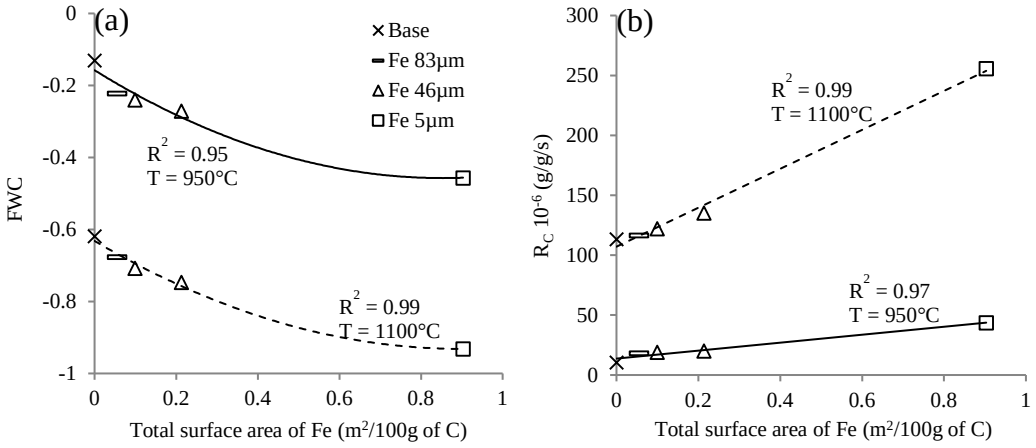

Figure 7-3: (a) A plot of FWC versus total surface area of elemental Fe with temperatures (950°C and 1100°C). The curves are 2nd order polynomial fits of the data. (b) A plot of R_C versus total surface area of elemental Fe with temperatures (950°C and 1100°C). The straight lines are linear fits of the data.

Inspection of Figure 7-3(a) and 7-3(b) shows that the reactivity as expressed by FWC (Figure 7-3(a)) has a non-linear behaviour with particle surface area, while the reactivity as expressed by R_C (Figure 7-3(b)) has a linear relationship with particle surface area. Though limited data sets are available for the other temperatures, the data are consistent with Figure 7-3(a) and (b). A full set of data are given in Appendix VII.

The difference in trends of FWC and R_C with particle surface area likely relate to the fact that R_C represents the early part of the analogue reaction (~10 minutes) and FWC all of the reaction over 2 hours. At the longer reaction times, it can be expected that there would be degradation of the analogue with respect to geometry. This would affect both the contact area of the carbon with CO_2 and that of carbon with the particle. The observations at the end of CO_2 reaction experiments captured in Table 4-20 support this.

Therefore it is likely the R_C versus particle surface area is a more robust representation of the particle contact area effect and has been used in subsequent analysis.

Elemental Fe versus Fe from readily reducible Fe_3O_4

This comparison is being carried out to establish the effects of elemental Fe and Fe added as Fe_3O_4 on the R_C of the coke analogue. A plot of R_C versus the total surface area of Fe (both as elemental Fe and Fe from reduced Fe_3O_4) at two different temperatures (950°C and 1100°C) is given in Figure 7-4.

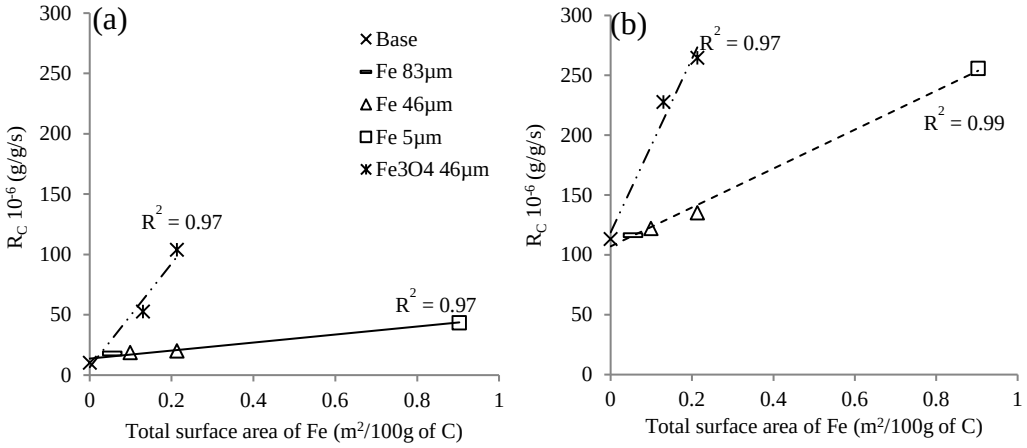

Figure 7-4: A plot of R_C versus total surface area of Fe (both as elemental Fe and Fe from reduced Fe_3O_4). The straight lines are linear fits of the data. (a) 950°C and (b) 1100°C.

From Figure 7-4 it can be seen that the effect of Fe from reduced Fe_3O_4 is different relative to Fe added in its elemental form, that is, the R_C for Fe from reduced Fe_3O_4 is significantly higher. In order to understand the behaviour of elemental Fe and Fe added as Fe_3O_4 on reactivity, four key observations (or results) of this study were considered as the baseline to identify why Fe_3O_4 is different relative to Fe. The observations are,

Initial porosity: As discussed previously in section 5.1.1, the initial porosity of all the coke analogues tested in this study is fixed and controlled (29.3% ± 2.3% for base, 31.9% for Fe 46µm, 31.4% for Fe 46µm (I), 29.7% for Fe_3O_4 46µm and 30.7% for Fe_3O_4 46µm). The controlled initial porosity of the coke analogues prepared with both

elemental Fe and Fe added as Fe_3O_4 suggest that the initial porosity is not significant a factor in the differences in reactivities of the coke analogues.

Localised graphitisation: As discussed previously in Chapter 6, both elemental Fe and Fe added as Fe_3O_4 increased sp^2 bonding in the carbon (as a localised effect). As the carbon bonding characters are very similar for both forms of Fe additions there are no clear differences in the sp^2 bonding. This may suggest that localised graphitisation is not a factor in the differences in reactivities of the coke analogues.

Concentration of additions (0.1 mol per 100g of C): On the basis of the concentration of the Fe and Fe_3O_4 added to the analogue, the mol cation of the additions were similar for both Fe 46µm and Fe_3O_4 46µm. This may suggest that concentration of additions is not a factor for the significant differences in reactivities of the coke analogues.

Particle surface area in the analogue ($0.21m^2$ per 100g C): On the basis of the total particle surface area in the coke analogue and with an assumption that all the particles are in close contact with coke analogue carbon, the particle surface area were similar for both Fe 46µm (I) and Fe added as Fe_3O_4 46µm (I). This may suggest that similar particle surface area is not a factor for the significant differences in reactivities of the coke analogues.

An alternative hypothesis may be that Fe from readily reducible magnetite (Fe_3O_4) is creating more active carbon sites relative to the Fe added as elemental Fe, that is, the reduced Fe from Fe_3O_4 increased reactivity more than elemental Fe because it created more active carbon sites. This is an issue that should be followed up in future research.

Summary of main points

- The addition of Fe (both elemental Fe and Fe added as Fe_3O_4) to coke analogue increases R_C and is a function of the Fe–coke analogue contact area.
- The effect of adding Fe initially in the form of Fe_3O_4 on reactivity is greater than that of elemental Fe.

8. Assessment of kinetic mechanisms for elemental Fe and Fe added as Fe_3O_4 effects on coke analogue reaction

This is being carried out to establish the possible kinetic mechanisms for the effect of Fe (both elemental Fe and Fe added as Fe_3O_4) on the reactivity of the coke analogue.

The previously suggested mechanisms in the literature for the catalytic effects of minerals and metals on reactivity of metallurgical coke and coal in CO_2 are [10, 44, 70, 82, 96, 97, 104, 116, 146, 147, 200-202, 204-207],

1. dissolution of carbon into Fe,
2. CO_2 gas dissociating on Fe surface,
3. redox reaction involving Fe and CO_2,
4. transfer of electrons from carbon into Fe, and
5. intercalation.

As mentioned previously in section 7-1, elemental Fe and Fe added as Fe_3O_4 increased the reactivity of the coke analogue. This increase appears to be a function of the particle surface area, with a linear relationship between R_C and particle surface area. In an attempt to fully understand the effects of Fe added as elemental Fe and Fe_3O_4 on the reactivity of the coke analogue, the experimental observations and results of this study will be discussed in the context of these mechanisms (1 to 5). A summary of the possible mechanisms and comments on experimental observations that support the mechanisms are given in Table 8-1. This table represents a summary of the text in this chapter.

Table 8-1: A summary of the possible mechanisms and comments on experimental observations that support the mechanisms

Mechanisms	**Elemental Fe and Fe added as Fe_3O_4**		Comments on experimental observations
	Fe	Fe_3O_4*	
Dissolution of carbon into Fe	Yes	Yes	(1) Localised graphitisation (Raman measurement), (2) Fe picking up carbon (LECO measurement), and (3) Graphite flakes within the Fe particles (microscopy analysis) are consistent with this mechanism
CO_2 gas dissociating on Fe surface	Yes	Yes	Removal of carbon from the Fe (LECO measurement) is consistent with this mechanism
Redox reaction involving Fe and CO_2, and iron oxide and carbon	Yes	Yes	(1) Observation of iron oxides around Fe particle, when the Fe particle is not in close contact with carbon (microscopy analysis), and (2) Observation of iron oxide post experimental (XRD analysis) are consistent with this mechanism
Transfer of Electrons from carbon into Fe	Yes	Yes	This mechanism can be viewed as another way of forming active carbon sites around Fe–carbon interface
Intercalation	No	No	No broadening of the (002) carbon peak (XRD analysis) indicates that intercalation did not occur with Fe and mineral addition.

Yes means experimental results are consistent with the mechanism
No means experimental results are not consistent with the mechanism
* Fe_3O_4 is reduced to Fe on firing of the coke analogue

8.1. Carbon dissolution into Fe

In this mechanism carbon dissolves into Fe [152, 154, 201, 202, 208, 215, 216]. When carbon dissolves into Fe, carbon–carbon bonds at the Fe–carbon interface in the coke analogue are weakened. The weakened carbon–carbon bonds increase the number of active carbon sites (C_f in equation 2-15, reproduced in the following text with equation 2-16) [44, 176, 181].

$$C_f + CO_{2(g)} \underset{j_1}{\overset{i_1}{\rightleftharpoons}} C(O) + CO_{(g)}$$

$$C(O) \xrightarrow{j_3} CO_{(g)}$$

An illustration of the carbon dissolution mechanism is given in Figure 8-1.

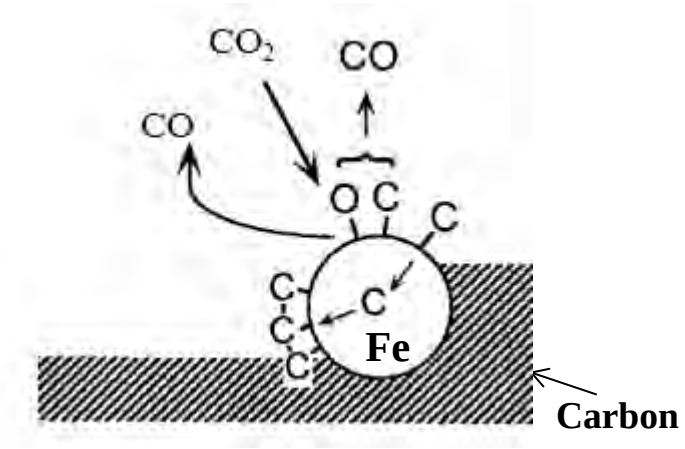

Figure 8-1: An illustration of carbon dissolution mechanism of elemental Fe and readily reducible Fe_3O_4 catalysed reaction of the coke analogue (modified from Tomita [207]).

In order to test whether this mechanism applies to the elemental Fe and readily reducible Fe_3O_4 added to the coke analogue, Raman, LECO and microscopy results were used as reference points.

The Raman results of this study indicated Fe (both elemental Fe and Fe added as Fe_3O_4) promoted localised graphitisation (see Figure 6-1). This is best explained in terms of graphitisation caused by dissolution of carbon into Fe during firing at temperature followed by precipitation of carbon from Fe during cooling. At the reaction temperature, it is expected that some of the precipitated carbon would diffuse back into the Fe forming new active sites at the Fe–carbon interface in the coke analogue [44, 176, 181].

The Raman result is complemented with LECO measurements and microscopy (SEM and optical) observations. Using LECO measurements, it was found that Fe picked up

carbon (the carbon level increased from 0.06 mass% to 1.72 mass%, see Table 4-21). Microscopy analysis (SEM and optical) provided further evidence in support of carbon pick up in coke analogue materials prepared with Fe and Fe_3O_4 (Figures 4-3, 4-4, III-3 to III-5). Graphite flakes were observed within the Fe particles. The increase in the carbon level in the Fe and observation of graphite flakes within the Fe particles are only possible if carbon had dissolved into the Fe.

Detailed non-polarised optical micrographs showing preferential loss of carbon around Fe particles in coke analogue–Fe 46µm are given in Figures III-14, III-15, III-20 and III-21. The samples were reacted at two different temperatures of 950°C and 1025°C for only 1 hour to ensure its initial cylindrical shape was maintained. That is, this was carried out for 1 hour to avoid the sample breaking up on transferring from the furnace alumina pedestal to sample container at 1025°C (see detailed post experimental dimensional observation captured in Table 4-20). A comparison of the unreacted and reacted coke analogue samples are given in Figure 8-2(a) and 8-2(b) respectively. Figure 8-2(a) and 8-2(b) were originally given in Figures II-19 and II-20 respectively.

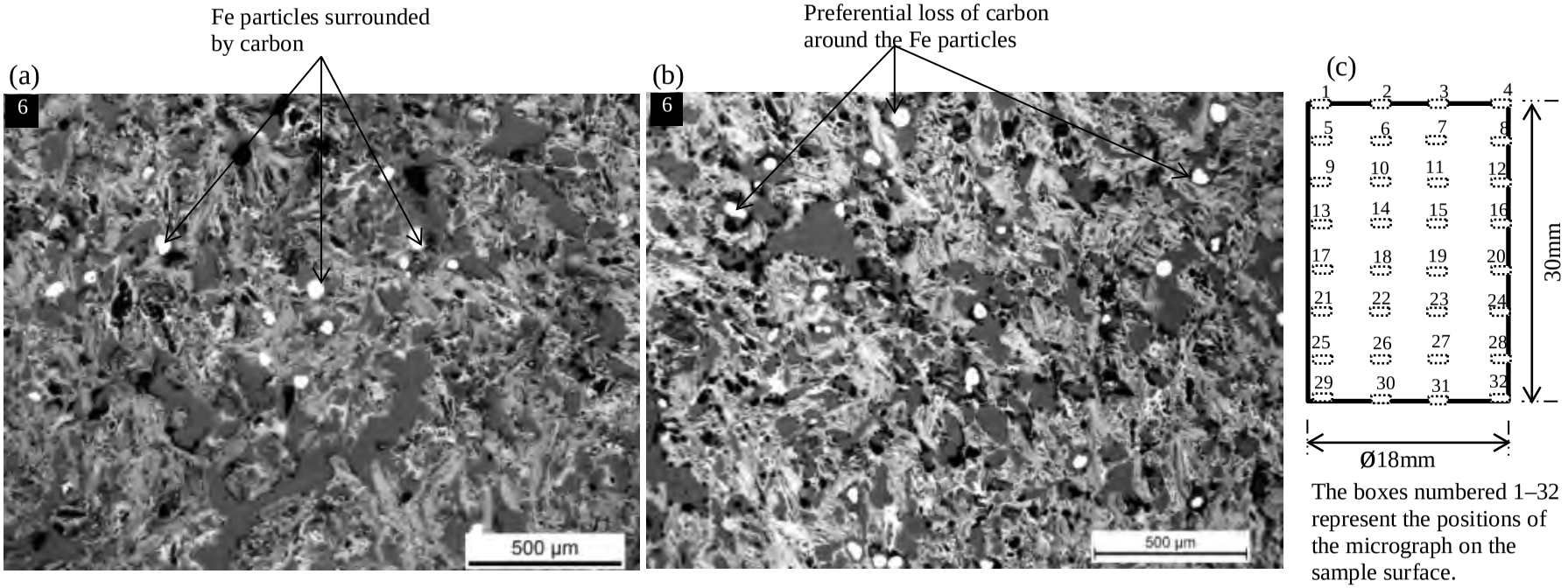

Figure 8-2: The non-polarised optical micrograph of coke analogue–Fe 46µm at position 6 showing (a) carbon around Fe particle before reaction, (b) preferential loss of carbon around Fe particle post reaction in CO_2 at 950°C for 1 hour and (c) illustration of approximate positions of the micrographs on the sample surface.

From a comparison of Figure 8-2(a) showing the unreacted sample with Figure 8-2(b) for the reacted sample, it can be seen that there was preferential loss of carbon around the Fe particles. This may suggest that there were more active carbon sites localised around the Fe particles.

The carbon dissolution mechanism is best explained as carbon diffusing into Fe at the reaction temperatures (900°C to 1350°C) to create active carbon sites, C_f, in the coke analogue carbon (Fe–carbon interface). This mechanism would probably be more favoured at low temperatures, that is, zone I where the CO_2 gas concentration is uniform throughout the bulk of the coke analogue and is equal to the concentration of the gas phase [15, 44, 77, 175, 181]. This proposition appears to be consistent with the R_C plots given in Figures 7-3(b) and 7-4, where R_C is linearly proportional to the Fe particle surface area.

8.2. CO_2 gas dissociating on Fe surface

This mechanism involves CO_2 gas dissociating on the Fe surface to form CO gas and absorbed oxygen atoms. These absorbed oxygen atoms can then react with the active carbon sites at the Fe–carbon interface, and can also spill over from the Fe surface to find an active carbon site [44, 97, 178, 199-201, 205, 206, 210-213]. An illustration of this mechanism is given in Figure 8-2.

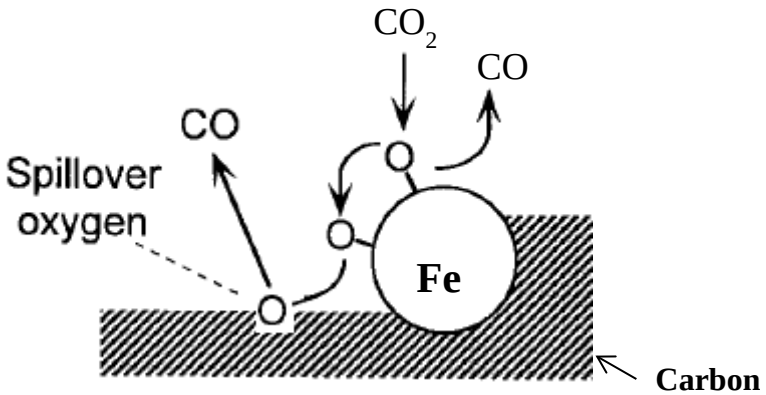

Figure 8-3: An illustration of CO_2 dissociation mechanism of elemental Fe and readily reducible Fe_3O_4 catalysed reaction of the coke analogue (modified from Tomita [207]).

In addition, at the reaction temperature, the dissolved carbon in the Fe is expected to react with CO_2 gas to form CO gas freeing the Fe surface of absorbed oxygen. This removal of carbon from the Fe regenerates the catalytic ability of the Fe. Under such circumstances, the Fe is able to continually dissociate CO_2 gas [215].

This is expected to maintain the increased reactivity in coke analogue containing Fe particles compared to the coke analogue containing no Fe particles (the base coke analogue). This is also consistent with the preferential loss of carbon around the Fe particles shown in Figure 8-2(b) above (see detailed micrographs in Figures III-14, III-15, III-20 and III-21).

The measurement of lower carbon levels in the Fe post reactivity testing of the coke analogue relative to pre reactivity testing has shown that the carbon in the Fe reacts with CO_2. The carbon levels in the Fe (1.72 mass% pre reaction) were lowered to 0.46 mass% and 0.48 mass% after reaction at 950°C and 1025°C respectively (see detailed assessment in Appendix V).

8.3. Redox reaction

The redox reaction mechanism suggests that Fe reacts with CO_2, yielding an iron oxide and CO, followed by a reaction between the iron oxide and carbon to give CO and Fe [200, 212, 213]. The Fe and CO_2 reaction is a gas–solid reaction vital for Fe oxidation, while the iron oxide and carbon reaction are needed for the transfer of oxygen to the carbon surface to form CO. Also, the Fe is continuously renewed. Maintaining Fe in its metallic form is crucial for continuous redox cycle. It would be expected that when Fe is not in close contact with carbon surface, there is the possibility that the Fe would react with CO_2 to form stable iron oxide phases.

In order to test whether redox reactions involving Fe and CO_2, and iron oxide and carbon could occur at the high temperatures used in this study, thermodynamic calculations (ΔG, equation 8-1) of reactions (8-2) to (8-7) over a range of temperatures were considered (see Figure 8-4).

$$\Delta G = \Delta G^\circ + RT\ln Q \qquad 8\text{-}1$$

$$Fe_{(s)} + CO_{2(s)} \rightarrow FeO_{(s)} + CO_{(g)} \qquad \Delta G^\circ = 20100 - 22.41T \text{ J.mol}^{-1} \text{ [63, 64]} \qquad 8\text{-}2$$

$$FeO_{(s)} + C_{(s)} \rightarrow Fe_{(s)} + CO_{(g)} \qquad \Delta G^\circ = 145200 - 148.35T \text{ J.mol}^{-1} \text{ [63, 64]} \qquad 8\text{-}3$$

$$3Fe_{(s)} + 4CO_{2(g)} \rightarrow Fe_3O_{4(s)} + 4CO_{(g)} \qquad \Delta G^\circ = 27740 - 27.09T \text{ J.mol}^{-1} \text{ [63, 64]} \qquad 8\text{-}4$$

$$Fe_3O_{4(s)} + 4C_{(s)} \rightarrow 3Fe_{(s)} + 4CO_{(g)} \qquad \Delta G^\circ = 633460 - 655.95T \text{ J.mol}^{-1} \text{ [63, 64]} \qquad 8\text{-}5$$

$$2Fe_{(s)} + 3CO_{2(g)} \rightarrow Fe_2O_{3(s)} + 3CO_{(g)} \qquad \Delta G^\circ = 28580 - 0.88T \text{ J.mol}^{-1} \text{ [63, 64]} \qquad 8\text{-}6$$

$$Fe_2O_{3(s)} + 3C_{(s)} \rightarrow 2Fe_{(s)} + 3CO_{(g)} \qquad \Delta G^\circ = 467320 - 511.40T \text{ J.mol}^{-1} \text{ [63, 64]} \qquad 8\text{-}7$$

The relationship between the reactants (partial pressure and activity) and the products (partial pressure and activity), and the reaction quotient Q in reactions (8-2) to (8-7) are given in Table 8-2.

Table 8-2: The reaction quotient Q in reactions (8-2) to (8-7)

Reaction	reaction quotient Q
8-2	$Q = \frac{a_{<FeO>} \cdot p_{CO}}{a_{<Fe>} \cdot p_{CO_2}}$
8-3	$Q = \frac{a_{<Fe>} \cdot p_{CO}}{a_{<FeO>} \cdot a_{<C>}}$
8-4	$Q = \frac{a_{<Fe_3O_4>} \cdot p_{CO}^4}{a_{<Fe>}^3 \cdot p_{CO_2}^4}$
8-5	$Q = \frac{a_{<Fe>}^3 \cdot p_{CO}^4}{a_{<Fe_3O_4>} \cdot a_{<C>}^4}$
8-6	$Q = \frac{a_{<Fe_2O_3>} \cdot p_{CO}^3}{a_{<Fe>}^2 \cdot p_{CO_2}^3}$
8-7	$Q = \frac{a_{<Fe>}^2 \cdot p_{CO}^3}{a_{<Fe_2O_3>} \cdot a_{<C>}^3}$

In Table 8-2 the values of $a_{<Fe>}$, $a_{<FeO>}$, $a_{<Fe2O3>}$, $a_{<Fe3O4>}$ and $a_{<C>}$ were assumed to be 1. The <C> reference state is pure graphite standard state. The p_{CO2} and p_{CO} values over the temperature range were obtained from Figure IV-1 (see detailed calculation in Appendix IV).

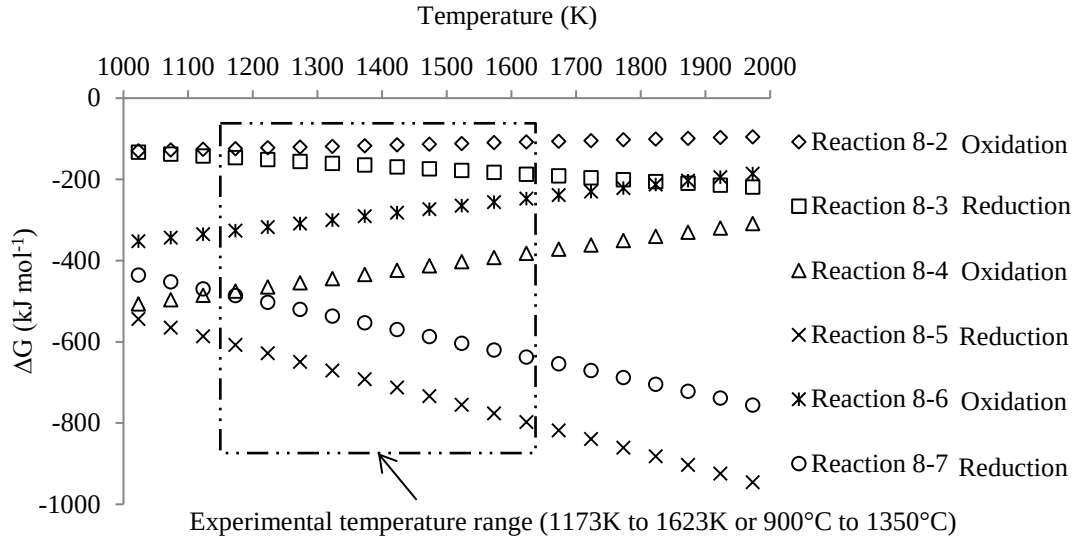

Figure 8-4: The plot of ΔG versus temperature for reactions 8-2 to 8-7.

From Figure 8-4, it can be seen that the oxide formation reactions (Reaction 8-2, 8-4 and 8-6) and the reduction of the iron oxides by carbon (Reaction 8-3, 8-5 and 8-7) are thermodynamically possible ($\Delta G < 0$). Due to the excess of carbon available at the early stage of the reactivity experiment, there is a lower probability that CO_2 gas would come in contact with Fe to oxidised the Fe via reactions 8-2, 8-4 and 8-6. When significant amounts of carbon have been reacted or removed from the analogue and the Fe is exposed to direct contact with CO_2, the oxidation of Fe with CO_2 could occur. From the thermodynamic analysis, the most likely oxidation product is Fe_3O_4 (Reaction 8-4). All the possible iron oxide products (Fe_3O_4, Fe_2O_3 and FeO) considered are reducible if they come in contact with coke analogue carbon. In this case, the iron oxide acts as an oxygen carrier to carbon surface to maintain the catalytic action of Fe. This is also consistent with the preferential loss of carbon around the Fe particles shown in Figure 8-2(b) above (see detailed micrographs in Figures III-14, III-15, III-20 and III-21).

Experimental observations (microscopy and XRD) indicate that the Fe (both in its elemental form and in a readily reduced form such as Fe_3O_4) reacts with CO_2 to form iron oxides (Fe_2O_3 and Fe_3O_4). The post-experimental XRD measurements of coke analogue–Fe 46μm and coke analogue–Fe_3O_4 46μm reacted at 1100°C for 2 hours indicated that only Fe_2O_3 and Fe_3O_4 phases were formed after reaction (see Figures II-3 and II-4). This is most likely to occur when significant amounts of carbon have been reacted or removed from the coke analogue. The observations at the end of the experiment are captured in Table 4-20. It can be seen that at 1100°C the geometry of the reacted samples had been degraded indicating significant loss of carbon. The final FWC values of the analogues prepared with Fe 46μm and Fe_3O_4 46μm are -0.71 and -0.85 respectively. The final FWC also indicates that most of the carbon had been reacted.

The post-experimental microscopy of the external surface of coke analogue–Fe 46μm reacted at 1100°C for only 20 minutes also showed the formation of iron oxide (Fe_2O_3 and Fe_3O_4) around the Fe particles. This occurred when the Fe particles were not in close contact with carbon (see Figures 4-12, 4-15 and Table 4-13). Further, after reaction for 1 hour at two different temperatures of 950°C and 1025°C dull reflection

thought to be iron oxides were observed closer to the external surface of the sample (Figures III-14, III-5, III-20, and III-21).

The XRD and microscopy results of the post reacted coke analogues prepared with elemental Fe and Fe_3O_4 are broadly consistent with the redox reaction mechanism suggested for Fe catalysed reaction of metallurgical coke and coal in CO_2 [44, 97, 178, 199-201, 205, 206, 210-213, 215, 217], but they only occurred when significant amounts of carbon had been reacted.

8.4. The transfer of electrons from carbon into Fe

According to Long and Sykes [206, 217], the transfer of electrons from carbon into Fe would catalyse the reaction of carbon in CO_2. The transfer of an electron from carbon to Fe (with the unfilled d-orbitals of Fe accepting electrons) results in a redistribution of π electrons in the carbon structure. This weakens the carbon–carbon bonds at the Fe–coke analogue carbon interface, with the weakened carbon–carbon bonds becoming active carbon sites (C_f) [44, 176, 181]. As before, an increase in C_f would increase the overall reaction of the coke analogue.

8.5. Intercalation

Intercalation is when an element or species sits (intercalates) between the graphite layers in the carbon structure. The formation of intercalates can cause an expansion of the coke carbon matrix, increase stress, modify the coke surface area, weaken coke microstrength and weaken coke structure to increase the reaction rate [70, 82, 104, 116, 146, 147].

In order to test for intercalation in this study, XRD data for coke analogues prepared with elemental Fe and magnetite (Fe_3O_4) were reviewed for evidence of intercalation. If there were significant intercalation taking place in the coke analogues, it would be observed in the broadening of the (002) carbon peak. A full width at half maximum

(FWHM) analysis of the (002) carbon peak was carried out. An example of the FWHM analysis was given in Figure 4-54, reproduced in the following text.

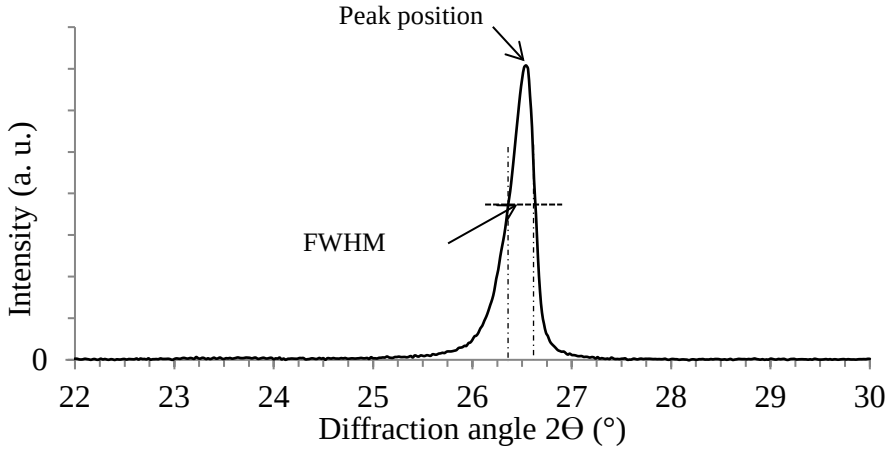

The XRD pattern of fired base coke analogue showing FWHM and position of the (002) carbon peak (see Figure 4-54).

A comparison of the FWHM values for the coke analogues prepared with elemental Fe and magnetite (Fe_3O_4) with the base coke analogue are given in Table 8-3.

Table 8-3: The FWHM and position of (002) peak in coke analogues

Coke analogue materials and graphite	FWHM (°)	Peak Position (°)
Base	0.286	26.54
Fe 5µm	0.226	26.56
Fe 46µm	0.218	26.58
Fe 83µm	0.240	26.54
Fe_3O_4 46µm	0.248	26.56

From Table 8-3 it can be seen that the FWHM values of the (002) carbon peak of all the coke analogues are relatively similar and if there is any trend, the FWHM is getting smaller with Fe and Fe_3O_4 additions. It appears that the elemental Fe and Fe added as Fe_3O_4 had no clear discriminating effect on the (002) carbon peak. There appears to be no intercalation effect of the Fe and Fe_3O_4 additions. This is also the same for all the other minerals tested (see Table 4-22).

8.6. Activation energies of the reaction of the coke analogues prepared with elemental Fe and Fe added as Fe_3O_4

The plots of ln R_C against 1/T for all the materials tested are given in Appendix VI. The activation energy values for zones I and II, and the temperature at the point of intersection between the zones for base coke analogue and coke analogues prepared with elemental Fe and Fe_3O_4 are given in Table 8-4.

Table 8-4: The activation energy values for base coke analogue and coke analogues prepared with elemental Fe and readily reducible Fe_3O_4.

Coke analogues	**Zone I kJ.mol^{-1}**	**Temperature at point of intersection (°C)**	**Zone II kJ.mol^{-1}**
Base	273.6±0.5	~1075	55.9±0.4
Fe 5µm	276.9±0.5	-	-
Fe 46µm	289.8±0.5	~1050	43.3±0.4
Fe 83µm	287.7±0.5	-	-
Fe_3O_4 46µm	238.7±0.5	~1025	30.7±0.4

- Reactivity not measured

From Table 8-4 it appears that the zone I activation energy values for the coke analogues are within a close range (though Fe_3O_4 46µm is lower) to the activation energy values of the base coke analogue and cokes (Table 5-3). No significant change in the zone I activation energy values for the coke analogues, indicates that there is no change in the rate controlling mechanism for the reaction of the coke analogue in CO_2. That is reaction 2-16, reproduced in the following text with reaction 2-15, is the rate controlling.

$$C_f + CO_{2(g)} \underset{j_1}{\overset{i_1}{\rightleftarrows}} C(O) + CO_{(g)}$$

$$C(O) \xrightarrow{j_3} CO_{(g)}$$

Though there is no change in the rate controlling mechanism, there was increased reactivity with elemental Fe and Fe added as Fe_3O_4 additions relative to the base coke analogue. This is best explained as increase in the number of active carbon sites (C_f) due to the catalytic effect of Fe. This increase in C_f increased reactivity but it is not substantial enough to change the rate controlling mechanism.

This suggestion is broadly consistent with the Raman measurement were elemental Fe and Fe from readily reducible Fe_3O_4 did not have a clear discriminating effect on the "bulk" carbon bonding of the coke analogue as assessed by $I_{(D)}/I_{(G)}$ versus $I_{(V)}/I_{(G)}$ plots. This is also consistent with the literature on minerals and metals that only increased the number of active carbon sites (C_f) in coke [178, 198, 211].

Summary of main points

- The addition of elemental Fe or Fe as Fe_3O_4 to the coke analogue increased reactivity relative to the base coke analogue by increasing the number of active carbon sites (C_f).
- The primary effect of Fe on the reactivity is considered to be an increase in the amount of active carbon sites, possibly through the following mechanisms
    - Carbon dissolution into Fe, and
    - Transfer of electrons from carbon into Fe.
- There are possible additional effects of Fe on reactivity relating to promotion of oxygen delivery to the active carbon sites that are consistent with the following mechanisms
    - Dissociation of CO_2 on the Fe surface, and
    - A redox reaction between Fe and CO_2 to form iron oxide and CO, followed by reduction of the iron oxide on reaction with carbon.
- Ultimately the results presented are consistent with all four mechanisms.

9. The comparative effects of elemental Fe and quartz (SiO_2) on reactivity of the coke analogue

The comparative effect of elemental Fe and quartz (SiO_2) on the reactivity of the coke analogue is discussed in this chapter.

A comparison of the effect of quartz (SiO_2) on the reactivity of the coke analogue relative to both coke analogue–Fe 46μm and base coke analogue is expressed as FWC plots at two different temperatures (see Figure 9-1). The two temperatures represent the lowest (900°C) and highest (1350°C) temperature points of the reactivity experiments. The trends of the reactivity data (speed of reaction) are consistent at all temperatures tested.

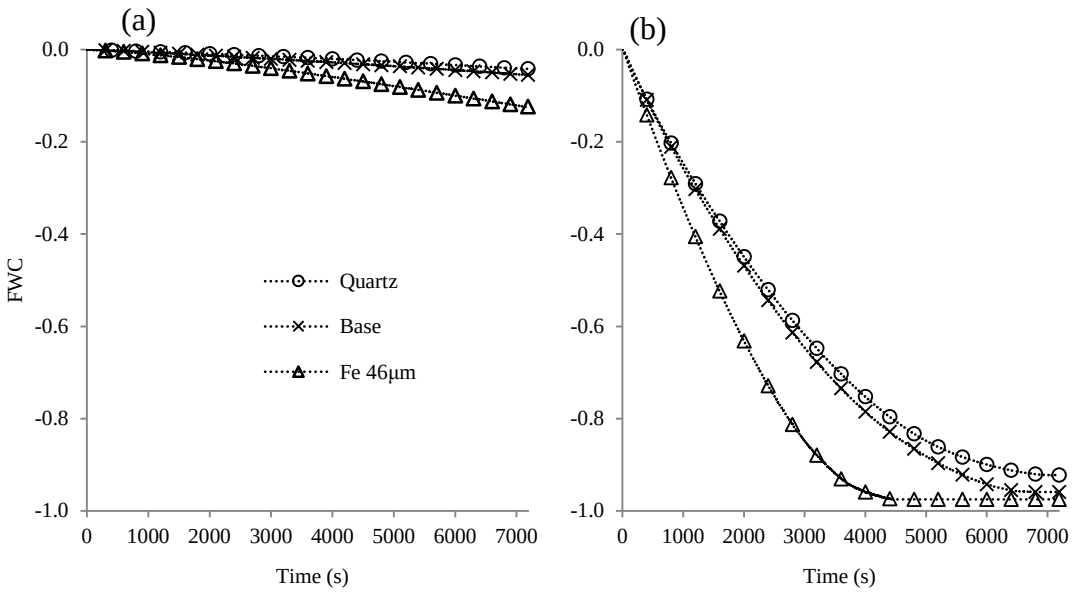

Figure 9-1: A comparison of the effects of elemental Fe and quartz (SiO_2) on the reactivity of the coke analogue expressed as a plot of FWC versus time with temperature. (a) 900°C and (b) 1350°C.

From Figure 9-1 it can be seen that reactivity increases with temperature, that is, with increasing temperature the FWC is more negative. Further, at the same temperature, it can be seen that elemental Fe increased reactivity relative to the base coke analogue while quartz decreased reactivity relative to the base coke analogue. The rate of the coke analogue reaction can be ranked as quartz < base < Fe 46μm.

As discussed previously in Chapters 7 and 8, elemental Fe was thought to both increase the number of active carbon sites in the analogue and promote oxygen delivery to the active carbon sites relative to the base coke analogue. The question would now be "how is quartz (SiO_2) reducing reactivity"?

In the coke literature [79, 89, 163, 168, 176, 186, 206, 218, 219], it was reported that some minerals (for example, aluminosilicates) reduced coke reactivity by covering the,

- pores and pore walls of coke, and
- coke surface.

In order to test for the possible effects of quartz (SiO_2) on the reactivity of the coke analogue, a number of measurements and analysis were carried out. The measurements and analysis were,

1. carbon bonding using Raman spectroscopy,
2. pore interconnectivity using neutron radiography (Dingo).

To facilitate a better understanding of the effect of quartz on reactivity, the results of the measurements (1 and 2) were compared with that of elemental Fe.

9.1. Effect of quartz on sp^2–sp^3 carbon bonding at the quartz–carbon interface

This was carried out to assess the effect of quartz (SiO_2) on the sp^2–sp^3 carbon bonding localised closer to the quartz–carbon interface, and by extension help to understand the effect of quartz (SiO_2) on reactivity.

As discussed previously in Chapter 5, elemental Fe and quartz (SiO_2) had no clear discriminating effect on the sp^2 and sp^2–sp^3 bonding of the coke analogue as characterised with the $I_{(D)}/I_{(G)}$ versus $I_{(V)}/I_{(G)}$ plot (see Figures 4-19(a) and 4-24(a)).

The effect of elemental Fe on the sp^2–sp^3 bonding was found to be local, that is, elemental Fe promotes sp^2 bonding at the Fe–coke analogue interface. This was discussed in detail in Chapter 6. The $I_{(V)}/I_{(G)}$ approach used to illustrate the effect of elemental Fe on sp^2–sp^3 bonding was also adopted to test the effects of quartz (SiO_2). The resulting plot is given in Figure 9-2. Figure 9-2(a) and 9-2(b) are amended graphics of Figures 4-19(c) and 4-24(c) respectively with the shaded area indicating the sp^2 bonding region.

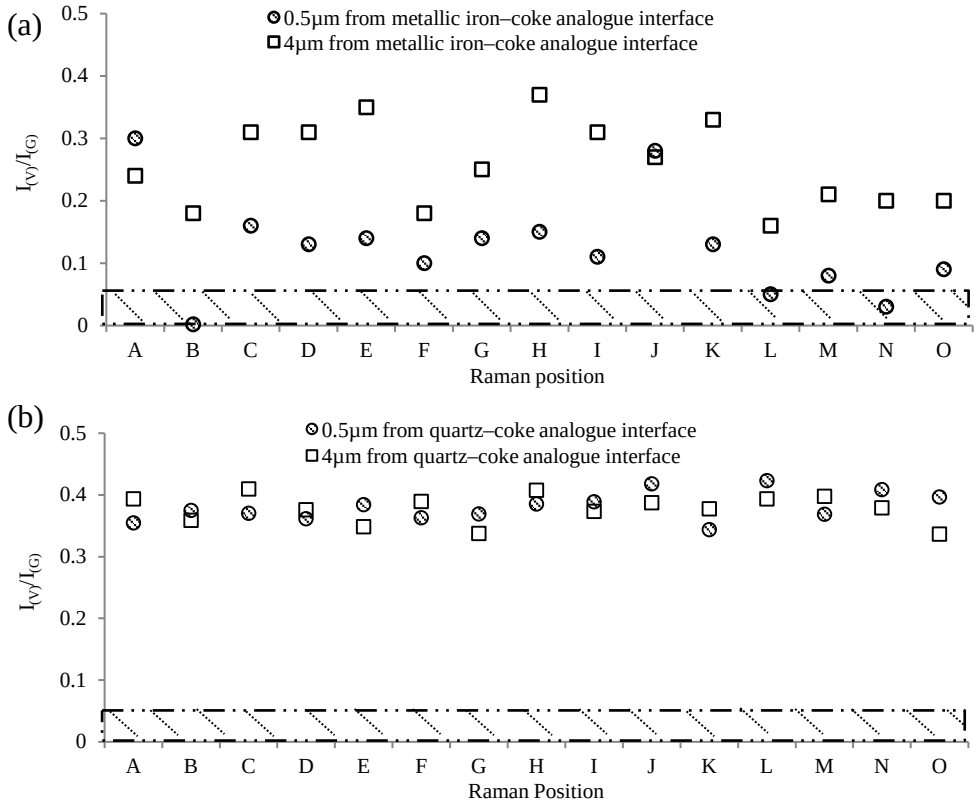

Figure 9-2: An illustration of sp^2–sp^3 bonding around particle in coke analogues. The hashed area is representative of the range of sp^2 bonding. (a) coke analogue–Fe 46µm and (c) coke analogue–quartz.

From a comparison of Figure 9-2(a) and (b) it appears that quartz (SiO_2) had no clear discriminating effect on the sp^2–sp^3 bonding. Also, the trend of the data in Figure 9-2(b) did not show a physical distortion effect, that is, an increase in the amount of sp^3 bonding at the quartz (SiO_2)–coke analogue interface. A physical distortion in carbon bonding is in the form of twisting, sliding or bending of graphene layers so that they are

not aligned with one another (see detail description in section 2.2.2 of the literature review chapter) [44, 130, 144].

As mentioned previously in Chapters 6, 7 and 8, the effect of elemental Fe on reactivity and bonding is often argued as a catalysing effect whereby elemental Fe promotes graphitisation (increase sp^2 bonding) and hence reactivity [4, 7, 10, 25, 26, 29, 30, 32, 33, 38, 40, 41, 43, 45-49, 52, 56, 59, 84, 96, 149-152, 180, 183-187]. With quartz (SiO_2) having no clear discriminating effect on sp^2–sp^3 bonding, it may be expected that it would not promote reactivity.

The suggestion of no clear discriminating effect on sp^2–sp^3 bonding appears to provide a basis to understand why quartz (SiO_2) did not increase reactivity, but it is not sufficient to answer the question of "how quartz (SiO_2) reduced reactivity".

9.2. Pore interconnectivity using neutron radiography (Dingo)

This is being carried out to assess whether the presence of quartz (SiO_2) particles in the analogue blocked the pores and pore walls. The result of this testing is compared to that of elemental Fe.

To facilitate a comparison of pore interconnectivity data for the coke analogues (base, Fe 46μm and quartz (SiO_2)), Figure 4-31 for the base coke analogue, Figure 4-32 for the coke analogue–Fe 46μm and Figure 4-34 for the coke analogue–quartz at 0.03mm, 0.10mm and 10.72mm slice thicknesses are given in Figure 9-3.

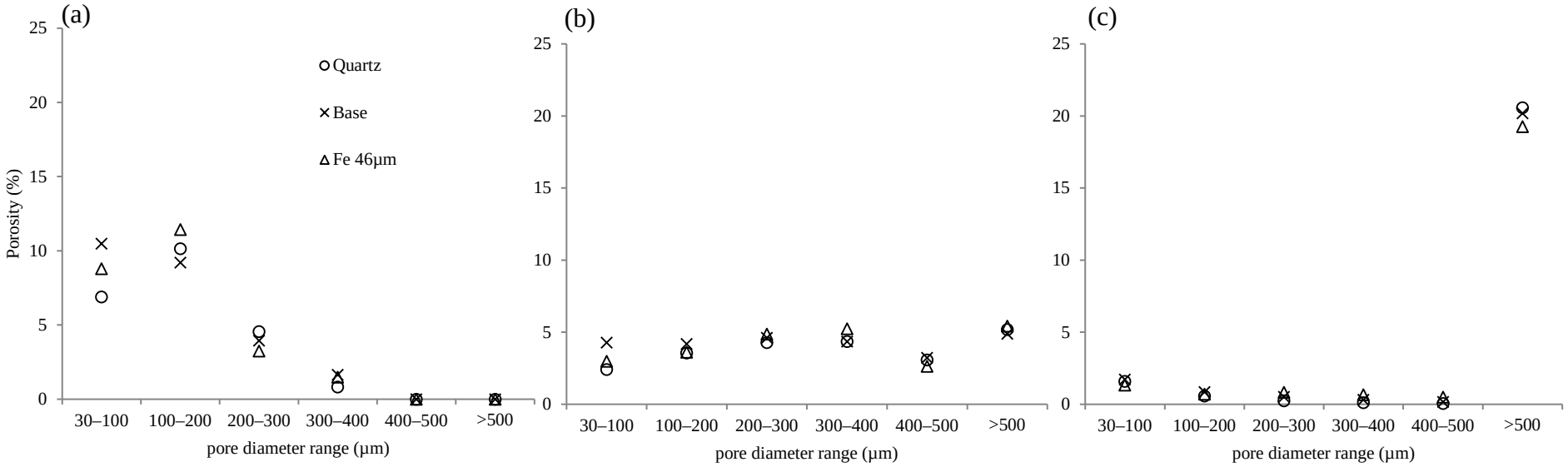

Figure 9-3: A plot of porosity versus pore diameter range of the coke analogues showing pore size distribution with slice thickness. (a) 0.03mm, (b) 0.10mm and (c) 10.72mm.

From Figure 9-3, it can be seen that the apparent pore sizes of the coke analogues increased with increasing thickness of the analogue sample indicating that the pores are interconnected. In each case, this suggests that the majority of the pores (~90%) and pore walls of the coke analogues are interconnected in 3D.

This high pore interconnectivity in the coke analogues would suggest that the pores and pore walls of the coke analogues are accessible for CO_2 gas penetration. With all things being equal it is unlikely that quartz (SiO_2) blocked pores and pore walls.

9.3. General comment on how quartz reduced reactivity

From the understanding of the effect of elemental Fe on reactivity which is best explained as elemental Fe increasing the number of active carbon sites (C_f in equation 2-15, reproduced in the following text with equation 2-16).

$$C_f + CO_{2(g)} \underset{j_1}{\overset{i_1}{\rightleftarrows}} C(O) + CO_{(g)}$$

$$C(O) \xrightarrow{j_3} CO_{(g)}$$

This increase in the number of active sites increased reactivity relative to the base coke analogue. It is apparent that quartz (SiO_2) reduced reactivity and it could be inferred that quartz (SiO_2) decreased the number of active carbon sites (C_f) available for the coke analogue reaction in CO_2.

As previously discussed in Chapter 8, elemental Fe is thought to increase reactivity through dissolution of carbon into Fe (section 8-1), CO_2 gas dissociating on Fe surface (section 8-2), redox reaction involving Fe and CO_2, and iron oxide and carbon (section 8-3), and transfer of electrons from carbon into Fe (section 8-4). Under the reaction conditions and results of this study, it could be suggested that these mechanisms (8-1 to 8-4) are not active with quartz (SiO_2) addition.

9.4. Activation energies of the reaction of the coke analogues prepared with elemental Fe and quartz (SiO_2)

The plots of ln R_C against 1/T for all the materials tested are given in Appendix VI. The activation energy values for zones I and II, and the temperature at the point of intersection between the zones for base coke analogue, coke analogue–Fe 46µm and coke analogue–quartz are given in Table 9-1.

Table 9-1: The activation energy values for base coke analogue, coke analogue–Fe 46µm and coke analogue–quartz.

Coke analogues	Zone I kJ.mol^{-1}	Temperature at point of intersection (°C)	Zone II kJ.mol^{-1}
Base	273.6±0.5	~1075	55.9±0.4
Fe 46µm	289.8±0.5	~1050	43.3±0.4
Quartz	247.7±0.4	~1100	54.6±0.3

From Table 9-1 it appears that the zone I and zone II activation energy values for the coke analogue–quartz are within a close range (though slightly lower) to the activation energy values of the base coke analogue and coke analogue–Fe 46µm. Though there has been a decrease in reactivity, likely due to the presence of quartz, this decrease is not substantial enough to significantly change the activation energy values.

Summary of main points

- The addition of quartz (SiO_2) to the coke analogue decreased its reactivity relative to the base coke analogue.
- Quartz (SiO_2) had no clear discriminating effects on the sp^2 and sp^2–sp^3 carbon bonding of the coke analogue from both "bulk" and "local" Raman measurements.
- It is not clear from the results obtained in this study why the addition of quartz lowered the reactivity of the coke analogue in CO_2.

10. The comparative effects of elemental Fe and Fe within a mineral on reactivity of the coke analogue

The comparative effect of elemental Fe and Fe bonded within enstatite ferroan ($Mg_{1.56}Fe_{0.44}Si_2O_6$) and phlogopite ferroan [$K(Mg,Fe)_3(Al,Fe)Si_3O_{10}(OH,F)_2$] on the reactivity of the coke analogue is discussed in this chapter.

A comparison of the effect of elemental Fe and Fe bonded within enstatite ferroan and phlogopite ferroan on the reactivity of the coke analogue relative to both coke analogue–Fe 46μm is expressed as FWC plots at two different temperatures (see Figure 10-1). The two temperatures represent the lowest (900°C) and highest (1350°C) temperature points of the reactivity experiments. The trends of the reactivity data (speed of reaction) are consistent at all temperatures tested.

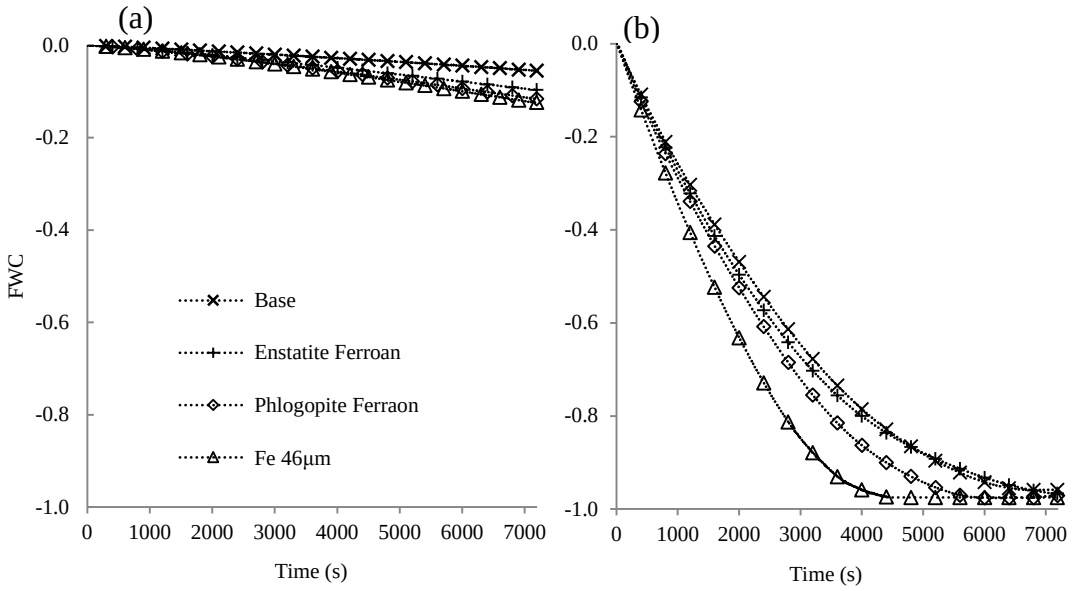

Figure 10-1: A comparison of the effects of elemental Fe and Fe bonded within enstatite ferroan ($Mg_{1.56}Fe_{0.44}Si_2O_6$) and phlogopite ferroan [$K(Mg,Fe)_3(Al,Fe)Si_3O_{10}(OH,F)_2$] on the reactivity of the coke analogue expressed as plot of FWC versus time with temperature. (a) 900°C and (b) 1350°C.

From Figure 10-1 it can be seen that reactivity increases with temperature, that is, with increasing temperature the FWC is more negative for the coke analogues. Further, at the same temperature conditions, it can be seen that elemental Fe, enstatite ferroan and phlogopite ferroan increased reactivity relative to the base coke analogue. The rate of

the coke analogue reaction can be ranked as base < enstatite ferroan ($Mg_{1.56}Fe_{0.44}Si_2O_6$) < phlogopite ferroan [$K(Mg,Fe)_3(Al,Fe)Si_3O_{10}(OH,F)_2$] < Fe 46μm.

As discussed previously in Chapters 7 and 8, elemental Fe was thought to increase the number of active carbon sites in the analogue and promote oxygen delivery to the active carbon sites relative to the base coke analogue.

To facilitate a better understanding of the effects of Fe bonded within enstatite ferroan ($Mg_{1.56}Fe_{0.44}Si_2O_6$) and phlogopite ferroan [$K(Mg,Fe)_3(Al,Fe)Si_3O_{10}(OH,F)_2$] on coke analogue reactivity, carbon bonding measurement using Raman spectroscopy was carried out to assess their effects on the sp^2–sp^3 carbon bonding localised closer to the particle–carbon interface.

10.1. Effects of Fe within a mineral on sp^2–sp^3 carbon bonding at the particle–carbon interface

This was carried out to assess the effects of Fe bonded within enstatite ferroan ($Mg_{1.56}Fe_{0.44}Si_2O_6$) and phlogopite ferroan [$K(Mg,Fe)_3(Al,Fe)Si_3O_{10}(OH,F)_2$] on the sp^2–sp^3 carbon bonding localised closer to the particle–carbon interface, and by extension understand their effect on reactivity. The result of this testing is compared to that of elemental Fe.

As discussed previously in Chapter 5, elemental Fe, enstatite ferroan and phlogopite ferroan had no clear discriminating effect on the sp^2 and sp^2–sp^3 bonding of the coke analogue as characterised with the $I_{(D)}/I_{(G)}$ versus $I_{(V)}/I_{(G)}$ plot (see Figures 4-19(a), 4-22(a) and 4-23(a)).

The effect of elemental Fe on the sp^2–sp^3 bonding was found to be local, that is, elemental Fe promotes sp^2 bonding at the Fe–coke analogue interface. This was

discussed in detail in Chapter 6. The $I_{(V)}/I_{(G)}$ approach used to illustrate the effect of elemental Fe on sp^2–sp^3 bonding was also adopted to test the effects of enstatite ferroan and phlogopite ferroan. The resulting plot is given in Figure 10-2. Figure 10-2(a), 10-2(b) and 10-2(c) are amended graphics of Figures 4-19(c), 4-22(c) and 4-23(c) respectively with the shaded area indicating the sp^2 bonding region.

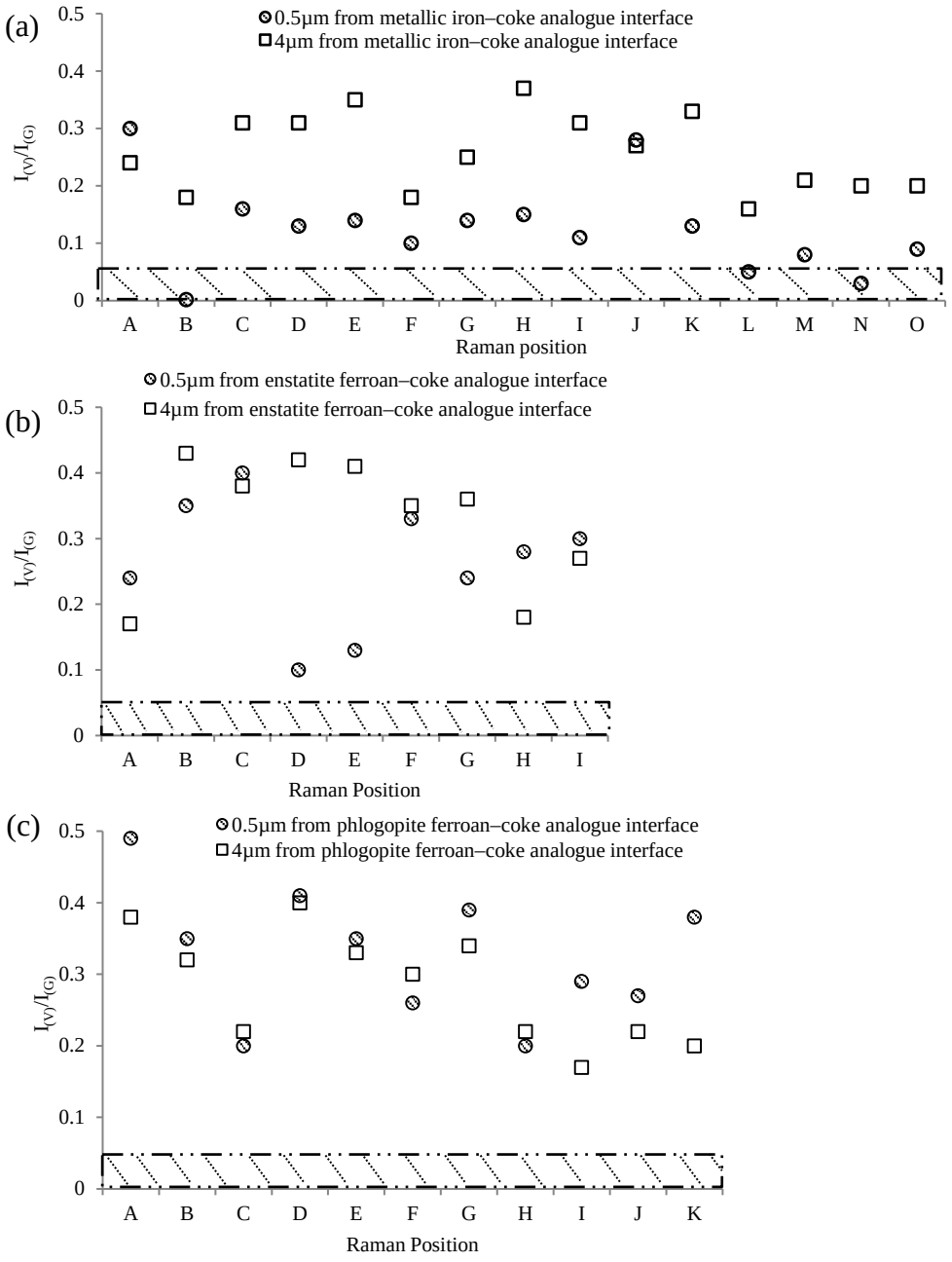

Figure 10-2: An illustration of sp^2–sp^3 bonding around particle in coke analogues. The hashed area is representative of the range of sp^2 bonding. (a) coke analogue–Fe 46µm and (c) coke analogue–enstatite ferroan and (c) coke analogue–phlogopite ferroan.

From a comparison of Figure 10-2(a), (b) and (c), the localised effects of elemental Fe and Fe bonded within enstatite ferroan and phlogopite ferroan on the sp^2–sp^3 bonding is summarised in Table 10-1.

Table 10-1: The localised effects of elemental Fe and Fe bonded within enstatite ferroan and phlogopite ferroan on sp^2–sp^3 bonding

Fe or Fe containing minerals	**Increased sp^2 bonding character at interface**	**Comments**
Fe 46µm	Yes	-
Enstatite ferroan ($Mg_{1.56}Fe_{0.44}Si_2O_6$)	No	Trace amounts of Ti in enstatite ferroan appears to cause an increase in sp^2 bonding for points D and E.
Phlogopite ferroan $K(Mg,Fe)_3(Al,Fe)Si_3O_{10}(OH,F)_2$	No	-

Yes means it increased sp^2 bonding,
No means it did not increase sp^2 bonding

Though not specifically investigated in this study, it would appear that Ti may be having a similar effect to Fe. There was trace amounts of Ti found in the enstatite ferroan ($Mg_{1.56}Fe_{0.44}Si_2O_6$). If we consider the Ti impurity in the enstatite ferroan, that is, position D and E of the non-polarised optical micrograph given in Figure 4-22(c) along with position D of the $I_{(V)}/I_{(G)}$ plot given in Figure 4-22(e). It can be seen that in this small region the carbon has been graphitised (increasing sp^2 bonding). Its effect on sp^2 bonding was captured in position D and E of Figure 10-2(b). This is consistent with what has been reported about Ti in the literature [32, 33, 52].

Due to the small amounts (trace) of Ti in the mineral and the fact that Ti was not the focus of this study no attempt was made to identify its phase. See Figure 10-3 for a more detailed micrograph and analysis of the Ti in the enstatite ferroan.

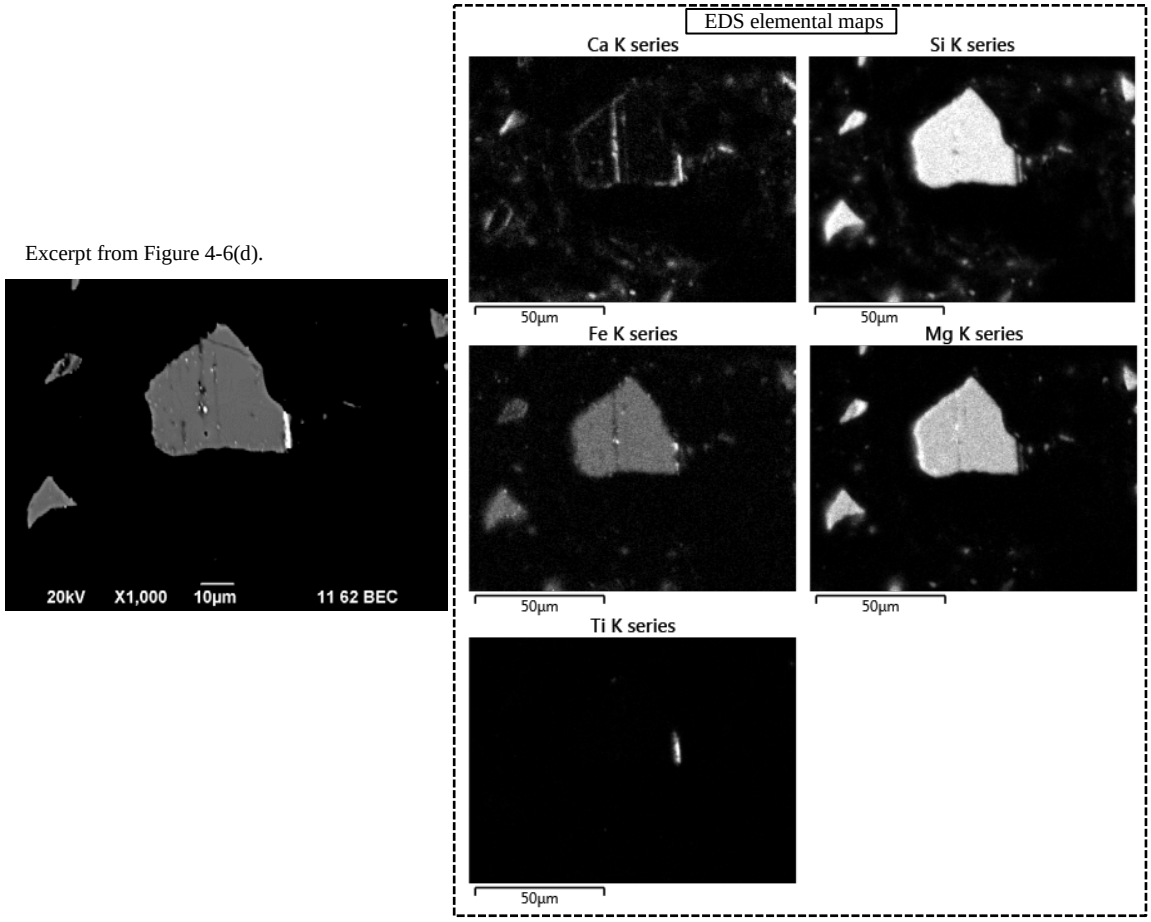

Figure 10-3: The backscattered SEM image focused on the enstatite ferroan ($Mg_{1.56}Fe_{0.44}Si_2O_6$) particle in the coke analogue and associated EDS elemental maps of the particle.

As mentioned discussed in Chapters 6, 7 and 8, elemental Fe promotes graphitisation (increase sp^2 bonding) and reactivity [4, 7, 10, 25, 26, 29, 30, 32, 33, 38, 40, 41, 43, 45-49, 52, 56, 59, 84, 96, 149-152, 180, 183-187]. In this case, Fe bonded within enstatite ferroan and phlogopite ferroan had no clear discriminating effect on the sp^2–sp^3 bonding, but increased reactivity. The unanswered question would then be “how did Fe bonded within these minerals increase reactivity”?

10.2. How did Fe bonded within a mineral increase reactivity?

An increase in reactivity due to the presence of elemental Fe and Fe bonded within enstatite ferroan ($Mg_{1.56}Fe_{0.44}Si_2O_6$) and phlogopite ferroan [$K(Mg,Fe)_3(Al,Fe)Si_3O_{10}(OH,F)_2$] is broadly consistent with the literature that have reported that Fe and Fe containing minerals increased the reactivity of coke, coal and coke analogue [12, 96, 97, 176, 187, 210].

Attempts were made to understand the effects of Fe bonded within enstatite ferroan ($Mg_{1.56}Fe_{0.44}Si_2O_6$) and phlogopite ferroan [$K(Mg,Fe)_3(Al,Fe)Si_3O_{10}(OH,F)_2$] on the reactivity of the coke analogue by comparing its data with elemental Fe. This was carried out by proportioning the amounts of Fe in the minerals in terms of mass%, mole% and particle surface area. The results indicated that there was no obvious correlation between Fe bonded within these minerals and elemental Fe.

As previously discussed in Chapter 8, elemental/metallic Fe is thought to increase reactivity through dissolution of carbon into Fe (section 8-1), CO_2 gas dissociating on Fe surface (section 8-2), redox reaction involving Fe and CO_2, and iron oxide and carbon (section 8-3), and transfer of electrons from carbon into Fe (section 8-4). Under the reaction conditions of this study, it is difficult to suggest whether these mechanisms (8-1 to 8-4) occurred with Fe bonded within a complex mineral (enstatite ferroan ($Mg_{1.56}Fe_{0.44}Si_2O_6$) and phlogopite ferroan [$K(Mg,Fe)_3(Al,Fe)Si_3O_{10}(OH,F)_2$]).

Using temperature programmed desorption (TPD) Kyotani et al. [210] found that Fe containing minerals in coal char can dissociate CO_2 gas to form CO gas and absorbed oxygen atoms. The TPD method is commonly used to examine the desorption of oxygen containing species on mineral surface [96, 210, 211]. It can be suggested that the formation of these absorbed oxygen atoms, due to the presence of Fe bonded within a mineral, is a possible reason for the increased reactivity.

10.3. Activation energies of the reaction of the coke analogues prepared with elemental Fe, enstatite ferroan and phlogopite ferroan

The plots of ln R_C against 1/T for all the materials tested are given in Appendix VI. The activation energy values for zones I and II, and the temperature at the point of intersection between the zones for base coke analogue, coke analogue–Fe 46µm, coke analogue–enstatite and coke analogue–phlogopite ferroan are given in Table 10-2.

Table 10-2: The activation energy values for base coke analogue, coke analogue–Fe 46µm, coke analogue–enstatite and coke analogue–phlogopite ferroan.

Coke analogues	**Zone I kJ.mol^{-1}**	**Temperature at point of intersection (°C)**	**Zone II kJ.mol^{-1}**
Base	273.6±0.5	~1075	55.9±0.4
Fe 46µm	289.8±0.5	~1050	43.3±0.4
Enstatite ferroan	261.3±0.5	~1035	37.2±0.4
Phlogopite ferroan	237.0±0.5	~1050	34.7±0.4

From Table 10-2 it appears that the zone I activation energy values for the coke analogues are within a close range (though phlogopite ferroan is slightly lower) to the activation energy values of cokes (Table 5-3).

Though there has been an increase in reactivity, likely caused by faster delivery of oxygen to the carbon surface. That is, the presence of Fe bonded within enstatite ferroan ($Mg_{1.56}Fe_{0.44}Si_2O_6$) and phlogopite ferroan [$K(Mg,Fe)_3(Al,Fe)Si_3O_{10}(OH,F)_2$]) increased oxygen delivery to carbon surface relative the base coke analogue. This increase in reactivity is not substantial enough to significantly change the activation energy values.

Summary of main points

- The effect of elemental Fe and Fe containing minerals effect on coke analogue reactivity can be ranked as base < enstatite ferroan ($Mg_{1.56}Fe_{0.44}Si_2O_6$) < phlogopite ferroan [$K(Mg,Fe)_3(Al,Fe)Si_3O_{10}(OH,F)_2$] < Fe 46µm.
- The addition Fe bonded within enstatite ferroan ($Mg_{1.56}Fe_{0.44}Si_2O_6$) and phlogopite ferroan [$K(Mg,Fe)_3(Al,Fe)Si_3O_{10}(OH,F)_2$] to the coke analogue increased reactivity by promoting oxygen delivery to the active carbon sites (C_f).

- Fe bonded within enstatite ferroan ($Mg_{1.56}Fe_{0.44}Si_2O_6$) and phlogopite ferroan [$K(Mg,Fe)_3(Al,Fe)Si_3O_{10}(OH,F)_2$] had no clear discriminating effects on the sp^2 and sp^2–sp^3 carbon bonding of the coke analogue from both "bulk" and "local" Raman measurements.

10.4. Use of analogue data in assessing coke performance in a blast furnace

In this study, the individual effects of minerals (elemental iron, magnetite, enstatite ferroan, phlogopite ferroan and quartz) on analogue reactivity has been evaluated. How can these data be used to predict coke performance in a blast furnace?

Coke performance in a blast furnace is often evaluated using the coke reactivity index (CRI)/coke strength after reaction (CSR) test [3, 21, 179, 188, 221, 224, 225] or equivalent. This test relates coke strength to reactivity. The coke analogue reactivity data will allow fine-tuning of current reactivity–strength models to improve coke performance in use predictions based on the mineralogy of the coke.

11. Conclusions

The use of metallurgical coke in laboratory studies is problematic. It is a complex material (carbonaceous forms, mineral components and pore structure) and displays significant heterogeneity on most metrics used to characterise it. While there have been many significant and important studies into metallurgical coke, its complexity and inherent homogeneity are factors that to some degree limit progress in our understanding of key fundamental issues relating to coke reactivity. To address the complexity and inherent heterogeneity of metallurgical coke an analogue has been developed that has a relatively simple structure and is controllable with respect to porosity, mineral addition and mineral size.

If the analogue is to be of use, it must first be established that it is representative of metallurgical coke in some key respects. This is the primary aim of this thesis. Assessment of the porosity, microstructure, carbon-bonding (sp^2–sp^3), general reaction mechanism in CO_2 and general reactivity behaviour, confirmed that the analogue was representative of metallurgical coke. The primary limitation being that it did not fully represent rank of a coke but something that approximates to a constant low rank material. Full details of the basis of this conclusion are given in points 1 to 7.

The analogue was then used to assess in detail the effects of elemental Fe and Fe added as magnetite (Fe_3O_4) on the carbon bonding and reactivity of the coke analogue. The findings of this assessment are given in points 8 to 10.

To extend the Fe addition work, evaluation of the effects of quartz and iron added as a complex mineral (enstatite ferroan ($Mg_{1.56}Fe_{0.44}Si_2O_6$) and phlogopite ferroan [$K(Mg,Fe)_3(Al,Fe)Si_3O_{10}(OH,F)_2$]) on carbon bonding and analogue reactivity were also studied. These effects were simply evaluated in comparison with Fe addition. The findings of this assessment are given in points 11 to 12.

1. Three different but complementary porosity measurements of the coke analogue were evaluated, these were optical microscopy, mercury porosimetry and neutron radiography (Dingo). It was found that the porosity and pore size distribution of the analogues are well controlled, reproducible and have less scatter than metallurgical coke.

2. The pores in the coke analogues and the metallurgical coke investigated in this study are highly interconnected in 3D and typical of that reported in the coke literature.

3. Optical and electro-optical microscopy revealed that the microstructure of the coke analogues is uniform and well controlled. The microstructure is made up of carbon (graphite grains and carbonised phenolic resin), Fe/minerals and pores. The graphite grains and carbonised phenolic resin of the fired analogue appear similar in character to the reactive maceral derived component (RMDC) type and inert maceral derived component (IMDC) type in metallurgical coke, respectively.

4. The coke analogue has a simpler but similar microstructure to that of metallurgical coke. To a large degree, the nature of the carbon component of the analogue was a constant in the experimental program, that is, the “rank” of the coke analogue was fixed. The mineral phase (size, composition and morphology) in the coke analogue is less complex, homogenous, well controlled and evenly dispersed relative to metallurgical coke.

5. The Raman spectroscopy assessment of the coke analogue established that the $I_{(D)}/I_{(G)}$ and $I_{(V)}/I_{(G)}$ ranges were 0.16–1.55 and 0–0.41 respectively. These values overlap with that found for metallurgical coke.

6. Using a large sample TGA, the reactivity of the coke analogues in CO_2 at temperatures between 900°C and 1350°C was established. In terms of trends with time and the effects of temperature, the kinetics of the reactivity of the coke analogue was in general similar to those of the metallurgical coke. The coke analogue had a greater repeatability than metallurgical coke.

7. Applying the Walker Arrhenius method, two temperature zones corresponding to different kinetic control regimes, chemical reaction controlled (zone I) and mixed controlled (zone II) were identified in the coke analogues. The zone I activation energy for the base coke analogue was comparable to that of metallurgical coke indicating that the reaction mechanism of the coke analogue is typical of metallurgical coke.

8. From Raman measurement of the effects of elemental/metallic Fe on the sp^2 and sp^2–sp^3 carbon bonding of the analogue it was found that the Fe increased the sp^2 graphite bonding character of the analogue. This effect was localised to near the Fe particle-carbon interface. The effects of both Fe added in its elemental form and readily reduced form of Fe_3O_4 on the sp^2–sp^3 bonding were discernible at a distance <5µm from the Fe–coke analogue interface. The localised graphitisation is similar to what is known about iron graphitised metallurgical coke found in the literature.

9. Elemental Fe and Fe added as Fe_3O_4 increased the reactivity of the analogue relative to the base coke analogue. It was thought that elemental Fe and Fe added as Fe_3O_4 increased the number of active carbon sites (C_f) in the coke analogue through carbon dissolution into Fe and the transfer of electrons from carbon into Fe.

10. The effects of Fe added as elemental Fe and Fe_3O_4 on the reactivity of the coke analogue were linearly proportional to the surface area of the Fe particles. There was a linear relationship between R_C and Fe particle surface area. The Fe added as Fe_3O_4 gave a higher reactivity of the coke analogue relative to elemental Fe at a constant concentration and similar total surface area.

11. Quartz (SiO_2) had no clear discriminating effects on the sp^2 and sp^2–sp^3 carbon bonding of the coke analogue from both "bulk" and "local" Raman measurements. The addition of quartz (SiO_2) to the coke analogue decreased its reactivity relative to the base coke analogue.

12. The addition of Fe bonded within a complex mineral (enstatite ferroan ($Mg_{1.56}Fe_{0.44}Si_2O_6$) and phlogopite ferroan [$K(Mg,Fe)_3(Al,Fe)Si_3O_{10}(OH,F)_2$]) had no clear discriminating effects on the sp^2 and sp^2–sp^3 carbon bonding of the coke analogue from both "bulk" and "local" Raman measurements. These Fe containing minerals increased the reactivity of the coke analogue relative to the base coke analogue. In comparison with elemental Fe their effects on coke analogue reactivity can be ranked as base < enstatite ferroan < phlogopite ferroan < Fe 46μm. The Fe containing minerals may have increased analogue reactivity by promoting oxygen delivery to the active carbon sites (C_f). That is, CO_2 gas may dissociate on the Fe containing minerals to increase the reactivity of the coke analogue.

This study has shown that the coke analogue can be used to study critical aspects of metallurgical coke behaviour in the ironmaking blast furnace and by extension other coke related applications. In addition, this investigation extends knowledge in the areas of fundamental understanding the effects of Fe/minerals on the carbon bonding and reactivity of metallurgical coke. Coke performance in a blast furnace is often evaluated using the coke reactivity index (CRI)/coke strength after reaction (CSR) test [3, 21, 179,

188, 221, 224, 225]. This test relates coke strength to reactivity. This new knowledge will allow fine-tuning of current reactivity–strength models to improve coke performance in use predictions.

12. Recommendations for future studies

During this work and on completion, some areas of more work were recognised. These areas are recommended for future study.

1. In addition to minerals investigated in this work, other commonly identified minerals in coke include alumina (Al_2O_3), mullite ($Al_6Si_2O_{13}$), spinel ($MgAl_2O_4$), calcite ($CaCO_3$) and iron sulphides (pyrrhotite ($Fe_{1-x}S$), troilite (FeS) and pyrite (FeS_2)). It is recommended that the Raman characterisation and TGA experimental approaches adopted in the study should be carried out on individual analogue materials prepared with these minerals. It is required to understand their effects on sp^2–sp^3 bonding and by extension on reactivity.

2. The Fe added as magnetite (Fe_3O_4) had a higher effect on reactivity compared to Fe added as elemental Fe, that is, reactivity was higher for reduced Fe from Fe_3O_4 compared to elemental Fe at a constant particle surface area of Fe. It was thought that the Fe added as Fe_3O_4 increased the number of active carbon sites more than the elemental Fe. It is recommended that further studies should be carried out to establish how the reduced Fe from Fe_3O_4 affected the concentration or number of active sites relative to elemental Fe.

3. It was found that reaction rate is directly proportional to the Fe (both elemental Fe and Fe added as Fe_3O_4) particle surface area. It is recommended that more robust studies should be carried out to establish a mathematic relationship between reaction rates and particle surface area of complex coke minerals. This is desirable to predict mineral effects on the reactivity of metallurgical cokes.

4. The Fe bonded within enstatite ferroan ($Mg_{1.56}Fe_{0.44}Si_2O_6$) and phlogopite ferroan [$K(Mg,Fe)_3(Al,Fe)Si_3O_{10}(OH,F)_2$] had no clear discriminating effect on sp^2–sp^3 bonding (bulk and localised Raman measurement), but increased reactivity relative to

the base coke analogue. It was thought that the Fe bonded within an oxide was able to dissociate CO_2 gas to increase reactivity. It is recommended that a temperature programmed desorption measurement should be carried out to test this suggestion. This would help to understand the CO_2 dissociating capability of Fe containing minerals and by extension other coke minerals.

5. The coke analogues prepared with Fe bonded within enstatite ferroan ($Mg_{1.56}Fe_{0.44}Si_2O_6$) and phlogopite ferroan [$K(Mg,Fe)_3(Al,Fe)Si_3O_{10}(OH,F)_2$], and quartz ($SiO_2$) had no significant discriminating effect on sp^2–sp^3 bonding (bulk and localised Raman measurement). It is recommended that these analogues should be produced at a higher temperature that would facilitate a reaction between quartz and coke analogue carbon (to form silicon carbide) and the decomposition of the Fe containing minerals in the coke analogue (to form metallic Fe). It is envisaged that at higher temperatures quartz and Fe containing minerals may affect the sp^2–sp^3 bonding. This would help to understand their effects on coke graphitisation in the high-temperature zone of the ironmaking blast furnace.

6. An attempt was made to use the BET to investigate gas contact area of the coke analogue, but baseline values proved difficult due to the degassing issues associated with the coke analogue. It is recommended that further investigation should be carried out to modify the BET measurement with the aim to eliminate these degassing challenges. This would help to understand gas–solid contact area.

References

[1]. A. K. Biswas, "Principles of Blast Furnace Ironmaking: Theory and Practice", Cootha Publishing House, Brisbane, Australia, (1981).

[2]. P. Loison, P. Foch, A. Boyer, "Coke Quality and Production", Butterworth and Co Press, London, UK, (1989).

[3]. P. Bennett, A. Reifenstein, G. O'Brien, B. Jenkins, "ACARP Project C12057: Coke Reactivity and Characterisation", ACARP Brisbane, Australia, (2008).

[4]. S. Gornostayev, J. Harkki, "Graphite Crystals in Blast Furnace Coke", Carbon, 45, 1145–1151, (2007).

[5]. N. Andriopoulos, C. E. Loo, R. Dukino, McGuire S. J., "Micro–Properties of Australian Coking Coals", ISIJ, 3, 1528–1537, (2003).

[6]. H. Bertling, "Coal and Coke for Blast Furnaces", ISIJ, 38, 617–624, (1999).

[7]. S. Gupta, D. French, R. Sakurovs, M. Grigore, H. Sun, T. Cham, T. Hilding, M. Hallin, B. Lindblom, V. Sahajwalla, "Minerals and Iron–Making Reactions in Blast Furnaces", Progress in Energy Combustion Science, 34, 155–197, (2008).

[8]. M. Diez, R. Alvarez, C. Barrocanal, "Coal For Metallurgical Coke Production: Predictions of Coke Quality and Future Requirements For Coke Making", International Journal of Coal Geology, 50, 389–412, (2002).

[9]. W. P. Hutny, G. K. Lee, J. T. Price, "Fundamentals of Coal Combustion During Injection into a Blast Furnace", Progress in energy and combustion science, 17, 373–395, (1991).

[10]. K. Li, R. Khanna, J. Zhang, Z. Liu, V. Sahajwalla, T. Yang, D. Kong, "The Evolution of Structural Order, Microstructure and Mineral Matter of Metallurgical Coke in a Blast Furnace: A Review", Fuel, 133, 194–215, (2014).

[11]. R. J. Longbottom, B. J. Monaghan, A. A. Chowdhury, M. H. Reid, G. Zhang, M. R. Mahoney, K. Hockings, "Effect of Mineral Matter on the Reactivity of Coke and Its Replication in a Coke Analogue", ISIJ, 56, 1553–1558, (2016).

[12]. M. H. Reid, M. R. Mahoney, B. J. Monaghan, "A Coke Analogue for the Study of the Effects of Minerals on Coke Reactivity", ISIJ, 54, 628–633, (2014).

[13]. R. J. Longbottom, B. J. Monaghan, G. Zhang, A. A. Chowdhury, M. R. Mahoney, K. Hockings, M. Reid, "The Effect of Binary and Ternary Mineral Combinations on the Reactivity of a Coke Analogue", 7th European Coke and Ironmaking Congree – ECIC Linz, Austria, 334–353, (2016).

[14]. R. J. Longbottom, B. J. Monaghan, M. W. Chapman, S. A. Nightingale, J. G. Mathieson, R. J. Nightingale, "Techniques in the study of carbon transfer in Ironmaking", Steel Research International, 82, 505–511, (2011).

[15]. A. S. Jayasekara, B. J. Monaghan, R. J. Longbottom, "The Kinetics of Reaction of a Coke Analogue in CO_2 Gas", Fuel, 154, 45 - 51, (2015).

[16]. R. J. Longbottom, B. J. Monaghan, A. A. Chowdhury, M. R. Mahoney, M. H. Reid, G. Zhang, K. Hockings, "The Effect of Combinations of Iron-Bearing Minerals and Quartz on Coke Reactivity", Ironmaking and Steelmaking, (2017).

[17]. M. Kawakami, T. Karato, T. Takenaka, S. Yokoyama, "Structure Analysis of Coke, Wood Charcoal and Bamboo Charcoal by Raman Spectroscopy and Their Reaction Rate with CO_2", ISIJ, 45, 1027–1034, (2005).

[18]. M. Kawakami, H. Kanba, K. Sato, T. Takenaka, S. Gupta, R. Chandratilleke, V. Sahajwalla, "Characterisation of Thermal Annealing Effects on the Evolution of Coke Structure Using Raman Spectroscopy and X-Ray Diffraction", ISIJ, 46, 1165–1170, (2006).

[19]. S. V. Vassilev, C. G. Vassileva, "Occurence, Abundance and Origin of Minerals in Coals and Coal Ashes", Fuel Processing Technology, 48, 85–106, (1996).
[20]. S. Gornostayev, O. Kerkkonen, J. Harkki, "Occurrence and Composition of Some Mineral Phases in Tuyere Coke", ISIJ, 45, 1–7, (2005).
[21]. J. Haapakangas, H. Suopajarvi, M. Iljana, A. Kemppainen, O. Mattila, E. Heikkinen, C. Samuelsson, T. Fabritius, "Coke Reactivity in Simulated Blast Furnace Shaft Conditions", Metallurgical and Materials Transaction B, 47B, 2357–2370, (2016).
[22]. M. W. Chapman, B. J. Monaghan, S. A. Nightingale, J. G. Mathieson, R. J. Nightingale, "Observations of the Mineral Matter Material Present at the Coke/Iron Interface During Coke Dissolution into Iron", ISIJ, 47, 973–981, (2007).
[23]. V. Croft,"In Situ Reduction of Blast Furnace Coke Ash", Ironmaking and Steelmaking, 116–122, (1980).
[24]. M. W. Chapman, "Insoluble Oxide Product Formation and its Effect on Coke Dissolution in Liquid Iron", University of Wollongong, (2009).
[25]. D. French, R. Sakurovs, M. Grigore, "ACARP Project C14074: Mineral Matter Reactions in Cokes", ACARP Brisbane, (2009).
[26]. W. Wang, K. M. Thomas, R. M. Poultney, R. R. Willmers, "Iron Catalysed Graphitisation in the Blast Furnace", Carbon, 33, 1525–1535, (1995).
[27]. B. Kim, S. Gupta, D. French, R. Sakurovs, V. Sahajwalla, "Effect of Thermal Treatment on Coke Reactivity and Catalytic Iron Mineralogy", Energy and Fuels, 23, 3694–3702, (2009).
[28]. V. Sahajwalla, S. Gupta, H. Sun, M. grigore, T. Cham, K. Kazuberns, B. Kim, N. Saha-Chaudhury, R. Sakurovs, D. French, "RR 85– Coke Quality and Performance Measures for Currents and Future BF Operations", CRC Pullenvale, Australia (2008).
[29]. E. T. Turkdogan, J. V. Vinters, "Catalytic Oxidation of Carbon", Carbon, 10, 97–111, (1972).
[30]. A. Oya, S. Otani, "Catalytic Graphitisation of Carbons by Various Metals", Carbon, 17, 131–137, (1979).
[31]. S. R. Dhakate, R. B. Mathur, O. P. Bahl, "Catalytic Effect of Iron Oxide on Carbon/Carbon Composites During Graphitization", Carbon, 35, 1753–1756, (1997).
[32]. A. S. Schwartz, J. C. Bokros, "Catalytic Graphitisation of Carbon by Titanium", Carbon, 5, 325–330, (1967).
[33]. H. Marsh, A. P. Warbutton, "Catalytic Graphitization of Carbon using Titanium and Zirconium", Carbon, 14, 47–52, (1976).
[34]. I. Mochida, R. Ohtsubo, K. Takeshita, H. Marsh, "Catalytic Graphitization of Non-graphitizable Carbon by Chromium and Manganese Oxides", Carbon, 18, 117–123, (1980).
[35]. M. Zhao, H. Song, "Catalytic Graphitisation of Phenolic Resin", Journal of Material Science and Technology, 27, 266–270, (2011).
[36]. H. N. Murty, D. L. Biedermann, E. A. Heintz, "Catalytic Graphitization of Model Compound Chars by Aluminium and Beryllium", Carbon, 11, 163–169, (1973).
[37]. M. Sevilla, A. B. Fuertes, "Catalytic Graphitization of Templated Mesoporous Carbons", Carbon, 44, 468–474, (2006).

[38]. W. Weisweiler, N. Subramanian, B. Terwiesh, "Catalytic Influence of Metal Melts on the Graphitisation of Monolithic Glass Like Carbon", Carbon, 9, 755–761, (1971).
[39]. H. Marsh, A. P. Warbutton, "Catalysis of Graphitisation", Journal of Applied Chemistry, 20, 133–142, (1970).
[40]. A. Oya, H. Marsh, "Phenomena of Catalytic Graphitization", Journal of Materials Science, 17, 309–322, (1982).
[41]. E. Fitzer, B. Kegel, "The Reaction of Vanadium Carbide Melt with Ordered and Disordered Carbon", Carbon, 6, 433–436, (1968).
[42]. A. Oya, S. Otani, "Influences of Particle Size of Metal on Catalytic Graphitisation of Non-graphitic Carbon", Carbon, 19, 391, (1981).
[43]. A. Oberlin, "Carbonisation and Graphitisation", Carbon, 22, 521–541, (1984).
[44]. H. Marsh, "Introduction to Carbon Science", Butterworth and Co., London, UK, (1989).
[45]. A. Oya, T. Fukatsu, S. Otani, H. Marsh, "Catalytic Graphitization of Cokes by Indigeneous Mineral Matter", Fuel, 60, 502–507 (1983).
[46]. D. Gonzalez, A. M. Montes-Moran, A. B. Gracia, "Influence of Inherent Coal Mineral Matter on the Structural Characteristics of Graphite Materials Prepared from Anthracites", Energy and Fuels, 19, 263–269, (2005).
[47]. P. J. Pappano, H. H. Schobert, "Effect of Natural Mineral Inclusions on the Graphitizability of a Pennyslvania Anthracite", Energy and Fuels, 23, 422–428, (2009).
[48]. J. Wang, K. Morishita, T. Takarada, "High-Temperature Interactions between Coal Char and Mixtures of Calcium Oxide, Quartz and Kaolinite", Energy and Fuels, 15, 1145–1152, (2001).
[49]. E. L. Evans, J. L. Jenkins, J. M. Thomas, "Direct Electron Microscopic Studies of Graphitic Regions in Heat-Treated Coals and Coal Extracts", Carbon, 10, 637–642, (1972).
[50]. M. Inagaki, "Graphitization and Sintering of Coals under Pressure", Carbon, 58, 741–744, (1979).
[51]. A. Onodera, Y. Irie, K. Higashi, "Graphitization of Amorphous Carbon at High Pressures to 15GPa", Journal of Applied Physics, 64, 2611–2617, (1991).
[52]. S. M. Irving, P. L. Walker Jr, "Interaction of Evaporated Carbon with Heated Metal Substrates", Carbon, 5, 399–402 (1967).
[53]. R. J. Longbottom, B. J. Monaghan, O. Scholes, M. R. Mahoney, "Development of a Metallurgical Coke Analogue to Investigate the Effects of Coke Mineralogy on Coke Reactivity", Scanmet IV, 4th International conference on process Development in Iron and Steelmaking, Lulea, Sweden, 147–156, (2012).
[54]. A. Jayasekara, B. J. Monaghan, R. J. Longbottom, "Dispersion of Lime in Coke Analogue and Its Effect on Gasification in CO_2", Fuel, 182, 73–79, (2016).
[55]. R. J. Longbottom, A. S. Jayasekara, B. J. Monaghan, "The Kinetics of the Reactivity of a Coke Analogue with Carbon Dioxide", 5th Australia-China-Japan Joint Symposium, Senda, Japan, (2014).
[56]. M. Grigore, R. Sakurovs, D. French, V. Sahajwalla, "Influence of Mineral Matter on Coke Reactivity with Carbon Dioxide", ISIJ, 46, 503–512, (2006).
[57]. R. Sakurovs, D. French, M. Grigore, "Quantification of Mineral Matter in Commercial Cokes and Their Parent Coals", International Journal of Coal Geology, 72, 81–88, (2007).

[58]. R. J. Longbottom, B. J. Monaghan, "ACARP Project C23049: A Coke Analogue to Examine the Effect of Mineralogy on Coke Reactivity", ACARP Brisbane, Australia, (2015).
[59]. G. Quinn, B. Faraj, R. Callcott, T. Callott, "ACARP Project C10054 Report: Elucidation of the Effects of Minerals on Coke Behaviour in the Blast Furnace", ACARP Brisbane, Australia, (2002).
[60]. M. Grigore, "Factors Influencing Coke Gasification with Carbon Dioxide", PhD Thesis, University of New South Wales, Australia, (2007).
[61]. H. L. George, "Liquid Flow Through a Reactive Packed Bed", PhD Thesis, University of Wollongong, Australia, (2013).
[62]. L. Smedowski, M. Krzesinska, W. Kwasny, M. Kozanecki, "Development of Ordered Structures in the High-Temperature (HT) Cokes from Binary and Ternary Coal Blends Studied by means of X-Ray Diffraction and Raman Spectroscopy", American Chemical Society, 25, 3142–3149, (2011).
[63]. E. T. Turkdogan, "Fundamentals of Steelmaking", Institute of Materials, London, UK, (1996).
[64]. D. R. Gaskell, "Introduction to the Thermodynamics of Materials", ed. 5th, Florida, US, (2008).
[65]. E. T. Turkdogan, "Physical Chemistry of High Temperature Technology", Academic Press, London, UK, (1980).
[66]. S. Gornostayev, J. Harkki, O. Kerkkonen, M. J. Fabritius, "Carbon Sphere in Metallurgical Coke", Carbon, 48, 4197–4214, (2010).
[67]. M. Grigore, R. Sakurovs, D. French, V. Sahajwalla, "Effect of Carbonisation Conditions on Mineral Matter in Coke", ISIJ, 47, 62–66, (2007).
[68]. S. Rodrigues, M. Marques, C. R. Ward, I. Suarez-Ruiz, D. Flores, "Mineral Transformations During High Temperature Treatment of Antracite",International Journal of Coal Geology, 94, 191–200, (2012).
[69]. X. Xing, H. Rogers, G. Zhang, K. Hockings, P. Zulli, O. Ostrovski, "Coke Degradation Under Simulated Blast Furnace Conditions", ISIJ, 56, 786–793, (2016).
[70]. T. Hilding, S. Gupta, V. Sahajwalla, B. Bjorkman, J. Wikstrom, "Degradation Behaviour of a High CSR Coke in an Experimental Blast Furnace: Effect of Structure and Alkali Reactions", ISIJ, 45, 1041–1050, (2005).
[71]. K. R. Horrocks, R. B. Cunningham, J. F. Ellison, R. J. Nightingale, "Coke Quality at BHP Steel Port Kembla", 4th European Coke and Ironmaking Congress, Paris, 1, 167–173, (2000).
[72]. D. C. Leonard, L. Bonte, A. Dufour, A. Ferstl, K. Raipala, P. Scmole, P. Schoone, J. L. Verduras, R. R. Willmers, "Coke Quality Requirements of European Blast Furnace Engineers (Joint EBFC-Paper)" in Proc. 3rd European Cokemaking Cong., CRM-VDEh, Gent, Belgium, 1–10, (1996).
[73]. K. H. Großpietsch, H. B. Lungen, G. Dauwels, A. Ferstl, T. Karjalahti, P. Negro, B. Velden, R. Willmers, "Coke Quality Requirements by European Blast Furnace Operators on the Turn of the Millennium", 4th European Coke and Ironmaking Congress, Paris, France, 2–11, (2000).
[74]. J. J. Poveromo, "Operarional Considerations for High-Level Blast Furnace Fuel Injection, in Proc 55th Ironmaking Conference ISSAIME", Pennsylvania, US, 79–92 (1996).
[75]. E. M. O'Donnell, J. J. Poveromo, "Coke Quality Requirements from a North American Perspective", 4th European Coke and Ironmaking Congress, Paris, France, 12–19, (2000).

[76]. D. A. Aderibigbe, J. Szekely, "Studies in Coke Reactivity: Part 2 Mathematical Model of Reaction with Allowance for Pore Diffusion and Experimental Verification", Ironmaking and Steelmaking, 1, 32–42, (1982).
[77]. D. A. Aderibigbe, J. Szekely, "Studies in Coke Reactivity: Part 1-Reaction of Conventionally Produced Coke with $CO–CO_2$ Mixtures over Temperature Range 850°C–1000°C", Ironmaking and Steelmaking, 1, 11–19, (1981).
[78]. S. Gornostayev, J. Harkki, "Spinel Crystal in Tuyere Coke", Metallurgical and Materials Transaction B, 36B, 303–305, (2005).
[79]. S. Gornostayev, J. Harkki, "Mechanism of Physical Transformation of Mineral Matter in The Blast Furnace Coke with Reference to Its Reactivity and Strength", Energy and Fuels, 20, 2632–2635, (2006).
[80]. S. Gornostayev, J. Harkki, O. Kerkkonen, "Transformations of Pyrite During Formation of Metallurgical Coke", Fuel, 88, 2032–2036, (2009).
[81]. M. Grigore, R. Sakurovs, D. French, V. Sahajwalla, "Mineral Reactions During Coke Gasification with Carbon dioxide", International Journal of Coal Geology, 75, 213–224, (2008).
[82]. K. Li, J. Zhang, M. Barati, R. Khanna, Z. Liu, J. Zhong, X. Ning, S. Ren, T. Yang, V. Sahajwalla, "Influence of Alkaline (Na, K) Vapors on Carbon and Mineral Behaviour in Blast Furnace Cokes", Fuel, 145, 202–213, (2015).
[83]. S. Gupta, M. Dubikova, D. French, V. Sahajwalla, "Characterization of the Origin and Distribution of the Minerals and Phases in Metallurgical Cokes", Energy and Fuels, 21, 303-313, (2007).
[84]. K. Li, J. Zhang, Y. Liu, M. Barati, Liu, Z., J. Zhong, B. Su, M. Wei, G. Wang, T. Yang, "Graphitization of Coke and Its Interaction with Slag in the Hearth of a Blast Furnace", Metallurgical and Materials Transactions B, 47B, 811–818, (2016).
[85]. K. Li, J. Zhang, Z. Liu, M. Barati, J. Zhong, M. Wei, G. Wang, K. Jiao, T. Yang, "Interfaces Between Coke Slag and Metal in the Tuyere Level of a Blast Furnace", Metallurgical and Materials Transactions B, 46B, 1104–1111, (2015).
[86]. G. L. Lecomte, J. P. Bonnet, P. Blanchart, "A Study of the Influence of Muscovite on the Thermal Transformations of Kaolinite from Room Temperature to 1100°C", Journal of Materials Science, 42, 8745–8752, (2007).
[87]. S. Gornostayev, J. Harkki, "Mineral Matter Crystallization and Crack Formation in Tuyere Coke", Fuel 85, 1047–1051, (2006).
[88]. G. P. Huffman, F. E. Huggins, A. A. Levasseur, O. Chow, S. Srinivasachar, A. K. Mehta, "Investigation of the Transformation of Pyrite in a Drop–Tube Furnace", Fuel, 68, 485–490, (1989).
[89]. S. Gornostayev, O. Kerkkonen, J. Harkki, "Importance of Mineralogical Data for Influencing Properties of Coke: A Reference on SiO_2 Polymorphs", Steel Research International, 77, 770–773, (2006).
[90]. Z. Ma, J. Bai, W. Li, Z. Bai, L. Kong, "Mineral Transformation in Char and Its Effect on Coal Char Gasification Reactivity at High Temperatures, Part 1: Mineral Transformation in Char", Energy and Fuels, 27, 4545−4554, (2013).
[91]. J. Wang, R. Ishida, T. Takarada, "Carbothernal Reactions of Quartz and Kaolinite with Coal Char", Energy and Fuels, 14, 1108–1114, (2000).
[92]. W. A. Deer, R. A. Howie, J. Zussman, "Rock-Forming Minerals: Framework Silicates", Longmans, Great Britain, (1965).
[93]. D. R. Lide, "CRC HandBook of Chemistry and Physics", CRC Press, Florida, US, (2003).

[94]. W. A. Bassett, D. M. Lapham, "A Thermal Increment Diffractometer",The American Mineralogist, 42, 548–555, (1957).
[95]. F. M. Wahl, R. E. Grim, R. B. Graf, "Phase Transformations in Silica as Examined By Continuous X-Ray Diffraction", The American Mineralogist, 46, 196–208, (1961).
[96]. H. Ohme, T. Suzuki, "Mechanisms of CO_2 Gasification of Carbon Catalyzed with Group VIII Metals. 1. Iron–Catalyzed CO_2 Gasification", Energy and Fuels, 10, 980–987, (1996).
[97]. E. Furimsky, P. Sears, T. Suzuki, "Iron–Catalyzed Gasification of Char in CO_2", Energy and Fuels, 2, 634–639, (1988).
[98]. S. Gupta, M. Dubikova, D. French, V. Sahajwalla, "Effect of CO_2 Gasification on the Transformations of Coke Minerals at High Temperatures", Energy and Fuels, 21, 1052–1061, (2007).
[99]. R. H. Davies, A. T. Dinsdale, J. A. Gisby, J. A. Robinson, S. M. Martin, "MTDATA–Thermodynamic and Phase Equilibrium Software from the National Physical Laboratory", Calphad, 26, 229–271, (2002).
[100]. C. W. Bale, P. Chartrand, S. A. Degterov, G. Erikssion, R. Hack, B. Mahfoud, J. Melancon, A. D. Pelton, S. Petersen, "FactSage Thermodynamic Software and Databases", Calphad, 26, 189–228, (2002).
[101]. C. D. Coin, "Coke Microtextural Description: Comparison of Nomenclature, Classification and Methods", Fuel, 66, 702–705, (1987).
[102]. R. J. Gray, K. F. Devanney, "Coke Carbon Form: Microscopic Classification and Industrial Applications", International Journal of Coal Geology, 6, 277–297, (1986).
[103]. L. G. Benedict, R. R. Thompson, "Coke/Carbon Reactions in the Study of Factors Affecting Coke Quality", International Journal of Coal Geology, 1, 19–34, (1980).
[104]. M. J. Shevlin, J. R. Fryer, T. Baird, "Microstructural Analysis of Metallurgical Cokes and Intercalated Species", Carbon, 24, 527–534, (1986).
[105]. D. Vogt, J. V. Weber, J. N. Rouzaud, M. Schneider, "Coke Proprieties and Their Microstructure: Part II Coke Carboxy Reactivity Relations to Their Texture", Fuel Processing Technology, 20, 155–162, (1988).
[106]. T. S. Cham, H. Sun, R. Sakurovs, V. Sahajwalla, "CCSD Technical Note 28: Coke Reactivity with Metal in Blast Furnace", CRC Queensland, Australia, (2007).
[107]. K. Koba, K. Sakata, S. Ida, "Gasification Studies of Cokes from Coals. The Effects of Carbonization Pressure on Optical Texture and Porosity", Fuel, 60, 499–506, (1981).
[108]. S. Pusz, M. Krzesinska, L. Smedowski, J. Majewska, B. Pilawa, B. Kwiecinska, "Changes in a Coke Structure Due to Reaction with Carbon Dioxide", Journal of Coal Geology, 81, 287–292, (2009).
[109]. C. Barriocanal, S. Hanson, J. W. Patrick, A. Walker, "The Characterization of Interfaces Between Textural Components in Metallurgical Cokes", Fuel, 73, 1842–1847 (1994).
[110]. B. Duval, J. M. Guet, J. R. Richard, J. N. Rouzaud, "Coke Properties and Their Microtexture. Part III: First Results About Relationship Between Microtexture and Reactivity of Some Cokes", Fuel Processing Technology, 20, 163–175, (1988).

[111]. M. Grigore, R. Sakurovs, D. French, V. Sahajwalla, "Properties and CO_2 Reactivity of the Inert and Reactive Maceral-Derived Components in Cokes", International Journal of Coal Geology, 98, 1–9, (2012).
[112]. K. Koba, S. Ida, "Gasification Reactivities of Metallurgical Cokes with Carbon Dioxide, Steam and Their Mixtures", Fuel, 59, 59–63, (1980).
[113]. A. Moreland, J. W. Patrick, A. Walker, "Optical Anistropy in Cokes from High-Rank Coals", Fuel, 67, 730–732, (1988).
[114]. P. D. Green, C. A. Johnson, M. K. Thomas, "Applications of Laser Raman Microprobe Spectroscopy to the Characterisation of Coals and Cokes", Fuel, 62, 1013–1023, (1983).
[115]. S. Dong, P. Alvarez, N. Paterson, D. R. Dugwell, R. Kandiyoti, "Study on The Effect of Heat Treatment and Gasification on The Carbon Structure of Coal Chars and Metallurgical Cokes Using Fourier Transform Raman Spectroscopy", Energy and Fuels, 23, 1651–1661, (2009).
[116]. S. Dong, N. Paterson, S. G. Karazian, D. R. Dugwell, R. Kandiyoti, "Characterisation of Tuyere-Level Core-Drill Samples from Blast Furnace Operation", Energy and Fuels, 21, 3446–3454, (2007).
[117]. G. Rantitsh, A. Bhattacharyya, J. Schenk, N. K. Lunsdorf, "Assessing the Quality of Metallurgical Coke by Raman Spectroscopy", International Journal of Coal Geology, 130, 1–7, (2014).
[118]. H. Marsh, "Structure in Carbons", J. L. Figueiredo, J. A. Moulijn, Eds., Carbon and Coal Gasification Martinus Nijhoff Publishers, Netherlands, (1986).
[119]. B. J. Monaghan, R. Nightingale, V. Daly, E. Fitzpatrick, "Determination of the Thermal Histories of Coke in a Blast Furnace Through X-Ray Analysis",Ironmaking and Steelmaking, 35, 38–42, (2008).
[120]. S. Pusz, B. Kwiecinska, A. Koszorek, M. Krzesinska, B. Pilawa, "Relationships Between the Optical Reflectance of Coal Blends and the Microscopic Characteristics of their Cokes", International Journal of Coal Geology, 77, 356–362, (2009).
[121]. H. Marsh, F. Rodriguez-Reinoso, "Activated Carbon", Elsevier, Oxford, UK, ed. 1st, (2006).
[122]. X. Xing, G. Zhang, H. Rogers, P. Zulli, O. Ostrovski, "Effects of Annealing on Microstructure and Microstrength of Metallurgical Coke", Metallurgical and Materials Transactions B, 45B, 106–112, (2014).
[123]. F. Tuinstra, J. L. Koenig, "Raman Spectrum of Graphite", Journal of Chemical Physics, 53, 1126–1130, (1970).
[124]. M. R. Ammar, J. N. Rouzaud, "How to Obtain a Reliable Structural Characterization by Raman Microspectroscopy", Journal of Raman Spectroscopy, 43, 207–211, (2010).
[125]. R. Vidano, D. B. Fischbachi, "New Lines in the Raman Spectra of Carbon and Graphite", Journal of America Ceramic Society, 61, 13–17, (1978).
[126]. A. C. Ferrar, J. Robertson, "Interpretation of Raman Spectra of Disordered and Amorphous Carbon", Physical Review B, 61, 14095–14106, (2000).
[127]. J. Schwan, V. Ulrich, V. Batori, H. Ehrhardt, "Raman Spectroscopy on Amorphous Carbon Films", Journal of Applied Physics, 80, 440–447, (1996).
[128]. X. Li, J. Hayashi, C. Li, "FT-Raman Spectroscopic Study of the Evolution of Char Structure During the Pyrolysis of a Victorian Brown Coal", Fuel, 85, 1700–1707, (2006).
[129]. X. Li, J. Hayashi, C. Li, "Volatilisation and Catalytic Effects of Alkali and Alkaline Earth Metallic Species During the Pyrolysis and Gasification of

Victorian Brown Coal. Part VII. Raman Spectroscopic Study on the Changes in Char Structure During the Catalytic Gasification in Air", Fuel, 1509–1517, (2006).
[130]. H. Hiura, T. W. Ebbesen, J. Fujita, K. Tanigaki, T. Takada, "Role of sp^3 Defect Structure in Graphite and Carbon Nanotubes", Nature, 367, 148–151, (1994).
[131]. O. Beyssac, B. Goffee, C. Chopin, J. N. Rouzaud, "Raman Spectra of Carbonaceous Material in Metasediments: A New Geothermometer", Journal of Metamorphic Geology, 20, 859–871, (2002).
[132]. Z. Ni, Y. Wang, T. Yu, Z. Shen, "Raman Spectrscopy and Imaging of Graphene", Nano Research, 1, 273–291, (2008).
[133]. K. Ohno, A. Babich, J. Mitsue, T. Maeda, D. Senk, H. W. Gudenau, M. Shimizu, "Effects of Charcoal Carbon Crystallinity and Ash Content on Carbon Dissolution in Molten Iron and Carburization Reaction in Iron–Charcoal Composite", ISIJ, 52, 1482–1488, (2012).
[134]. A. Guedes, B. Valentim, A. C. Prieto, S. Rodrigues, F. Noronha, "Micro-Raman Spectroscopy of Collotelinite, Fusinite and Macrinite", International Journal of Coal Geology, 83, 415–422, (2010).
[135]. E. V. Ulyanova, A. N. Molchanov, I. Y. Prokhorov, V. G. Grinyov, "Fine Structure of Raman Spectra in Coals of Different Rank", International Journal of Coal Geology, 121, 37–43, (2014).
[136]. S. Reich, C. Thomsen, "Raman Spectroscopy of Graphite", Philosophical Transactions of The Royal Society A, 2271–2288, (2004).
[137]. A. Cuesta, P. Dhamelincourt, J. Laureyns, A. Martinez-Alonzo, J. M. Tascon, "Raman Microscope Studies on Carbon Materials", Carbon, 32, 1523–1532, (1994).
[138]. B. Kwiecinska, I. Suárez-Ruiz, C. Paluszkiewicz, S. Rodriques, "Raman Spectroscopy of Selected Carbonaceous Samples" International Journal of Coal Geology, 84, 206–212, (2010).
[139]. L. Lu, V. Sahajwalla, C. Kong, D. Harris, "Quantitative X–Ray Diffraction Analysis and Its Application to Various Coals", Carbon, 39, 1821–1833, (2001).
[140]. Q. Lin, J. M. Guet, "Characterization of Coals and Macerals by X-Ray Diffraction", Fuel, 69, (1990).
[141]. S. Gupta, V. Sahajwalla, J. Burgo, P. Chaubal, P. Youman, "Carbon Structure of Coke at High Temperatures and Its Influence on Coke Fines in Blast Furnace Dust", Metallurgical and Materials Transactions B, 36B, 385–394, (2005).
[142]. Y. Hishiyama, M. Nakamura, "X–ray Diffraction in Oriented Carbon Films with Turbostratic Structure", Carbon, 33, 1399–1403, (1995).
[143]. A. L. Patterson, "The Scherrer Formula for X–Ray Particle Size Determination", Physical Review 56, 978–982, (1939).
[144]. N. Grobert, T. Seeger, G. Seifert, M. Ruhle, "Processing, Characterisation and Theory of Carbon Nanotubes Containing SiO_X–Based Composite", Journal of Ceramic Processing Research, 4, 1–5, (2003).
[145]. J. Goma, M. Oberlin, "Graphitisation of Thin Carbon Films", Thin Solid Films, 65, 221–232, (1980).
[146]. K. C. Chan, K. M. Thomas, H. Marsh, "The Intercalations of Carbons with Potassium", Carbon, 31, 1071–1082, (1993).
[147]. Gornostayev S. S., E. Heikkinen, J. J. Heino, S. M. M. Huttunen, M. J. Fabritius, "Behaviour of Alkali-Bearing Minerals in Coking and Blast Furnace", Steel Research International, 87, 1144–1153, (2016).

[148]. R. E. Franklin, "Crystallite Growth in Graphitizing and Non-Graphitizing Carbon", Proc. R. Soc. (London) A, A209, 196–218, (1951).
[149]. S. B. Austerman, S. M. Myron, J. W. Wagner, "Growth and Characterisation of Graphite Single Crystals", Carbon, 5, 549–557, (1967).
[150]. A. Oberlin, F. Rousseaux, J. P. PRouchy, "Microscopy and Electron Diffraction of Partial Graphitisation of Hard Carbons Promotor Effect", J. De Chimie Physique Et De Physico-Chimie Biologique, 160, (1969).
[151]. A. Oberlin, J. P. Rouchy, "Transformation Des Carbones Non Graphitables Par Traitment Thermique En Presence De Fer", Carbon, 9, 39, (1971).
[152]. W. L. Holstein, R. D. Moorhead, H. Poppa, M. Boudart, "The Palladium Catalyzed Conversion of Amorphous to Graphitic Carbon", P. Thrower, Ed. Marcel Dekker, New York, 18, 139-171, (1982).
[153]. A. Rist, J. Chipman, "Activity of Carbon in Liquid Iron–Carbon Solutions (ASTIA Report AD94193)", Armed Services Technical Information Agency, (1956).
[154]. R. P. Smith, "Equilibrium of Iron–Carbon Alloys with Mixtures of $CO–CO_2$ and $CH_4–H_2$", Journal of the American Chemical Society, 68, 1163–1175, (1946).
[155]. D. R. Poirier, G. H. Geiger, "Transport Phenomena in Materials Processing", The Minerals, Metals and Materials Society, Pennysylvania, US, (1994).
[156]. W. D. Callister, "Materials Science and Engineering: An Introduction", John Wiley and Sons Inc, Utah, US, ed. 5th, (2003).
[157]. M. Grigore, R. Sakurovs, D. French, V. Sahajwalla, "Mineral Matter in Coals and Their Reactions During Coking", International Journal of Coal Geology, 76, 301–308, (2008).
[158]. C. R. Ward, "Analysis and Significance of Mineral Matter in Coal Seams", International Journal of Coal Geology, 1–4, 135–168, (2002).
[159. F. Moore, A. Esmaeili, "Mineralogy and Geochemistry of the Coals from the Karmozd and Kiasar Coal Mines, Mazandaran Province, Iran", International Journal of Coal Geology, 96-97, 9–21, (2012).
[160]. M. G. Yossifova, "Petrography, Mineralogy and Geochemistry of Balkan Coals and Their Waste Products", International Journal of Coal Geology, 122, 1–20, (2014).
[161]. K. S. Sing, D. H. Everett, R. A. Haul, L. Moscow, R. A. Pierotti, J. Rouquerol, T. Siemieniewska, "Reporting Physisorption Data for Gas/Solid Systems with Special Reference to the Determination of Surface Area and Porosity", Pure and Applied Chemistry, 57, 603, (1985).
[162]. K. S. W. Sing, "The Use of Physisorption for the Characterization of Microporous Carbons", Carbon, 27, 5–11, (1989).
[163]. E. T. Turkdogan, R. G. Olsson, J. V. Vinters, "Pore Characteristics of Carbons", Carbon, 8, 545–564, (1970).
[164]. K. M. Steel, R. E. Dawson, D. R. Jenkins, R. Pearce, M. R. Mahoney, "Use of Rheometry and Micro-CT Analysis to Understand Pore Structure Development in Coke", Fuel Processing Technology, 155, 106–113, (2017).
[165]. J. W. Patrick, A. Walker, "Macroporosity in Cokes: Its Significance, Measurement and Control", Carbon, 27, 117–123, (1989).
[166]. K. Nishioka, S. Yoshida, "Strength Estimation of Coke as Porous Material", Transactions ISIJ, 23, 475–481, (1983).
[167]. X. Xing, G. Zhang, M. DellAmico, G. Ciezki, Q. Meng, O. Ostrovski, "Effect of Annealing on Properties of Carbonaceous Materials. Part II Porosity and Pore Geometry",Metallurgical and Materials Transactions B, 44B, 862–868, (2013).

[168]. O. Kerkkonen, E. Mattila, R. Heiniemi, The Correlation Between Reactivity and Ash Mineralogy of Coke "in 55th Ironmaking conference proceedings". Iron and Steel Society Ironmaking Division, Pennyslvania, US, 275 - 281. (1996).
[169]. H. Giesche, "Mercury Porosimetry: A General (Practical) Overview", Particle and Particle Systems Characterization, 23,1–11, (2006).
[170]. L. C. Drake, "Pore-Size Distribution in Porous Materials", Industrial and Engineering Chemistry, 41, 780–785, (1949).
[171]. D. R. Jenkins, M. R. Mahoney, R. Roest, H. Lomas, R. Pearce, R. Li, S. Mayo, D. Wang, "Micro-CT Analysis of Coke and Its Relationship to Coke Quality Indicators", 7th International Congress on the Science and Technology of Ironmaking, Cleveland, US, (2015).
[172]. M. Mahoney, R. Roest, H. Lomas, R. Fetscher, D. R. Jenkins, R. Pearce, S. Mayo, "Examination of Coke Formation Through Microsctructure of Sole–Heated Oven Tests", METEC and 2nd ESTAD Dusseldorf, Germany, 1–8, (2015).
[173]. S. Lowell, J. E. Shields, M. A. Thomas, M. Thommes, "Characterization of Porous Solids and Powders: Surface Area, Pore Size and Density", Kluwer Academic Publishers, Netherlands, ed. 1, (2004).
[174]. S. J. Ergun, "Kinetics of The Reaction of Carbon Dioxide with Carbon",Journal of Physical Chemistry, 60, 480–485, (1956).
[175]. J. Szekely, J. W. Evans, H. Y. Sohn, "Gas–Solid Reactions", Academic Press, (1976).
[176]. N. M. Laurendeau, "Heterogeneous Kinetics of Coal Char Gasification and Combustion", Progress in Energy and Combustion Science, 4, 221–270, (1978).
[177]. J. Gadsby, J. F. Long, P. Sleightholm, K. W. Sykes, "The Mechanism of the Carbon Dioxide–Carbon Reaction", Proceedings of the Royal Society A, 193, 357–376, (1948).
[178]. H. Freund, "Gasification of Carbon by CO_2 : A Transient Kinetic Experiment", Fuel, 65, 63–66, (1986).
[179]. J. A. Menendez, R. Alvarez, J. J. Pis, "Determination of Metallurgical Coke Reactivity at INCAR: NSC and ECE-INCAR Reactivity Tests", Ironmaking and Steelmaking, 2, 117–121, (1999).
[180]. P. L. Walker, E. J. Hippo, "Factors Affecting Reactivity of Coal Chars", American Chemical Society Division Fuel Chemistry Preprints, 20, 45–51, (1975).
[181]. P. L. Walker, F. Rusinko, G. Austin, "Gas Reactions of Carbon", Advances in Catalysis, 11, 133–215, (1959).
[182]. P. A. Tesner, "The Activation Energy of Gas Reactions With Solid Carbon", Symposium (International) on Combustion, 8,807–814, (1961).
[183]. B. van-der-Velden, J. Trouw, R. Chaigneau, J. Van den Berg, "Coke Reactivity Under Simulated Blast Furnace Conditions", Ironmaking Conference Proceedings, 58, 275–285, (1999).
[184]. K. N. Tran, S. K. Bhatia, "Air Reactivity of Petroleum Cokes: Role of Inaccessible Porosity", Industrial and Engineering Chemistry, 46, 3265–3274, (2007).
[185]. M. Sakawa, Y. Sakurai, Y. Hara, "Influence of Coal Characteristics on CO_2 Gasification", Fuel, 61, 717–720, (1982).
[186]. W. W. Gill, N. A. Brown, C. D. A. Coin, M. R. Mahoney, "Influence of Ash on the Weakening of Coke", 44th ISS-AIME Ironmaking Conference, Detroit, US, 233–238, (1985).

[187]. S. Tanaka, T. Uemura, K. Ishizaki, K. Nagoyoshi, N. Ikenaga, H. Ohme, T. Suzuki, H. Yamashita, M. Ampo, "CO_2 Gasification of Iron-Loaded Carbons: Activation of the Iron Catalyst with CO", Energy and Fuels, 9, 45–52, (1995).
[188]. R. Sakurovs, L. Burke, "Influence of Gas Composition on the Reactivity of Cokes", Fuel Processing Technology, 92, 1220–1224, (2011).
[189]. R. H. Tien, E. T. Turkdogan, "Incomplete Pore Diffusion Effect on Internal Burning of Carbon", Carbon, 8, 607–621, (1970).
[190]. D. J. Harris, I. W. Smith, "Intrinsic Reactivity of Coke and Char to Carbon Dioxide", Am. Chem. Soc. Div. Fuel Chem. Prepr., 34, 94–101, (1989).
[191]. R. J. Tyler, I. W. Smith, "Reactivity of Petroleum Coke to Carbon Dioxide between 1030 and 1180K", Fuel, 54, 99–104, (1975).
[192]. M. Malekshahian, J. M. Hill, "Kinetic Analysis of CO_2 Gasification of Petroleum Coke at High Pressures", Energy and Fuels, 25, 4043–4048, (2011).
[193]. H. F. Liu, M. Kaneko, C. Luo, S. Kato, T. Kojima, "Effect of Pyrolysis Time on the Gasification Reactivity of Char with CO_2 at Elevated Temperatures", Fuel, 83, 1055–1061, (2004).
[194]. E. T. Turkdogan, V. Koump, J. V. Vinters, T. F. Perzak, "Rate of Oxidation of Graphite in Carbon Dioxide", Carbon, 6, 467–484 (1968).
[195]. A. Jess, A. K. Anderson, "Influence of Mass Transfer on Thermogravimetric Analysis of Combustion and Gasification Reactivity of Coke", Fuel, 89, 1541–1548, (2010).
[196]. H. J. Zou, Z. J. Zhou, F. C. Wang, W. Zhang, Z. H. Dai, H. F. Liu, Z. H. Yu, "Modeling Reaction Kinetics of Petroleum Coke Gasification with CO_2" Chemical Engineering and Processing, 46, 630–636, (2007).
[197]. D. W. McKee, "Mechanisms of the Alkali Metal Catalysed Gasification of Carbon", Fuel, 60, 170–175, (1983).
[198]. K. Otto, L. Bartosiewicz, M. Shelef, "Effects of Calcium, Strontium and Barium as Catalysts and Sulphur Scavengers in the Steam Gasification of Coal Chars", Fuel, 58, 565–572, (1979).
[199]. P. L. Walker, S. Matsumoto, T. Hanzawa, T. Muira, I. M. K. Ismail, "Catalysis of Gasification of Coal–Derived Cokes and Chars", Fuel, 62, 140–149, (1983).
[200]. P. L. J. Walker, M. Shelef, R. A. Anderson, "in Chemistry and Physics of Carbon", P. L. W. Jr., Ed. Marcel Dekker, New York, vol. 4, pp. 287-383. (1968).
[201]. E. A. Gulbransen, K. F. Andrew, "Reaction of Carbon Dioxide with Pure Artificial Graphite at Temperatures of 500° to 900°C", Industrial and Engineering Chemistry, 44, 1048–1051, (1952).
[202]. Y. Tamai, H. Watanabe, A. Tomita, "Catalytic Gasification of Carbon with Steam, Carbon Dioxide and Hydrogen", Carbon, 15, 103–106, (1977).
[203]. C. Liu, T. R. Cundari, A. K. Wilson, "CO_2 Reduction on Transition Metals (Fe, Co, Ni and CU) Surfaces: In Comparison with Homogeneous Catalysis", Journal of Physical Chemistry, 116, 5681–5688, (2012).
[204]. C. L. Spiro, D. W. McKee, P. G. Kosky, E. J. Lamby, D. H. Maylotte, "Significant Parameters in the Catalysed CO2 Gasification of Coal Chars", Fuel, 62, 323–330, (1983).
[205]. G. Hermann, K. J. Huttinger, "Mechanism of Iron–Catalyzed Water Vapour Gasification of Carbon", Carbon, 24, 429–435, (1986).
[206]. F. J. Long, K. W. Sykes, "The Effect of Specific Catalysts on the Reactions of the Steam–Carbon System", Proceeding of the Royal Society of London A, 100–110, (1952).

[207]. A. Tomita, "Catalysis of Carbon–Gas Reactions", Catalysis Surveys, 5, (2001).
[208]. W. L. Holstein, M. Boudart, "Transition Metal and Metal Oxide Catalysed Gasification of Carbon by Oxygen, Water and Carbon Dioxide", Fuel, 62, 162–165, (1983).
[209]. G. R. Hennig, "Catalytic Oxidation of Graphite", Journal of Inorganic and Nuclear Chemistry, 24, 1129–1137, (1962).
[210]. T. Kyotani, Z. Zhang, S. Hayashi, A. Tomita, "TPD Study on H_2O–Gasified and O_2–Chemisorbed Coal Chars", Energy and Fuels, 2, 136–141, (1988).
[211]. F. Kapteijn, H. Porre, J. A. Moulijn, "CO_2 Gasification of Activated Carbon Catalyzed by Earth Alkaline Elements", AIChE Journal, 32, 691–695, (1986).
[212]. S. P. Mehrotra, V. K. Sinha, "Catalytic Effect of Iron on the Carbon–Carbon Dioxide Reaction Kinetics", Transactions ISIJ, 23, 723–730, (1983).
[213]. F. J. Vastola, P. L. Walker,"The Reaction of Graphite Wear Dust with Carbon Dioxide and Oxygen at Low Pressures",Journal de Chimie Physique 58,20–24, (1961).
[214]. W. L. Holstein, M. Boudart, "Uncatalyzed and Platinum–Catalyzed Gasification of Carbon by Water and Carbon Dioxide", Journal of Catalysis, 75, 337–353, (1982).
[215]. J. F. Rakszawski, F. Rusinko, P. L. Walker, Catalysis of the Carbon–Carbon Dioxide Reaction by Iron "in Proceedings of the Fifth Carbon Conference". Pergamon, Oxford, UK, (1962).
[216]. S. Ban-Ya, J. F. Elliott, J. Chipman, "Thermodynamics of Austenitic Fe–C Alloys", Metallurgical Transactions,1, (1970).
[217]. F. J. Long, K. W. Sykes, "The Catalysis of the Oxidation of Carbon", Journal de Chimie Physique, 47, 361–378, (1950).
[218]. E. J. Hippo, "The Role of Active Sites in the Inhibition of Gas–Carbon Reactions", Carbon, 27, (1989).
[219]. D. E. Pearson, "Influence of Geology on CSR (Coke Strength After Reaction With CO_2)", Pearson Coal Petrography, British Columbia, Canada, (1989).
[220. ASTM D5341/D5341M-14: Standard Test Method for Measuring Coke Reactivity Index (CRI) and Coke Strength After Reaction (CSR)", ASTM International (2014).
[221]. A. Koszorek, M. Krzesinska, S. Pusz, B. Pilawa, B. Kwiecinska, "Relationship Between the Technical Parameters of Cokes Produced from Blends of Three Polish Coals of Different Coking Ability", International Journal of Coal Geology, 77, 363–371, (2009).
[222]. J. I. Rodero, J. Sancho-Gorostiaga, M. Ordiales, D. Fernandez-Gonzalez, J. Mochon, I. Ruiz-Bustina, A. Fuentes, L. F. Verdeja, "Blast Furnace and Metallurgical Coke's Reactivity and its Determination by Thermal Gravimetric Analysis", Ironmaking and Steelmaking, 42, 618–625, (2015).
[223]. B. Gao, J. Zhang, H. Zuo, C. Qi, Y. Rong, Z. Wang, "CO_2 Gasification Characteristics of High and Low Reactivity Cokes", Journal of Iron and Steel Research, International, 21, 723–728, (2014).
[224]. M. Krzesinska, S. Pusz, L. Smedowski, "Characterization of the Porous Structure of Cokes Produced from the Blends of Three Polish Bituminous Coking Coals", International Journal of Coal Geology, 78, 169–176, (2009).
[225]. D. V. Miroshnichenko, "Preliminary Estimation of Coke’s CRI and CSR Values on the Basis of the Physical Properties of Coal Ash ", Coke and Chemistry,447–450, (2008).

[226]. D. W. McKee, "Gasification of Graphite in Carbon Dioxide and Water Vapor–The Catalytic Effects of Alkali Metal Salts", Carbon, 20, 59–66, (1982).
[227]. E. Diaz-Faes, C. Barriocanal, M. A. Diez, R. Alvarez, "Applying TGA Parameters in Coke Quality Prediction Models", Journal of Analytical and Applied Pyrolysis, 79, 154–160, (2007).
[228]. Z. Wang, R. J. Longbottom, B. J. Monaghan, "ACARP Project C23049 Part II: A Coke Analogue to Examine the Effect of Mineralogy on Coke Reactivity", ACARP Brisbane, Australia (2016).
[229]. L. Lutterotti, "Total Pattern Fitting for the Combined Size–Strain–Stress–Texture Determination in Thin Film Diffraction", Nuclear Instruments and Methods in Physics Research B, 268, 334–340, (2010).
[230]. S. Grazulis, A. Daskevic, A. Merkys, D. Chateigner, L. Lutterotti, M. Quiros, N. R. Serebryanaya, P. Moeck, R. T. Downs, A. L. Bail, "Crystallography Open Database (COD): An Open-Access Collection of Crystal Structures and Platform for World-Wide Collaboration", Nucleic Acids Research, 40, D420–D427, (2012).
[231]. GBC-Scientific-Equipment: "XRD Software – Automation Software", USA.
[232]. T. G. Fawcett, S. N. Kabbekodu, J. Faber, F. Needham, F. Mcclune, "Evaluating Experimental Methods and Techniques in X–Ray Diffraction Using 280,000 Data Sets in The Powder Diffraction File", Advances in X–Ray Analysis, 47, 156–164, (2004).
[233]. ASTM E1621-13: "Standard Guide for Elemental Analysis by Wavelength Dispersive X-Ray Fluorescence Spectrometry", ASTM International, (2013)
[234]. T. Ko, W. Kuo, Y. Chang, "Microstructural Changes of Phenolic Resin During Pyrolysis", Journal of Applied Polymer Science, 81, 1084–1089, (2001).
[235]. T. Ko, W. Kuo, Y. Chang, "Raman Study of the Microstructure Changes of Phenolic Resin During Pyrolysis", Polymer Composites, 21, 745–750, (2000).
[236]. S. Tzeng, Y. Chr, "Evolution of Microstructure and Properties of Phenolic Resin-Based Carbon/Carbon Composites during Pyrolysis", Materials Chemistry and Physics, 73, 162–169, (2002).
[237]. K. A. Trick, T. E. Saliba, "Mechanisms of the Pyrolysis of Phenolic Resin in a Carbon/Phenolic Composite", Carbon, 33, 1509–1515, (1995).
[238]. Z. Lausevic, S. Marinkovic, "Mechanical Properties and Chemistry of Carbonization of Phenol Formaldehyde Resin", Carbon, 24, 575–580, (1986).
[239]. E. Fitzer, W. Shaefer, S. Yamada, "The Formation of Glasslike Carbon by Pyrolysis of Polyfurfuryl Alcohol and Phenolic Resin", Carbon, 7, 643–648, (1969).
[240]. M. C. Domeneghetti, G. M. Molin, V. Tazzoli, "Crystal–Chemical Implications of the Mg^{2+}–Fe^{2+} Distribution in Orthopyroxenes", American Mineralogist, 70, 987–995, (1985).
[241]. Leica Microsystems Handbook: "Imaging Software Integrates Leica Automated Microscopes and Digital Cameras Leica Application Suite", Australia.
[242]. ASTM 1019-03: "Standard Test Method for Determination of Carbon, Sulphur, Nitrogen and Oxygen in Steel and in Iron, Nickel and Cobalt Alloys", ASTM International, (2003).
[243]. Leitz Orthoplan Microscope Handbook, Germany.
[244]. H. Rogers, "SEM-EDS of Coke Analogue Doped with Metallic Iron", Pyrometallurgy Group–University of Wollongong, (unpublished, 2016).
[245]. C. Payne, A. R. Barron, "Surface–Enhanced Raman Spectroscopy for the Study of Surface Chemistry", (2006).

[246]. Horiba-Scientific: 'LabSpec 6 Software Technical Note– Searching Spectra Databases with LabSpec 6', (2016).
[247]. R. Wayne, "ImageJ, Version 1.48", National Institutes of Health, Maryland, US, (2008).
[248]. ISO 15901–1: 'Pore Size Distribution and Porosity of Solid Materials by Mercury Porosimetry and Gas Adsorption– Part I Mercury Porosimetry", International Organisation for Standardization, (2005).
[249]. U. Garbe, N. T. Randall, C. Hughes, G. Davidson, S. Pangelis, S. J. Kennedy, "A New Neutron Radiography/Tomography/Imaging Station DINGO at OPAL", Physics Procedia 69, 27–32, (2015).
[250]. M. Dierick, B. Masschaele, L. Van-Hoorebeke, "Octopus, A Fast and User–Friendly Tomographic Reconstruction Package Developed in Labview", Measurement Science and Technology, 15, 1366–1370, (2004).
[251]. VGStudio-MAX 2.0, 'Application Software for Visualization and Documentation of Industrial Computer Tomography/Voxel Data', Volume Graphics GMBH, Heidelberg, Germany (2014).
[252]. M. I. Joseph, "LECO–Corporation: Carbon and Sulphur in Steel, Nickel-base and Cobalt–Base Alloys", (2007).
[253]. H. H. Ku, "Notes on the Use of Propagation of Error Formulas", Journal of Research of the National Bureau of Standards - C. Engineering and Instrumentation, 70C, 263–273, (1966).
[254]. J. C. Taylor, "Computer Programs for Standardless Quantitative Analysis of Minerals Using the Full Powder Diffraction Profile", Powder Diffraction, 6, 2–9, (1991).
[255]. P. Atkins, J. De Paula, "Atkins' Physical Chemistry", Oxford University Press, New Delhi, India, ed. 8th (2008).

LIST OF PUBLICATIONS

Refereed Journal Paper

O. A. Aladejebi, B. J. Monaghan, M. H. Reid, M. in het Panhuis, R. J. Longbottom, "Metallic Iron Effects on Coke Analog Carbon Bonding and Reactivity", *Steel Research Int.*, **87**, 9999, (2017)

Refereed Conference Paper

B. J. Monaghan, R. J. Longbottom, M. Reid, **O. A. Aladejebi**, A. S. Jayasekara, M. In het Panhuis, "A New Approach to Investigating Coke Reactivity", in *TMS Annual Meeting and Exhibition,* John Wiley and Sons, USA (2014)

Non-Refereed Conference Paper

O. A. Aladejebi, B. J. Monaghan, M. H. Reid, M. In het Panhuis, "Characterisation of Coke Analogue", in *6th High Temperature Processing Symposium,* Swinburne University, Australia (2014)

Table I-1: The list of suppliers and impurity details of the materials used in this study.

Materials	Suppliers	Product Number	Description / Size	Purity* (%)	Batch Number	Major Impurities (Mass %)	Minor Impurities (ppm)
Graphite powder 1	Sigma-Aldrich	496596	Dark grey powder <45µm	>99.99	02819TD	ND	Na 18, Ca 5, K 3, Mg <2, Fe 2, Al 2, (Zr, W, Ti, Ta, Sn, Pb, Mo, Li, Cu, Co, Bi, Be, BA, Cr, Mn, B <1)
					09525JE	ND	Mg 5, Ca 4, Na 3, (W, Ti, Ta, K, Hf, Cu, Cr, Al, Fe, Zr, Zn, Sn, Sb, Pb, Mo, As, V, Ni, Mn, Be, Ba, B, Li <1)
Graphite powder 2	Sigma-Aldrich	496588	Dark grey powder <150µm	>99.99	08108HE	ND	Na 10, Mg <5, Ca 5, Al 3, K 2, (W, Ti, Ta, Hf, Cr, Fe, Zr, Sn, Sb, Pb, Mo, Cu, Co, Be, BA <1)
					06527JD	ND	Al 5, Na 4, Ca 3, Mg <2, Fe 2, (Zr, W, Ti, Sn, Nb, Mo, Cr, No, K, Zn, V, Sb, Pb, Li, Cu, Co, Ba, B, Be, Mn <1)
Metallic iron 1	Sigma-Aldrich	267953	<10µm powder	>99.9	MKBR1415V	ND	Al 13.5, Ba 6.1, Bi 19.1, Ca 1.3, Cd 24.2, Co 3.8, Cr 2.1, Mg 37.9, Mn 0.7, Na 5.1, Ni 114.6, Pb 116.7, Pt 9.3, Sb 35.6, Sn 15.9, W 80.9, Zr 3.0.
Metallic iron 2	Höganas	AHC 100.29	<150µm powder	>99.5	-	Si 0.003, Cr 0.08, Ni 0.05, Cu 0.09, Mo 0.02, Mn 0.20, P 0.008, S 0.01, C <0.02, O <0.17	ND
Magnetite	Höganas	1646383	<500µm powder	72 mass% of Fe, with O as balance	031314	C 0.008, S 0.003, P 0.01, Al_2O_3 0.15, Cr_2O_3 0.002, MnO 0.03, SiO_2 0.10, TiO_2 0.15, V_2O_5 0.12.	ND
LCAK steel	Bluescope	-	2mm x 7mm x 9mm	99.62	-	C 0.056, Mn 0.210, Cr 0.015, Cu 0.013, Mo 0.003, Nb 0.001, Ni 0.10, P 0.015, S 0.01, Si 0.005, Sn 0.002, Ti 0.002, V 0.003	-

ND – No trace of impurities detected
* – as reported by supplier

Appendix II XRD and XRF measurements

This is being carried out to establish the chemical composition and phases of the non-carbonaceous materials used in this study. The XRD data of the coke analogues were assessed to check for intercalation in the (002) carbon peak.

II.1. XRD analysis of non-carbonaceous materials used to make the coke analogues.

A GBC MMA XRD unit was used to characterise the phases of non-carbonaceous materials used to make the coke analogue and their stability in the coke analogue system. The coke analogue materials were detailed in Table 3-5. The XRD analysis was carried out with Copper Kα radiation (wavelength λ = 1.54Å). The XRD patterns were recorded using a Visual XRD software ViX122D [231] over 2θ diffraction angle range 20–70°. The generated patterns were subsequently processed using Trace X-ray processing software V6 combined with the international centre for diffraction data (ICDD) database system [231, 232].

The phases of the non-carbonaceous materials prior to addition to the coke analogue and the result phases in the fired and post reacted coke analogue samples were also confirmed. The reactivity testing was carried out in CO_2 at 1100°C for 2 hours. At 1100°C, the FWC of the reacted samples was ≥-0.65. The post reacted samples maintained their initial cylindrical shape with powdered external surface but broke up on transferring from the furnace alumina pedestal to a sample container (except for coke analogue–magnetite 46um that deviated significantly from the initial shape and in powdered form). The XRD patterns are given in Figures II-1 to II-7.

The XRD patterns of ashed enstatite ferroan and phlogopite ferroan are given in Figures II-8 and II-9 respectively. The minerals were fired in graphite to 1200°C and then ashed at 520°C in air.

Where more than one mineral phase was identified, Maud diffraction software version 2.55 [229] linked to crystallography database of crystal structure [230] were used to quantify the phases in weight%. The letters used as phase identifier on the XRD pattern, the mineral name, chemical formula and card numbers of the phases are given in Table II-1.

Table II-1: List of the letters, mineral names, chemical formula and card numbers of the phases identified on the XRD pattern

Letters	**Mineral names**	**Chemical formula**	**Card Number** [231, 232]
A	Anothite	$(Ca,Na)(Si,Al)_4O_8$	18-1202
C	Graphite	C	41-1487
D	Gedrite	$(Fe,Mg,Al)_7Al_2Si_6O_{22}(OH)_2$	13-0506
E	Enstatite ferroan	$Mg_{1.56}Fe_{0.44}Si_2O_6$	88-1911
F	Fosterite	Mg_2SiO_4	34-0189
G	Gehlenite	$Ca_2Si(AlSi)O_7$	89-5917
H	Hematite	Fe_2O_3	33-0664
I	α-Iron	Fe	06-0696
M	Magnetite	Fe_3O_4	07-0322
O	Osumilite	$KMg_2Al_3(Si_{10}Al_2)O_{30}$	29-1016
P	Phlogopite ferroan	$K(Mg,Fe)_3(Al,Fe)Si_3O_{10}(OH,F)_2$	42-1437
Q	α-quartz	SiO_2	05-0490
q	β-quartz	SiO_2	11-0252
R	Iron Rhodium	FeRh	25-1408
S	Sanidine	$KAlSi_3O_8$	80-2107
U	Augite	$Ca(Mg,Fe,Al)(Si,Al)_2O_6$	41-1483

In Figures II-1 to II-7, the graphite peaks have been truncated to enable the resolution of the non-carbonaceous peaks. The inherent non-carbonaceous phases identified in the base coke analogue were anothite [$(Ca,Na)(Si,Al)_4O_8$] and gehlenite ($Ca_2Si(AlSi)O_7$). These phases are low level impurities (< 1 mass%) in the coke analogue. The phases of the non-carbonaceous materials used to make the coke analogue and their states in the fired and post reacted coke analogues are given in Table II-2.

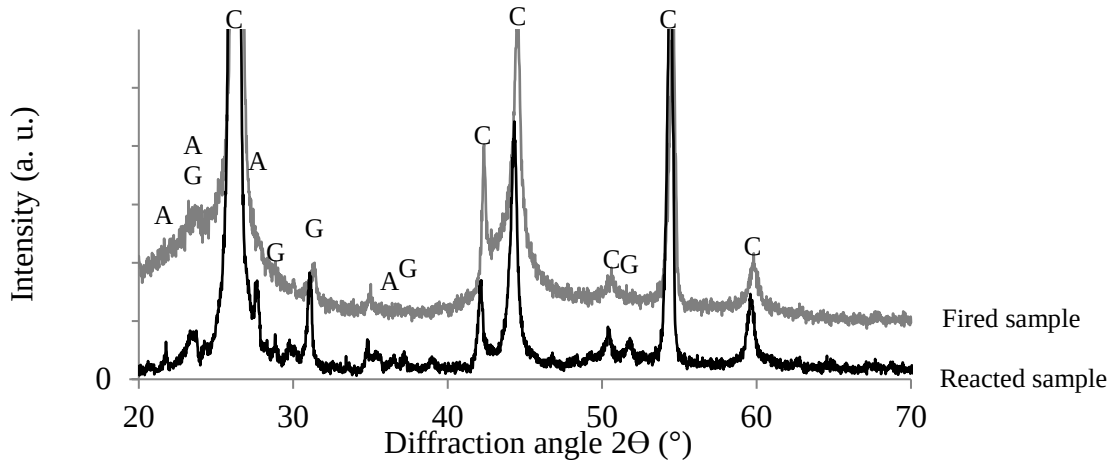

Figure II-1: An XRD pattern of the base coke analogue. The letters A, C and G represent phases given in Table II-1.

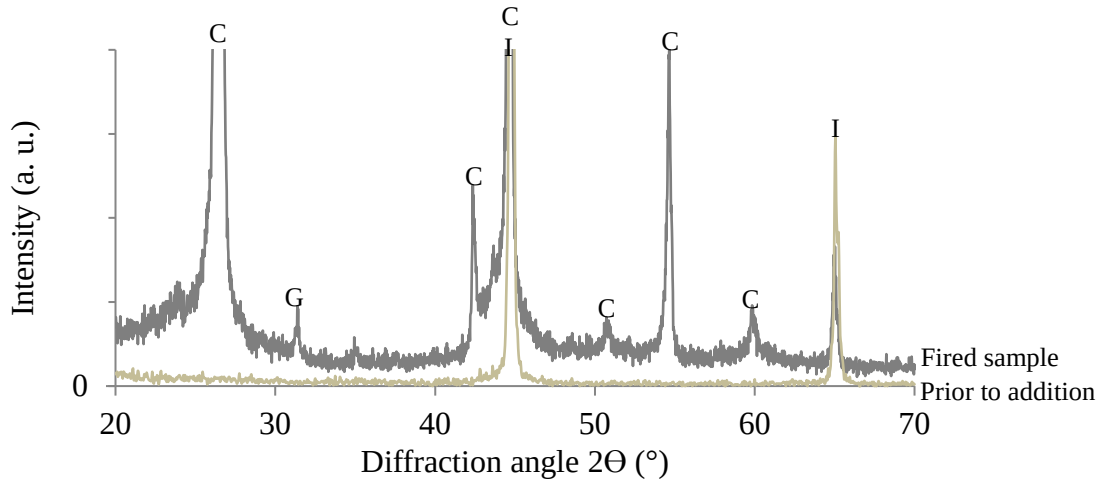

Figure II-2: An XRD pattern of metallic iron 1 (Fe) prior to addition to the coke analogue and its stability in the fired coke analogue. The letters A, C, G, H, I and M represent phases given in Table II-1.

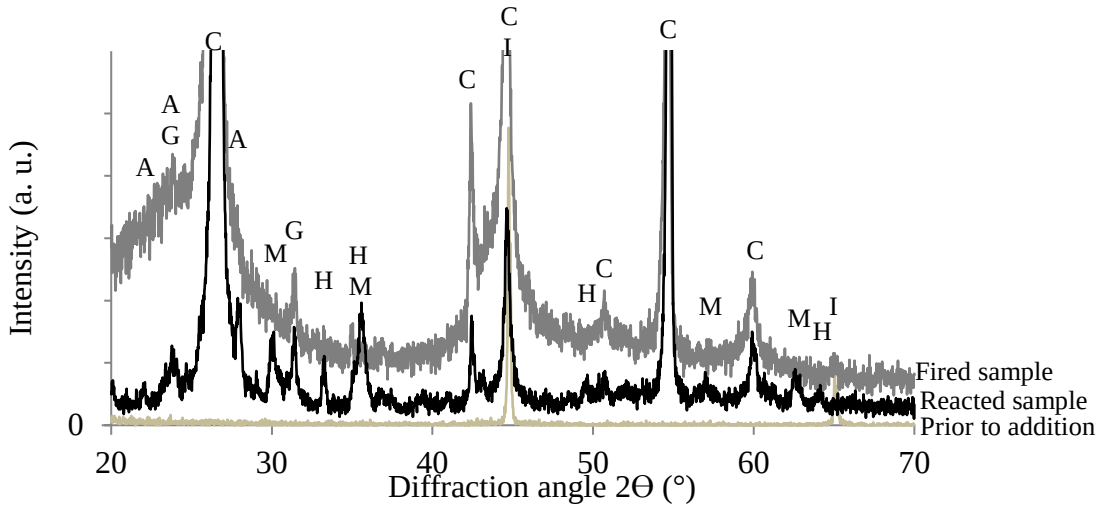

Figure II-3: An XRD pattern of metallic iron 2 (Fe) prior to addition to the coke analogue and its stability in the coke analogue (fired and post reacted conditions). The letters A, C, G, H, I and M represent phases given in Table II-1.

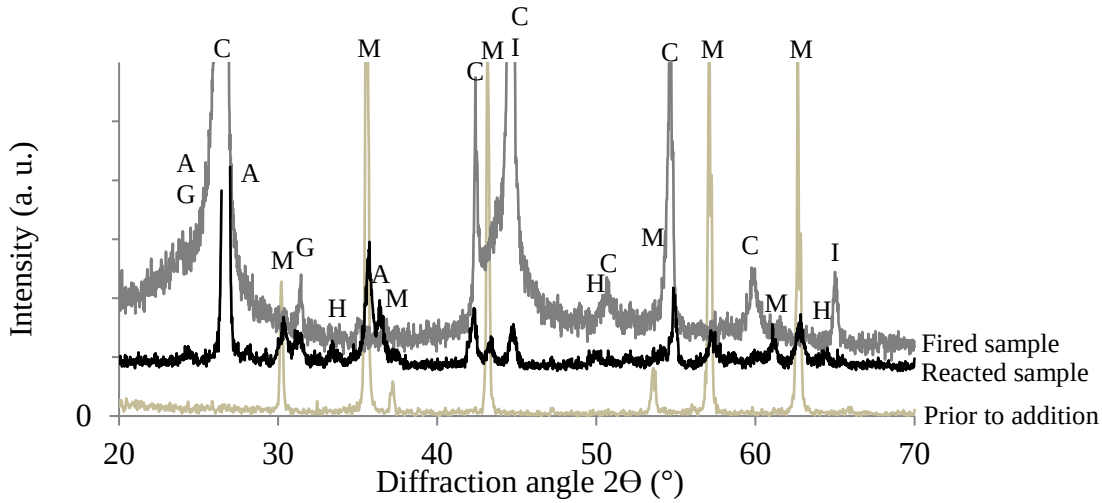

Figure II-4: An XRD pattern of magnetite (Fe_3O_4) prior to addition to the coke analogue and its stability in the coke analogue (fired and post reacted conditions). The letters A, C, G, H, I and M represent phases given in Table II-1.

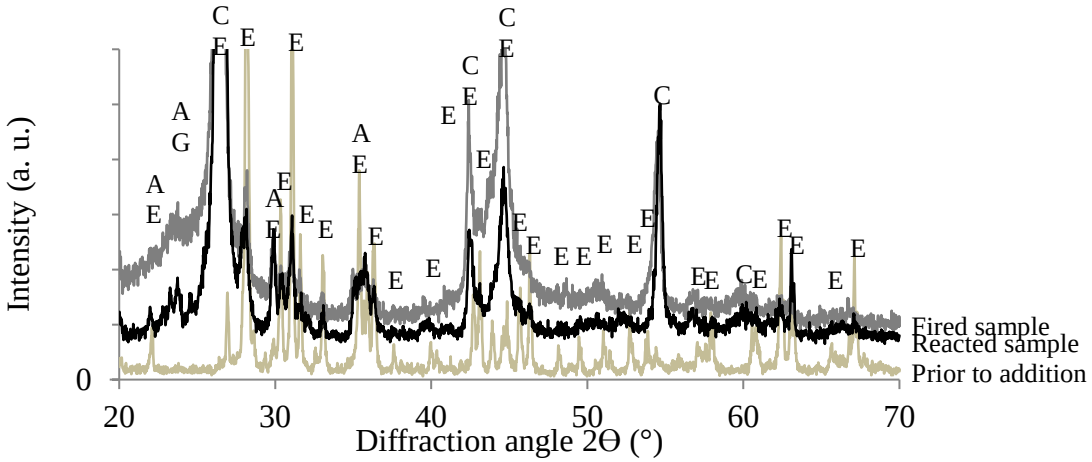

Figure II-5: An XRD pattern of enstatite ferroan ($Mg_{1.56}Fe_{0.44}Si_2O_6$) prior to addition to the coke analogue and its stability in the coke analogue (fired and post reacted conditions). The letters A, C, E and G represent phases given in Table II-1.

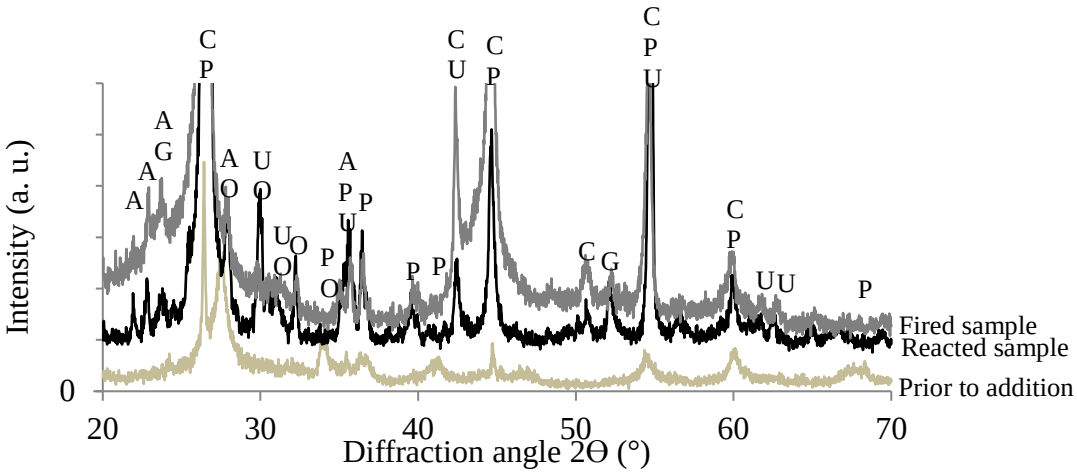

Figure II-6: An XRD pattern of phlogopite ferroan [$K(Mg,Fe)_3(Al,Fe)Si_3O_{10}(OH,F)_2$] prior to addition to the coke analogue and its stability in the coke analogue (fired and post reacted conditions). The letters A, C, G, O, P, and U represent phases given in Table II-1.

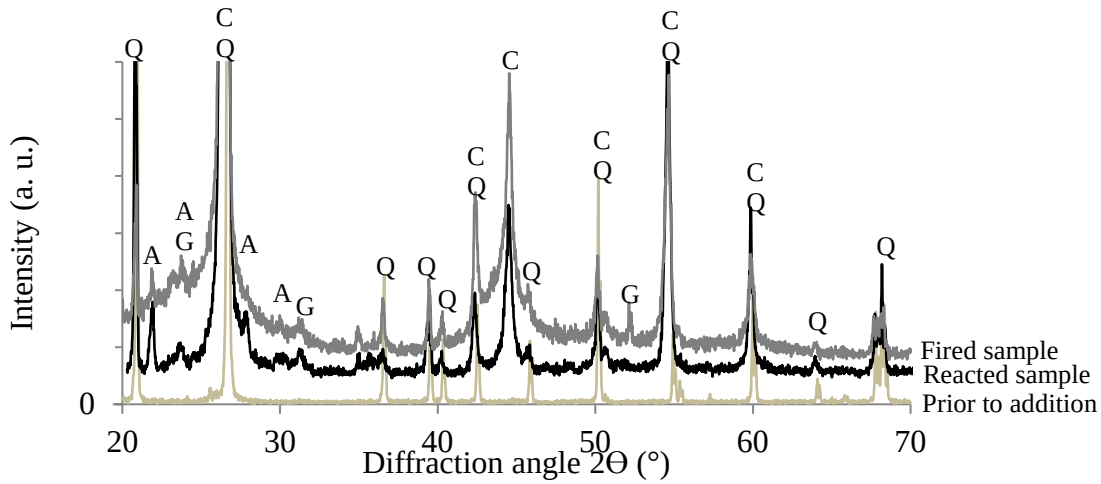

Figure II-7: An XRD pattern of quartz (SiO_2) prior to addition to the coke analogue and its stability in the coke analogue (fired and post reacted conditions). The letters A, C, G and Q represent phases given in Table II-1.

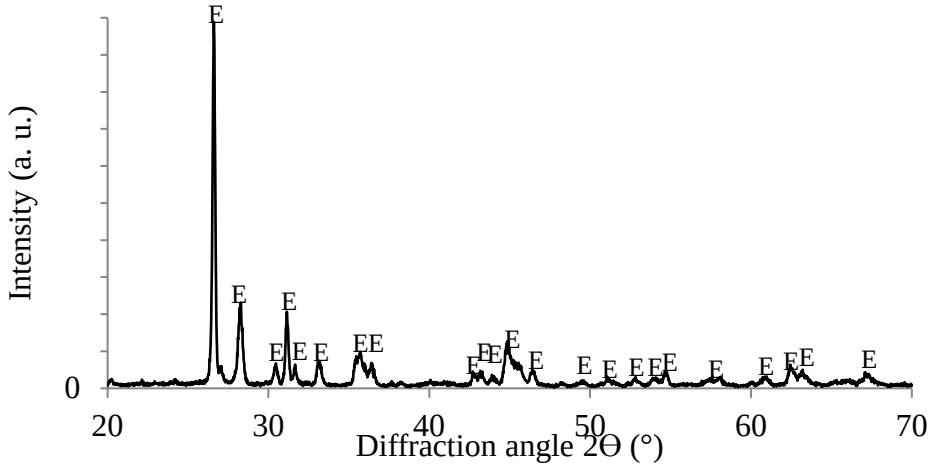

Figure II-8: An XRD pattern of the enstatite ferroan after ashing at 520°C. The letter E represents phase given in Table II-1.

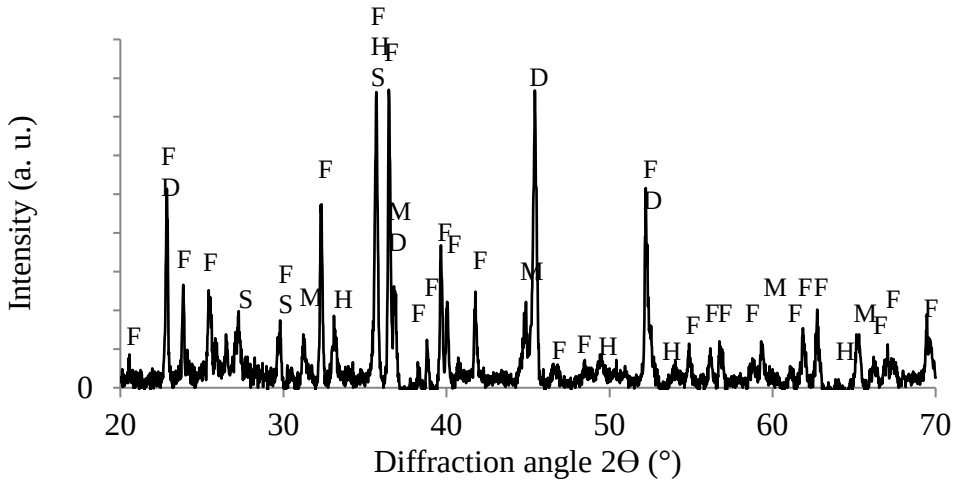

Figure II-9: An XRD pattern of the phlogopite ferroan after ashing at 520°C. The letters D, E, F, H, M and S represent phases given in Table II-1.

Table II-2: The phases of the non-carbonaceous materials used to make the coke analogue and their stability in the coke analogue as measured by XRD.

Non-carbonaceous materials	**Prior to addition**	**Post fired coke analogue (fired at 1200°C for 1 hour)**	**Post fired coke analogue and followed by ashing at 520°C**	**Post reacted coke analogues (CO_2 at 1100°C for 2 hours)**
Metallic iron 1 (Fe)	α-Iron (Fe)	α-Iron (Fe)	–	–
Metallic iron 2 (Fe)	α-Iron (Fe)	α-Iron (Fe)	–	Magnetite (Fe_3O_4) 97.5%, and hematite (Fe_2O_3) 2.5%
Magnetite (Fe_3O_4)	Magnetite (Fe_3O_4)	α-Iron (Fe)	–	Magnetite (Fe_3O_4) 84.5%, and hematite (Fe_2O_3) 15.5%
Enstatite Ferroan ($Mg_{1.56}Fe_{0.44}Si_2O_6$) Phlogopite Ferroan $[K(Mg,Fe)_3(Al,Fe)Si_3O_{10}(OH,F)_2]$	Enstatite ferroan ($Mg_{1.56}Fe_{0.44}Si_2O_6$) Phlogopite ferroan $[K(Mg,Fe)_3(Al,Fe)Si_3O_{10}(OH,F)_2]$ 81.3% and osumilite ($KMg_2Al_3(Si_{10}Al_2)O_{30}$) 18.7%.	Enstatite ferroan ($Mg_{1.56}Fe_{0.44}Si_2O_6$) Phlogopite ferroan $[K(Mg,Fe)_3(Al,Fe)Si_3O_{10}(OH,F)_2]$ 14.7% and osumilite ($KMg_2Al_3(Si_{10}Al_2)O_{30}$) 85.3%	Enstatite ferroan ($Mg_{1.56}Fe_{0.44}Si_2O_6$) Forsterite ($Mg_2SiO_4$) 50.9%, sanidine ($KAlSi_3O_8$) 41.1%, gedrite $[(Fe,Mg,Al)_7Al_2Si_6O_{22}(OH)_2]$ 4.6%, hematite (Fe_2O_3) 3.4% and magnetite (Fe_3O_4) (trace amount)	Enstatite ferroan ($Mg_{1.56}Fe_{0.44}Si_2O_6$) Phlogopite ferroan $[K(Mg,Fe)_3(Al,Fe)Si_3O_{10}(OH,F)_2]$ 7.6%, osumilite ($KMg_2Al_3(Si_{10}Al_2)O_{30}$) 9.7% and augite $Ca(Mg,Fe,Al)(Si,Al)_2O_6$ 82.7%
Quartz (SiO_2)	α-Quartz (SiO_2)	α-Quartz (SiO_2)	–	α-Quartz (SiO_2)

–Not measured

II.2. Assessment of intercalation

Intercalation has been assessed by considering the broadening of the (002) carbon peak. The assessment of the full width at half maximum (FWHM) of the (002) carbon peak is being carried out to establish the effects of iron and minerals. The FWHM and peak position of the (002) carbon peak of the analogues are given in Table II-3. The XRD profile over diffraction angle 22–30° is given in Figures II-10 to II-17.

Table II-3: The FWHM and position of (002) peak in the coke analogues

Coke analogues	Fired		Post experimental at 1100°C for 2hrs	
	FWHM (°)	Peak Position (°)	FWHM (°)	Peak Position (°)
Base	0.286	26.54	0.336	26.58
Fe 5µm	0.226	26.56	–	–
Fe 46µm	0.218	26.58	0.222	26.64
Fe 83µm	0.240	26.54	–	–
Fe_3O_4 46µm	0.248	26.56	0.332	26.52
Enstatite ferroan ($Mg_{1.56}Fe_{0.44}Si_2O_6$)	0.296	26.50	0.302	26.56
Phlogopite ferroan [$K(Mg,Fe)_3(Al,Fe)Si_3O_{10}(OH,F)_2$]	0.250	26.58	0.256	26.60
Quartz (SiO_2)	0.244	26.58	0.284	26.52

– Not measured

From Table II-3, it can be seen that FWHM of the coke analogues is relatively similar both in the fired and post reacted conditions. It appears Fe and mineral additions did not affect the (002) carbon peak, that is no broadening of the peak. That is there appears to be no intercalation effect of these minerals.

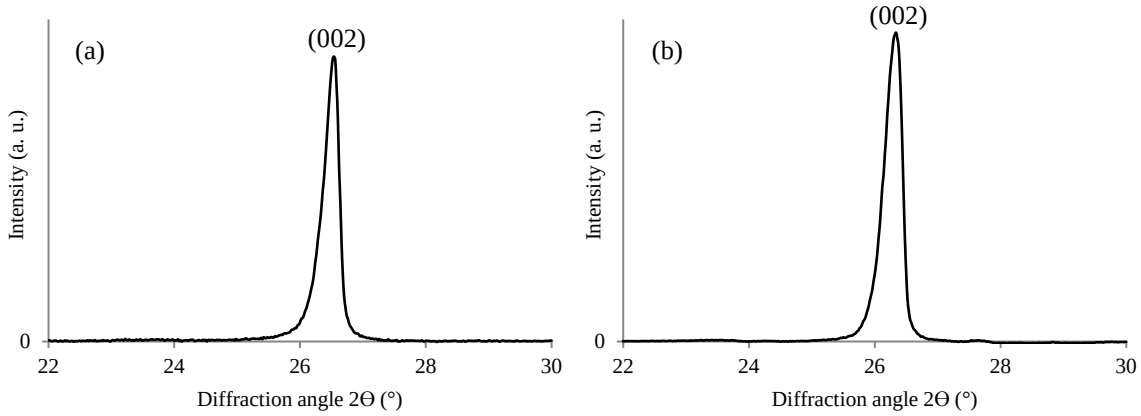

Figure II-10: An XRD pattern of base coke analogue showing the (002) carbon peak. (a) fired and (b) post reaction in CO_2 at 1100°C for 2 hours.

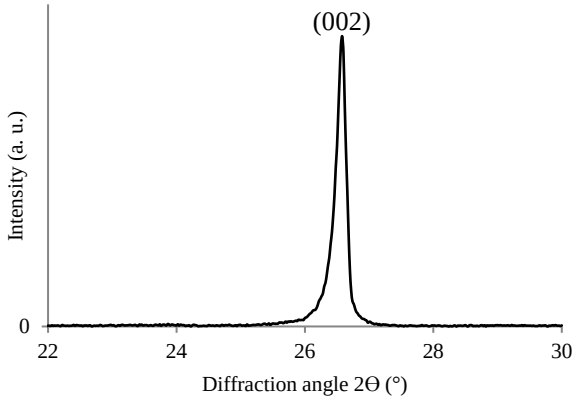

Figure II-11: An XRD pattern of fired coke analogue–Fe 5µm showing the (002) carbon peak.

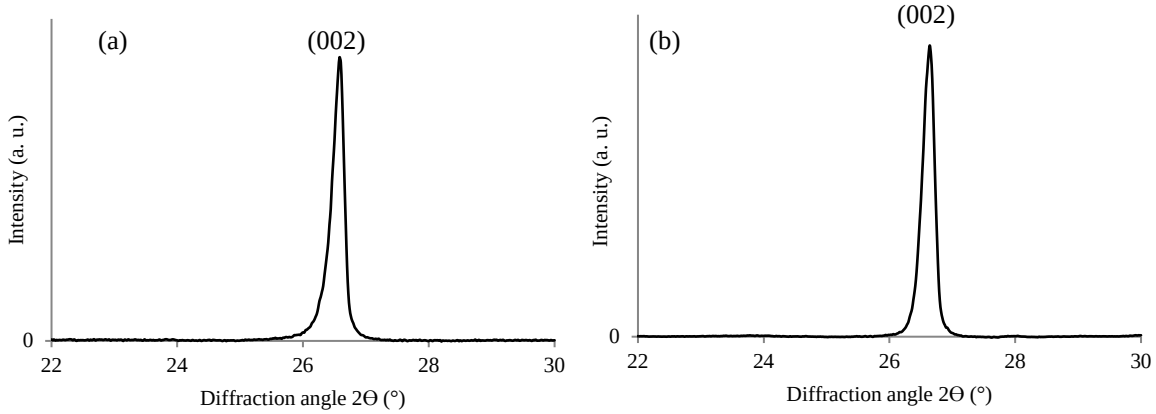

Figure II-12: An XRD pattern of fired coke analogue–Fe 46µm showing the (002) carbon peak. (a) fired and (b) post reaction in CO_2 at 1100°C for 2 hours.

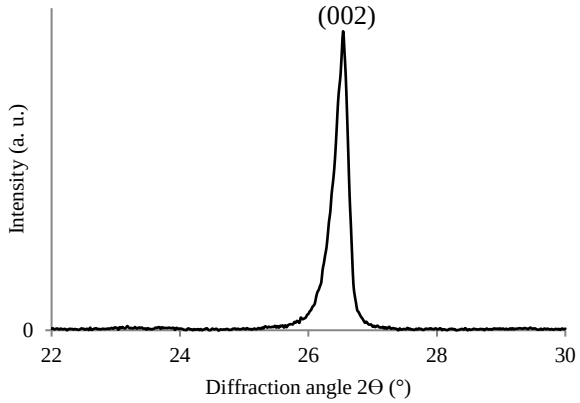

Figure II-13: An XRD pattern of fired coke analogue–Fe 83µm showing the (002) carbon peak

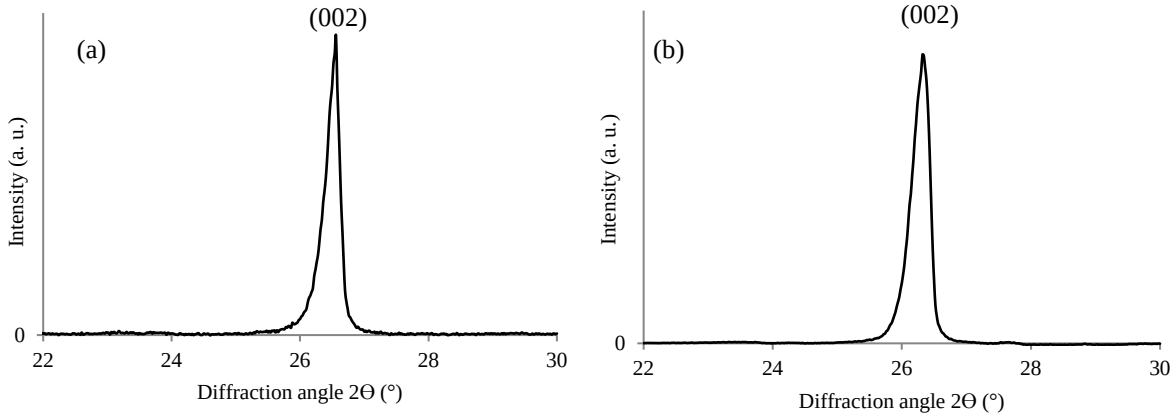

Figure II-14: An XRD pattern of fired coke analogue–Fe_3O_4 46µm showing the (002) carbon peak. (a) fired and (b) post reaction in CO_2 at 1100°C for 2 hours.

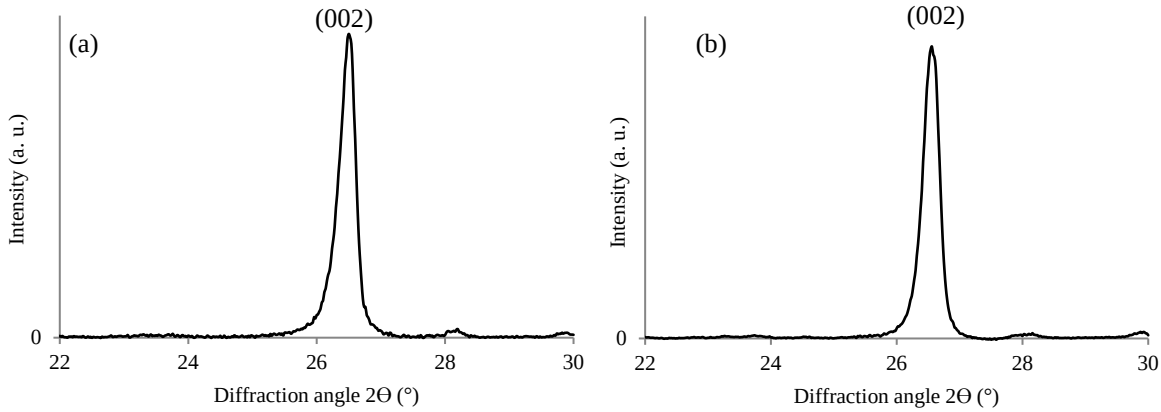

Figure II-15: An XRD pattern of fired coke analogue–enstatite ferroan showing the (002) carbon peak. (a) fired and (b) post reaction in CO_2 at 1100°C for 2 hours.

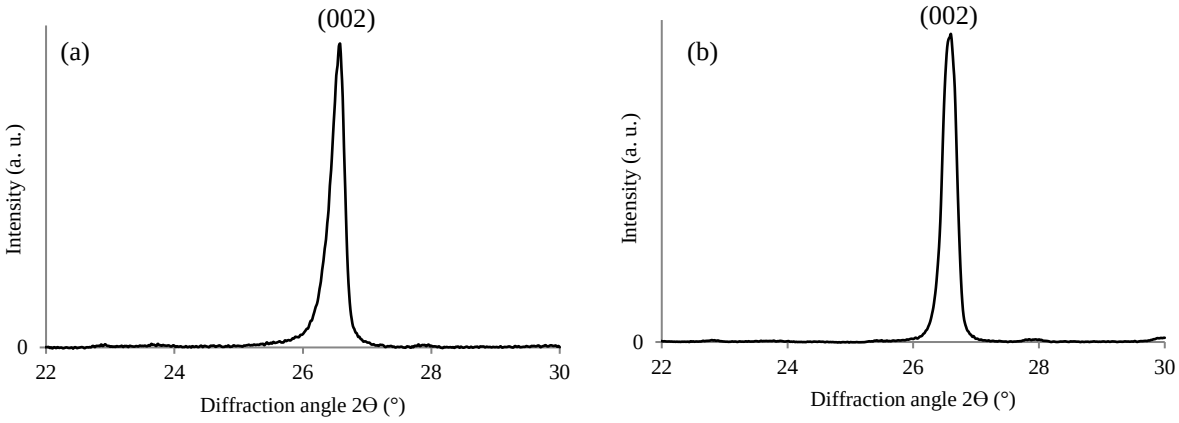

Figure II-16: An XRD pattern of fired coke analogue–phlogopite ferroan showing the (002) carbon peak. (a) fired and (b) post reaction in CO_2 at 1100°C for 2 hours.

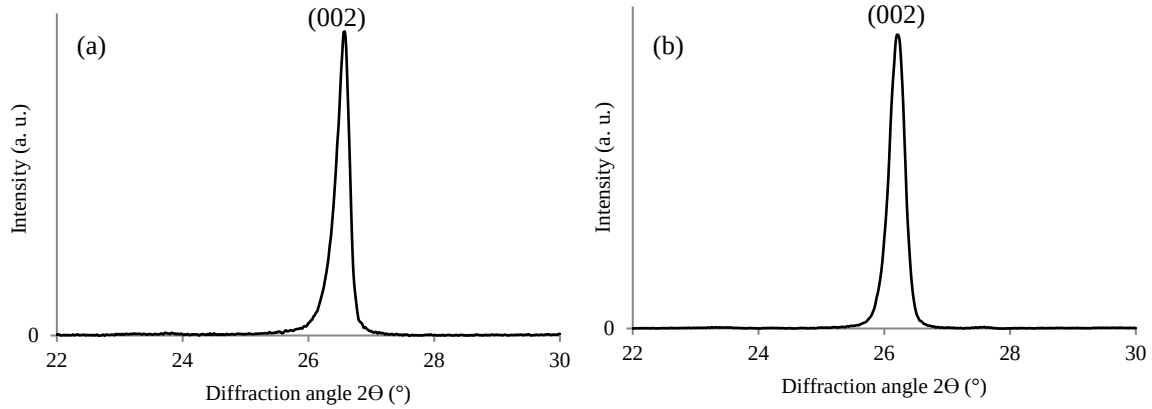

Figure II-17: An XRD pattern of fired coke analogue–quartz (SiO_2) showing the (002) carbon peak. (a) fired and (b) post reaction in CO_2 at 1100°C for 2 hours.

II.3. XRF analysis of enstatite ferroan and phlogopite ferroan used to make the coke analogue

A SPECTRO XEPOS energy dispersive X-ray fluorescence spectrometer was used to determine the chemical composition of the enstatite ferroan ($Mg_{1.56}Fe_{0.44}Si_2O_6$) and phlogopite ferroan [$K(Mg,Fe)_3(Al,Fe)Si_3O_{10}(OH,F)_2$] used to make the coke analogue. The XRF analysis complied with the ASTM E1621 'standard guide for elemental analysis by wavelength dispersive X-ray fluorescence spectrometry' [233] with the data given in Table II-4.

Table II-4: XRF analysis of enstatite ferroan and phlogopite ferroan used to make the coke analogue.

Mineral name	**Composition in mass%**										
	Na_2O	MgO	Al_2O_3	SiO_2	P_2O_5	SO_3	K_2O	CaO	TiO_2	MnO	Fe_2O_3
Enstatite ferroan	*	24.4	4.7	52.2	*	*	*	*	*	*	18.7
Phlogopite ferroan	*	25.4	14.9	44.5	*	*	5.1	*	*	*	10.1

*trace amount

Appendix III Non-polarised optical microscopy

A Leica DM/RM optical microscope equipped with a Leica DFC295 digital camera (see schematic given in Figure 3-11) was used to take non-polarised optical micrographs of the coke analogues. This was carried out to ensure representative characterisation of the microstructure of the coke analogues.

The non-polarised optical micrographs of the fired coke analogues and a metallurgical coke used in this work are given in Figures III-1 to III-9. The micrographs were acquired at 250x magnification using the approach illustrated in Figure 3-12 and reproduced in the following text.

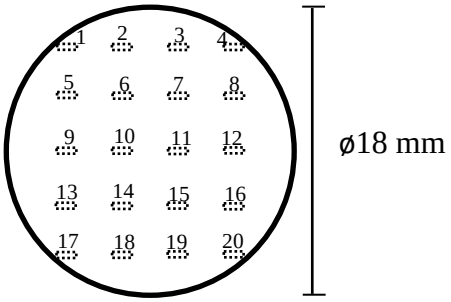

A schematic of the positions where the micrographs were taken on the sample horizontal cross section. The boxes numbered 1–20 represent the approximate positions of the micrographs (Figure 3-12).

The non-polarised optical micrographs of the coke analogues (base and metallic iron 46µm) are given in Figures III-10 to III-21. The micrographs were acquired at 50x magnification using the horizontal and vertical approaches illustrated in Figures 3-12 and 3-13 respectively. The vertical approach (Figure 3-13) is reproduced in the following text. These magnification and approaches were adopted to ensure a wider area in both the horizontal and cross sectional views of the coke analogues (fired and post reacted) microstructure were characterised.

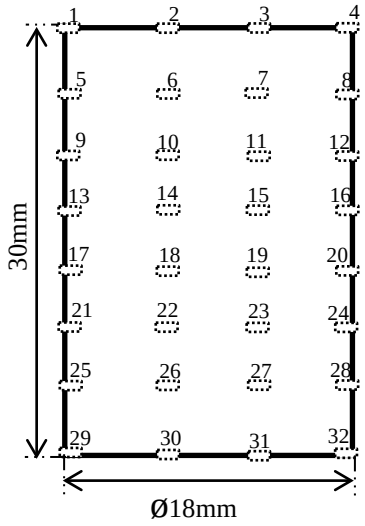

A schematic of the positions where the micrographs were taken on the sample vertical cross section. The boxes numbered 1–32 represent the approximate positions of the micrographs (Figure 3-13).

Given the uniformity of the coke analogues microstructure, only selected micrographs are labelled.

Key summary of the non-polarised optical microscopy

Figure III-1 shows the microstructure of the fired base coke analogue. The graphite grains in the base coke analogue appeared to be of similar size to the graphite powders (<45µm and <150µm particle size range) used to make it. The carbonised phenolic resin appeared to be of less obvious or little grain structure and associated with smaller sized pores. If there is a grain structure, it is likely to be <1µm in size and not resolved at the magnification used in this study. The size of the pores in the base coke analogue appeared to be in the range of 10–500µm.

Figures III-2 to III-8 show the microstructure of the fired coke analogues containing metallic iron and minerals. The graphite grains, carbonised phenolic resin and pores were similar to the base coke analogue. Iron (Fe) particles in the coke analogues (Figures III-2 to III-5) appeared to have sizes similar to the initial particle sizes (Figures 3-1(a) to 3-1(d)). The Fe particles are more rounded morphology than the original particle addition for metallic iron (Figure 3-1(b) and 3-1(c)) and magnetite (Figure 3-

1(d)), indicating they may have gone through a liquid Fe phase during coke analogue firing. There was evidence of graphite flake within the iron particles (Figures III-3 to III-5). It is difficult to resolve the morphology and graphite flake within the metallic iron with <10µm particle size at the magnification used in this study. Enstatite ferroan ($Mg_{1.56}Fe_{0.44}Si_2O_6$), phlogopite ferroan ($K(Mg,Fe)_3(Al,Fe)Si_3O_{10}(OH,F)_2$) and quartz ($SiO_2$) particles in the coke analogues (Figures III-6, III-7 and III-8 respectively) have sizes similar to the initial particle sizes (Figures 3-1(e), 3-1(f) and 3-1(g) respectively). They also have angular morphology similar to the initial angular morphology used to make the coke analogue.

Figure III-9 shows the microstructure of the metallurgical coke used in this study. The reactive maceral derived components (RMDC) appeared to have a grain structure with size of approximately 50µm or larger. The inert maceral derived component (IMDC) appeared to have a less obvious grain structure at the magnification used in this study. The IMDC is associated with minerals and smaller sized pores. The mineral phase in the metallurgical coke has high variability in their sizes, morphology and distribution.

Given the magnification used to characterise the microstructure of the coke analogues given in Figures III-10 to III-21, the particle size range of the graphite grains and metallic iron particles were not specified. The sizes of the graphite grains are expected to be similar to the initial graphite grains (<45µm and <150µm) used to make the coke analogue. The metallic iron particles are expected to have particle sizes similar to the initial particle size range (38–53µm) with a round morphology (relative to the initial morphology of agglomerated small spherical particles (Figure 3-1(b)).

Figures III-10 to III-12 and III-16 to III-18 show the microstructure of the fired and reacted (post experimental) base coke analogue in horizontal and vertical views respectively. The reactivity testing was carried out in CO_2 and arrested after 1 hour at two different temperatures of 950°C and 1025°C. The samples were reacted for only 1 hour to ensure its initial cylindrical shape was maintained. That is, to avoid the sample breaking up on transferring from the furnace alumina pedestal to sample container at

1025°C. The microstructure of the post reacted samples (Figures III-11, III-12 and III-17, III-18) was relatively similar to the microstructure of the fired sample (Figures III-10 and III-16), but there was evidence of preferential loss of carbonised phenolic resin compared to graphite grains (remaining only particles of the size similar to the particle size of the initial graphite used to make the coke analogue) in the post reacted samples. The preferential loss was evident at the external surface of the post reacted sample, but difficult to resolve closer to interior of the post reacted sample at the magnification used in the study.

Figures III-13 to III-15 and III-19 to III-21 show the microstructure of the fired and reacted (post experimental) coke analogue–metallic iron 46μm in horizontal and vertical views respectively. The reactivity testing was similar to the base coke analogue above. The microstructure of the post reacted samples (Figures III-14, III-15 and III-20, III-21) was similar to the microstructure of the fired sample (Figures III-13 and III-19), but there was evidence of preferential loss of carbonised phenolic resin (similar to the base coke analogue). There was an appearance of preferential loss of carbon around the iron particles. Furthermore, closer to the external surface of the post reacted samples, there were darker phase on the surface of the iron particles and is thought to be iron oxide (Figures III-14, III-15 and III-20, III-21).

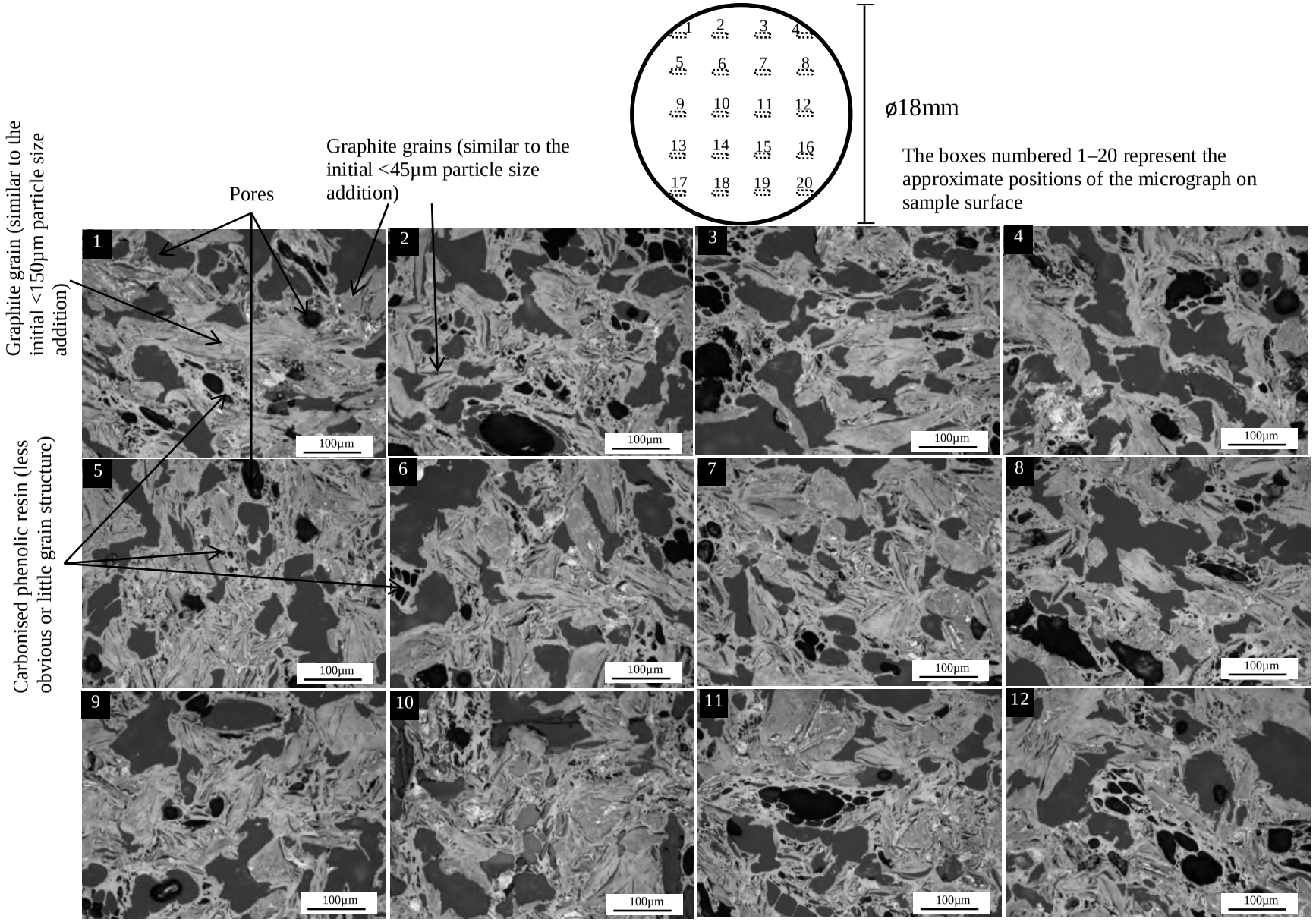

Figure III-1: The non-polarised optical micrographs of the fired base coke analogue.

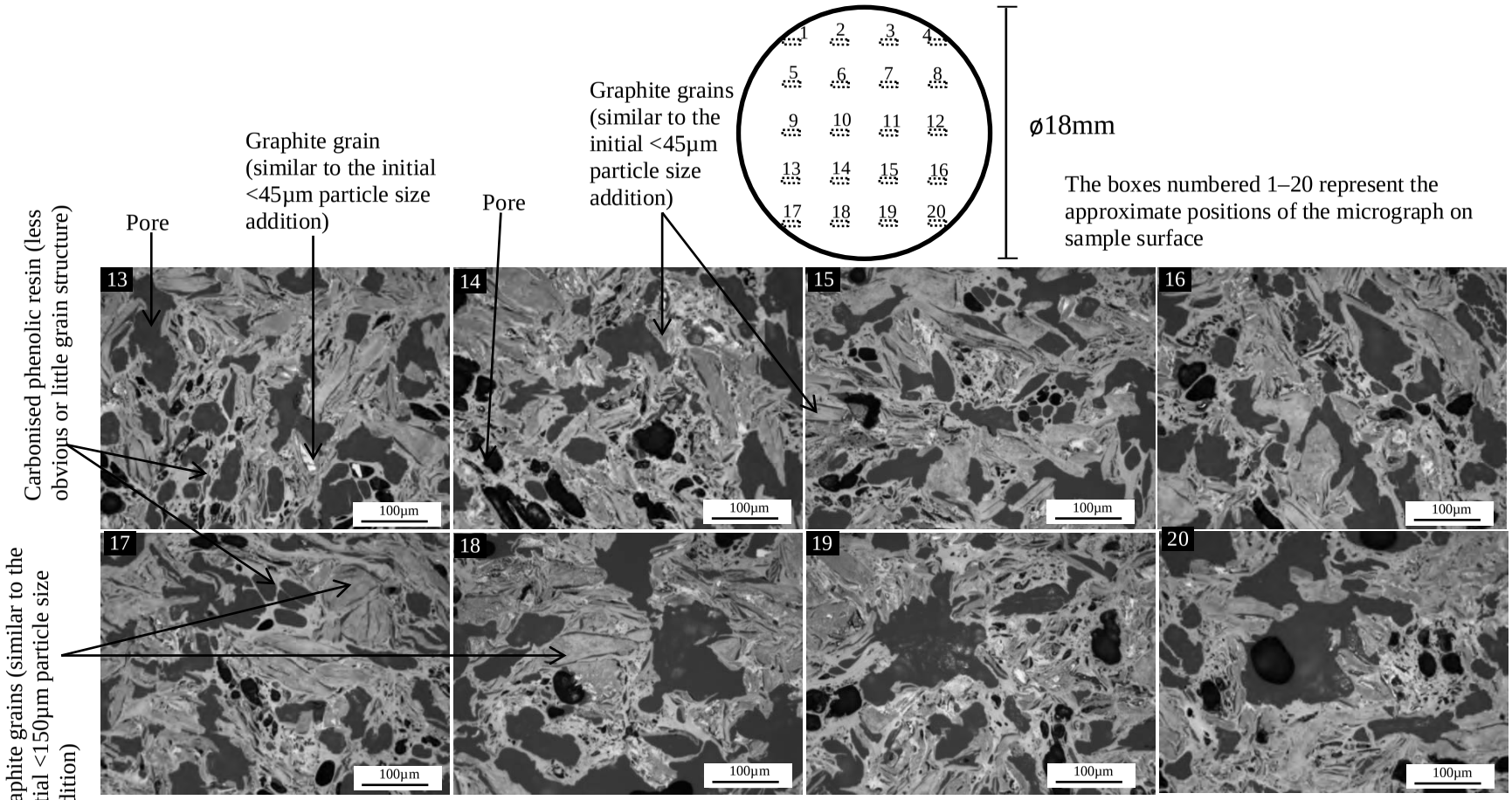

Figure III-1 (continued)**:** The non-polarised optical micrographs of the fired base coke analogue.

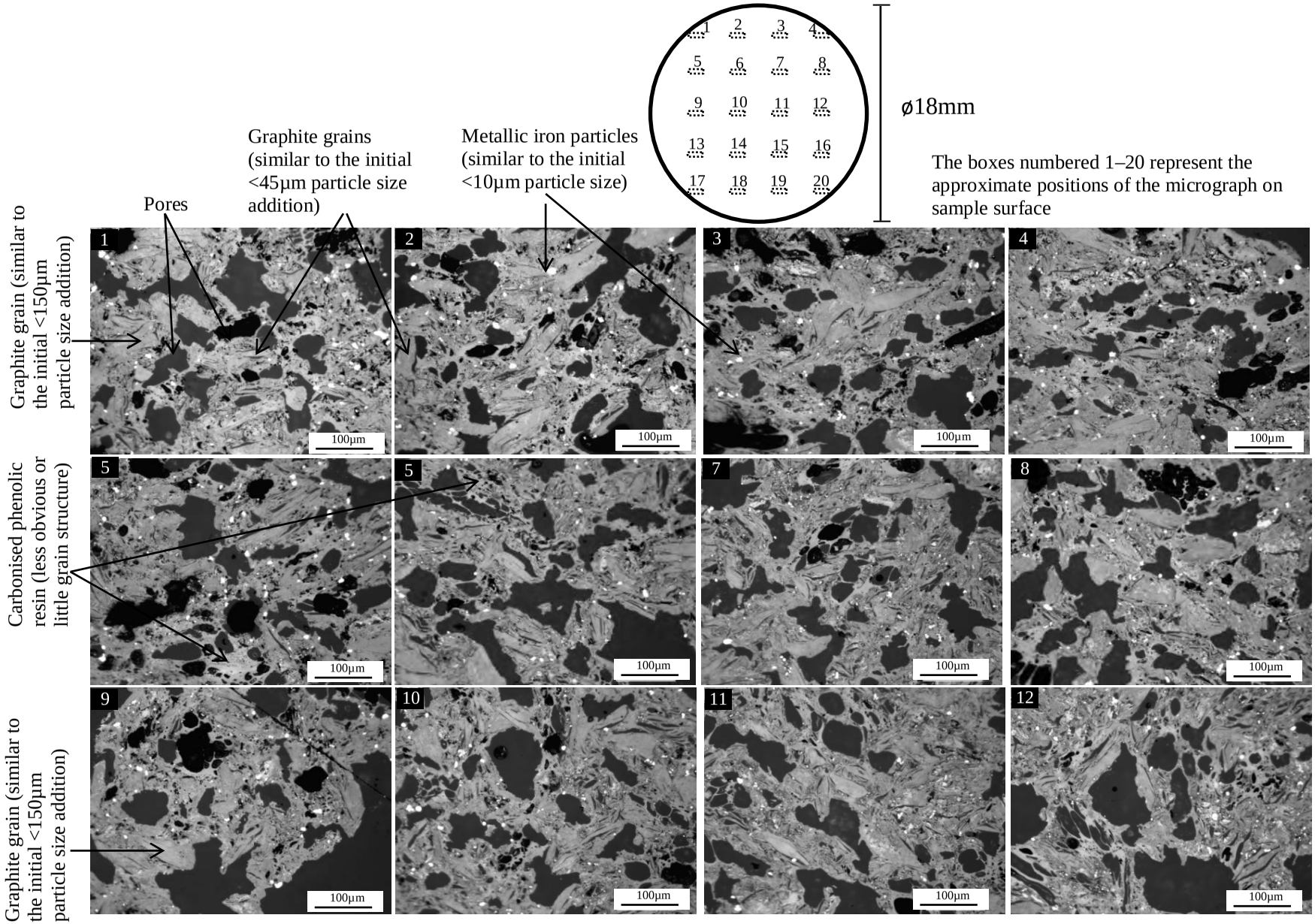

Figure III-2: The non-polarised optical micrographs of the fired coke analogue–metallic iron 5µm.

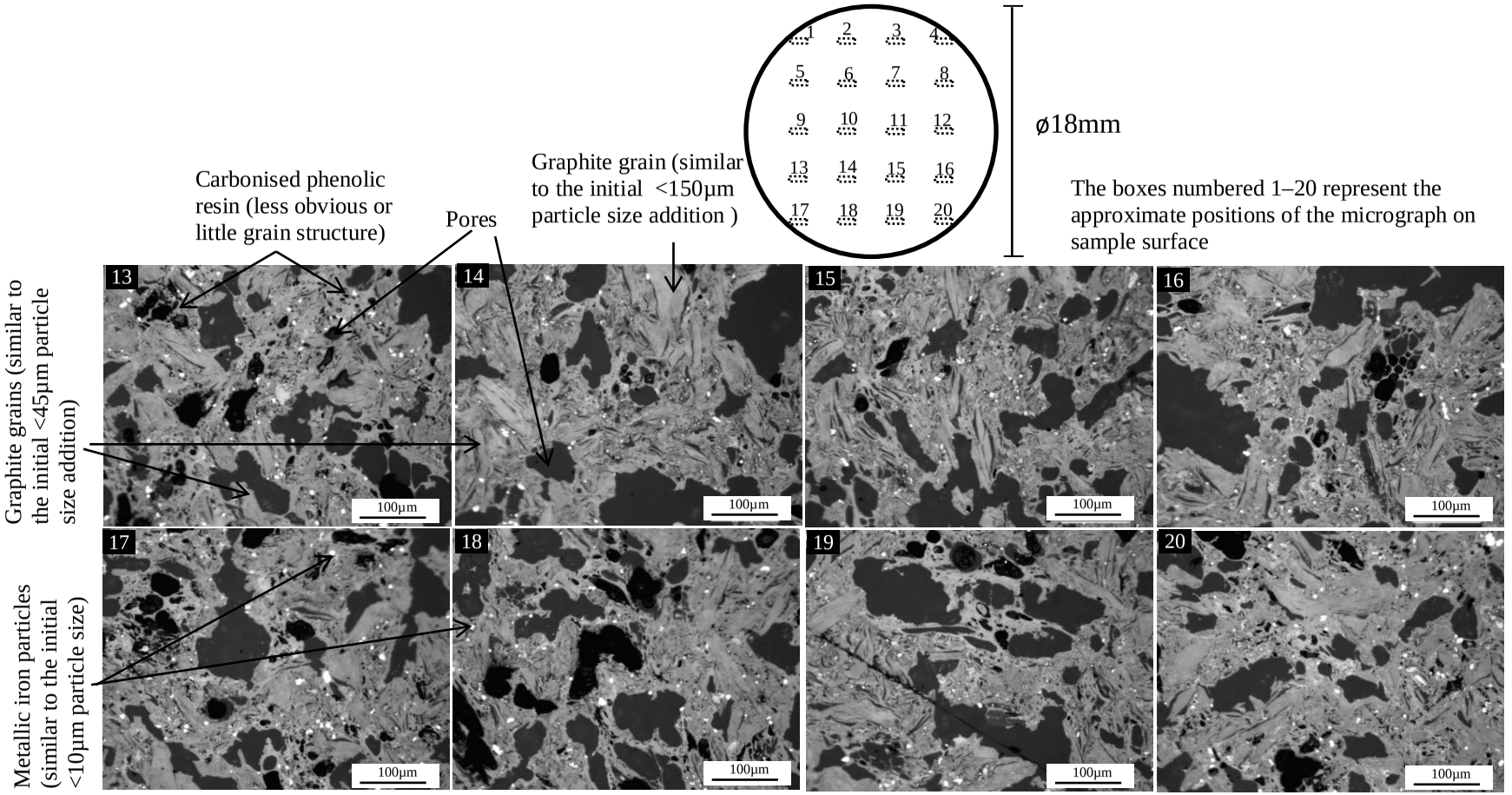

Figure III-2 (continued)**:** The non-polarised optical micrographs of the fired coke analogue–metallic iron 5µm.

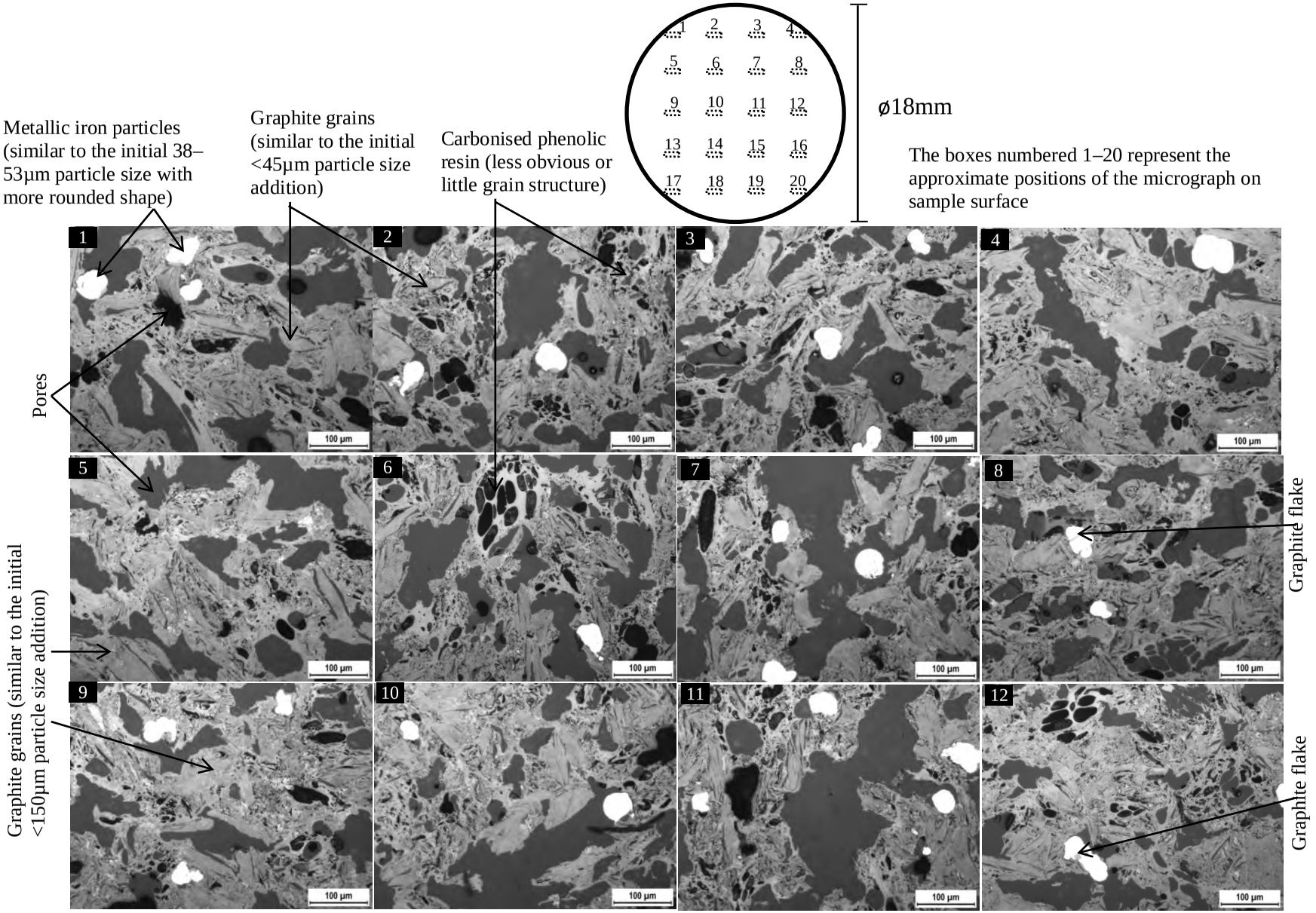

Figure III-3: The non-polarised optical micrographs of the fired coke analogue–metallic iron 46µm.

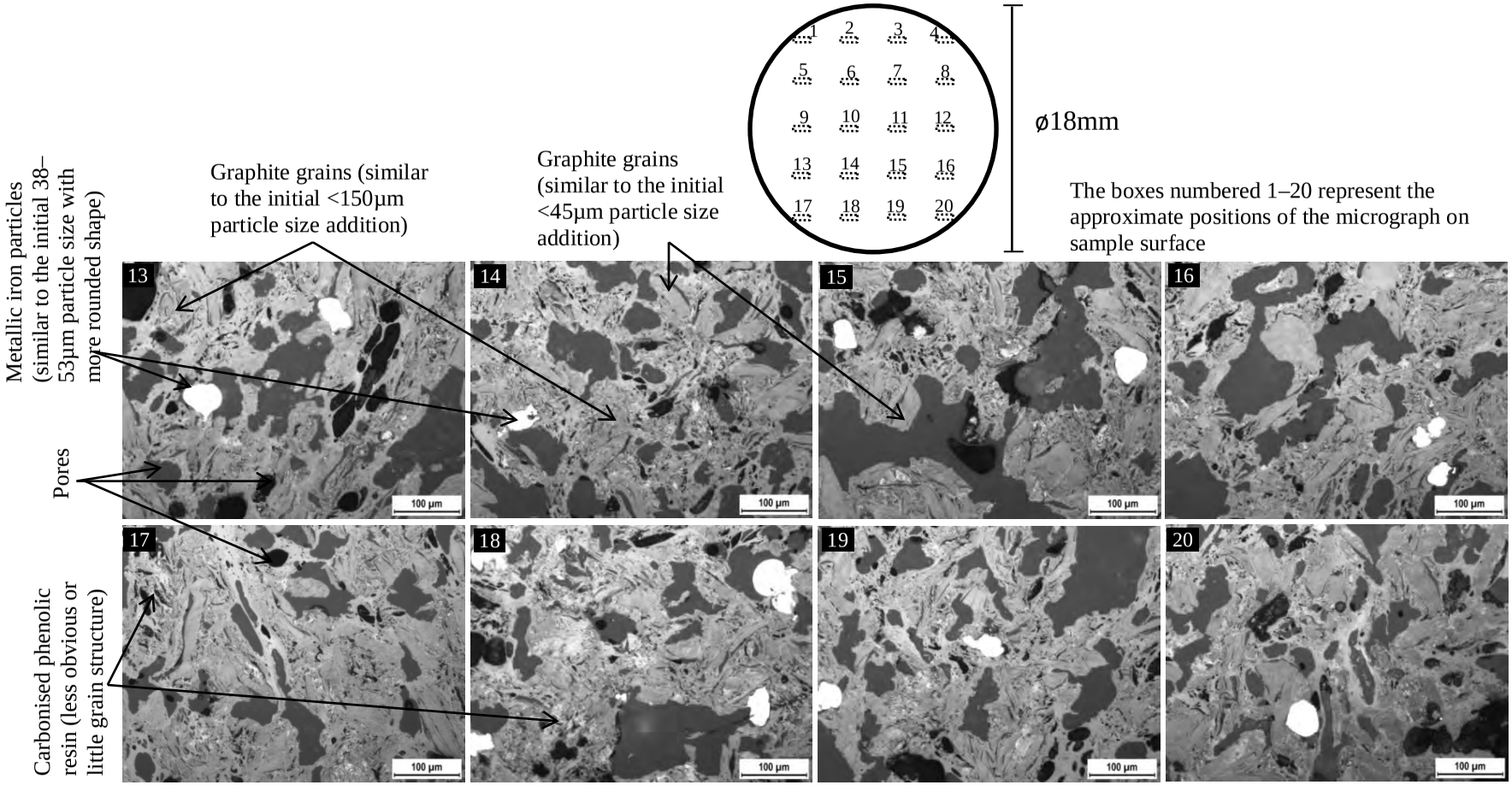

Figure III-3 (continued)**:** The non-polarised optical micrographs of the fired coke analogue–metallic iron 46µm.

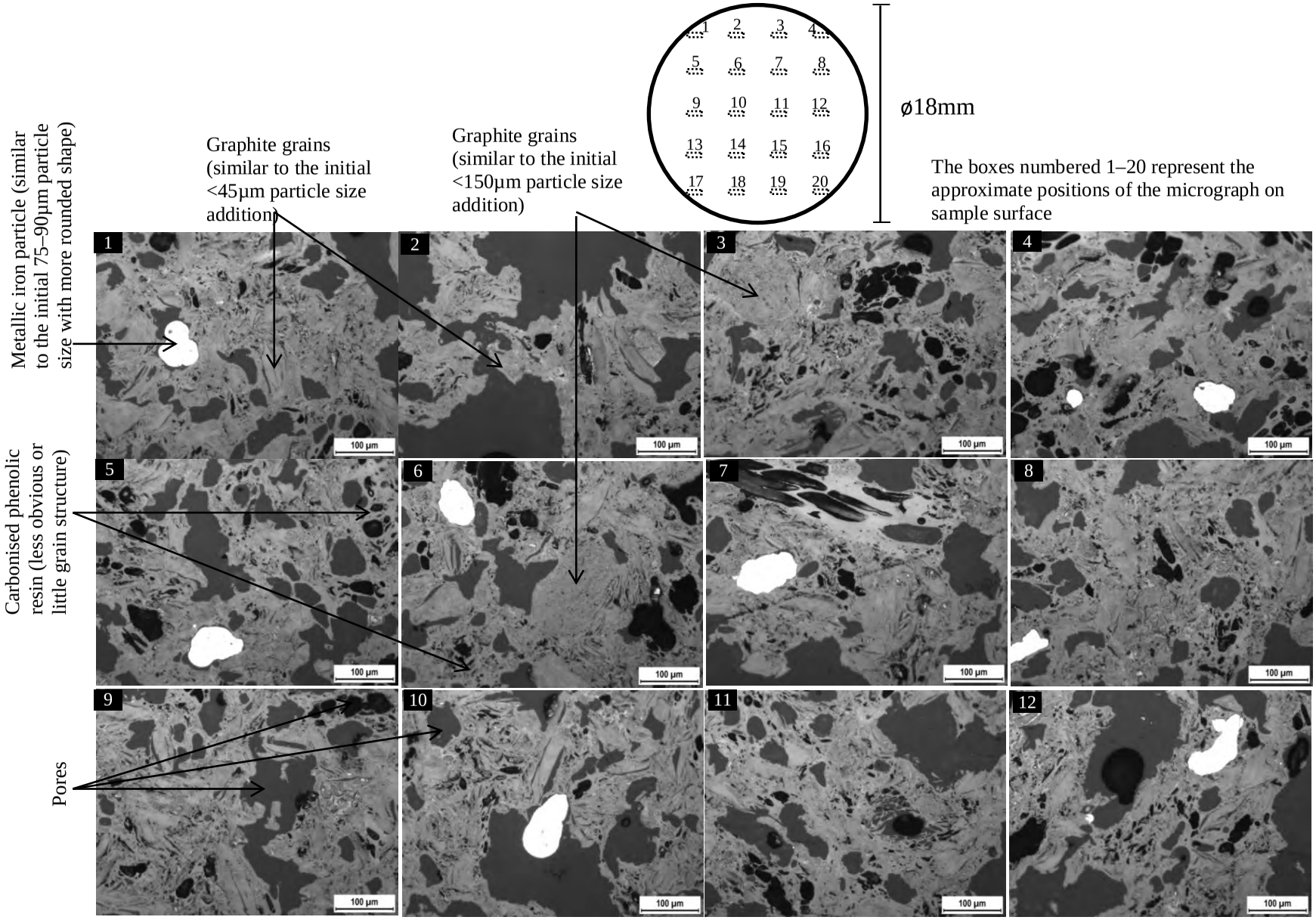

Figure III-4 The non-polarised optical micrographs of the fired coke analogue–metallic iron 83µm.

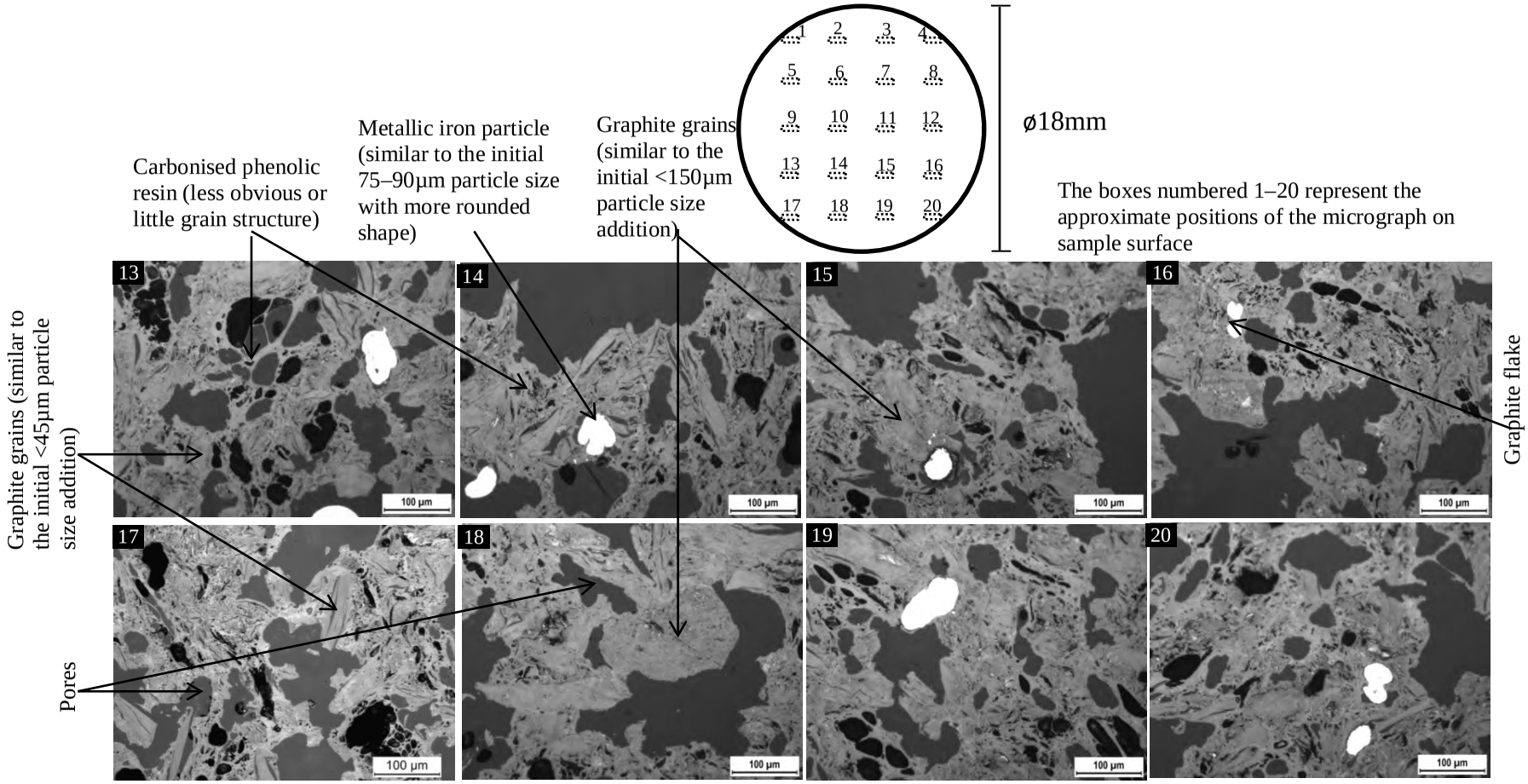

Figure III-4 (continued)**:** The non-polarised optical micrographs of the fired coke analogue–metallic iron 83µm.

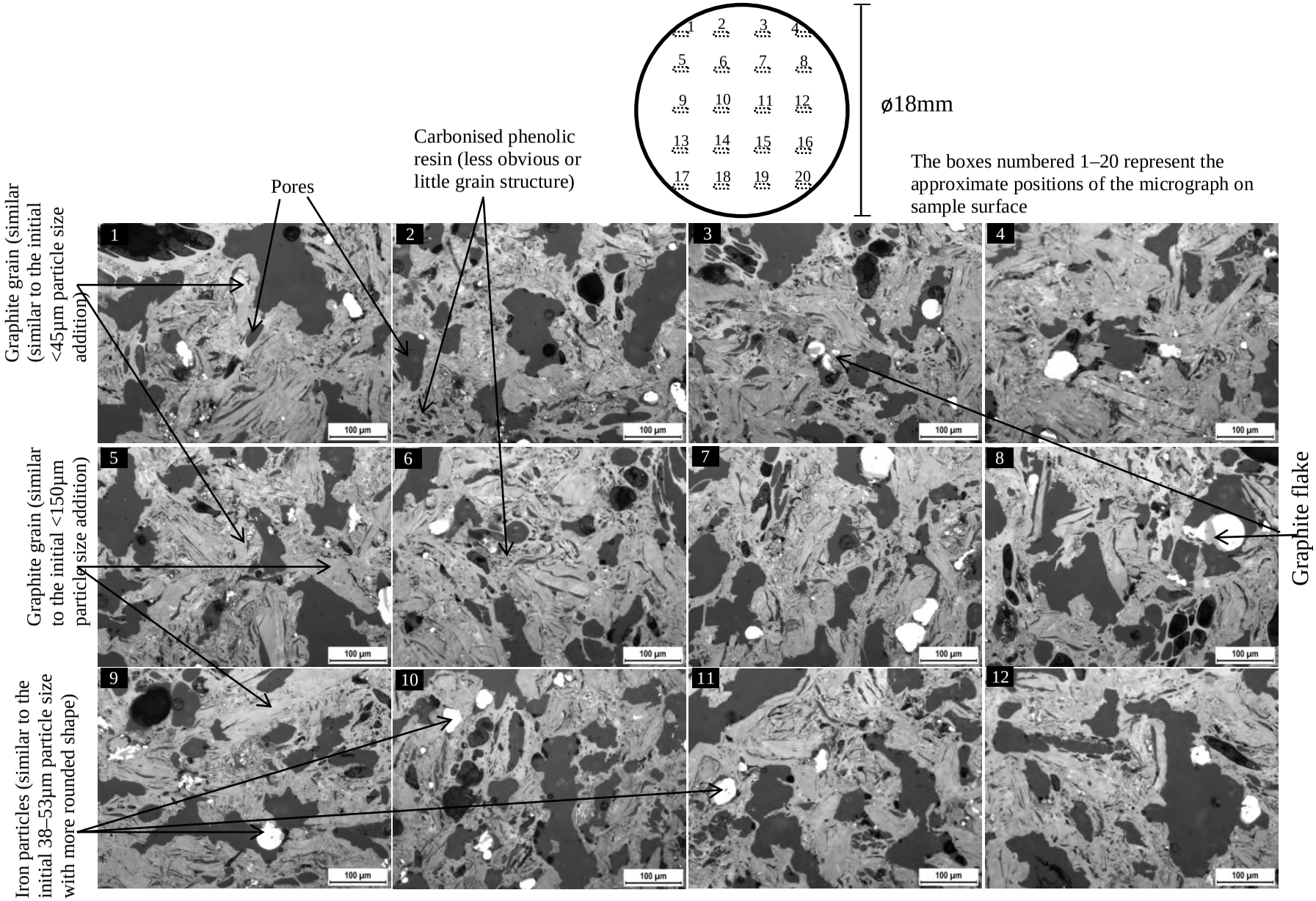

Figure III-5: The non-polarised optical micrographs of the fired coke analogue–magnetite 46µm.

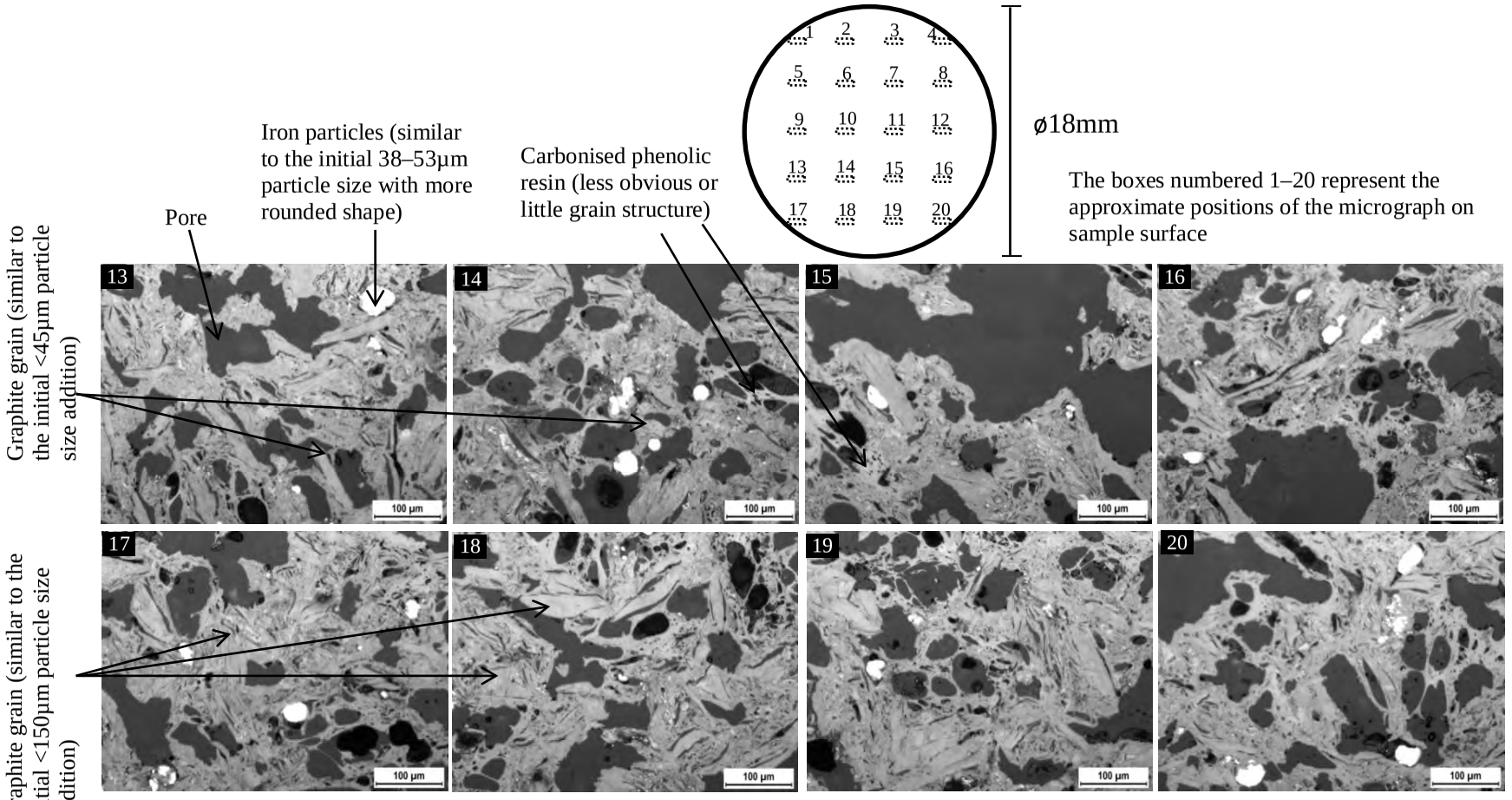

Figure III-5 (continued)**:** The non-polarised optical micrographs of the fired coke analogue–magnetite 46µm.

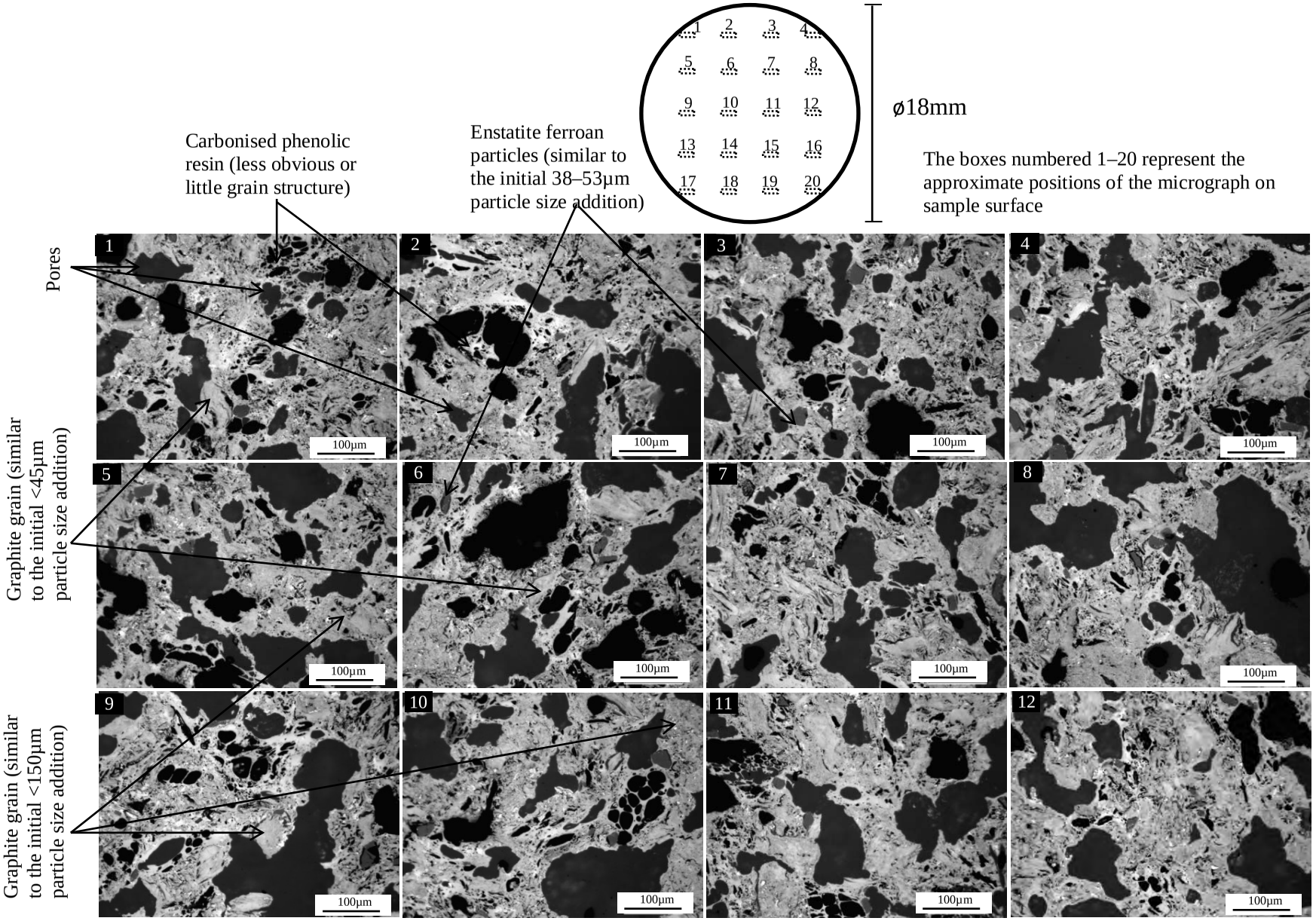

Figure III-6: The non-polarised optical micrographs of the fired coke analogue–enstatite ferroan.

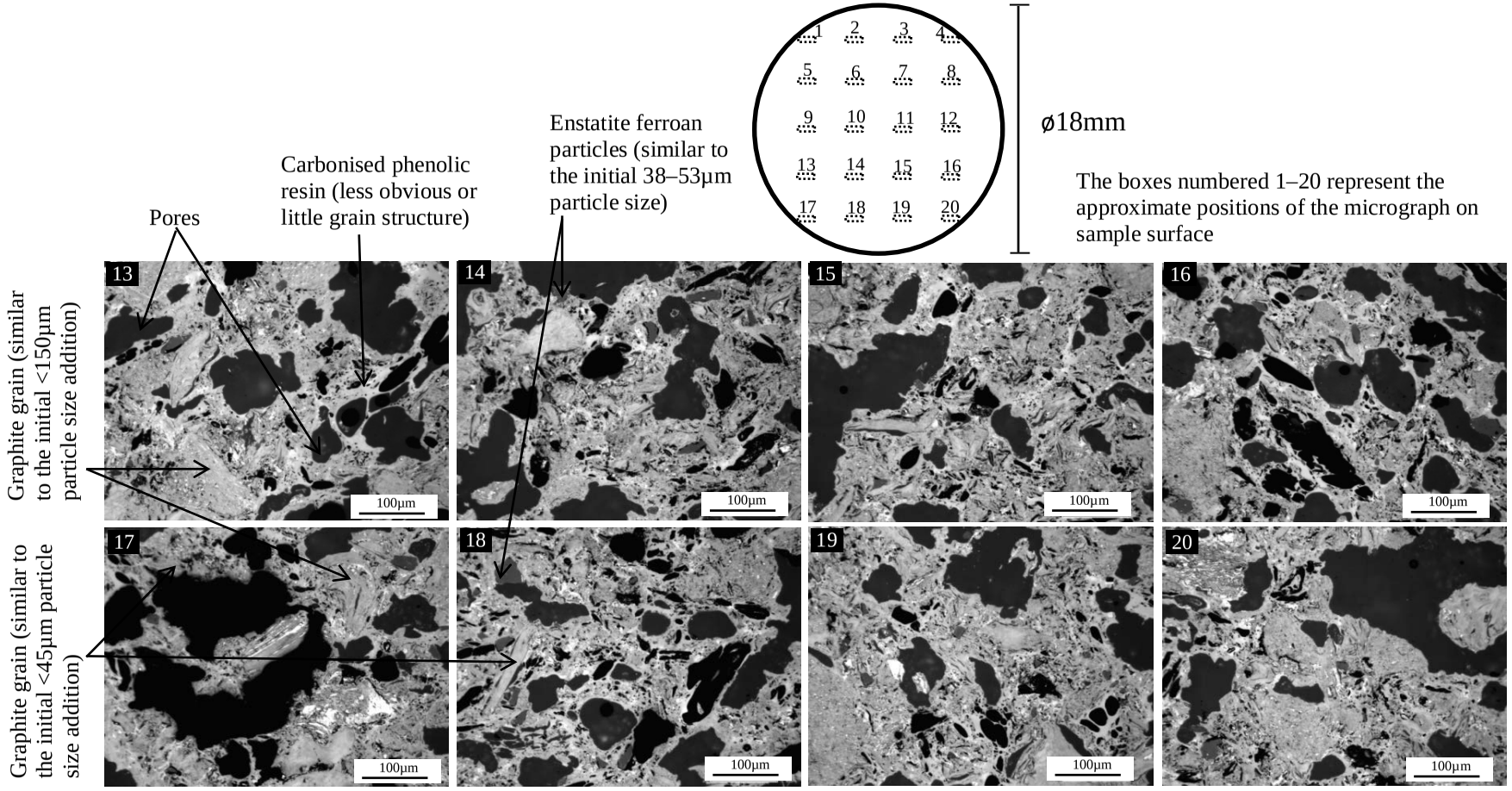

Figure III-6 (continued)**:** The non-polarised optical micrographs of the fired coke analogue–enstatite ferroan.

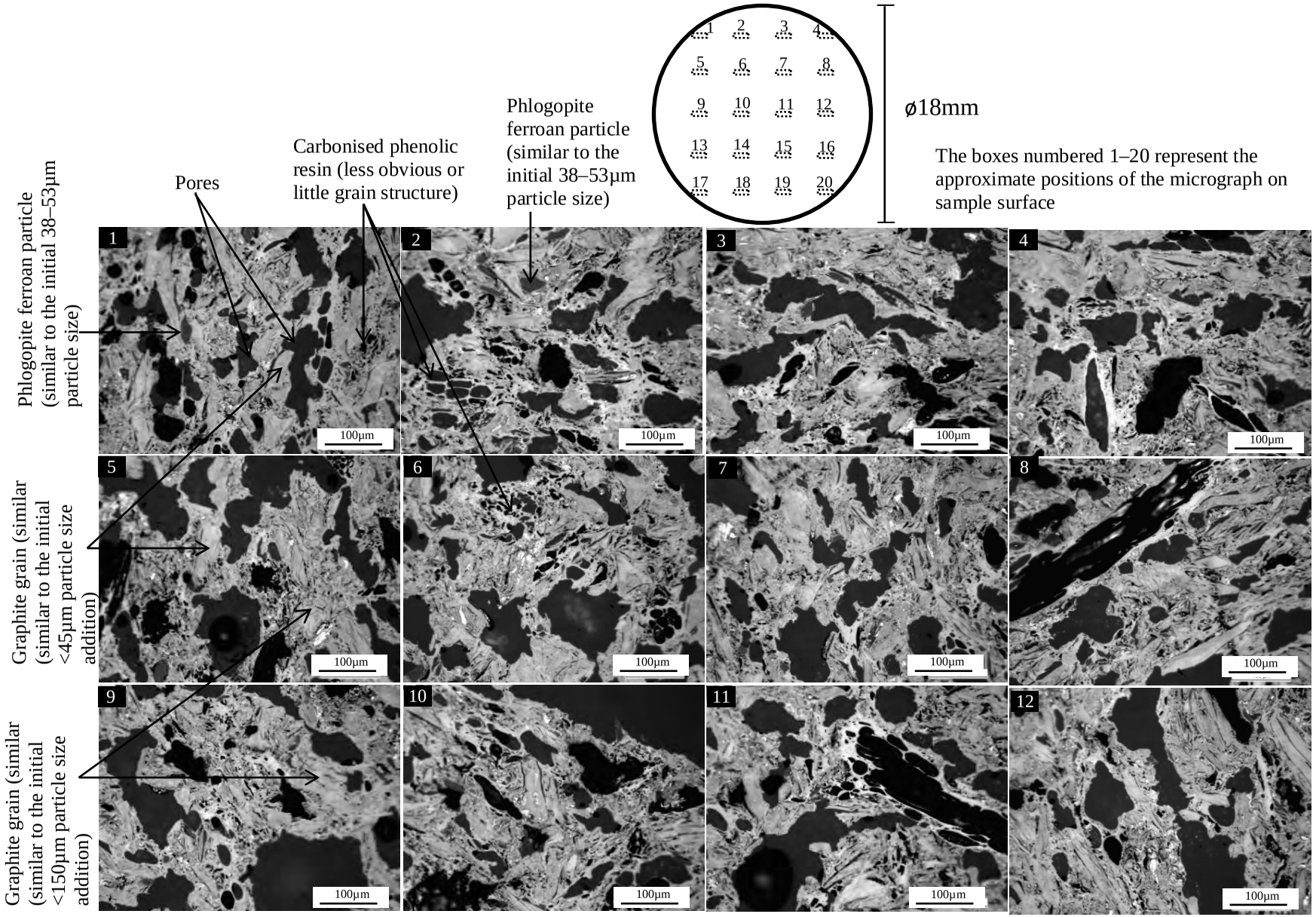

Figure III-7: The non-polarised optical micrographs of the fired coke analogue–phlogopite ferroan.

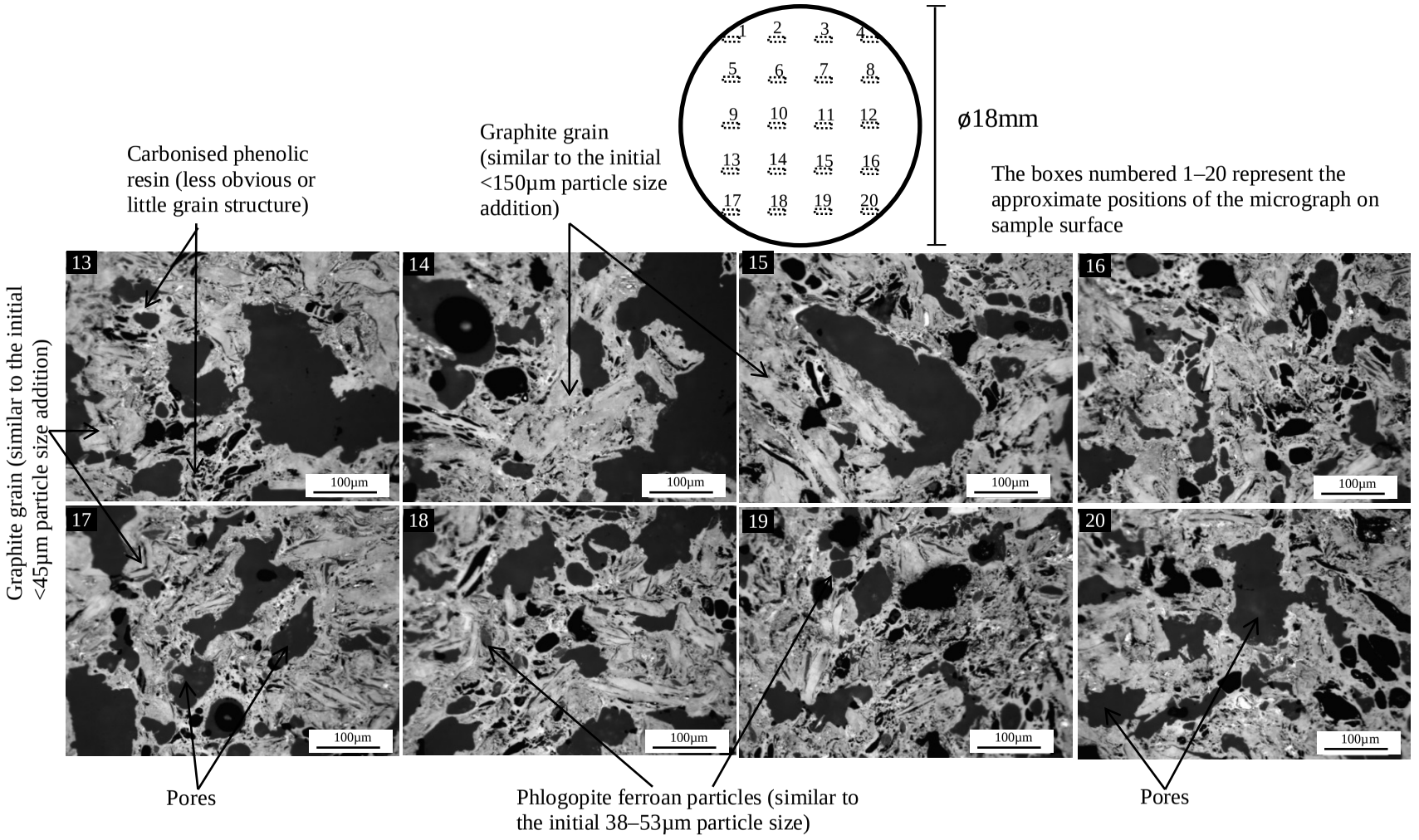

Figure III-7 (continued)**:** The non-polarised optical micrographs of the fired coke analogue–phlogopite ferroan.

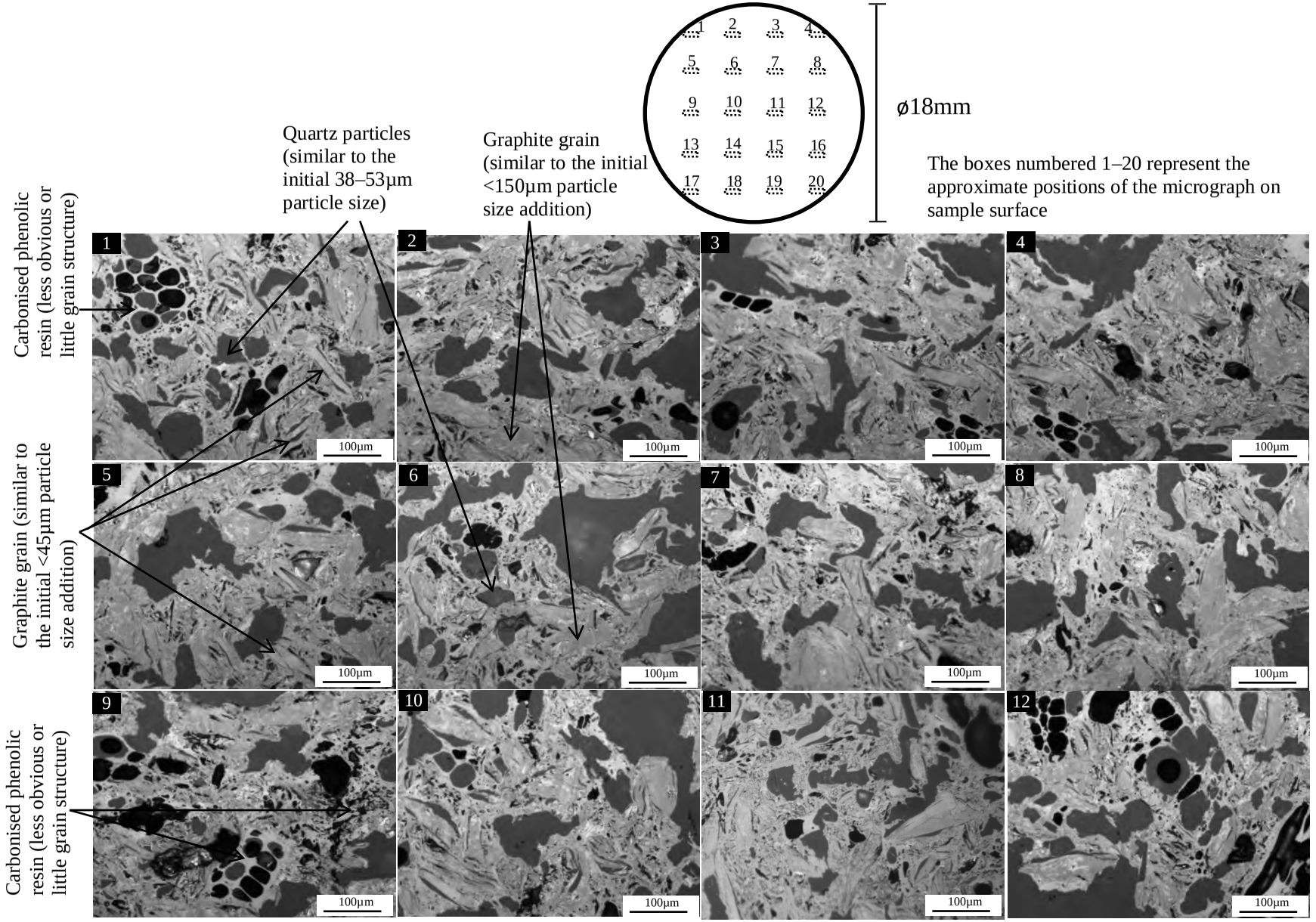

Figure III-8: The non-polarised optical micrographs of the fired coke analogue–quartz.

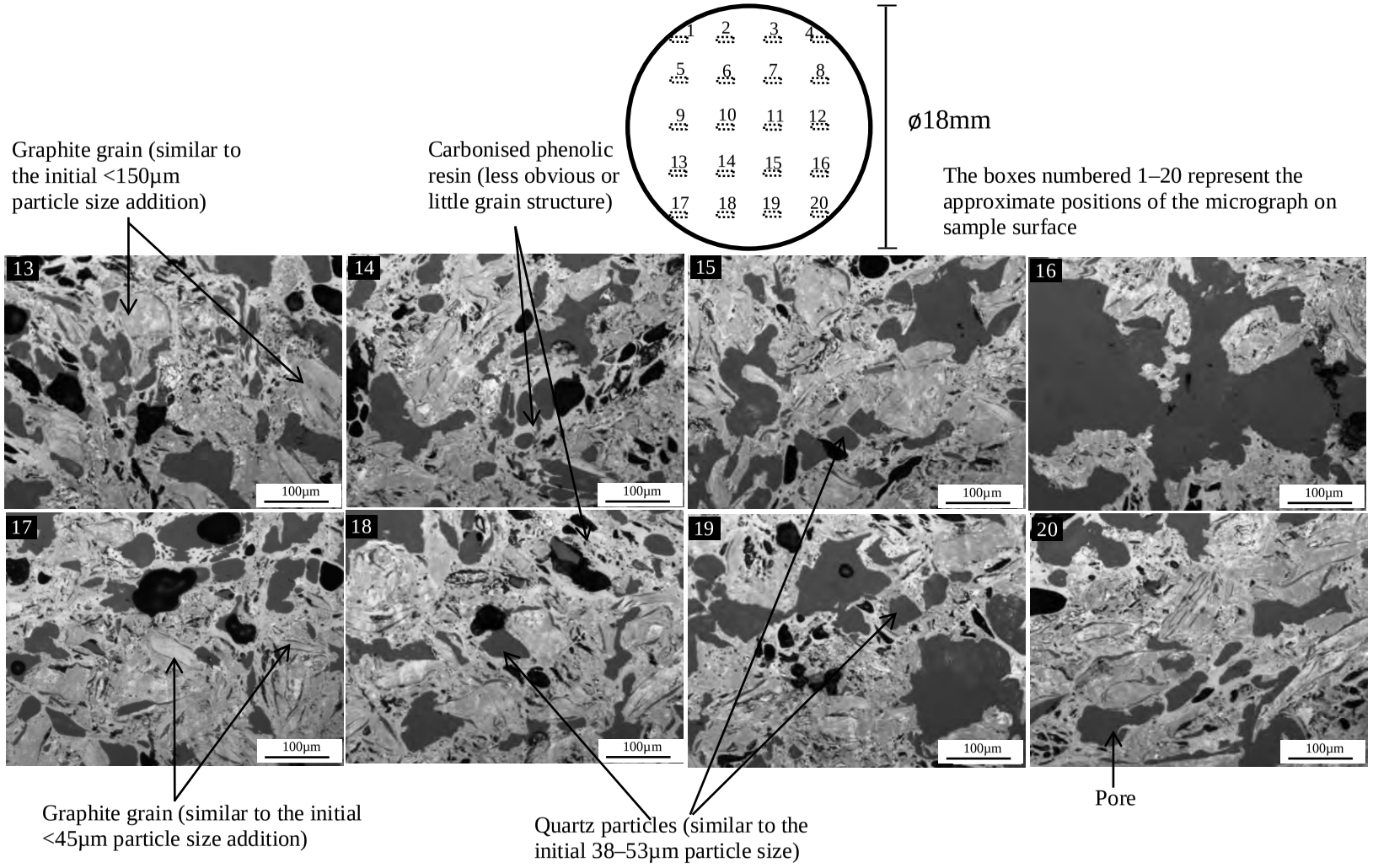

Figure III-8 (continued)**:** The non-polarised optical micrographs of the fired coke analogue–quartz.

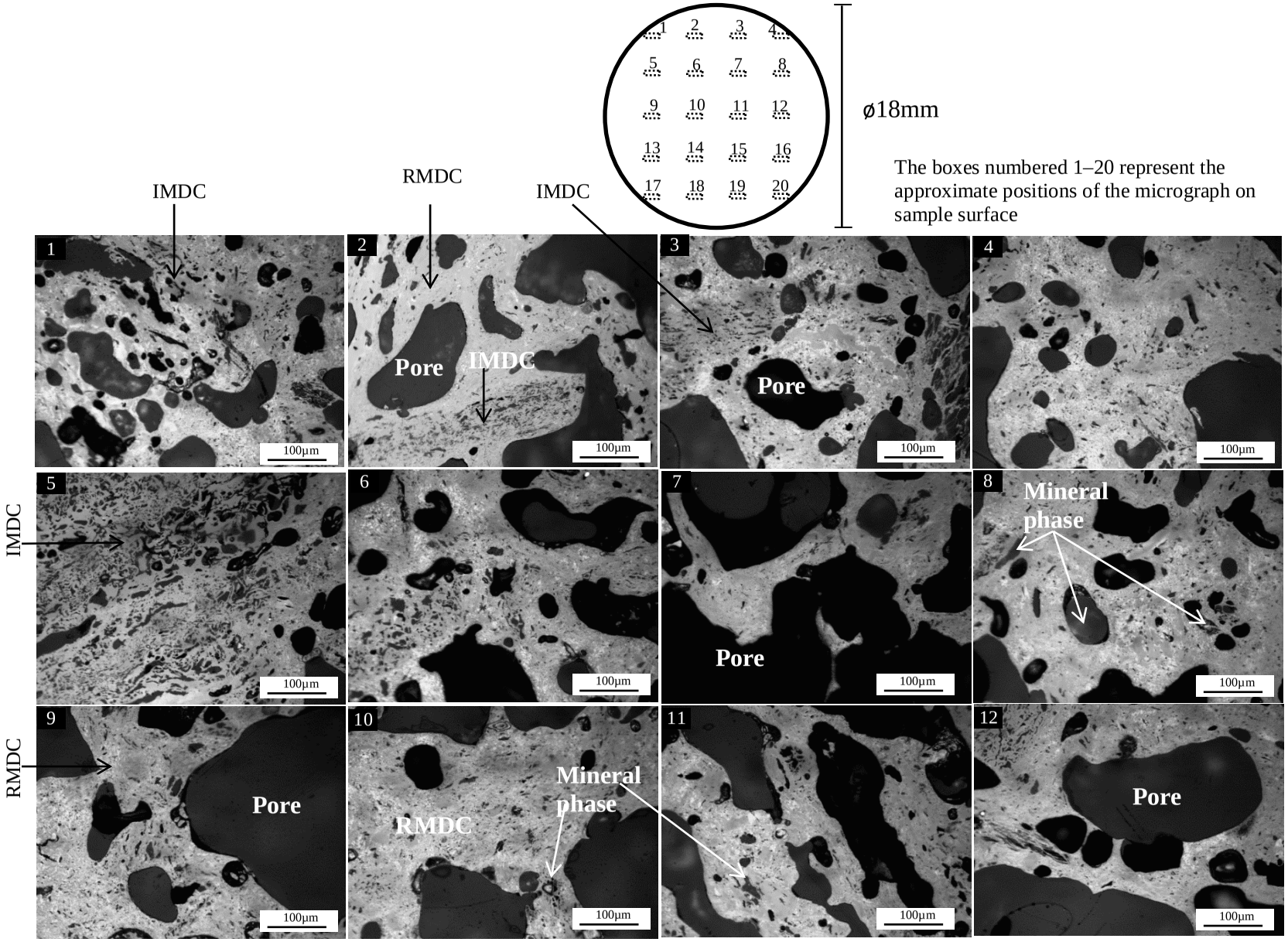

Figure III-9: The non-polarised optical micrographs of the metallurgical coke.

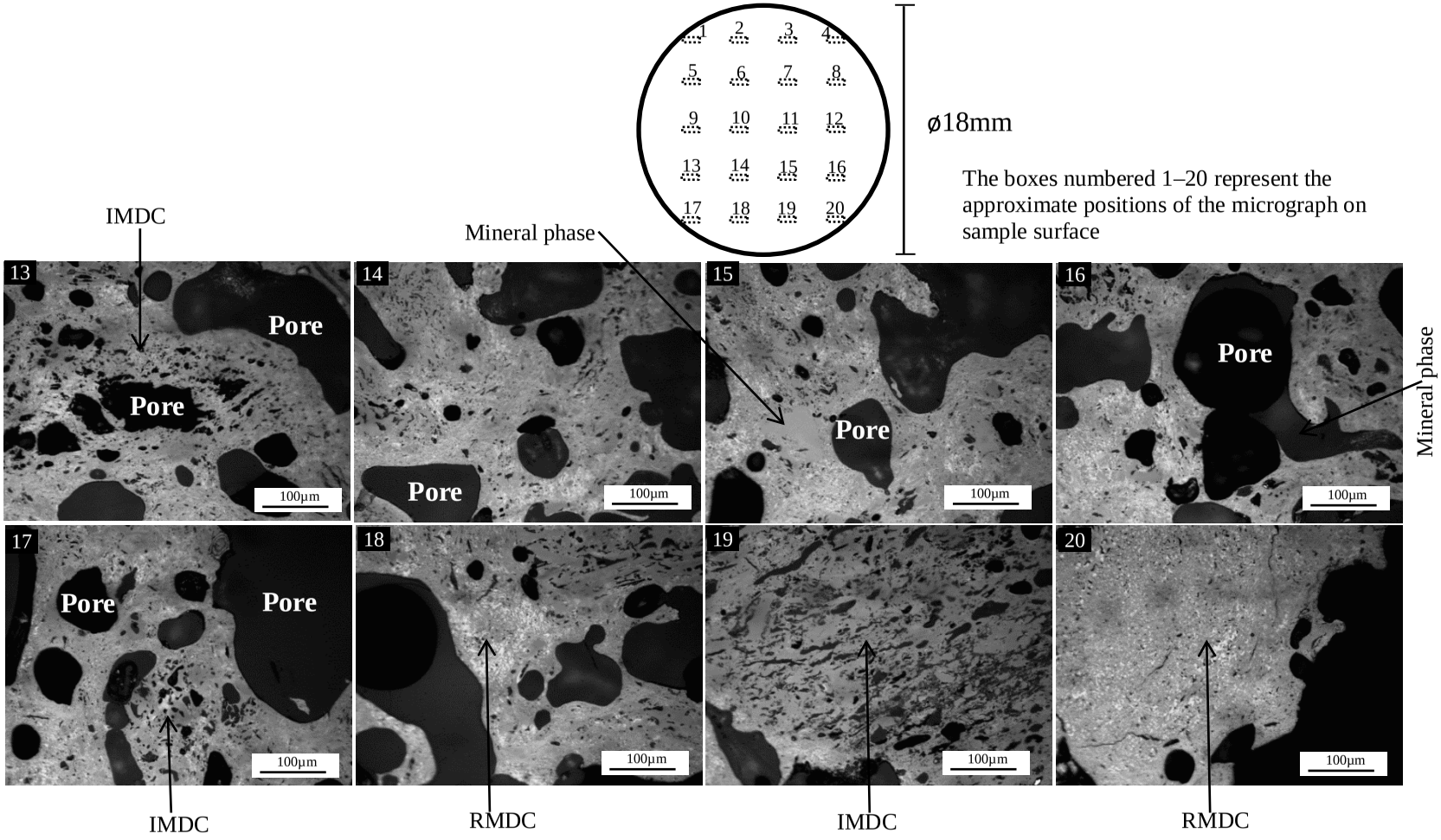

Figure III-9 (continued)**:** The non-polarised optical micrographs of the metallurgical coke.

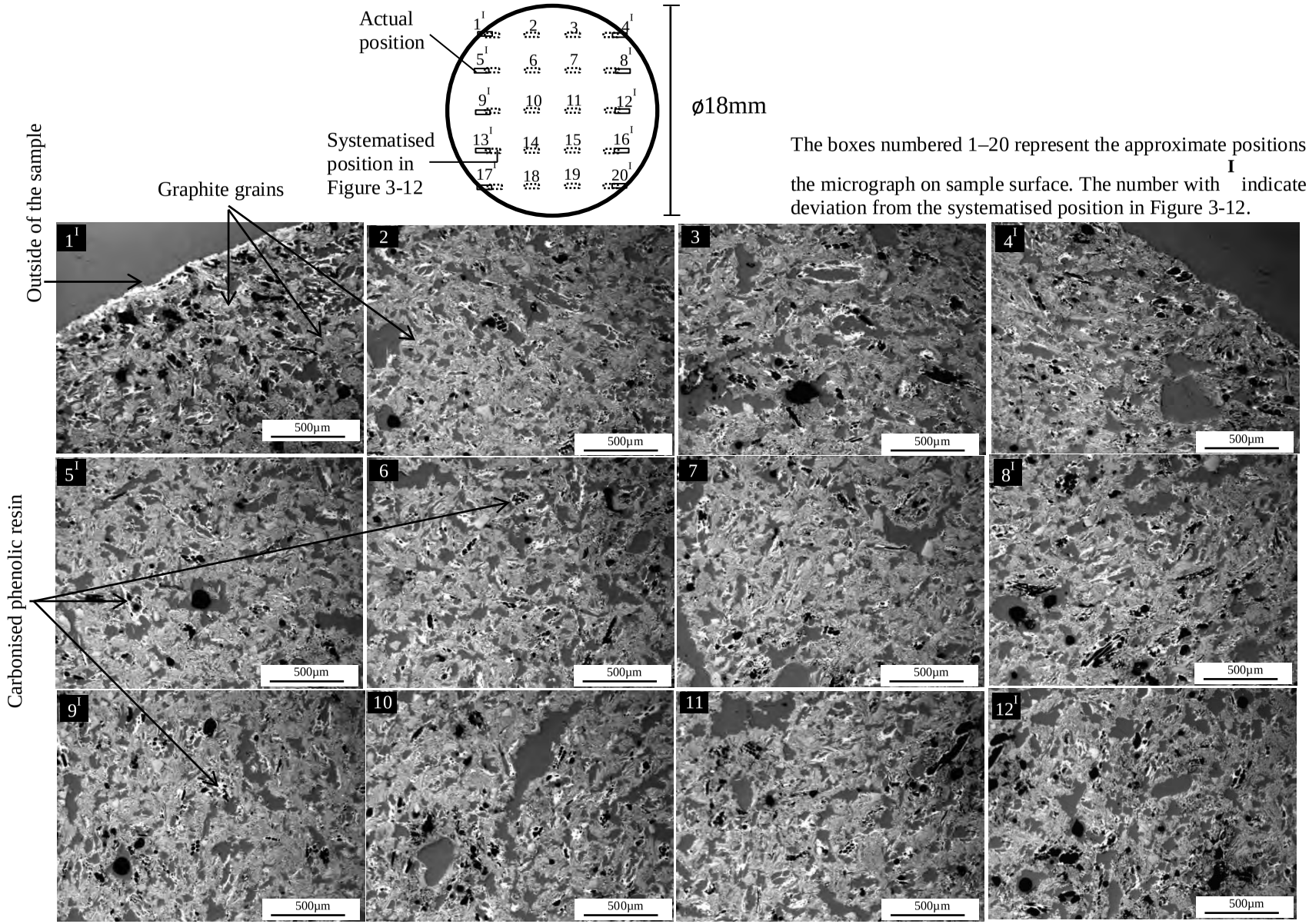

Figure III-10: The non-polarised optical micrographs of the fired base coke analogue, in horizontal view.

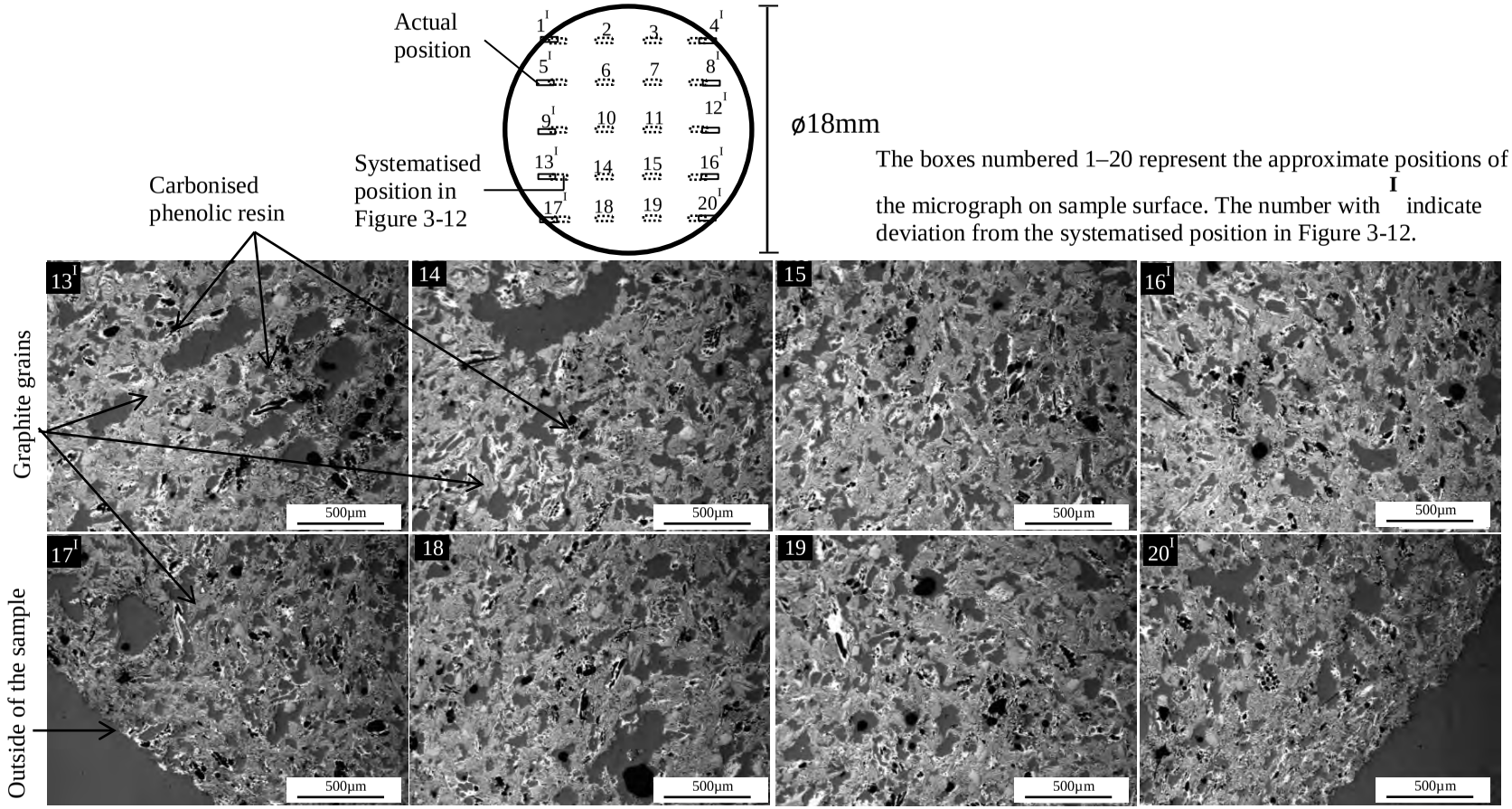

Figure III-10 (continued)**:** The non-polarised optical micrographs of the fired base coke analogue, in horizontal view.

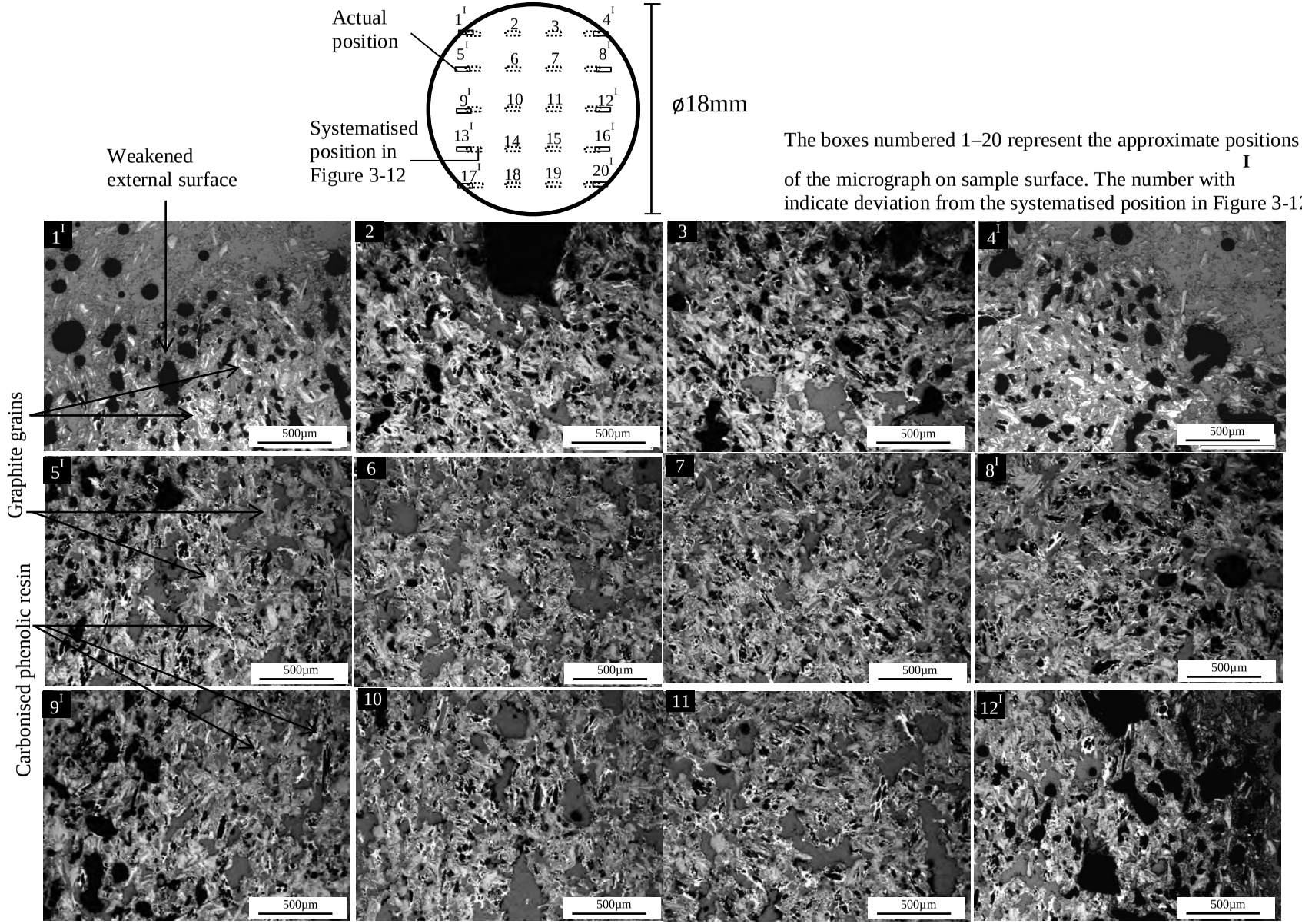

Figure III-11: The non-polarised optical micrographs of the post reacted base coke analogue, in CO_2 at 950°C for 1 hour, horizontal view.

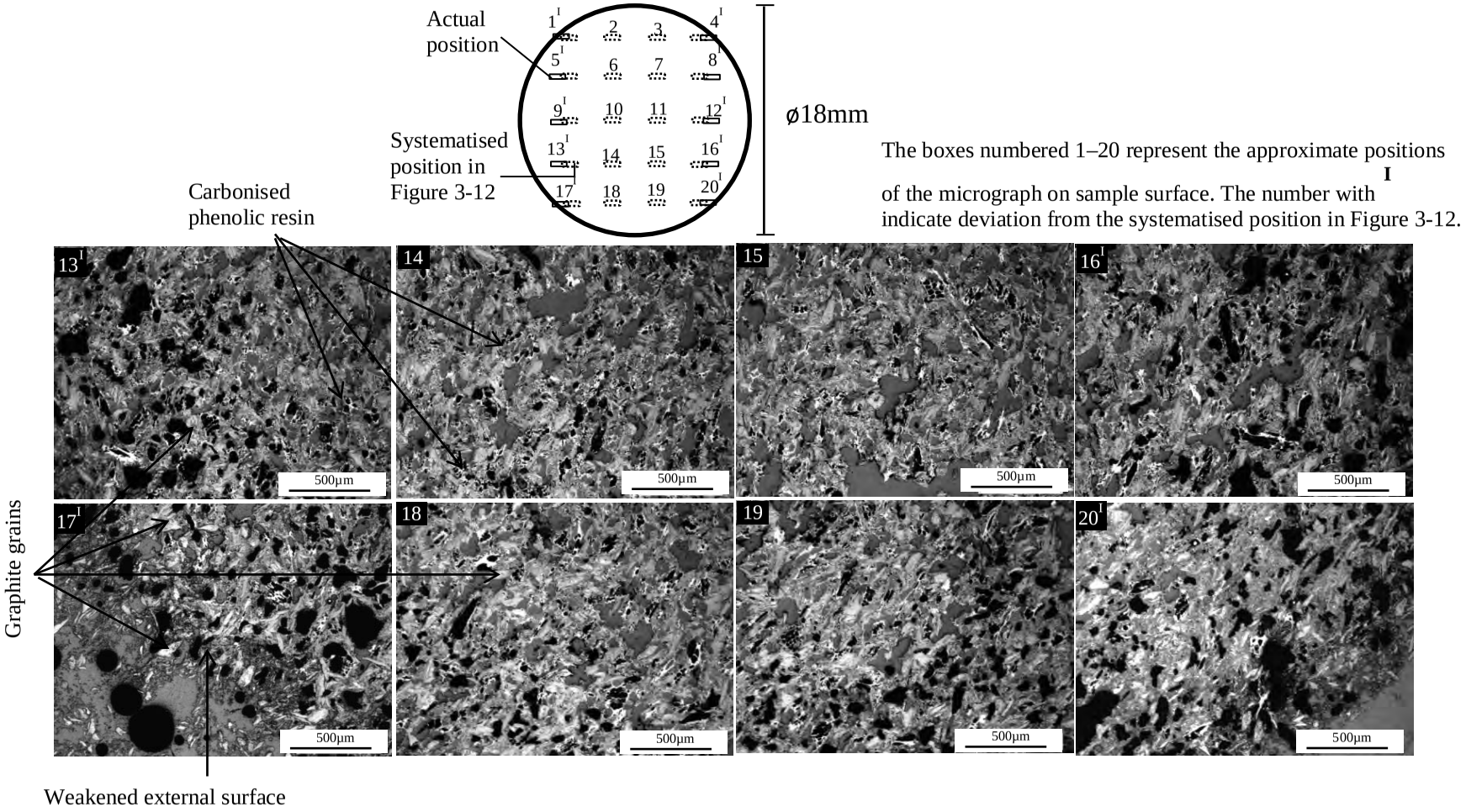

Figure III-11 (continued)**:** The non-polarized optical micrographs of the post reacted base coke analogue, in CO_2 at 950°C for 1 hour, horizontal view.

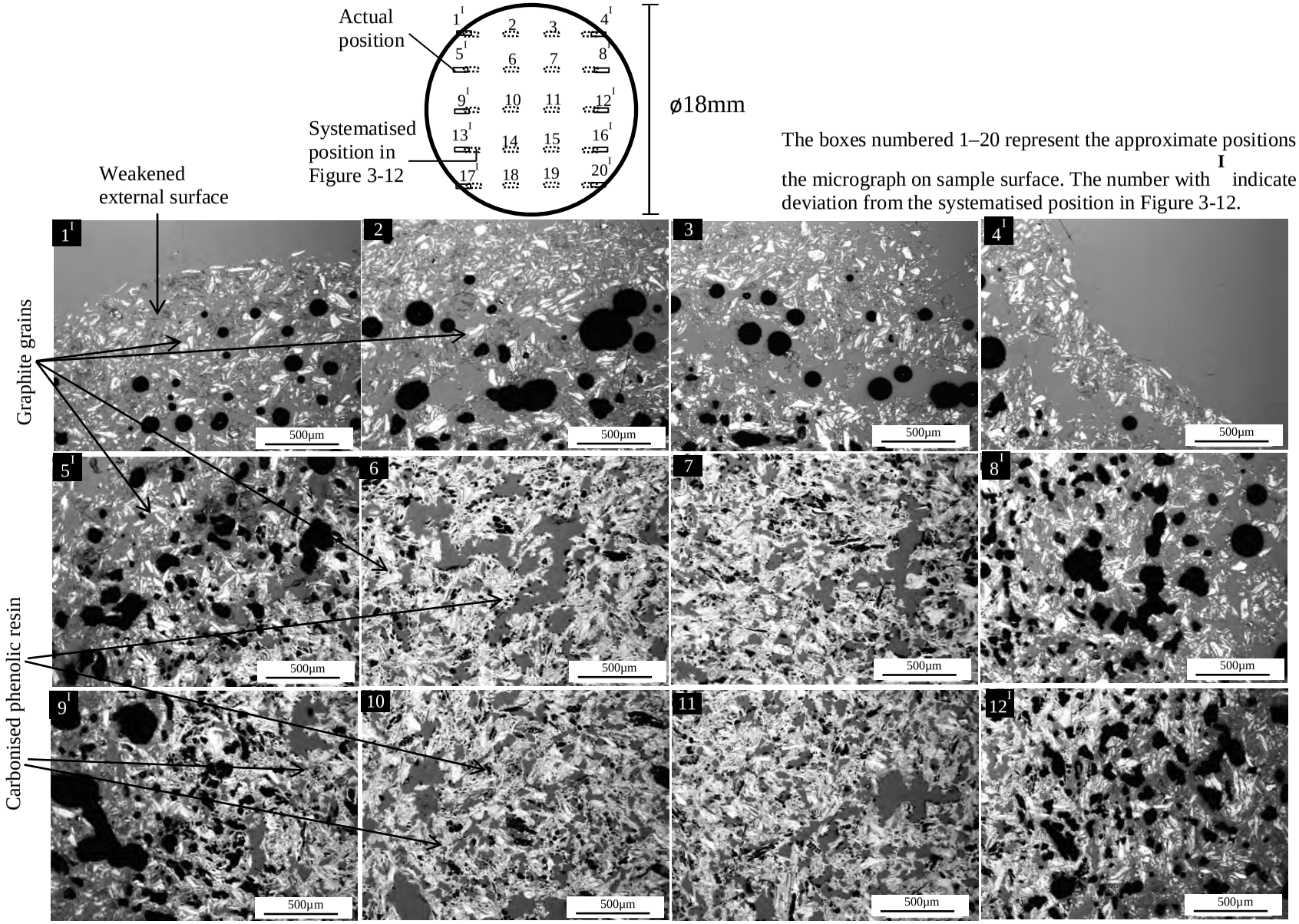

Figure III-12: The non-polarised optical micrographs of the post reacted base coke analogue, in CO_2 at 1025°C for 1 hour, horizontal view.

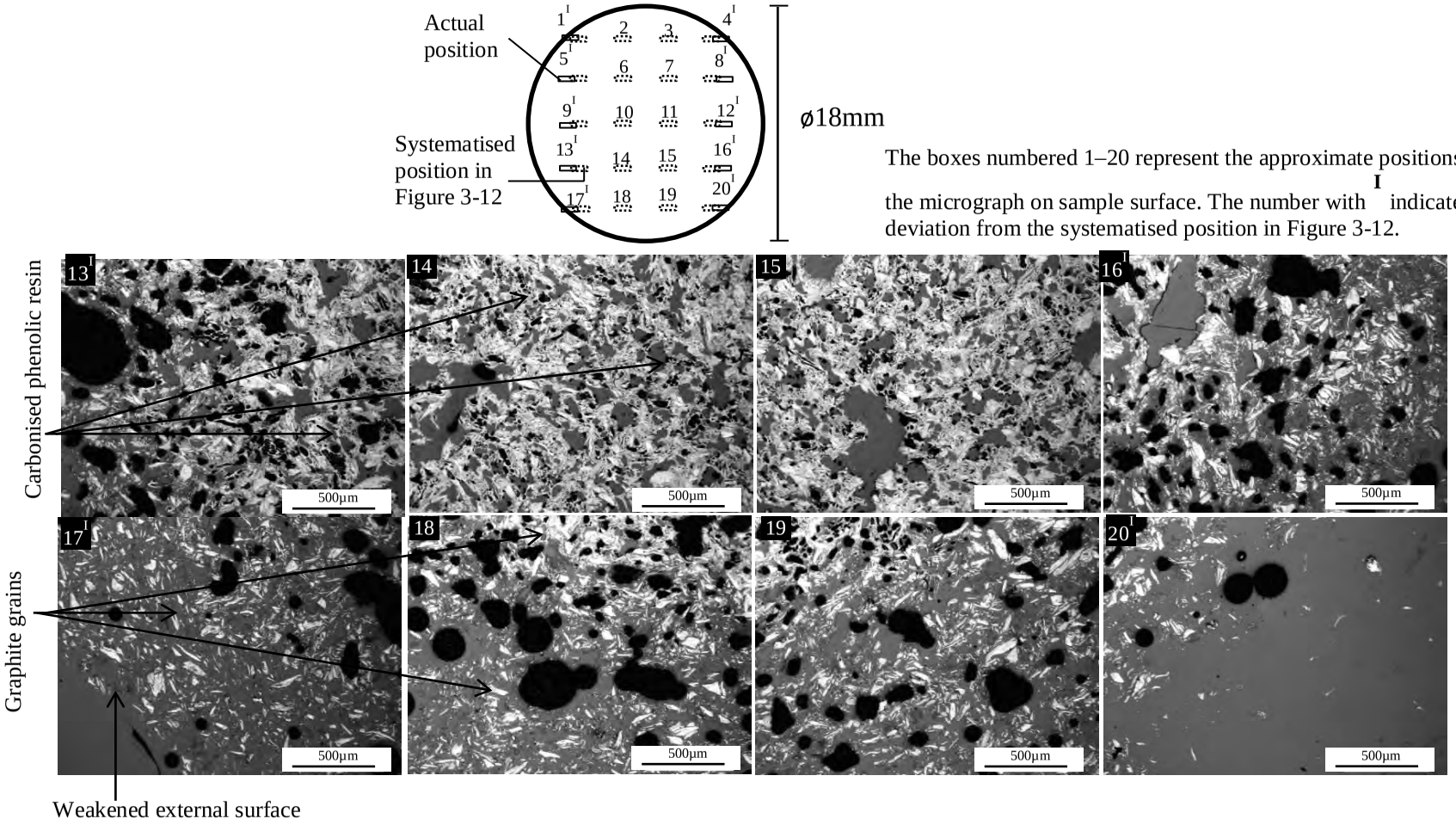

Figure III-12 (continued)**:** The non-polarised optical micrographs of the post reacted base coke analogue, in CO_2 at 1025°C for 1 hour, horizontal view.

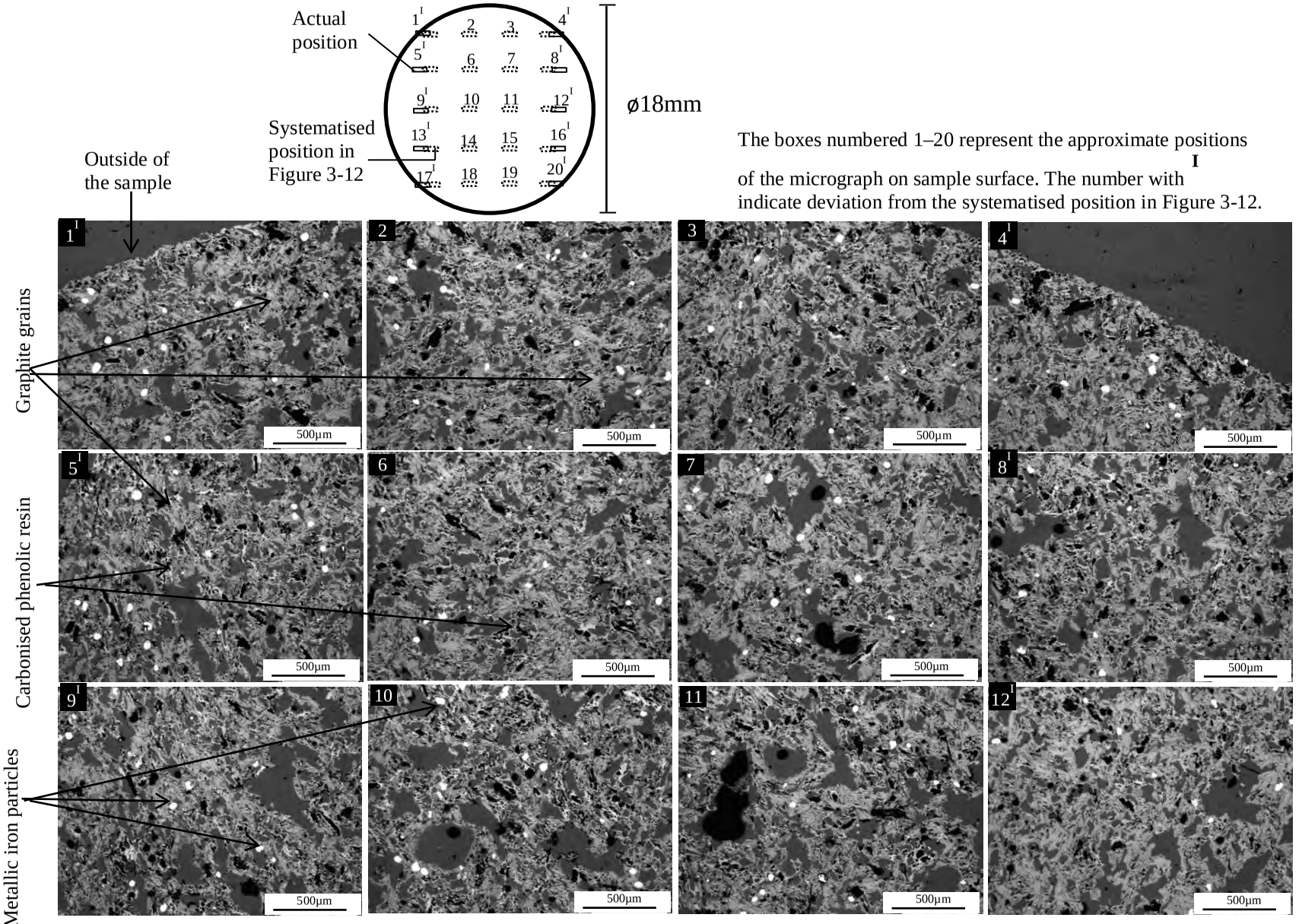

Figure III-13: The non-polarised optical micrographs of the fired coke analogue–metallic iron 46µm, in horizontal view.

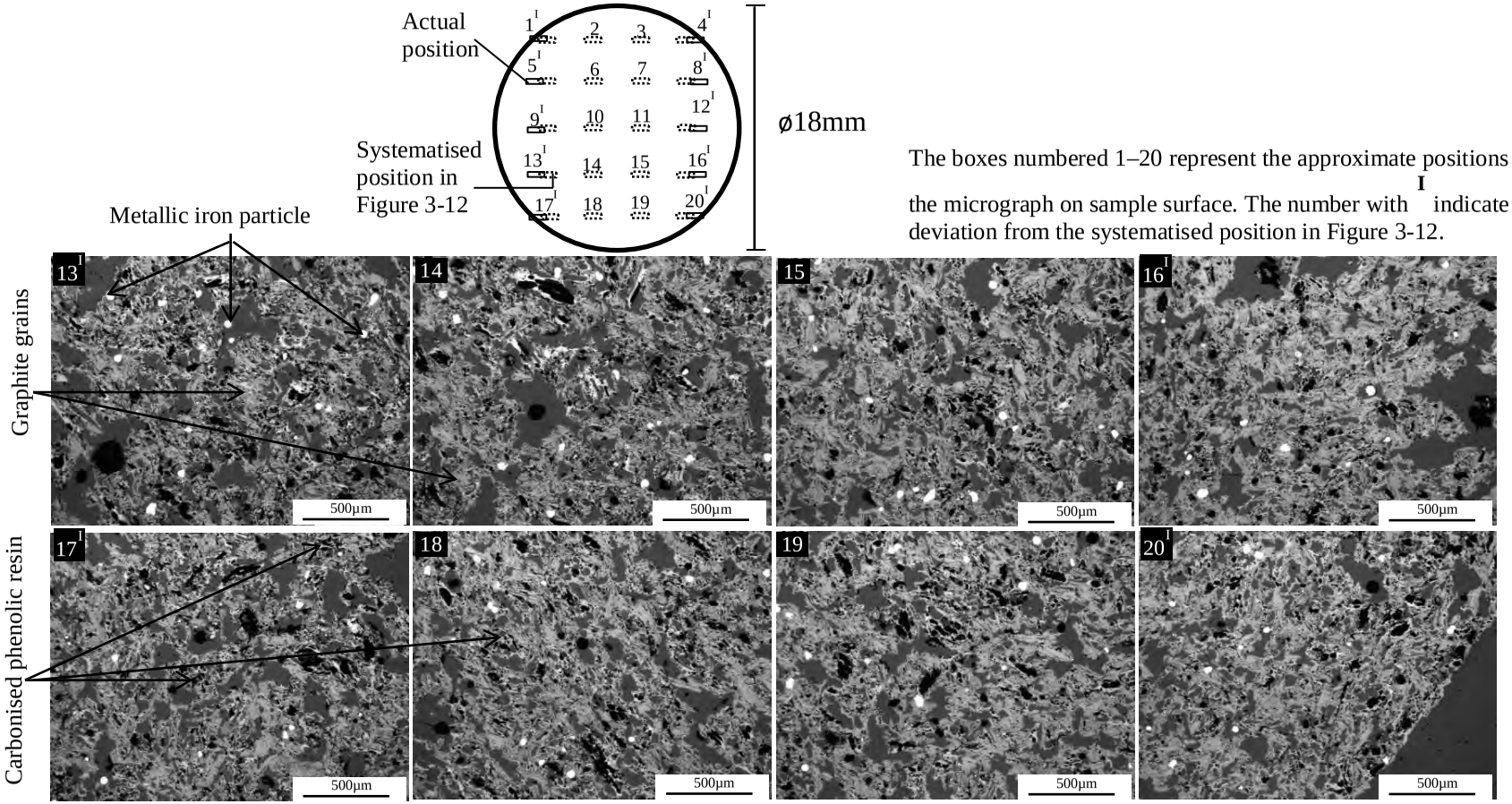

Figure III-13 (continued)**:** The non-polarised optical micrographs of the fired coke analogue–metallic iron 46µm, in horizontal view.

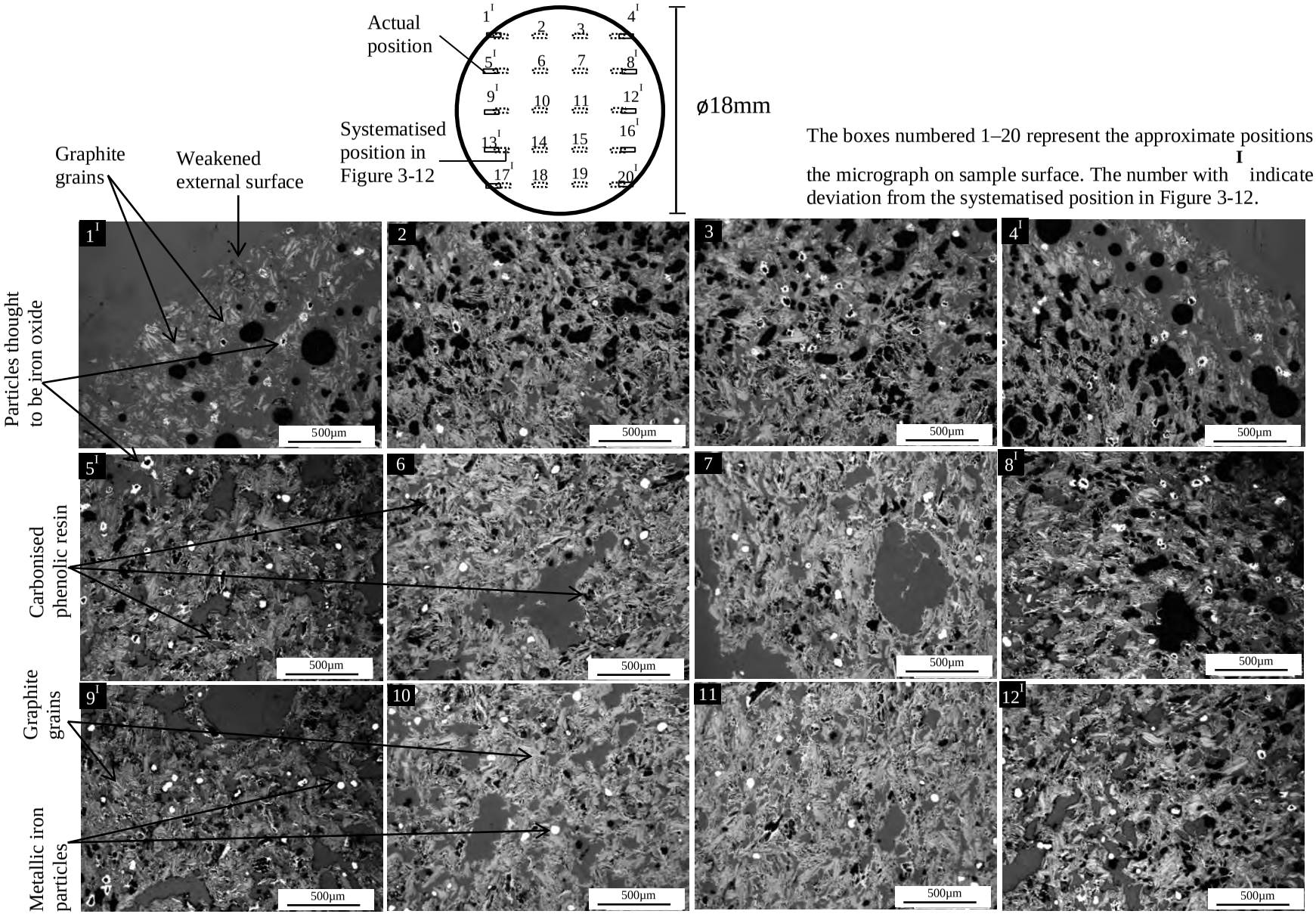

Figure III-14: The non-polarised optical micrographs of the post reacted coke analogue–metallic iron 46µm, in CO_2 at 950°C for 1 hour, horizontal view.

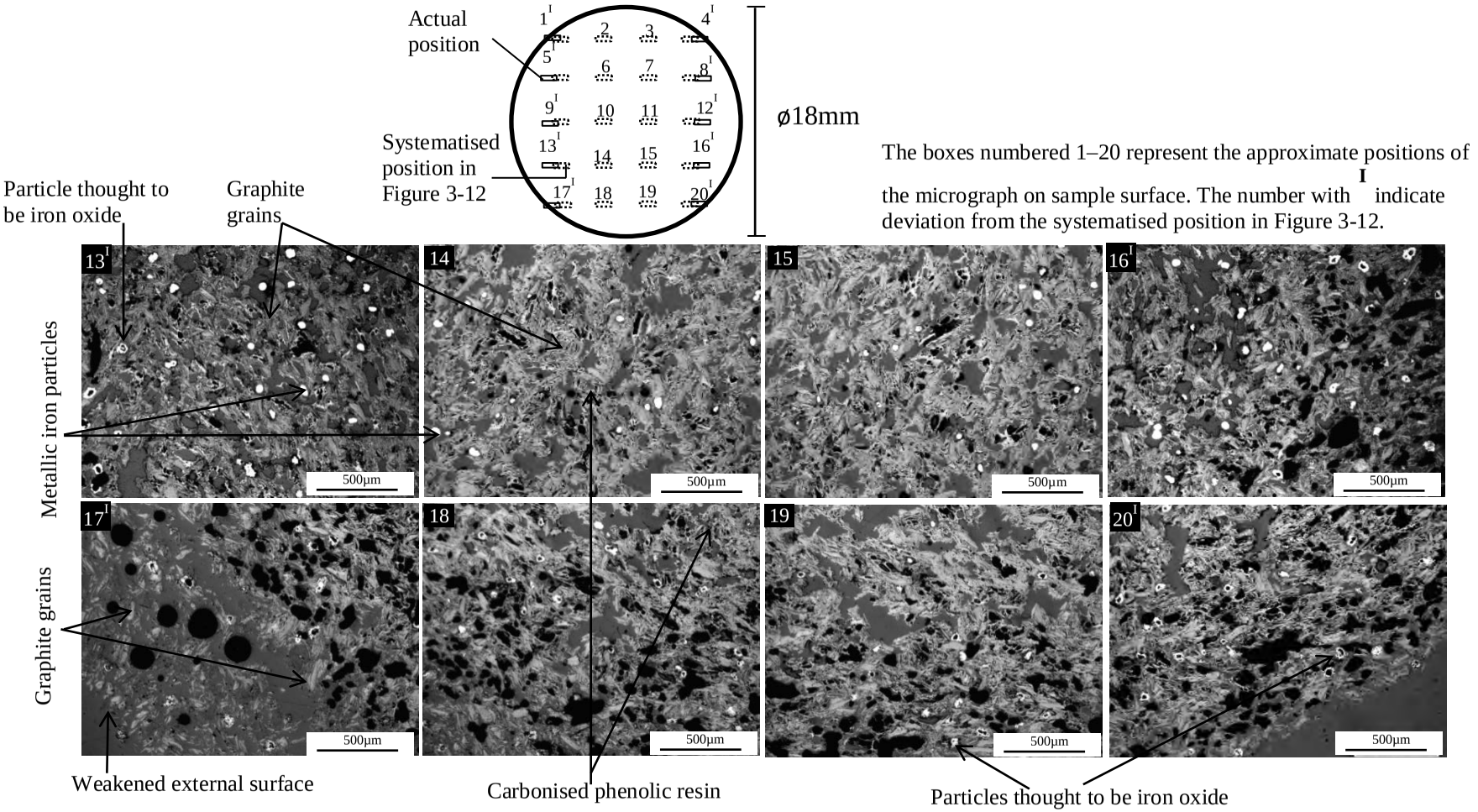

Figure III-14 (continued)**:** The non-polarised optical micrographs of the post reacted coke analogue–metallic iron 46µm, in CO_2 at 950°C for 1 hour, horizontal view.

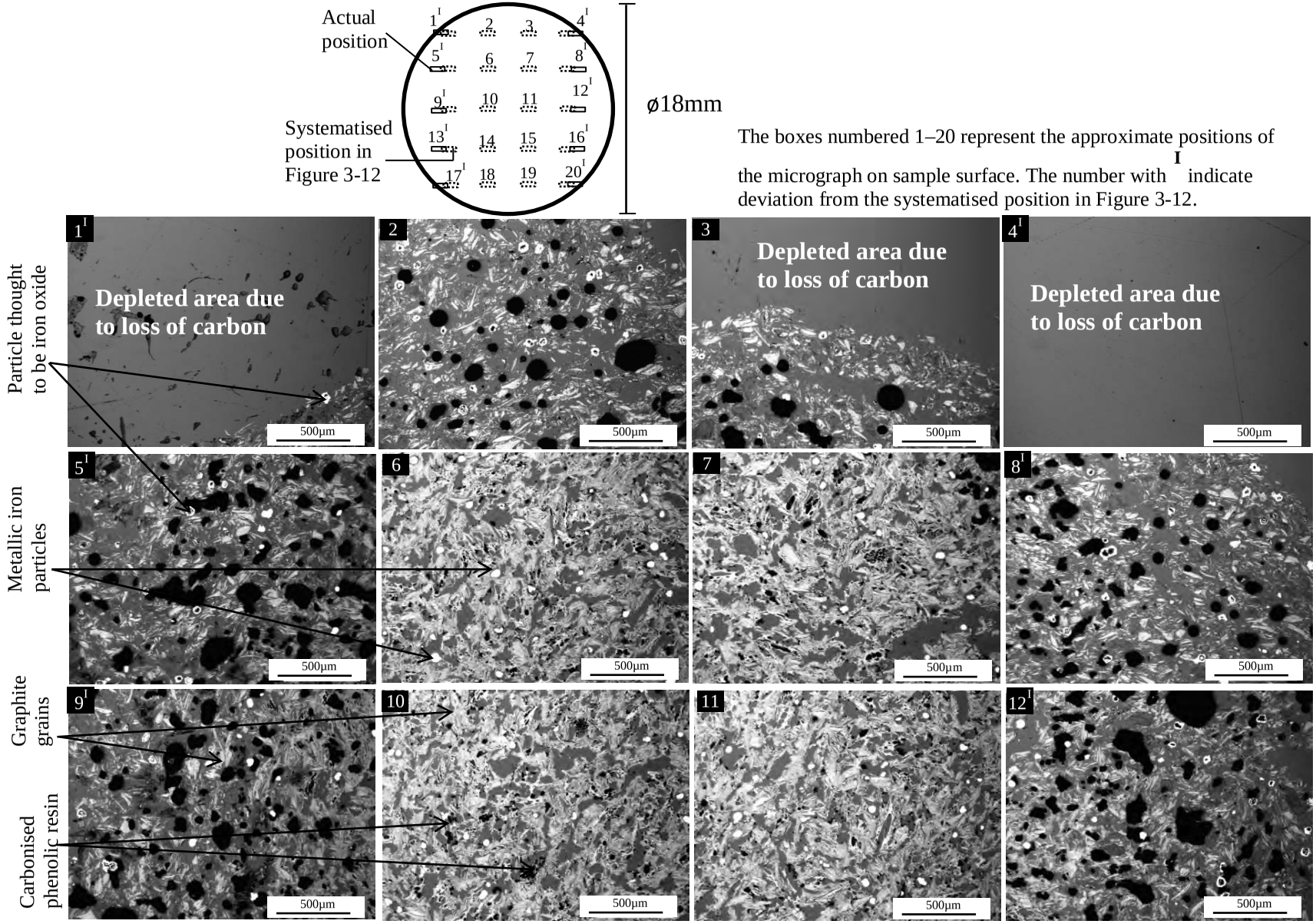

Figure III-15: The non-polarised optical micrographs of the post reacted coke analogue–metallic iron 46µm, in CO_2 at 1025°C for 1 hour, horizontal view.

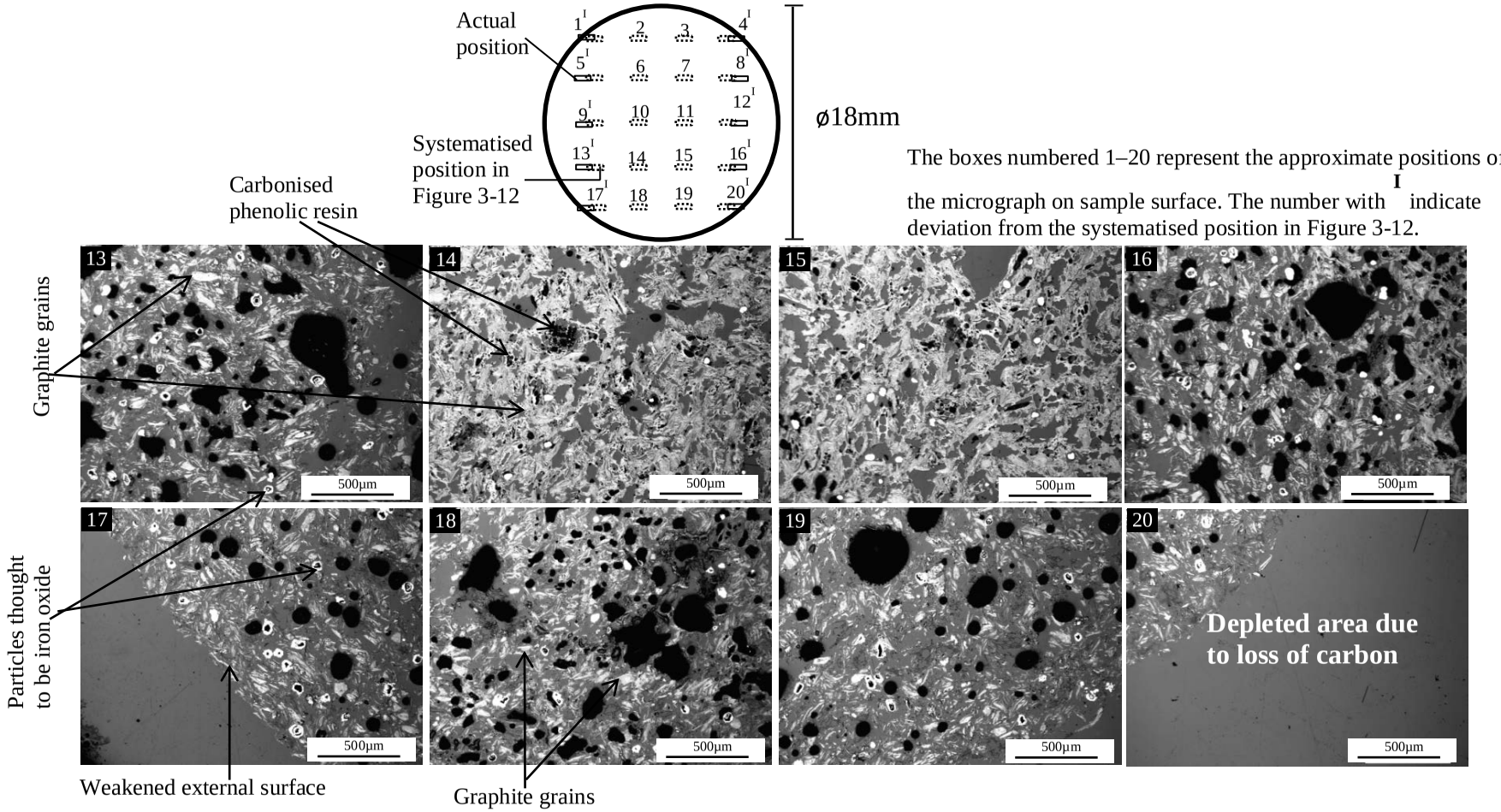

Figure III-15 (continued)**:** The non-polarised optical micrographs of the post reacted coke analogue–metallic iron 46µm, in CO_2 at 1025°C for 1 hour, horizontal view.

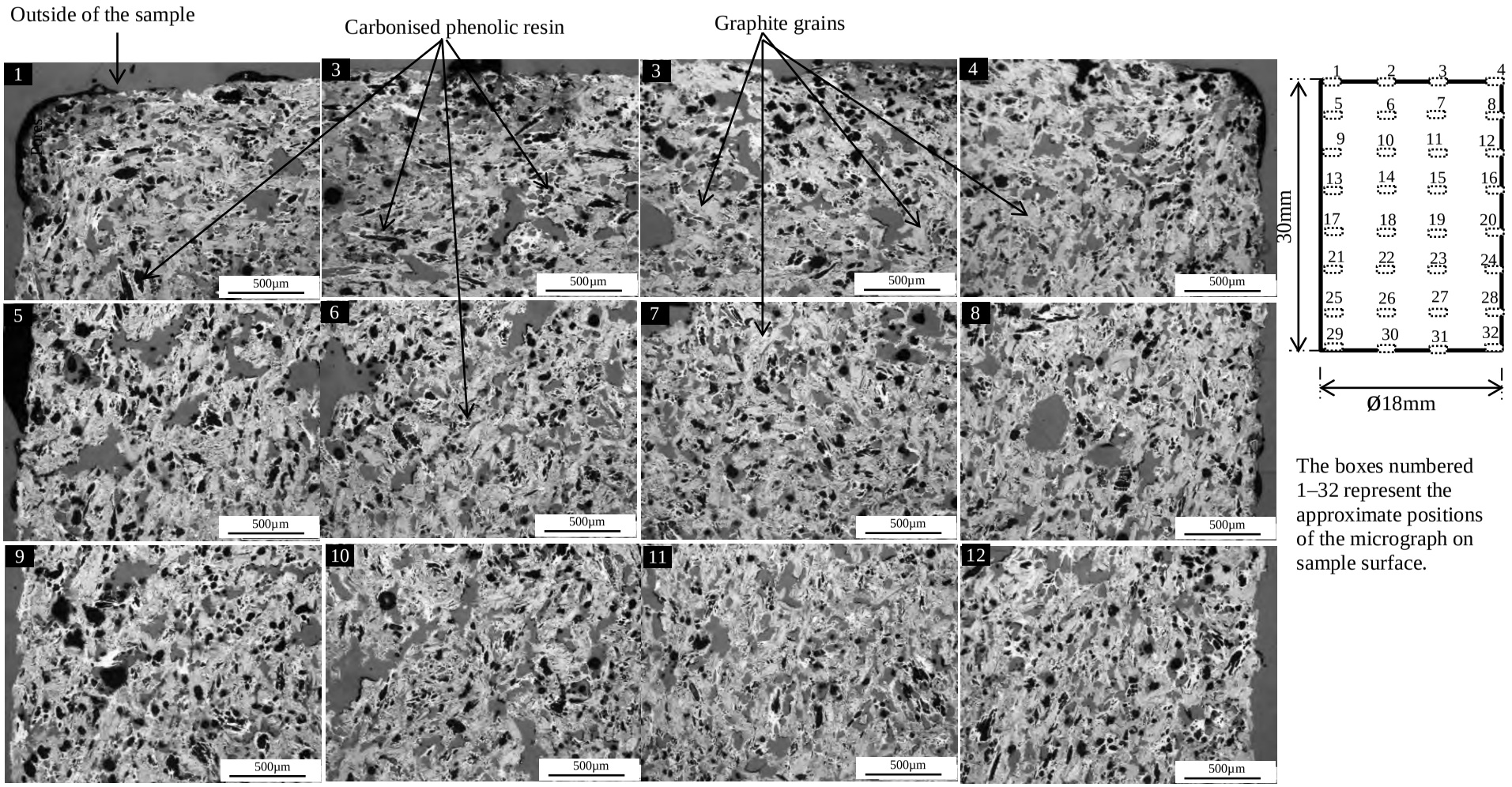

Figure III-16: The non-polarised optical micrographs of the fired base coke analogue, in vertical view.

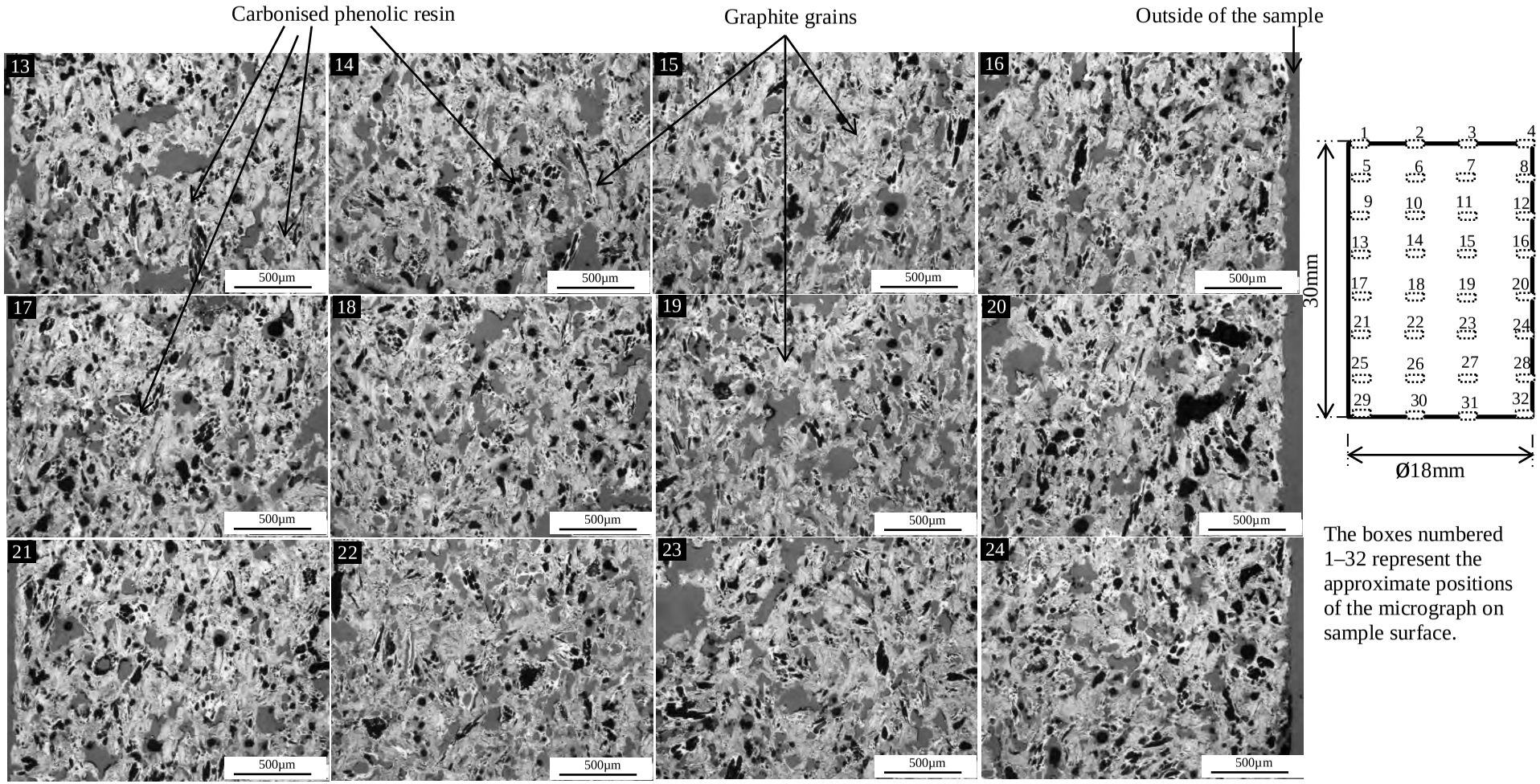

Figure III-16 (continued)**:** The non-polarised optical micrographs of the fired base coke analogue, in vertical view.

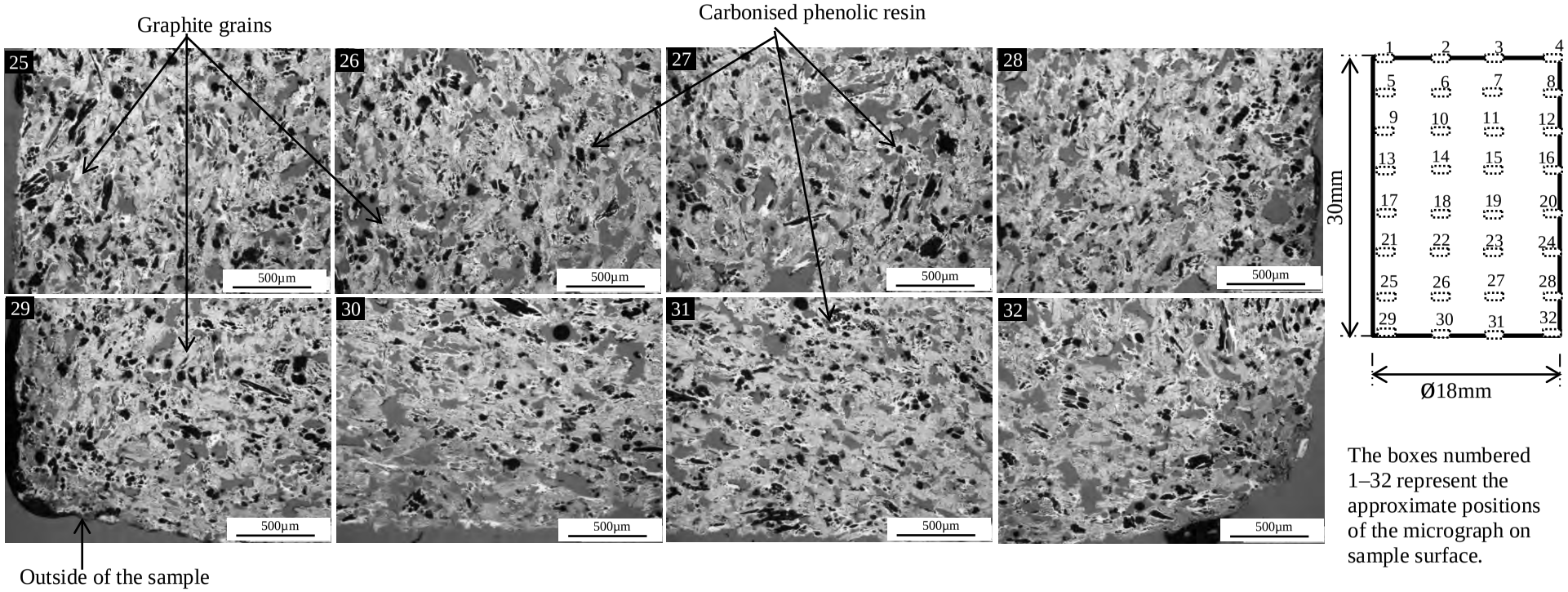

Figure III-16 (continued)**:** The non-polarised optical micrographs of the fired base coke analogue, in vertical view.

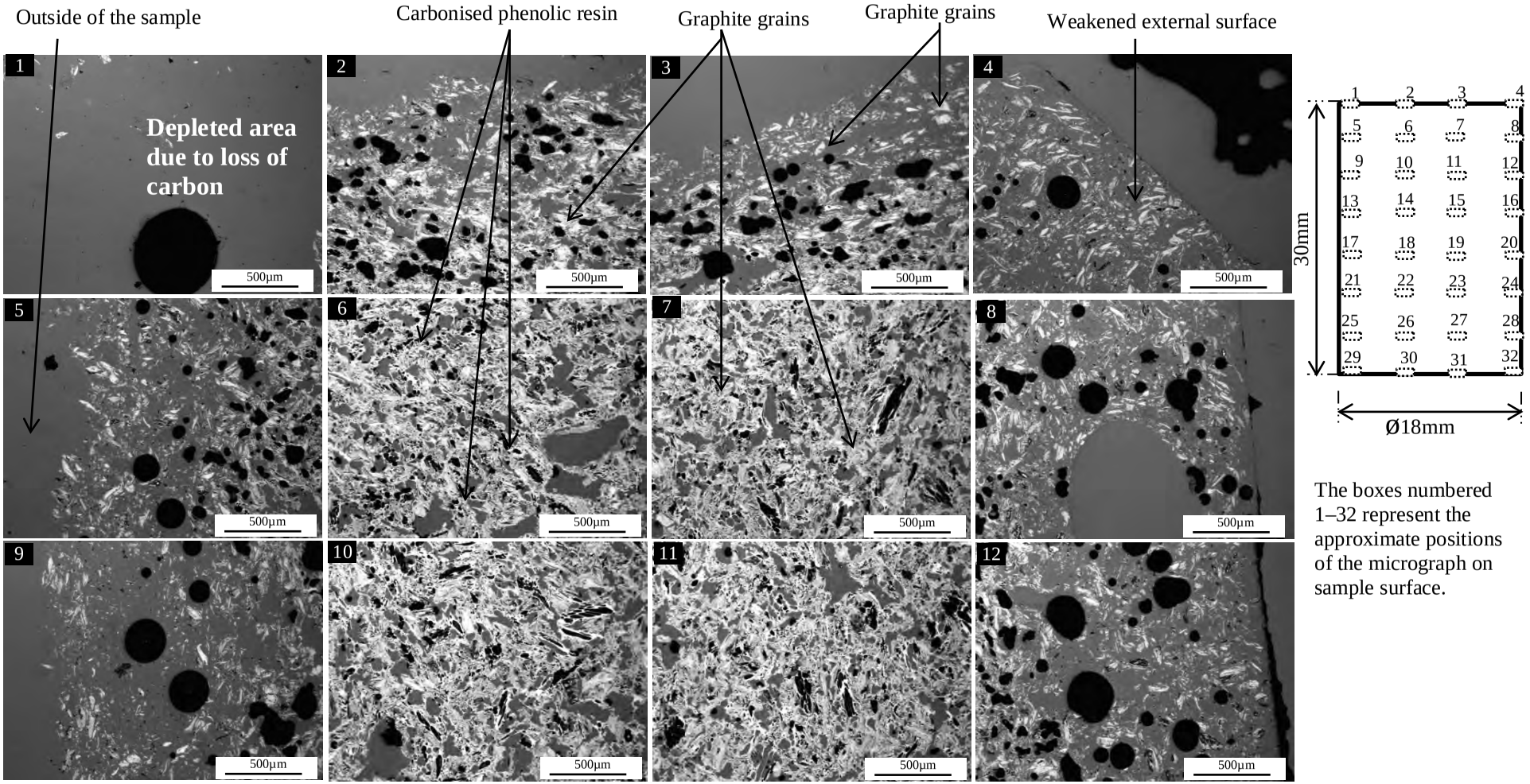

Figure III-17: The non-polarised optical micrographs of the post reacted base coke analogue, in CO_2 at 950°C for 1 hour, vertical view.

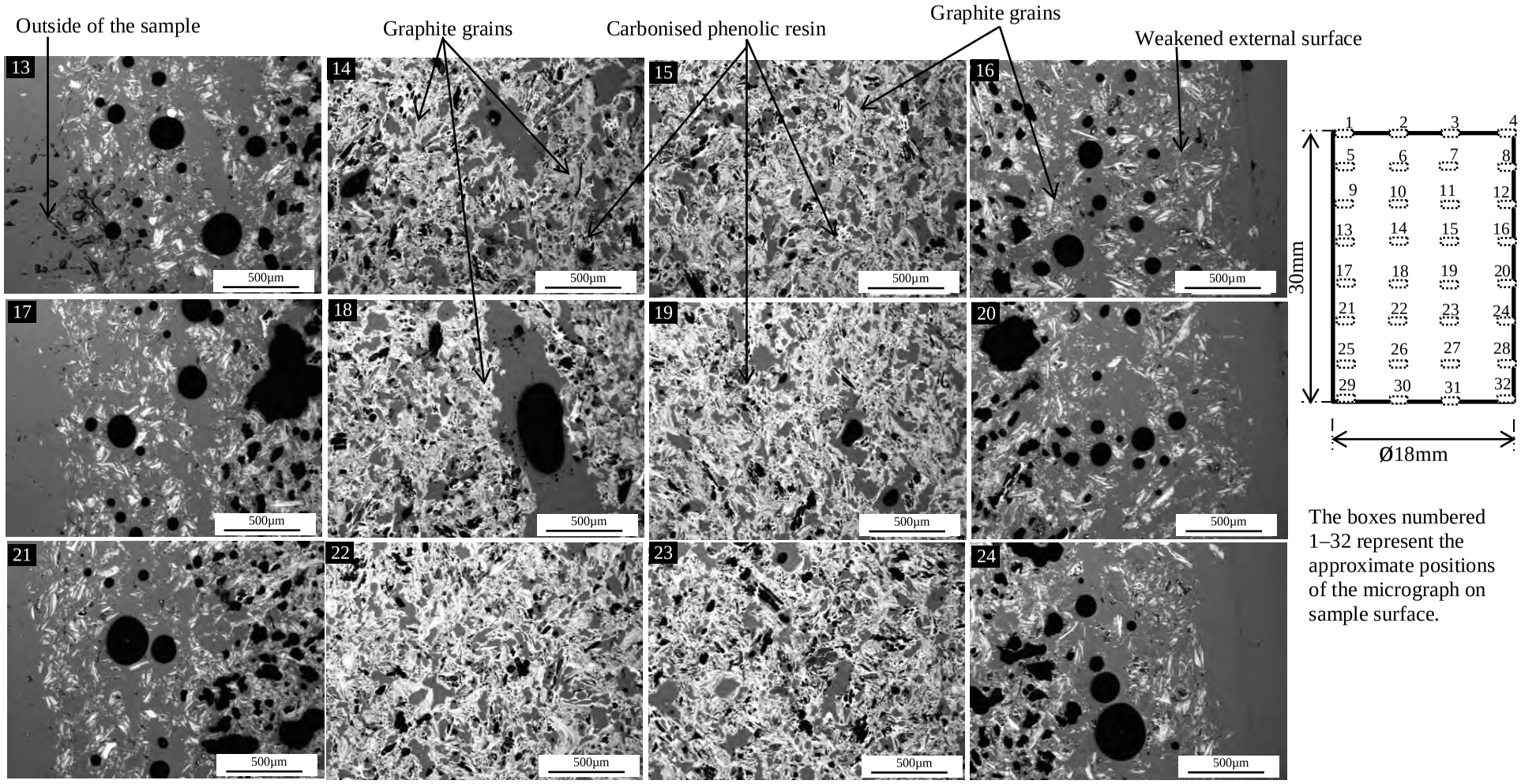

Figure III-17 (continued)**:** The non-polarised optical micrographs of the post reacted base coke analogue, in CO_2 at 950°C for 1 hour, vertical view.

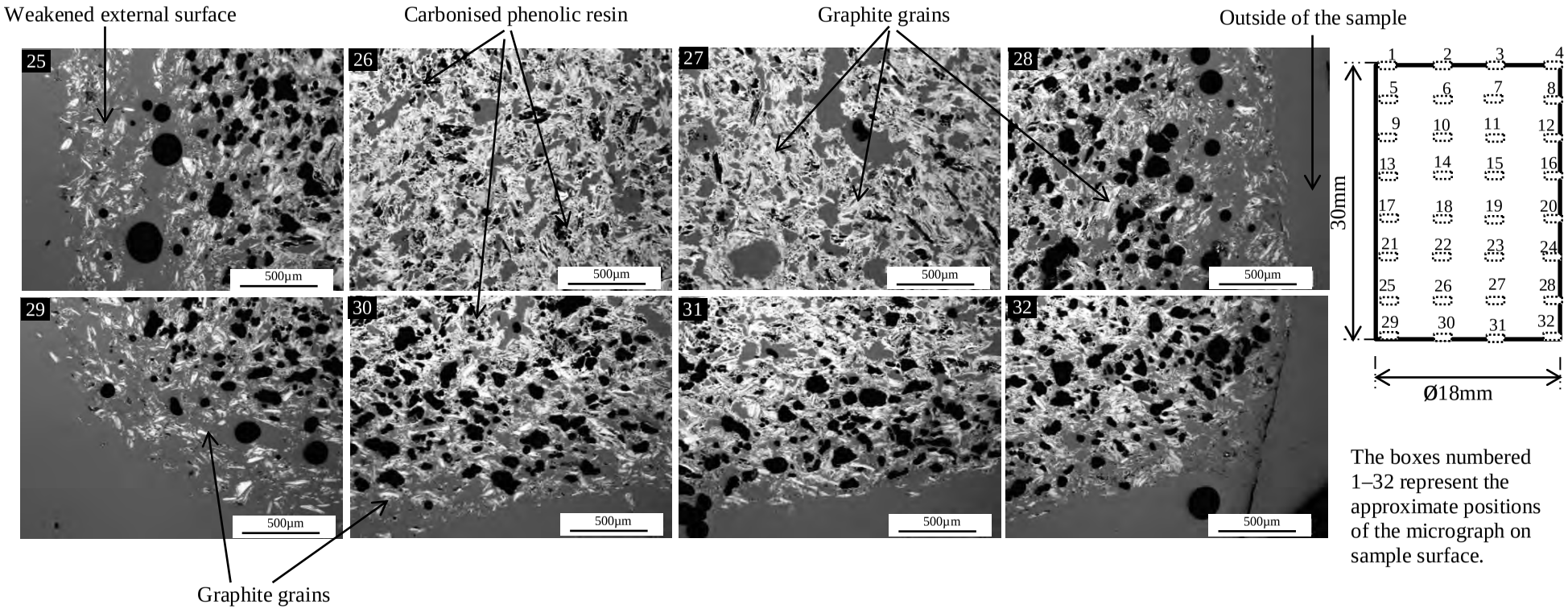

Figure III-17 (continued)**:** The non-polarised optical micrographs of the post reacted base coke analogue, in CO_2 at 950°C for 1 hour, vertical view.

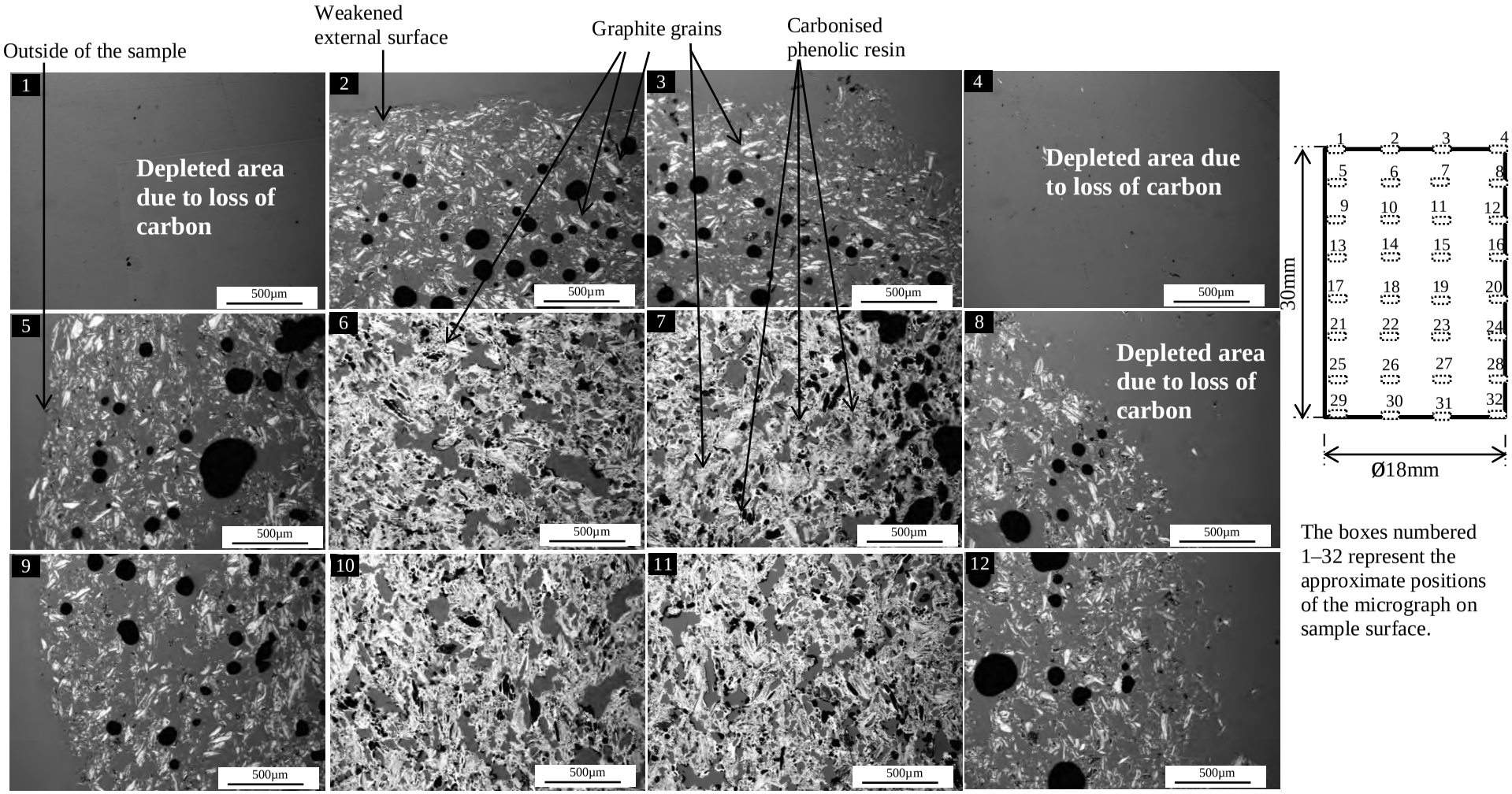

Figure III-18: The non-polarised optical micrographs of the post reacted base coke analogue, in CO_2 at 1025°C for 1 hour, vertical view.

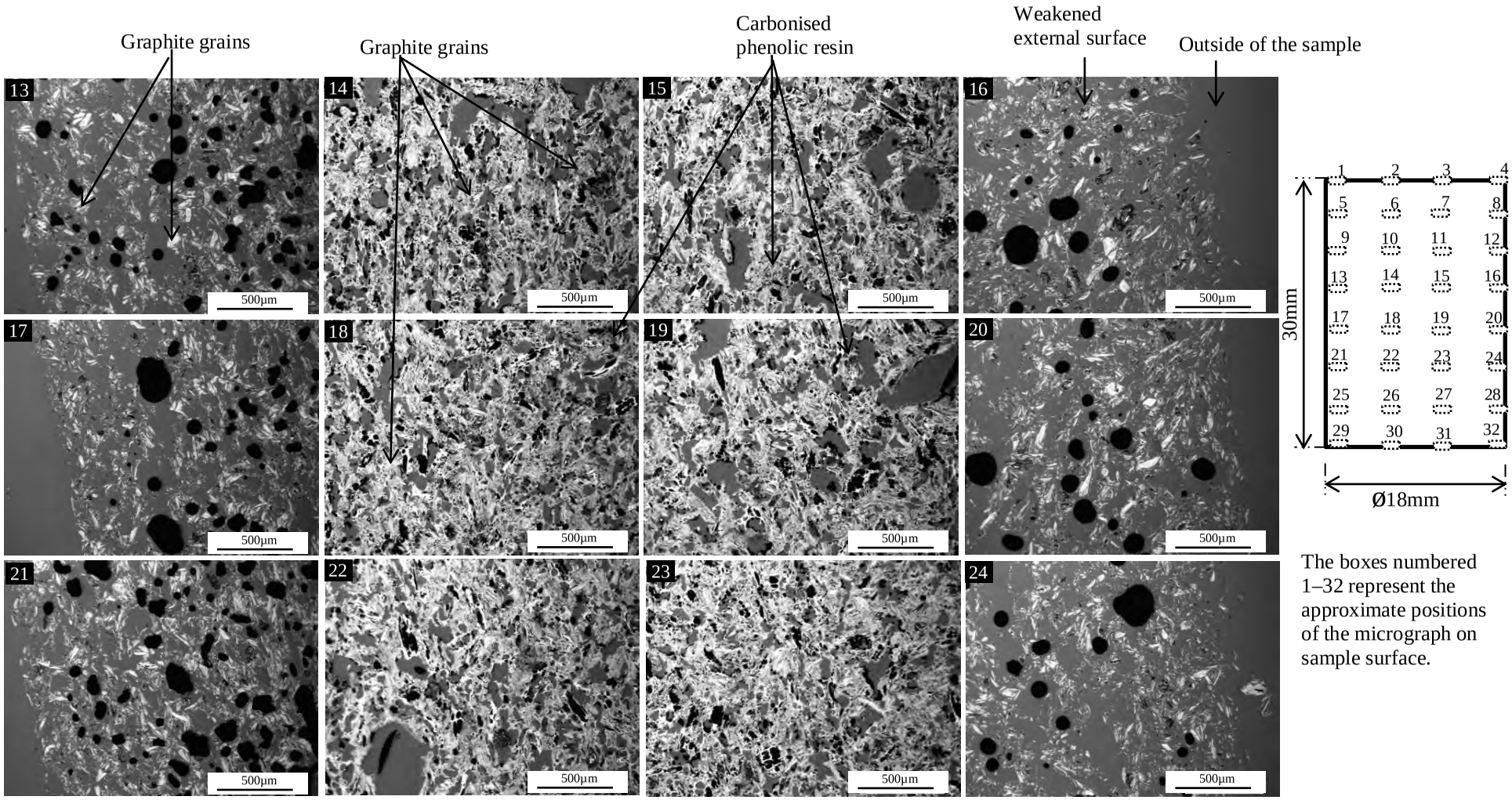

The boxes numbered 1–32 represent the approximate positions of the micrograph on sample surface.

Figure III-18 (continued)**:** The non-polarised optical micrographs of the post reacted base coke analogue, in CO_2 at 1025°C for 1 hour, vertical view.

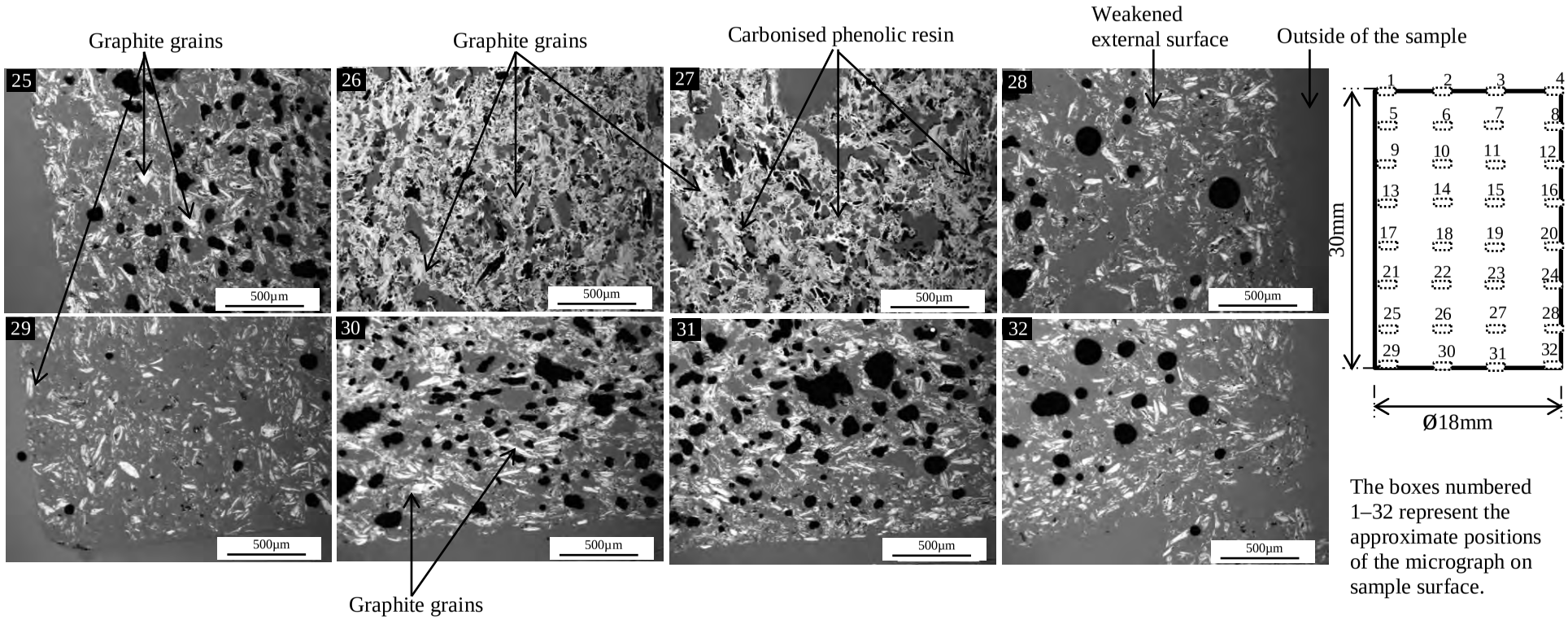

Figure III-18 (continued)**:** The non-polarised optical micrographs of the post reacted base coke analogue, in CO_2 at 1025°C for 1 hour, vertical view.

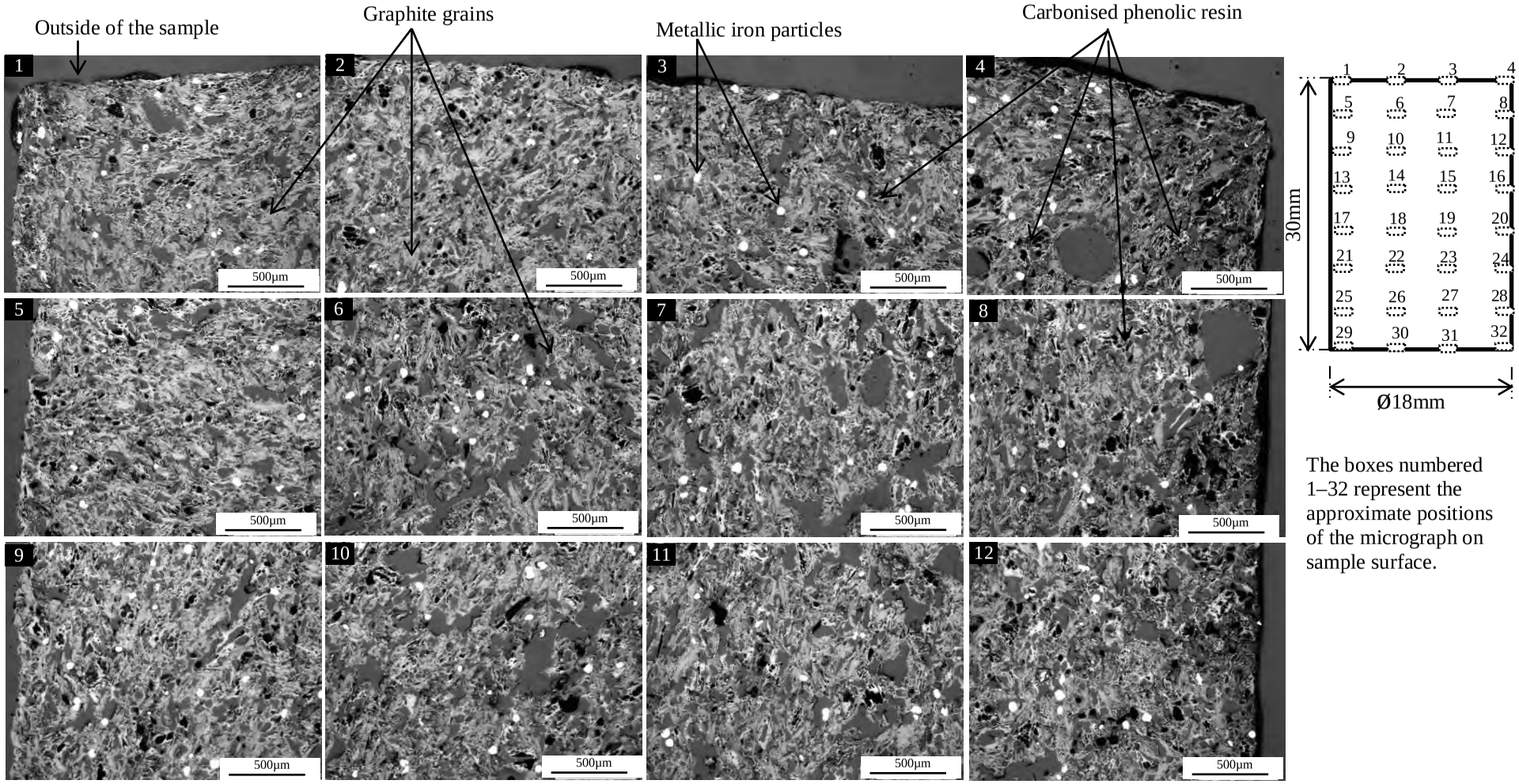

Figure III-19: The non-polarised optical micrographs of the fired coke analogue–metallic iron 46µm, in vertical view.

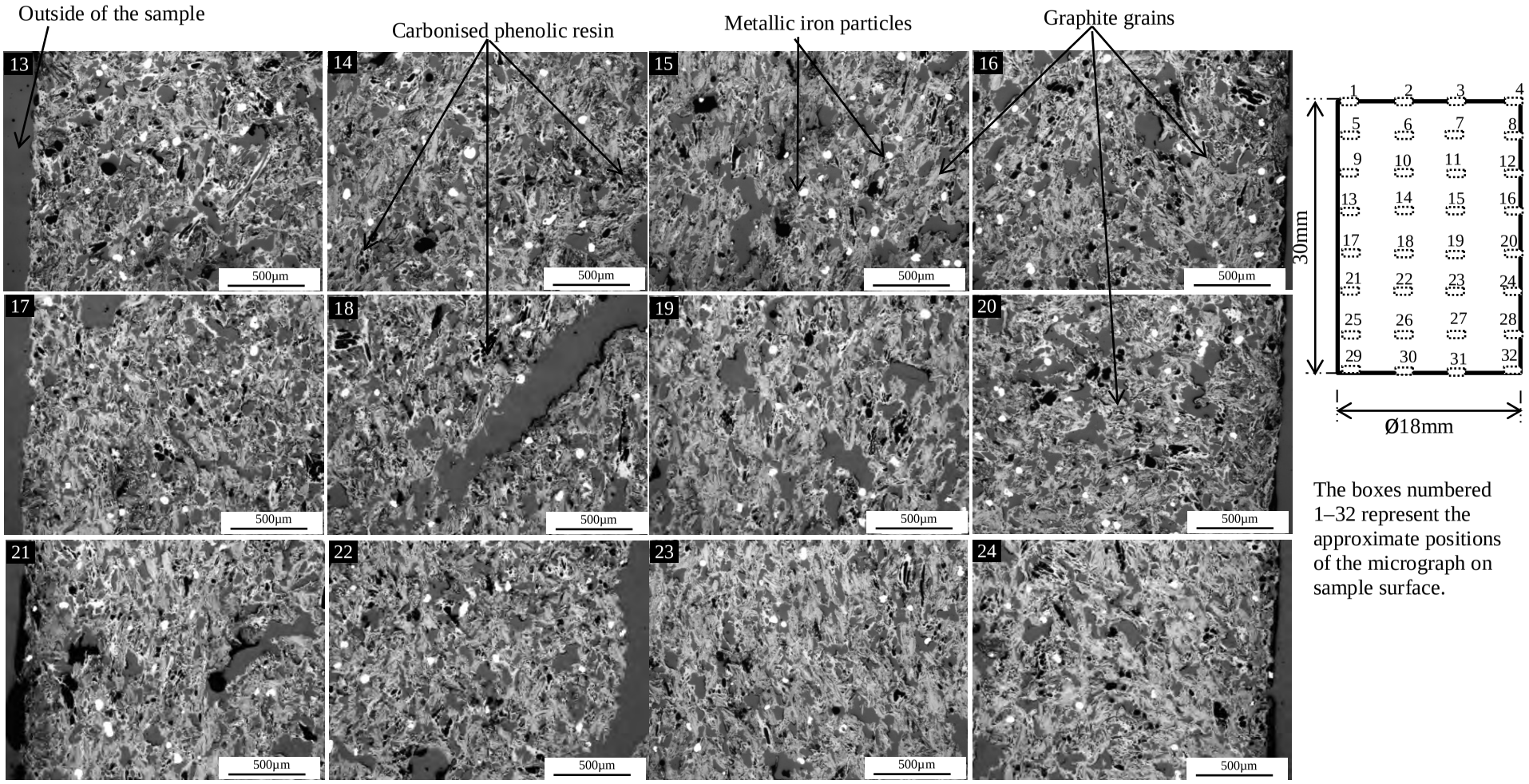

Figure III-19 (continued)**:** The non-polarised optical micrographs of the fired coke analogue–metallic iron 46µm, in vertical view.

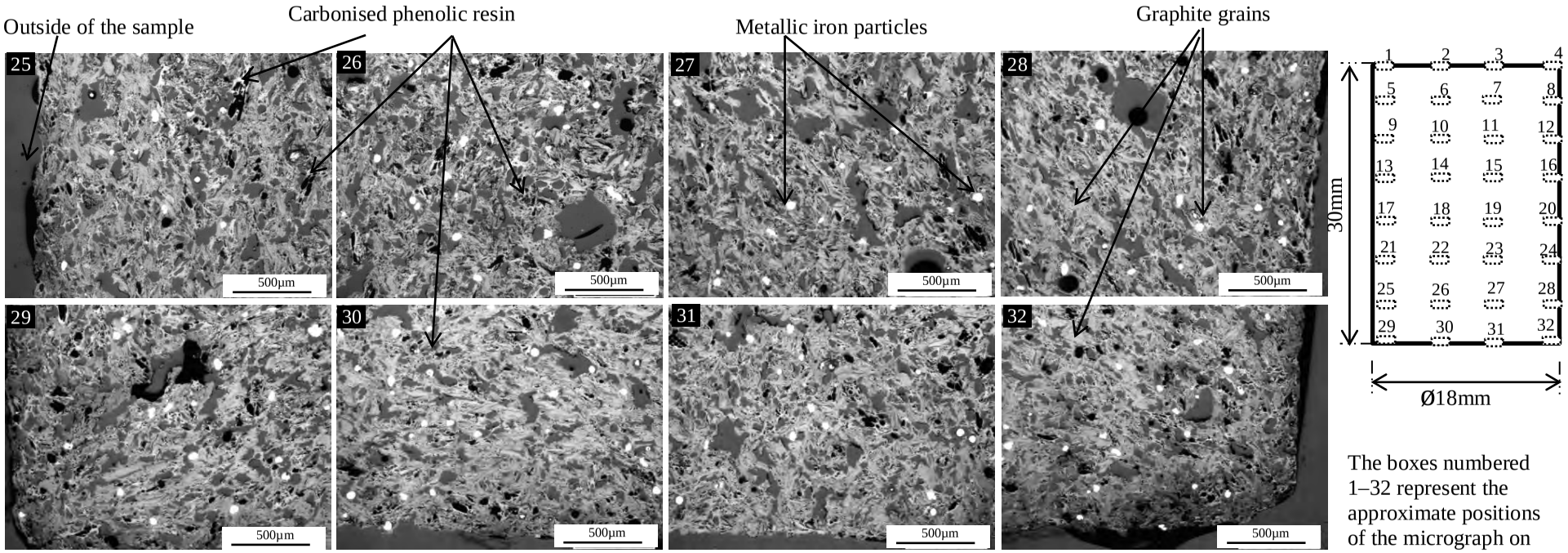

The boxes numbered 1–32 represent the approximate positions of the micrograph on sample surface.

Figure III-19 (continued)**:** The non-polarised optical micrographs of the fired coke analogue–metallic iron 46µm, in vertical view.

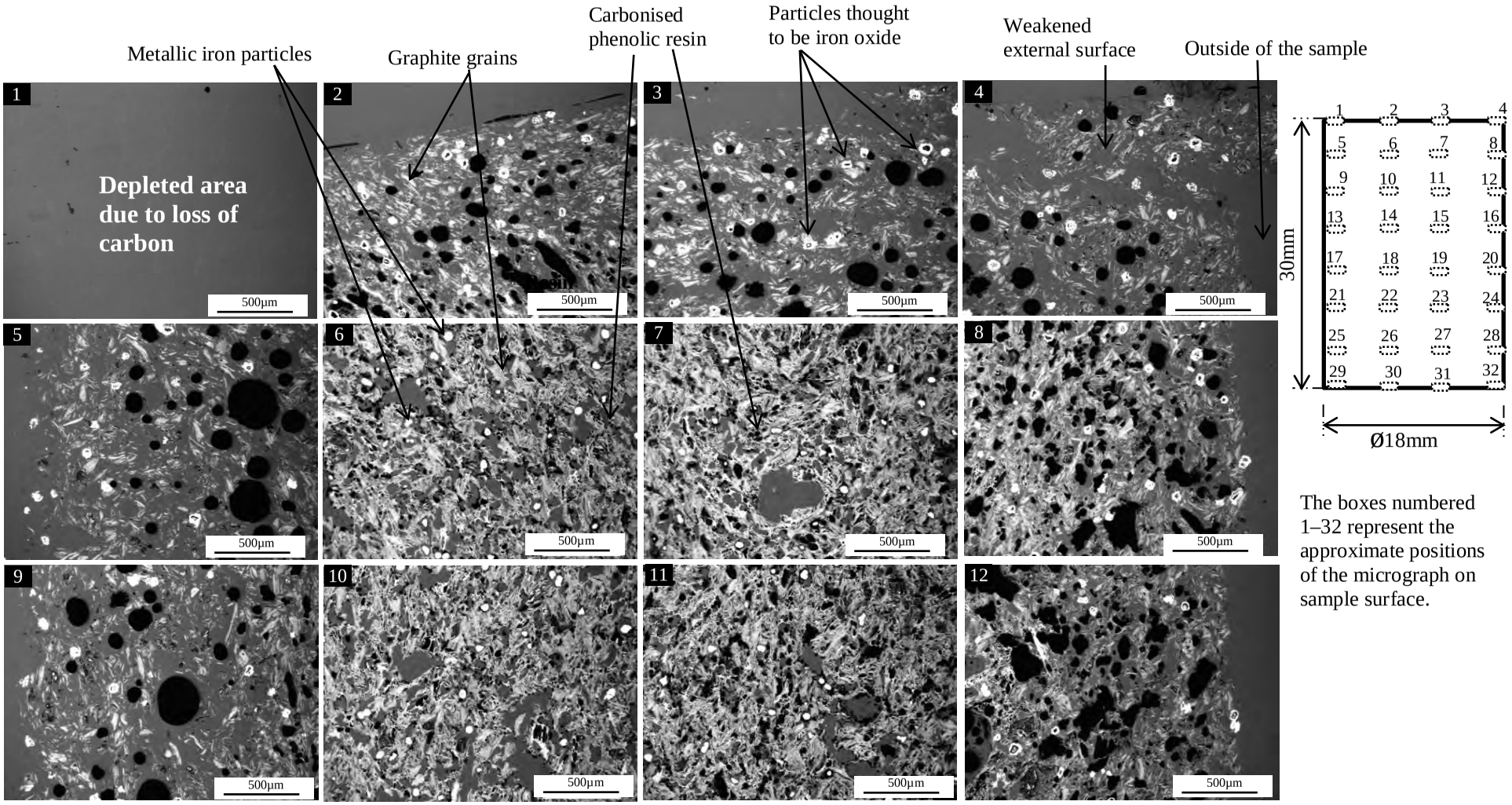

Figure III-20: The non-polarised optical micrographs of the post reacted coke analogue–metallic iron 46µm, in CO_2 at 950°C for 1 hour, vertical view.

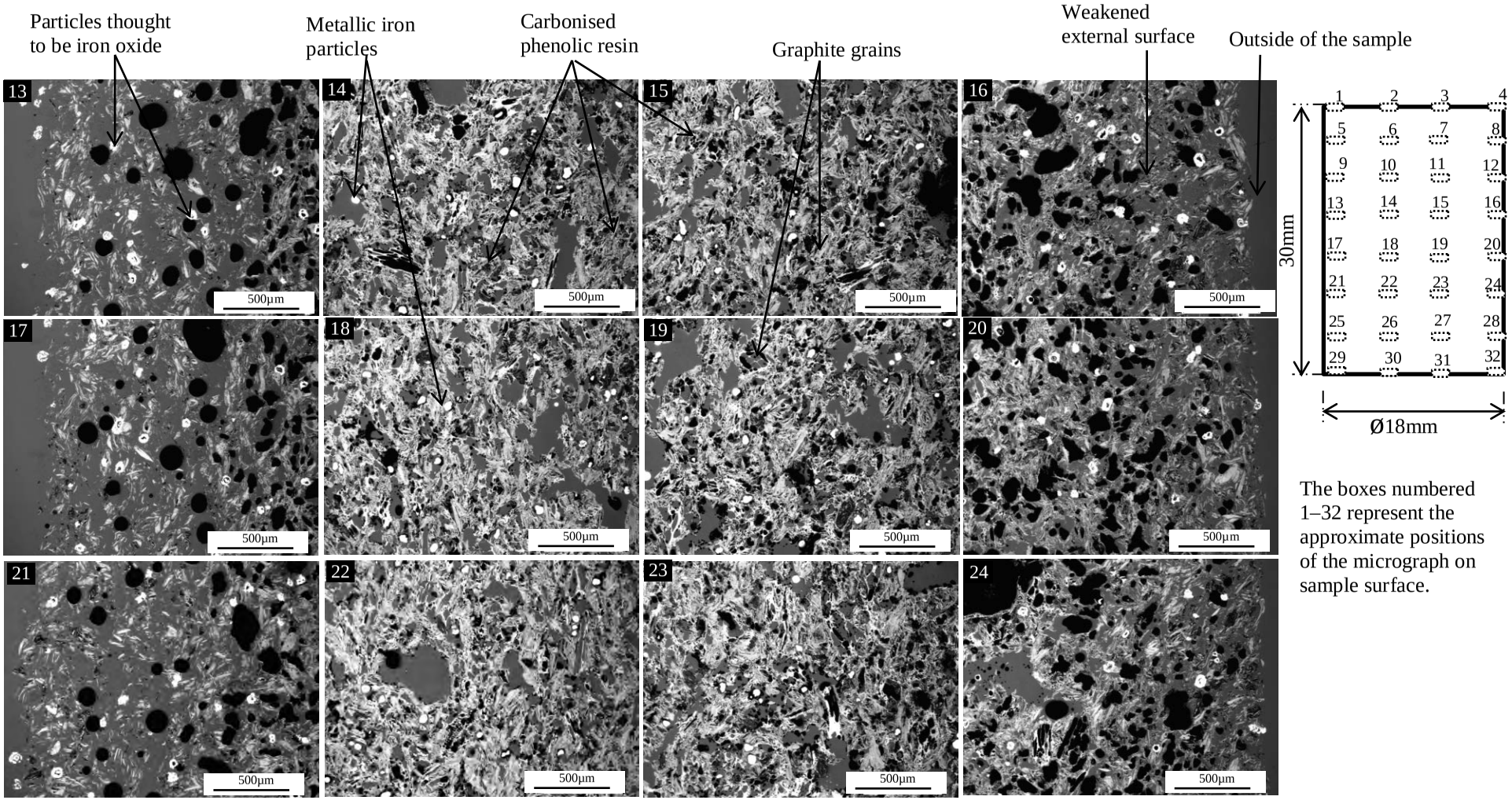

Figure III-20 (continued)**:** The non-polarised optical micrographs of the post reacted coke analogue–metallic iron 46µm, in CO_2 at 950°C for 1 hour, vertical view.

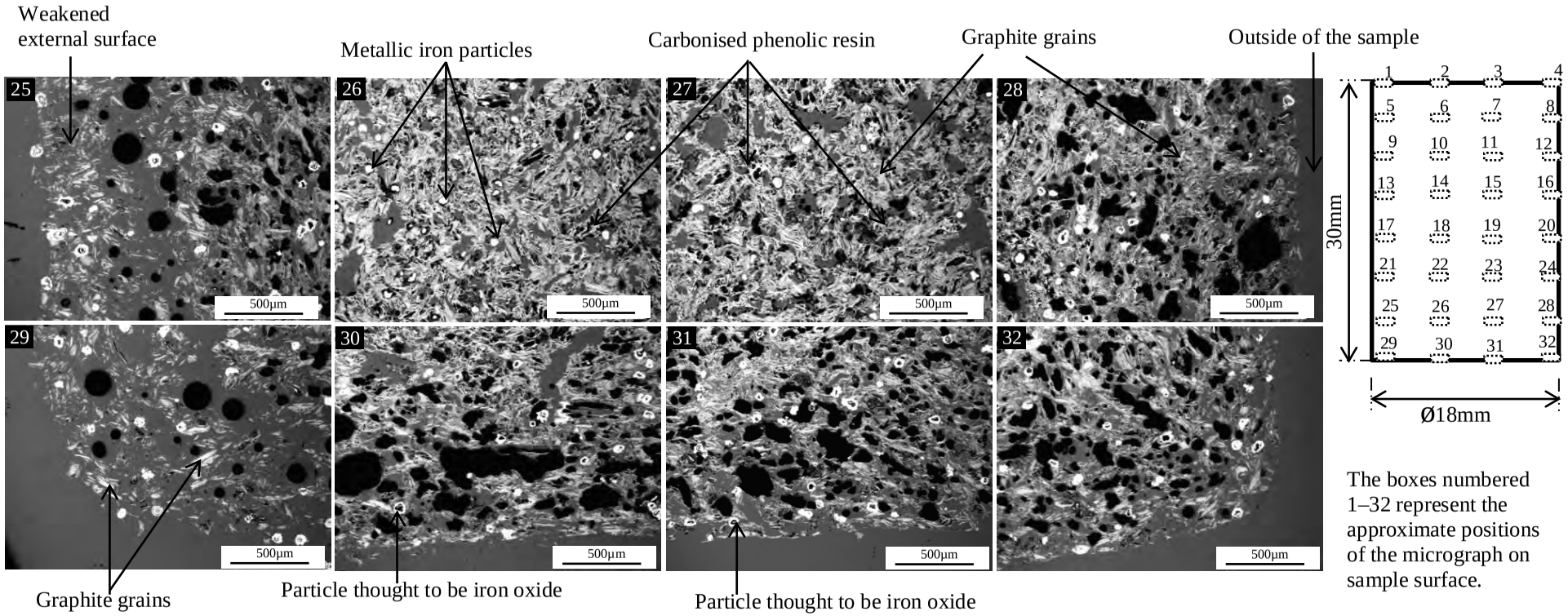

Figure III-20 (continued)**:** The non-polarised optical micrographs of the post reacted coke analogue–metallic iron 46µm, in CO_2 at 950°C for 1 hour, vertical view.

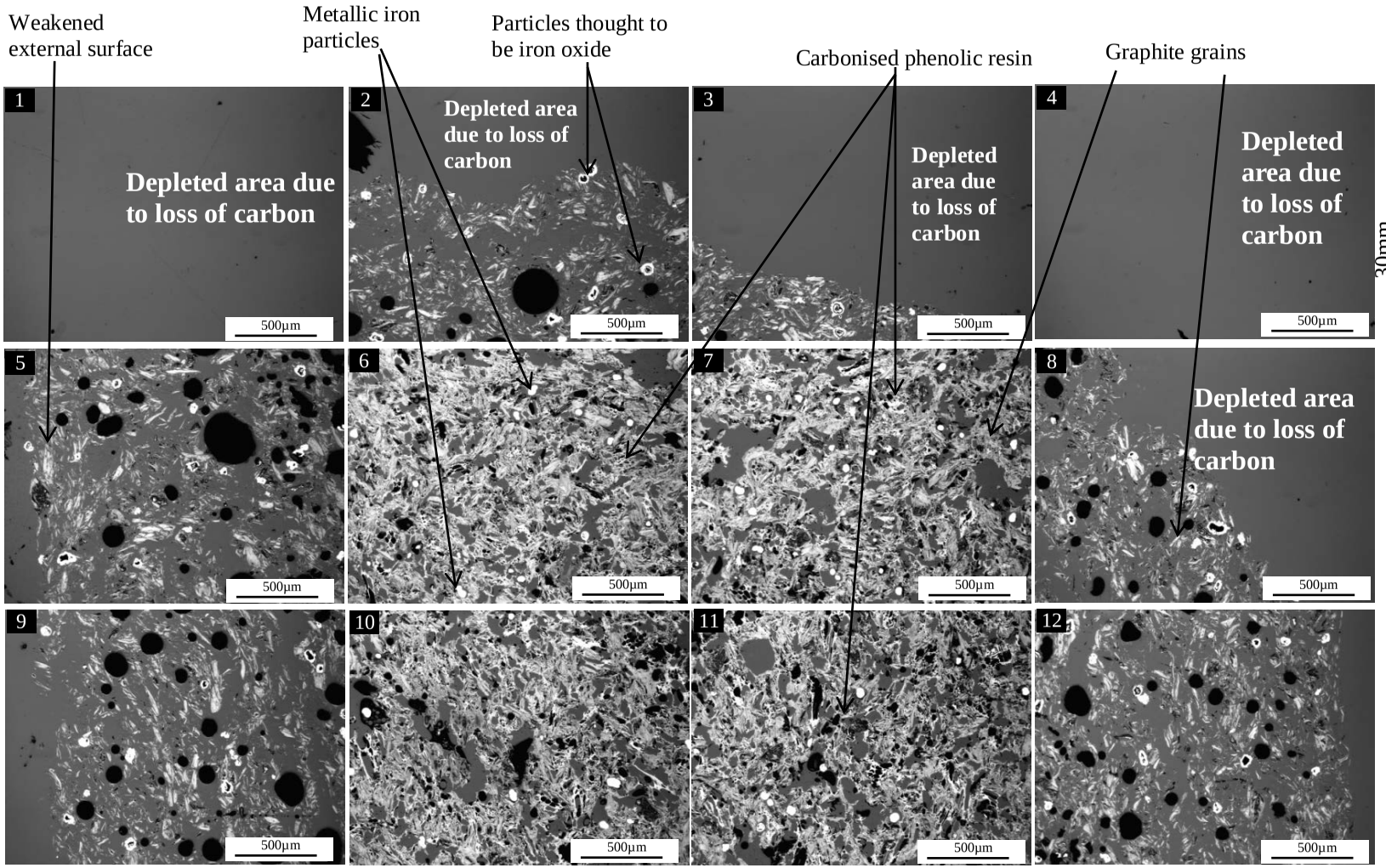

The boxes numbered 1–32 represent the approximate positions of the micrograph on sample surface.

Figure III-21: The non-polarised optical micrographs of the post reacted coke analogue–metallic iron 46µm, in CO_2 at 1025°C for 1 hour, vertical view.

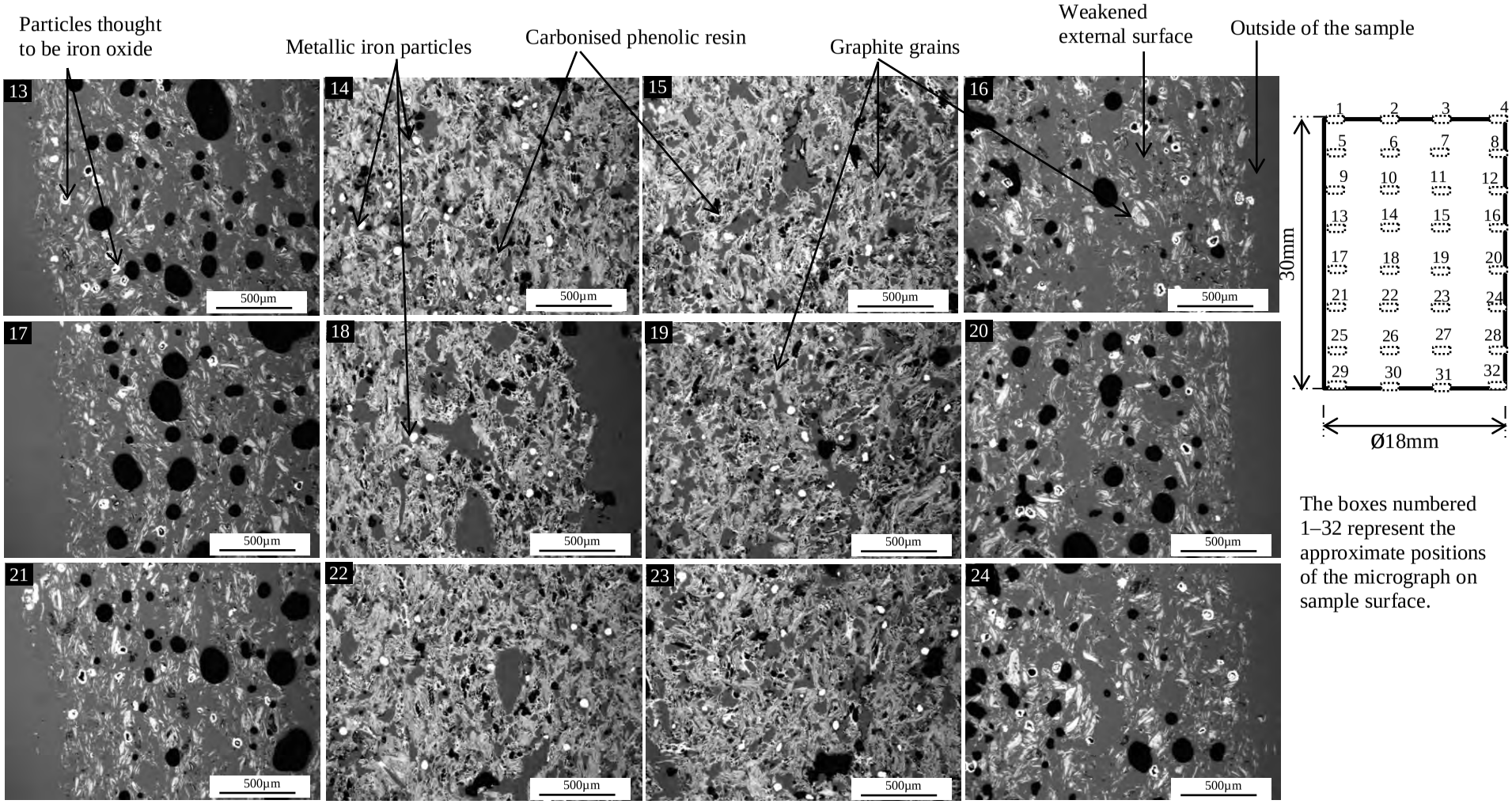

Figure III-21 (continued)**:** The non-polarised optical micrographs of the post reacted coke analogue–metallic iron 46µm, in CO_2 at 1025°C for 1 hour, vertical view.

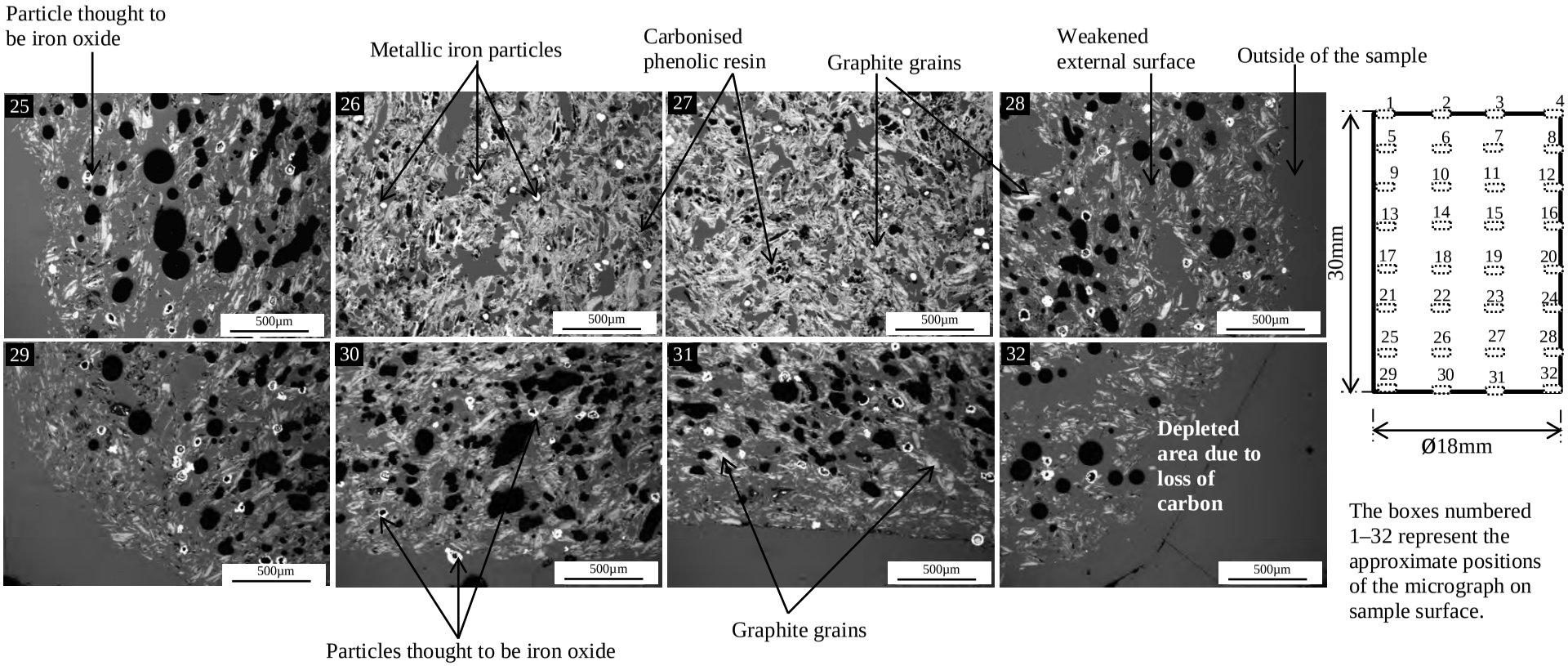

Figure III-21 (continued)**:** The non-polarised optical micrographs of the post reacted coke analogue–metallic iron 46µm, in CO_2 at 1025°C for 1 hour, vertical view.

Appendix IV The partial pressure of CO_2, CO and O_2 in the absence of carbon

This calculation is being carried out to establish the CO_2, CO and O_2 levels in the supply gas prior to the reaction with carbon. The partial pressure of CO_2, CO and O_2 in the absence of carbon can be determined by establishing the reaction IV-1 [63, 64].

$$CO_{2(g)} \rightarrow CO_{(g)} + \frac{1}{2}O_{2(g)} \qquad \Delta G° = 279700 - 84.96T \quad J.mol^{-1} \qquad \text{IV-1}$$

The relationship between the partial pressures of CO_2, CO and O_2 and the equilibrium constant K in reaction IV-1 is,

$$K = \frac{pCO.\sqrt{pO_2}}{pCO_2} \qquad \text{IV-2}$$

where pCO_2, pCO and pO_2 are the partial pressures of CO_2, CO and O_2 respectively

If the total pressure in the reaction is 1 atmosphere, then

$$pCO_2 + pCO + \sqrt{pO_2} = 1 \qquad \text{IV-3}$$

Reaction IV-4 was derived from the stoichiometry of reaction IV-1 [63,64].

$$(1-X)CO_{2(g)} \rightarrow XCO_{(g)} + \frac{X}{2}O_{2(g)} \qquad \text{IV-4}$$

Total number of moles of the reaction IV-4 is,

$$1 - X + X + \frac{X}{2} = \frac{2+X}{2} \qquad \text{IV-5}$$

where (1- X), X and $\frac{X}{2}$ are number of moles of CO_2, CO and O_2 respectively,

then,

$$pCO_2 = \frac{1-X}{\frac{2+X}{2}} \qquad \text{IV-6}$$

$$pCO = \frac{X}{\frac{2+X}{2}} \qquad \text{IV-7}$$

$$pO_2 = \frac{\frac{X}{2}}{\frac{2+X}{2}} \qquad \text{IV-8}$$

by putting the values of pCO_2, pCO and pO_2 into IV-2 gives,

$$K = \frac{\frac{X}{\frac{2+X}{2}} \cdot \sqrt{\frac{\frac{X}{2}}{\frac{2+X}{2}}}}{\frac{1-X}{\frac{2+X}{2}}} \qquad \text{IV-9}$$

A simplified form of equation IV-9 can be written as,

$$K^2(1-X)^2.(2+X) - X^3 = 0 \qquad \text{IV-10}$$

solving equation IV-10 graphically for values of $0 < n \leq 1$, the values of pCO_2, pCO and pO_2 can be determined.

The plot of pCO_2, pCO and pO_2 with temperature is given in Figure IV-1.

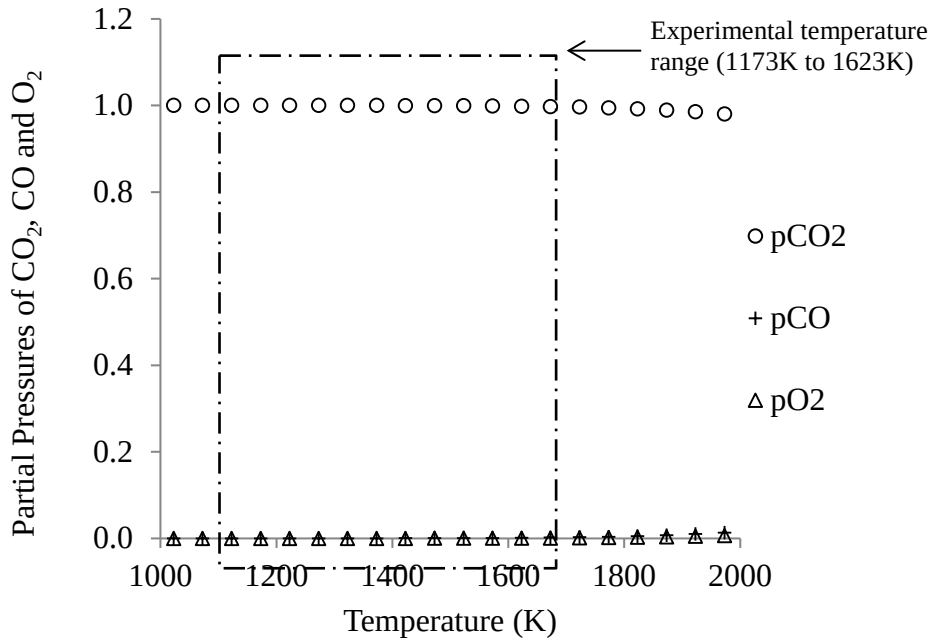

Figure IV-1: A plot of partial pressures of CO_2, CO and O_2 with temperature.

From this figure it can be seen that under the experimental temperature (950°C to 1350°C) of this study, the partial pressure of O_2 (0.0000029 to 0.0005702) and CO (0.0000057 to 0.0011404) are negligible, such that the partial pressure of CO_2 (0.9999914 to 0.9982894) is stable.

Appendix V Assessment of carbon pick up and loss from the iron during firing and reaction with CO_2 respectively

This calculation is being carried out to complement the LECO measurement of carbon pick up and loss from iron during analogue firing and reaction with CO_2 respectively.

Pick up of carbon in Fe during firing

The suggestion that Fe is picking up carbon at the firing temperature of the coke analogue (1200°C) can be evaluated using the Fick's second law for non-steady state diffusion (equation 2-14, reproduced in the following text) [155, 156].

$$\frac{\overline{C} - C_s}{C_i - C_s} = \frac{8}{\pi^2}\exp\left[\frac{-\pi^2}{4}.\frac{Dt}{L^2}\right]$$

where C_s is the carbon concentration at the surface, C_i is the initial carbon concentration of the Fe, $\overline{C}$ is the average carbon concentration of the Fe at time t, D is the diffusion coefficient and L is the semi-thickness.

The variables/parameters in equation 2-14 for the firing condition are given in Table V-1.

Table V-1: Pick up of carbon in Fe during firing

Temp. (°C)	D (cm^2/sec) [155]	t* (sec)	L# (cm)	C_i (mass%)	C_s (mass%)
1200	$1.5x10^{-6}$	3600	0.1	0.06	~1.77 (MTDATA plot given in Figure 6-2).

* the analogue was held for 1 hour (3600 seconds)
\# semi thickness of the Fe used is 1 mm (0.1 cm)

$$\frac{\overline{C} - C_s}{C_i - C_s} = 0.21 \qquad \text{V-1}$$

$$\overline{C} = 0.21(C_i - C_S) + C_S \qquad \text{V-2}$$

$$\overline{C} = 1.41\% \qquad \text{V-3}$$

From the above calculations, it can be seen that $\overline{C}$ after firing (1.41 mass%) is consistent with the value measured with LECO (1.72 mass%). This indicates that the Fe picked up carbon after firing. It increased from 0.06 mass% to 1.72 mass%.

Loss of carbon in Fe on reacting with CO_2 during reactivity testing

This situation is likely to occur when regions become carbon depleted and the Fe is exposed to CO_2 gas. Under such circumstances, we can consider this Fe containing carbon reacting with the furnace input CO_2/CO gas as established in Appendix IV.

To test for this situation, reactivity testing was carried out at different temperatures (950°C and 1025°C) for 2 hours (7200 seconds).

The C_s carbon concentration at the surface of the Fe (austenite) is established from equation 2-31 (reproduced in the following text),

$$<C> + CO_{2(g)} \rightarrow 2CO_{(g)} \qquad \Delta G° = 165300 - 170.76T \text{ J.mol}^{-1} \text{ [63, 64]}$$

<C> reference state is graphite.

the relationship between the partial pressures of CO_2 and CO, the activity of <C> and the equilibrium constant K in 2-31 is,

$$K = \frac{p_{CO}^2}{p_{CO_2} \cdot a_{<C>}} \qquad \text{V-4}$$

the relationship between the Gibbs free energy $\Delta G°$ and the equilibrium constant K is,

$$\Delta G° = -RT\ln K \qquad \text{V-5}$$

putting the expression for K in V-4 into V-5 gives

$$\Delta G^\circ = -RT \ln \frac{p_{CO}^2}{p_{CO_2} \cdot a_{<C>}} \qquad \text{V-6}$$

the above expression can be rewritten as a function of $a_{<C>}$ to give,

$$a_{<C>} = \frac{p_{CO}^2}{p_{CO_2}} . e^{\frac{\Delta G^\circ}{RT}} \qquad \text{V-7}$$

The variables/parameters in equation V-7 for the reactivity testing conditions are given in Table V-2.

Table V-2: The values of $a_{<C>}$ and the corresponding C_s as calculated from V-7

Temp	p_{CO}*	p_{CO2}*	ΔG° ($J.mol^{-1}$)	R ($J.mol^{-1}.K^{-1}$)	$a_{<C>}$ [63]	C_s (mass%)# [63]
950°C (1223K)	0.000012	0.999981	-43539.5	8.314	1.99×10^{-12}	Negligible
1025°C (1298K)	0.000026	0.999962	-56346.5	8.314	3.65×10^{-12}	Negligible

* data were obtained from Figure IV-1 (Appendix IV)

\# the corresponding C_s data was obtained from the plot of activity of carbon in austenite given in the literature [63].

Using the Fick's second law for non-steady state diffusion (equation 2-14, reproduced in the following text) [155, 156], the average carbon concentration of the Fe ($\overline{C}$) after reactivity testing can be established.

$$\frac{\overline{C} - C_s}{C_i - C_s} = \frac{8}{\pi^2} \exp\left[\frac{-\pi^2}{4} . \frac{Dt}{L^2}\right]$$

The variables/parameters in equation 2-14 for the reactivity testing conditions are given in Table V-3.

Table V-3: The loss of carbon in Fe on reacting with CO_2 during reactivity testing

Temp. (°C)	D (cm^2/sec) [63, 155]	t (sec)	L (cm)	C_i (%)	C_s (%)
950	$4.0x10^{-7}$	7200	0.1	1.41	Negligible
1025	$4.8x10^{-7}$	7200	0.1	1.41	Negligible

At 950°C

$$\frac{\overline{C} - C_s}{C_i - C_s} = 0.40 \qquad \text{V-8}$$

$$\overline{C} = 0.40(C_i - C_S) + C_S \qquad \text{V-9}$$

$$\overline{C} = 0.56\% \qquad \text{V-10}$$

At 1025°C

$$\frac{\overline{C} - C_s}{C_i - C_s} = 0.34 \qquad \text{V-11}$$

$$\overline{C} = 0.34(C_i - C_S) + C_S \qquad \text{V-12}$$

$$\overline{C} = 0.48\% \qquad \text{V-13}$$

It can be seen that the average carbon concentration of the Fe ($\overline{C}$) after reactivity testing at two different temperatures (0.56 mass % at 950°C and 0.48 mass% at 1025°C) are consistent with the values measured with LECO (0.48 mass % at 950°C and 0.46 mass% at 1025°C). This indicates that the Fe lost carbon on reacting with CO_2 during the coke analogue reactivity testing. This is consistent with the literature [154, 215, 216].

Appendix VI Assessment of activation energies for the reaction of the coke analogues

This calculation is being carried out to establish the effect of elemental Fe, Fe added in the form of oxides such as magnetite (Fe_3O_4), enstatite ferroan ($Mg_{1.56}Fe_{0.44}Si_2O_6$) and phlogopite ferroan [$K(Mg,Fe)_3(Al,Fe)Si_3O_{10}(OH,F)_2$] and quartz ($SiO_2$) on the activation energy values of the reaction of coke analogue in CO_2.

The plot of ln R_C against 1/T for the reaction of the coke analogues in CO_2 is given in Figure VI-1.

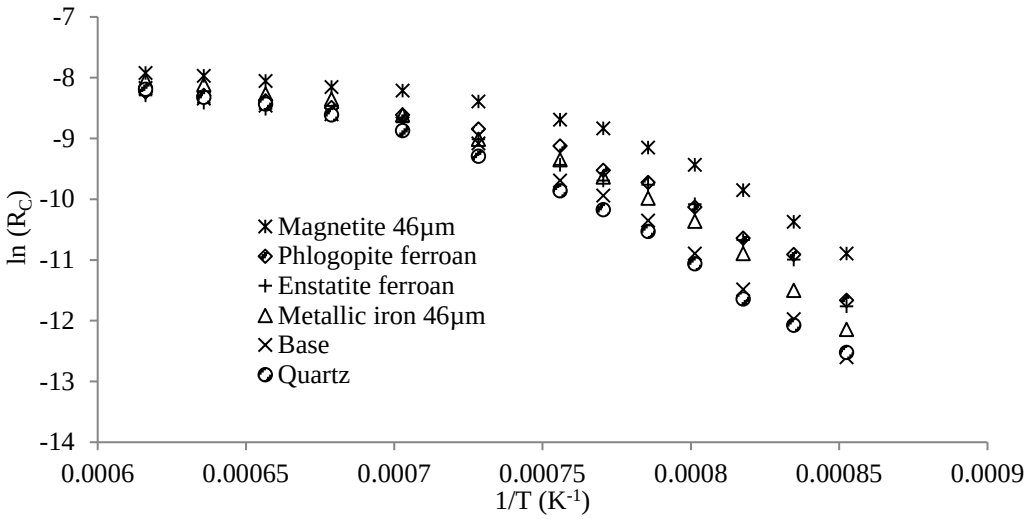

Figure VI-1: The plot of ln(R_C) against 1/T for coke analogues (Base, Fe 46µm, Fe_3O_4 46µm, enstatite ferroan ($Mg_{1.56}Fe_{0.44}Si_2O_6$), phlogopite ferroan [$K(Mg,Fe)_3(Al,Fe)Si_3O_{10}(OH,F)_2$] and quartz ($SiO_2$)) reacted in CO_2 with temperature.

From this figure, the effect of Fe, Fe containing minerals and quartz on the kinetic of the reaction of the coke analogues in CO_2 can be evaluated. The linear relationship between the plot of ln(R_C) against 1/T is given in Figures VI-2 to VI-7.

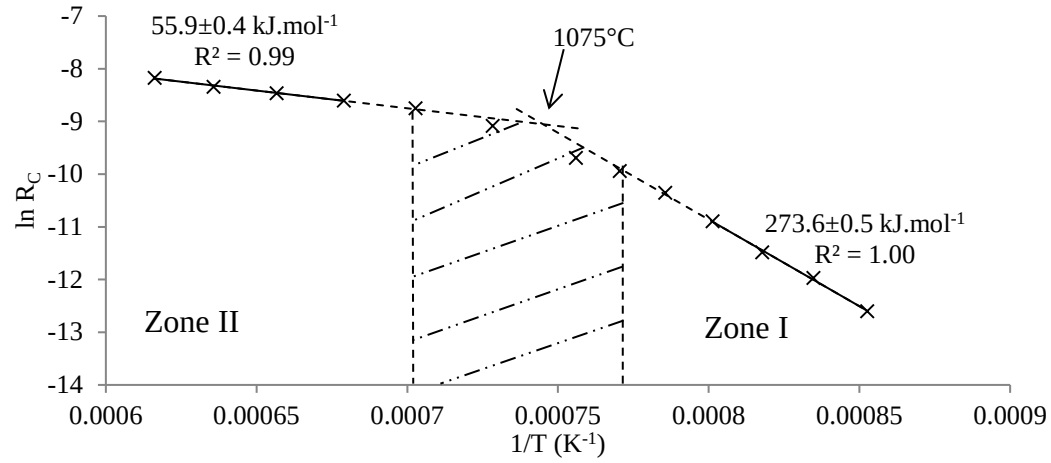

Figure VI-2: The plot of ln R_C against 1/T for base coke analogue reacted in CO_2 with temperature and showing reaction zones.

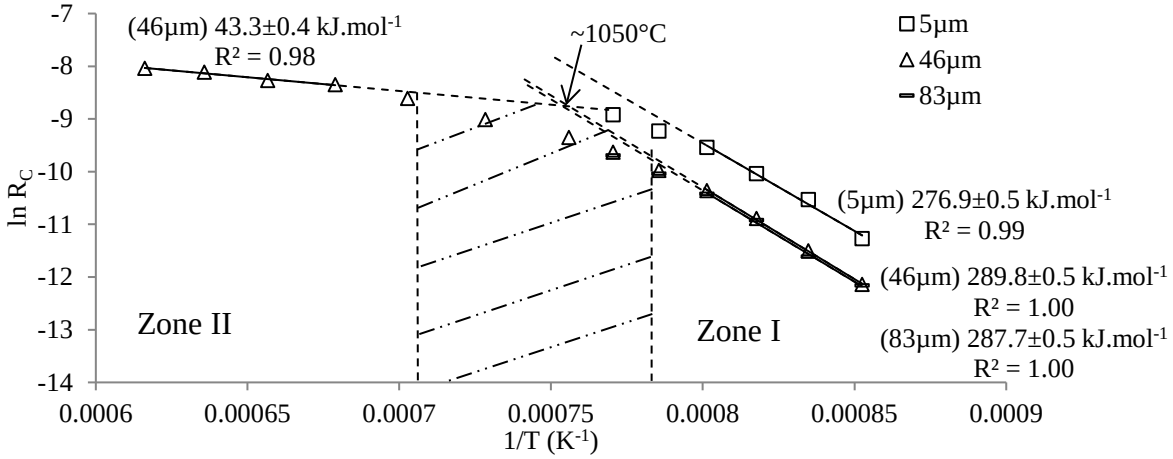

Figure VI-3: The plot of ln(R_C) against 1/T for coke analogues (prepared with Fe of different particle sizes) reacted in CO_2 with temperature and showing reaction zones.

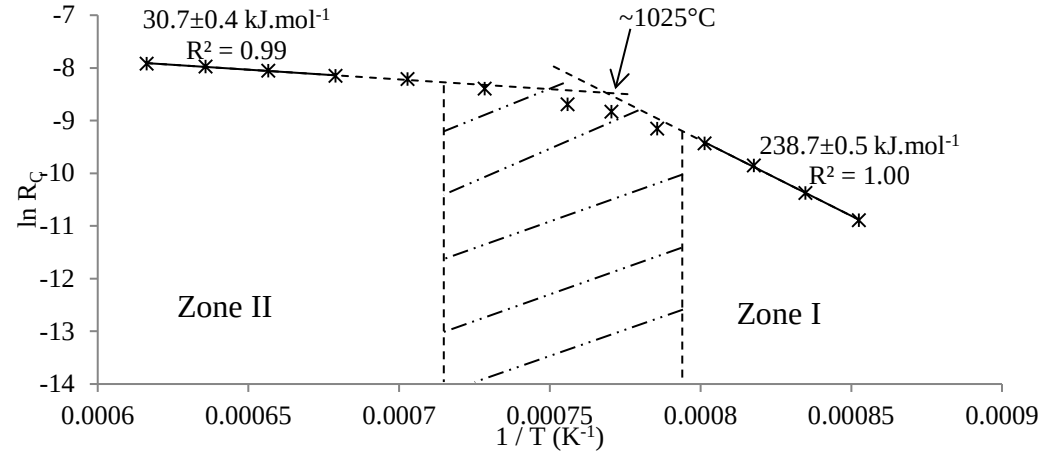

Figure VI-4: The plot of ln(R_C) against 1/T for coke analogue–Fe_3O_4 46µm reacted in CO_2 with temperature and showing reaction zones.

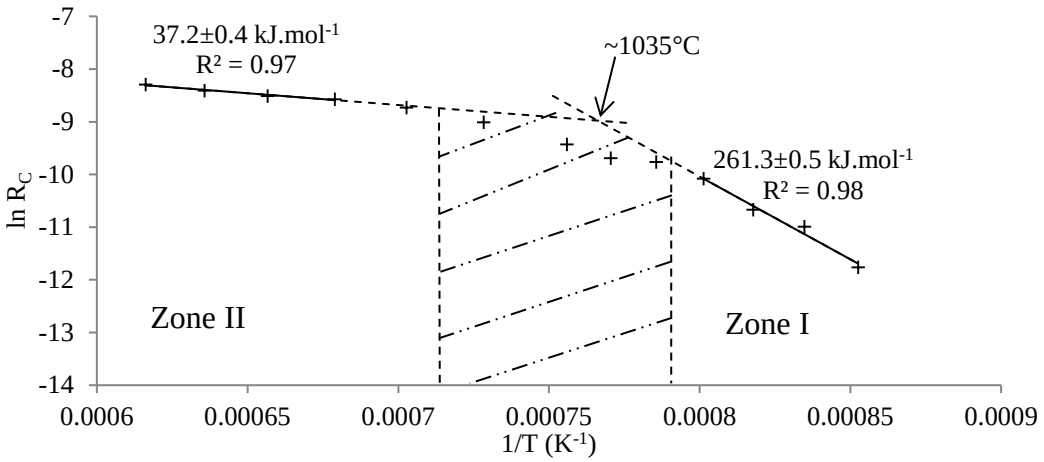

Figure VI-5: The plot of ln(R_C) against 1/T for coke analogue–enstatite ferroan reacted in CO_2 with temperature and showing reaction zones.

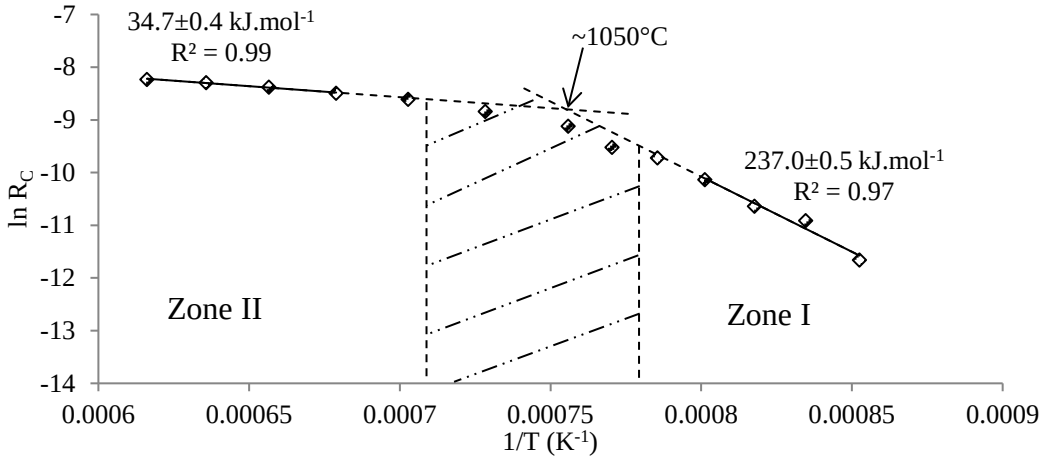

Figure VI-6: The plot of ln(R_C) against 1/T for coke analogue–phlogopite ferroan reacted in CO_2 with temperature and showing reaction zones.

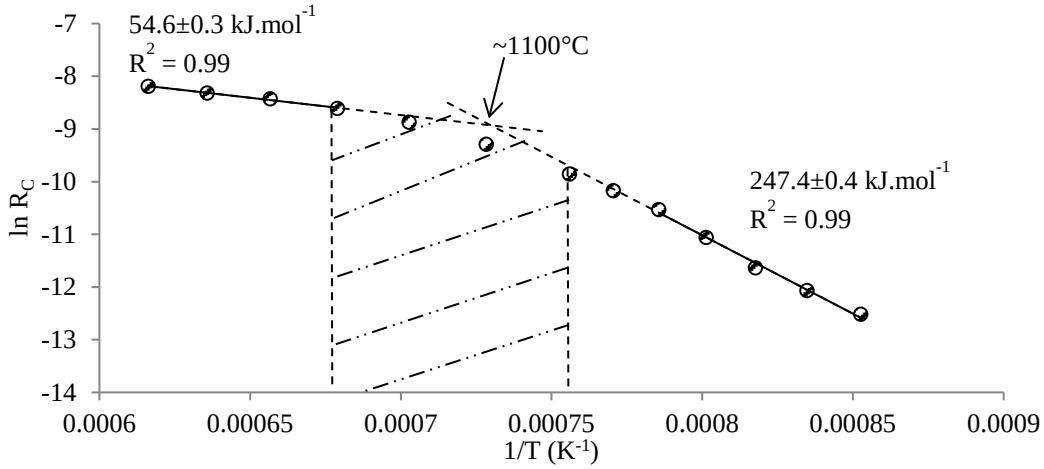

Figure VI-7: The ln(R_C) against 1/T for coke analogue–quartz (SiO_2) reacted in CO_2 with temperature and showing reaction zones.

The activation energies for the coke analogues are given in Table VI-1.

Table VI-1: The activation energy values for the coke analogues reacted in CO_2.

Coke analogues	**Zone I kJ.mol^{-1}**	**Temperature at point of intersection (°C)**	**Zone II kJ.mol^{-1}**
Base	273.6±0.5	~1075	55.9±0.4
Fe 5µm	276.9±0.5	-	-
Fe 46µm	289.8±0.5	~1050	43.3±0.4
Fe 83µm	287.7±0.5	-	-
Fe_3O_4 46µm	238.7±0.5	~1025	30.7±0.4
Enstatite ferroan	261.3±0.5	~1035	37.2±0.4
Phlogopite ferroan	237.0±0.5	~1050	34.7±0.4
Quartz (SiO_2)	247.4±0.4	~1100	54.6±0.4

- Reactivity not measured

From Table VI-1 it can be seen that the zone I activation energies for the coke analogues prepared with elemental Fe and minerals are within a close range and similar to the activation energies of base coke analogue and cokes (Table 5-3). This is broadly consistent with the "bulk" Raman measurement where elemental Fe and mineral additions to the coke analogue did not have a clear discriminating effect on the sp^2 bonding and sp^2–sp^3 bonding of the coke analogue as assessed by $I_{(D)}/I_{(G)}$ versus $I_{(V)}/I_{(G)}$ plots. Also, the zone II activation energies for the coke analogues prepared with elemental Fe and minerals are similar to that of the base coke analogue.

With no significant change in the zone I activation energy values for the coke analogues, it indicates that there is no change in the rate controlling mechanism for the reaction of the coke analogue in CO_2. That is reaction 2-16, reproduced in the following text, is the rate controlling.

$$C(O) \xrightarrow{j_3} CO_{(g)}$$

Though there is no change in the rate controlling mechanism, there was increased reactivity with elemental/metallic Fe. It was thought that elemental Fe and Fe added as Fe_3O_4 increased the number of active carbon sites in the coke analogue through the carbon dissolution into Fe and the transfer of electrons from carbon into Fe. Further possible additional effects of Fe relating to the promotion of oxygen delivery to the active carbon sites through the dissociation of CO_2 on Fe surface and redox reaction

between Fe and CO_2 to form iron oxide and CO, followed by reduction of the iron oxide on reaction with carbon.

On comparative with elemental Fe, Fe bonded within a complex mineral (enstatite ferroan ($Mg_{1.56}Fe_{0.44}Si_2O_6$) and phlogopite ferroan [$K(Mg,Fe)_3(Al,Fe)Si_3O_{10}(OH,F)_2$]) increased the coke analogue reactivity while quartz (SiO_2) addition decreased the coke analogue reactivity relative to the base coke analogue.

Summary of main points

- The addition of elemental Fe and Fe as Fe_3O_4 to the coke analogue did not significantly change the zone I and zone II activation energy values of the reaction of the coke analogue in CO_2 relative to the base coke analogue.
- On comparative with elemental Fe, Fe containing mineral (enstatite ferroan ($Mg_{1.56}Fe_{0.44}Si_2O_6$) and phlogopite ferroan [$K(Mg,Fe)_3(Al,Fe)Si_3O_{10}(OH,F)_2$]) and quartz ($SiO_2$) did not significantly change the activation energy values (zones I and II) of the reaction of the coke analogue in CO_2 relative to the base coke analogue.

Appendix VII Testing for the effect of particle surface area of elemental Fe on coke analogue reactivity

This is being carried out to test the effect of contact area of elemental Fe on coke analogue reactivity. In an attempt to evaluate the effect of contact area, the Fe particle surface area was varied by,

- changing the size of the Fe particles at constant mass, and
- changing the amount or mass of Fe added at constant particle size.

The FWC plot with temperature for the Fe particles (5μm, 46μm and 83μm) is given in Figure VII-1. The (I) denotes higher mass of Fe addition at two different temperatures of 950°C and 1100°C.

Figure VII-1 show that reducing the particle size of Fe and increasing the mass addition of the Fe all resulted in an increased reaction rate (lower FWC). Both the smaller particle size and the increased mass result in an increased surface area of Fe. Therefore the result from this figure is consistent with what might be expected with increased contact area effects on a heterogeneous reaction, that is, increased contact area of reagents increasing the rate of reaction.

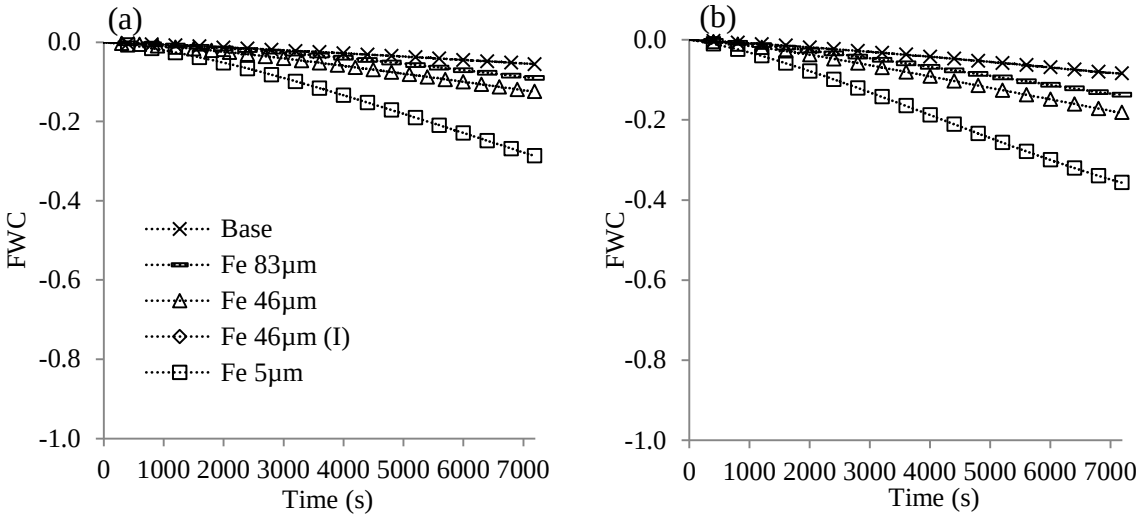

Figure VII-1: The FWC versus time of the base coke analogue and coke analogues prepared with metallic iron (Fe) reacted in CO_2 at different temperatures. (a) 900°C, (b) 925°C, (c) 950°C, (d) 975°C, (e) 1000°C, (f) 1025°C and (g) 1100°C.

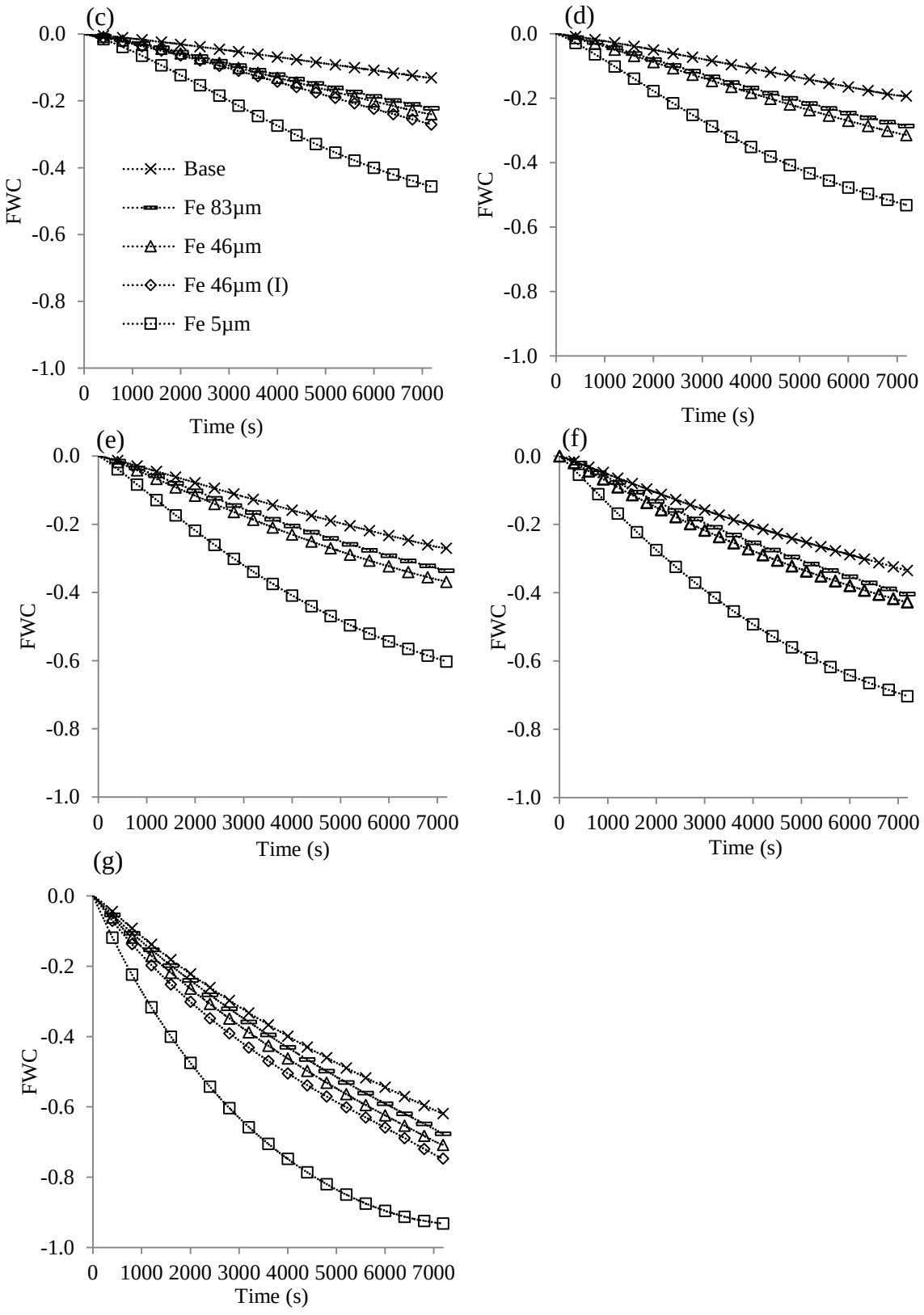

Figure VII-1 (continued): The FWC versus time of the base coke analogue and coke analogues prepared with metallic iron (Fe) reacted in CO_2 at different temperatures. (a) 900°C, (b) 925°C, (c) 950°C, (d) 975°C, (e) 1000°C, (f) 1025°C and (g) 1100°C.